Computational Studies Towards the Expansion of Supraicosahedral Heteroborane Chemistry

David McKay

Submitted for the degree of

Doctor of Philosophy

School of Engineering and Physical Sciences

Heriot-Watt University

December 2010

Abstract

This thesis describes a series of density functional theory (DFT) studies that investigate the processes underlying the synthesis of supraicosahedral (>12 vertex) heteroboranes.

The reduction of carborane isomers, *closo*-$C_2B_{12}H_{12}$ to [*nido*-$C_2B_{12}H_{12}$]$^{2-}$, was modelled, where the results were consistent with experiment. The oxidation of [7,9-R_2-7,9-*nido*-$C_2B_{12}H_{10}$]$^{2-}$ was found to be dependent on R, where the reducing potential (ΔE_{OX}) was 4.8 kcal mol^{-1} for R = H. Electron withdrawing *p*-$C_6F_4CF_3$ groups (ΔE_{OX} = 60.8 kcal mol^{-1}) were suggested as synthetic targets.

The structural chemistry of 12- and 13-vertex stannacarboranes and related platinacarboranes was investigated. The degree of slip in these species was found, in general, to be controlled by steric interactions between the metal and carborane fragments.

Structural preferences in 12- and 13-vertex heteroboranes, $X_2B_{n-2}H_n$ and $Y_2B_{n-2}H_{n-2}$ (X = C, Si, Ge, Sn; Y = P, As, Sb, Bi) were investigated. Phosphaboranes were suggested for polyhedral expansion as they showed the largest number of stable isomers.

Observation of C–C cleavage of an arene in a bis(carborane) species was rationalised computationally. The reaction was found to proceed *via* an internal REDOX pathway, whereby cleavage was invoked by electron transfer from a *nido* carborane cage to the central arene of a triple-decker intermediate.

To my parents, Tom and Helen and my brother, Neil

To my fiancée, Lauren

Acknowledgments

Firstly, I would like to thank my supervisors, Professors Stuart Macgregor and Alan Welch. Their enthusiasm and encouragement throughout my time at Heriot-Watt have made me the chemist I am today.

I would like to thank my parents and my brother, Neil, for the support and advice they've given me over the last 8 years at university. It's been a huge comfort knowing you're just a phone call away.

I'd especially like to thank Lauren. Since we first met at the start of our undergraduate degrees, and through my PhD, she has been there to motivate and inspire me. Thank you Lauren, for keeping me going, making me smile and cooking me dinner!

My two groups, The Boron Group and The Computational Inorganic Chemistry Group, have been fantastic to work with over the past three years and I wish to thank past and present members of both groups. Particularly Brian, Dave, Hugo, Peter and Ross for the challenges they've sent my way. I'd like to thank Amalia, Jenni, Julien, Abu and Jonas for their friendship and the great atmosphere they created in the lab.

I'd like to thank my group of friends from halls and the few more we've picked up along the way. Our regular get-togethers and your interest in my progress have given me kept me driven and focussed.

ACADEMIC REGISTRY
Research Thesis Submission

Name*:*	David McKay		
School/PGI:	Engineering and Physical Sciences		
Version: *(i.e. First, Resubmission, Final)*	Final	Degree Sought (Award **and** Subject area)	Doctor of Philosophy (Chemistry)

Declaration

In accordance with the appropriate regulations I hereby submit my thesis and I declare that:

1) the thesis embodies the results of my own work and has been composed by myself
2) where appropriate, I have made acknowledgement of the work of others and have made reference to work carried out in collaboration with other persons
3) the thesis is the correct version of the thesis for submission and is the same version as any electronic versions submitted*.
4) my thesis for the award referred to, deposited in the Heriot-Watt University Library, should be made available for loan or photocopying and be available via the Institutional Repository, subject to such conditions as the Librarian may require
5) I understand that as a student of the University I am required to abide by the Regulations of the University and to conform to its discipline.

* *Please note that it is the responsibility of the candidate to ensure that the correct version of the thesis is submitted.*

Signature of Candidate*:*		Date:	

Submission

Submitted By *(name in capitals):*	
Signature of Individual Submitting:	
Date Submitted:	

For Completion in Academic Registry

Received in the Academic Registry by *(name in capitals):*			
Method of Submission *(Handed in to Academic Registry; posted through internal/external mail):*			
*E-thesis Submitted (**mandatory for final theses from January 2009)***			
Signature:		Date:	

Please note this form should bound into the submitted thesis.

Updated February 2008, November 2008, February 2009

Table of Contents

List of Publications

1. B. W. Hutton, F. MacIntosh, D. Ellis, F. Herisse, S. A. Macgregor, D. McKay, V. Petrie-Armstrong, G. M. Rosair, D. S. Perekalin, H. Tricas and A. J. Welch, *Chem. Commun.*, 2008, 5345-5347.

2. P. D. Abram, D. McKay, D. Ellis, S. A. Macgregor, G. M. Rosair, R. Sancho and A. J. Welch, *Dalton Trans.*, 2009, 2345-2351.

3. P. D. Abram, D. McKay, D. Ellis, S. A. Macgregor, G. M. Rosair and A. J. Welch, *Dalton Trans.*, 2010, **39**, 2412-2422.

4. G. Scott, A. McAnaw, D. McKay, A. S. F. Boyd, D. Ellis, G. M. Rosair, S. A. Macgregor, A. J. Welch, F. Laschi, F. Rossi and P. Zanello, *Dalton Trans.*, 2010, **39**, 5286-5300.

5. D. Ellis, D. McKay, S. A. Macgregor, G. M. Rosair and A. J. Welch, *Angew. Chem. Int. Ed.*, 2010, **49**, 4943-4945.

Chapter 1 – Introduction

1.1. Introduction

The background in boron cluster chemistry required by the reader of this thesis is provided in this introduction. The structural characteristics, synthesis and reactivity of boranes and heteroboranes will be discussed along with theories of skeletal bonding and electron counting.

1.2. Polyhedral geometries

The geometries of clusters will be familiar. The shapes they adopt were known in ancient Greece as the Platonic Solids. Indeed the beauty of these geometries has been a source of fascination to humans for many thousands of years; the Scottish Carved Stone Balls, mostly tetrahedra and octahedra, date back to *ca.* 3200 BC.[1]

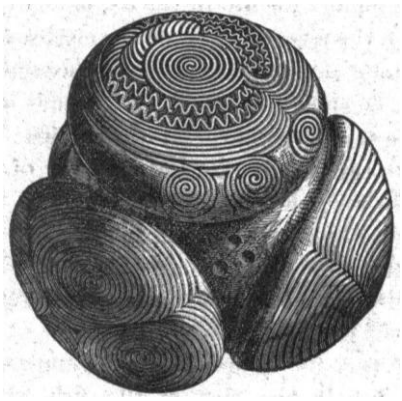

Figure 1.1 – Tetrahedral carved stone ball from Towie, Aberdeenshire, around 2500 BC.

The structures of boranes fit into a series based upon the number of electrons in the skeleton.[2] Before the structures of these compounds were determined, they were known to be electron deficient, in that their electron counts were too few to allow two centre two electron (2c2e) bonding between each pair of atoms,[3] challenging the existing bonding theories of that time. The resolution of the geometry of diborane, B_2H_6, through vibrational spectroscopy, led to the idea of the 3c2e bond.[4] Later, the use of low temperature X-Ray crystallographic techniques revealed the structures unambiguously.[5] The link between theory and experiment is strong in this field of chemistry: as will be described below, the empirical Polyhedral Skeletal Electron Pair (PSEP) theory which allows the prediction of structures from stoichiometric data has its basis in molecular orbital (MO) theory.[6]

1.2.1. Wade-Williams-Rudolph structural matrix

The development of carborane chemistry, through research into rocket fuels in the 1950s, rapidly expanded the family of known (hetero)borane geometries. In 1971,[2] Williams produced a pattern relating *closo* (meaning "cage"), *nido* (meaning "nest") and *arachno* (meaning "web") polyhedra. Examples of these structures are given in Figure 1.2, below and the structural matrix relating them is given in Figure 1.3 (adapted from ref. 7). Boron hydrides of the form $[B_nH_n]^{2-}$ exhibit *closo* deltahedral structures (having only triangular faces) and vertices within the deltahedra are defined by the number of connections to that site, *k*.

Nido structures are related to the (*n* + 1) *closo* species (on the same row) by removal of one vertex (formally one $\{BH\}^{2+}$ fragment) of the largest *k* value with additional protons making up the charge. These extra hydrogen atoms adopt BHB bridging positions on the open face of the fragment.

Arachno structures are related to the (*n* + 2) *closo* species by removal of two adjacent vertices and to the (*n* + 1) *nido* fragment by removal of a vertex on the open face with the largest *k* value. Stable *arachno* species exhibit hydrogen atoms in BHB bridging positions as well as $B–H_{endo}$ centres (where these H atoms lie on the pseudo-spherical surface of the cage; see Figure 1.2, below).

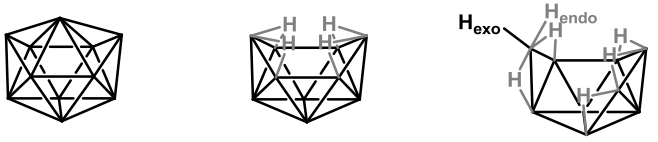
H
H
H

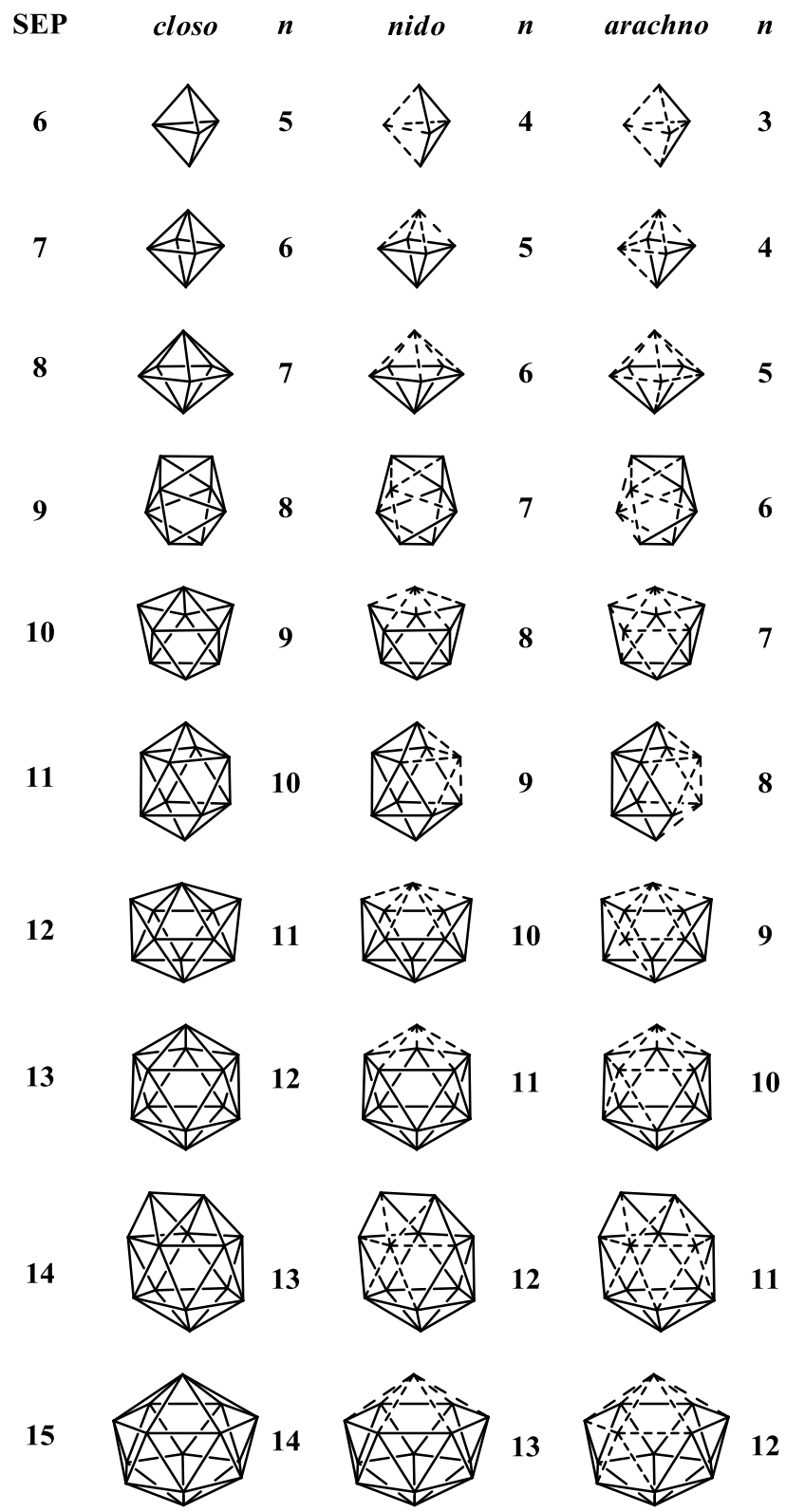

Figure 1.3 – Wade-Williams-Rudolph structural matrix relating deltahedra to skeletal electron pairs (SEP) and number of vertices, *n*.

Since the first recognition of this pattern, the structural family has been further expanded to include *hypercloso* species, B_nH_n, and more opened structures, *e.g. hypho* (meaning "net") structurally related to the (n + 1) *arachno* or (n + 3) *closo* species.

1.3. Polyhedral Skeletal Electron Pair (PSEP) theory

PSEP theory is an empirical method for rationalising the geometries of polyhedra, also known as Wade's Rules[8] (analogous to the 18 electron rule in transition metal chemistry and the octet rule in main group compounds). This theory sees *closo* polyhedra as having [*n* + 1] SEPs, *nido* with [*n* + 2] SEPs, *arachno* with [*n* + 3] SEPs, *etc*. It is applied by dividing a polyhedron into fragments and assigning those fragments an electron count, *s*, based on the valence of the central atom. This is given by (for a main group fragment):

$$s = v + x - 2 \qquad \text{(Eq. 1.1)}$$

where, *v* is the valency of the central element of the fragment and *x* the number of electrons contributed to the central atom by its substituent and the number 2 accounts for the 2c2e B–H bond (or similar), which will not contribute to the skeletal electron count. In the {BH} fragment, boron has 3 valence electrons and hydrogen has one, so the fragment contributes two electrons to the polyhedral skeleton. The $[B_7H_7]^{2-}$ species, for example, has 14 electrons from {BH} fragments and a further 2 from the charge, giving [*n* + 1] SEPs and predicting a *closo* structure. This is indeed found experimentally in a pentagonal bipyramidal geometry (Figure 1.4, below).

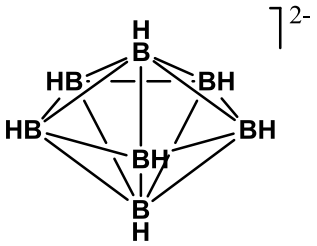

Figure 1.4 – [*closo*-$B_7H_7]^{2-}$.

1.4. Molecular orbital view of polyhedral bonding

Polyhedral geometries of boron hydrides can be further rationalised by considering the construction of molecular orbitals (MOs) from the valence orbitals of boron-centred fragments. Each fragment is considered as contributing three orbitals to skeletal bonding. In the case of the sp-hybridised {BH} fragment this is an occupied sp_z orbital and two empty unhybridised p_x and p_y atomic orbitals, where sp_z is a 'radial' orbital, pointing towards the centre of the polyhedron and p_x and p_y are 'tangential' to the pseudo-spherical cluster surface (see Figure 1.5).

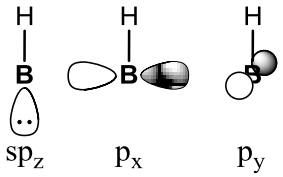

Figure 1.5 – {BH} fragment orbitals.

Linear combinations of these fragment orbitals then give molecular orbitals of the clusters (illustrated in Figure 1.6 through the octahedron). MOs arising from linear combinations of the radial orbitals ('r') include the a_{1g} bonding molecular orbital (BMO), where all are in phase, and two sets of antibonding molecular orbitals (ABMOs) making up the t_{1u}* and e_g* sets. A further 6 BMOs, of t_{2g} and t_{1u} symmetry, are generated through linear combinations of the tangential orbitals ('t') thus accounting for the [*n* + 1] SEPs required for a *closo* geometry (*i.e.* through a filled set of 7 BMOs in this case). Mixing of the radial orbital-based and tangential orbital-based t_{1u} sets occurs to give 3 bonding and 3 antibonding orbitals (labelled 'r/t').

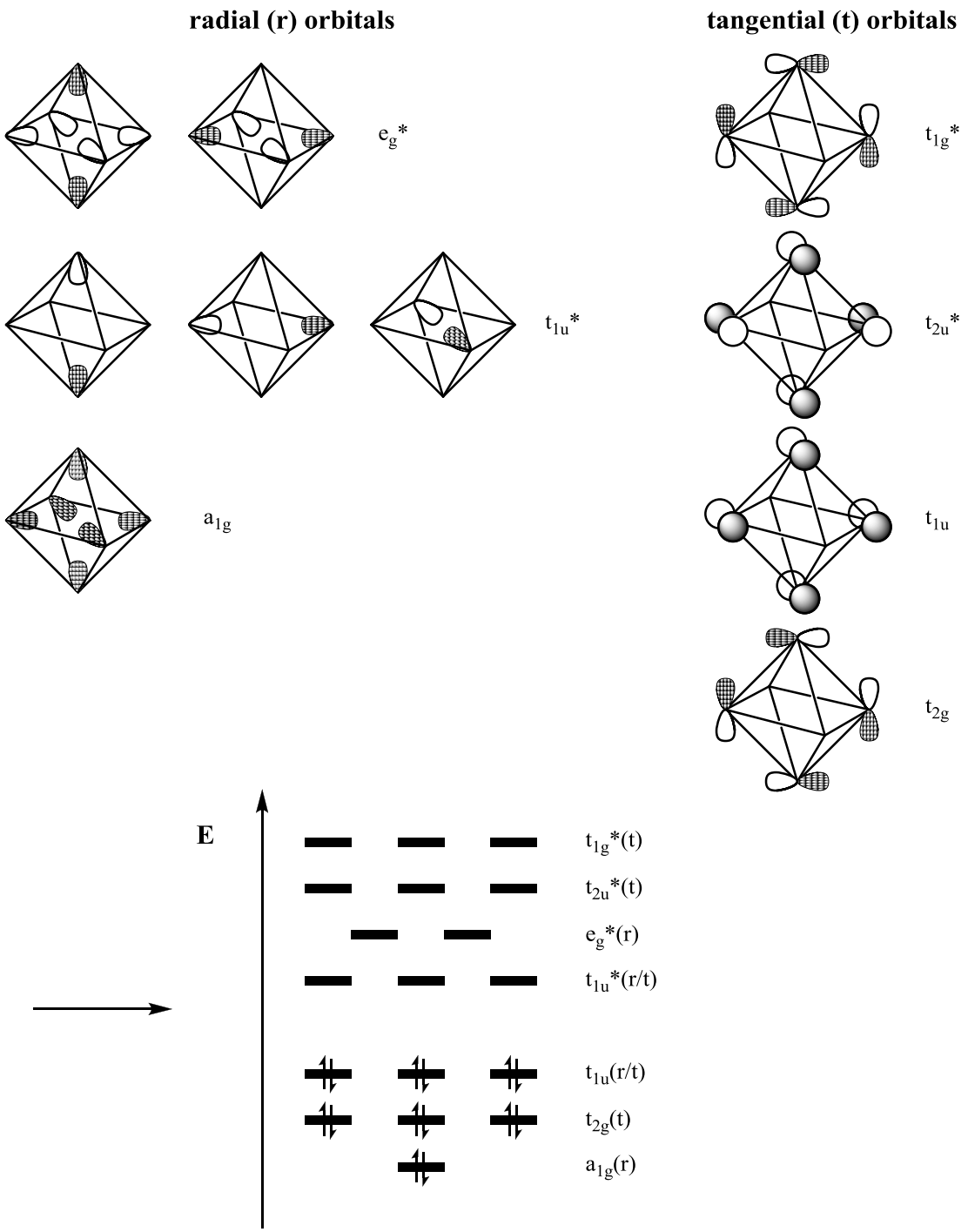

Figure 1.6 – Construction of the skeletal MOs of an octahedron from radial and tangential orbitals giving a filled set of 7 BMOs.

The MO approach to boron cluster bonding has been successful in predicting electronic features such as 3-dimensional aromaticity[5] and a rationalisation of the formation of triangular faces by maximising overlap of tangential orbitals as suggested by Stone.[9] Particularly notable was the prediction, through MO theory, of the stability of $[B_{12}H_{12}]^{2-}$ by H. C. Longuet-Higgins and M. de V. Roberts in 1955,[10] before its first isolation.[11]

1.5. Isolobality

Fragment contributions to skeletal bonding can be extended to heteroatom-based (non-boron) species through the theory of isolobality, developed by Hoffmann.[12] Two fragments are said to be isolobal if they are isoelectronic and their frontier molecular orbitals (FMOs) exhibit comparable shapes and energies. In heteroborane chemistry, fragments that are isolobal with {BH} are adopted. Isolobal fragments are shown linked by a double-ended arrow with a lobe in the centre (see Figure 1.7, below).

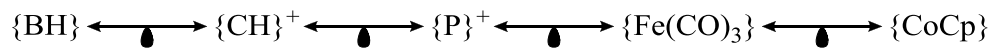

Figure 1.7 – Selection of isolobal fragments important to heteroborane chemistry.

The main group fragments above have been incorporated into heteroboranes and have the same construction as the {BH} fragment FMOs. Similarly, the number of electrons contributed by a transition metal (TM) fragment is given by:

$$s = v + x - 12 \qquad \text{(Eq. 1.2)}$$

where v is the valence electron count of the metal, and x is the number of electrons contributed by the ligands, giving 12 electrons in the ML_3 bonds and the $1a_1$ and 1e NBMOs. Figure 1.8 shows the NBMOs and FMOs of this fragment, derived from an octahedral ML_6 complex.[13] The $\{d^8\text{-}ML_3\}$ and $\{d^9\text{-}MCp\}$ transition metal fragments have been important in the development of the metallaboranes and metallacarboranes.

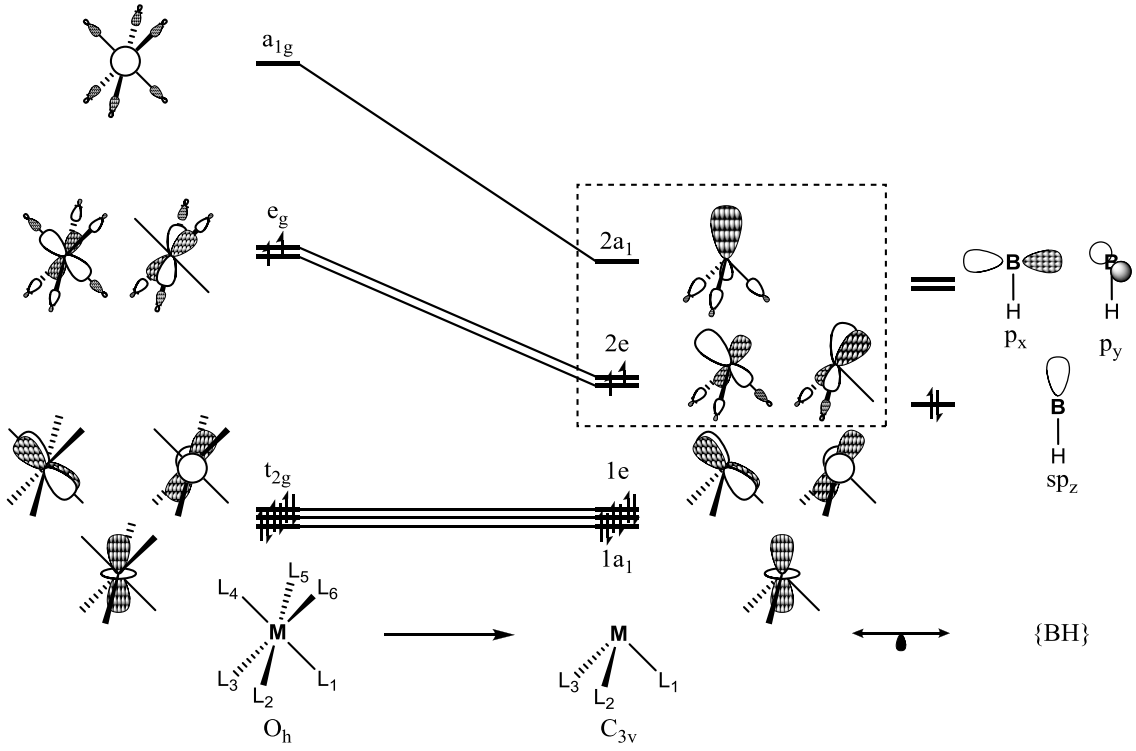

Figure 1.8 – FMOs of the d^8 ML_6 fragment as derived from octahedral ML_6.

1.6. Heteroboranes and Metallaheteroboranes

Heteroborane chemistry is dominated by the carboranes, which will be the subject of Chapters 2 and 3 of this thesis. However, elements from all areas of the Periodic Table have been adopted as heteroatoms into boron cluster chemistry. Further examples pertinent to this work include {Sn} and $\{Pt(PR_3)_2\}$, studied in Chapter 4, as well as $\{XH\}^+$ and $\{Y\}^+$ (X = Group 14 element; Y = Group 15 element) in Chapter 5.

1.6.1. Numbering of polyhedra

The numbering scheme for (hetero)boranes depends upon the fragment type (*closo*, *nido*, *etc.*) the vertex types (*k* values) and presence of heteroatoms. In *closo* species, numbering begins with the vertex with the lowest *k*. Numbering is done either consistently clockwise or consistently anticlockwise around each level of vertices, then continues downwards through the levels of the cage. The first vertex of the next lower belt is that forming a triangle with the first two vertices of the upper belt (see the B2-B3-B7 triangle in example 'a' of Figure 1.3, below). Numbering is done in a way that gives any heteroatoms the lowest numbers (see examples 'a' and 'b' in Figure 1.9). In open structures, numbering begins with the vertex opposite the open face then continues as the *closo* numbering (see examples 'c' and 'd' in Figure 1.9, below).

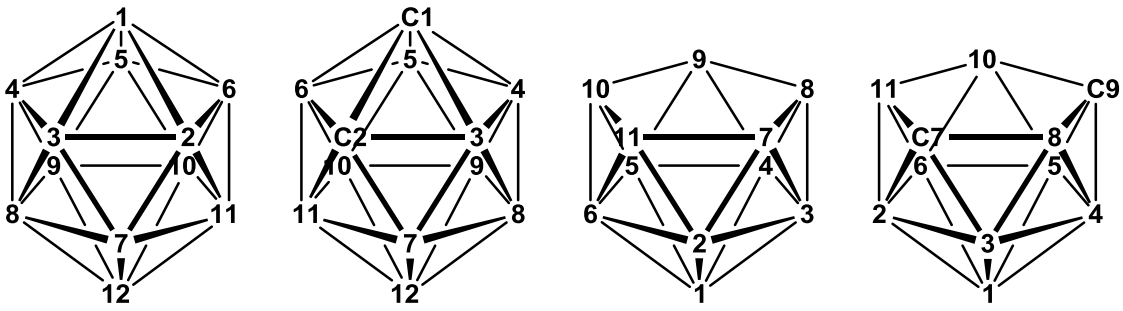

a **b** **c** **d**

Figure 1.9 – Numbering of: a) [*closo*-$B_{12}H_{12}]^{2-}$; b) 1,2-*closo*-$C_2B_{10}H_{12}$; c) [*nido*-$B_{11}H_{11}]^{4-}$ and d) [7,9-*nido*-$C_2B_9H_{11}]^{2-}$.

1.6.2. General synthesis and reactivity

1.6.2.1. Boranes

The starting point for the syntheses of boranes is diborane, which is produced industrially by reduction of BF_3. Larger boranes can be produced through condensation and pyrolysis (see Figure 1.10, below).

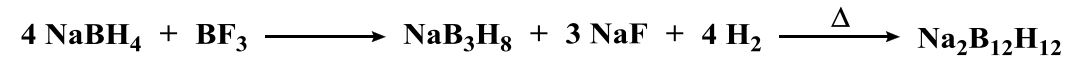

Figure 1.10 – Condensation reaction forming NaB_3H_8 followed by pyrolysis to give dodecaborate, where the product is usually precipitated as the caesium salt.

The common reactivity of boranes includes electrophilic substitution, nucleophilic substitution by Lewis bases and deprotonation by strong bases. Dodecaborate is relatively inert, however it does undergo B–H insertion reactions to form $[B_{12}H_{11}SH]^{2-}$, which was the first polyhedral compound used in Boron Neutron Capture Therapy (BNCT).[14]

1.6.2.2. Carboranes

Ortho-carborane (1,2-*closo*-$C_2B_{10}H_{12}$, a key species in this thesis) and its derivatives are synthesised by reaction of decaborane[14] with the appropriate alkyne (Figure 1.11, below).[15] Other isomers are produced through pyrolysis at 450 °C to give *meta*-carborane (1,7-*closo*-$C_2B_{10}H_{12}$)[16] and at 700 °C to give *para*-carborane (1,2-*closo*-$C_2B_{10}H_{12}$).[17]

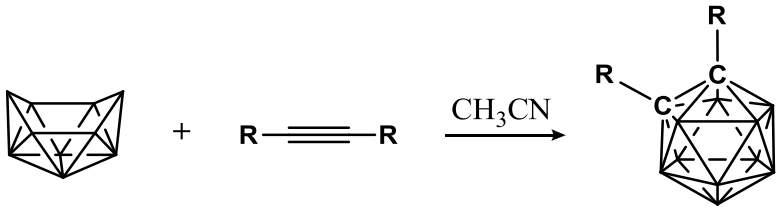

Figure 1.11 – Synthesis of *ortho*-carborane in acetonitrile solvent.

The reactivity of carboranes is summarised in Figure 1.12. Their chemistry includes substitution at the acidic C–H positions, through lithiation and reaction with organic halides, electrophilic substitution at the boron positions, polyhedral expansion chemistry (reduction followed by capitation or metallation) and decapitation.

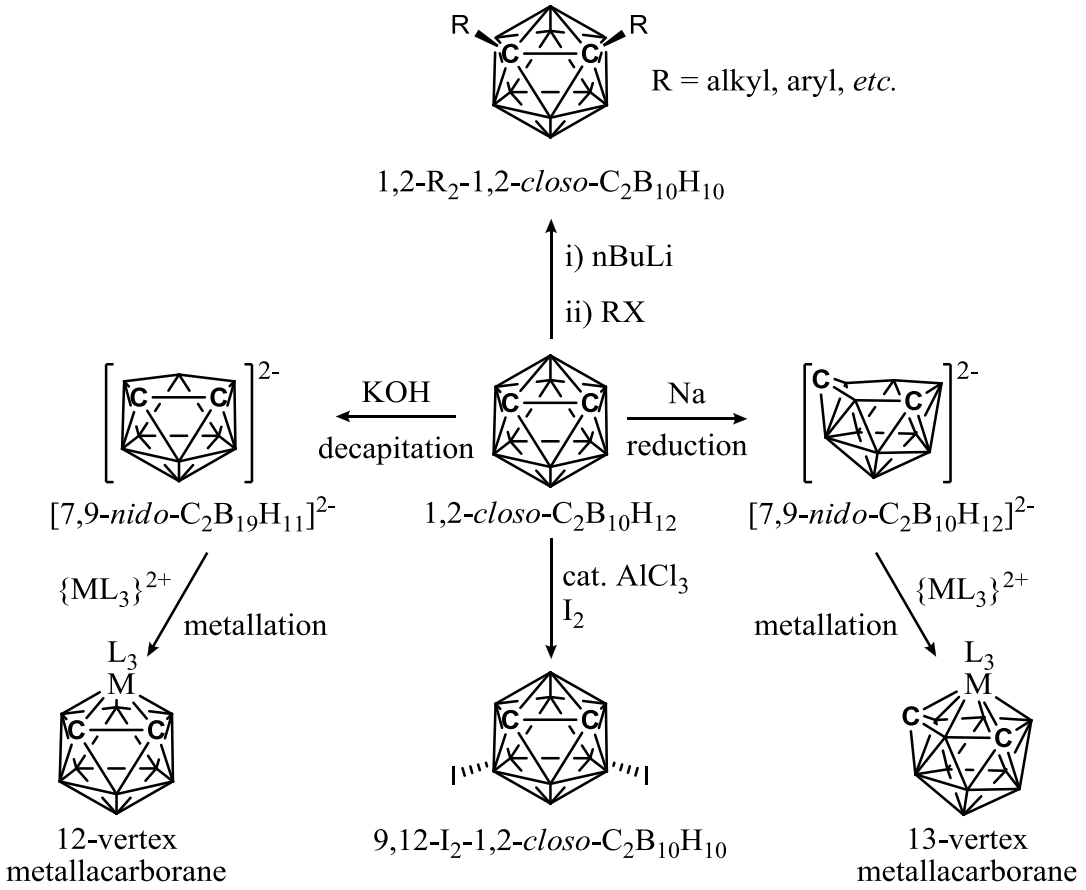

Figure 1.12 – Reactivity of carboranes.

1.6.3. Supraicosahedral heteroboranes

The reduction and capitation (or, more commonly, metallation) reaction, which increases the number of vertices in the cage, is known as polyhedral expansion.[18] Polyhedral expansion of 12-vertex carboranes is discussed in detail in Chapter 2. Through this method, experimental workers produce supraicosahedral (n > 12) heteroboranes, by sequential polyhedral expansion processes. The synthesis of supraicosahedral heteroboranes is not straightforward however, due to the relative stability of the 12-vertex species over those with more than 12 vertices. Frequently, this is termed the "synthetic bottleneck" of supraicosahedral heteroborane chemistry and is related to boron hydride chemistry in the step of the archetypal $[B_{12}H_{12}]^{2-}$ to the as yet unknown $[B_{13}H_{13}]^{2-}$. Schleyer[19] rationalised this through the cumulative enthalpy of addition of {BH} fragments to [*closo*-B_nH_n]$^{2-}$ (see Figure 1.13, below). Icosahedral $[B_{12}H_{12}]^{2-}$ is found to be much more stable than the energetic trend.

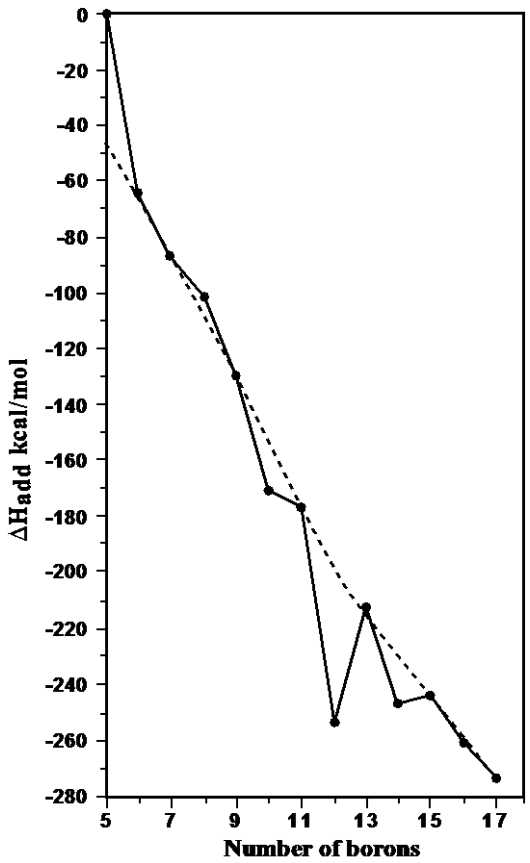

Figure 1.13 – Plot of the ΔH_{add} of {BH} fragments to *closo* boranes versus the number of vertices.

1.7. Summary and overall aims

The main aim of this work is to contribute to the field of supraicosahedral heteroborane chemistry by computational modelling of reduction reactions and by rationalising the structures of supraicosahedral species. The mechanism of the reduction process is key to the understanding of supraicosahedral products as the structure adopted by the reduced species determines the form of the final product. The research group of Prof. Alan Welch is concerned mainly with the reduction and capitation of heteroboranes, where breakthroughs such as the first supraicosahedral carborane[20] and first p-block supraicosahedral metallacarborane[21] have been made. Computational work aims to predict and rationalise experimental results and, where possible, to reveal fundamental driving forces behind heteroborane reactions.

The thesis will be divided into six further chapters. Chapter 2 concerns fundamental problems of the thermal isomerisation and REDOX chemistry of carboranes. This work is extended in Chapter 3 to include C-substituted carboranes, where the specific problem of stabilisation of reduced carboranes is addressed. In Chapter 4, supraicosahedral stannacarboranes are investigated in a structural study. A known problem of carboranes is that the carbon atoms cannot stabilise high-connected sites

(*e.g.* k = 6) which appear as n becomes large. Chapter 5 therefore departs from carboranes and considers alternative main group heteroatoms of groups 14 and 15 of the Periodic Table. The final results chapter, Chapter 6, is an investigation into the polyhedral expansion of bis(carboranes), which exhibit two carborane cages directly linked by a single connection, where the combination of two REDOX active carborane clusters provides interesting novel reactivity.

1.8. References

1. *Carved Stone Ball, Towie, Aberdeenshire*, National Museums of Scotland, Edinburgh, Record X.AS 10.
2. R. E. Williams, *Inorg. Chem.*, 1971, **10**, 210-214.
3. A. Stock, *The Hydrides of Boron and Silicon*, Cornell University Press, New York, USA, 1933.
4. H. C. Longuet-Higgins and R. P. Bell, *J. Chem. Soc.*, 1943, 250-255.
5. W. N. Lipscomb, *Boron Hydrides*, W. A. Benjamin, New York, USA, 1963.
6. K. Wade, *J. Chem. Soc. D*, 1971, 792-793.
7. M. A. Fox and K. Wade, *Pure Appl. Chem.*, 2003, **75**, 1315-1323.
8. K. Wade, *Adv. Inorg. Chem. Radiochem.*, 1976, **18**, 1-66.
9. a) A. J. Stone, *Inorg. Chem.*, 1981, **20**, 563-571; b) A. J. Stone and M. J. Alderton, *Inorg. Chem.*, 1982, **21**, 2297-2302.
10. H. C. Longuet-Higgins and M. de V. Roberts, *Proc. R. Soc. Lond. A*, 1955, **230**, 110-119.
11. A. R. Pitochelli and M. F. Hawthorne, *J. Am. Chem. Soc.*, 1960, **82**, 3228-3229.
12. a) R. Hoffmann, *Angew. Chem. Int. Ed.*, 1982, **21**, 711-800; b) R. Hoffmann, *Nobel Lectures, Chemistry 1981-1990*, World Scientific Publishing Co., Singapore, 1992.
13. a) T. A. Albright, J. K. Burdett and M.-H. Whangbo, *Orbital Interactions in Chemistry*, John Wiley & Sons, Inc., New York, USA, 1985; b) Y. Jean, *Molecular Orbitals of Transition Metal Complexes*, Oxford University Press, New York, USA, 2005.
14. I. B. Sivaev, V. I. Bregadze and N. T. Kuznetsov, *Russ. Chem. Bull.*, 2002, **51**, 1362-1374.
15. M. M. Fein, J. Bobinski, N. Mayes, N. Schwartz and M. S. Cohen, *Inorg. Chem.*, 1963, **2**, 1111-1115.
16. D. Grafstein and J. Dvorak, *Inorg. Chem.*, 1963, **2**, 1128-1133.

17. a) S. Papetti and T. L. Heying, *J. Am. Chem. Soc.*, 1964, **86**, 2295-2295; b) V. I. Stanko, V. A. Brattsev and Y. V. Gol'tyapin, *Zh. Obshch. Khim.*, 1969, **39**, 2686-2688.
18. G. B. Dunks, R. J. Wiersema and M. F. Hawthorne, *J. Am. Chem. Soc.*, 1973, **95**, 3174-3179.
19. P. v. R. Schleyer, K. Najafian and A. M. Mebel, *Inorg. Chem.*, 1998, **37**, 6765-6772.
20. A. Burke, D. Ellis, B. T. Giles, B. E. Hodson, S. A. Macgregor, G. M. Rosair and A. J. Welch, *Angew. Chem.-Int. Edit.*, 2003, **42**, 225-228.
21. N. M. M. Wilson, D. Ellis, A. S. F. Boyd, B. T. Giles, S. A. Macgregor, G. M. Rosair and A. J. Welch, *Chem. Commun.*, 2002, 464-465.

Chapter 2 – REDOX and Isomerisation of Carboranes

2.1. Introduction

The rearrangement of boranes and heteroboranes has been studied theoretically for many years, the seminal work being that by Lipscomb,[1] where the *diamond-square-diamond* (D-S-D) mechanism (Figure 2.1a) was introduced. Isomerisations between *closo*-$C_2B_{10}H_{12}$ (carborane) isomers were hypothesised to be the result of single, highly symmetrical, D-S-D processes. The mechanism has since been recognised as key to *closo* borane rearrangement, however most isomerisations are described as multiple sequential D-S-D processes. Another appealing mechanism is the *triangular face rotation* (TFR) suggested by Zakharkin and Kalinin (Figure 2.1b), which can also be described as three concerted D-S-D processes.[2]

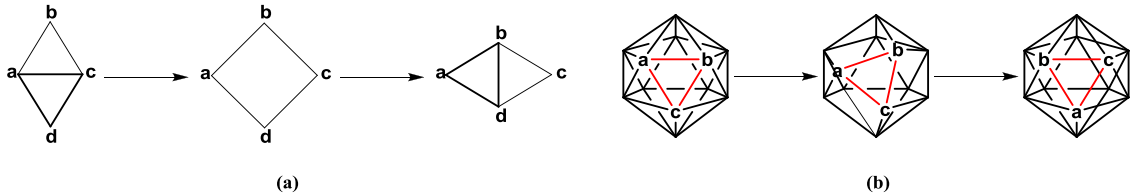

Figure 2.1 – (a) The Diamond-Square-Diamond mechanism; (b) the Triangular Face Rotation mechanism.

The potential energy surfaces (PES) of $[B_{12}H_{12}]^{2-}$ and $C_2B_{10}H_{12}$ were explored by Wales at the Hartree-Fock (HF) level.[3] High energy, multistep pathways linking the three carborane isomers 1,2-*closo*-$C_2B_{10}H_{12}$, 1,7-*closo*-$C_2B_{10}H_{12}$ and 1,12-*closo*-$C_2B_{10}H_{12}$ (*ortho*-, *meta*- and *para*-carborane respectively) were described (see Figure 2.2, below). Pathways were found to consist, mostly, of D-S-D derived steps, though two examples of TFR processes were also seen. Higher symmetry and *closo-nido-closo* processes (in which the cage opens and recloses *via* a "pseudo-*nido*" intermediate) are discounted as they are either very high in energy, exhibit higher order stationary points or since no stationary point was located. Wales' method for exploring the PES, by locating both transition states and connected minima, was a sophisticated modified eigenvector following (EF) method. The true power of this technique was the combination of the ability to choose the vibrational mode of a minimum to follow in order to discover a corresponding isomerisation and the ability to follow the chosen eigenvector extremely rigorously. The unmodified EF method,[4] available in the Gaussian 03 package[5] shares the same theoretical basis and retains the ability to choose the desired eigenvector, however it appears to fall down where two vectors are relatively close in energy and

often fails to find a viable stationary point, that is, it does not follow the vibrational mode as rigorously. It has therefore been superseded (in this study) by the DIIS algorithm[6] which locates transition states effectively, through the 'TS' option, while losing the eigenvector selection option – opting to always follow the lowest in energy, which in most cases, as stated by Wales, is adequate.

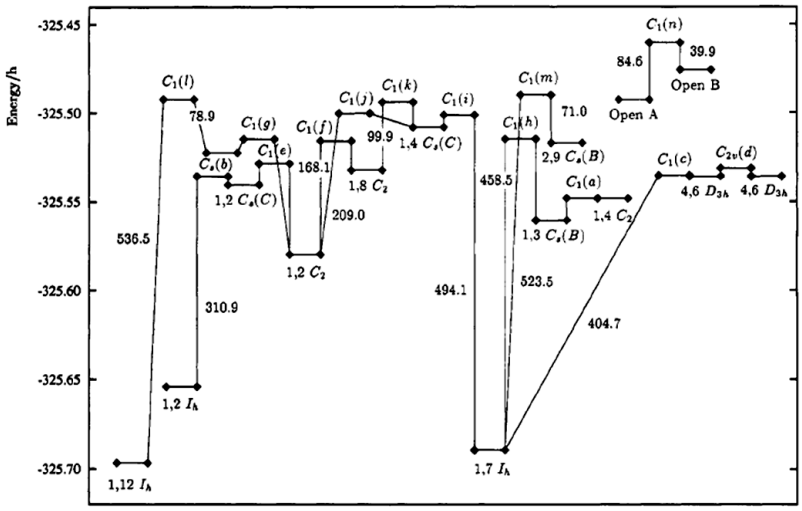

Figure 2.2 – 12-vertex *closo* carborane isomerisation profile reported by Wales. Energies in hartrees.

Rearrangements in *closo*-$[B_{12}H_{12}]^{2-}$ and carborane were revisited by Brown and McKee[7] at the hybrid Density Functional Theory (DFT) level, through the B3LYP method (see Figure 2.3, below).[8] They showed that shorter pathways existed between carborane isomers. This included single TFR steps between carborane isomers, which were shown to be the lower energy process in the *ortho*- to *meta*-carborane case but higher in energy than a two step 'non-TFR' pathway connecting *meta*- and *para*-carborane. The non-TFR pathways reported, however, involved pseudo-*nido* geometries, earlier discounted by Wales.

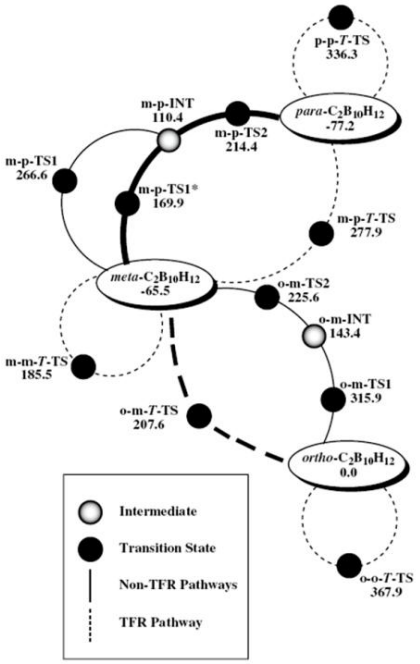

Figure 2.3 – 12-vertex *closo* carborane isomerisation pathways as reported by Brown and McKee. Energies in kJ mol^{-1}.

A key step towards the polyhedral expansion of heteroborane clusters is their chemical 2e reduction. This is known, in the case of the icosahedron, to result in formation of a *nido* fragment of a 13-vertex cluster, consistent with Wade's Rules.[9] Experiment verifies this; by metallating with, e.g. {Ru(*p*-cymene)}$^{2+}$ or {CoCp}$^{2+}$ fragments, the corresponding neutral 13-vertex *closo* compound can be produced, effectively trapping out *nido* species present in solution and preventing further isomerisation,[†] a process known as REDMET (reduction and metallation).

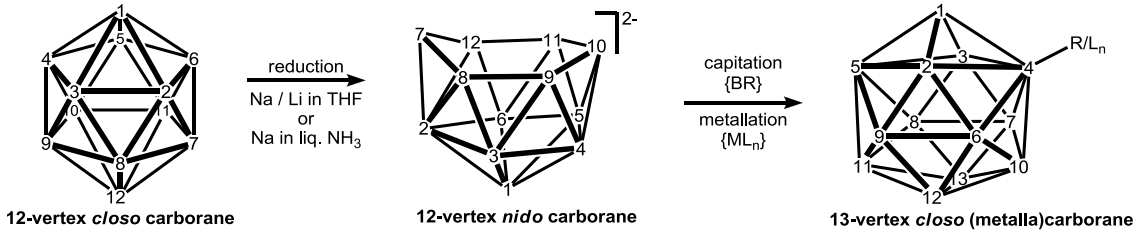

Figure 2.4 – The REDCAP/REDMET synthesis of supraicosahedral (metalla)carboranes.

In addition, Hermansson *et al.*[10] carried out theoretical work at the HF/6-31G** level, optimising the carborane isomers and reoptimising with the addition of one and two electrons, with the basis sets lowered to the 6-31G* level for dianions. Only in the case of *meta*-carborane 2e reduction was a *nido*-like geometry found by this method, closely resembling [7,9-*nido*-$C_2B_{10}H_{12}]^{2-}$ (**7,9**), which is inferred experimentally as the product of chemical reduction by Hawthorne.[11] However the same *nido* species is suggested to

[†] In general, calculations show isomerisation barriers in *closo* species are higher than those in *nido* species.

be produced by *ortho*-carborane reduction, where Hermansson *et al.* see a distorted *closo* geometry, involving only a slight opening of the cage (see Figure 2.5).

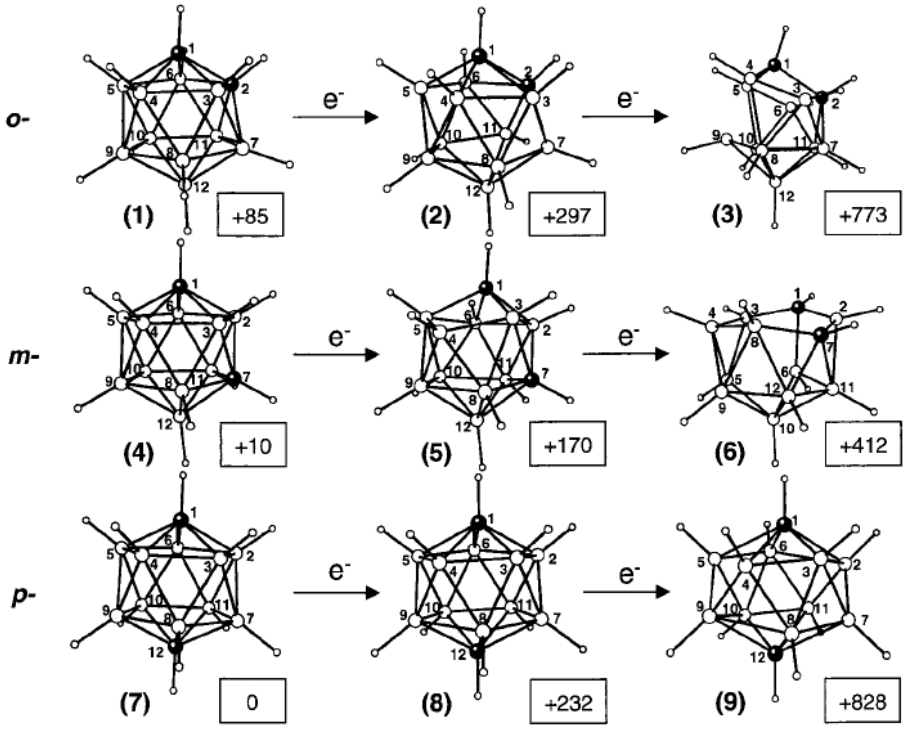

Figure 2.5 – 12-vertex carborane reductions reported by Hermansson. Energies in kJ mol^{-1}.

Most recently, Welch, Macgregor *et al.* reported that the reduction of *para*-carborane gives a complex array of products experimentally (see Figure 2.6, below).[12] *Nido* products inferred by experiment through metallation with {Ru(*p*-cymene)}$^{2+}$ and characterised by NMR and X-Ray crystallography include [1,7-*nido*-$C_2B_{10}H_{12}]^{2-}$ (**1,7**), [3,7-*nido*-$C_2B_{10}H_{12}]^{2-}$ (**3,7**), [4,7-*nido*-$C_2B_{10}H_{12}]^{2-}$ (**4,7**), [7,9-*nido*-$C_2B_{10}H_{12}]^{2-}$ (**7,9**) and [7,10-*nido*-$C_2B_{10}H_{12}]^{2-}$ (**7,10**).

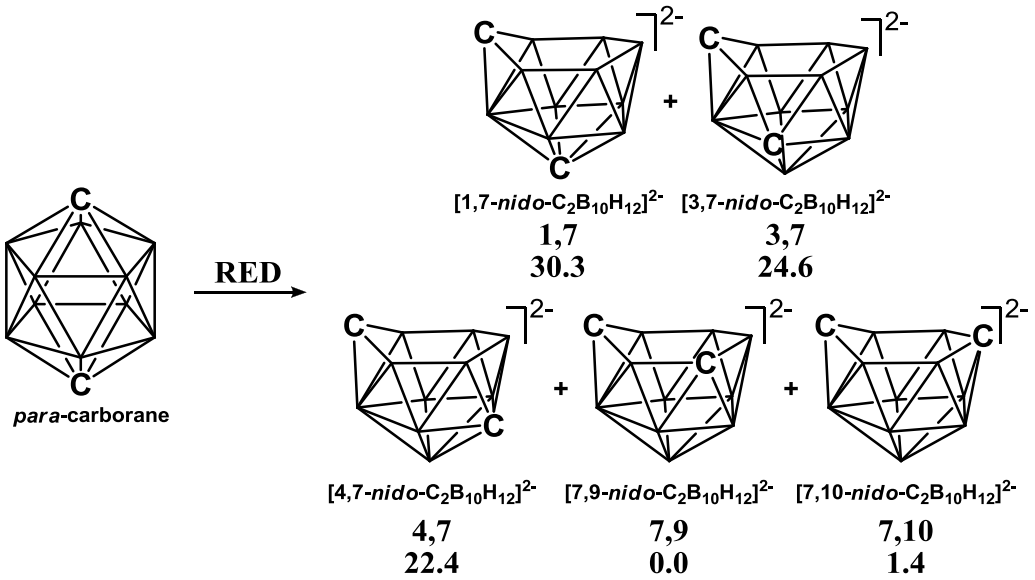

Figure 2.6 – 2e$^-$ reduction of *para*-carborane giving five *nido* products implied by experiment through capitation with {Ru(*p*-cymene)}$^{2+}$ with relative energies in kcal mol^{-1}.

Alongside this computational results were given, revealing the process of the 2e reduction of *para*-carborane by successive electron addition and optimisation at the BP86/6-31G** level. The results are depicted in Figure 2.7, where numbering is consistent with *para*-carborane on the left hand side and with the movement of the atoms thereafter. *Para*-carborane was found to be reduced initially to two intermediate geometries, **A** and **B**, where **B** is 4.5 kcal mol^{-1} more stable than **A** and they are related by a single transition state (TS) at $\Delta E^{\ddagger}$ = 4.8 kcal mol^{-1}. Subsequent isomerisation steps were discovered, giving **1,7** and **4,7** as the first *nido* species formed.

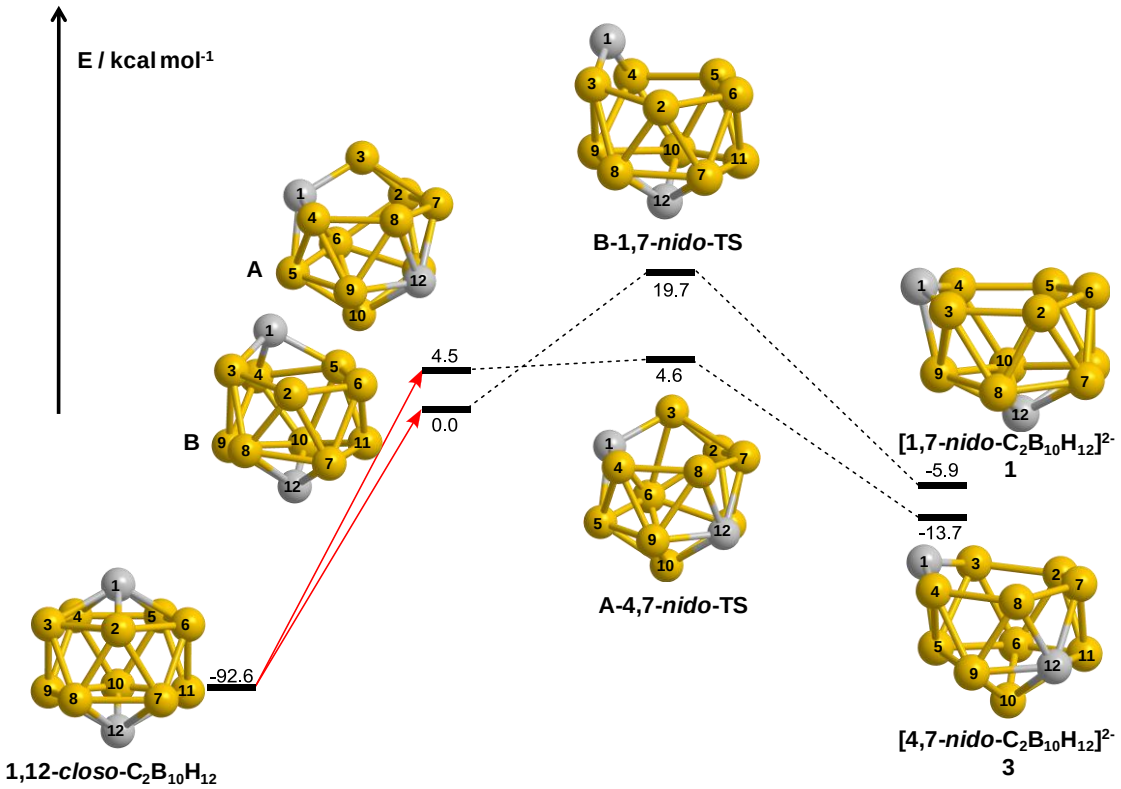

Figure 2.7 – Computed reduction of *para*-carborane to two initial *nido* products.

A and **B** are topologically equivalent, where both exhibit a 4-membered and a 5-membered face sharing the C1–B3 edge. In forming **A**, D-S-D processes are seen in the B4–B3–B8–B9, B2–B6–B7–B11 and C1–B6–B2–B3 diamonds, where in the first, the B3···B4 and B3···B8 connections are lengthened to 2.589 Å and 2.561 Å respectively, giving a five-membered face and in the last the D-S-D is incomplete, leaving a four-membered face with a B3···B6 distance of 2.121 Å, which shares a C–B edge with the five-membered face. The formation of **B** is perhaps easier to visualise in that there are no complete D-S-D processes relating it back to *para*-carborane. The C1···B2 and C1···B6 distances are lengthened from 1.714 Å in *para*-carborane (where they are symmetrically equivalent) to 2.827 Å and 2.707 Å respectively in **B**, producing a five-membered face. A four-membered face is again produced through a partial D-S-D and shares a C–B edge with the five-membered face, here in the C1–B3–B9–B4 diamond where the B3–B4 connection is lengthened from 1.792 Å to 2.330 Å. The transition states are also equivalent in terms of their topology as well as the process corresponding to their negative mode. In each case, the exposed C–B edge falls into the smaller 4-membered face, resulting in a 6-membered face and giving a *nido* fragment of a 13-vertex docosahedron, where carbon occupies the least connected vertex 7. **A** was found to then isomerise to **4,7** with a minimal energy barrier of 0.1 kcal mol^{-1} and ΔE = -18.2

kcal mol^{-1} while **B** may isomerise to **1,7**, where the energy barrier to be overcome is more significant at 19.7 kcal mol^{-1} and the step is less exothermic; ΔE = -5.9.

In this work our aim was to continue to follow the isomerisation on the dianionic potential energy surface in order to discover pathways to the remaining experimentally inferred products, **3,7**, **7,9** and **7,10**. We also fully characterise the reduction pathways for the simpler cases of *ortho*- and *meta*-carborane, both of which result in formation of **7,9**. Furthermore we report a pathway linking **7,9** and **7,10**, a transformation that has been observed experimentally.[13] In carrying out this work we uncover a new family of dianionic heteroborane structures and interesting, novel processes involved in their interconversion. Following this the oxidation processes of *nido* dianions are investigated, where experimental and computational results are compared.

2.2. Isomerisations of dianionic carboranes

The aim of the study was to discover pathways connecting the *nido* isomers previously computed, **1,7** and **4,7** with the remaining isomers found experimentally, **3,7**, **7,9** and **7,10**. It was also hoped that a library of common intermediate topologies and common mechanistic processes for dianionic 12 vertex carboranes could be compiled. At first glance it appears *nido* isomers can be closely related by single rotations of triangular faces. For instance in **1,7**, **3,7**, and **4,7** the higher connected carbon vertices all lie in the 1–3–4 triangle and thus its rotation should interchange them. Moreover, vertex 4, occupied by C in **4,7**, shares a triangle with vertices 9 and 10, occupied by C in **7,9** and **7,10** respectively. Therefore the first possibility was to carry out potential energy surface searching (or scanning) calculations attempting to influence TFR processes.

After several attempts from both **1,7** and **4,7** it became clear scanning for triangular rotation processes both gave large increases in energy without producing maxima, with respect to the coordinate scanned, and proved extremely difficult to control. Several atoms close to those being scanned had to be fixed in space to prevent undesired isomerisation of the molecule. The suggestion was, therefore, that the rotation of a single triangle, though seen in neutral carboranes, was higher in energy than other processes seemingly allowed by the increased flexibility of the *nido* fragment over the *closo* species.

By visualising the vibrational modes of **1,7** and **4,7**, it can be seen that the lowest energy vibration represents rotation of the 6-membered face over the 5-membered B2–B3–B/C4–B5–B6 ring, with the greatest movement at the C7 position. In the case of **4,7** it was thought possible this could correspond to a process interchanging **4,7** and **3,7** by multiple concerted D-S-D steps, giving a ca. 72° rotation of the 6-membered ring, even though such high symmetry processes were shown to be high in energy in *closo* carboranes. To pursue this, the DIIS optimisation algorithm was used along with 'TS', 'verytight' convergence constraints, an 'ultrafine' integration grid and by calculating the force constants of the starting geometry. These options, along with the input geometry which was slightly perturbed from the optimised *nido* structure, were designed to prevent geometry convergence in the first step and influence the algorithm to follow the lowest energy mode to the first saddle point along its corresponding vector. This technique will be termed 'mode following'.

Calculations adopting the mode following approach gave more promising results than initial scans, and located transition states from both **1,7** and **4,7**. The two transition states exhibited similar topologies and represented equivalent geometrical changes with respect to the input *nido* geometry. In each case the 3-connected C7 is moved to a 4-connected position and a 4-connected boron vertex adjacent to C7 on the 6-membered open face (*i.e.* B8/B12 in Figure 2.3) is moved into a 3-connected position in a single D-S-D process. These saddle points, as is our standard practise, were then subjected to Intrinsic Reaction Coordinate (IRC) calculations. As expected, the reverse direction of the reaction coordinate gave the *nido* geometry from which the transition state was discovered in each case. The unknown forward direction, where **1,7** was found to isomerise to **7,9** (ΔE = -30.3 kcal mol^{-1}, Figure 2.8) and **4,7** rearranged to **7,10** (ΔE = -21.1 kcal mol^{-1}, Figure 2.13), are subsequently discussed in detail.

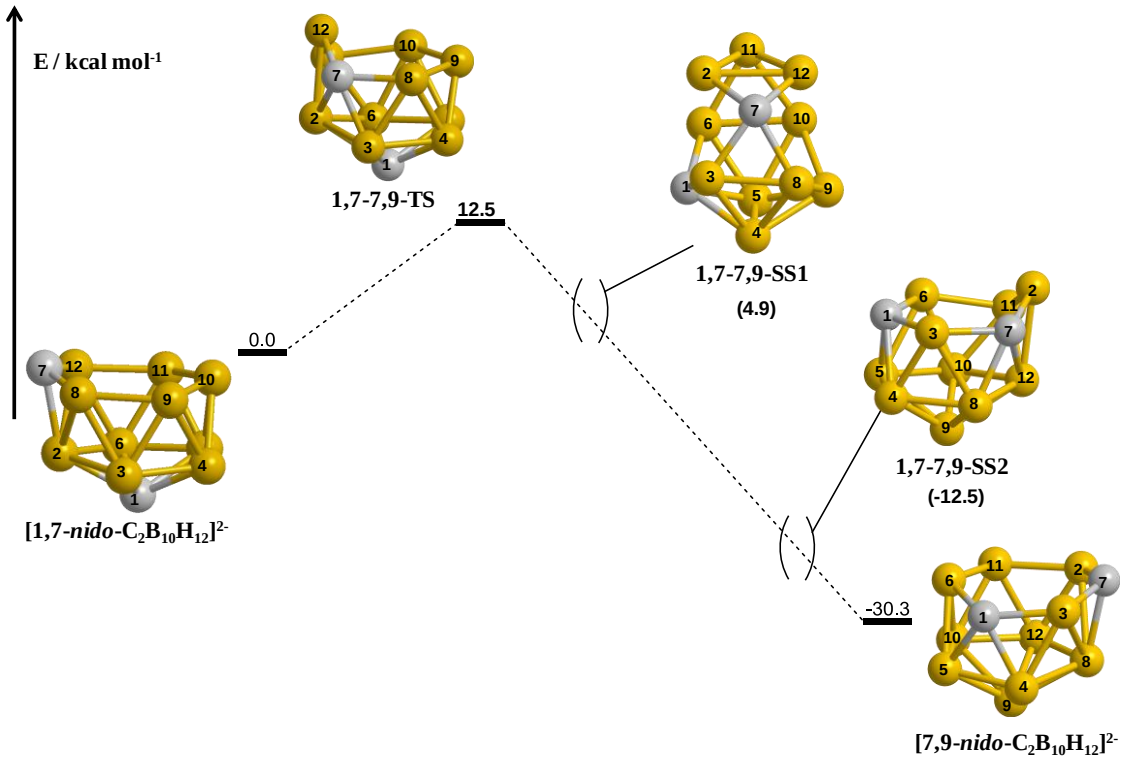

Figure 2.8 – Isomerisation of 1,7 to 7,9; $\Delta E^{\ddagger}$ = 12.5 kcal mol^{-1}.

2.2.1. Isomerisation of [1,7-*nido*-$C_2B_{10}H_{12}$]$^{2-}$ to [7,9-*nido*-$C_2B_{10}H_{12}$]$^{2-}$

The single transition state between **1,7** and **7,9** (**1,7-7,9-TS** in Figure 2.8) exhibits a 3-connected boron vertex, B12, which protrudes from the 6-membered open face by 0.806 Å with respect to the least squares mean plane through the remaining vertices of the open face. This is large in comparison to the protrusion of C7 from the open face in **1,7** of 0.277 Å (0.273 Å in **7,9**) and is accompanied by a lengthening of the B2–C1 distance

from 1.731 Å in **1,7** to 1.867 Å. The single negative eigenvector of **1,7-7,9-TS** (highlighted in Figure 2.9, below) shows movement of B12 in and out of the open face with a frequency of -200.5 cm^{-1}, where the B12–B9 distance is 3.005 Å at the transition state geometry.

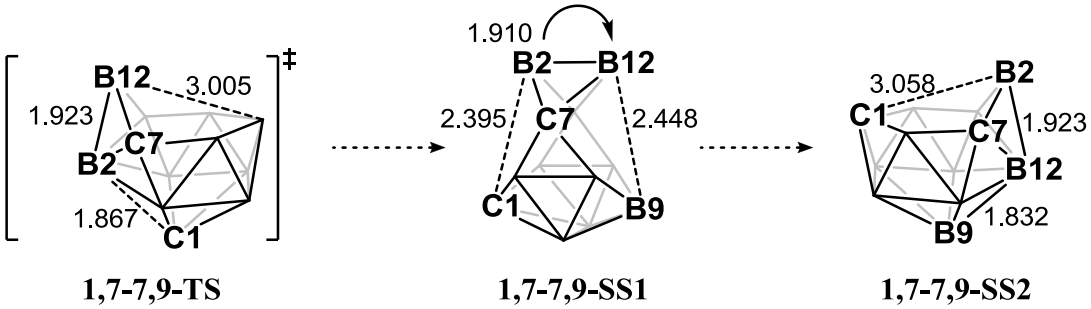

1,7-7,9-TS **1,7-7,9-SS1** **1,7-7,9-SS2**

Figure 2.9 – Schematic of the structural evolution from 1,7-7,9-TS with distances in ångstroms.

Following the forward reaction coordinate through IRC calculation and subsequent optimisation gives **7,9** directly. Visualisation of the IRC calculation shows a very interesting evolution of the geometry (Figure 2.9, above). The C7–B12–B11–B2 diamond of **1,7-7,9-TS** is seen to pivot about its long diagonal. At the midpoint (in terms of distance) of this pivot (**1,7-7,9-SS1** in Figures 2.8 and 2.9), where the diamond is parallel to the B3–B8–B10–B6 plane, the molecule exhibits two inequivalent 6-membered faces. The inequivalence arises from C1 in the left-hand C1–B3–C7–B2–B11–B6 face versus B9 in the right-hand B9–B10–B11–B12–C7–B8 face, where the previously 5-connected C1 fully loses its connection to B2 and previously 4-connected B9 begins to connect to B12 as the 6-membered face is transferred from one side of the cage to the other. At the second snap shot, **1,7-7,9-SS2**, shown in Figures 2.8 and 2.9, B2 is 3-connected, adjacent to 4-connected C7, with a local geometry mirroring that of the transition state. We therefore see a D-S-D process mirroring that which gives **1,7-7,9-TS** from **1,7** to finally give **7,9**, where C7 returns to a 3-connected position on the open face but now with C1 also on the open face, separated from C7 by a single B-vertex. Since it is known from experiment that carbon prefers to adopt lower connected sites within carborane cages, and given the ΔE of this isomerisation, movement of C1 to the open face is thought to be the driving force behind this seemingly large transformation.

The lowest energy vibrational mode of **7,9**, 173.6 cm^{-1}, can be followed to give a C_s transition state at +11.4 kcal mol^{-1}, which exchanges the two carbon vertices, suggesting equivalent C chemical environments in solution. This is reflected in the NMR spectra

of 4,1,6-*M*$C_2B_{10}H_{12}$, formed by metallation of **7,9**, which shows effective C_s symmetry with a typical barrier of *ca.* 40 kJ mol^{-1}.[14]

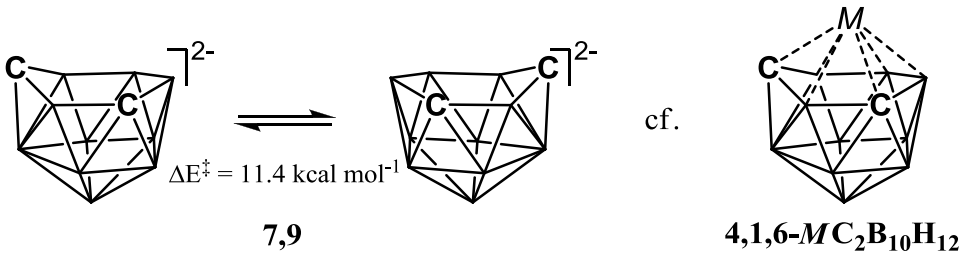

7,9 **4,1,6-*M*$C_2B_{10}H_{12}$**

Figure 2.10 – Comparison of [7,9-*nido*-$C_2B_{10}H_{12}$]$^{2-}$ with its metallated form showing the source of its effective C_s symmetry.

2.2.2. Isomerisation of [4,7-*nido*-$C_2B_{10}H_{12}$]$^{2-}$ to [7,10-*nido*-$C_2B_{10}H_{12}$]$^{2-}$

In contrast to the single step isomerisation of **1,7** to **7,9**, the isomerisation of **4,7** to **7,10** was found to be a multistep process (given in Figure 2.14), with four transition states and three intermediates. By virtue of the relative forward and backward barrier heights from each intermediate, it was possible to characterise the entire pathway by sequential mode following and IRC calculations, since mode following consistently locates the lower energy transition state. As is mentioned above, the initial saddle point in the **4,7** to **7,10** isomerisation process (**4,7-7,10-TS1**, Figure 2.11, below) is related to **4,7** by a single D-S-D process involving vertices C7–B8–B3–B2, which can be closely related to the change in topology from **1,7** to **1,7-7,9-TS**. The 6-membered face of **4,7-7,10-TS1** is more planar than in **1,7-7,9-TS**, where the 3-connected boron vertex protrudes from the least squares mean plane of the five remaining atoms in the face by 0.564 Å. As seen in **1,7-7,9-TS**, a C–B connection in the lower part of the cage is lengthened as the D-S-D occurs. Here the B3–C4 connection lengthens from 1.671 Å to 2.012 Å, producing a 4-membered B1–B3–B9–C4 face.

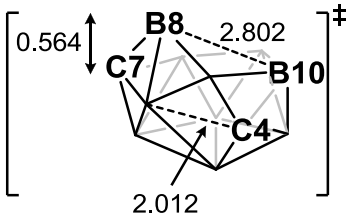

Figure 2.11 – Schematic of 4,7-7,10-TS1 with distances in ångstroms.

The single negative mode at -174.8 cm^{-1} differs from that of **1,7-7,9-TS** however, showing atomic motion involving rotation of the triangular faces which share B9, hinging about the shared vertex, not the motion into and out of the open face of the 3-connected B as was seen in **1,7-7,9-TS**. This movement further elongates the B3–C4

connection to 2.567 Å while making the B8–B10 connection (shortened to 2.802 Å from 2.969 Å in **4,7-7,10-TS1**) seen in **4,7-7,10-INT1** (see Figure 2.12, below).

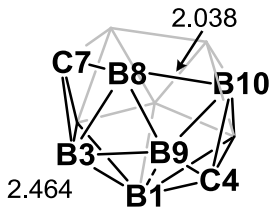

Figure 2.12 – Schematic of 4,7-7,10-INT1 with distances in ångstroms.

This first intermediate in the **4,7** to **7,10** isomerisation exhibits two inequivalent faces with more than 3 vertices. The lower, 4-membered face, has disconnected diagonals, where the B1···B9 distance is 2.464 Å and the B3···C4 distance is 2.567 Å. In the upper, 5-membered C7–B12–B11–B10–B8 face, B10 is 5-connected despite its facial location (normally only 3- or 4-connected sites are seen on an open face). This is coupled with a very long B8···B10 contact of 2.038 Å. The lowest energy mode of **4,7-7,10-INT1** corresponds to motion of B8 into and out of the 5-membered face. Following this eigenvector yields **4,7-7,10-TS2**, where B8 moves into the 5-membered face and its connections to B3 and B9 are lengthened but not broken (1.903 and 1.738 Å respectively in **4,7-7,10-TS2** *cf.* 1.798 and 1.677 Å respectively in **4,7-7,10-INT1**). The B3···B1 connection is broken however, lengthening to 2.107 Å in **4,7-7,10-TS2** from 1.993 Å in **4,7-7,10-INT1**. The motion of B8 is continued from **4,7-7,10-TS2** to **4,7-7,10-INT2** (see Figure 2.13, below) where the B8···B3 and B8···B9 connections are broken (lengthening to 2.472 Å and 2.222 Å respectively) and B8···B12 and B8···B11 connections made. The result is a geometry lower in energy than the starting *nido* species, **4,7**, by 4.8 kcal mol^{-1}. **4,7-7,10-INT2** is topologically similar to intermediates **A** and **B**, formed via 2e$^-$ reduction of *para*-carborane described earlier, which were C_1 and had 4- and 5-membered faces. Here, however, by virtue of the positions of the carbon atoms, C_2 symmetry is exhibited and there are two equivalent 5-membered faces with a common edge represented by the B3–B9 connection.

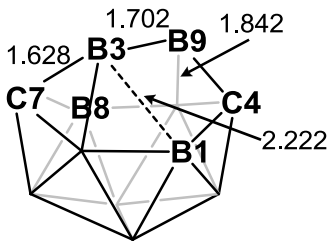

Figure 2.13 – Schematic of 4,7-7,10-INT2 showing key distances in ångstroms.

On following the lowest energy eigenvector from here we see a process equivalent to those seen from **A** and **B** to form *nido* fragments. Following the lowest energy eigenvector from **4,7-7,10-INT2**, **4,7-7,10-TS3** is found directly and shows a disconnection of the B3···B2 contact (lengthening from 1.841 Å to 2.254 Å) and a connection reformed between B9 and B8 at 2.022 Å. Visualising the single negative eigenvector of **4,7-7,10-TS3** shows movement of B3 between the 6-membered B3–B9–C4–B1–B2–C7 face and the 4-membered B3–B9–B8–C7 face, with a frequency of -236.2 cm^{-1}. IRC calculations from this saddle point give back **4,7-7,10-INT2** and the next intermediate along the pathway, **4,7-7,10-INT3**, where the B3–B8 distance is 1.901 Å. Here the *nido* topology is regained with B3 occupying the 3-connected site adjacent to 4-connected C7. Hence we again see a single D-S-D process to exchange these atoms, lowering the connectivity of the carbon. Although there is an intermediate located in this case, the potential energy surface is shown to be extremely flat and the D-S-D process effectively barrierless. The product, **7,10** is formed where C4 now occupies vertex 10 of the fragment and the B8–B9–B3 triangle has effectively passed across the open face of **4,7** to effect the transformation.

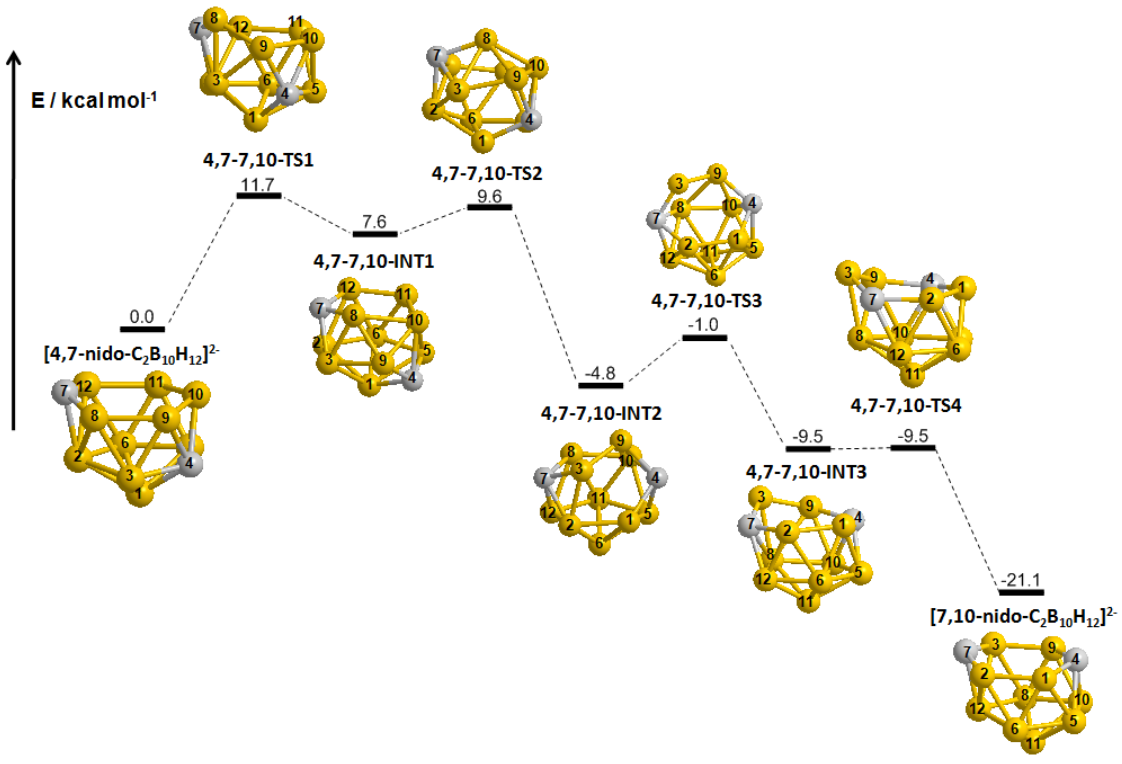

Figure 2.14 – Isomerisation of 4,7 to 7,10; $\Delta E^{\ddagger}$ = 11.7 kcal mol^{-1}.

Overall this isomerisation has an energy barrier of 11.7 kcal mol^{-1} and ΔE = -21.1 kcal mol^{-1}. In comparison to the isomerisation of **1,7** to **7,9** ($\Delta E^{\ddagger}$ = 12.5 kcal mol^{-1}; ΔE = -30.3 kcal mol^{-1}) here there is a slightly lower activation energy and a slightly less

stable fragment is formed. Most significantly, the large exothermicity corroborates the previous conclusion that movement of a carbon vertex towards the open face is the driving force of the isomerisation.

2.2.3. Summary and observations

We have now seen two pathways for isomerisation of *nido* dianions of carboranes. These pathways were discovered simply by seeking saddle points from minima as input geometries, a technique made possible by the nature of these molecules, where the lowest energy vibrational modes are related to structural deformations. This has allowed the discovery of pathways that would not have otherwise been trivial to predict. The one remaining isomerisation sought by this study, however, should not be possible to locate in this way. As stated before, mode following from a minimum follows the lowest energy vibrational mode from that minimum to a transition state along the related eigenvector. Since here we have used this technique from both of our starting geometries we must now use other techniques to located the remaining pathway.

The final *nido* product, [3,7-*nido*-$C_2B_{10}H_{12}$]$^{2-}$ (**3,7**) is found to be between **1,7** and **4,7** in energy, where, relative to **4,7**, **3,7** is located at 2.2 kcal mol^{-1} and **1,7** at 7.9 kcal mol^{-1} higher in energy. There would therefore be a requirement for an exothermic pathway from **1,7** and an endothermic pathway from **4,7**. Given the flexibility shown by these species in the previously calculated pathways, it was considered possible that the seemingly larger transformation (by inspecting the starting and end point geometries) from **1,7** to **3,7** may actually be possible to undertake, to lower the total energy of the system. A possible pathway from **4,7** to **3,7** was not discounted however – the geometries appear more closely related, by rotation of the upper 6-membered CB_5 ring with respect to the 5-membered CB_4 ring, but in the knowledge that higher symmetry pathways tend to have higher energy barriers and that the transformation would have to be endothermic this seemed the less likely route to formation of **3,7**.

Below, the processes seen so far will be summarised, with a view to applying previously seen processes to the current isomerisation problem of connecting **1,7** and **3,7**.

(i) In both isomerisations seen before, the first step was to move the 3-connected C7 atom into a 4-connected position, by a single D-S-D process. Also, this process in **1,7** leads to a local topology of the carbon atoms equivalent to that in **3,7**, where they lie in the non-bonded diagonal positions of a C–B–C–B diamond.

(ii) Low-connected atoms move over the open faces of the molecules in a spherical motion (as if around the surface of a sphere) with relative ease in downhill processes which generally push carbon vertices towards a low-connected position. This is particularly striking in the **1,7** to **7,9** transformation where movement of a group of atoms around the cage is found to be a one step process. However it is also seen in the **4,7** to **7,10** isomerisation where, perhaps equally remarkably, a triangle of boron atoms (B8–B9–B3) is seen to move from one side of the molecule to the other *via* a two step process.

(iii) The second new process seen in the **4,7** to **7,10** transformation is that from **4,7-7,10-TS1** to form **4,7-7,10-INT1**. Here two vertex sharing triangles (B8–B9–B3 and B9–B10–C4) rotate in opposite directions to form a third triangle (B8–B10–B9) and move the shared B9 vertex away from the open face.

(iv) Some intermediates were found to resemble 12-vertex fragments of the docosahedron, these include of course the five *nido* dianions which are defined in this way, but also high energy intermediates such as **4,7-7,10-INT1** which has two open faces and may be related to the docosahedron by capitation of the 5-membered face. This is an important point towards identifying possible intermediates along a pathway to form **3,7**.

(v) We have also seen a new topology, which we have termed a 'basket' intermediate. This is seen in the initial reduction and isomerisation in Figure 2.7 that forms **1,7** and **4,7**, where intermediates **A** and **B** fall into this category. Also in the **4,7** to **7,10** isomerisation, **4,7-7,10-INT2** is a relatively stable basket intermediate with C_2 rotational symmetry. All three of these basket structures are related to *nido* geometries by the bridging atoms falling into an open face, increasing their connectivity and producing *nido* topologies. Such processes will be termed 'basket collapse'.

Given these observations, a D-S-D process was sought from **1,7** through scanning along the C7···B6 coordinate, following process (i) above. This was thought to be set up to give a first transition state in a multistep pathway towards formation of **3,7**. However problems arose whereby the lower energy process of forming **7,9** via a single step was difficult to avoid. After several attempts to realise the required transformation it

became clear that the **1,7** to **7,9** transformation was so facile and the structure so flexible that it was very difficult to prevent.

We therefore sought a reverse pathway from **3,7**. The lowest energy vibration of **3,7** was inspected but found to be a fluxional process with $\Delta E^{\ddagger}$ = 6.8 kcal mol^{-1}. Scans were then conducted from **3,7** in order to locate one or more of the processes summarised above. These included a D-S-D process to give a 3-connected boron on the open face, analogous to (i) and rotations of the C1–B8–B3 and B8–B2–C7 triangles about the shared vertex 8, as in process (iii). The D-S-D process was not located, however, the second double triangular hinging movement about B8 appeared promising at this point, though not fully resolved. This was because for the scan to work, much of the rest of the molecule had to be constrained and the selection of a single coordinate relating to the motion desired was difficult.

Given these circumstances, a Synchronous Transit-Guided Quasi-Newton (STQN) method was investigated, where, in Gaussian 03, there are two options available; QST2 requests this method, given two different input geometries representing the reactant and product molecules and QST3 requests an STQN method given three input geometries, where the third is a guess transition state.

2.2.4. Isomerisation of [1,7-*nido*-$C_2B_{10}H_{12}$]$^{2-}$ to [3,7-*nido*-$C_2B_{10}H_{12}$]$^{2-}$

The pathway of isomerisation from [1,7-*nido*-$C_2B_{10}H_{12}$]$^{2-}$ to [3,7-*nido*-$C_2B_{10}H_{12}$]$^{2-}$ is given in Figure 2.15, below.

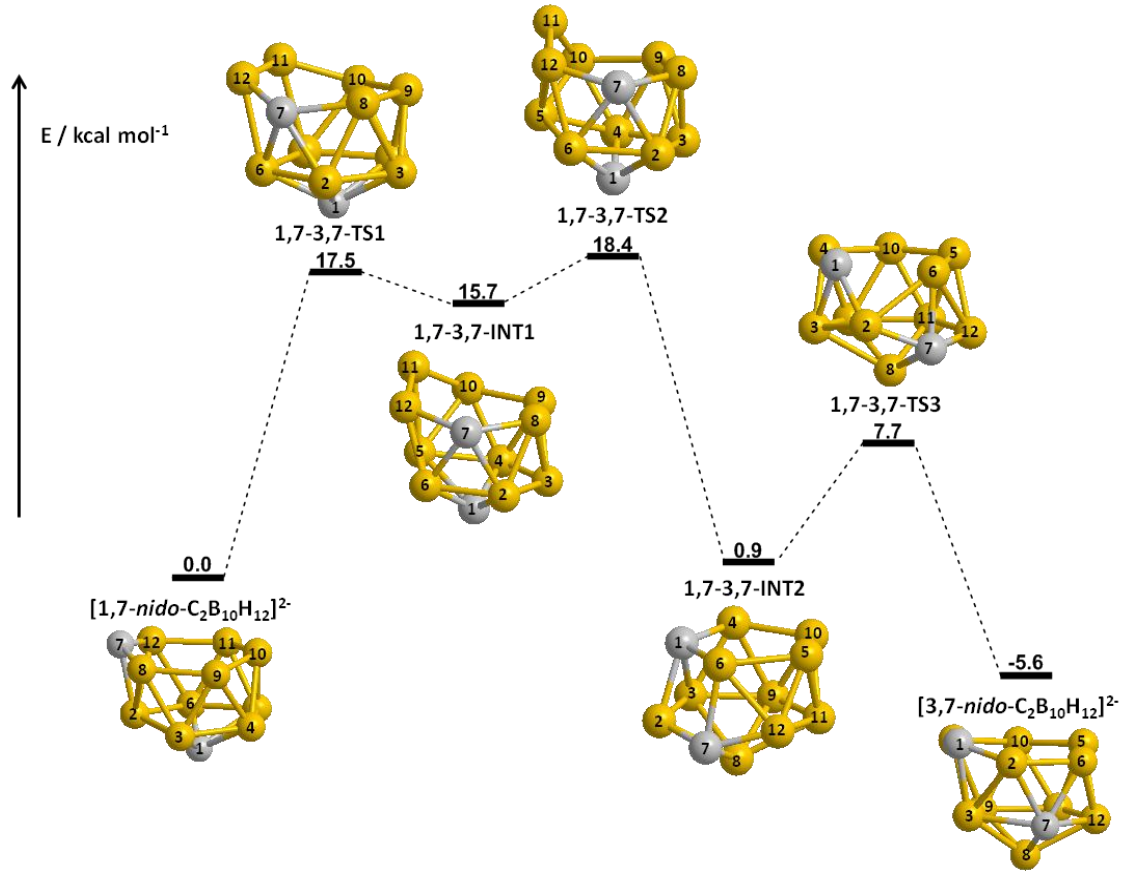

Figure 2.15 – Isomerisation of 1,7 to 3,7; $\Delta E^{\ddagger}$ = 18.4 kcal mol^{-1}.

Here the QST2 option was adopted where **3,7** was given as the reactant molecule and what is now known to be **1,7-3,7-INT2** as the product, with atoms numbered to reflect the movement of B2 to and from the open face by rotation of C1–B2–B3 and B2–B6–C7 triangles, accompanied by a D-S-D process forming the B2–B8 connection (1.912 Å in **1,7-3,7-INT2** *cf.* 3.004 Å in **3,7**) in the B3–B2–C7–B8 diamond. **1,7-3,7-INT2** was in fact previously found via a scan from **3,7**, however the scan did not yield a transition state relating it to **3,7**, nor at that time was the importance of this geometry known, although noted was its relatively similar energy to **1,7** and **3,7**. Through the QST2 calculation and subsequent transition state optimisation, **1,7-3,7-TS3** was characterised and shown to link **1,7-3,7-INT2** to **3,7** through IRC calculations, showing a second process involving vertex sharing rotation of two neighbouring triangles in a carborane dianion (process (iii) in section 2.2.4). The challenge now was to connect **1,7-3,7-INT2** to **1,7** and therefore complete the isomerisation pathway. The lower and right part of the **1,7-3,7-INT2** cage contains atoms C7–B8–B9–B10–B11–B12. These vertices become the 6-membered open face in **1,7**, hence their numbering, which is again based upon the formal number of the fragment on the left hand side of the profile, **1,7**. To gain the relative positioning of carbon atoms in **1,7** from here, as the 6-membered face is opened up, vertex B5 must move towards C1 to leave the carbon at the bottom of the

cage while a 6-membered face is opened. To achieve this one may envisage a process analogous to that seen in the **1,7** to **7,9** transformation, (process (ii) in section 2.2.4) where here pivoting of the B5–B10–B11–B12 diamond about the long B12–B10 diagonal may open up a 6-membered face in the lower part of the cluster while closing the C1–B4–B10–B5–B6 5-membered face. This was sought through scanning the B5···C1 distance (from 2.862 Å in **1,7-3,7-INT2** to 1.683 Å in **1,7**) while carefully monitoring of the B5–B11 distance (see Figure 2.16, below) and resulted in location of a transition state, **1,7-3,7-TS2**, which is similar to **1,7-7,9-TS** except that the 3-connected facial boron atom (B11) is not directly bound to the facial carbon atom.

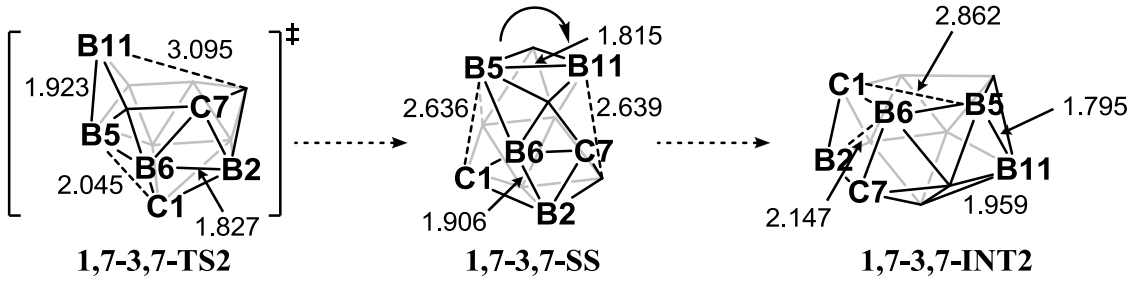

Figure 2.16 – Schematic of the structural evolution from 1,7-3,7-TS2 to 1,7-3,7-INT2, distances in ångstroms. Dotted arrows refer to the reaction coordinate.

Characterisation of **1,7-3,7-TS2** gives back **1,7-3,7-INT2** along with **1,7-3,7-INT1**, where B11 remains 3-connected and the B5···C1 is shortened from 2.045 Å in **1,7-3,7-TS2** to 1.799 Å in **1,7-3,7-INT1**. In the forward direction from **1,7-3,7-TS2** to **1,7-3,7-INT2** the movement of atoms is analogous to the movement of a diamond over the open face in a rotational motion (process (ii) in section 2.2.4) as hypothesised. Here the motion is similar in that the B5–B10–B11–B12 diamond rotates about the B12···B10 axis, however in this case there is also a partial D-S-D process seen in the C1–B6–C7–B2 diamond at the front of the fragment, as shown. Most clearly illustrated in Figure 2.16, this partial D-S-D processes appears to stabilise B5, which, were the process exactly analogous to that between **1,7** and **7,9**, would lose a connection to B6. Meanwhile, C7 would be pushed to a position farther from the open face and higher connected, similarly to B8 in **7,9** (as numbered in the **1,7** to **7,9** pathway, Figure 2.8). Again, this emphasises the idea that carboranes are stabilised by having low connected C vertices and high connected B vertices and will distort considerably to achieve this.

The final process located was that connecting **1,7-3,7-INT1** to **1,7**, by two sequential D-S-D processes. This process was located by mode following from **1,7-3,7-INT1**, where the lower energy TS shown was found directly and characterisation confirms its

position in the pathway, connecting **1,7** to **1,7-3,7-INT1**, completing the **1,7** to **3,7** isomerisation pathway.

2.2.5. Conclusions from *para*-carborane reduction and isomerisation

Pathways have been discovered connecting the initial products of the reduction of *para*-carborane to each of the five *nido* fragments inferred experimentally. Through doing this, several new intermediate topologies and isomerisation processes have been characterised; basket intermediates, basket collapse (giving a *nido* intermediate), the movement of atoms across the open face of a *nido* fragment, as if tracing the surface of a sphere, by single or multistep processes and common starting processes in isomerisations which initially destabilise the molecule by increasing the connectivity of a carbon atom on the open face. Each process has re-emphasised the idea that the cage is more stable when its lower-connected sites are occupied by carbon and its higher-connected sites by boron.

The initial step in isomerisation processes is common to *nido* species where only one carbon atom is located on the open face (**1,7**, **3,7** and **4,7**). This is where the 3-connected C7 exchanges with a 4-connected boron on the open face, giving a 3-connected B and 4-connected C. This increases the total the energy of the system, but seems to also increase its flexibility, since the 3-connected boron atom undergoes the most movement in the following steps of the mechanism. A powerful combination of mode following, scanning and STQN calculations has led to successful characterisation of these pathways with minimal presupposition or constraint being placed upon the system.

2.3 Further questions posed by experimental results

It follows logically, then to attempt to answer more questions that come out of experimental work towards supraicosahedral (metalla)carboranes. The reduction and metallation of either *ortho*- or *meta*-carborane, for instance, leads solely to the production of 4,1,6-*closo*-$MC_2B_{10}H_{12}$ species, derived from **7,9**.[11] Why is no mixture of products seen? Also, more recent experimental work has highlighted the existence of a pathway exchanging **7,9** and **7,10** C-phenyl derivatives at low temperatures.[13] What is the mechanism of this process? These questions are addressed below.

Experimental studies by Zlatogorsky *et al.* showed that if 2e reduction of 1,12-*closo*-$C_2B_{10}H_{12}$ is carried out with Na in liquid NH_3 and subsequently heated at THF reflux, before metallation, 4,1,6-*closo*-$MC_2B_{10}H_{12}$ species (derived from metallation of **7,9**) are characterised as the product. When this work was carried out it was thought that [7,10-*nido*-$C_2B_{10}H_{12}$]$^{2-}$ (**7,10**) was the only product of *para*-carborane reduction,[15] although it is now clear there are a possible five products of this process. However this does show that one remaining process, namely an isomerisation from **7,10** to **7,9**, can occur in solution. THF reflux is required in the case of unsubstituted carboranes, however can be effected at room temperature with C-phenyl derivatives, this suggests significant substituent effects on isomerisation barriers, and this will be discussed in the following chapter.

2.3.1 Location of a 7,10 to 7,9 isomerisation pathway

For the unsubstituted carborane dianions, **7,10** is 1.4 kcal mol^{-1} higher in energy than **7,9**, consistent with the experimental observation that **7,9** is the thermodynamic product of reduction. The first attempt to locate this pathway was carried out by scanning from **7,10** to shorten the distance between the carbon vertices (3.160 Å in **7,10** cf. 2.750 Å in **7,9**). This failed, however; due to the symmetry of **7,10** the scan merely strained the structure without yielding a maximum with respect to the chosen coordinate.

A C_1 structure showing a 5-membered face where a carbon atom sits over three boron vertices of a lower CB_4 pentagon (topology given in Figure 2.17, below) was seen in investigating other pathways. It is possible to envisage D-S-D processes in diamonds C1–B5–B8–B3 and C1–B4–B7–B3 giving a 7,10- and a 7,9-*nido*-C_2B_{10} geometry respectively. It was therefore considered as an intermediate in an isomerisation pathway exchanging **7,9** and **7,10**. The C_1 fragment can be thought of as a *nido* fragment of a 13-vertex heteroborane where vertex 2 has been removed (as opposed

vertex 4) to give a 5-membered face, as opposed to vertex 4, which is typically that removed given its high number of connections.

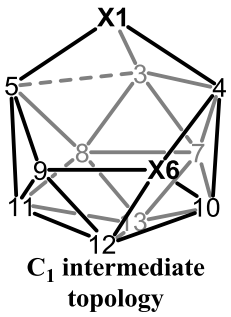

Figure 2.17 – Topology of the C_1 intermediate of the 7,9 to 7,10 isomerisation, numbered as a fragment of a docosahedral heteroborane after loss of vertex 2.

To discover pathways from the C_1 intermediate (Figure 2.16, above) scan coordinates can easily be set up to effect the D-S-D processes described above whereby either the C1···B7 distance is shortened, leaving the carbon vertices separated by B4, giving **7,9** or the C1···B8 distance is shortened to give **7,10**, where the carbons are separated by vertices B3 and B4 (clockwise from C1) and by vertices B5 and B9 (anti-clockwise from C1). The pathway resulting from these scans is given in Figure 2.17 where the numbering is adjusted to reflect the movement of vertices in the isomerisation.

The energy of the C_1 intermediate is relatively comparable to the *nido* intermediates, **7,9** and **7,10**; $\Delta E = +3.2$ kcal mol^{-1} with respect to **7,9**. Its topology is equivalent to that of **B** (see Figure 2.7) where the higher-connected carbon now lies on the open face – reasonably assumed to be the source of the its relative accessibility. A disconnection is observed between B5 and B3 (in Figure 2.16) where the B5···B3 distance is 2.364 Å. This reflects the structures seen previously in asymmetric basket intermediates where two open faces of four and five members are exhibited, adding to this new family of carborane dianion geometries.

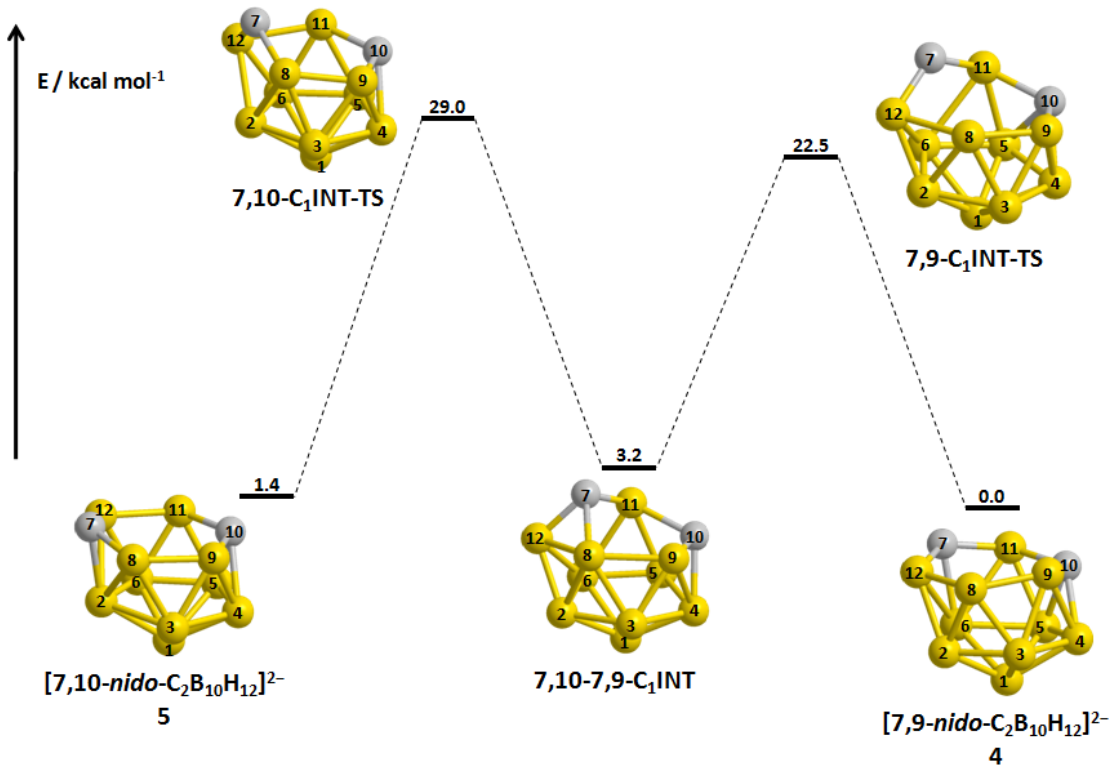

Figure 2.18 – Isomerisation of 7,10 to 7,9; $\Delta E^{\ddagger}$ = 27.6 kcal mol^{-1}.

Starting from **7,10**, with formal numbering of the [7,10-*nido*-$C_2B_{10}H_{12}]^{2-}$ fragment, we can see the first D-S-D process within the C7–B8–B2–B12 quadrangle to form **7,10-7,9-C_1INT**. The C7···B2 connection is broken – lengthening from 1.759 Å in **7,10** to 2.312 Å in **7,10-C_1INT-TS**, alongside (to a lesser extent) the B8···B12 distance shortening from 2.744 Å to 2.642 Å and lengthening of the B11···B12 connection from 1.783 Å in **7,10** to 1.875 Å. In forming **7,10-7,9-C_1INT**, the B8···B12 connection is formed (1.882 Å) the B11···B12 connection is lost (2.364 Å) and a short C7···B11 connection is formed (1.594 Å). In **7,9-C_1INT-TS**, the C7···B8 connection is lengthened from 1.680 Å in **7,10-7,9-C_1INT** to 2.323 Å, and the C7···B6 distance is shortened from 2.588 Å to 2.233 Å. Finally the C7···B6 connection is formed, giving **7,9**, where the C7···B6 distance is 1.757 Å and the C7···B8 distance is 2.864 Å. Formation of **7,9** from **7,10-7,9-C_1INT** is both the more exothermic process and that with the lower energy barrier. Overall, $\Delta E^{\ddagger}$ = 27.6 kcal mol^{-1} for isomerisation of **7,10** to **7,9**, which is consistent with the experimental requirement to reflux in THF. It is expected that the relatively high energy barriers here will be lowered by substitution of phenyl substituents onto the carbon vertices since experimentally [7,10-Ph_2-7,10-*nido*-$C_2B_{10}H_{10}]^{2-}$ will isomerise to [7,9-Ph_2-7,9-*nido*-$C_2B_{10}H_{10}]^{2-}$ at room temperature. The effect of changing the carbon substituents is investigated in Chapter 3.

In conclusion, the reduced species, [7,10-*nido*-$C_2B_{10}H_{10}]^{2-}$ (**7,10**) has been shown to isomerise to the thermodynamically more stable [7,9-*nido*-$C_2B_{10}H_{10}]^{2-}$ (**7,9**) by calculations, in agreement with experiment.

A new addition to the family of relatively stable dianionic basket intermediates has been found; the C_1 basket intermediate located in the two step isomerisation pathway between **7,9** and **7,10**, which is less stable than only these two minima; just 3.2 kcal mol^{-1} higher in energy than **7,9** and 1.8 kcal mol^{-1} above **7,10**.

2.4 *Ortho*- and *meta*-carborane reductions

In contrast to the reduction and metallation of *para*-carborane, analogous experiments performed on *ortho*- and *meta*-carborane give just one product – 4,1,6-*closo*-MC$_2$B$_{10}$H$_{12}$, derived from metallation of **7,9**.[11] Previous work by Hermansson *et al.*[10] showed the first optimised geometries of *ortho*-, *meta*- and *para*-carborane with addition of 1e and 2e; the 2e reduced fragment derived from *meta*-carborane (geometry **(6)** in ref. 10) closely resembled **7,9**, whereas all others reported are better described as distorted icosahedra. Our approach, as with the reduction of *para*-carborane, is equivalent to that of Hermansson, *et al.*, though using DFT (BP86/6-31G**).

2.4.1 2e reduction of *meta*-carborane

The 2e reduction of *meta*-carborane (shown in Figure 2.18 and schematically in Figure 2.19(a)) gives **7,9** directly. The reaction profile therefore shows the evolution of the geometry from the optimisation of *meta*-carborane after addition of 2e. As the optimisation is followed, a lengthening of the C1–B3 connection is seen (shown in ***meta*-RED-SS1**). This is followed by further lengthening of the B2–C1 and B6–B3 connections and reformation of the C1–B3 connection, to give the B2–C7–B6–C1–B3–B8 6-membered open face (in ***meta*-RED-SS2**). At this second snap-shot of the optimisation a common picture of a 3-connected B adjacent to C is seen. This is the result of a D-S-D process in the B2–B8–B12–C7 diamond, showing that it is movement of boron atoms (most markedly of B2) that takes place in the relaxation of this structure. Here the final stage of the process is a barrierless D-S-D in the C7–B2–B12–B11 diamond to form **7,9**, where the more stable arrangement with 3-connected C7 is obtained and the C1–B3 connection is shortened again to 1.665 Å.

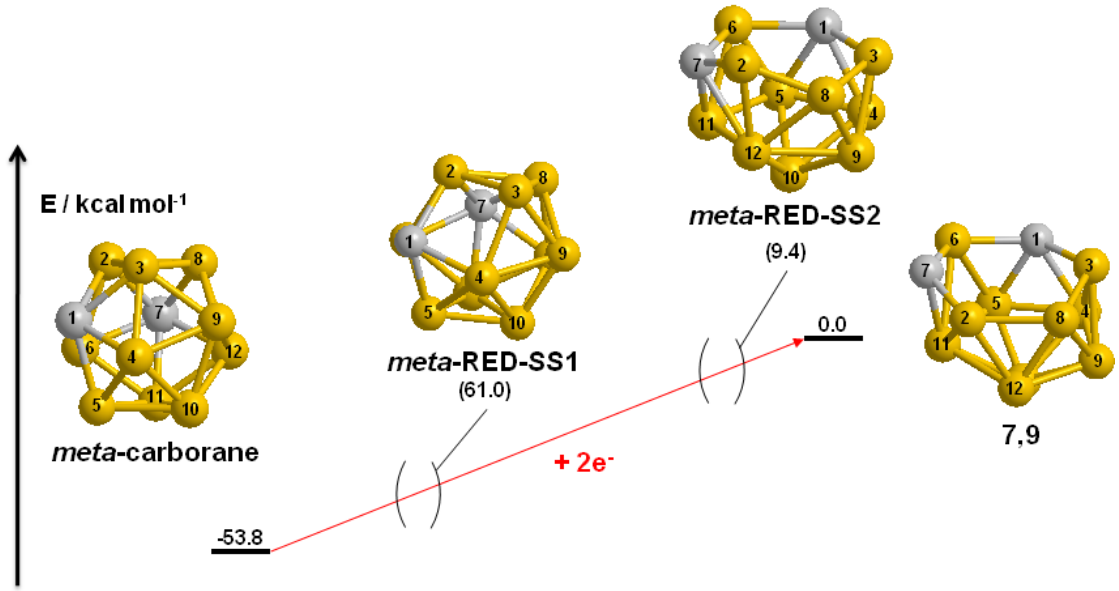

Figure 2.19 - Computed reduction of *meta*-carborane directly giving 7,9.

The optimised structure of the monoanion (shown as a line drawing in Figure 2.19(b)) formed by addition of 1e to *meta*-carborane, has a distorted icosahedral structure, where the icosahedron has partially opened by a lengthening of the C1···B3 connection from 1.720 Å to 2.404 Å. This mirrors to initial behaviour of the direct optimisation of the dianion. A lengthening of the same bond from 1.716 Å to 2.419Å with 1e reduction was previously reported by Hermansson[10] (differences in bond lengths between these studies can be attributed to the differing levels of computational theory adopted).

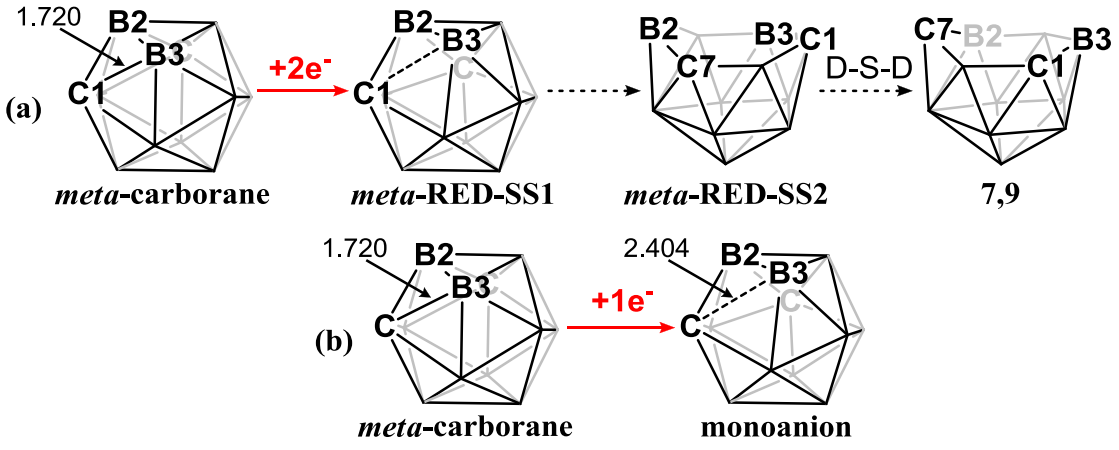

Figure 2.20 – (a) 2e reduction and (b) 1e reduction of *meta*-carborane.

2.4.2 2e reduction of *ortho*-carborane

With the addition of 2e to *ortho*-carborane the C–C bond is preserved throughout the optimisation. This gives **C**, which is the second C_2 symmetric basket intermediate located in this study and has not been characterised previously. The first C_2 basket was **4,7-7,10-INT2** (Figure 2.13), where the bridge was B3–B9 and the carbon vertices

were in symmetrical positions connected to the bridging vertices. Here the structure is analogous since we now have a C1–C2 bridge, C_2 rotational symmetry and two equivalent 5-membered faces. The two carbon atoms then fall into one of the faces by a basket collapse process to give **C-7,9-TS**, where the negative eigenvector shows movement of C1 into and out of the open face with a frequency of -484.5 cm^{-1}. Characterisation of this transition state shows that C1 moves directly into its position seen in **7,9**. This transition state and its transformation along the reaction coordinate to give **7,9** is very similar in geometry to **7,9-C_1INT-TS** (Figure 2.17). However, **C-7,9-TS** is 32.5 kcal mol^{-1} higher in energy than **7,9-C_1INT-TS**. The only major structural difference between these saddle points and presumably the source of the relative instability of **C-7,9-TS** appears to be the disconnection exhibited in B5···B11 at 2.135 Å, which is 0.177 Å longer than the same connection in **7,9-C_1INT-TS**, possibly introducing strain into the structure. The result of this is that the transition state is less product-like and so is less stable, given that **7,9** is the global minimum of the dianionic potential energy surface.

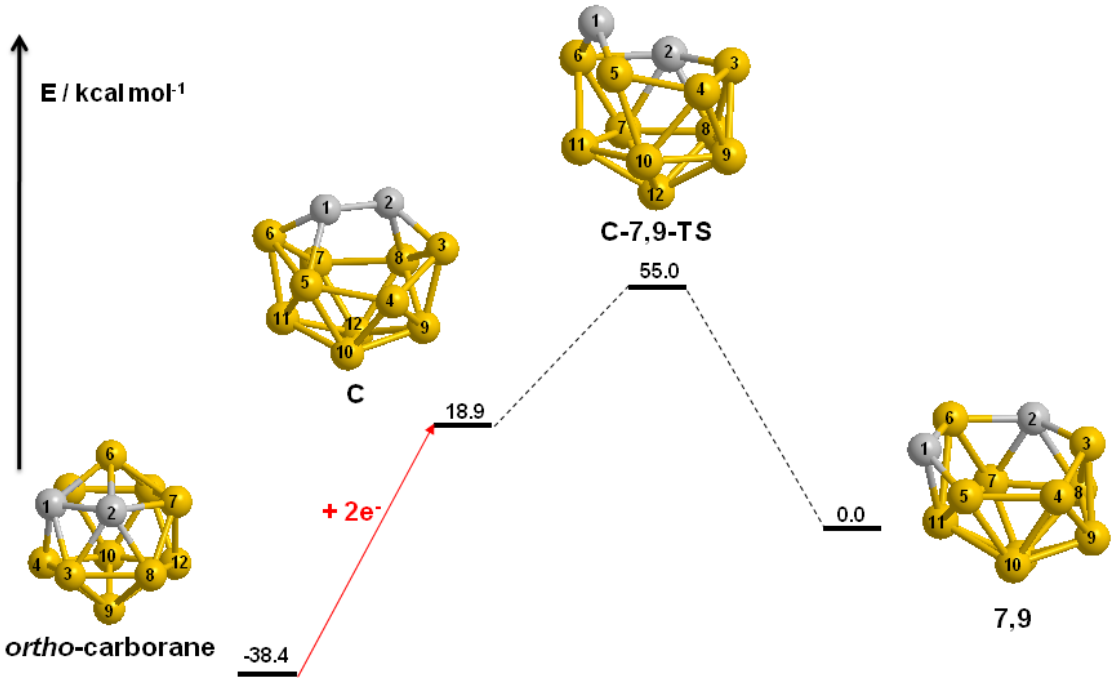

Figure 2.21 – Computed reduction of *ortho*-carborane, giving 7,9 after a single step isomerisation from a basket intermediate, C.

These calculations show that the kinetic product of the $2e^-$ reductions of both *ortho*- and *meta*-carborane is **7,9**. They are therefore in agreement with experiment in that the only *nido* geometry inferred experimentally is **7,9** and it is calculated to be both the kinetic and the thermodynamic product of reduction, the latter, crucially determining that there is no further isomerisation after formation of **7,9**.

The reduction of *ortho*-carborane has again added to the library of basket intermediates and as well as an associated process of basket collapse to a *nido* fragment geometry.

2.5 Oxidation of dianionic [*nido*-$C_2B_{10}H_{12}]^{2-}$ species

Collation of the pre-2007 literature on the thermal isomerisation of neutral 12-vertex carboranes, together with their reported REDOX chemistry gives Figure 2.21, below, where *para*-carborane is reduced to **7,10**,[15] which in turn is oxidised to *meta*-carborane,[16] *ortho*- and *meta*-carborane are reduced to **7,9**[11] which is oxidised to *ortho*-carborane.[2]

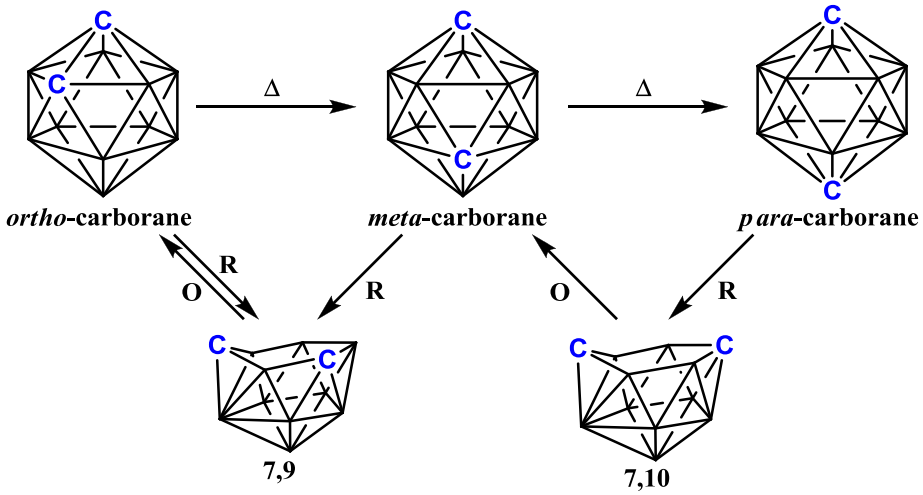

Figure 2.22 – Literature picture of thermal isomerisation and REDOX chemistry of carboranes.

In this study, the reduction of *para*-carborane has been shown, computationally, to be much more complex than previously thought, whereas the computational reduction of *ortho*- and *meta*-carboranes is in agreement with historical data. The next step was to investigate the oxidation processes to complete the updated picture.

The oxidation and subsequent isomerisations of **7,9** and **7,10** were investigated since these species are the most stable dianionic *nido* intermediates. The remaining *nido* fragments listed previously, along with [7,8-*nido*-$C_2B_{10}H_{12}]^{2-}$, from which the precursor to the first 13-vertex carborane was derived,[17] were investigated in terms of their first 2e oxidised intermediate only, where the energy difference between that and the *nido* geometry is defined as ΔE_{OX}. This allowed for a ranking of the dianions in terms of their reducing potential (see Figure 2.22).

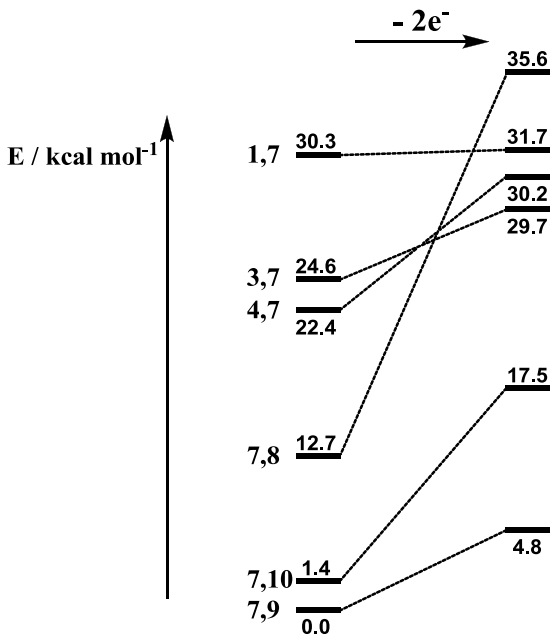

Figure 2.23 - First steps in the oxidation of nido fragments. Energies in kcal mol^{-1}.

From the above schematic, one may conclude that the oxidations of **1,7**, **3,7** and **7,9** are relatively facile, with ΔE_{OX} = +1.4, +5.1 and +4.8 kcal mol^{-1} respectively. Oxidation of **4,7** is intermediate in terms of ΔE_{OX} = +7.8 kcal mol^{-1}. **7,10** has a large ΔE_{OX} = +16.1 kcal mol^{-1} and the largest computed is that for **7,8** at ΔE_{OX} = +22.9 kcal mol^{-1}

This provides an important insight into the stability of the dianions towards oxidation. Oxidation is thought to be in competition with capitation, preventing the formation of 13-vertex carboranes. This is illustrated well by the reduction of *ortho*-carborane or *meta*-carborane to give **7,9**, followed by additions of $\{BH\}^{2+}$, $\{Sn\}^{2+}$ and $\{CpCo\}^{2+}$ as capitating fragments. When $\{BH\}^{2+}$ is added, *ortho*-carborane is produced, not a 13-vertex carborane, suggesting that oxidation occurs. When $\{CpCo\}^{2+}$ is added, 4-Cp-4,1,6-*closo*-$CoC_2B_{10}H_{12}$ is formed, showing capitation to be successful, whilst the addition of $\{Sn\}^{2+}$ produces a *ca.* 50:50 mixture of the capitated 4,1,6-*closo*-$SnC_2B_{10}H_{12}$ species and the oxidised *ortho*-carborane.

With gas phase calculations such as those performed in this study it is not viable to study the mechanism of capitation of the dianionic carborane fragments by dicationic capitating fragments. This is due to the nature of the extremely large energy difference between these ionic species at infinite separation and at bound distances. Consequently an unrealistic model of the experimental system, which is largely dependent on solvent, would be produced.

Hence, these calculations use the benchmark that 1,2-μ$(CH_2)_3$-1,2-*closo*-$C_2B_{10}H_{10}$ may be reduced to [7,8-μ$(CH_2)_3$-7,8-*nido*-$C_2B_{10}H_{12}]^{2-}$ and subsequently capitated with a $\{BPh\}^{2+}$ fragment, where μ$(CH_2)_3$ is a tether used to prevent the C–C connection from breaking with reduction. The oxidation reaction thought to be competing with this successful capitation is approximated by ΔE_{OX} of [7,8-*nido*-$C_2B_{10}H_{12}]^{2-}$ (μ$(CH_2)_3$ replaced by H) which, is +22.9 kcal mol^{-1} (see Figure 2.22, above).

Substituent effects upon ΔE_{OX} were investigated in attempting to discover a derivatives of **7,9** with a $\Delta E_{OX} \geq 22.9$ kcal mol^{-1} (where the underivatised form exhibits ΔE_{OX} = +4.8 kcal mol^{-1}). The overall aim of this work was to provide data to experimental workers to allow the production of an untethered 13-vertex carborane by a new synthetic route. The results of that work are discussed in Chapter 3.

2.5.1 Oxidation of [7,9-*nido*-$C_2B_{10}H_{12}]^{2-}$

The procedure adopted in computing the oxidation processes was equivalent to the reduction calculations in that both stepwise (removal of 1e followed by optimisation then removal of the second electron and optimisation) and direct 2e oxidations were calculated. It was concluded that the oxidation procedure had no effect on the nature of the final minimum located.

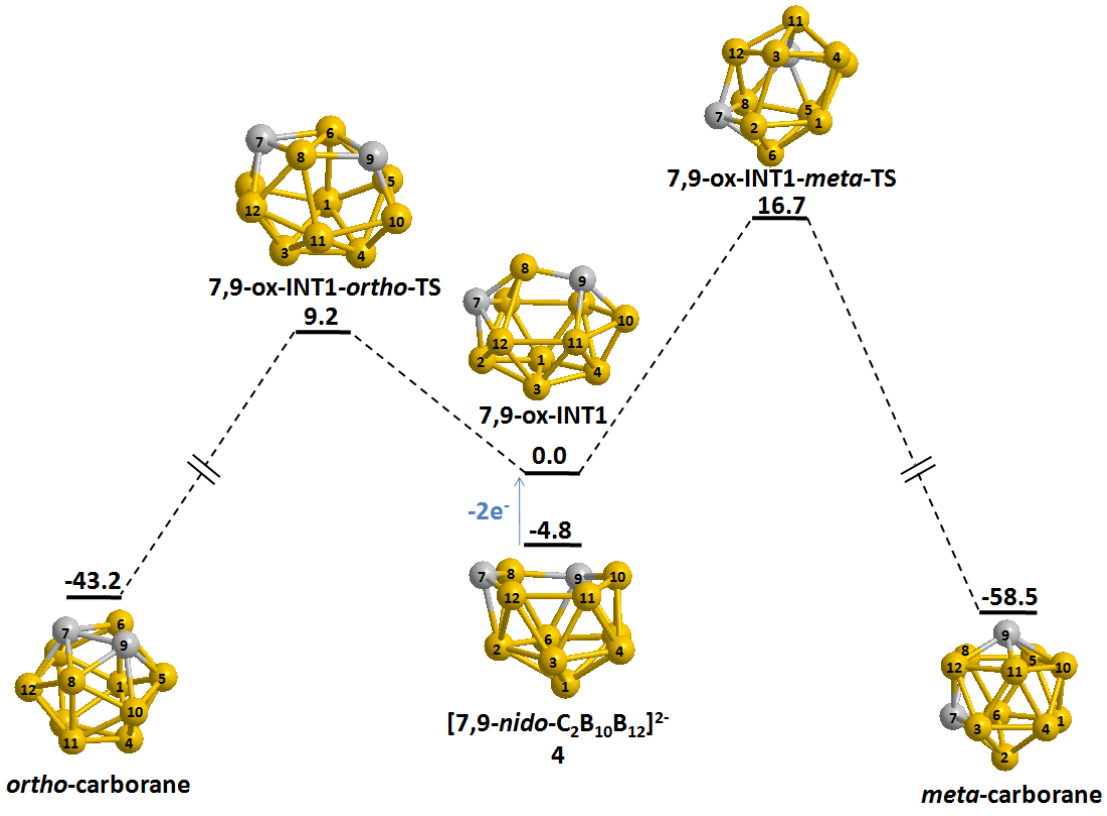

Figure 2.24 - Oxidation of 7,9, giving a basket intermediate, then *ortho*-carborane and *meta*-carborane through respective barriers of 9.2 and 16.7 kcal mol^{-1}.

In the case of 2e oxidation of **7,9** (Figure 2.23), on removal of 2e and optimisation a C_s symmetric, neutral basket intermediate, **7,9-ox-INT1** (E = 0.0), was located. The basket intermediate was subjected to a mode following calculation, which located **7,9-ox-INT1-*ortho*-TS** at +9.2 kcal mol^{-1} which in turn was found by IRC calculations to connect the basket to *ortho*-carborane. In this process, the bridge of the basket intermediate first rotates to form the C7–B6–C9–B8 diamond with lengthened connections to the rest of the vertices in the C_2 transition state. From **7,9-ox-INT1-*ortho*-TS** there is a D-S-D process in this diamond, resulting in the formation of the C–C bond as well as the B8–B10 and B2–B6 connections seen in *ortho*-carborane.

To locate a pathway to *meta*-carborane, QST2 calculations were adopted, where the input geometries used were **7,9-ox-INT1** as the reactant and *meta*-carborane as the product. The transition state, **7,9-ox-INT1-*meta*-TS**, was located, corresponding to the transition states of two concerted D-S-D processes in the C7–B12–B3–B2 and B2–B3–B4–B1 diamonds.

The neutral intermediate, **7,9-ox-INT1** as well as **7,9-ox-INT1-*meta*-TS** were located by Brown and McKee as part of a non-TFR pathway for isomerisation of *ortho*- to *meta*-carborane.[7] However their pathway from *ortho*-carborane to the basket involved a *closo-nido-closo* process far higher in energy than **7,9-ox-INT1-*ortho*-TS** with $\Delta E^{\ddagger}$ = 43.2 kcal mol^{-1} *cf.* 9.2 kcal mol^{-1} in the above pathway. The result, therefore, is that the route presented above, *via* **7,9-ox-INT1** represents the lowest energy process so far characterised for the thermal isomerisation from *ortho*- to *meta*-carborane.

Overall the oxidation of **7,9** is in agreement with experiment since the lower energy process characterised gives *ortho*-carborane.[18]

2.5.2 Oxidation of [7,10-*nido*-$C_2B_{10}H_{12}$]$^{2-}$

The computational oxidation of **7,10** did not give as straightforward a picture as that shown in Figure 2.23. The initial optimised minimum after removal of 2e was a pseudo-*nido* geometry, **7,10-ox-INT1** (E = 0.0), that is it exhibits a *nido*-like topology, but has the 2*n*+2 skeletal electron count of a *closo* compound.[19] Pathways were subsequently located to all three *closo* isomers, where that to *ortho*-carborane was the lowest in energy with $\Delta E^{\ddagger}$ = 2.2 kcal mol^{-1} (see Figure 2.24). Formations of *meta*- and *para*-carboranes have the same initial step and lower energy subsequent steps and so have the same overall energy barrier of $\Delta E^{\ddagger}$ = 4.5 kcal mol^{-1}.

Performing scans across the 6-membered open face of the pseudo-*nido* **7,10-ox-INT1** produced the initial transition states shown, where scanning the C7–C10 distance and optimising the located maximum for a transition state gave **INT1-*ortho*-TS**. Here the C7–B2 connection has lengthened from 1.873 Å to 2.168 Å. From **INT1-*ortho*-TS** to *ortho*-carborane C7 moves into the face of the pseudo-*nido* geometry and closes the cage, directly forming *closo ortho*-carborane. Alternatively, scanning a coordinate diagonally across the face between B8 and B11 resulted in the location of **INT1-INT2-TS**. Here the B8–B2 connection has been lengthened from 1.995 Å in **7,10-ox-INT1** to 2.467 Å. The face is then closed as B8 and B9 form connections to B12 and B11, giving **7,10-ox-INT2**, where both C vertices are 4-connected and two boron vertices (B3 and B11) are 6-connected. This geometry and subsequent geometries in the right-hand-side of the pathway as shown were located by Brown and McKee in their non-TFR pathway for *meta*- to *para*-carborane isomerisation.[7]

7,10-ox-INT2 was first seen by Wales,[3] as the "$\mathbf{C_2}$ intermediate" in the isomerisations of neutral carboranes. Wales originally characterised two step pathways from $\mathbf{C_2}$ to *ortho*-, *meta*- and *para*-carborane, in contrast to the one step pathways here and by Brown and McKee. As predicted by Wales, **7,10-ox-INT2**, is more stable than the open-faced, pseudo-*nido* **7,10-ox-INT1** geometry. **7,10-ox-INT2** can also be related to the neutral basket located in the oxidation of [7,9-*nido*-$C_2B_{10}H_{12}]^{2-}$, **7,9-ox-INT1**, with rows of 2, 6 and 4 vertices. However, **7,10-ox-INT2** does not exhibit any 4-membered faces, possibly due to the relative positions of the carbon-based vertices, where neither are in the 2-vertex row.

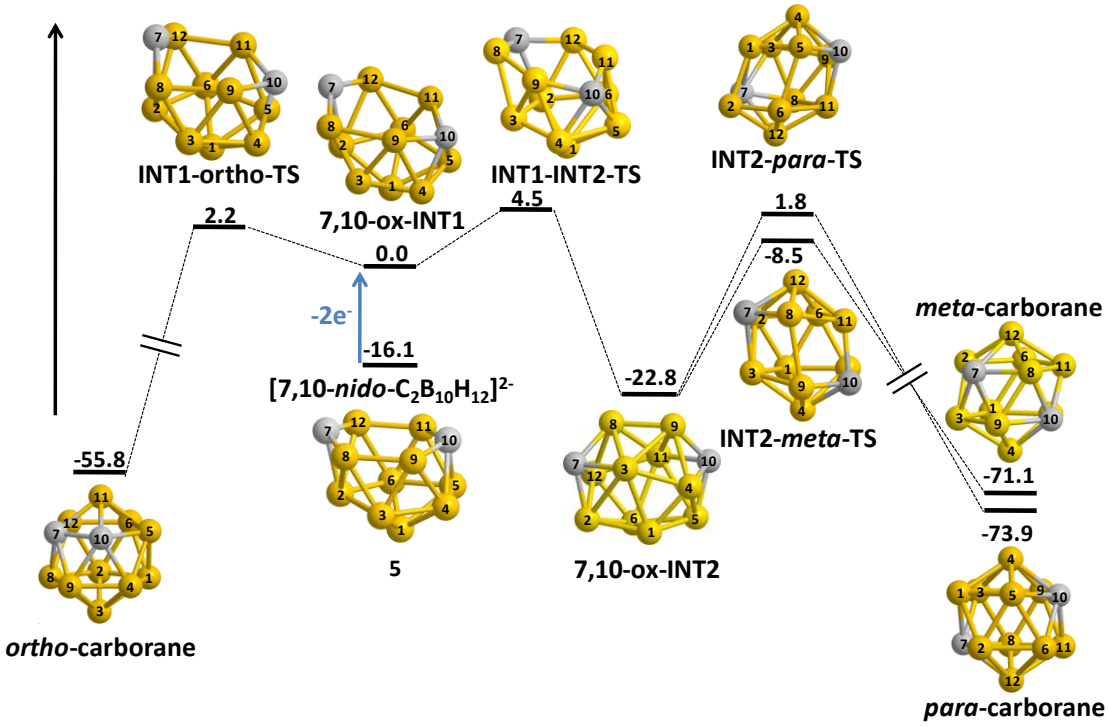

Figure 2.25 – Oxidation of 7,10, initially giving a pseudo-*nido* intermediate

The transformations giving *meta*- and *para*-carborane, located through QST2 calculations from **7,10-ox-INT2** and appropriately numbered *meta*- and *para*-carborane cages, each involve two concerted D-S-D processes. These either bring the C vertices closer together by D-S-D processes in the C7–B8–B9–B3 and B8–B11–C10–B9 diamonds to form *meta*-carborane, or maintain the distance between C atoms during the double D-S-D in the B1–B5–B6–B2 and B5–C10–B11–B6 diamonds to form *para*-carborane. In each case the overall symmetry is increased, from C_2 in the basket intermediate to C_{2v} in *meta*-carborane or D_{5d} in *para*-carborane.

These double D-S-D processes are equivalent to that giving the formation of *meta*-carborane from **7,9-ox-INT1** and, indeed, were located through the same QST2 methodology. Though the formations of *meta*- and *para*-carboranes have the same energy barrier in terms of the oxidation, the activation energy required for the formation of *meta*-carborane from **7,10-ox-INT2** is lower.

To form **INT2-*para*-TS** from **7,10-ox-INT2**, there is an initial lengthening of the B1–B6 and B5···B11 connections (1.790 Å and 2.119 Å respectively in **7,10-ox-INT2** and 2.274 Å and 2.387 Å respectively in **INT2-*para*-TS**) at the bottom of the basket as shown in Figure 2.24. As the D-S-D processes proceed, the B5···B2 and C10···B6 distances are shortened from 2.853 Å and 2.678 Å respectively in **INT2-*para*-TS** to give *para*-carborane, where B5–B2 is 1.775 Å and C10–B6 is 1.714 Å.

Following two similar concerted D-S-D process on the top of the molecule, as viewed in Figure 2.24, gives **INT2-*meta*-TS**, where B3–B8 and B9–B11 have lengthened each from 1.907 Å (since they are equivalent by C_2 symmetry) in **7,10-ox-INT2** to 2.834 Å in the transition state, which maintains the symmetry of the intermediate. The processes are completed as the equivalent C7···B9 and B8···C10 distances shorten from 2.696 Å in **INT2-*meta*-TS** to 1.701 Å in *meta*-carborane.

These processes give insight into the lower energy of **INT2-*meta*-TS** in comparison to **INT2-*para*-TS** as both diamonds involved in the isomerisation to the *meta* product involve the carbon vertices. Therefore the carbon atoms in **INT2-*meta*-TS** have on average fewer connections and boron atoms have more connections on average than in the higher energy transition state to form *para*-carborane. As it has already been seen that the relative stability of carborane isomers increases where carbon adopts low-connected sites within the cage, this hypothesis would appear to apply to the difference in energy barriers seen here.

The conclusion of the computational study is that the oxidation of **7,10** would lead to the formation of *ortho*-carborane. This is in disagreement to experiment which suggests the oxidation produces *meta*-carborane. Since all other computational results support experimentally determined results which show the REDOX chemistry of carboranes to be far more complex than previously thought, these calculations suggest the chemical oxidation should be reinvestigated. Recent work in the group on biscarboranes[20] (see Figure 2.26, below) suggests the concurrent capitation and oxidation of two *nido* fragments of 7,10 topology linked by a C–C connectivity. Such species are formed with 4e reduction of 1,1′-bis(*para*-carborane) by Na in liquid NH_3. On metallation by $\{Ni(dppe)\}^{2+}$ (where 2 equivalents of $Ni(dppe)Cl_2$ are added to the reduced carborane solution) a biscarborane product, 1-[4′-dppe-4′,1′,10′-*closo*-$NiC_2B_{10}H_{11}$]-2-*closo*-$C_2B_{10}H_{11}$, is observed. In this species, one cage has been metallated to give a nickelacarborane of 4,1,10-*closo*-NiC_2B_{10} architecture and the other has been oxidised to produce a 1,2-*closo*-C_2B_{10} architecture, verifying an experimental oxidation route from 7,10 to *ortho*-carborane.

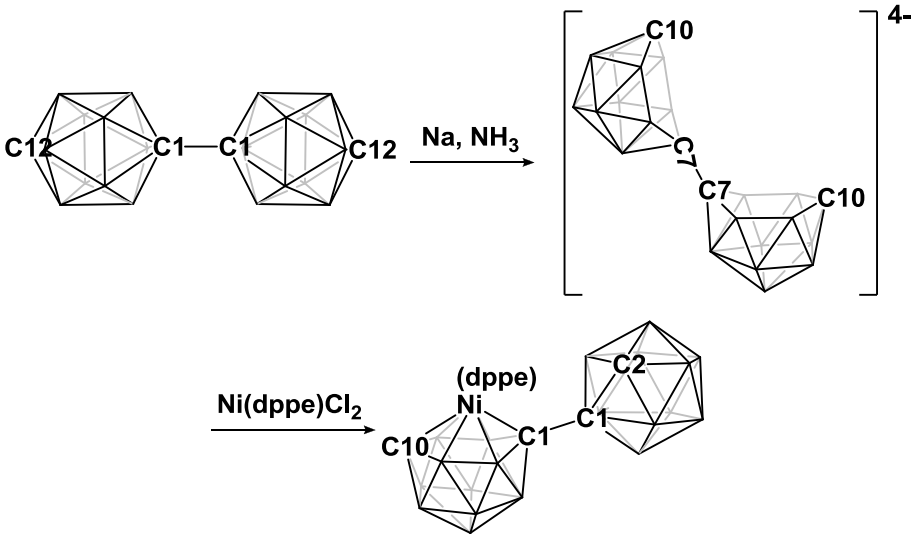

Figure 2.26 – Reduction and metallation/oxidation of 1,1′-bis(*para*-carborane).

The product of metallation, exhibiting a 13-vertex metallacarborane linked to a 12-vertex carborane by a C1–C1′ connection was characterised by ^{11}B NMR and X-Ray crystallography (Figure 2.27). The combination of architectures of both cages implies the reduced species exhibits 7,10-*nido* topology and therefore a link from **7,10** to *ortho*-carborane.

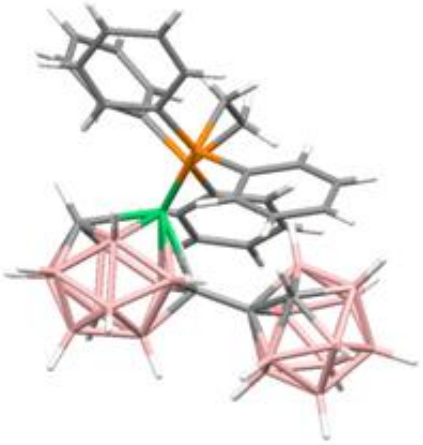

Figure 2.27 – View of the crystallographically characterised product of metallation/oxidation.

2.6 Summary and Conclusions

For completion and to put all of the profiles discussed in this chapter into context, Figure 2.28 was constructed. This figure shows the calculated dianionic carborane potential energy surface (black lines) and the neutral carborane potential energy surface (blue lines). The "connections" between these surfaces in terms of 2e reductions (red arrows) and 2e oxidations (blue arrows) are shown, where these are equivalent to direct or stepwise removal or addition of electrons from the calculation, followed by relaxation of the geometry to the first optimised minimum.

The three neutral isomers, *ortho*-, *meta*- and *para*-carborane, and five dianionic *nido* fragment isomers found are shown on a larger scales than other geometries for clarity. Also highlighted are the new family of "basket intermediates" discovered, where they are shown to be abundant on the dianionic PES (orange caption text) but also appear as intermediates on the neutral PES (green caption text).

Common processes discovered on the dianionic PES are shown in red text; 3-connected boron vertices are seen often as transition states or first intermediates from *nido* fragments. Where basket geometries are found, "basket collapse" is seen as the common process for their loss to the lower energy *nido* fragment.

The TFR transition state located between *ortho*- and *meta*-carborane is shown for comparison with the lower energy pathway discovered in this study through investigation of the oxidation process, where the intermediate is a neutral basket structure.

D-S-D processes have not been labelled on Figure 2.16 due to their being extremely common on both surfaces, they are, however, described in their individual sections.

Finally, an additional, C_2, intermediate is shown, which fits into the **7,9** to **7,10** isomerisation pathway, replacing the C_1 intermediate, depending on the C-substituents used and so will feature in Chapter 3 of this thesis. Although it does not directly connect to other dianionic species located here, it was optimised with an energy of +1.6 kcal mol^{-1} with respect to **7,9**.

In conclusion, the aims of the study described in this chapter have been successfully realised. The isomerisation studies have shown the pathways from previously reported products of *para*-carborane to the remaining concurrently-reported experimental products. A final isomerisation pathway was found to link the two most stable *nido*

carboranes, [7,9-*nido*-$C_2B_{10}H_{12}]^{2-}$ and [7,10-*nido*-$C_2B_{10}H_{12}]^{2-}$. The intermediate in this pathway, along with many others on the dianionic carborane PES were shown to share similar topologies and have been recognised as basket intermediates. A library of common processes in isomerisation of dianionic carboranes has also been built up.

The reductions of *ortho*- and *meta*-carborane were shown to be simpler cases in comparison to the reduction of *para*-carborane, as is indeed the case experimentally, and computed and experimental results are in agreement.

Finally, the oxidation processes producing neutral carboranes were investigated, where historical experimental evidence was compared and contrasted to computational results. The oxidation of the global minimum, **7,9**, was shown, as expected from experimental observation, to yield *ortho*-carborane. A competing pathway was also shown, where *meta*-carborane was produced and this resulted in the construction of the lowest energy pathway known for the thermal isomerisation from *ortho*- to *meta*-carborane.

Oxidation of **7,10**, however, did not shown an agreement with experiment, where *meta*-carborane is the sole reported product. Here, the computed pathways see the production of *ortho*-carborane by a very low barrier, 2.2 kcal mol^{-1}, as well as *meta*- and *para*-carboranes with an overall barrier of 4.5 kcal mol^{-1}, suggesting all three would be found experimentally. This leads to the possibility that the experimental environment favours the formation of *meta*-carborane in a way that is not modelled computationally.

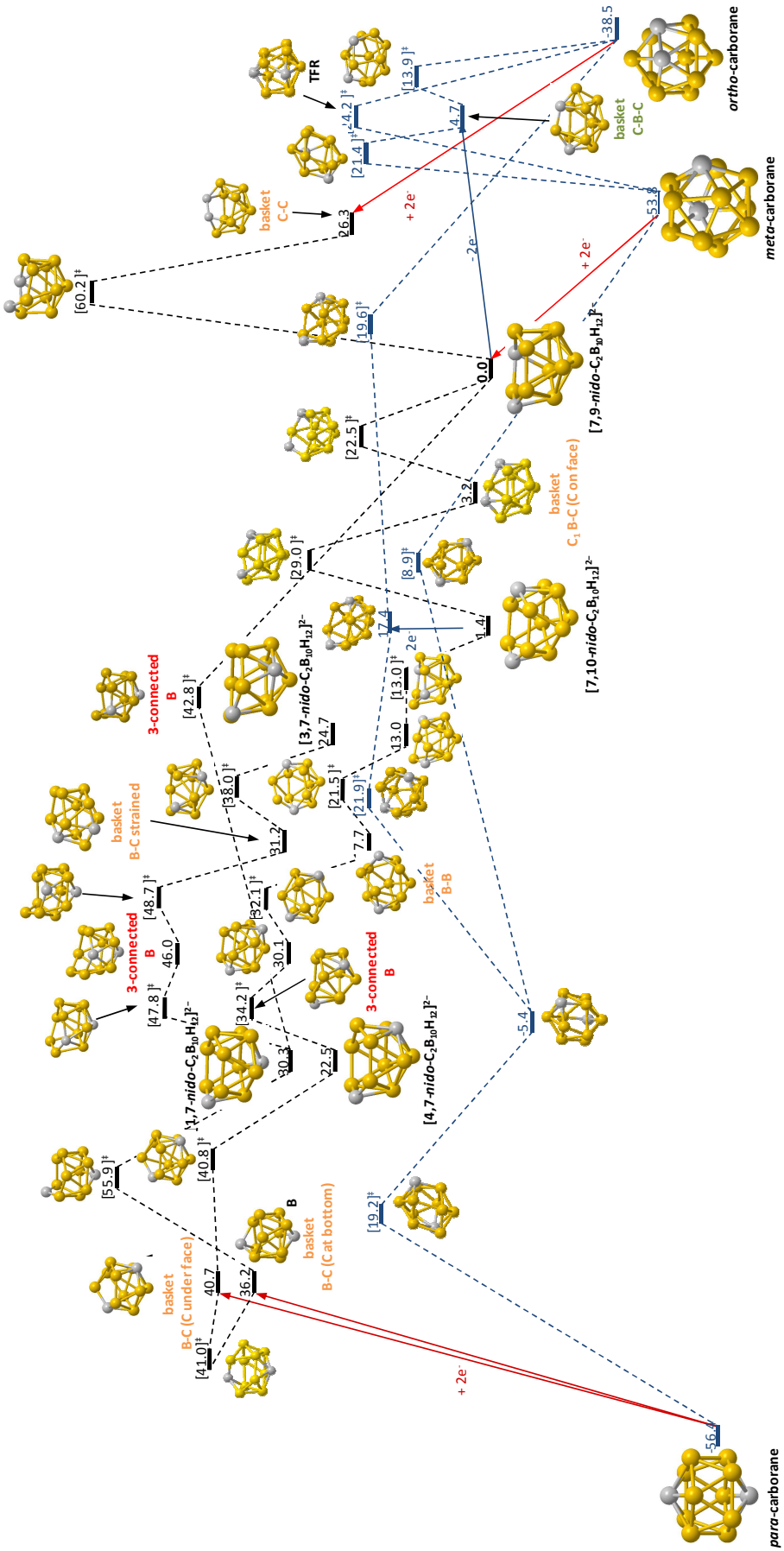

Figure 2.28 – The superimposed potential energy surfaces for dianionic (black lines) and neutral (blue lines) carboranes, with energies in kcal mol^{-1} relative to [7,9-*nido*-$C_2B_{10}H_{12}$]$^{2-}$.

2.7 References

1. W. N. Lipscomb, *Science*, 1966, **153**, 373-378.
2. L. I. Zakharkin and V. N. Kalinin, *Dokl. Akad. Nauk SSSR*, 1966, **169**, 590.
3. D. J. Wales, *J. Am. Chem. Soc.*, 1993, **115**, 1557-1567.
4. a) J. Baker, *J. Comp. Chem.*, 1986, **7**, 385-395; b) J. Baker, *J. Comp. Chem.*, 1987, **8**, 563-574.
5. M. J. Frisch, G. W. Trucks, H. B. Schlegel, G. E. Scuseria, M. A. Robb, J. R. Cheeseman, J. A. Montgomery, Jr., T. Vreven, K. N. Kudin, J. C. Burant, J. M. Millam, S. S. Iyengar, J. Tomasi, V. Barone, B. Mennucci, M. Cossi, G. Scalmani, N. Rega, G. A. Petersson, H. Nakatsuji, M. Hada, M. Ehara, K. Toyota, R. Fukuda, J. Hasegawa, M. Ishida, T. Nakajima, Y. Honda, O. Kitao, H. Nakai, M. Klene, X. Li, J. E. Knox, H. P. Hratchian, J. B. Cross, V. Bakken, C. Adamo, J. Jaramillo, R. Gomperts, R. E. Stratmann, O. Yazyev, A. J. Austin, R. Cammi, C. Pomelli, J. W. Ochterski, P. Y. Ayala, K. Morokuma, G. A. Voth, P. Salvador, J. J. Dannenberg, V. G. Zakrzewski, S. Dapprich, A. D. Daniels, M. C. Strain, O. Farkas, D. K. Malick, A. D. Rabuck, K. Raghavachari, J. B. Foresman, J. V. Ortiz, Q. Cui, A. G. Baboul, S. Clifford, J. Cioslowski, B. B. Stefanov, G. Liu, A. Liashenko, P. Piskorz, I. Komaromi, R. L. Martin, D. J. Fox, T. Keith, M. A. Al-Laham, C. Y. Peng, A. Nanayakkara, M. Challacombe, P. M. W. Gill, B. Johnson, W. Chen, M. W. Wong, C. Gonzalez and J. A. Pople, *Gaussian 03*, *Revision D.01*, Gaussian, Inc., Wallingford CT, 2004.
6. a) P. Császár and P. Pulay, *J. Mol. Struct.*, 1984, **114**, 31-34; b) Ö. Farkas, *PhD (CsC) Thesis*, Eötvös Loránd University and Hungarian Academy of Sciences, 1995; c) O. Farkas and H. B. Schlegel, *J. Chem. Phys.*, 1999, **111**, 10806-10814.
7. C. A. Brown and M. L. McKee, *J. Mol. Model.*, 2006, **12**, 653-664.
8. a) A. D. Becke, *J. Chem. Phys.*, 1993, **98**, 5648-5652; b) C. Lee, W. Yang and R. G. Parr, *Phys. Rev. B*, 1988, **37**, 785-789; c) P. J. Stephens, F. J. Devlin, C. F. Chabalowski and M. J. Frisch, *J. Phys. Chem.*, 1994, **98**, 11623-11627; d) S. H. Vosko, L. Wilk and M. Nusair, *Can. J. Phys.*, 1980, **58**, 1200-1211.
9. K. Wade, *J. Chem. Soc. D*, 1971, 792-793.
10. K. Hermansson, M. Wójcik and S. Sjöberg, *Inorg. Chem.*, 1999, **38**, 6039-6048.
11. G. B. Dunks, R. J. Wiersema and M. F. Hawthorne, *J. Am. Chem. Soc.*, 1973, **95**, 3174-3179.
12. S. Zlatogorsky, M. J. Edie, D. Ellis, S. Erhardt, M. E. Lopez, S. A. Macgregor, G. M. Rosair and A. J. Welch, *Angew. Chem. Int. Ed.*, 2007, **46**, 6706-6709.

13. S. Zlatogorsky, D. Ellis, G. M. Rosair and A. J. Welch, *Chem. Commun.*, 2007, 2178-2180.
14. a) M. A. Laguna, D. Ellis, G. M. Rosair and A. J. Welch, *Inorg. Chim. Acta*, 2003, **347**, 161-167; b) A. Burke, D. Ellis, D. Ferrer, D. L. Ormsby, G. M. Rosair and A. J. Welch, *Dalton Trans.*, 2005, 1716-1721.
15. D. Ellis, M. E. Lopez, R. McIntosh, G. M. Rosair, A. J. Welch and R. Quenardelle, *Chem. Commun.*, 2005, 1348-1350.
16. V. I. Stanko, Y. V. Gol'tyapin and V. A. Brattsev, *J. Gen. Chem. USSR*, 1969, 1142.
17. A. Burke, D. Ellis, B. T. Giles, B. E. Hodson, S. A. Macgregor, G. M. Rosair and A. J. Welch, *Angew. Chem.-Int. Edit.*, 2003, **42**, 225-228.
18. B. W. Hutton, F. MacIntosh, D. Ellis, F. Herisse, S. A. Macgregor, D. McKay, V. Petrie-Armstrong, G. M. Rosair, D. S. Perekalin, H. Tricas and A. J. Welch, *Chem. Commun.*, 2008, 5345-5347.
19. M. A. Fox and K. Wade, *Pure Appl. Chem.*, 2003, **75**, 1315-1323.
20. D. Ellis and A. J. Welch, *Unpublished Results*.

Chapter 3 – C-Substituent Effects in Carborane REDOX Chemistry

3.1. Introduction

3.1.1. Common carborane substituents

The use of carboranes provides flexibility to heteroborane chemistry, in terms of REDOX chemistry, as the carbon vertices give neutral *closo* species, and the carbon centres are readily functionalised. Phenyl and methyl carbon substituents are most commonly used in carborane chemistry. This is a result of the synthesis of the carborane itself, which is formed through reaction of *nido*-decaborane ($B_{10}H_{14}$) with acetylene derivatives. 1,2-dimethylacetylene and 1,2-diphenylacetylene give 1,2-Me_2-1,2-*closo*-$C_2B_{10}H_{10}$ and 1,2-Ph_2-1,2-*closo*-$C_2B_{10}H_{10}$ respectively and reaction with acetylene itself gives *ortho*-carborane. Furthermore, the relative acidity of the C–*H* atoms allows their substitution with, for example, alkyl groups *via* lithiation followed by nucleophilic attack at a C–X bond (X = halide).

The nature of the carbon substituents is generally thought to have little effect on the reactivity of carboranes (for example in thermolysis or REDOX chemistry), however there is experimental evidence for changes in reaction rates with changing C-substituents. In particular, when phenyl C-substituents are used, experiment suggests a reduction in the barrier height for isomerisation from [7,10-Ph_2-7,10-*nido*-$C_2B_{10}H_{10}$]$^{2-}$ to [7,9-Ph_2-7,9-*nido*-$C_2B_{10}H_{10}$]$^{2-}$.[1]

The main reason for having non-hydrogen C-substituents in carborane chemistry is due to the fact that the most effective technique for characterisation of reaction products is X-Ray crystallography. In practice, X-Ray crystallography, which resolves atomic positions in a crystal through providing an electron density map, does not distinguish well between carbon and boron centres. The use of non-hydrogen C-substituents alleviates this issue by unambiguously defining the positions of the carbon vertices.

3.1.2. *Nido* dianion reoxidation versus capitation with {BR}$^{2+}$

The process adopted in producing 13-vertex metallacarboranes is the polyhedral expansion method, where a 12-vertex carborane is first reduced, *via* a 2 electron process, to a dianionic *nido* fragment and is subsequently metallated with a metal fragment, typically {CoCp}$^{2+}$ or {Ru(arene)}$^{2+}$.[2] This has been carried out successfully on many occasions to produce a range of supraicosahedral metallacarboranes. Thus far, however, it has not been possible to use the same chemistry to produce supraicosahedral

carboranes (through capitation with a $\{BR\}^{2+}$ fragment) without the use of an exopolyhedral tether (see Section 3.1.3). Instead, *ortho*-carborane is seen, possibly the result of reoxidation of the *nido* fragment (see Figure 3.1, below). Alternatively, formation of a transient 13-vertex carborane before "boron loss" would give the same result. There is some experimental evidence for this, where an attempt to reduce and capitate *ortho*-carborane with $\{BI\}^{2+}$ (from BI_3) produced a mixture of 1,2-*closo*-$C_2B_{10}H_{12}$ and 3-I-1,2-*closo*-$C_2B_{10}H_{11}$.[3]

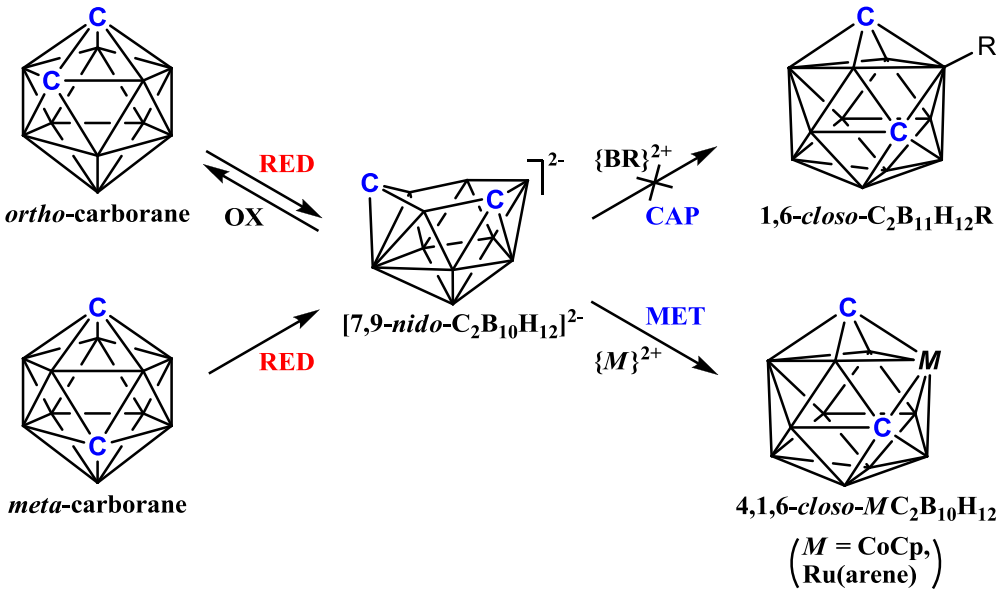

Figure 3.1 – Competition between capitation and reoxidation of 12-vertex carboranes.

As shown in Figure 3.1, the reduction of either *ortho*- or *meta*-carborane (normally done with Li/Na metal in THF in the presence of naphthalene as a charge carrier) produces [7,9-*nido*-$C_2B_{10}H_{12}$]$^{2-}$. Experimental studies have shown that this can then be metallated to give 4,1,6-*closo*-*M*$C_2B_{10}H_{12}$ but cannot be capitated with $\{BR\}^{2+}$. Studies into supraicosahedral main group metallacarboranes, where $\{Sn\}^{2+}$ is used as the metallating fragment in the polyhedral expansion of *meta*-carborane derivatives highlights this competition, where the supraicosahedral 4,1,6-*closo*-SnC_2B_{10} product and *ortho*-carborane formed through reoxidation are seen in a near 1:1 ratio.[4]

Unfortunately it would not be viable to attempt to model either of the capitation or boron loss processes through computational methods. The limitation of the gas phase computational technique is particularly apparent in situations such as this, where the association of two opposing charges is to be modelled, in that their combination will *always* be favourable due to the unrealistic (with respect to solution phase experiment) electrostatic energy contributions. Furthermore there is little insight from experiment as

to the exact nature of the capitating species or the involvement or otherwise of other species present in solution and the solvent itself.

Where calculations can provide useful data to experimental co-workers is in the oxidation process (as described in Chapter 2, Section 2.5) and how this is affected by changes in the carbon substituents.

The role of the calculations, therefore, would be to aid the discovery of substituents that disfavour oxidation while favouring the unknown capitation process and, if possible, be readily available. An added challenge also exists, where the initial carborane derivative (be it of *ortho*- or *meta*-carborane) must, of course, remain chemically reducible.

3.1.3. *Ortho*-tethered carboranes

The use of an exopolyhedral μ-($C_6H_4(CH_2)_2$) tether, whereby the cage C atoms are linked, led to the formation of the first supraicosahedral carborane.[3] The tether prevents the carbon atoms from moving apart upon reduction, giving the [7,8-μ-($C_6H_4(CH_2)_2$)-7,8-*nido*-$C_2B_{10}H_{10}$]$^{2-}$ fragment. This was verified experimentally by protonation of the *nido* dianion to form [7,8-μ-($C_6H_4(CH_2)_2$)-7,8-*nido*-$C_2B_{10}H_{11}$]$^{-}$, which was characterised crystallographically. The {BPh}$^{2+}$ fragment (from $BPhCl_2$) was used to capitate the *nido* dianion, forming henicosahedral 4-Ph-1,2-μ-($C_6H_4(CH_2)_2$)-1,2-*closo*-$C_2B_{10}H_{10}$. A second, more simple μ-$(CH_2)_3$ *ortho*-tether was adopted in producing a further series of supraicosahedral metallacarboranes with adjacent carbon vertices.[5]

The main limitation of the *ortho*-tether is that the supraicosahedral carborane formed is constrained by the tether to have adjacent carbon vertices, which is known to be relatively less stable than isomers where the carbon atoms are apart. Since the ultimate aim is to produce clusters of 14, 15, 16, or more vertices, alternative routes to a 13-vertex carborane were sought. With this limitation in mind, Xie *et al.*[6] developed a silyl tether (μ-($SiMe_2(CH_2)_2$) which produced the same henicosahedral 13-vertex architecture as the previous hydrocarbyl-based *ortho*-tethers with the important exception that the tether is readily lost upon chromatography on silica. The first example of an untethered 13-vertex carborane, 1,2-Me_2-1,2-$C_2B_{11}H_{11}$, was so produced. Welch *et al.*[7] later used the silyl tether to produce 4-indenyl-1,2-Me_2-$CoC_2B_{10}H_{10}$, the first example of an untethered supraicosahedral metallacarborane with adjacent C vertices.

There are two major effects the *ortho*-tether has on the carborane cage. The first is that the flexibility of the cage is reduced. The second is that the stability of the reduced

species towards oxidation is increased, where the computed reducing potential of [7,8-μ$(CH_2)_3$-7,8-*nido*-$C_2B_{10}H_{12}]^{2-}$ is large (35.4 kcal mol^{-1}) *cf.* that of [7,9-*nido*-$C_2B_{10}H_{12}]^{2-}$ (4.8 kcal mol^{-1}) as seen in Chapter 2, Section 2.5. Either of these may be the effect that allows capitation of the reduced species to occur. Therefore both were investigated in order to design systems that allow capitation, but do not suffer from the limitation of *ortho*-tethered carboranes of having adjacent carbon-based vertices.

3.1.4. Possible alternative solutions

In view of the oxidation pathway of the 'carbons apart' [7,9-*nido*-$C_2B_{10}H_{12}]^{2-}$ fragment, which sees formation of *ortho*-carborane, one possible solution may be to prevent the carbon vertices from coming together. To investigate this reduction in carborane flexibility, systems with i) bulky carbon substituents and ii) a '*meta*-tether' were designed.

The effect of the reducing potential of the *nido*-carborane was investigated by changing the R groups in [7,9-R_2-7,9-*nido*-$C_2B_{10}H_{10}]^{2-}$, with the aim of finding substituents that cause an increase in the reducing potential, with a target value of 35.4 kcal mol^{-1}.

Before attempting to design new carborane substituents, however, the general assumption that phenyl substituents have little effect on carborane reactivity was to be tested. This was done by characterising the computational reductions of diphenyl-*ortho*- and diphenyl-*meta*-carboranes.

3.2. Reductions of diphenyl-*ortho*- and diphenyl-*meta*-carboranes

Phenyl groups are commonly used carborane C-substituents. They have been shown to lower isomerisation barriers in reduced species[1] and many examples of supraicosahedral (metalla)carboranes contain $\{CPh\}^+$ vertices.

In order to increase the understanding of the effects that phenyl C-substituents have on carboranes, particularly in their REDOX chemistry, the reductions of diphenyl-*ortho*- and diphenyl-*meta*-carborane were computed for comparison with their unsubstituted analogues, described in Chapter 2, Section 2.2.9. The complex reduction pathways of *para*-carborane were not fully recomputed with phenyl C-substituents, however their effect on the [7,10-*nido*-C_2B_{10}]$^{2-}$ to [7,9-*nido*-C_2B_{10}]$^{2-}$ isomerisation was investigated for comparison with experimental observations.

3.2.1. 2e reduction of diphenyl-*ortho*-carborane

In the case of unsubstituted *ortho*-carborane, it was shown that reduction proceeds to give a C_2 symmetrical basket intermediate where the key result was preservation of the C1–C2 connection. The single-step pathway to [7,9-*nido*-$C_2B_{10}H_{12}$]$^{2-}$ then involved breaking of this C–C bond with rearrangement of the cage to give a 6-membered open face, where the isomerisation barrier, after 2e reduction, was 36.1 kcal mol^{-1}. The two electron reduction of diphenyl-*ortho*-carborane was computed and is shown in Figure 3.2, below.

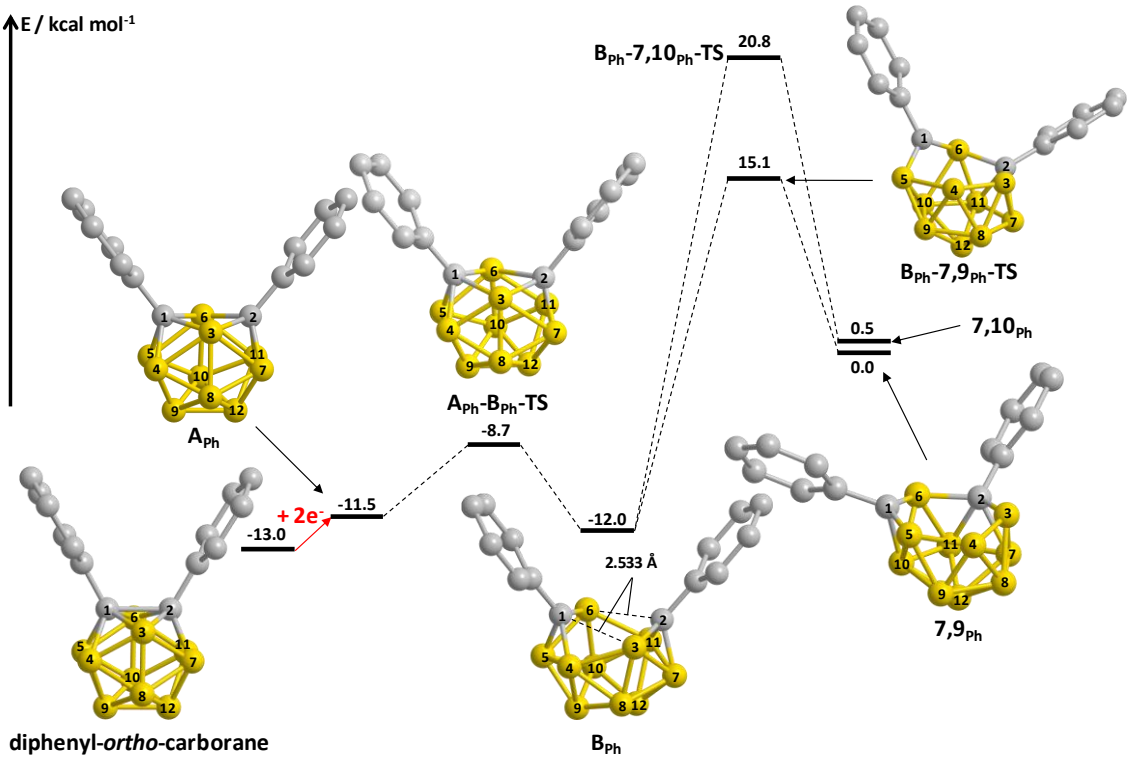

Figure 3.2 – 2e reduction of diphenyl-*ortho*-carborane.

In stark contrast with the pathway computed for *ortho*-carborane reduction, the bond initially broken by the addition of 2e to diphenyl-*ortho*-carborane was the C–C connection, where the C–C distance of 1.786 Å is increased to 2.524 Å in $\mathbf{A_{Ph}}$. The computed energy change on reduction is relatively small in the case of diphenyl-*ortho*-carborane at $\Delta E = +1.5$ kcal mol^{-1} *cf.* $\Delta E = +57.3$ kcal mol^{-1} in *ortho*-carborane. $\mathbf{A_{Ph}}$ is C_{2v} symmetric and it was found that lowering the symmetry to C_2 gave intermediate $\mathbf{B_{Ph}}$, in which the C1–B3 and C2–B6 connections were lengthened from 1.719 Å to 2.533 Å through an energy barrier of $\Delta E^{\ddagger} = 2.8$ kcal mol^{-1}. $\mathbf{B_{Ph}}$ is closely related to **7,10-7,9-C$_1$INT**, seen in Chapter 2, Figure 2.17, by shortening of the C2···B6 connection and so isomerisations from it to $\mathbf{7,9_{Ph}}$ and $\mathbf{7,10_{Ph}}$ were sought. Similar to **7,10-7,9-C$_1$INT**, $\mathbf{B_{Ph}}$ is shown to be an intermediate in the isomerisation pathway connecting $\mathbf{7,9_{Ph}}$ and $\mathbf{7,10_{Ph}}$ however in this case it is more stable than the open-faced *nido* species. This corroborates the experimental result first seen by Tolpin and Lipscomb in 1973[8] that in reducing and protonating a diphenyl-carborane, the resulting monoanion can be crystallised and shows a partially ejected {CHPh} fragment bridging two boron vertices of a Ph-$CB_{10}H_{10}$ cage (see Figure 3.3, below). This represents the first computational insight into the formation of this structure.

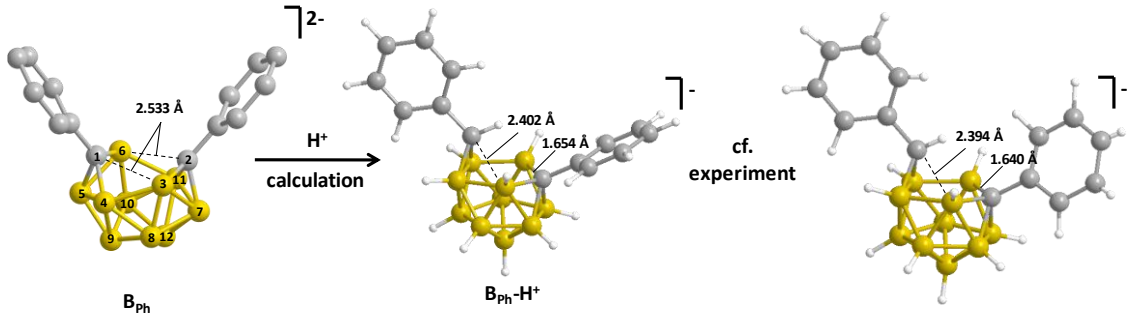

Figure 3.3 – Computational protonation of B_{Ph} in comparison with the crystallographically determined structure of reduced and protonated diphenyl-carborane.

As discussed in Chapter 2, the isomerisation of **7,10$_{Ph}$** to **7,9$_{Ph}$** at room temperature was suggested, where the reduction and metallation of 1,12-Ph_2-1,12-$C_2B_{10}H_{10}$ afforded products of metallation of **7,9$_{Ph}$** rather than the expected metallation of **7,10$_{Ph}$**.[1] The computational results, however, suggest the nature of the reduced species is different to that expected. The true reason for metallation of **7,9$_{Ph}$** over **7,10$_{Ph}$** experimentally may be down to population of **B$_{Ph}$** as the global minimum. This species may not be liable to metallation as it does not exhibit a 6-membered open face. Therefore, isomerisation to **7,9$_{Ph}$** and **7,10$_{Ph}$** may occur upon metallation. These results therefore suggest that phenyl C-substituents, used commonly in carborane chemistry, may have a larger effect on carborane reactivity than previously thought.

*3.2.1.1. Why do diphenyl-*ortho*-carborane and* ortho*-carborane have different mechanisms of reduction?*

The origin of the different way in which diphenyl-*ortho*-carborane distorts on reduction, in comparison with *ortho*-carborane, was then investigated. This was done pictorially, in terms of the frontier molecular orbitals (FMOs) of neutral *ortho*- and diphenyl-*ortho*-carborane. Components of the LUMO that had bonding contributions between a pair of atoms were suggested as initially strengthening their interaction upon addition of an electron, whereas a component of the orbital between two atoms with anti-bonding character was thought to initially weaken the interaction.

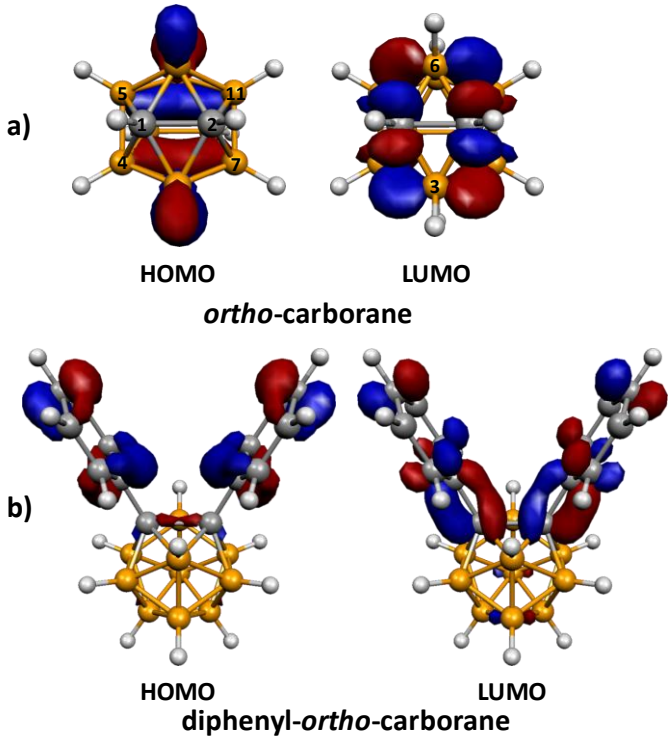

Figure 3.4 – Frontier molecular orbitals of *ortho*- and diphenyl-*ortho*-carborane.

Figure 3.4, above, shows the FMOs of *ortho*- and diphenyl-*ortho*-carborane. The HOMO of *ortho*-carborane is B–H and B–B bonding in character with a node in the mirror plane containing the carbon atoms of the C_{2v} symmetric geometry. There is therefore no carbon contribution to this orbital. In contrast the HOMO orbital of diphenyl-*ortho*-carborane is phenyl-based and largely π-bonding in character with a small contribution for cage carbon atoms, showing a C1–C2 σ-interaction.

The LUMO of *ortho*-carborane exhibits π-antibonding character between the C vertices and is σ-bonding between boron vertices, B3–B7, B3–B4, B5–B6 and B6–B7 which lie opposite the C vertices in C-B-B triangles. A large σ-antibonding character is seen across the triangular faces, between the C vertices and the B–B σ-bonding lobes. Occupation of this orbital would therefore see initial weakening of the C–B bonds, strengthening of the B–B bonds circling the C–C fragment and weakening of the C–C interaction.

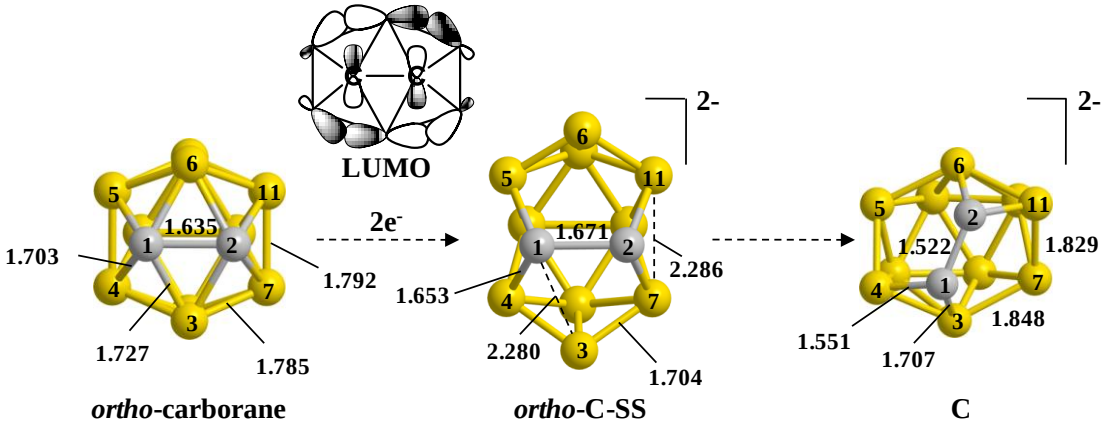

Figure 3.5 – Cage distortions seen in *ortho*-carborane upon addition of 2e, showing the orbital to be occupied. *Ortho*-C-SS represents a 'snap shot' taken from the geometry optimisation. Selected distances in Ångstroms.

In the initial steps of the mechanism (see Figure 3.5, above), these bond strengthening and weakening effects are indeed seen as shortening and lengthening connections. The C1–C2 distance is lengthened from 1.635 Å in *ortho*-carborane to 1.671 Å in ***ortho*-C-SS**, C–B3 and C–B6 distances are lengthened from 1.727 Å in *ortho*-carborane to 2.280 Å in ***ortho*-C-SS**, and the B3–B7 (and equivalent B–B) connection is shortened from 1.785 Å to 1.704 Å in ***ortho*-C-SS**. The C1–B4 distance is also shortened from 1.703 Å in *ortho*-carborane to 1.653 Å and the B7–B11 connection is lengthened from 1.792 Å to 2.286 Å in ***ortho*-C-SS**, which can be attributed to (less visible) C–B bonding and B–B antibonding interactions in the LUMO of *ortho*-carborane (see Figure 3.5). From ***ortho*-C-SS**, the cage then distorts further, presumably along with a change in orbital hybridisation, to give a basket intermediate, **C**.

In the case of diphenyl-*ortho*-carborane, the LUMO is again largely phenyl-based. It is π-antibonding with respect to C_{ipso}–C_{ortho} of the phenyl ring, however, it is π-bonding with respect to the C_{cage}–C_{ipso} interactions. Significantly, this orbital is antisymmetric with respect to the mirror plane relating C1 and C2, resulting in a large antibonding coefficient between these carbons. One would expect the C–C bond to weaken with reduction of diphenyl-*ortho*-carborane, along with a shortening of the C_{cage}–C_{ipso} connection and some distortion of the phenyl rings.

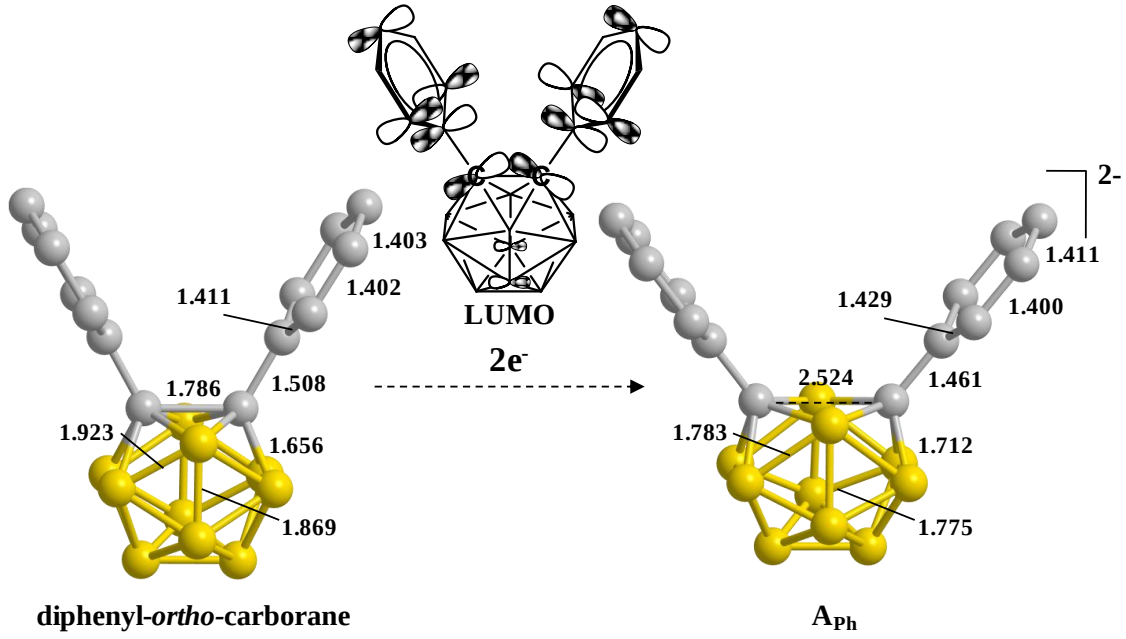

Figure 3.6 – Cage distortions seen in diphenyl-*ortho*-carborane upon addition of 2e, showing the orbital to be occupied. Selected distances in Ångstroms.

The distortions in diphenyl-*ortho*-carborane on addition of 2e, are shown in Figure 3.6, above. The C1–C2 connection is broken on reduction, lengthening from 1.786 Å to 2.524 Å in **A_{Ph}**. The C_{cage}–C_{ipso} bond is significantly shortened, while the C_{ipso}–C_{ortho} bond is lengthened. This matches perfectly with the LUMO of diphenyl-*ortho*-carborane and displays that, where distortion upon reduction is small, it is entirely predicted by visualisation of the LUMO of the neutral species.

3.2.2. 2e reduction of diphenyl-*meta*-carborane

The reduction of *meta*-carborane was found to proceed *via* the initial lengthening of the C1–B3 connection, going through to form [7,9-*nido*-$C_2B_{10}H_{10}]^{2-}$ directly, where C1-B3-B8-B2-C7-B6 form the 6-membered open face (see Chapter 2, Section 2.2.9.1). Reduction of diphenyl-*meta*-carborane, however does not give formation of a 6-membered faced *nido* structure directly (see Figure 3.7, below). In the initial steps of the optimisation, the geometry is seen to distort by initial rotation of the phenyl substituents to give B6-C1-C_{ipso}-C_{ortho} and B11-C7-C_{ipso}-C_{ortho} dihedral angles of *ca.* 90° followed by simultaneous lengthening of the C1–B6 and C7–B11 connections. The C_s symmetry is then lost as the C7–B11 connection is shortened again. The result is a lengthened C7–B2 connection from 1.719 Å in diphenyl-*meta*-carborane to 1.938 Å, while the C1–B5 and C1–B6 connections are lengthened from 1.731 Å to 2.643 Å and from 1.737 Å to 2.734 Å respectively, to give a shallow minimum, **C_{Ph}**, at ΔE = 23.8 kcal mol^{-1} with respect to **$7,9_{Ph}$**. This intermediate has a topology related to that of **B_{Ph}**

by exchange of C7 and B5 vertices, meaning one C vertex remains 5-connected in the first intermediate after 2e reduction. Indeed, **C_{Ph}** is 35.3 kcal mol^{-1} higher in energy than the first intermediate in the 2e reduction of diphenyl-*ortho*-carborane, **A_{Ph}**, and this energy difference matches well with the difference in topology and the relative ease in the experimental reduction of diphenyl-*ortho*-carborane.[9] From **C_{Ph}**, the long C7–B2 connection (1.938 Å) was then increased, giving **C_{Ph}-7,9$_{Ph}$-TS** at ΔE = 24.0 kcal mol^{-1}. Finally, IRC characterisation of **C_{Ph}-7,9$_{Ph}$-TS** returned **C_{Ph}** and **7,9$_{Ph}$**. The pathway to the global minimum, **B_{Ph}**, would then proceed as shown in Figure 3.2 *via* an energy barrier of $\Delta E^{\ddagger}$ = 15.1 kcal mol^{-1}. This is in good agreement with experiment, where 13-vertex, metallated products imply the [7,9-Ph_2-7,9-*nido*-$C_2B_{10}H_{10}$]$^{2-}$ reduced species.

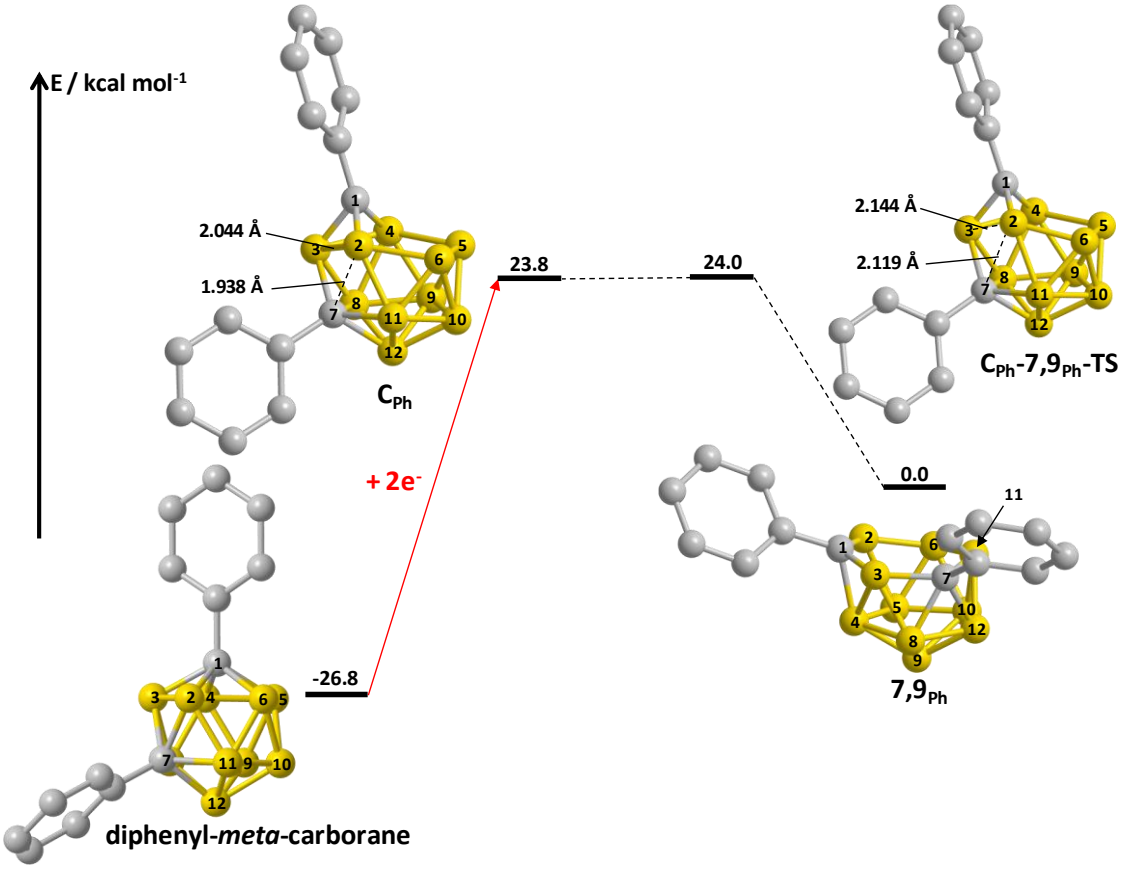

Figure 3.7 – 2e reduction of diphenyl-*meta*-carborane.

The initial distortion seen in the reduction of diphenyl-*meta*-carborane was again considered in view of its LUMO (see Figure 3.8, below).

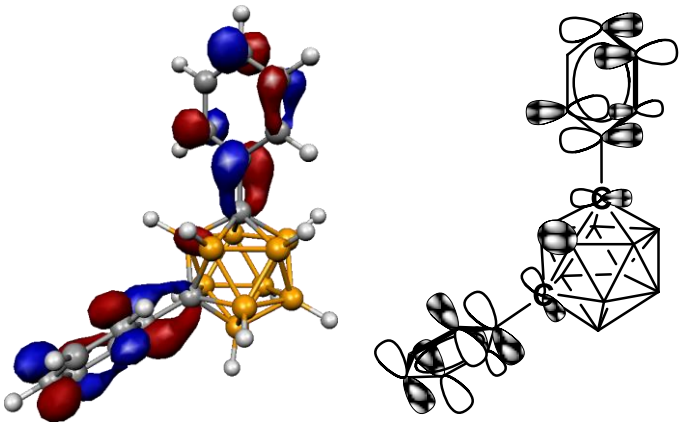

Figure 3.8 – LUMO of diphenyl-*meta*-carborane.

The LUMO of diphenyl-*meta*-carborane is mainly located on the phenyl substituents and features a π-bonding interaction between C_{cage} and C_{ipso} centres. Additionally, there is an antibonding interaction between the C_{cage}–C_{ipso} π interactions and the B2–B3 σ-bonding contribution. It may therefore be predicted that the C vertices would move away from the B2–B3 edge upon reduction. However, this is not the case, and as seen above the major distortion upon reduction is a lengthening of the C1–[B5-B6] interaction. The reduction of diphenyl-*meta*-carborane is therefore less well predicted through its LUMO than that of diphenyl-*ortho*-carborane. This may be a result of low symmetry isomerisation processes generally requiring lower energy than high symmetry processes such as that predicted here.[10]

3.3. Oxidation of modified [7,9-*nido*-C_2B_{10}]$^{2-}$ fragments

3.3.1. Solving the re-oxidation problem I - The *meta*-tether

As an alternative to the *ortho*-tether, the *meta*-tether has been suggested. This exopolyhedral tether would have a rigid geometry, where its bite distance is matched to the H–C···C–H distance in *meta*-carborane. The aim of this would be to allow reduction of *meta*-carborane to [7,9-μ(R)-7,9-*nido*-$C_2B_{10}H_{10}$]$^{2-}$, where R is some tether, but block the pathways to oxidation by preventing the carbon atoms coming together. The hope would be that the capitation process would be more competitive with an oxidative route back to *meta*-carborane. In parallel experimental studies, the anthracene derivative, 1,8-bis[bromomethyl(ethynyl)]-anthracene was synthesised (Figure 3.9, below), in five steps from 1,8-dichloroanthraquinone with an overall 10% yield.[9] This was then reacted with lithiated *meta*-carborane to give, in modest yield, 'tethered *meta*-carborane' which was characterised by mass spectrometry (MS) and nuclear magnetic resonance (NMR) spectroscopy.

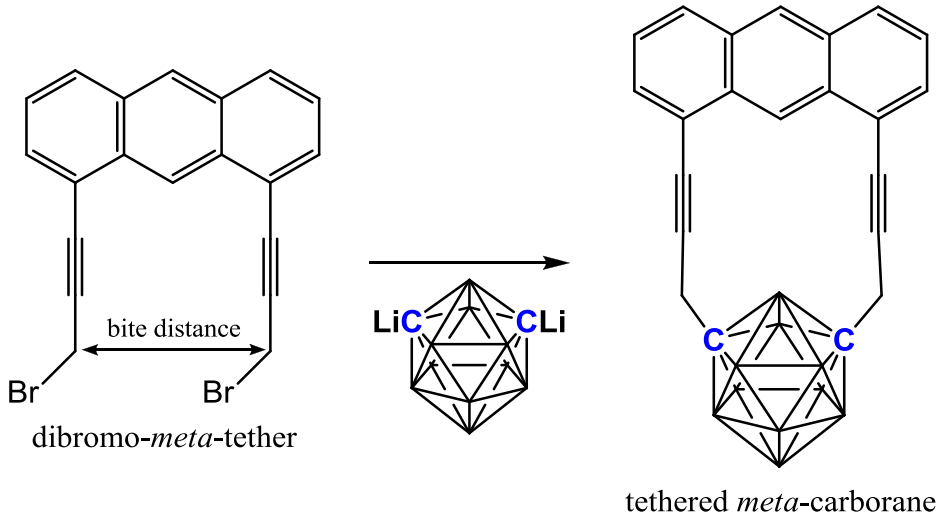

Figure 3.9 – The production of tethered *meta*-carborane.

Attempts to reduce and capitate tethered *meta*-carborane have thus far been unsuccessful. This is thought to be due to the conjugated, anthracene-derived tether interfering with [naphthalene]$^{-}$, which is used as a charge carrier in carborane reduction experiments. *Meta*-carborane, naphthalene, anthracene and alternative *meta*-tethers (see Figure 3.10, below) were therefore investigated, in order to address this result in terms of the energy of the LUMO and the energy of the SOMO of their optimised anions.

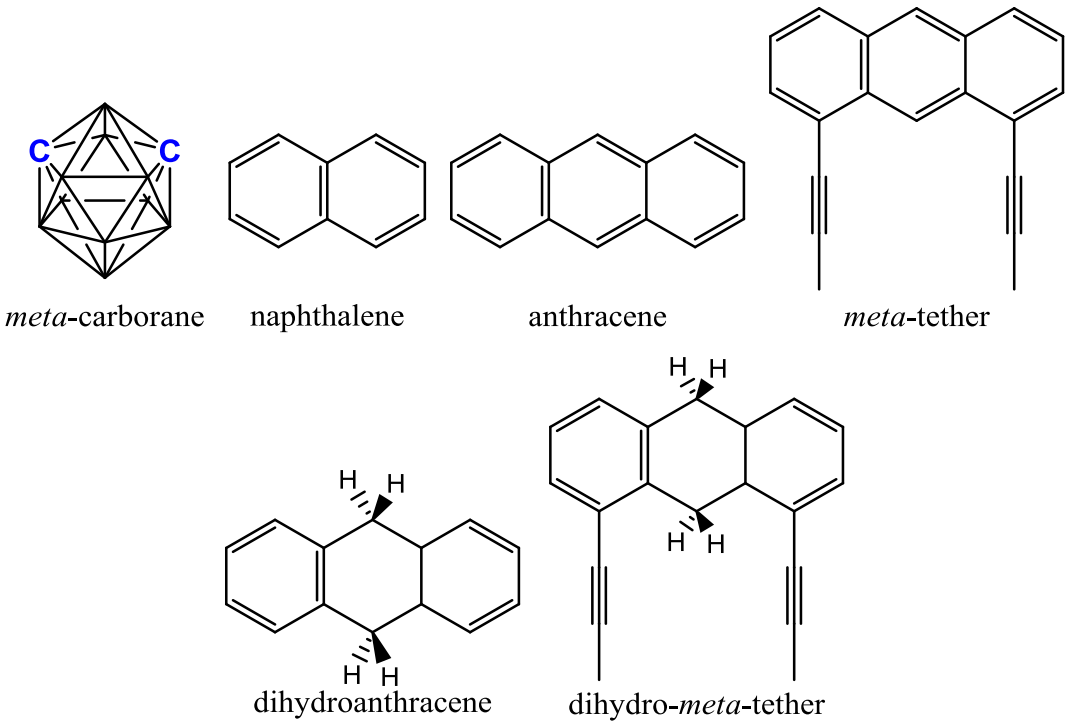

Figure 3.10 – Species used in the reduction of tethered *meta*-carborane.

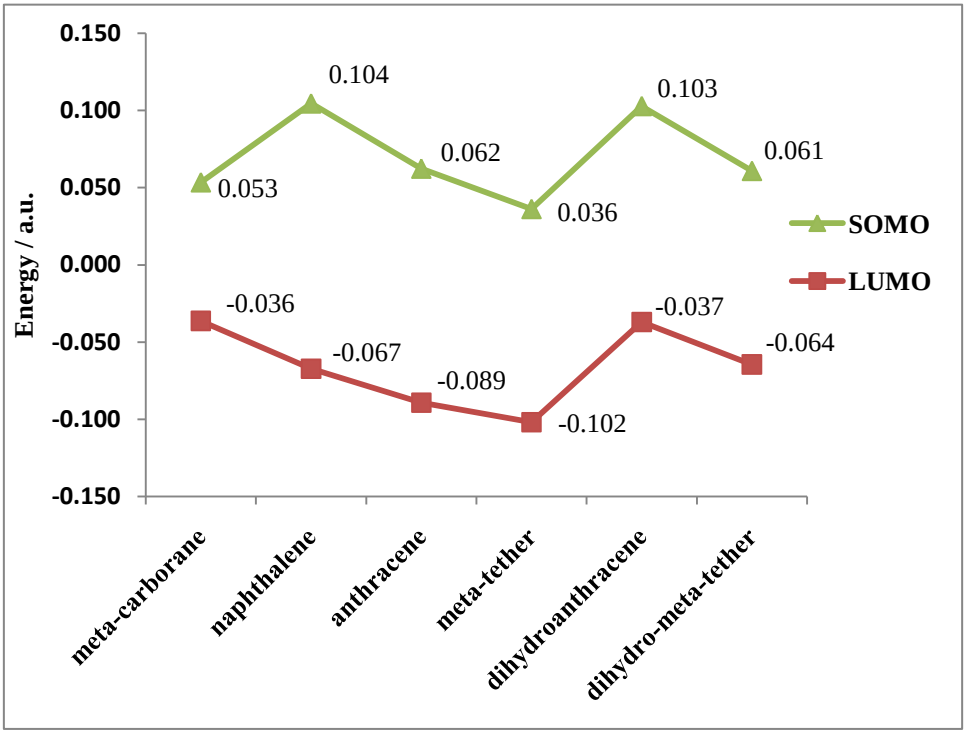

Figure 3.11 – Plot of energies (in Hartrees) of orbitals involved in tethered *meta*-carborane REDOX.

There are two criteria for a successful *meta*-carborane reduction in this case. Firstly, the charge carrier (conjugated organic molecule) must have a low energy LUMO in order to be itself reducible: experimentally, naphthalene is used and so charge carriers with LUMO energies of the order of E_{LUMO}(naphthalene) = -0.067 a.u. are considered as reducible (see Figure 3.11). Secondly, the SOMO energies of the anions must be higher

than that of *meta*-carborane, producing a favourable energy for charge transfer to *meta*-carborane. For example, Figure 3.11, above, shows that an electron transfer from [naphthalene]$^-$ to *meta*-carborane would give a net stabilisation to the system, since E_{SOMO}([naphthalene]$^-$) > E_{SOMO}([*meta*-carborane]$^-$). The opposite would be true if an electron were to be transferred from the *meta*-tether anion to *meta*-carborane since the anion of the *meta*-tether has the most stable SOMO computed here. Thus the experimental observation that tethered *meta*-carborane is not reducible is rationalised by the *meta*-tether to *meta*-carborane electron transfer corresponding to an overall decrease in stability in the system. The effects on the orbital energies of doubly reducing anthracene (by addition of 2 H) and the *meta*-tether (at the C-H centres of the central C_6 ring) are shown as dihydroanthracene and dihydro-*meta*-tether respectively. These were investigated since doubly reducing effectively splits the conjugation in these molecules into two regions, separated by two sp^3 carbon atoms, which, upon reduction, would produce a less stable anion. This is indeed the case, as the SOMO energies of their anions are raised, giving E_{SOMO}([dihydro-*meta*-tether]$^-$) > E_{SOMO}([*meta*-carborane]$^-$), however their energy difference is not as marked as that seen in comparing *meta*-carborane with naphthalene. The dihydro-*meta*-tether has not been synthesised, however the above suggests that it may produce a chemically reducible system.

3.3.2. Solving the re-oxidation problem II – Bulky C-substituents

A second *meta*-carborane derivative was sought, 1,7-R_2-1,7-$C_2B_{10}H_{10}$ with bulky R groups. Reducing this would produce [7,9-R_2-7,9-*nido*-$C_2B_{10}H_{10}$]$^{2-}$, which, it was hoped, would be prevented from reoxidising to *ortho*-carborane by the bulky groups impeding the carbon vertices from coming together.[11] As with the *meta*-tether, this approach leaves open the possibility of reoxidation still occurring and simply proceeding to *meta*-carborane, rather than *ortho*-carborane, and so relies on a capitation process being at least competitive with reoxidation.

Substituted fulvenes (see Figure 3.12, below) were chosen due as substituents to their bulk, their possession of customisable substituents at the α-carbon and their ready reactivity with lithiated carboranes. They also offer further functionality in that their cyclopentadiene rings may be reduced, giving the possibility of reaction with {FeCp}$^+$ to give pendant ferrocenyl functions. These would serve to further increase the bulk of these substituents, and also possibly produce molecules with interesting electrochemical activity, i.e. a single molecule with two remote REDOX active centres.

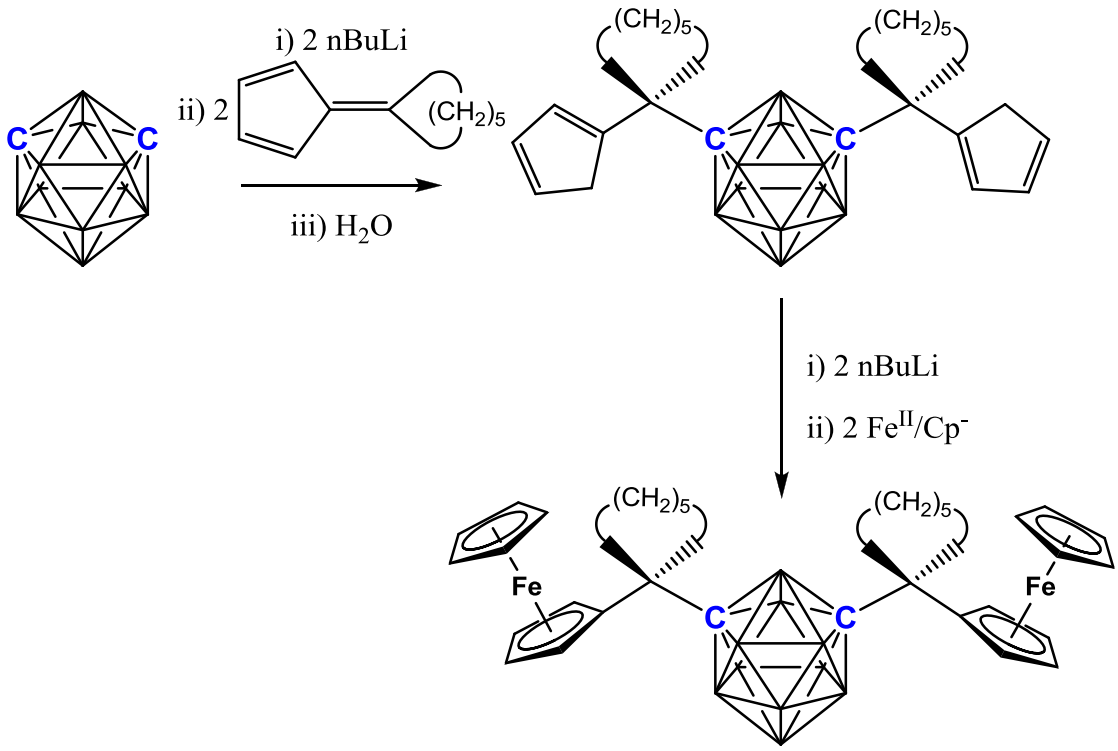

Figure 3.12 – Synthesis of bulky *meta*-carborane derivatives. Lithiated *meta*-carborane is reacted with pentamethylfulvenes, which are then interconverted to ferrocenyl groups.

The same reaction with *ortho*-carborane was shown to give only singly substituted 1-R-1,2-*closo*-$C_2B_{10}H_{11}$. This result suggested that the direct formation of a bulky *ortho*-carborane derivative was unfavourable and so the next step was taken to reduce and then oxidise the bulky *meta*-carboranes. However, in spite of the bulk of these groups, the carbon vertices became adjacent, as products of the reduction and reoxidation were fully characterised as *ortho*-carborane derivatives. A view of the crystallographically determined structure of the product with the most bulky carbon substituents (where the C_5 rings of the pentamethylenylfulvene groups have been converted to ferrocenyl groups) is shown below (Figure 3.13). This was found to exhibit an unusually long C···C connection of 2.156(4) Å. Further evidence showing the extent of the strain in the molecule can be seen in the ferrocenyl group of Fe2, where C21 is out of the plane of the attached C_5 ring by 0.303 Å and where the C_5 rings of the ferrocenyl are not co-parallel, their least-squares planes meeting at an angle of 11.65°. The ferrocenyl group centred on Fe1 is shown to be less strained as C11 is just 0.106 Å out of the plane of the adjacent ring and the angle between the C_5 rings is smaller, at 4.97°. Though not fulfilling its original objective, this synthesis now represents a route to highly strained, truly *closo*, *ortho*-carboranes. Furthermore, this species may only be formed through the REDOX of a parent *meta*-carborane. Previous examples showing long C–C

connections had arguably > (2*n*+2) skeletal electron counts,[12] where a *closo* heteroborane has strictly (2*n*+2) skeletal electrons.[13]

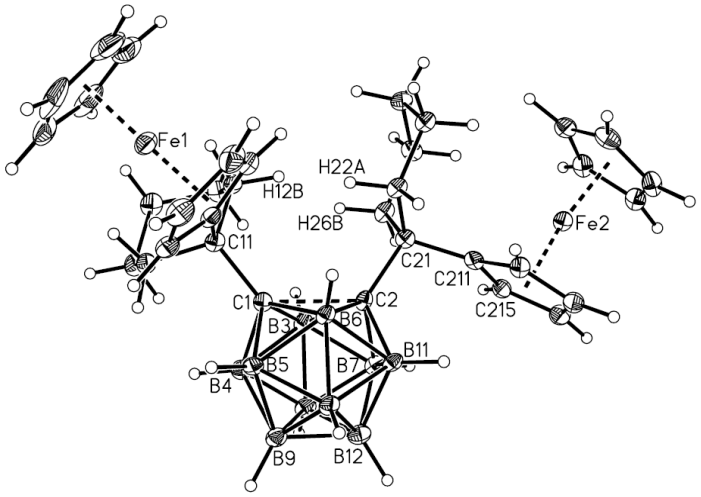

Figure 3.13 – A view of the *ortho*-carborane derivative showing ferrocenyl functionalised pentamethylenylfulvene groups.

3.3.2.1. Computational investigation of the effects of C-substituent bulk

In order to rationalise the experimental observation that the bulky C-substituents do not prevent the formation of R_2-*ortho*-carborane on reoxidation, the computational oxidation of [7,9-R_2-7,9-*nido*-$C_2B_{10}H_{10}$]$^{2-}$ (R = Me, ^{t}Bu) was carried out, where ^{t}Bu was used to model the bulky R groups used experimentally. The results were then compared with the computed reaction pathway for the oxidation of [7,9-*nido*-$C_2B_{10}H_{12}$]$^{2-}$ given in Chapter 2, Section 2.5.1 (Figure 3.14, below).

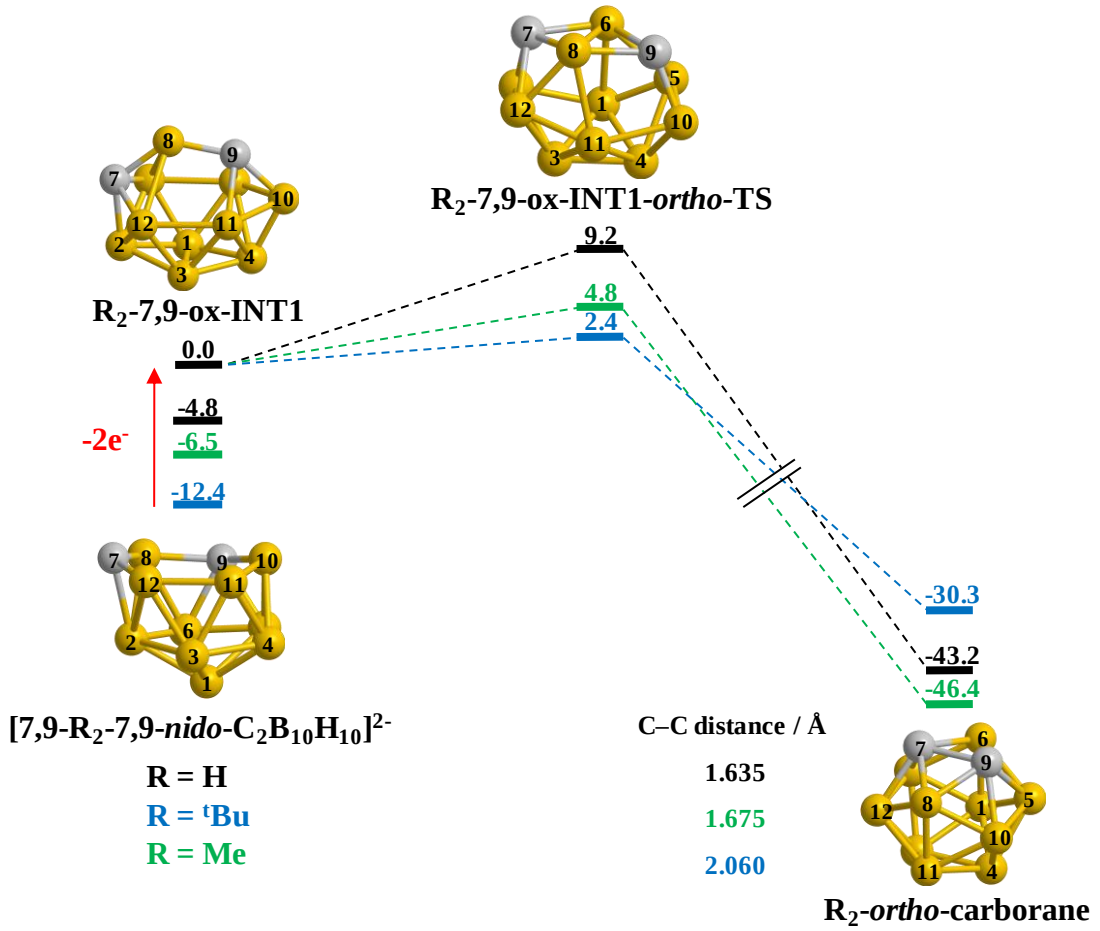

Figure 3.14 – The effect of changing C-substituents, R, on the oxidation of [7,9-R_2-7,9-*nido*-C_2B_{10}]$^{2-}$ (R = H, Me, ^{t}Bu). Energies in kcal mol^{-1}.

As found in the experimental studies, the computational oxidation of **[7,9-R_2-7,9-$C_2B_{10}H_{10}$]$^{2-}$** gives **R_2-*ortho*-carborane** as the kinetic product with all R. The process giving **R_2-*meta*-carborane** was characterised as consistently having a higher energy barrier and more stable final product, as seen in Chapter 2 with R = H. The effect of R on the pathway to **R_2-*ortho*-carborane** is discussed below.

As shown in Figure 3.14, there are significant changes in the computed oxidation profile with R. The initial effect is seen in the energy difference between **R_2-7,9-ox-INT1** and **[7,9-R_2-7,9-*nido*-$C_2B_{10}H_{10}$]$^{2-}$** where ΔE increases with R = H < R = Me < R = ^{t}Bu. From the first oxidation intermediate, **R_2-7,9-ox-INT1**, the barrier to formation of **R_2-*ortho*-carborane** was found to decrease with increasing bulk of R ($\Delta E^{\ddagger}$ = 9.2, 4.8 and 2.4 kcal mol^{-1} for R = H, Me and ^{t}Bu respectively). **R_2-7,9-ox-INT1-*ortho*-TS** is an early transition state in terms of the C–C bond formation (C···C distances were computed as 2.778 Å, 2.813 Å and 2.844 Å with R = H, Me and ^{t}Bu respectively) and so is considered as sterically similar to **R_2-7,9-ox-INT1** (C···C distances of 2.858 Å, 2.965 Å and 3.019 Å with R = H, Me and ^{t}Bu respectively). Therefore, the trend in

stability is likely only due to electronic effects, whereby increasing σ-donation from large alkyl groups gives increasing transition state stability.

In contrast, the differences in stability and C···C distance of **R_2-*ortho*-carborane** with R suggest opposing electronic effects and steric interactions. Changing R = H for R = Me gives a stabilisation of 3.2 kcal mol^{-1}. The C–C distance changes little (from 1.635 to 1.675 Å), therefore this is likely to be an electronic effect, where increased electron donation gives a more electron rich, and therefore stabilised, cluster. With R = ^{t}Bu, however, there is a destabilisation of 12.9 kcal mol^{-1} (with respect to R = H), suggesting steric interactions override increased σ-donation in this case. This is mirrored by the increased C–C distance from 1.635 to 2.060 Å.

3.3.2.2. Probing C-substituent electronic effects

To probe the electronic effect of R, the profile for oxidation of **[7,9-R_2-7,9-*nido*-$C_2B_{10}H_{10}$]$^{2-}$** to **R_2-*ortho*-carborane** was recomputed with R = trifluoromethyl (CF_3), as a strong electron withdrawing group (EWG).[14]

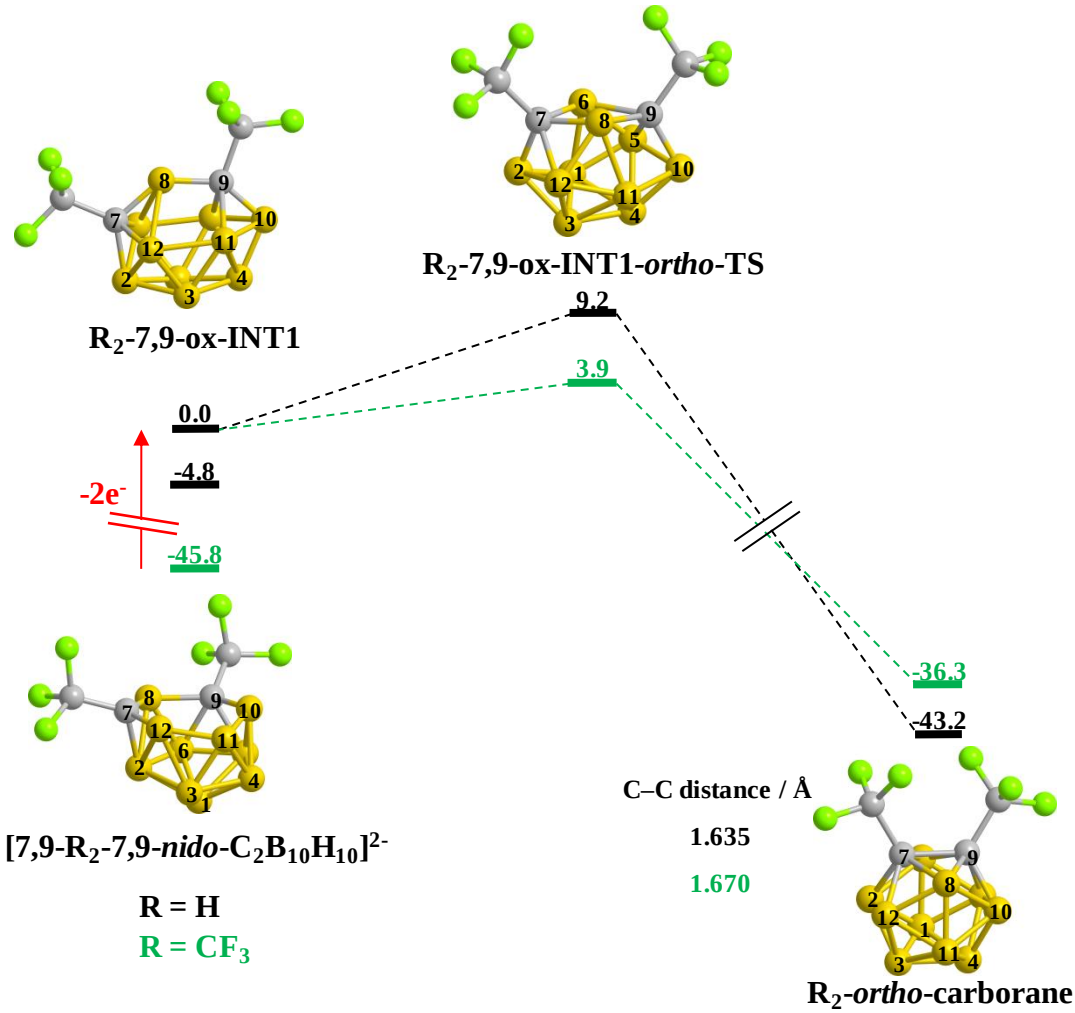

Figure 3.15 – The effect of changing C-substituents, R, on the oxidation of $[7,9\text{-}R_2\text{-}7,9\text{-nido-}C_2B_{10}]^{2-}$ (R = H, CF_3). Energies in kcal mol^{-1}.

The profile produced (Figure 3.15, above), however, shows unexpected changes with R = CF_3 in comparison with R = H. The transition state energy is decreased where an increase was expected and **R_2-*ortho*-carborane** is destabilised despite there being no evidence for steric interactions in the geometry (C–C = 1.670 Å). Perhaps the most striking feature of the profile with R = CF_3, however, is the large stabilisation of **$[7,9\text{-}R_2\text{-}7,9\text{-}nido\text{-}C_2B_{10}H_{10}]^{2-}$** with respect to **$R_2$-7,9-ox-INT1**, which will be discussed later.

The C···C distance in **R_2-7,9-ox-INT1-*ortho*-TS** is short, at 2.764 Å, possibly suggesting a later transition state than that seen with R = H, Me and ^{t}Bu. The barrier height is most similar to that of R = Me ($\Delta E^{\ddagger}$ = 4.8 and 3.9 kcal mol^{-1} with R = Me and CF_3 respectively). The opposite effect is seen in **R_2-*ortho*-carborane**. Where R = Me, **R_2-*ortho*-carborane** is stabilised by 3.2 kcal mol^{-1} with respect to R = H, whereas with R = CF_3 **R_2-*ortho*-carborane** is *destabilised* by 6.9 kcal mol^{-1}. This suggests, paradoxically, that CF_3 groups produce similar effects to methyl groups in the transition

state but the opposing effects in **R_2-*ortho*-carborane**, despite the effects being predominantly electronic in nature in both cases.

To investigate this, natural charges were calculated.[15] These have been used previously to explain the unusual electronic behaviour of CF_3 groups, where an excess in negative charge was found to be located on the *β*-position with respect to one or more fluoride centres, known as the *β*-effect.[16] This is seen, for example in 1,1,1-trifluoroethane, where π-donation from a fluoride centre results in a resonance form with a formally negatively-charged *β*-carbon (Figure 3.16).

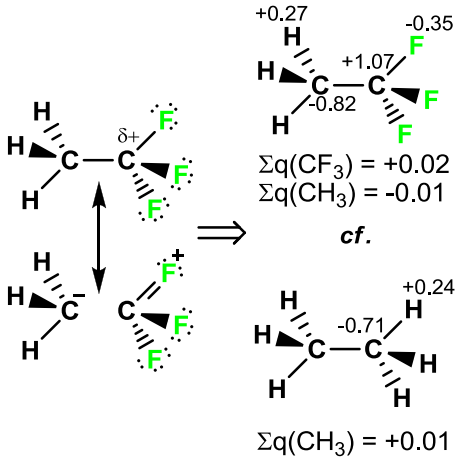

Figure 3.16 – The *β*-effect in 1,1,1-trifluoroethane *cf.* ethane showing resonance effect of π-electron donation from fluoride (left) and computed natural charges (right).

In order to carry out the same comparison in R_2-$C_2B_{10}H_{10}$, natural charges were computed for R = Me and CF_3 for the neutral geometries involved in the computational oxidation of **[7,9-R_2-7,9-*nido*-$C_2B_{10}H_{10}$]$^{2-}$**. Selected charges, summations of charges and average charges for selected centres are given in Figure 3.17, below.

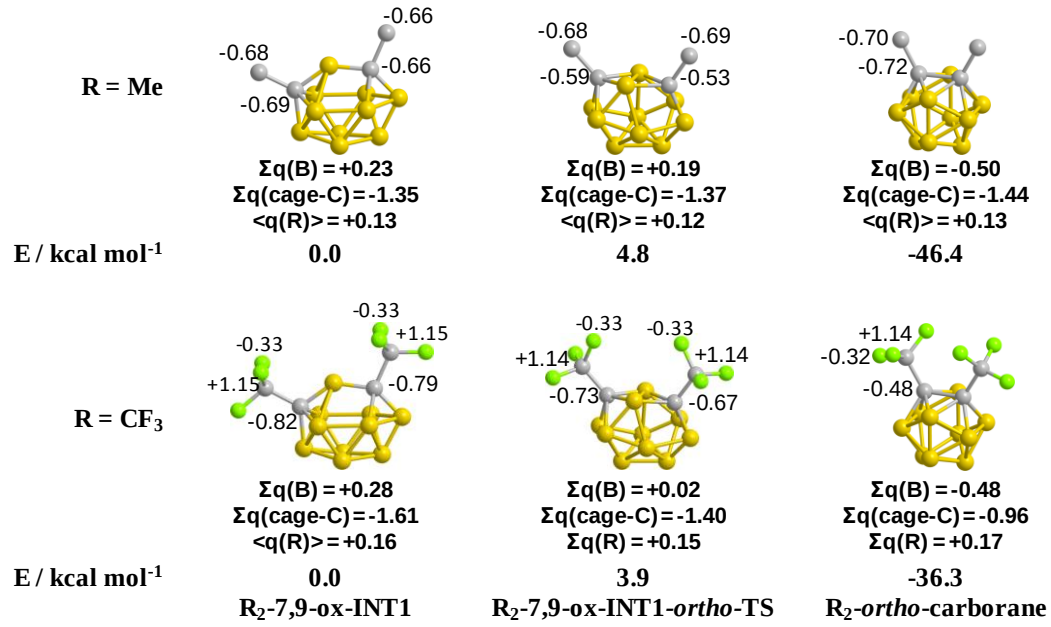

Figure 3.17 – Computed natural charges in neutral R_2-$C_2B_{10}H_{10}$ geometries (R = CH_3, CF_3).

Along the reaction coordinate, the total charge on the boron atoms becomes less positive, from +0.23 and +0.28 for R = Me and CF_3 respectively in **R_2-7,9-ox-INT1**, to +0.19 and +0.02 for R = Me and CF_3 respectively in **R_2-7,9-ox-INT1-*ortho*-TS**. This continues to **R_2-*ortho*-carborane** where the charges become negative (-0.50 and -0.48 for R = Me and CF_3 respectively). The cage carbon atoms carry a larger proportion of charge than the boron atoms, where ∑q(cage-C) in **R_2-7,9-ox-INT1** is -1.35 and -1.61 for R = Me and CF_3 respectively. This then becomes less negative on isomerisation to **R_2-*ortho*-carborane** (-0.72 and -0.96 for R = Me and CF_3 respectively). These results therefore suggest a transfer of electron density from carbon to boron centres during isomerisation of the cage.

The average total charge on the C-substituents, <q(R)>, is relatively similar with R = Me and CF_3. However, the carbon centre in both the Me and CF_3 groups reveals the largest difference in these species. The charge on the substituent carbon centre is consistently around -0.68 for R = Me but much more positive at *ca.* +1.14 for R = CF_3. The charge on the cage carbon atom is more negative with R = CF_3 in **R_2-7,9-ox-INT1** and **R_2-7,9-ox-INT1-*ortho*-TS**, however, in **R_2-*ortho*-carborane**, the cage carbon centres are more negative with R = Me. The first two are therefore in agreement with the resonance views depicted in Figure 3.16, while there is no evidence for a *β*-effect in **R_2-*ortho*-carborane** with R = CF_3. However, in going from R = Me to R = CF_3 the average charge on boron centres in the cage becomes more positive in all cases, suggesting the fluorinated groups have a net electron withdrawing effect on the cluster.

The conclusion is, therefore, that CF_3 groups stabilise "carbons apart" carboranes by increasing the negative charge on the relatively (in comparison to boron) electronegative carbon vertices and increasing the positive charge on the more electropositive boron vertices. The exception to this is **R_2-*ortho*-carborane**, which is least stable where R = CF_3. This may be due to the association of like charges as the carbon vertices move together.

3.3.3. Solving the re-oxidation problem III – Electron withdrawing C-substituents

A relatively large stabilisation is seen in **[7,9-R_2-7,9-*nido*-$C_2B_{10}H_{10}$]$^{2-}$** with respect to **R_2-7,9-ox-INT1** where R = CF_3, representing an increase by a factor of ten over the ΔE_{OX} (the change in energy that coincides with 2e oxidation) with R = H. Indeed, this is the first case seen in this study where a dianionic *nido* intermediate is more stable than a neutral *closo* intermediate (**R_2-*ortho*-carborane** with R = CF_3).

The observation that one may heavily stabilise a dianionic *nido* fragment with respect to the first oxidation intermediate, by inclusion of simple fluorinated C-substituents, was very significant to the re-oxidation problem. This led to a third parallel computational and experimental study in which a library of electron withdrawing groups (EWG) was assessed. EWGs were ranked by their effect on the computed **R_2-7,9-ox-INT1** versus **[7,9-R_2-7,9-*nido*-$C_2B_{10}H_{10}$]$^{2-}$** energy difference (ΔE_{OX}), their commercial availability and their viability for use in carborane REDOX chemistry. An additional advantage was also seen in that either *ortho*- or *meta*-carborane derivatives could be used as carborane precursors as the R groups being used are less bulky than previous examples (see Section 3.3.2).

Figure 3.18, below shows the process which is to be monitored against R. The effect of R on the geometries of dianionic and neutral intermediates is relatively small, therefore only the energy change is shown (in Table 3.1).

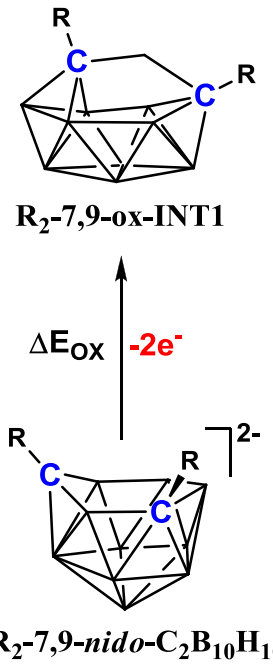

Figure 3.18 – The initial step in the oxidation of [7,9-*nido*-C_2B_{10}]$^{2-}$ derivatives.

As discussed in section 3.1.4, the computed oxidation barrier for *ortho*-tethered [7,8-μ$(CH_2)_3$-7,8-*nido*-$C_2B_{10}H_{10}$]$^{2-}$, which has been successfully capitated, is 35.4 kcal mol^{-1}. This was therefore set as the target value of ΔE_{OX} and groups shown to produce a ΔE_{OX} exceeding this target, and meeting the practical requirements, would be tested experimentally. Table 3.1, below, shows the library of R groups that was constructed. R = H, CH_3, $C(CH_3)_3$ and CF_3 are shown again for ease of comparison. Groups giving an oxidation barrier greater than the target value are colour coded in green.

Table 3.1 – Oxidation barrier (ΔE_{OX}) of [7,9-R_2-7,9-*nido*-$C_2B_{10}H_{10}$]$^{2-}$ for selected R groups.

R Group	ΔE_{OX} / kcal mol^{-1}
H	4.8
CH_3	6.5
$C(CH_3)_3$	12.4
CF_3	45.8
CCl_3	66.5
F	30.7
COOH	43.6
CF_2CH_3	36.9
CH_2CF_3	31.8
p-$C_6F_4CF_3$ [b]	60.8
p-C_6H_4F	36.2
o,*o*-$C_6H_3F_2$	29.4
m,*m*-$C_6H_3F_2$	44.9
o,*o*,*p*-$C_6H_2F_3$	35.5
m,*m*,*p*-$C_6H_2F_3$	50.5
o,*o*,*m*,*m*-C_6HF_4	43.9
C_6F_5 [b]	49.3
p-$C_6H_4CF_3$ [b]	50.1
C_6H_5 [a]	29.8
o-pyridyl	26.0
m-pyridyl	41.4
p-pyridyl	46.8

[a] Parent *ortho*- or *meta*-carborane previously synthesised
[b] Parent *ortho*- or *meta*-carborane synthesised in this study

As before, those R groups producing the largest oxidation barriers in [7,9-R_2-7,9-*nido*-$C_2B_{10}H_{10}$]$^{2-}$ were noted as those generally considered to be most highly electron withdrawing. The initial, computational, comparison produced a list of potential R groups. The CCl_3 and COOH groups (ΔE_{OX} = 66.5 and 43.6 kcal mol^{-1} respectively) may be discounted as carboranes containing these groups are known to be unstable under reducing conditions. Also, R_2-*ortho*- or R_2-*meta*-carboranes with R = CF_3 (ΔE_{OX} = 45.8 kcal mol^{-1}) were not successfully synthesised. However, by far the most promising fluorinated EWG from the computational study was the *p*-$C_6F_4CF_3$ group, which produced ΔE_{OX} = 60.3 kcal mol^{-1} and was experimentally viable. This substituent therefore received most of the computational and experimental attention and is discussed in the following section.

3.3.4. Solving the re-oxidation problem IV – *p*-$C_6F_4CF_3$ C-Substituents

3.3.4.1. Initial 2e reduction of (p-$C_6F_4CF_3$)$_2$-meta-*carborane*

It was possible for the experimental workers to prepare and characterise diperfluorotolyl derivatives of *ortho*- and *meta*-carborane (1,2-(*p*-$C_6F_4CF_3$)$_2$-1,2-*closo*-$C_2B_{10}H_{10}$ and 1,7-(*p*-$C_6F_4CF_3$)$_2$-1,7-*closo*-$C_2B_{10}H_{10}$ respectively). Initially, the latter was adopted for polyhedral expansion experiments. However, when the reduction and metallation of 1,7-(*p*-$C_6F_4CF_3$)$_2$-1,7-*closo*-$C_2B_{10}H_{10}$ was attempted, despite a colour change from colourless to yellow-brown being observed in the reduction stage, no 13-vertex metallacarboranes were formed.[9] Therefore the reduction pathway was investigated computationally.

Until now, only the oxidation of the *nido* dianion with *p*-$C_6F_4CF_3$ C-substituents has been considered. However, given that chemical reduction and metallation of 1,7-(*p*-$C_6F_4CF_3$)$_2$-1,7-*closo*-$C_2B_{10}H_{10}$ was unsuccessful, more calculations were carried out into the nature of the reduced species and, subsequently, the reduction pathways. Figure 3.19, below, shows the HOMOs of **7,9** and **7,9**$_{p\text{-}C_6F_4CF_3}$ which can act as donor orbitals towards metallating fragments (for full analyses of carborane-metal bonding, see Chapter 4).

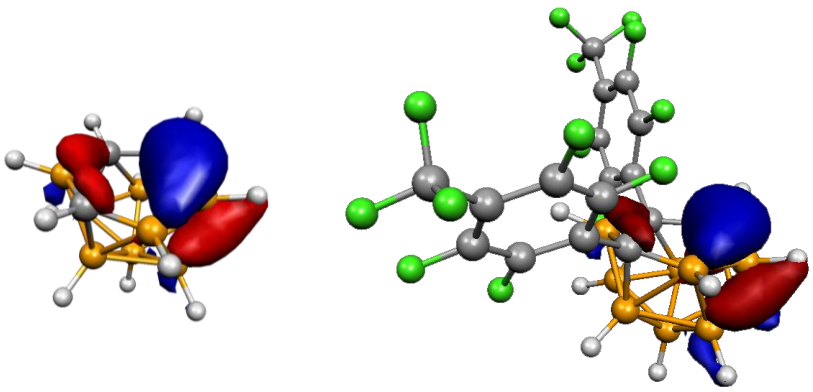

7,9 **7,9**$_{p\text{-}C_6F_4CF_3}$

Figure 3.19 – HOMOs of [7,9-*nido*-$C_2B_{10}H_{12}$]$^{2-}$ and [7,9-(*p*-$C_6F_4CF_3$)$_2$-*nido*-$C_2B_{10}H_{10}$]$^{2-}$.

Visually, there is no significant difference between these orbitals and so it appears that metallation of **7,9**$_{p\text{-}C_6F_4CF_3}$ should occur. The experimental evidence suggests a reduction does occur, as a colour change was observed on addition of reducing agent. Therefore the product of reduction of 1,7-(*p*-$C_6F_4CF_3$)$_2$-1,7-*closo*-$C_2B_{10}H_{10}$ does not appear to be **7,9**$_{p\text{-}C_6F_4CF_3}$.

To provide further insight, it was therefore necessary to compute the reduction pathway of diperfluorotolyl-*meta*-carborane. Earlier in this chapter, it was shown that

visualisation of the LUMO of a neutral carborane derivative could be used to predict the initial distortion of the cage on reduction. The LUMO of diperfluorotolyl-*meta*-carborane, shown in Figure 3.20, is similar to that of diphenyl-*meta*-carborane (shown in Figure 3.8), however it exhibits a smaller contribution on the cage. Furthermore, there is no contribution on the cage C-vertices, meaning there is no antibonding overlap on the cage. This suggests that perhaps the colour change seen experimentally was due to the perfluorotolyl substituents being themselves reduced, rather than the carborane cage.

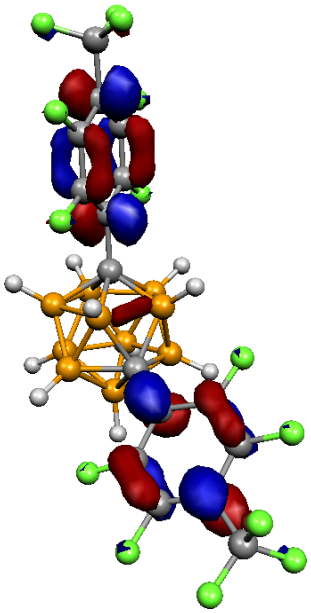

Figure 3.20 – LUMO of 1,7-(*p*-$C_6F_4CF_3$)$_2$-1,7-*closo*-$C_2B_{10}H_{10}$.

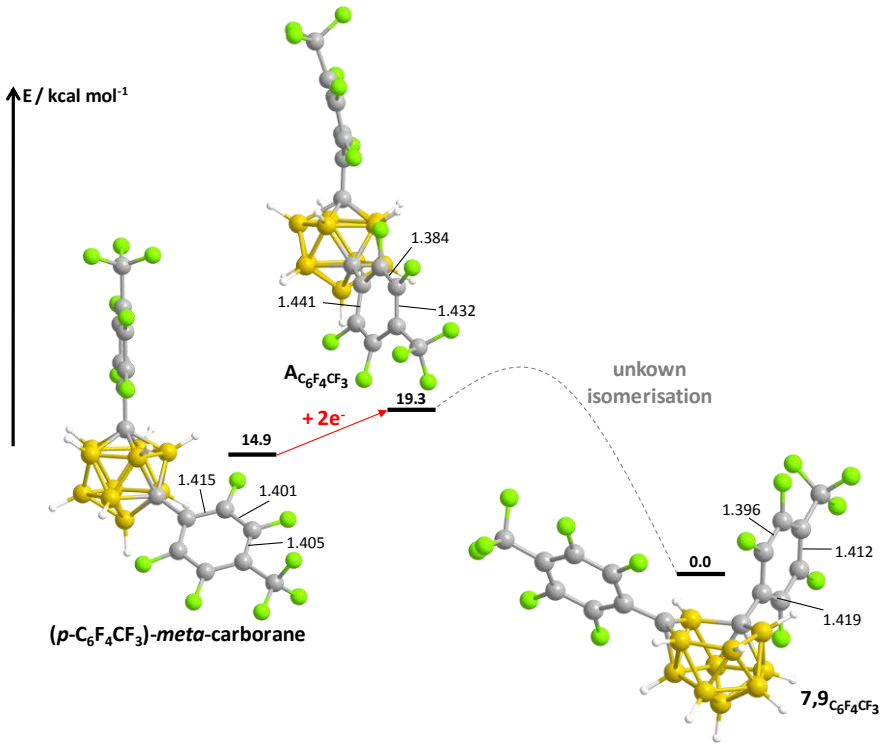

Figure 3.21 – First step of 1,7-(*p*-$C_6F_4CF_3$)$_2$-1,7-*closo*-$C_2B_{10}H_{10}$ reduction. Energies relative to [7,9-(*p*-$C_6F_4CF_3$)$_2$-7,9-*nido*-$C_2B_{10}H_{10}$]$^{2-}$.

The computed reduction of diperfluorotolyl-*meta*-carborane is given in Figure 3.21, above, and appears to show that the perfluorotolyl groups are, indeed, reduced. The cage is relatively unchanged, whereas the planarity of the perfluorotolyl C_6 rings is lost, consistent with loss of aromaticity on reduction to $\mathbf{A}_{C_6F_4CF_3}$. Loss of aromaticity is confirmed by the C–C bond distances in the aryl rings, which are all relatively similar in 1,7-(*p*-$C_6F_4CF_3$)$_2$-1,7-*closo*-$C_2B_{10}H_{10}$ and range between 1.401 and 1.415 Å then fall into "short" and "long" C–C bonds, in $\mathbf{A}_{C_6F_4CF_3}$, of 1.384, 1.432 and 1.441 Å, indicative of a degree of bond alternation. In [7,9-(*p*-$C_6F_4CF_3$)$_2$-7,9-*nido*-$C_2B_{10}H_{10}$]$^{2-}$ (which was calculated directly, rather than seeking the full isomerisation pathway) the aromaticity is restored in the aryl rings, where the C–C bonds range between 1.396 and 1.419 Å. Charge transfer from the *p*-$C_6F_4CF_3$ groups to the carborane cage may then be the barrier to formation of [7,9-(*p*-$C_6F_4CF_3$)$_2$-7,9-*nido*-$C_2B_{10}H_{10}$]$^{2-}$ and is not achieved experimentally.

*3.3.4.2. Initial 2e reduction of (*p-$C_6F_4CF_3$)$_2$-ortho-*carborane*

Given the contrasting pathways found for diphenyl-*ortho*- and diphenyl-*meta*-carborane reduction, it was suggested that where a *meta*-carborane derivative is not chemically reducible, the analogous *ortho*-carborane derivative may be. The LUMO of 1,2-(*p*-$C_6F_4CF_3$)$_2$-1,2-*closo*-$C_2B_{10}H_{10}$, which exhibits larger cage contributions to the orbital than seen in 1,7-(*p*-$C_6F_4CF_3$)$_2$-1,7-*closo*-$C_2B_{10}H_{10}$, is shown in Figure 3.22, below. The cage contributions are similar to those seen in diphenyl-*ortho*-carborane – the dominant feature is an antibonding interaction between C1 and C2. This suggests that its reduction pathway will resemble that seen in diphenyl-*ortho*-carborane in terms of the initial cage distortions.

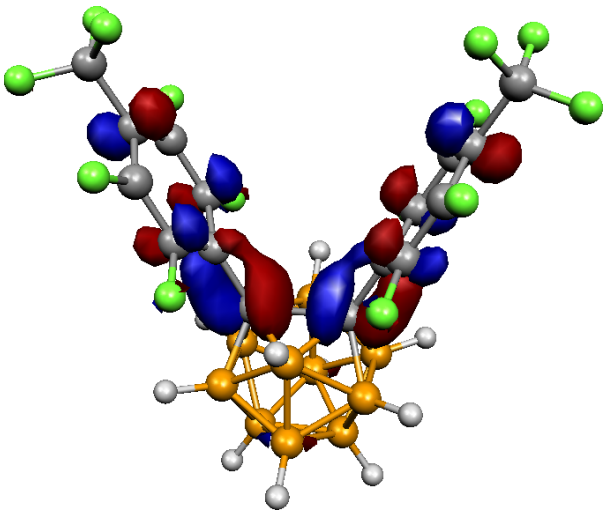

Figure 3.22 – LUMO of 1,2-(p-$C_6F_4CF_3$)$_2$-1,2-*closo*-$C_2B_{10}H_{10}$.

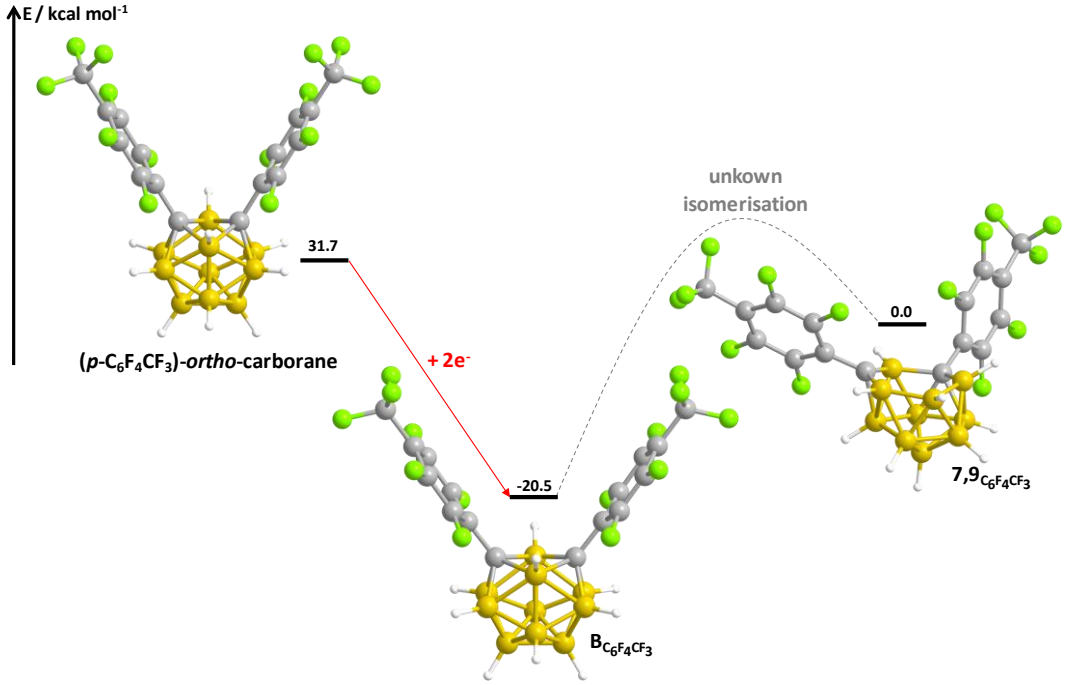

Figure 3.23 – First step of 1,2-(p-$C_6F_4CF_3$)$_2$-1,2-*closo*-$C_2B_{10}H_{10}$ reduction. Energies relative to [7,9-(p-$C_6F_4CF_3$)$_2$-7,9-*nido*-$C_2B_{10}H_{10}$]$^{2-}$.

As shown in Figure 3.23, above, it is indeed the case that the cage is distorted by lengthening of the C1–C2 connection upon the addition of 2e, from 1.983 Å in 1,2-(p-$C_6F_4CF_3$)$_2$-1,2-*closo*-$C_2B_{10}H_{10}$ to 2.506 Å in $\mathbf{B}_{C_6F_4CF_3}$. The effect of the perfluorotolyl substituents on the energy change upon reduction is very apparent in Figure 3.23. Where $\mathbf{7,9}_{Ph}$ was 13.0 kcal mol^{-1} less stable than diphenyl-*ortho*-carborane, $\mathbf{7,9}_{C_6F_4CF_3}$ is 31.7 kcal mol^{-1} *more* stable than diperfluorotolyl-*ortho*-carborane. The endothermic isomerisation pathway from $\mathbf{B}_{C_6F_4CF_3}$ to $\mathbf{7,9}_{C_6F_4CF_3}$ was not computed, however it is not unreasonable to assume this would be analogous to the isomerisation of reduced diphenyl-*ortho*-carborane to $\mathbf{7,9}_{Ph}$ or $\mathbf{7,10}_{Ph}$ as described in Figure 3.2.

3.3.4.3. Chemical reduction of (p-$C_6F_4CF_3$)$_2$-ortho-*carborane*

Given the above information, the chemical reduction of (*p*-$C_6F_4CF_3$)$_2$-*ortho*-carborane was attempted by the experimental coworkers.[9] A clean colour change from colourless to deep red is immediately seen in the solution, suggesting that reduction had taken place and that the product is different from that of chemically reduced (*p*-$C_6F_4CF_3$)$_2$-*meta*-carborane (yellow-brown suspension). Exposure of the deep red solution to air, which normally gives fast aerial oxidation of dianionic carborane species, did not immediately cause loss of colour. Here, in contrast, full loss of colour requires overnight stirring. This demonstrates, encouragingly, that reduced (*p*-$C_6F_4CF_3$)$_2$-*ortho*-carborane is more stable towards aerial reoxidation than methyl or phenyl disubstituted analogues.

Thus far, 13-vertex metallacarboranes incorporating {CoCp}, {CoCp*} and {Ru(benzene)} fragments have been produced through the reduction and metallation of (*p*-$C_6F_4CF_3$)$_2$-*ortho*-carborane. In previous studies, reduction and metallation of *ortho*-carborane derivatives has given 4,1,6-MC_2B_{10} species. 4,1,12-MC_2B_{10} isomers may then be produced through thermolysis. Reduction and metallation of (*p*-$C_6F_4CF_3$)$_2$-*ortho*-carborane is unusual, however, in that all metallacarboranes produced are of the 4,1,12-MC_2B_{10} isomeric form (see Figure 3.24, below).

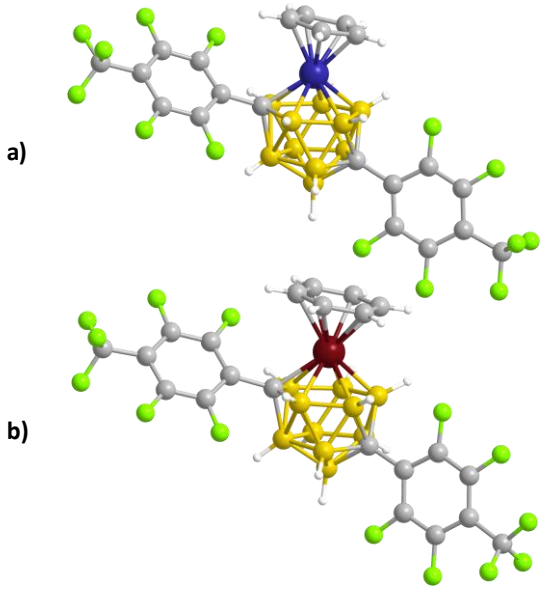

Figure 3.24 – Crystallographically determined structures of a) 4-(η-C_5H_5)-1,12-(*p*-$C_6F_4CF_3$)$_2$-4,1,12-*closo*-$CoC_2B_{10}H_{10}$ and b) molecule A of 4-(η-C_6H_6)-1,12-(*p*-$C_6F_4CF_3$)$_2$-4,1,12-*closo*-$RuC_2B_{10}H_{10}$ (two molecules per asymmetric unit).

Production of these isomers suggests one of two mechanistic pathways; either the metal induces isomerisation of the cage (with or following metallation) or the cage isomerises

before metallation to the implied *nido* fragment, [4,7-(*p*-$C_6F_4CF_3$)$_2$-4,7-*nido*-$C_2B_{10}H_{10}$]$^{2-}$. The latter is generally thought to be more likely in that metallation is accepted to 'trap out' *nido* species present in solution. However, in this case, the steric bulk of the perfluorotolyl group may allow isomerisation with or following metallation and, moreover, the relative stability of $\mathbf{B}_{C_6F_4CF_3}$ shown in Figure 3.23, makes isomerisation free of the metal appear less likely. In order to shed light on this result, the energetic order of *nido* fragments (as given in Chapter 2, Figure 2.22 with R = H) was recomputed for R = *p*-$C_6F_4CF_3$ (Figure 3.25, below).

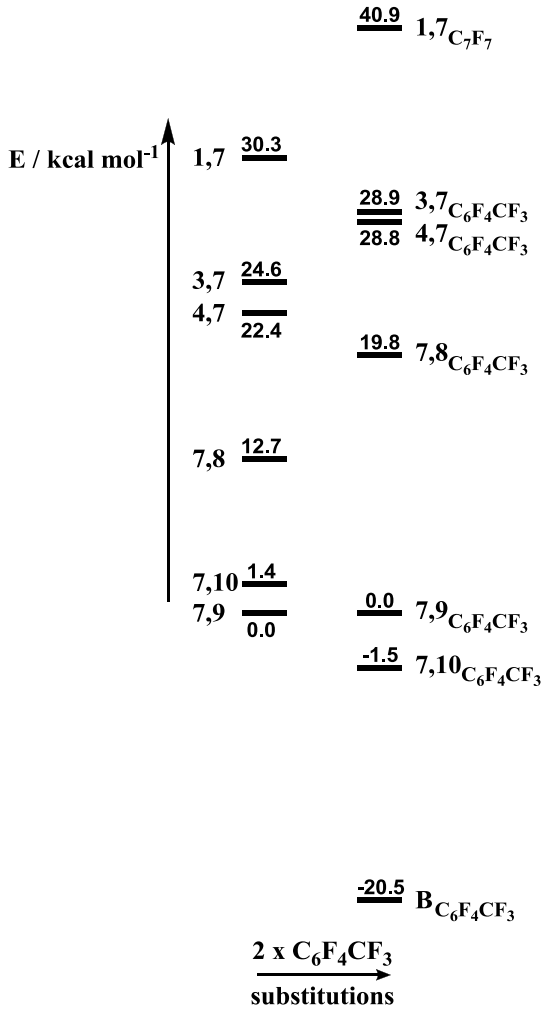

Figure 3.25 – Energetic order of *nido* fragments R = H and *p*-$C_6F_4CF_3$.

The above shows that the presence of [4,7-(*p*-$C_6F_4CF_3$)-4,7-*nido*-$C_2B_{10}H_{10}$]$^{2-}$ in solution is very unlikely. Furthermore, these C-substituents appear to increase the stabilisation brought about by having the carbon vertices on the open face of the *nido* cage. Figure 3.25 suggests, in combination with the reduction pathways computed, that the open-faced *nido* isomers most likely to be present in solution are $\mathbf{7,9}_{C_7F_7}$ and $\mathbf{7,10}_{C_7F_7}$ and that $\mathbf{B}_{C_6F_4CF_3}$, which doesn't exhibit an open face, is the most stable geometry. Isomerisation

to 4,1,12-*closo*-MC_2B_{10} is presumed therefore to occur from either the 4,1,6- or 4,1,10-*closo*-MC_2B_{10} isomer if an open face is required for association to a metal fragment, formed through metallation of **7**,**9**$_{C_7F_7}$ and **7**,**10**$_{C_7F_7}$ respectively, or through metal-induced isomerisation of **B**$_{C_6F_4CF_3}$ to give the observed 4,1,12-*closo*-MC_2B_{10} topology.

3.3.4.4. Electrochemical study of carborane isomers with R = p-$C_6F_4CF_3$

To further increase understanding of the REDOX chemistry of (p-$C_6F_4CF_3$)$_2$-*ortho*- and (p-$C_6F_4CF_3$)$_2$-*meta*-carborane, samples were provided by experimental coworkers for electrochemical analysis by Zanello *et al.*, at the *Università di Siena*, Italy. Shown below (Figure 3.26) are cyclic voltammograms recorded at a gold electrode in THF.

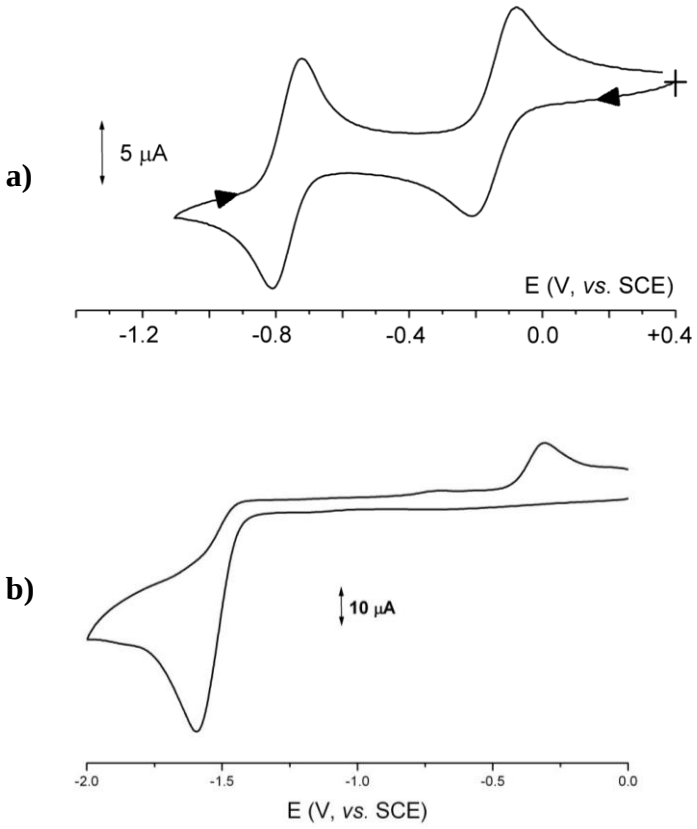

Figure 3.26 – Cyclic voltammograms of a) (p-$C_6F_4CF_3$)$_2$-*ortho*-carborane ($1.1x10^{-3}$ M, 0.05 Vs^{-1} scan rate) and b) (p-$C_6F_4CF_3$)$_2$-*meta*-carborane ($1.8x10^{-3}$ M, 0.2 Vs^{-1}). Recorded at a gold electrode in THF at 293 K. [NBu_4][PF_6] supporting electrolyte (0.2 M).

Zanello *et al.* concluded from the above that (p-$C_6F_4CF_3$)$_2$-*ortho*-carborane displays two separate reductions at E° = –0.15 V and –0.76 V, respectively. In contrast, (p-$C_6F_4CF_3$)$_2$-*meta*-carborane does not exhibit reversible reductions. Instead it is irreversibly reduced at E_p = –1.60 V. On exhaustive reduction at –1.8 V, it was reported that the colorless solution of (p-$C_6F_4CF_3$)$_2$-*meta*-carborane turns brown, in agreement with experimental observations.

Further analysis of the electrochemistry of (p-$C_6F_4CF_3$)$_2$-*ortho*-carborane showed that the voltammetric trend exhibited suggested a chemically and electrochemically reversible electron transfer. The solution was exhaustively reduced at –0.4 V (corresponding to the first reduction). This produced a purple solution of the monoanion, [(p-$C_6F_4CF_3$)$_2$-*ortho*-carborane]$^-$, which displayed a reversible reduction

corresponding to the second reversible reduction seen in Figure 3.29a. These observations suggested that the reduction is a stepwise 2e process, going through a monoanionic intermediate that is stable on the timescale of the cyclic voltammetry experiment.

3.4. Conclusions

Understanding of the polyhedral expansion of carborane derivatives by the REDCAP method has been extended through combined computational and experimental work. Previous work showed only *ortho*-tethered carboranes could be successfully expanded, and this was thought to arise from either their constrained geometries (C vertices held in adjacent positions) or the high barrier to oxidation of their reduction products.

An experimental study showed that a *meta*-tethered carborane could be produced (aiming to constrain the cage by preventing C vertices from moving together, which is associated with undesirable oxidation), however its reduction remains a challenge. Calculations suggested the tether is itself more reducible than the carborane cage whereas a doubly-protonated tether (with higher energy LUMO) was suggested as a viable alternative.

The use of *meta*-carborane derivatives with very bulky C-substituents was investigated in order to prevent C vertices from becoming adjacent. These did not, however, prevent oxidation, nor did they prevent formation of the *ortho*-carborane derivative. Indeed, the computed oxidation pathways suggest the bulky C-substituents considered actually reduce the barrier to formation of the *ortho*-carborane derivative.

Electron withdrawing C-substituents were seen, computationally, to stabilise [7,9-R_2-7,9-*nido*-$C_2B_{10}H_{10}$]$^{2-}$ (R = EWG) with respect to the first intermediate of its oxidation. A library of potential R groups was built up in close collaboration with experimental co-workers. The most promising group found was the perfluorotolyl group.

Perfluorotolyl carborane derivatives proved to have interesting REDOX chemistry, in that the C-substituents rendered the *meta*- and *para*-carborane derivatives irreducible while promoting the reduction of the *ortho*-carborane derivative and leading to reduced products of unprecedented stability. Here computational, electrochemical and chemical results were in very good agreement. 13-vertex metallacarboranes of the form 4,1,12-*closo*-MC_2B_{10} (M = Cp*Co, CpCo and Ru(*p*-cymene)) have since been synthesised through the reduction and metallation of diperfluorotolyl-*ortho*-carborane, where the reduced species goes through, presumably, a metal-mediated isomerisation process.

3.5. Current aims and future work

A 13-vertex carborane has not, thus far, been produced through this investigation and *ortho*-tethering remains the only successful synthetic route to supraicosahedral carboranes in reasonable yield. The knowledge gained through this work, however, promises the discovery of unconnected C-substituents that produce a supraicosahedral carborane, given the major problem being faced, the reoxidation of reduced carborane fragments, has been overcome.

Further development of the chemistry of carboranes with electron withdrawing C-substituents is the most promising part of this work. Current efforts involve the inclusion of electron withdrawing B-substituents and their effects on the carborane cages. For example adjacent C-Ph and B-Ph may give the same cage antibonding interaction seen in diphenyl-*ortho*-carborane, but now between C and B vertices, leading to different reduction mechanisms.

The most exciting future aim would be to produce a 13-vertex carborane as a result of stabilisation, towards oxidation, of a *nido* fragment by electron withdrawing groups.

3.6. References

1. S. Zlatogorsky, D. Ellis, G. M. Rosair and A. J. Welch, *Chem. Commun.*, 2007, 2178-2180.
2. M. F. Hawthorne and G. B. Dunks, *Science*, 1972, **178**, 462-471.
3. A. Burke, D. Ellis, B. T. Giles, B. E. Hodson, S. A. Macgregor, G. M. Rosair and A. J. Welch, *Angew. Chem.-Int. Edit.*, 2003, **42**, 225-228.
4. N. M. M. Wilson, D. Ellis, A. S. F. Boyd, B. T. Giles, S. A. Macgregor, G. M. Rosair and A. J. Welch, *Chem. Commun.*, 2002, 464-465.
5. R. McIntosh, D. Ellis, J. Gil-Lostes, K. J. Dalby, G. M. Rosair and A. J. Welch, *Dalton Trans.*, 2005, 1842-1846.
6. J. Zhang, L. Deng, H.-S. Chan and Z. Xie, *J. Am. Chem. Soc.*, 2006, **129**, 18-19.
7. G. Scott, A. McAnaw, D. McKay, A. S. F. Boyd, D. Ellis, G. M. Rosair, S. A. Macgregor, A. J. Welch, F. Laschi, F. Rossi and P. Zanello, *Dalton Trans.*, 2010, **39**, 5286-5300.
8. E. I. Tolpin and W. N. Lipscomb, *Inorg. Chem.*, 1973, **12**, 2257-2262.
9. H. Tricas, *PhD Thesis*, Heriot-Watt University, 2010.
10. D. J. Wales, *J. Am. Chem. Soc.*, 1993, **115**, 1557-1567.
11. B. W. Hutton, F. MacIntosh, D. Ellis, F. Herisse, S. A. Macgregor, D. McKay, V. Petrie-Armstrong, G. M. Rosair, D. S. Perekalin, H. Tricas and A. J. Welch, *Chem. Commun.*, 2008, 5345-5347.
12. a) D. A. Brown, W. Clegg, H. M. Colquhoun, J. A. Daniels, I. R. Stephenson and K. Wade, *J. Chem. Soc., Chem. Commun.*, 1987, 889-891; b) T. D. Getman, C. B. Knobler and M. F. Hawthorne, *Inorg. Chem.*, 1992, **31**, 101-105; c) K. Chui, H.-W. Li and Z. Xie, *Organometallics*, 2000, **19**, 5447-5453; d) L. A. Boyd, W. Clegg, R. C. B. Copley, M. G. Davidson, M. A. Fox, T. G. Hibbert, J. A. K. Howard, A. Mackinnon, R. J. Peace and K. Wade, *Dalton Trans.*, 2004, 2786-2799.
13. K. Wade, *J. Chem. Soc. D*, 1971, 792-793.
14. K. Uneyama, *Organofluorine Chemistry*, Blackwell, Oxford, UK, 2006.
15. E. D. Glendening, A. E. Reed, J. E. Carpenter and F. Weinhold, *NBO, Version 3.1*, University of Wisconsin, Madison WI, 1994.
16. a) J. A. Pople and M. Gordon, *J. Am. Chem. Soc.*, 1967, **89**, 4253-4261; b) S. A. Holmes and T. D. Thomas, *J. Am. Chem. Soc.*, 1975, **97**, 2337-2341; c) J. Goodman, V. V. Grushin, R. B. Larichev, S. A. Macgregor, W. J. Marshall and D. C. Roe, *J. Am. Chem. Soc.*, 2009, **131**, 4236-4238.

Chapter 4 – Main Group Metallacarborane Chemistry – Stannacarboranes and Model Platinacarboranes

4.1. Introduction

4.1.1. Donor/acceptor properties of stannacarboranes

Icosahedral 1,2-R_2-3,1,2-*closo*-$SnC_2B_9H_9$ (R = H, Me)[1, 2] and subicosahedral (less than 12 vertices), e.g. 2,3-$(SiMe_3)_2$-1,2,3-*closo*-$SnC_2B_4H_4$[3] stannacarboranes were first reported forty years ago. These species displayed Lewis acidity in forming adducts with Lewis bases such as pyridine and 2,2'-bipyridine (bipy), where formation of adducts reveals (through orientation of the base) a stereochemically active lone pair on the naked Sn vertex. However no adducts are formed with classical Lewis acids, illustrating the Sn lone pair is chemically inactive.

More recent work by Wesemann *et al.* has shown that the related icosahedral stannaborate, [*closo*-$SnB_{11}H_{11}]^{2-}$,[4] *does* form adducts with Lewis acids such as Au(III) (see Figure 4.1 (left), below)[5] moreover, the monocarbon analogue, [1,2-*closo*-$SnCB_{10}H_{11}]^-$,[6] exhibits both σ-donor and π-acceptor properties. This series of [1,2-*closo*-$SnC_nB_{11-n}H_{11}]^{-2+n}$ (n = 0, 1, 2), was investigated in terms of σ-donor and π-acceptor properties by Fox, Marder and Wesemann through DFT calculations.[7] The changes in frontier molecular orbitals (FMOs) through the series, in terms of shapes and energies, were used to rationalise experimental observations. The orbitals were found to decrease in energy with each isolobal replacement of $\{BH\}^{2+}$ with $\{CH\}^{3+}$, reflecting the experimental trend in σ-donor ability (from the Sn lone pair in the HOMO) and increase in π-acceptor character into the LUMO. This was attributed to the overall charge of the cluster decreasing from the dianionic stannaborate to the neutral stannacarborane as well as the substitution of more electronegative C vertices for B vertices in the cage.

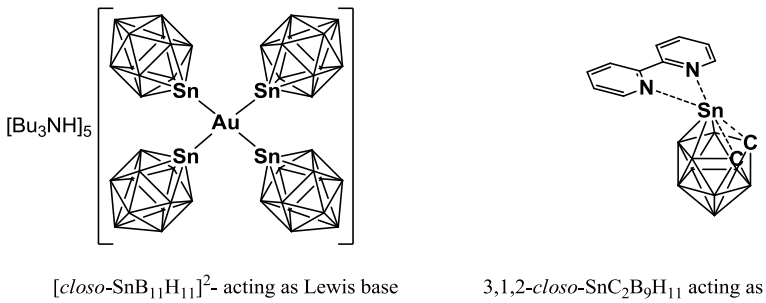

[*closo*-$SnB_{11}H_{11}]^{2-}$ acting as Lewis base 3,1,2-*closo*-$SnC_2B_9H_{11}$ acting as Lewis acid

Figure 4.1 – Stannaborate dianion as a Lewis base (left)[5] and stannacarborane as Lewis acid with stereochemically active lone pair (right).[1]

In 2002, Welch *et al.* reported the first examples of a supraicosahedral p-block metallacarborane; 'carbons apart' 4,1,6-*closo*-$SnC_2B_{10}H_{12}$, in which the two carbon vertices are separated by a single boron vertex, and its C-dimethyl analogue, 1,6-Me_2-4,1,6-*closo*-$SnC_2B_{10}H_{10}$, which each exhibit a naked Sn vertex in the 4 position.[8] In addition, the supraicosahedral 'carbons adjacent' stannacarborane, 1,2-μ-$(CH_2)_3$-4,1,2-*closo*-$SnC_2B_{10}H_{10}$, has been synthesised.[9, 10] Section 4.2 of this chapter extends the investigations of donor/acceptor properties of stannacarboranes into supraicosahedral dicarbon species by crystallographic analysis of their adducts with Lewis bases and DFT calculations.[11]

4.1.2. Slip distortion in metallacarboranes

The slip distortion, Δ, in a metallacarborane is a measure of the extent to which the metal fragment is horizontally displaced with respect to the carborane ligand, measured by reference to the centroid, *c*, of the lower B_5 belt (see Figure 4.2, below). Slipping distortions were characterised around 30 years ago in $(L_2M)C_2B_9$ species (M = Pt or Pd, L = phosphine) in 'carbons apart' 2,1,7-MC_2B_9[12] and 'carbons adjacent' 3,1,2-MC_2B_9.[13]

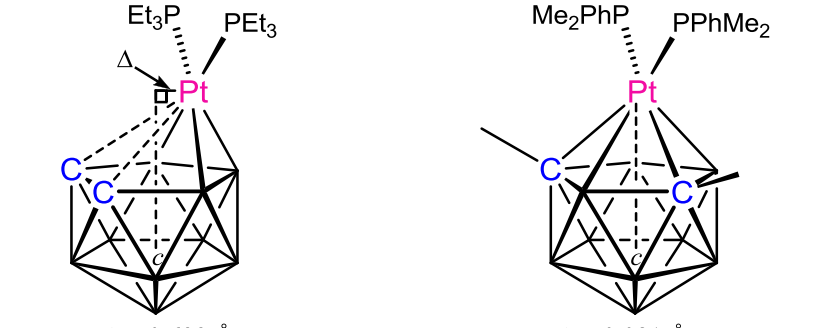

Figure 4.2 – Slipped platinacarboranes, where Δ is large in 3,1,2-MC_2B_9 and small in 2,1,7-MC_2B_9.

It was found that Δ was greater in the 'carbons adjacent' species, which was rationalised by Welch and Mingos through molecular orbital (MO) calculations of the idealised, C_s symmetric, neutral fragments ({$Pt(PH_3)_2$} and {*nido*-$C_2B_9H_{11}$}) at the extended Hückel (EHMO) level.[13]

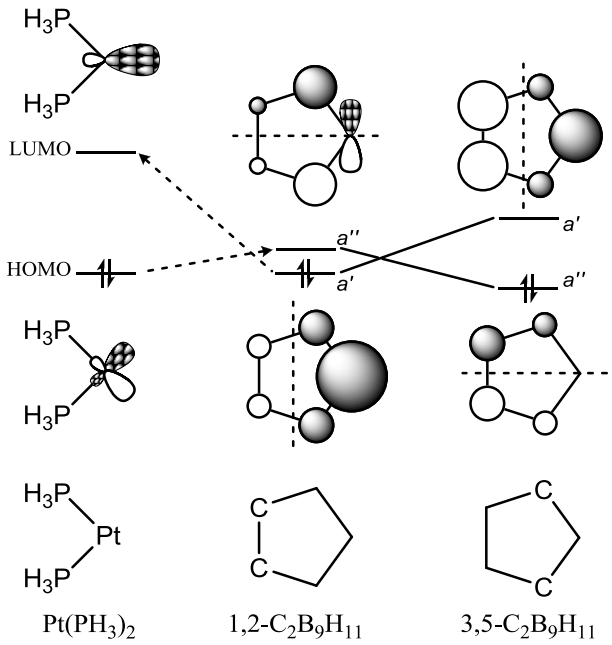

Figure 4.3 – EHMO view of orbital contributions in {$Pt(PH_3)_2$} and {*nido*-$C_2B_9H_{11}$} fragments.

It was found that the {$Pt(PH_3)_2$} fragment would have a π-donor HOMO and a σ-acceptor LUMO. These orbitals would interact with a carborane fragment whereby the π-interaction would define the orientation of the metal-based fragment and the σ-interaction would define the direction and magnitude of slip. Applied to the 'carbons adjacent' carborane fragment, {*nido*-1,2-$C_2B_9H_{11}$}, the π-donor orbital on platinum would maximise overlap with the unoccupied *a''* orbital, resulting in an orientation parallel to the C–C connection in the cage. Slip could then occur whereby the metal fragment is free to move horizontally (as shown in Figure 4.3) retaining C_s symmetry. It is clear, then, that for optimal σ-donation from carborane to metal, a large slip away from the cage carbon atoms would be required. Now considering the 'carbons apart' carborane fragment, 3,5-$C_2B_9H_{11}$, which has a small experimental *Δ*, the *a'* and *a''* orbital energies have been inverted. The π-interaction therefore results in a metal fragment orientation perpendicular to the C···C vector and, significantly, the carborane *a''* to metal LUMO σ-donation is non-bonding in C_s symmetry, meaning this interaction cannot be strengthened by any slip distortion in the cluster. It was concluded from this that the trend in slip seen experimentally could be attributed to orbital control.

In supraicosahedral stannacarboranes, however, the opposite trend is seen, where the 'carbons apart' 4,1,6-*closo*-$SnC_2B_{10}H_{12}$[11] was found to have a larger slip distortion than the 'carbons adjacent' 1,2-μ-$(CH_2)_3$-4,1,2-*closo*-$SnC_2B_{10}H_{10}$.[10] This trend was then found to exist in 13-vertex platinacarboranes 4,4-$(PMe_2Ph)_2$-4,1,6-*closo*-$PtC_2B_{10}H_{12}$[14]

and 1,2-μ-$(CH_2)_3$-4,4-$(PMe_2Ph)_2$-4,1,2-*closo*-$PtC_2B_{10}H_{10}$[15] with concurrent computational studies showed strong agreement with experiment.

In Section 4.3 of this chapter the computational rationalisation of slip distortions in icosahedral and supraicosahedral 'carbons apart' and 'carbons adjacent' platinacarboranes ($(PH_3)_2PtC_2B_9H_{11}$ and $(PH_3)_2PtC_2B_{10}H_{12}$) is discussed. Calculations were conducted at the DFT level of theory using fully optimised geometries, meaning there are analyses available that were not possible in previous work of Welch and Mingos. The comparison of steric and orbital interaction energy contributions is now available, through the energy decomposition scheme available in the Amsterdam Density Functional (ADF) code[16] (see Section 4.3.2). Here the platinacarboranes are considered as models of the stannacarborane species as they share the same trends in experimental slip distortion, but the platinacarboranes have the added benefit of providing information about orientation of the fragment through the metal phosphine ligands as was described previously for the icosahedral case through EHMO calculations.

4.2. Supraicosahedral stannacarboranes and their Lewis base adducts

The first examples of 13-vertex stannacarboranes were 'carbons apart' 4,1,6-*closo*-$SnC_2B_{10}H_{12}$ and 1,6-Me_2-4,1,6-*closo*-$SnC_2B_{10}H_{10}$, **1** (see Figure 4.4), which each exhibit a naked Sn vertex in the 4 position. These were produced *via* the REDMET method (discussed in previous chapters) whereby a THF solution of Na_2[7,9-*nido*-$C_2B_{10}H_{12}$] was reacted with 1 equivalent of $SnCl_2$ at 0 °C. 4,1,6-*closo*-$SnC_2B_{10}H_{12}$ and **1** were formed in 44% and 31% yields respectively after recrystallisation. The crystal structure of **1** was analysed along with the structures of the new compounds synthesised by the experimental collaborators in this work and are discussed in the next section of this chapter.

The 'carbons adjacent' isomer, **6** (discussed later), has since been synthesised through the same method, starting from μ-$(CH_2)_3$-*ortho*-carborane, and exhibits a high percentage docosahedral character (see Section 4.2.2 for definition) which is relatively rare in 'carbons adjacent' 13-vertex metallacarboranes.[10]

4.2.1. Experimental structures and analysis of 4,1,6-*closo*-SnC_2B_{10} species

In order to probe the Lewis acidic properties of 13-vertex stannacarboranes, **1** was reacted with classic bidentate Lewis bases (L_2). It was found to form bright yellow adducts, in toluene, with 2,2'-bipyridine (bipy), 1,10-phenanthroline (*o*-phen), 4,4'-dimethyl-2,2'-bipyridine (Me_2bipy) and 4,4'-diphenyl-2,2'-bipyridine (Ph_2bipy), of the form 1,6-Me_2-4-(L_2)-4,1,6-*closo*-$SnC_2B_{10}H_{10}$, numbered **2-5** respectively.

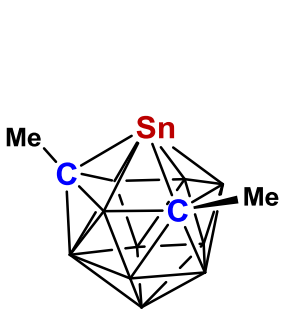

1,6-Me_2-4,1,6-*closo*-$SnC_2B_{10}H_{10}$

1

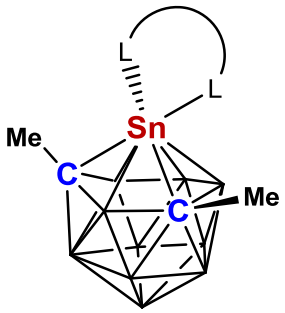

1,6-Me_2-4-(L_2)-4,1,6-*closo*-$SnC_2B_{10}H_{10}$

2-5

Figure 4.4 – 'Carbons apart' 13-vertex stannacarborane, 1 and its adducts with Lewis bases, 2-5. L_2 = bipy, *o*-phen, Me_2bipy and Ph_2bipy in 2-5 respectively.

Compounds **1-5** were subjected to crystallographic studies, the key molecular parameters from which are summarised in Table 4.1. The slip distortion, Δ, the change

in slip on adduct formation, Δ_Δ, the vertical displacement of Sn4 from the lower B_5 belt, z and the angle of inclination of the Lewis base with respect to the same 5B pentagon, θ, were measured. These parameters are illustrated in Figure 4.5.

The non-standard molecular parameters given above, Δ, Δ_Δ, z and θ, were calculated using Mercury[17] through Equations 4.1-4.4, below. For this, two least squares planes B5B9B12B13B8 (p_1) and Sn4N41CCN42 (p_2) were defined, where the angle between these planes gives θ. Also, a right-angled triangle is defined, involving Sn4 and the centroid of the B_5 belt (c), with the Pythagoras theorem then providing Δ.

$$z = \mathrm{R}(\mathrm{Sn4},p_1) \qquad \textit{(Eq. 4.1)}$$

$$\Delta = \mathrm{sqrt}(\mathrm{R}(\mathrm{Sn4},c)^2 - z^2) \qquad \textit{(Eq. 4.2)}$$

$$\Delta_\Delta = \Delta_{(\mathrm{adduct})} - \Delta_{(\mathbf{1})} \qquad \textit{(Eq. 4.3)}$$

$$\theta = \mathrm{A}(p_1,p_2) \qquad \textit{(Eq. 4.4)}$$

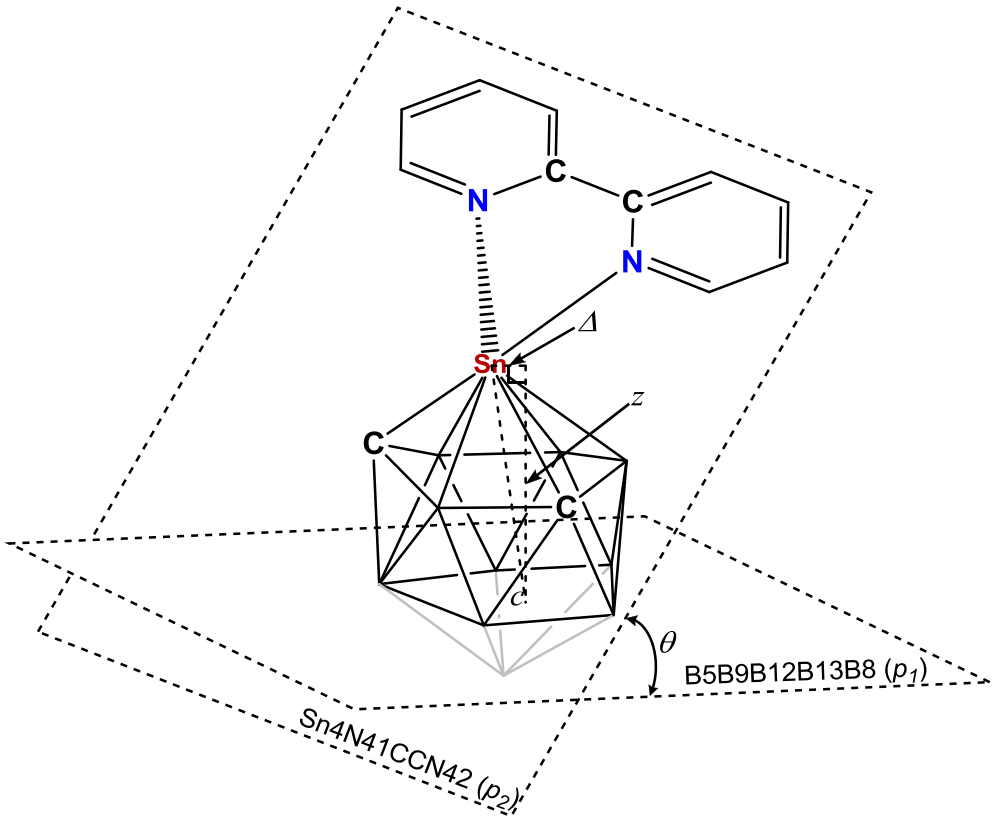

Figure 4.5 – Definition of molecular parameters in supraicosahedral stannacarborane adducts with Lewis bases.

Table 4.1 – Selected molecular parameters (Å, °) in compounds 1-5 from crystallographic studies.

	1	**2**	**3**	**4**	**5**
Sn4–C1	2.411(3)	2.717(3)	2.725(3)	2.7502(14)	2.692(7)
Sn4–B2	2.639(4)	3.033(4)	3.027(3)	3.0642(17)	3.008(8)
Sn4–C6	2.672(4)	3.173(4)	3.064(3)	3.1182(15)	3.205(7)
Sn4–B10	2.425(4)	2.620(4)	2.547(3)	2.5561(17)	2.530(9)
Sn4–B7	2.453(4)	2.471(4)	2.463(3)	2.4135(17)	2.473(11)
Sn4–B3	2.592(4)	2.717(4)	2.750(3)	2.7215(17)	2.7552(7)
Sn4–N41		2.389(3)	2.425(2)	2.3854(12)	2.374(6)
Sn4–N42		2.384(3)	2.397(2)	2.3611(13)	2.347(7)
Δ	0.274	0.651	0.582	0.665	0.549
Δ_{Δ}		0.377	0.308	0.391	0.275
z	3.407	3.689	3.665	3.656	3.650
θ		21.2	20.6	26.4	19.0

Perspective views of the crystallographically determined molecular structures are given in Figures 4.6-4.8.

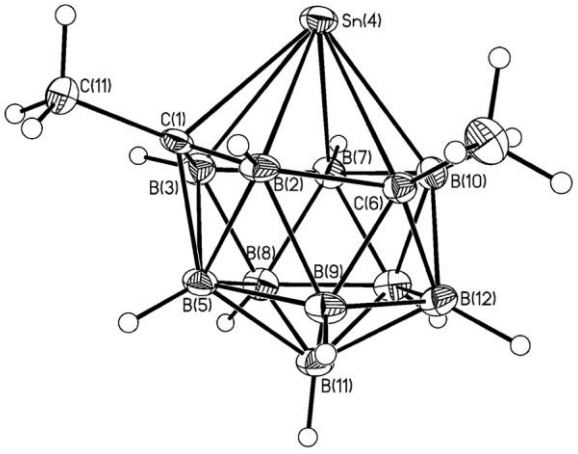

Figure 4.6 – Perspective view of 1 with thermal ellipsoids at 50% probability (except H).[8]

Through this analysis, it can be seen that the slip distortion increases upon adduct formation from 0.274 Å in the original naked tin species, **1**, to an average Δ = 0.612 Å for adducts. The vertical displacement, *z*, of Sn from p_1 also increases on adduct formation, from 3.407 Å in **1** to an average *z* = 3.655 Å in **2-5**. The final parameter, θ, measures the hinging of the Lewis base with respect to the carborane fragment which indicates the presence of a stereochemically active lone pair on tin, as is seen in icosahedral stannacarboranes. The largest θ is seen in **4**, θ = 26.4°. **4** also exhibits the largest Δ of 0.665 Å. This trend is seen across all four adducts, suggesting these parameters vary according to the same effect. There is not a strong correlation, however, between *z* and θ or Δ. Given that Δ is increased upon adduct formation, it seems reasonable to assume that both Δ and θ are directly proportional to the strength of the donor/acceptor interaction.

In adduct **2** (Figure 4.7a) the Lewis base, bipy, was expected to have intermediate σ-donor strength with respect to its derivatives, Me_2bipy (methyl groups electron donating to N) and Ph_2bipy (phenyl groups electron withdrawing from N), owing to decreasing electron density at the nitrogen atoms in the order Me_2bipy > bipy > Ph_2bipy. Verification of this can be achieved computationally by comparing the HOMO energies, where a higher energy suggests a better donor and the natural charges of the nitrogen centres where a more negative nitrogen suggests a better donor. The HOMOs of bipy, Me_2bipy and Ph_2bipy are partially delocalised and include out of phase contributions from both nitrogen lone pairs. The energy of this orbital was found to be -5.22 eV in bipy and -5.09 and -5.20 eV in Me_2bipy and Ph_2bipy respectively. Therefore the orbital energies suggest Me_2bipy is a better donor than bipy, as expected, but that Ph_2bipy has the same, or slightly better, donor strength as bipy. Evaluation of natural charges in these Lewis bases shows nitrogen charges of -0.407 in bipy and -0.412 and -0.408 in Me_2bipy and Ph_2bipy respectively. Natural charges are therefore in agreement with HOMO energies that Me_2bipy is the strongest donor and bipy and Ph_2bipy have similar donor strengths. This result may be rationalised by considering opposing inductive and resonance effects of the phenyl substituent, where electron donation through the σ-bonded framework of the molecule increases the energy of the nitrogen lone pairs, while the electron withdrawal through the π-system reduces the charge on the nitrogen centres. In adduct **3** (Figure 4.7b), *o*-phen is used as the Lewis base. Its σ-donor strength is thought to be less than that of bipy as it has the added conjugation of the central aromatic ring. It also possesses enforced planarity, which appears to weaken the interaction with the stannacarborane Lewis acid, since **2** clearly exhibits a non-planar bipy in its crystal structure. Therefore, an overall ordering of donor/acceptor interaction strength in adducts is expected as **4** > **2** ≈ **5** > **3**. Experimentally, the order of Δ and of θ is **4** > **2** > **3** > **5**. This therefore suggests that these molecular parameters are somewhat related to the strength of the donor/acceptor interaction in adducts **2**-**5**.

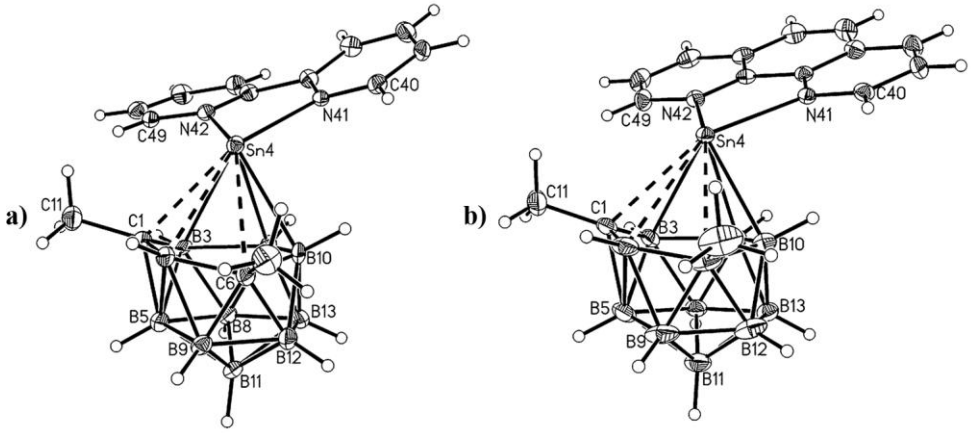

Figure 4.7 – a) Perspective view of 2 and b) perspective view of 3 with thermal ellipsoids as Fig. 4.6.

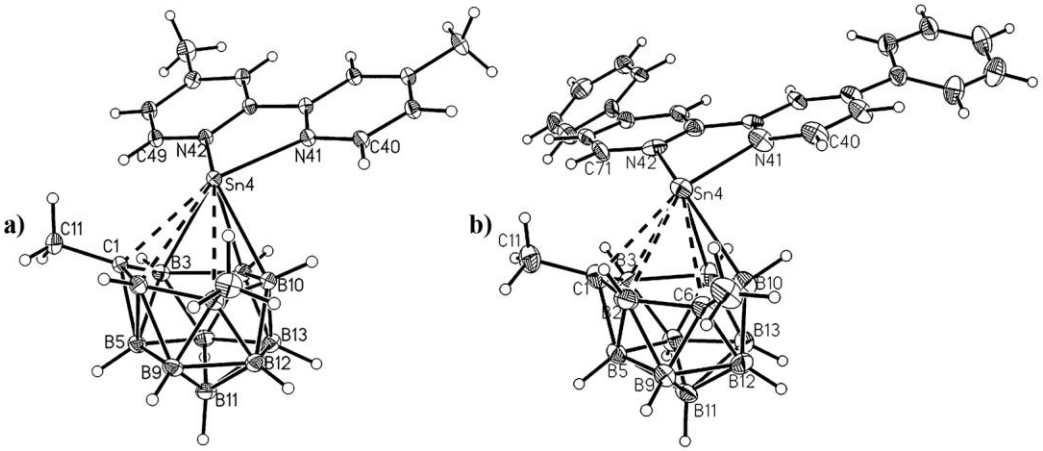

Figure 4.8 – a) Perspective view of 4 and b) perspective view of 5 with thermal ellipsoids as Fig. 4.6.

4.2.2. Experimental structures and analysis of 4,1,2-*closo*-SnC_2B_{10} species

As remarked upon in the introduction to this section, the naked tin 'carbons adjacent' 13-vertex stannacarborane, 1,2-μ-$(CH_2)_3$-4,1,2-*closo*-$SnC_2B_{10}H_{10}$ (**6**, Figure 4.10) is described as having a high percentage docosahedral character. Its adducts with Lewis bases (**7**-**9**, Figure 4.10), however, are best described as having henicosahedral structures (see Figure 4.9, below).

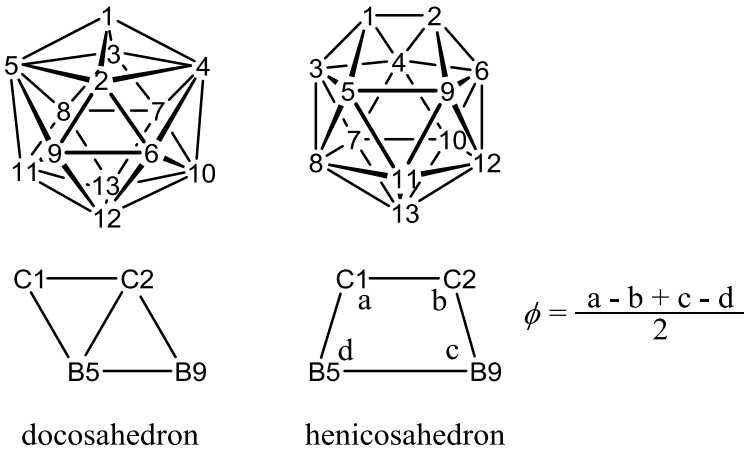

Figure 4.9 – The docosahedron (left) and henicosahedron (right) related by the presence or absence of the C2–B5 connection.

The position of a compound on the continuum between these two forms can therefore be used as an additional geometrical handle on the interaction strength in adducts of 'carbons adjacent' stannacarboranes. Two further molecular parameters, ϕ and x, are therefore defined. The former is the average difference between angles C1-C2-B9 and C2-C1-B5 and angles C2-B9-B5 and B9-B5-C1 and the latter as the 'percentage docosahedral character', where the henicosahedron has ϕ = 0° by symmetry and the 'most docosahedral' species known in the literature is the nickelacarborane[15] 1,2-μ-$(CH_2)_3$-4-dppe-4,1,2-*closo*-$NiC_2B_{10}H_{10}$ with ϕ = 41.55°.

$$\phi = (|C1\text{-}C2\text{-}B9 - C2\text{-}C1\text{-}B5| + |C2\text{-}B9\text{-}B5 - B9\text{-}B5\text{-}C1|) / 2 \qquad \textit{(Eq. 4.5)}$$

$$x = (\phi / 41.55) \times 100\ \% \qquad \textit{(Eq. 4.6)}$$

The Lewis acidic properties of **6** were probed through the method used above (for **1**) using bipy, *o*-phen and Ph_2bipy to form bright yellow adducts **7**, **8** and **9** respectively.

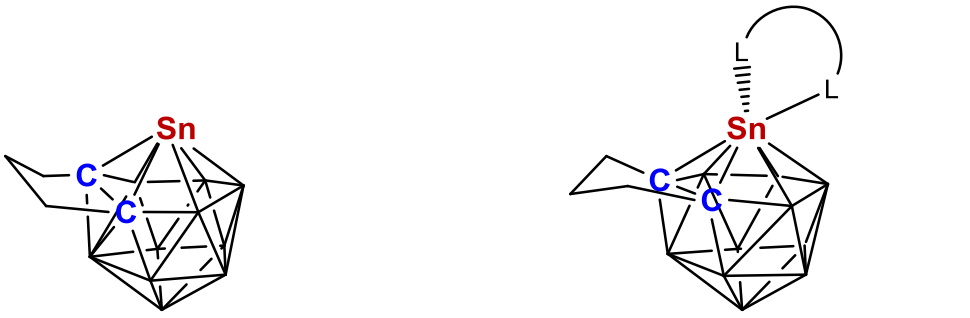

1,2-μ-$(CH_2)_3$-4,1,2-*closo*-$SnC_2B_{10}H_{10}$
6

1,6-Me_2-4-(L_2)-4,1,6-*closo*-$SnC_2B_{10}H_{10}$
7-9

Figure 4.10 – 'Carbons adjacent' 13-vertex stannacarborane, docosahedral 6 and its henicosahedral adducts with Lewis bases, 7-9. L_2 = bipy, *o*-phen and Ph_2bipy.

Compounds **6-9** were subjected to structural analysis as before and the results of this are given in Table 4.2, below. Perspective views of the crystallographically determined molecular structures are given in Figures 4.11 and 4.12 (adducts **7** and **9** were seen to crystallise with two molecules in the asymmetric unit cell, Figure 4.11b shows only **7α** while Figure 4.12b shows **9β**).

Table 4.2 – Selected molecular parameters (Å, °) in compounds 6-9 from crystallographic studies.

	6	**7α**	**7β**	**8**	**9α**	**9β**
Sn4–C1	2.545(2)	2.813(17)	2.879(18)	2.803(2)	2.821(4)	2.782(4)
Sn4–C2	2.727(3)	2.92(2)	2.824(17)	2.820(2)	2.797(4)	2.864(5)
Sn4–B6	2.582(3)	2.95(2)	2.82(2)	2.899(3)	2.732(5)	2.988(6)
Sn4–B10	2.375(3)	2.50(2)	2.43(2)	2.521(2)	2.469(5)	2.604(6)
Sn4–B7	2.492(3)	2.46(2)	2.47(2)	2.448(2)	2.585(5)	2.441(5)
Sn4–B3	2.692(3)	2.786(19)	2.897(19)	1.433(3)	1.431(6)	1.420(6)
C1–C2	1.445(3)	1.40(3)	1.44(3)	2.755(2)	2.949(5)	2.671(5)
C2–B5[a]	2.056(4)	2.33(3)	2.45(3)	2.410(3)	2.359(7)	2.378(7)
Sn4–N41		2.419(16)	2.399(15)	2.4481(17)	2.433(4)	2.462(4)
Sn4–N42		2.396(15)	2.396(14)	2.4460(18)	2.419(4)	2.415(4)
Δ	0.144	0.392	0.410	0.341	0.331	0.400
Δ_Δ		0.248	0.266	0.197	0.187	0.256
z	3.455	3.644	3.644	3.631	3.648	3.635
θ		24.26	25.68	30.16	27.13	16.04
ϕ	33.37	7.46	0.97	4.68	8.98	6.76
x	80.3	18.0	0.02	11.3	21.6	16.3

[a] For the henicosahedral species **7-9** the smaller of the C2−B5 and C1−B9 distances is quoted, since these molecules could be numbered in one of two enantiomorphic ways.

Through this analysis the docosahedral description of **6** is now quantified as x = 80.3 % and its adducts confirmed as essentially henicosahedral with x in the range 0.02-21.6 %. Δ is again systematically increased with adduct formation, with Δ_Δ in the range 0.187 to 0.266 Å. As seen in the 'carbons apart' adducts, θ values clearly indicate the presence of a stereochemically active lone pair on Sn. Δ and θ are not well correlated in compounds **7-9** and indeed neither are strongly correlated with the σ-donor strength of the associated Lewis base. This may be due to greater flexibility of the cage in 'carbons adjacent' species than in 'carbons apart' species, as well as the increased complexity of the analysis due to the asymmetric nature of the crystallised adducts **7** and **9**, somewhat masking the subtle trends in other molecular parameters (namely Δ and θ).

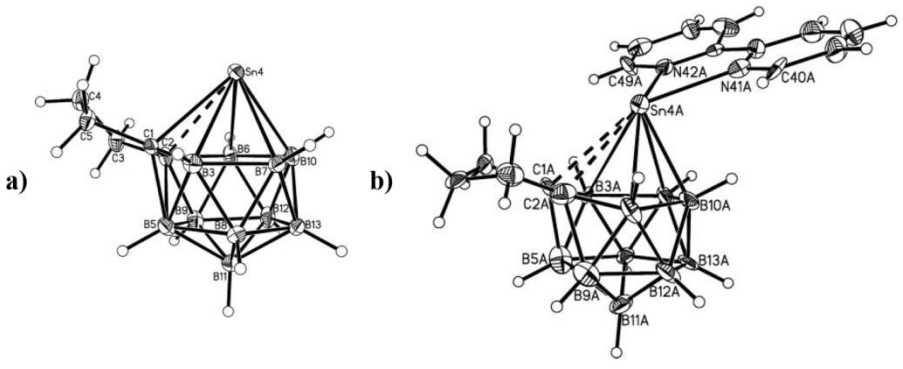

Figure 4.11 – a) Perspective view of 6 and b) perspective view of 7α, thermal ellipsoids as Fig. 4.6.

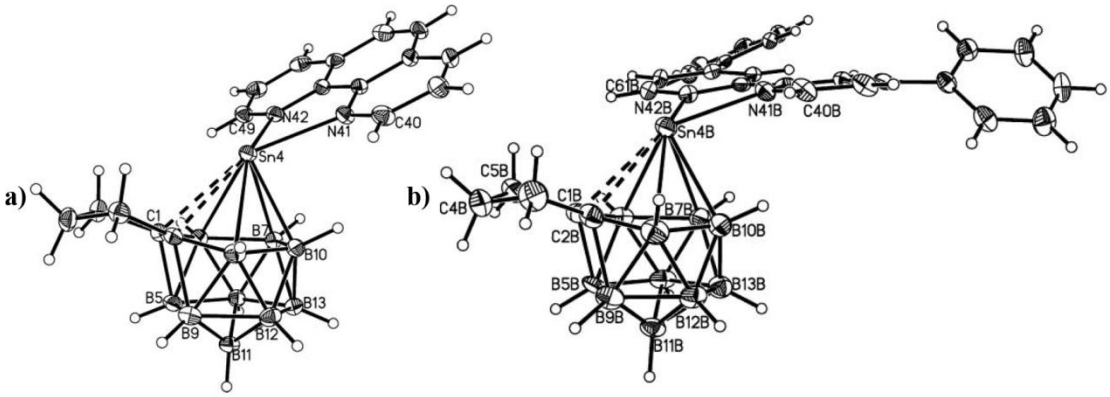

Figure 4.12 – a) Perspective view of 8 and b) perspective view of 9β, thermal ellipsoids as Fig. 4.6.

4.2.3. Computational structures and comparison with experiment

DFT calculations were carried out in an attempt to understand the structural trends seen in supraicosahedral stannacarboranes and their adducts. Geometries were optimised in Gaussian 03[18] employing the BP86 exchange correlation functional. The Stuttgart relativistic ECP and associated basis sets[19] and additional d-polarization functions[20] were used for Sn while 6-31G** basis sets were used for B, C, H and N atoms. Analytical frequency calculations were carried out to confirm optimised geometries as minima. The 'carbons apart' stannacarboranes, **1**, **2**, **4** and **5**, and 'carbons adjacent' species, **6** and **7**, were optimised in the gas phase, giving computed geometries **A**-**F** respectively (Figure 4.13), where exopolyhedral carbon substituents (Me in **1**, **2**, **4** and **5** and μ-$(CH_2)_3$ is **6** and **7**) were simplified to H. Optimised geometries were then analysed using the same methodology as described for experimental structures. The results of this analysis are summarised in Table 4.3, below.

Table 4.3 – Selected molecular parameters (Å, °) in computed geometries A-F; values given in brackets represent the error in the parameter with respect to that determined experimentally.[a]

	A	**B**	**C**	**D**	**E**	**F**[b]
Sn4–C1	2.416	2.582	2.594	2.595	2.549	2.832
	(-0.005)	(0.135)	(0.056)	(0.097)	(0.004)	(0.019)
Sn4–2[c]	2.652	2.923	2.937	2.937	2.762	2.787
	(-0.013)	(0.110)	(0.127)	(0.071)	(0.035)	(-0.13)
Sn4–6[d]	2.700	2.992	3.005	3.005	2.560	2.742
	(-0.028)	(0.181)	(0.113)	(0.020)	(-0.022)	(-0.21)
Sn4–B10	2.433	2.541	2.548	2.547	2.365	2.458
	(-0.008)	(0.079)	(0.008)	(-0.017)	(-0.010)	(-0.04)
Sn4–B7	2.471	2.468	2.471	2.469	2.514	2.535
	(-0.018)	(0.003)	(-0.058)	(0.004)	(0.022)	(0.08)
Sn4–B3	2.634	2.689	2.695	2.694	2.675	2.903
	(-0.042)	(0.028)	(0.027)	(0.061)	(-0.017)	(-0.117)
C1–C2					1.463	1.437
					(0.018)	(0.037)
C2–B5					1.954	2.434
					(-0.102)	(0.10)
Sn4–N41		2.638	2.619	2.618		2.623
		(-0.249)	(-0.234)	(-0.244)		(0.204)
Sn4–N42		2.593	2.573	2.570		2.608
		(-0.209)	(-0.212)	(-0.223)		(0.212)
Δ	0.287	0.517	0.525	0.525	0.117	0.330
	(-0.013)	(0.134)	(0.140)	(0.024)	(-0.027)	(-0.062)
Δ_Δ		0.230	0.238	0.238		0.212
		(0.147)	(0.153)	(0.037)		(-0.036)
z	3.419	3.596	3.606	3.605	3.432	3.612
	(0.012)	(0.093)	(0.050)	(0.045)	(-0.023)	(-0.032)
θ		27.2	26.6	26.8		31.2
		(-6.0)	(-0.2)	(-7.8)		(6.97)
ϕ					28.8	3.25
					(-4.57)	(-4.21)
x					69.2	7.82
					(-11.1)	(-10.2)

[a] Standard accuracy for computational values is 4 sig. figs. for distances and 3 sig. figs. for angles. Differences between computed and experimental parameters are given in brackets.
[b] Errors with respect to experiment for model **F** are given with respect to **7α**.
[c] Vertex 2 is a boron atom in structures **A**-**D** and a carbon atom in structures **E** and **F**.
[d] Vertex 6 is a carbon atom in structures **A**-**D** and a boron atom in structures **E** and **F**.

From the above, it is clear that the computed geometries of naked tin species are in very good agreement with experiment. Errors in molecular parameters in **A** are all within 0.05 Å of those determined experimentally and those in **E** are all within 0.10 Å of experiment and also correspond well to those of Fox *et al.*[7] Calculations also agree with experiment in terms of the high percentage docosahedral character of **E** (**6**), where the computed ϕ is within 5° of the experimental value, giving x = 69.2%.

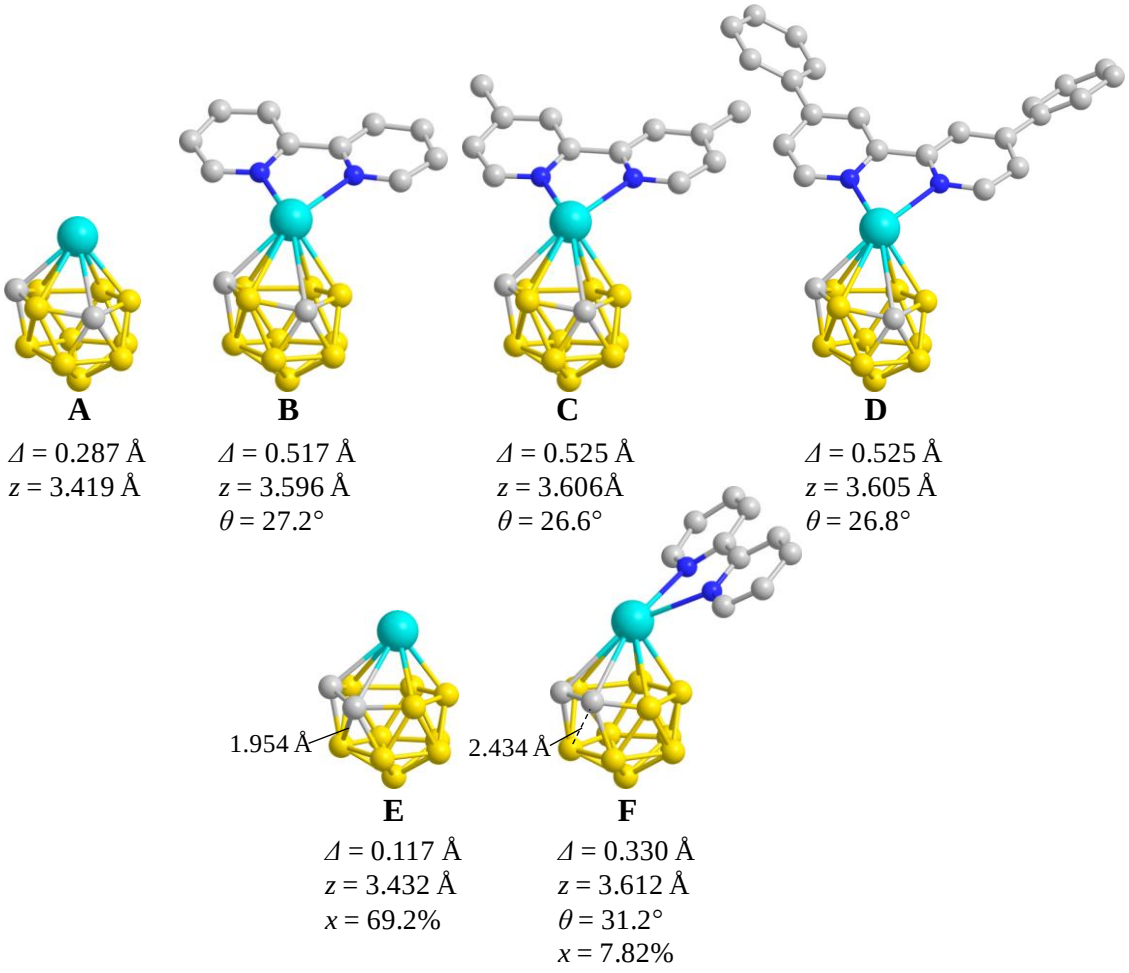

Figure 4.13 – Computed geometries for models A-F showing selected molecular parameters from Table 4.3. Hydrogen atoms are removed for clarity.

The molecular orbitals of **A** were computed, revealing HOMO and LUMO energies of -6.72 and -3.25 eV respectively, again in good agreement with those published by Fox *et al.*[7] Views of the FMOs of **A** are given in Figure 4.14, below. The HOMO is largely comprised of the Sn lone pair, while the first three lowest energy unoccupied orbitals are also largely Sn-based and are well set up to receive electron density from Lewis bases, L_2.

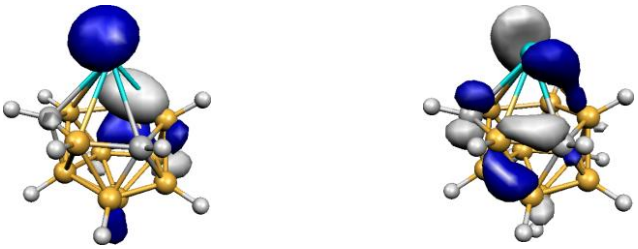

HOMO, E = -6.72 eV **LUMO**, E = -3.25 eV

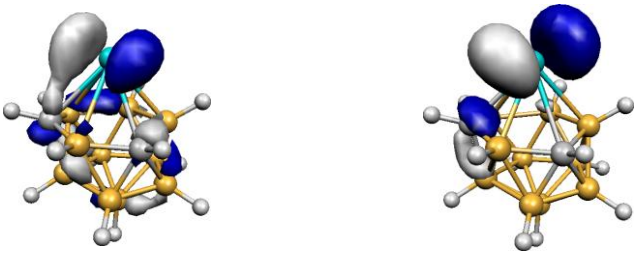

LUMO+1, E = -2.79 eV **LUMO+2**, E = -2.28 eV

Figure 4.14 – Frontier molecular orbitals of A.

The orientation of the incoming L_2 base can then be rationalised by these unoccupied MOs, as shown in Figure 4.15, below.

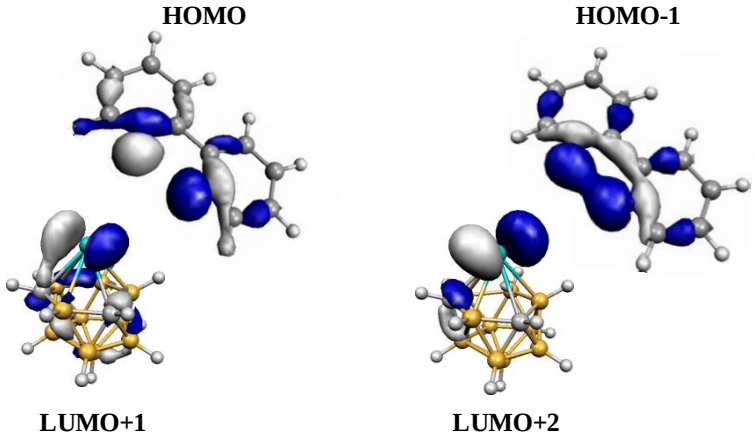

Figure 4.15 – A view of how the HOMO (left) and HOMO-1 (right) of bipy could interact with the LUMO+1 and LUMO+2 of A respectively.

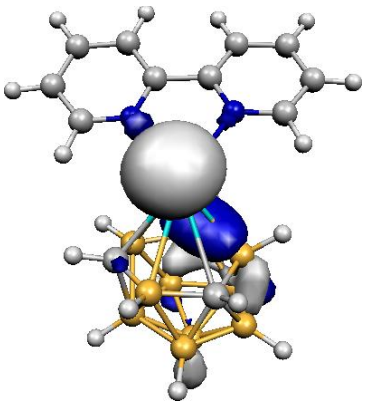

Figure 4.16 – The HOMO of B, confirming large contribution of Sn lone pair to stereochemistry.

Computing the molecular orbitals of **B** confirms the Sn lone pair dominates the HOMO (Figure 4.16, above) as inferred from both computationally and experimentally determined structures. The frontier molecular orbitals of **E** were also computed, showing similar results to **A**, and are summarised in Figure 4.17, below.

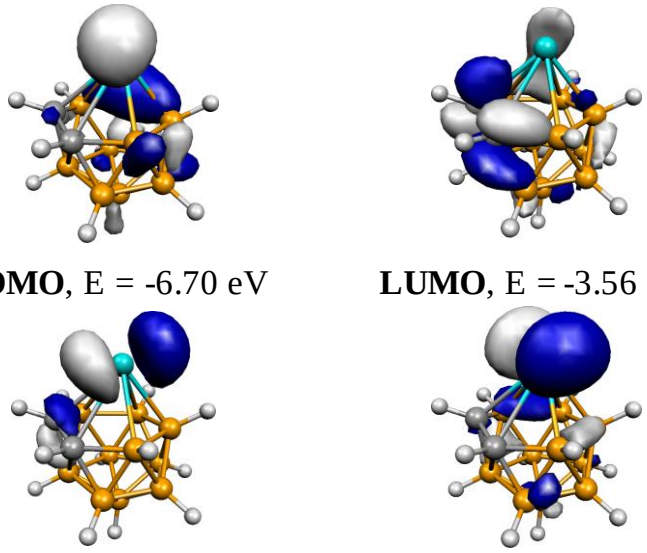

HOMO, E = -6.70 eV **LUMO**, E = -3.56 eV

LUMO+1, E = -2.82 eV **LUMO+2**, E = -2.33 eV

Figure 4.17 – Frontier molecular orbitals of E.

Computed geometries **B**, **C**, **D** and **F** represent experimental adducts **2**, **4**, **5** and **7**. Structural parameters pertaining to the stannacarborane cage are reproduced relatively well, however large discrepancies are seen between computed and experimental Sn–N bond lengths. These are found to be on average 0.223 Å (8.6%) longer in the computed geometries than in experiment. In compensation for this systematic overestimation of Sn–N bond lengths, Sn–cage distances in **B**-**D** are generally shorter in computed geometries. This is carried through to molecular parameters, Δ (and therefore Δ_Δ) and *z*, which are also underestimated, the culmination of which is the failure of these calculations to reproduce the experimental trend in Δ with respect to Lewis base σ-donor strength in these adducts. For example the computed slip in **C** is *equal* to that in **D** at Δ = 0.525 Å, despite their associated Lewis bases appearing at opposing ends of the range in σ-donor strength in this work.

Somewhat curiously, Δ in **F** corresponds well with that in **7**, despite the same systematic overestimation of Sn–N distances (which are included in the average given above). This may be related to the directionality of slip distortion (see Section 4.3) reducing the dependence of slip on donor/acceptor interaction strength, as in the 'carbons adjacent' stannacarborane adducts slip is small and approximately perpendicular to the Sn–base

direction while in the 'carbons apart' isomers the slip direction is approximately collinear with the Sn4–N42 bond. Finally, the change in *x* between naked tin 'carbons adjacent' and its adducts is successfully reproduced in computed geometries, whereby **F** and **7α** are henicosahedral (*x* = 7.8% and 18% respectively) and **E** and **6** are docosahedral (*x* = 69% and 80% respectively).

4.2.4. Computed vs. experimental Sn–N bond lengths

In order to address the discrepancies seen between computed and measured Sn–N distances, **A**-**D** were reoptimised using a range of different methods and basis sets. These included DFT methodologies: the B3LYP hybrid functional;[21] the TPSS *meta*-GGA;[22] the recent M06 hybrid functional,[23] which includes dispersion effects and the MP2 wavefunction-based method.[24] All optimisation were conducted with standard basis sets (6-31G**/SDD(d)). Triple-ζ polarised (6-311G**) and diffuse double-ζ polarised (6-31++G**) basis sets (for B, C, H and N centres) were also tested with the standard DFT method (BP86). Geometries generated from these tests are numbered with superscripts 1-6 respectively. **B**-**D** were also recomputed at the standard level with Sn–N interatomic distances fixed at those found experimentally *via* constrained optimisations, giving geometries $\mathbf{B^{13}}$-$\mathbf{D^{13}}$. Fully optimised geometries $\mathbf{A^{1\text{-}6}}$-$\mathbf{D^{1\text{-}6}}$, $\mathbf{A^{7\text{-}12}}$-$\mathbf{B^{7\text{-}12}}$ (described later) and constrained geometries $\mathbf{B^{13}}$-$\mathbf{D^{13}}$ were then analysed using the same method as before, using Mercury. In the case of geometries with fixed Sn–N distances, the small energy differences with respect to fully optimised geometries (ΔE = 2.8, 2.9 and 3.1 kcal mol^{-1} for $\mathbf{B^{13}}$, $\mathbf{C^{13}}$ and $\mathbf{D^{13}}$, respectively) are of particular note and will be discussed later.

Table 4.4 – Selected molecular parameters (Å, °) from functional testing in 'carbons apart' stannacarborane, A and adducts B-D (B3LYP and TPSS).[a]

	B3LYP/6-31G**/SDD(d)				TPSS/6-31G**/SDD(d)			
	A[1]	**B[1]**	**C[1]**	**D[1]**	**A[2]**	**B[2]**	**C[2]**	**D[2]**
Sn4–C1	2.413	2.596	2.608	2.610	2.416	2.575	2.586	2.588
	(-0.002)	(0.121)	(0.042)	(0.082)	(-0.005)	(0.142)	(0.064)	(0.104)
Sn4–B2	2.653	2.928	2.943	2.944	2.655	2.922	2.935	2.937
	(-0.014)	(0.105)	(0.121)	(0.064)	(-0.016)	(0.111)	(0.129)	(0.071)
Sn4–C6	2.716	3.016	3.030	3.031	2.678	2.974	2.986	2.987
	(-0.044)	(0.157)	(0.088)	(-0.006)	(-0.006)	(0.199)	(0.132)	(0.038)
Sn4–N41		2.668	2.647	2.645		2.626	2.610	2.603
		(-0.279)	(-0.262)	(-0.271)		(-0.237)	(-0.225)	(-0.229)
Sn4–N42		2.615	2.590	2.589		2.572	2.554	2.551
		(-0.231)	(-0.229)	(-0.242)		(-0.188)	(-0.193)	(-0.204)
Δ	0.310	0.551	0.565	0.565	0.274	0.510	0.517	0.517
	(-0.036)	(0.100)	(0.100)	(-0.016)	(0.000)	(0.141)	(0.148)	(0.032)
z	3.420	3.598	3.608	3.608	3.412	3.591	3.599	3.600
	(-0.013)	(0.091)	(0.048)	(0.042)	(-0.005)	(0.098)	(0.057)	(0.050)
θ		25.2	24.5	24.7		24.3	23.4	24.2
		(-4.0)	(2.0)	(-5.7)		(-3.1)	(3.1)	(-5.2)

[a] Standard accuracy for computational values is 4 sig. figs. for distances and 3 sig. figs. for angles. Differences between computed and experimental parameters are given in brackets.

Table 4.5 – Selected molecular parameters (Å, °) from functional testing in 'carbons apart' stannacarborane, A and adducts B-D (M06 and MP2).[a]

	M06/6-31G**/SDD(d)				MP2/6-31G**/SDD(d)			
	A[3]	**B[3]**	**C[3]**	**D[3]**	**A[4]**	**B[4]**	**C[4]**	**D[4]**
Sn4–C1	2.385	2.523	2.530	2.527	2.403	2.542	2.549	2.548
	(0.026)	(0.194)	(0.120)	(0.165)	(0.008)	(0.175)	(0.101)	(0.144)
Sn4–B2	2.644	2.880	2.890	2.887	2.639	2.882	2.891	2.690
	(-0.005)	(0.153)	(0.174)	(0.121)	(0.000)	(0.151)	(0.173)	(0.318)
Sn4–C6	2.645	2.916	2.927	2.926	2.669	2.933	2.944	2.943
	(0.027)	(0.257)	(0.191)	(0.099)	(0.003)	(0.240)	(0.174)	(0.082)
Sn4–N41		2.962	2.667	2.673		2.642	2.521	2.628
		(-0.573)	(-0.282)	(-0.299)		(-0.253)	(-0.136)	(-0.254)
Sn4–N42		2.601	2.582	2.582		2.535	2.627	2.519
		(-0.217)	(-0.221)	(-0.235)		(-0.151)	(-0.266)	(-0.172)
Δ	0.297	0.510	0.478	0.478	0.286	0.464	0.465	0.465
	(-0.023)	(0.141)	(0.187)	(0.071)	(-0.012)	(0.187)	(0.072)	(0.084)
z	3.376	3.591	3.555	3.554	3.406	3.576	3.584	3.584
	(0.031)	(0.098)	(0.101)	(0.096)	(0.001)	(0.113)		(0.066)
θ		24.3	18.3	17.8		15.6	15.2	14.7
		(-3.1)	(8.1)	(1.2)		(5.6)	(11.3)	(4.3)

[a] Standard accuracy for computational values is 4 sig. figs. for distances and 3 sig. figs. for angles. Differences between computed and experimental parameters are given in brackets.

Tables 4.4 and 4.5, above, show that for models **A[1-4]** the effect of changing the computational methodology is minimal for the five relevant molecular parameters given. The method producing the smallest average error with respect to experiment was MP2, closely followed by TPSS with mean absolute errors of 0.005 and 0.006 Å respectively. BP86 produces a mean absolute error of 0.014 Å for these parameters and B3LYP and M06 are less accurate with respect to experiment, both having mean absolute errors of 0.022 Å.

For models **B**$^{1\text{-}4}$-**D**$^{1\text{-}4}$, no marked improvement is made upon the BP86 computed Sn–N distances with respect to experiment. The average overestimation of Sn–N distances from BP86 is 0.230 Å. From the above, for B3LYP, this average overestimation is 0.252 Å, for TPSS it is 0.212 Å, for M06 it is 0.268 Å and for MP2 it is 0.205 Å. Therefore, it is clear from these values that while some improvement in Sn–N distances may be made, the error with respect to experiment remains greater than a factor of ten larger than errors seen in molecular parameters in species **A** and **A**$^{1\text{-}4}$. As a result, changing the methodology adopted in computing these geometries does not alleviate the overall failure to reproduce experimental trends in Δ with respect to Lewis base σ-donor strength.

Table 4.6 – Selected molecular parameters (Å, °) from basis set testing in 'carbons apart' stannacarborane, A and adducts B-D (6-311G and 6-31++G**).**[a]

	BP86/6-311G**/SDD(d)				BP86/6-31++G**/SDD(d)			
	A^5	**B**^{5}	**C**^{5}	**D**^{5}	**A**^{6}	**B**^{6}	**C**^{6}	**D**^{6}
Sn4–C1	2.421	2.596	2.606	2.608	2.419	2.588	2.599	2.601
	(-0.010)	(0.121)	(0.044)	(0.084)	(-0.008)	(0.129)	(0.051)	(0.091)
Sn4–B2	2.654	2.931	2.944	2.945	2.655	2.928	2.943	2.944
	(-0.015)	(0.102)	(0.120)	(0.063)	(-0.016)	(0.105)	(0.121)	(0.064)
Sn4–C6	2.711	3.006	3.019	3.020	2.706	3.001	3.014	3.014
	(-0.039)	(0.167)	(0.099)	(0.005)	(-0.034)	(0.172)	(0.104)	(0.011)
Sn4–N41		2.635	2.619	2.615		2.642	2.624	2.620
		(-0.246)	(-0.234)	(-0.241)		(-0.253)	(-0.239)	(-0.246)
Sn4–N42		2.588	2.569	2.567		2.592	2.571	2.570
		(-0.204)	(-0.208)	(-0.220)		(-0.208)	(-0.210)	(-0.223)
Δ	0.287	0.525	0.539	0.533	0.299	0.525	0.532	0.532
	(-0.013)	(0.126)	(0.126)	(0.016)	(-0.025)	(0.126)	(0.133)	(0.017)
z	3.426	3.608	3.616	3.617	3.424	3.604	3.614	3.614
	(-0.019)	(0.081)	(0.040)	(0.033)	(-0.017)	(0.085)	(0.042)	(0.036)
θ		26.0	25.2	25.6		26.1	25.1	25.3
		(-4.8)	(1.2)	(-6.6)		(-4.9)	(1.3)	(-6.3)

[a] Standard accuracy for computational values is 4 sig. figs. for distances and 3 sig. figs. for angles. Differences between computed and experimental parameters are given in brackets.

On enlarging the basis set within the standard BP86 method (Table 4.6, above), the same overestimation is seen in Sn–N distances. The average overestimation with respect to experiment in **B**^{5}-**D**^{5}, where the basis sets for B, C, H and N atoms was increased from double- to triple-ζ, is 0.226 Å, which corresponds to an average improvement of just 0.004 Å on the double-ζ computed values. In models **B**^{6}-**D**^{6}, diffuse functions have been added to the double-ζ basis sets. The result is significantly different, as the overall average overestimation of Sn–N interatomic distances is 0.230 Å.

A and **B** were also subjected to optimisation (at the BP86/6-31G**/SDD(d) standard level) in solvent through the polarised continuum model (PCM) with a range of solvents

covering dielectric constants from ε = 2.379 (toluene) to 36.64 (acetonitrile), producing new geometries for **A** and **B**, numbered with superscripts 7-12.

Table 4.7 – Selected molecular parameters (Å, °) from PCM solvent model testing in 'carbons apart' stannacarborane, A and adduct B (toluene, diethylether and trichloromethane).[a]

	Toluene ε = 2.379		Diethylether ε = 4.335		$CHCl_3$ ε = 4.9	
	$\mathbf{A}^{7}$	$\mathbf{B}^{7}$	$\mathbf{A}^{8}$	$\mathbf{B}^{8}$	$\mathbf{A}^{9}$	$\mathbf{B}^{9}$
Sn4–C1	2.429	2.640	2.439	2.673	2.442	2.681
	(-0.018)	(0.077)	(-0.028)	(0.044)	(-0.031)	(0.036)
Sn4–B2	2.663	2.991	2.674	3.026	2.677	3.034
	(-0.024)	(0.042)	(-0.035)	(0.007)	(-0.038)	(-0.001)
Sn4–C6	2.719	3.057	2.727	3.089	2.729	3.096
	(-0.047)	(0.116)	(-0.055)	(0.084)	(-0.057)	(0.077)
Sn4–N41		2.564		2.531		2.525
		(-0.175)		(-0.142)		(-0.136)
Sn4–N42		2.526		2.496		2.493
		(-0.142)		(-0.112)		(-0.109)
Δ	0.299	0.568	0.288	0.583	0.288	0.590
	(-0.025)	(0.083)	(-0.014)	(0.068)	(-0.014)	(0.061)
z	3.440	3.647	3.457	3.676	3.461	3.682
	(-0.033)	(0.042)	(-0.050)	(0.013)	(-0.054)	(0.007)
θ		26.1		25.6		
		(-4.9)		(-4.4)		

[a] Standard accuracy for computational values is 4 sig. figs. for distances and 3 sig. figs. for angles. Differences between computed and experimental parameters are given in brackets.

Table 4.8 – Selected molecular parameters (Å, °) from PCM solvent model testing in 'carbons apart' stannacarborane, A and adduct B (tetrahydrofuran, trichloromethane and acetonitrile).[a]

	THF ε = 7.58		DCM ε = 8.93		Acetonitrile ε = 36.64	
	$\mathbf{A}^{10}$	$\mathbf{B}^{10}$	$\mathbf{A}^{11}$	$\mathbf{B}^{11}$	$\mathbf{A}^{12}$	$\mathbf{B}^{12}$
Sn4–C1	2.446	2.700	2.447	2.709	2.456	2.739
	(-0.035)	(0.017)	(-0.036)	(0.008)	(-0.045)	(-0.022)
Sn4–B2	2.681	3.054	2.682	3.061	2.691	3.090
	(-0.042)	(-0.021)	(-0.043)	(-0.028)	(-0.052)	(-0.057)
Sn4–C6	2.736	3.113	2.736	3.119	2.750	3.145
	(-0.064)	(0.060)	(-0.064)	(0.054)	(-0.078)	(0.028)
Sn4–N41		2.509		2.504		2.484
		(-0.120)		(-0.115)		(-0.095)
Sn4–N42		2.478		2.474		2.458
		(-0.094)		(-0.090)		(-0.074)
Δ	0.289	0.598	0.289	0.598	0.290	0.613
	(-0.015)	(0.053)	(-0.015)	(0.053)	(-0.016)	(0.038)
z	3.469	3.699	3.472	3.705	3.487	3.730
	(-0.062)	(-0.010)	(-0.065)	(-0.016)	(-0.080)	(-0.041)
θ		24.7		24.5		23.7
		(-3.5)		(-3.3)		(-2.5)

[a] Standard accuracy for computational values is 4 sig. figs. for distances and 3 sig. figs. for angles. Differences between computed and experimental parameters are given in brackets.

Selected parameters for optimised geometries, $\mathbf{A}^{7\text{-}12}$-$\mathbf{B}^{7\text{-}12}$, are given in Tables 4.7 and 4.8, above. Experimentally, solvents used included tetrahydrofuran (THF), toluene and dichloromethane (DCM, or its deuterated analogue), for reactions and spectroscopic analysis and 40-60° petroleum ether for growing crystals. These were therefore modelled computationally through geometry optimisations in PCM, with the additions

of acetonitrile (CH_3CN), trichloromethane ($CHCl_3$) and diethylether (Et_2O) to cover a greater range of dielectric constants.

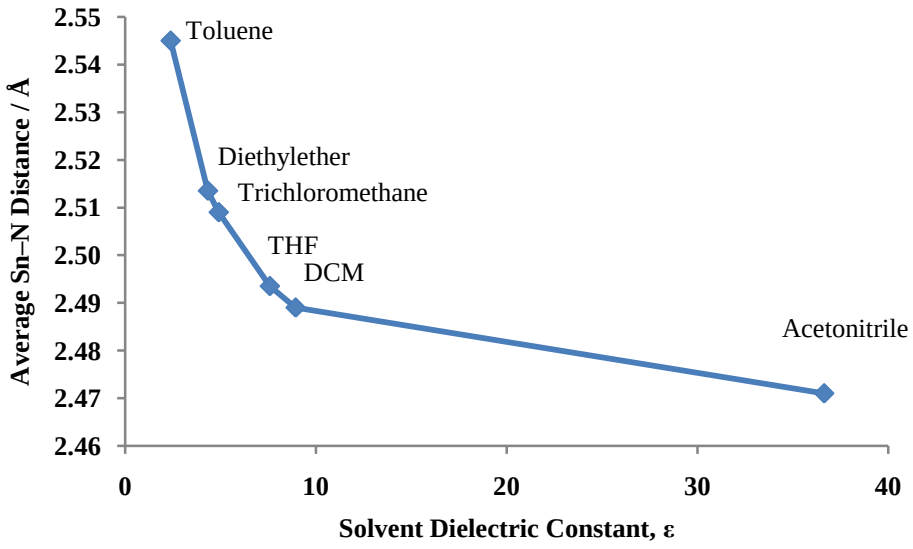

Figure 4.18 – Plot of the average Sn–N interatomic distances in $B^{7\text{-}12}$ versus solvent dielectric constant.

A trend is now seen in the Sn–N distances with respect to solvent dielectric constant and is illustrated in Figure 4.18, above. This sees average errors with respect to the experimental Sn–N distances decrease from 0.159 Å in toluene to 0.103 Å in DCM and is further decreased to 0.085 Å in acetonitrile, though this solvent is not used experimentally.

With solvent corrections, therefore, the discrepancies between computed and experimental Sn–N bond lengths are minimised. Indeed, the absolute errors in molecular parameters with respect to experiment are of the same order of magnitude for the Sn–N distance as for the stronger Sn–cage bonds and the Δ, z and θ parameters in **B** at high dielectric constant.

As noted in the introduction to this sub-section, if models **B**-**D** are reoptimised with Sn–N distances fixed at those determined experimentally, giving $\mathbf{B^{13}}$-$\mathbf{D^{13}}$, only small energy differences, with respect to fully optimised geometries, are found (*ca.* 3 kcal mol^{-1}). The conclusion from this is that there is a relatively soft potential related to the donor/acceptor interaction in there adducts. Coupled with the above dependence upon dielectric constant in solvent calculations, this observation suggests the Sn–N interatomic distances are highly sensitive to the phase in which they are measured or computed. Gas phase calculations, independent of the level of theory, do not model these distances well, while solvent calculations go some way to correcting the

discrepancies seen. It is also worth noting that mass spectrometry of these species only sees separate Lewis acid and Lewis base fragments and not a $[M]^+$ corresponding to the intact adduct.[9] The key conclusion is, therefore, that the discrepancies observed between computational results and experimental measurements (recorded in the solid state) appear to be related to the environment in which the molecules are placed.

4.3. Slip distortions in 12- and 13-vertex metallacarboranes

As seen in Section 4.2, the slip distortions, *Δ*, of supraicosahedral stannacarboranes **1** and **6** show *Δ* is larger for 'carbons apart' 4,1,6- than for 'carbons adjacent' 4,1,2-*closo*-SnC_2B_{10}. This trend is also apparent from adducts of **1** and **6** with Lewis bases (**2-5** and **7-9** respectively) where *Δ* is increased on adduct formation, but always remains larger for 'carbons apart' isomers. Moreover, the trend is supported by published geometries of supraicosahedral platinacarboranes.[14, 15] Experimental results are corroborated by computational results, though subtle trends between adducts were not reproduced by DFT.

The opposite trend is seen in icosahedra, where smaller slip distortions are seen in 'carbons apart' 2,1,7- than in 'carbons adjacent' 3,1,2-*closo*-PtC_2B_9 species.[12, 13]

In this section, the cause of slip distortion in metallacarboranes will be investigated through DFT calculations on models of known platinacarboranes; icosahedral 3,3-$(PEt_3)_2$-3,1,2-*closo*-$PtC_2B_9H_{11}$[13] (**10**) and 1,7-Me_2-2,2-$(PMe_2Ph)_2$-2,1,7-*closo*-$PtC_2B_9H_9$[12] (**11**) and supraicosahedral 1,2-μ-$(CH_2)_3$-4,4-$(PMe_2Ph)_2$-4,1,2-*closo*-$PtC_2B_{10}H_{10}$[15] (**12**) and 4,4-(PMe_2Ph_2)-4,1,6-*closo*-$PtC_2B_{10}H_{12}$[14] (**13**). In computational models of **10-13**, numbered **G-J** respectively, exopolyhedral C-substituents and P-substituents have been substituted with H. Geometries were initially optimised with the Gaussian program, through the BP86 method utilising SDD ECPs and associated basis sets for Pt and P with additional d-orbital polarisation for P and 6-31G** basis sets for B, C and H centres. The optimised geometries produced are then compared to published experimental geometries. Analysis of interaction energies between the platinum-based $\{Pt(PH_3)_2\}^{2+}$ and $\{nido\text{-}C_2B_nH_{n+2}\}^{2-}$ (n = 9, 10) carborane fragments were then computed through ADF with the BP86 method and ZORA/TZ2P basis sets on all atoms and this will be discussed in detail in Section 4.3.2. 'Carbons adjacent' and 'carbons apart' 12-vertex models, **G** and **H**, were optimised in C_s symmetry, allowing for more a detailed analysis of orbital interactions to be carried out (see Section 4.3.2). In agreement with previous work,[14] 13-vertex 'carbons adjacent' model **I** exhibits a C_1 geometry when fully optimised (and is docosahedral), however it exhibits a low lying, henicosahedral, C_s symmetric transition state, $\mathbf{I}_{\mathbf{C_s}}$, at E = 7.3 kcal mol^{-1} with respect to **I**, which is the transition state responsible for exchanging the carbon vertices and giving the species effective C_s symmetry on the NMR timescale. This is employed to simplify the orbital interaction analysis and allowing the C_s and unsimplified, C_1, models to be

compared. The 'carbons apart' 13-vertex isomer was also found to be C_1 symmetric, again in agreement with the published computational structure, however a low lying geometry of C_s symmetry was not located.

4.3.1. Optimised geometries of platinacarboranes

Computational models, **G-J**, (Figure 4.19) agree well with published experimental structures (determined through X-ray diffraction). Selected structural parameters are given in Table 4.9. These include interatomic distances around Pt (to the C_2B_3 or C_2B_4 face of the carborane fragment and to phosphine P atoms), Δ, calculated as in Section 4.2 and χ, which is a measure of the orientation of the platinum bisphosphine fragment with respect to the C···C vector of the carborane fragment, given by the P1-P2-C1-C dihedral angle.

Table 4.9 – Selected molecular parameters (Å, °) experimental 12-vertex platinacarboranes 10 and 11 and computed model geometries G and H.

	10	**G**		**11**	**H**
CCDC	EPTBOR10		CCDC	CMPBPT20	
Pt3–C1	2.530(7)	2.794	Pt3–C1	2.442(7)	2.465
Pt3–C2	2.613(7)	[a]	Pt3–C7	2.452(8)	[a]
Pt3–B4	2.283(8)	2.240	Pt3–B6	2.261(8)	2.283
Pt3–B7	2.277(8)	[a]	Pt3–B11	2.255(9)	[a]
Pt3–B8	2.264(8)	2.212	Pt3–B3	2.270(9)	2.253
Pt3–P1	2.2759(18)	2.379	Pt3–P1	2.303(2)	2.381
Pt3–P2	2.2843(18)	[a]	Pt3–P2	2.249(2)	2.342
Δ	0.411	0.699	Δ	0.141	0.081
χ	16.5	0	χ	88.9	90

[a] Value as above by symmetry.

Table 4.10 – Selected molecular parameters (Å, °) experimental 13-vertex platinacarboranes 12 and 13 and computed model geometries I, I_{C_s} and J.

	12	**I**	**I_{C_s}**		**13**	**J**
CCDC	GAQHUC			CCDC	HEYZOB	
Pt3–C1	2.381(8)	2.396	2.406	Pt3–C1	2.1652(12)	2.153
Pt3–C2	2.626(8)	2.855	[a]	Pt3–B2	2.4438(15)	2.439
Pt3–B3	2.322(8)	2.299	2.311	Pt3–B3	2.3961(14)	2.442
Pt3–B6	2.301(7)	2.292	[a]	Pt3–C6	2.8131(13)	2.894
Pt3–B7	2.305(7)	2.279	2.310	Pt3–B7	2.2631(14)	2.230
Pt3–B10	2.265(7)	2.236	[a]	Pt3–B10	2.3692(14)	2.412
Pt3–P1	2.3046(18)	2.383	2.377	Pt3–P1	2.2710(3)	2.346
Pt3–P2	2.3001(17)	2.398	[a]	Pt3–P2	2.3129(4)	2.420
Δ	0.080	0.195	0.079	Δ	0.518	0.583
χ	2.0	10.2	0	χ	62.7	68.5
x[b]	68.4%	100.1%	0%			

[a] Value as above by symmetry.
[b] x calculated as in Section 4.2.2 through Equations 4.5 and 4.6.

The largest discrepancies were seen between computed and experimentally derived geometries in relation to the Pt–C distances. Pt–C1 and Pt–C2 in **G** have equivalent

computed distances of 2.794 Å where they are inequivalent experimentally with distances of 2.530(7) and 2.613(7) Å respectively (in **10**). Also, Pt–C2 in **I** has a computed distance of 2.855 Å and an experimental distance of 2.626(8) Å in **12**. The effect of this overestimation in Pt–C bond lengths is a large computed slip distortion; Δ = 0.699 Å in **G** *cf.* 0.411 Å in **10** and Δ = 0.195 Å in **I** *cf.* 0.080 Å in **12**. Views of the computed geometries are given in Figure 4.19, below.

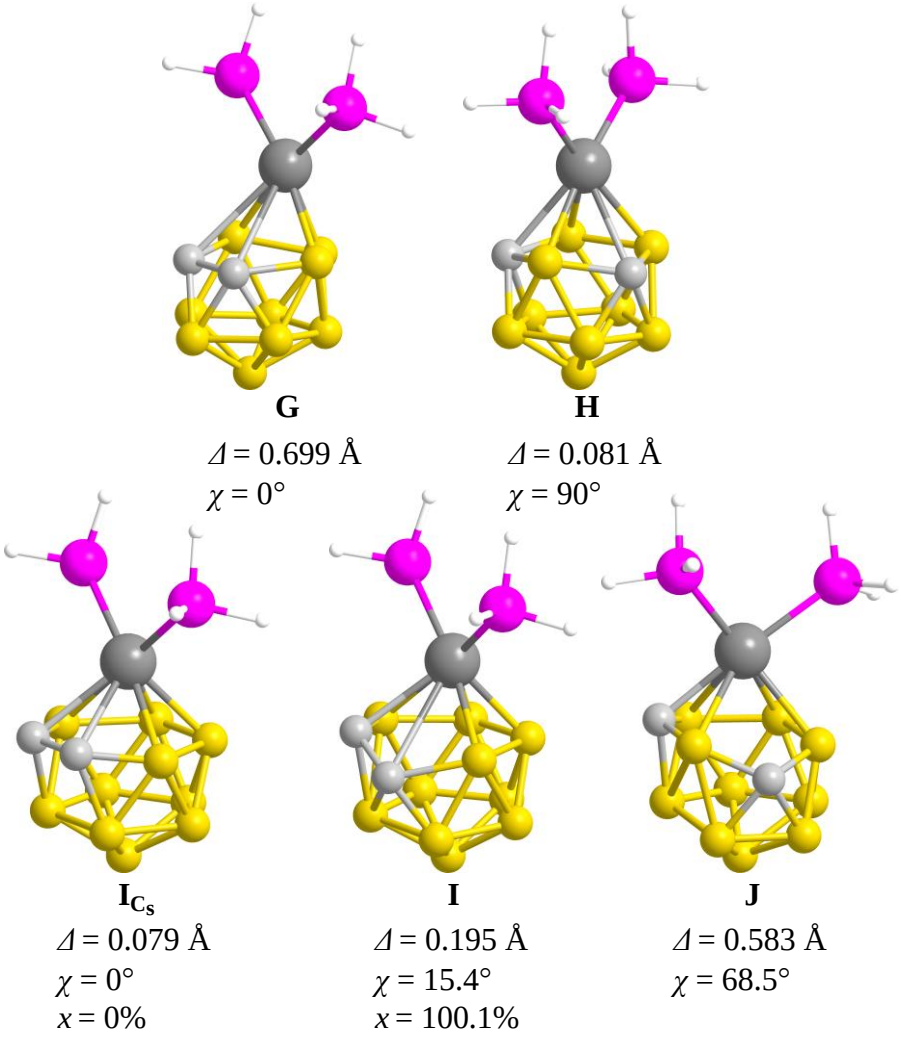

Figure 4.19 – Optimised geometries of models G-J to be used in slip distortion analysis. Δ, χ and *x* are given (where applicable). Cage hydrogens are ommited for clarity.

4.3.2. Computational analysis of Δ in platinacarboranes

In order to assess the changes in the interaction energy between $\{Pt(PH_3)_2\}^{2+}$ and $\{nido\text{-}C_2B_nH_{n+2}\}^{2-}$ (n = 9, 10) fragments, the energy decomposition scheme available in the ADF code was used. In this approach, the interaction between two (or more) fragments may be represented as a sum of "steric" and "orbital interaction" energy terms (Eq. 4.7).

$$E_{total} = E_{steric} + E_{orbital} \qquad \textit{(Eq. 4.7)}$$

$$E_{orbital} = E_{a'} + E_{a''} \text{ (for a } C_s \text{ molecule)} \qquad \textit{(Eq. 4.8)}$$

The steric term is made up of stabilising electrostatic interactions, derived from charge distributions within the fragments, and a Pauli repulsion term, which arises from the interaction of occupied orbitals on one fragment with occupied orbitals on another and is overall destabilising. The orbital interaction term is the stabilisation due to overlap between occupied orbitals on one fragment with unoccupied orbitals on another. The orbital interaction energy term is itself represented as a sum of terms related to different orbital symmetries (Eq. 4.8). The existence of symmetry in the molecule being examined, therefore, greatly enhances these analyses; hence **G**, **H**, (12-vertex, carbons adjacent and apart respectively) and $\mathbf{I}_{C_s}$ (13-vertex, carbons adjacent) are computed in C_s symmetry. Since for **I** and **J** (13-vertex, carbons adjacent and apart respectively, in C_1 symmetry) interaction energy decomposition can go no further than calculation of "steric" and "orbital interaction" energy terms, it is crucial to the analysis of **J** that conclusions drawn from $\mathbf{I}_{C_s}$ are reasonably related to those from **I**, in that a lack of the ability to decompose the orbital interaction energy into orbital symmetries should not to be prohibitive to the analysis.

4.3.2.1. Analysis of Δ in 12-vertex platinacarboranes

In order to analyse the changes in interaction energies between $\{Pt(PH_3)_2\}^{2+}$ and {*nido*-$C_2B_nH_{n+2}\}^{2-}$ fragments, first the optimised geometries must be described in internal coordinates. This allows two "dummy atoms", X and X^c to be added (see Figure 4.20), where X is the position Pt would adopt at $\Delta = 0$ and X^c represents the centroid of the lower B_5 ring, *c*, as defined in Section 4.2.1. By varying the Pt···X distance between 0 and ±2 Å in 0.1 Å steps the platinum fragment is displaced along a horizontal vector passing through the optimised Δ position and exploring extremes in Δ. Through this model, geometries were generated where neither the fragments nor the vertical distance between the fragments were allowed to relax. Interaction energy terms will therefore inevitably be exaggerated; however, trends within these terms should remain reliable.

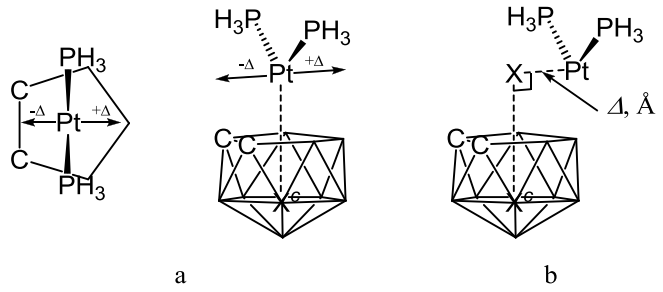

a b

Figure 4.20 – a) Trajectory of the $\{Pt(PH_3)_2\}^{2+}$ fragment above in 3,3-$(PH_3)_2$-3,1,2-$PtC_2B_9H_{11}$, G, in plan and perspective views at Δ = 0 Å and b) the dummy atom points, where the Pt···X distance represents Δ. X^c represents the centroid of the lower B_5 ring in both a) and b).

In previous work, slip distortions in icosahedral platinacarboranes were rationalised through maximised overlap of frontier molecular orbitals (as seen in Figure 4.3). This view of the bonding in this system may now be updated to include charged fragments taken from the fully optimised geometries of **G** and **H**. However, the overall orbital picture is unchanged (Figure 4.21, below).

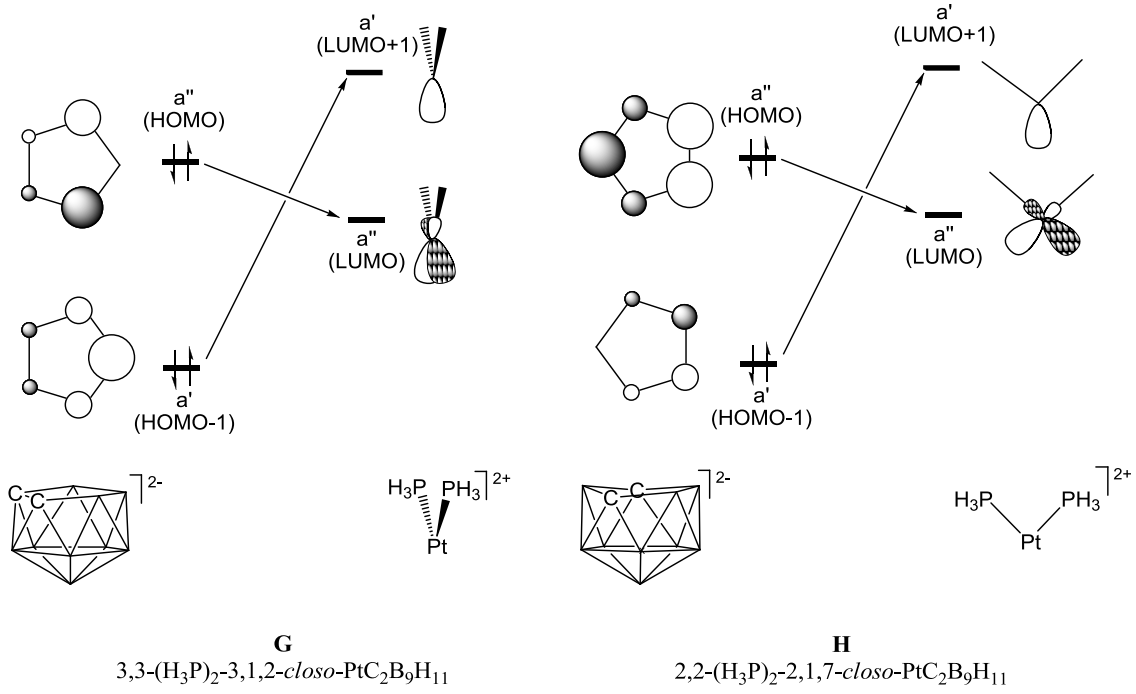

G
3,3-$(H_3P)_2$-3,1,2-*closo*-$PtC_2B_9H_{11}$

H
2,2-$(H_3P)_2$-2,1,7-*closo*-$PtC_2B_9H_{11}$

Figure 4.21 – Frontier molecular orbital interactions in G and H

As discussed in Section 4.1.2, the relative orientation of the two fragments is defined by the overlap of *a″* orbitals, which is associated with the overlap of carborane HOMO with platinum bisphosphine LUMO. In the EHMO calculations, neutral fragments were used, however here the charge partitioning reflects that accepted for these fragments, as a dianionic, 4 electron donor carborane and a dicationic transition metal fragment (in the context of Figure 4.21, above). As seen in EHMO calculations, and confirmed by DFT, in going from 'carbons adjacent' to 'carbons apart' $\{nido\text{-}C_2B_9H_{11}\}^{2-}$, the nodal planes

of the HOMO and HOMO-1 are rotated 90° (shown in Figure 4.3 as a cross over in energies of HOMO and LUMO orbitals). Thus the orientation of the platinum bisphosphine is parallel with the C–C connection in **G** and perpendicular to C···C in **H**. The large slip distortion in **G** was rationalised by the enhanced overlap of the σ-acceptor orbital on $\{Pt(PH_3)_2\}^{2+}$ at large Δ, where larger lobes are seen in the a' orbital of the carborane. In **H**, the a' carborane orbital is non-bonding with the platinum σ-acceptor, the overlap of these orbitals would therefore not be dependent upon Δ, rationalising the small slip distortion seen experimentally.

Figure 4.22, below, shows the energy decomposition analysis for **G** (left) and **H** (right). Plots (a) show the total interaction energies, plots (b) show the steric (green) and orbital (purple) interaction energies and plots (c) show the a' (red) and a'' (blue) contributions to the orbital interaction energy vs. slip distance, Δ.

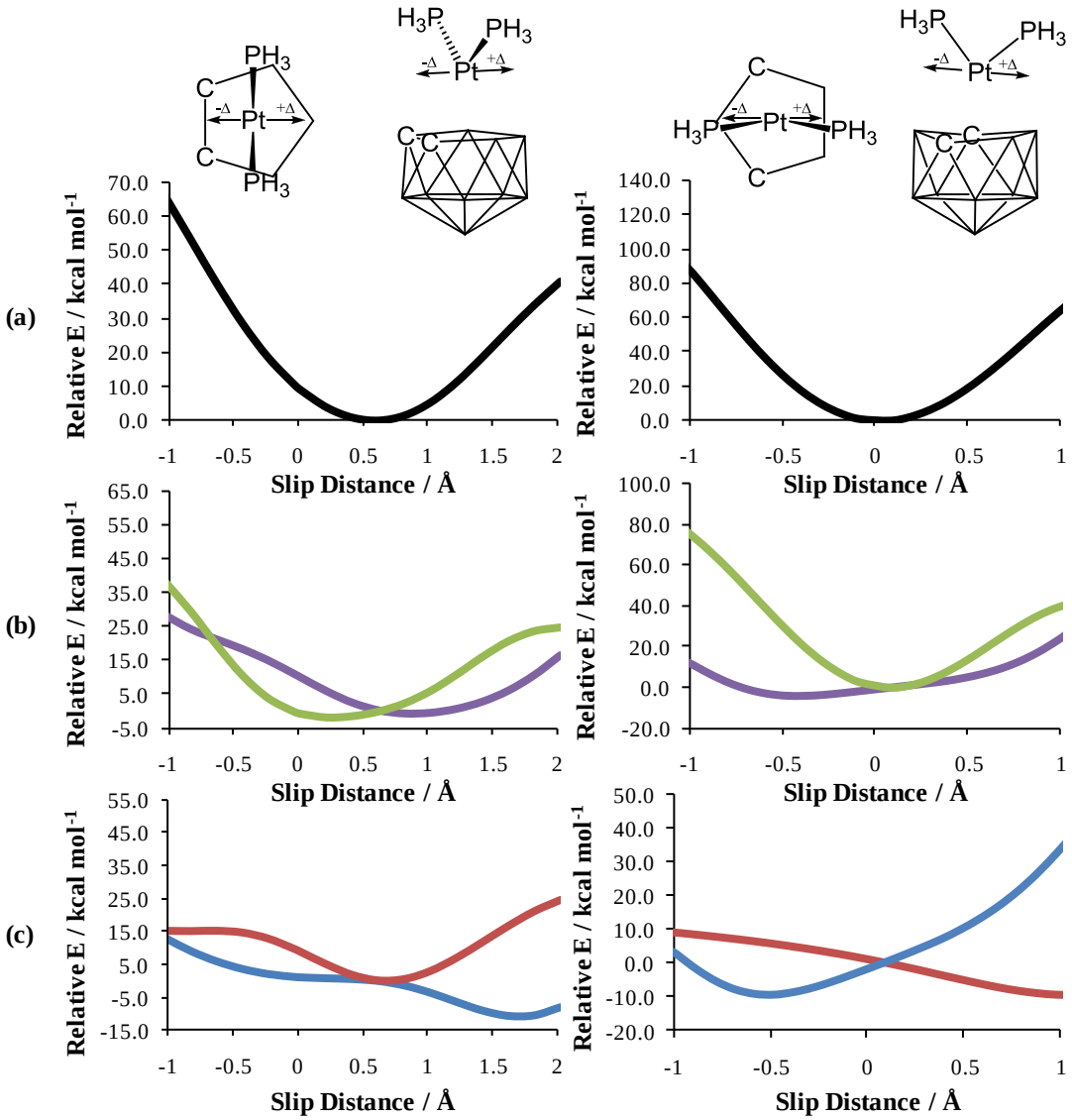

Figure 4.22 – Energy decomposition analyses for G (left) and H (right). Plots show (a) total interaction energy, (b) steric (green) and orbital (purple) interaction energy terms and (c) *a′* (red) and *a″* (blue) orbital interaction terms against slip distortion, *Δ*.

The total interaction energy in **G** finds a minimum at $\Delta \approx +0.7$ Å, in agreement with optimised structures. Plot (b) for **G** reveals that this is a compromise between minimised steric interactions (green line) (at $\Delta \approx +0.2$ Å) and minimised orbital interaction (purple line) (at $\Delta \approx +1.0$ Å). Finally, plot (c) shows that the *a″* orbital interaction (between the HOMO of $\{nido\text{-}C_2B_9H_{11}\}^{2-}$ and LUMO of $\{Pt(PH_3)_2\}^{2+}$) is the more significant contribution to the orbital interaction energy, since it is most stabilising at high *Δ* values (blue line). The red line shows the *a′* orbital interaction, which is also stabilised at positive slip. Thus, the slip distortion in **G** is enhanced by both *a′* (as suggested by previous work) and *a″* orbital interactions, however the role played by steric interactions is found, by this approach, to be significant, in order to obtain a thorough description of *Δ*.

In the case of **H**, the dominant interaction is found to be due to steric interaction. A relatively steep well, centred on *Δ ca.* +0.1 Å is seen for the steric interaction in plot (b). The orbital interaction has only a weak dependence upon *Δ* in comparison, seen as a relatively flat plot (in purple). This relatively unchanging interaction was predicted by previous work and so the overall conclusion of small slip distortion in **H** is consistent. However the relative large dependence on steric interactions rather than orbital interactions is only visible to the approach adopted here and, indeed, is found to be of paramount importance to the understanding of *Δ*.

4.3.2.2. Analysis of Δ in 13-vertex platinacarboranes

The large dependence of *Δ* on the steric interaction energy between $\{Pt(PH_3)_2\}^{2+}$ and the carborane *nido* fragment seen in the "carbons apart" 12-vertex species, **H**, is reflected in the analysis of 13-vertex platinacarboranes. For the "carbons adjacent" 4,4-$(PH_3)_2$-4,1,2-*closo*-$PtC_2B_{10}H_{10}$ isomer in its C_s form, $\mathbf{I}_{\mathbf{C_s}}$, the total interaction energy (Figure 4.23, left hand plots) is minimised at $\Delta \approx -0.1$ Å. This is almost superimposable onto the steric interaction plot in (b). However the relatively flat orbital interaction term (purple line) infact is least stabilising at this point. Plots (c) show that both orbital symmetries are least stabilising at *Δ ca.* 0 Å. The slip distortion is therefore solely dependent on the minimisation of the steric interactions between $\{Pt(PH_2)_3\}^{2+}$ and "carbons adjacent" $\{nido\text{-}C_2B_{10}H_{12}\}^{2-}$. As discussed in the introduction to Section 4.3.2, the fully optimised geometry of 4,4-$(PH_3)_2$-4,1,2-*closo*-$PtC_2B_{10}H_{10}$ does not, however, exhibit C_s symmetry. The right hand side of Figure 4.23 shows the same analysis for the fully optimised model, **I**. The trajectories are again computed with the position of the Pt centre passing through the optimised coordinates and through $\Delta = 0$. As the C_s symmetry has been removed, this trajectory does not exactly bisect the polyhedral C–C connection as in $\mathbf{I}_{\mathbf{C_s}}$. The same plots are reproduced, though slightly shifted to higher *Δ* (as seen in the optimised structures in Table 4.10). In addition, the total interaction energy and steric interaction energy plots exhibit steeper curves toward negative *Δ* and shallower curves towards positive *Δ*. This is most likely due to the less symmetrical concave face (w.r.t. slip direction) in **I** compared to that in $\mathbf{I}_{\mathbf{C_s}}$, caused by the protruding C1 vertex in **I**. Overall, the energy decomposition analysis of **I** satisfactorily returns the same trends as the more detailed analysis that is possible in $\mathbf{I}_{\mathbf{C_s}}$. This gives confidence in the following results for **J**, where no relatively low-lying C_s geometry exists, and so the same comparison cannot be made.

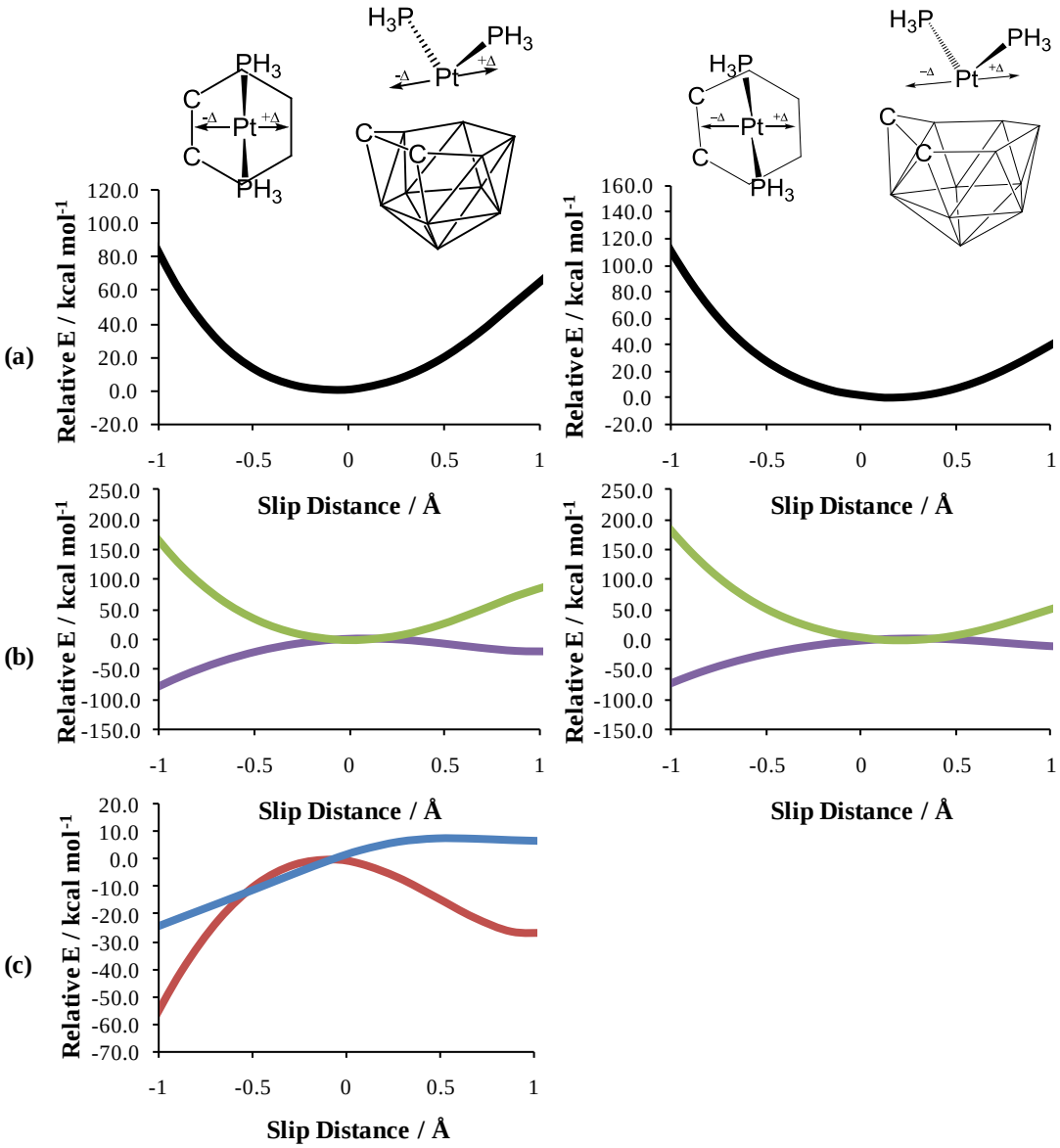

Figure 4.23 – Energy decomposition analyses for I_{C_s} (left) and I (right). Plots show (a) total interaction energy, (b) steric (green) and orbital (purple) interaction energy terms and (c) *a'* (red) and *a''* (blue) orbital interaction terms against slip distortion, *Δ*.

In the final energy decomposition analysis of **J**, the steric interaction term is again shown to predominate (see Figure 4.24, below). **J** is unique in that the direction of slip, in a trajectory along a diagonal of the 6-membered carborane face, means that the steric interation energy plot becomes relatively flat at large *Δ* and appears to become competitive with orbital interactions. However, where the steric interaction energy finds a minimum at *Δ* ≈ +0.5 Å, the orbital interaction only slightly adjusts the total interaction energy minimum to a *Δ* of *ca.* +0.6 Å and in fact the contributes to the increased slope of the total interaction energy curve at large positive *Δ*. It is apparent that, the total interaction energy curve is more flat in this case than those seen

previously, possibly due to the direction of slip, which may suggest a wider range of experimental Δ values in the 4,1,6-MC_2B_{10} than the 4,1,2-MC_2B_{10} isomers.

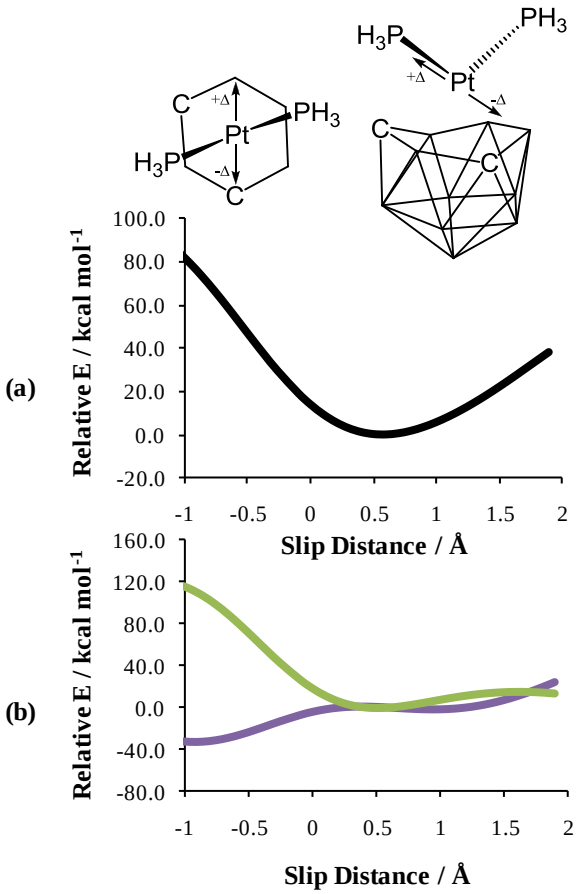

Figure 4.24 – Energy decomposition analyses for J. Plots show (a) total interaction energy, (b) steric (green) and orbital (purple) interaction energy terms against slip distortion, Δ.

4.4. Conclusions

"Carbons adjacent" and "carbons apart" supraicosahedral carboranes have been shown through parallel experimental and computational studies to act as Lewis acids in forming adducts with a range of bidentate Lewis bases. The slip distortion, Δ, of Sn above the carborane cage was found to increase upon adduct formation. The orientation and hinging, θ, of the chelating bases was shown to be caused by the presence of a chemically inert lone pair on Sn in a similar manner to that in icosahedral and subicosahedral stannacarboranes.

Experimental results showed a correlation between Δ and θ values in adducts and suggested the σ-donor strength of the Lewis bases may be a factor. Calculations, however, do not reproduce these more subtle trends as the Sn–N bond distances themselves are overestimated. This was investigated through geometry optimisations *via* TPSS *meta*-GGA, B3LYP hybrid DFT and MP2 wavefunction methodologies as well as increased (triple-ζ and diffuse) basis set size and PCM solvent calculations, benchmarked against the standard BP86/6-31G**/SDD method. These tests suggested that the failure of calculations to reproduce Sn–N bond distances and related structural trends seen experimentally was a result of the nature of the comparison, where calculations were performed in the gas phase and experimental parameters were derived from solid state structural data.

The observation was made from experimental Δ measurements, and corroborated by calculated geometries, that "carbons adjacent" supraicosahedral stannacarboranes are less distorted than the "carbons apart" isomers. This is in contrast to the trend seen in the superficially related "carbons adjacent" and "carbons apart" icosahedral species. This phenomenon was investigated through in related platinacarboranes the energy decomposition scheme made available in the ADF code, whereby interactions between molecular fragments may be factored into "steric" and "orbital interaction" energy terms and, where possible, the orbital interactions are further decomposed into terms related to the symmetry of the system.

In agreement with previous work on icosahedral platinacarboranes, the large slip distortion in the "carbons adjacent" icosahedral species was rationalised by the maximisation of favourable orbital interactions. However, this hypothesis was found not to extend to the "carbons apart" icosahedron nor to the supraicosahedra, where steric

interactions between metal and carborane fragments, not present in the original calculations, were found to dominate interaction energy profiles.

4.5. References

1. P. Jutzi, P. Galow, S. Abuorabi, A. M. Arif, A. H. Cowley and N. C. Norman, *Organometallics*, 1987, **6**, 1024-1031.
2. R. W. Rudolph, R. L. Voorhees and R. E. Cochoy, *J. Am. Chem. Soc.*, 1970, **92**, 3351-3354.
3. a) N. S. Hosmane, R. D. Barreto, M. A. Tolle, J. J. Alexander, W. Quintana, U. Siriwardane, S. G. Shore and R. E. Williams, *Inorg. Chem.*, 1990, **29**, 2698-2701; b) N. S. Hosmane, P. De Meester, N. Maldar, S. B. Potts, S. S. C. Chu and R. H. Herber, *Organometallics*, 1986, **5**, 772-778; c) N. S. Hosmane, N. N. Sirmokadam and R. H. Herber, *Organometallics*, 1984, **3**, 1665-1669.
4. R. W. Chapman, J. G. Kester, K. Folting, W. E. Streib and L. J. Todd, *Inorg. Chem.*, 1992, **31**, 979-983.
5. T. Gädt and L. Wesemann, *Organometallics*, 2007, **26**, 2474-2481.
6. D. Joosten, I. Weissinger, M. Kirchmann, C. Maichle-Mössmer, F. M. Schappacher, R. Pöttgen and L. Wesemann, *Organometallics*, 2007, **26**, 5696-5701.
7. M. A. Fox, T. B. Marder and L. Wesemann, *Canad. J. Chem.*, 2009, **87**, 63-71.
8. N. M. M. Wilson, D. Ellis, A. S. F. Boyd, B. T. Giles, S. A. Macgregor, G. M. Rosair and A. J. Welch, *Chem. Commun.*, 2002, 464-465.
9. P. D. Abram, *PhD Thesis*, Heriot-Watt University, 2009.
10. P. D. Abram, D. McKay, D. Ellis, S. A. Macgregor, G. M. Rosair and A. J. Welch, *Dalton Trans.*, 2010, **39**, 2412-2422.
11. P. D. Abram, D. McKay, D. Ellis, S. A. Macgregor, G. M. Rosair, R. Sancho and A. J. Welch, *Dalton Trans.*, 2009, 2345-2351.
12. A. J. Welch, *J. Chem. Soc., Dalton Trans.*, 1975, 1473-1478.
13. D. M. P. Mingos, M. I. Forsyth and A. J. Welch, *J. Chem. Soc., Dalton Trans.*, 1978, 1363-1374.
14. K. J. Dalby, D. Ellis, S. Erhardt, R. D. McIntosh, S. A. Macgregor, K. Rae, G. M. Rosair, V. Settels, A. J. Welch, B. E. Hodson, T. D. McGrath and F. G. A. Stone, *J. Am. Chem. Soc.*, 2007, **129**, 3302-3314.
15. R. McIntosh, D. Ellis, J. Gil-Lostes, K. J. Dalby, G. M. Rosair and A. J. Welch, *Dalton Trans.*, 2005, 1842-1846.
16. E. J. Baerends, J. Autschbach, D. Bashford, A. Bérces, F. M. Bickelhaupt, C. Bo, P. M. Boerrigter, L. Cavallo, D. P. Chong, L. Deng, R. M. Dickson, D. E. Ellis, M. van Faassen, L. Fan, T. H. Fischer, C. F. Guerra., A. Ghysels, A.

Giammona, S. J. A. van Gisbergen, A. W. Götz, J. A. Groeneveld, O. V. Gritsenko, M. Grüning, F. E. Harris, P. van den Hoek, C. R. Jacob, H. Jacobsen, L. Jensen, G. van Kessel, F. Kootstra, M. V. Krykunov, E. van Lenthe, D. A. McCormack, A. Michalak, M. Mitoraj, J. Neugebauer, V. P. Nicu, L. Noodleman, V. P. Osinga, S. Patchkovskii, P. H. T. Philipsen, D. Post, C. C. Pye, W. Ravenek, J. I. Rodríguez, P. Ros, P. R. T. Schipper, G. Schreckenbach, M. Seth, J. G. Snijders, M. Solà, M. Swart, D. Swerhone, G. te Velde, P. Vernooijs, L. Versluis, L. Visscher, O. Visser, F. Wang, T. A. Wesolowski, E. M. van Wezenbeek, G. Wiesenekker, S. K. Wolff, T. K. Woo, A. L. Yakovlev and T. Ziegler, *ADF2009.01*, SCM, Theoretical Chemistry, Vrije Universiteit, Amsterdam, The Netherlands, 2009.

17. *Mercury, Version 1.4.2*, Cambridge Crystallographic Data Center, Cambridge, UK, 2006.

18. M. J. Frisch, G. W. Trucks, H. B. Schlegel, G. E. Scuseria, M. A. Robb, J. R. Cheeseman, J. A. Montgomery, Jr., T. Vreven, K. N. Kudin, J. C. Burant, J. M. Millam, S. S. Iyengar, J. Tomasi, V. Barone, B. Mennucci, M. Cossi, G. Scalmani, N. Rega, G. A. Petersson, H. Nakatsuji, M. Hada, M. Ehara, K. Toyota, R. Fukuda, J. Hasegawa, M. Ishida, T. Nakajima, Y. Honda, O. Kitao, H. Nakai, M. Klene, X. Li, J. E. Knox, H. P. Hratchian, J. B. Cross, V. Bakken, C. Adamo, J. Jaramillo, R. Gomperts, R. E. Stratmann, O. Yazyev, A. J. Austin, R. Cammi, C. Pomelli, J. W. Ochterski, P. Y. Ayala, K. Morokuma, G. A. Voth, P. Salvador, J. J. Dannenberg, V. G. Zakrzewski, S. Dapprich, A. D. Daniels, M. C. Strain, O. Farkas, D. K. Malick, A. D. Rabuck, K. Raghavachari, J. B. Foresman, J. V. Ortiz, Q. Cui, A. G. Baboul, S. Clifford, J. Cioslowski, B. B. Stefanov, G. Liu, A. Liashenko, P. Piskorz, I. Komaromi, R. L. Martin, D. J. Fox, T. Keith, M. A. Al-Laham, C. Y. Peng, A. Nanayakkara, M. Challacombe, P. M. W. Gill, B. Johnson, W. Chen, M. W. Wong, C. Gonzalez and J. A. Pople, *Gaussian 03*, *Revision D.01*, Gaussian, Inc., Wallingford CT, 2004.

19. a) A. Bergner, M. Dolg, W. Kuechle, H. Stoll and H. Preuss, *Mol. Phys.*, 1993, **80**, 1431-1441; b) M. Dolg, H. Stoll, H. Preuss and R. M. Pitzer, *J. Phys. Chem.*, 1993, **97**, 5852-5859; c) M. Kaupp, P. v. R. Schleyer, H. Stoll and H. Preuss, *J. Chem. Phys.*, 1991, **94**, 1360-1366.

20. A. Hollwarth, M. Bohme, S. Dapprich, A. W. Ehlers, A. Gobbi, V. Jonas, K. F. Kohler, R. Stegmann, A. Veldkamp and G. Frenking, *Chem. Phys. Lett.*, 1993, **208**, 237-240.

21. A. D. Becke, *J. Chem. Phys.*, 1993, **98**, 5648-5652.
22. J. Tao, J. P. Perdew, V. N. Staroverov and G. E. Scuseria, *Phys. Rev. Lett.*, 2003, **91**, 146401-146404.
23. Y. Zhao and D. Truhlar, *Theor. Chem. Acc.*, 2008, **120**, 215-241.
24. J. A. Pople, R. Krishnan, H. B. Schlegel and J. S. Binkley, *Int. J. Quantum Chem.*, 1979, **16**, 225-241.

Chapter 5 – Main Group Heteroborane Chemistry – Alternatives to Carboranes

5.1. Introduction

As highlighted in Chapter 2, carboranes hold an inherent problem that the carbon-based vertices, having more contracted frontier molecular orbitals in comparison with their boron-based equivalents, prefer to adopt lower-connected sites. The complement to this is that a polyhedral cluster with high-connected sites, such as the 13-vertex docosahedron, which has two 6-connected vertices, is destabilised by the inclusion of carbon. Hence the use of alternative heteroatoms, which have better compatibility with boron, may allow the synthesis of supraicosahedral heteroboranes where a synthetic bottle-neck has arisen in carborane chemistry.

Most main group diheteroborane clusters reported, apart from carboranes, involve a single carbon vertex along with the other main group heteroatom.[1] Additionally, Little *et al.*[2] synthesised a range of $PEB_{10}H_{10}$ (E = As, Sb, Bi) derivatives. However, in this study, diheteroboranes with only a single heteroatom type are to be considered. Thus far, synthesised examples have been contributed by Little *et al.* and, more recently, by Wesemann *et al.* and include dianionic stannaborates[3] and neutral silaboranes,[4] germaboranes,[5] phosphaboranes[2, 6] arsenaboranes[7] and stibaboranes.[8]

Heteroboranes have been studied computationally by Hofmann *et al.* who considered relative energies in heteroborane and -borate isomers.[9-12] A comprehensive series of studies introduced "structural increments" and "connection increments" which can be assigned *via* DFT calculations and subsequently used as a predictive tool for relative energies of structural isomers. In this scheme, the lowest energy isomer is described as having no unfavourable structural features, therefore its energy, E^0_{inc} is the sum of connection increments (Eq. 5.1, below), arising from the number of heteroatom–B connections (Het–B), Het–Het connections and Het–Het' connections (in cases of two different heteroatom types, usually in heterocarboranes). Each other possible isomer is then given energy "penalties" based upon its structure. These energy penalties are additive; each disfavourable structural feature increments upon the relative energy of the isomer (Eq. 5.2). Finally, the relative energies calculated through structural increments are tested against the computed (DFT[9, 10, 12] or MP2[11]) energies, E_{calc} (Eq. 5.3).

$$E^0_{inc} = \sum E_{inc} \text{ (connection increments)} \qquad \textit{(Eq. 5.1)}$$

$$E_{inc}{}^{rel} = \sum E_{inc} \text{ (connection \& structural increments)} - E^{0}{}_{inc} \qquad \textit{(Eq. 5.2)}$$

$$\Delta E = E_{inc}{}^{rel} - E_{calc} \qquad \textit{(Eq. 5.3)}$$

The structural types covered by Hofmann and co-workers include heteroboranes and -borates of 6-,[11] 10-,[12] 11-,[9, 10] and 12-vertices.[9] The key result from the icosahedral *closo*-heteroborane work by Kiani and Hofmann was that the Het–Het structural increment changes from positive (destabilising) to negative as we go down the Periodic Table. Therefore, while carboranes favour the 1,12-*closo*-$C_2B_{10}H_{12}$ isomer, heavy main group elements, such as tin, favour the 1,2-isomer.

5.1.1. This study – towards REDCAP of 12-vertex heteroboranes

This chapter discusses a computational study into the effects of exchanging {BH} vertices in 12- and 13-vertex *closo*-borates with either $\{XH\}^+$, to give $X_2B_{10}H_{12}$ and $X_2B_{11}H_{13}$ (X = C, Si, Ge, Sn) or with $\{Y\}^+$, to give $Y_2B_{10}H_{10}$ and $Y_2B_{11}H_{11}$ (Y = P, As, Sb, Bi) diheteroboranes. A list of the elements considered, along with the key properties of electronegativity and atomic radius, is given in Figure 5.1. Elements with electronegativities and atomic radii close to that of boron are expected to give more stable heteroboranes by counteracting the preferences seen in carboranes for low-connected and separated carbon vertices.

13	14	15
B 2.04 85	**C** 2.55 70	**N** 3.04 65
Al 1.61 125	**Si** 1.90 110	**P** 2.19 100
Ga 1.81 130	**Ge** 2.01 125	**As** 2.18 115
In 1.78 155	**Sn** 1.96 145	**Sb** 2.05 145
Tl 1.62 190	**Pb** 2.33 180	**Bi** 2.02 160

Figure 5.1 – Section of the Periodic Table including elements assessed, showing Pauling electronegativities[13] and empirical atomic radii in pm.[14]

In comparison with the work of Kiani and Hofmann,[9] this study aims to reproduce trends for 12-vertex *closo*-heteroboranes, and extend the work to include neutral 13-

vertex *closo*-heteroboranes and dianionic 12-vertex *nido*-heteroboranes (the intermediate between 12- and 13-vertex *closo*-heteroboranes). The aim will be to provide experimental co-workers with data as to the heteroatoms most viable for polyhedral expansion experiments and predictions of structural isomers that may be expected (see Figure 5.2).

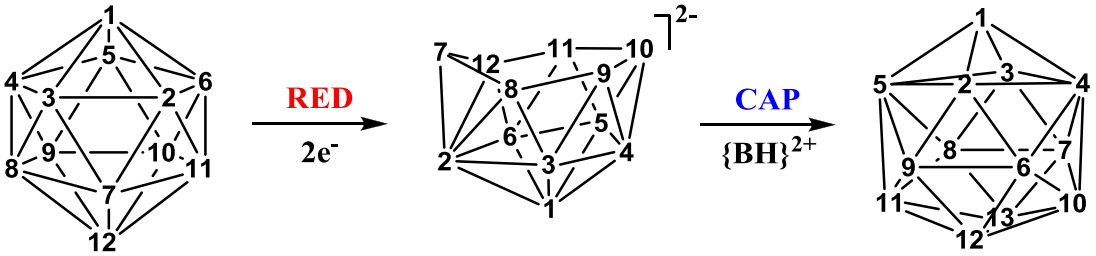

neutral 12-vertex
1,a-*closo*-$X_2B_{10}H_{12}$

dianionic 12-vertex
$[b,c\text{-}nido\text{-}X_2B_{10}H_{12}]^{2-}$

13-vertex
d,e-*closo*-$X_2B_{11}H_{13}$

Figure 5.2 – REDCAP of a Group 14 heteroborane, where letters a-e are vertex numbers of heteroatoms. Neutral 12-vertex diheteroborane (3 possible isomers; a = 2, 7, 12), dianionic *nido*-diheteroborane (38 possible isomers) then a 13-vertex diheteroborane (28 possible isomers).

5.2. Icosahedral diheteroboranes $X_2B_{10}H_{12}$ (X = C, Si, Ge, Sn) and $Y_2B_{10}H_{10}$ (Y = P, As, Sb, Bi)

The relative stabilities of *closo*-$X_2B_{10}H_{12}$ (X = C, Si, Ge, Sn) and *closo*-$Y_2B_{10}H_{10}$ (Y = P, As, Sb, Bi) were investigated. This was carried out first by optimising the parent icosahedron, [*closo*-$B_{12}H_{12}$]$^{2-}$, then exchanging {BH} fragments for {XH}$^{+}$ and {Y}$^{+}$, giving neutral compounds with the same (n + 1) skeletal electron pair count. Geometries were then optimised, giving *ortho*-, *meta*- and *para*-heteroboranes for each heteroatom type and these are given in Figure 5.3, below.

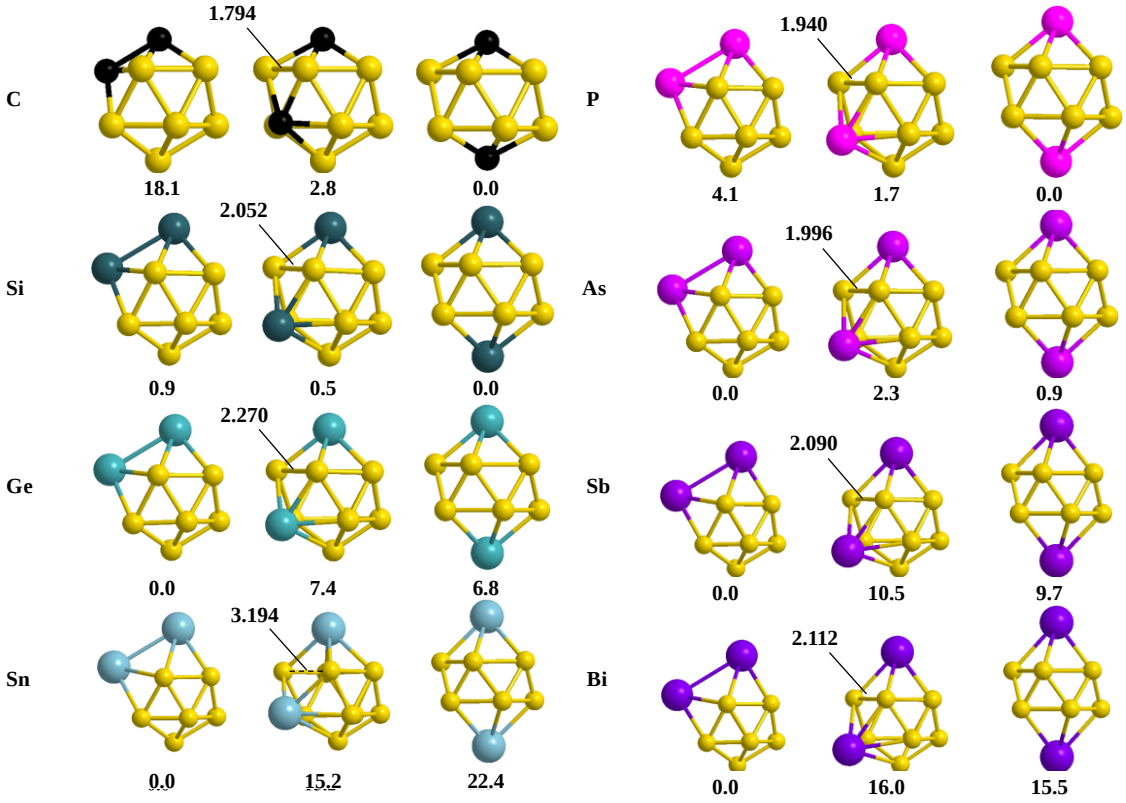

Figure 5.3 – Optimised geometries of 12-vertex diheteroboranes, *closo*-$X_2B_{10}H_{12}$ and *closo*-$Y_2B_{10}H_{10}$. Energies given in kcal mol^{-1} and selected bond distances given in Ångstroms.

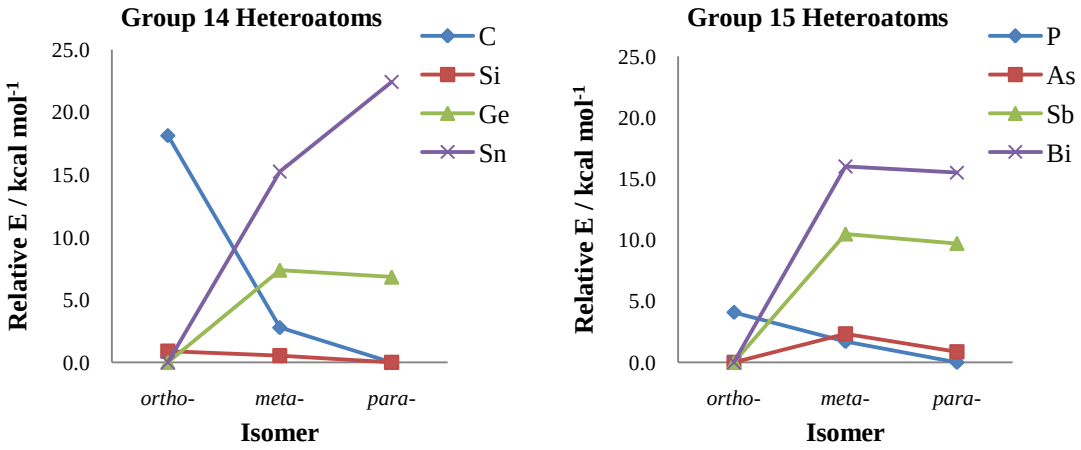

Figure 5.4 – Relative energies (in kcal mol^{-1}) of 12-vertex diheteroborane isomers.

The above graphs (Figure 5.4) show the computed relative energies of *closo*-$X_2B_{10}H_{12}$ and *closo*-$Y_2B_{10}H_{10}$ isomers. Each plot is relative to the lowest energy isomer for that heteroatom. The trends seen reproduce previous work, in that the well known thermodynamic order of stability in carboranes, *ortho* < *meta* < *para*, holds true for only the early main group elements, C, Si and P.

For the carboranes, with *para*-carborane set to zero in energy, *ortho*- and *meta*-carborane are computed at +18.1 and +2.8 kcal mol^{-1} respectively. The energy range is reduced for silaboranes, where the three isomers are within 1 kcal mol^{-1}, with *ortho*- and *meta*-silaborane at +0.9 and +0.5 kcal mol^{-1} respectively, above *para*-silaborane. This thermodynamic order changes round in the germaboranes, where now *ortho*-germaborane is the most stable isomer and the *meta* and *para* isomers are found at +7.4 and +6.8 kcal mol^{-1} respectively, *i.e. meta* < *para* < *ortho*. This order is further modified in the stannaboranes, to *para* < *meta* < *ortho*, where *meta* and *para* isomers have energies of +15.2 and +22.4 kcal mol^{-1} respectively.

For the group 15 heteroatoms, the same reversal in favoured isomers is seen going down the group. The phosphaboranes exhibit the smallest range in energies, where with *para*-phosphaborane set to zero, *ortho*- and *meta*-phosphaborane are located at +4.1 and +1.7 kcal mol^{-1} respectively. This smaller range in energy may be due to the closer electronegativities of phosphorus and boron in comparison to carbon and boron (see Figure 5.1) giving a lesser preference for the heteroatoms to be apart through improved electron delocalisation. In the arsenaboranes, the order of thermodynamic stability is established as *meta* < *para* < *ortho*. *Ortho*- and *para*-arsenaborane are relatively close in energy at 0.0 and +0.9 kcal mol^{-1} respectively, whereas *meta*-arsenaborane is 2.3 kcal mol^{-1} higher in energy than *ortho*-arsenaborane. The order of *meta* < *para* < *ortho* is

maintained through the antimony and bismuth containing heteroboranes, where the difference in energy between *meta* and *para* isomers remains relatively constant and *ortho* isomers become increasingly more stable relative to these.

The trends seen appear to indicate two competing effects in the stability of main group diheteroboranes. The preference for the heteroatoms to be apart is related to the electronegativity of the heteroatom compared to that of boron, where a mismatch increases the difference in charge between boron and heteroatoms. Separation of the heteroatoms therefore minimises destabilising Coulombic effects=. The second competing effect is a preference for metal-metal bonding due to a size mis-match between the heteroatoms and boron. Thus bonding becomes less effective between the heteroatoms and the cage boron atoms and localised metal-metal bonding appears to become more stabilising than delocalised skeletal bonding. As we move down the Periodic Table, the second effect (size) becomes dominant over the first (electronegativity). This agrees with the energy penalty treatment adopted by Kiani and Hofmann, where the Het–Het energy penalty is positive for early main group heteroatoms and negative for late main group elements.

These findings have an effect on the potential isomers available experimentally. The synthesis of diheteroboranes is typically carried out by introducing the heteroatom containing fragment into decaborane ($B_{10}H_{14}$), giving the *ortho* isomer. The production of *meta* and *para* isomers then relies on thermal isomerisation. The relative energies of $X_2B_{10}H_{12}$ and $Y_2B_{10}H_{10}$ suggest this route would only give access to all three isomers in sila- and phosphaboranes (and possibly in arsenaboranes due to the relatively small range in energies), since all other elements studied here see the *ortho*-heteroborane isomer as the most thermodynamically stable.

5.3. 13-vertex monoheteroboranes $[XB_{12}H_{13}]^-$ (X = C, Si, Ge, Sn) and $[YB_{12}H_{12}]^-$ (Y = N, P, As, Sb)

There are many different environments in the docosahedron, as opposed to the icosahedron where all vertices are equivalent. Therefore to ease the analysis of the relative energies of X_2/Y_2B_{11} species, monoheteroboranes were also computed. Figure 5.5, below shows the plots of relative energies of the different isomers of group 14 $[XB_{12}H_{13}]^-$ and group 15 $[YB_{12}H_{12}]^-$ monoheteroboranes.

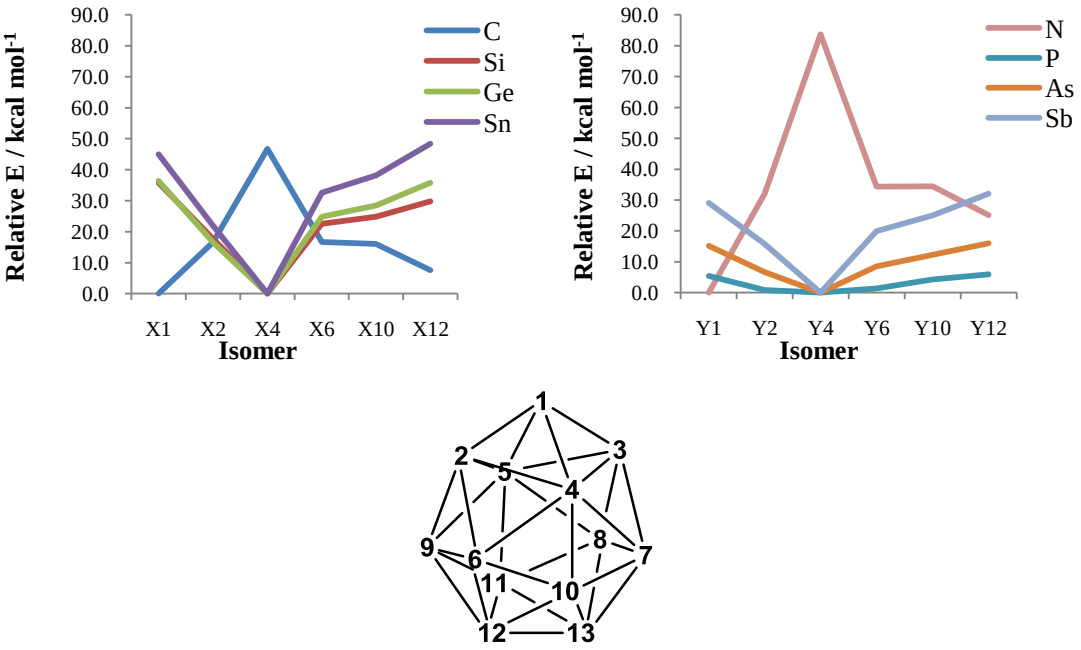

Figure 5.5 – Plots of relative stabilities of group 14 and 15 13-vertex monoheteroboranes with numbered geometry.

Figure 5.5 reveals the preference for heteroatoms to adopt a position based only on the number of connections. Vertex 1 is 4-connected, vertices 4 and 5 are 6-connected and the remaining vertices are 5-connected. Vertices 2 & 3 are equivalent, as are 6, 7, 8 & 9, 10 & 11 and 12 & 13. The plots allow for elements to be placed into two groups; those preferring fewer connections, C and N (which are smaller than boron), and those preferring more connections, Si, Ge, Sn, P, As, Sb (larger than boron), where the plots of the latter are essentially the inverted plots of the former. The energetic trend is relatively simple, in that the preference for a site is directly related to the atomic radius of the heteroatom and inversely related to its electronegativity. At this stage, phosphorus appears most closely-matched with boron, in agreement with its atomic radius and electronegativity, as it exhibits the smallest range in relative energies of monoheteroboranes, where all isomers fall within a range of *ca.* 10 kcal mol^{-1}. Nitrogen, due to its relatively small atomic radius and high electronegativity, exhibits

the same properties as carbon in heteroboranes. Indeed, the deficiencies are enhanced with nitrogen, where there is an even greater preference for the low-connected vertex 1 and the cage is even more destabilised where N adopts high-connected vertex 4. Nitrogen will therefore not be considered as a viable heteroatom in supraicosahedral heteroboranes.

5.4. Supraicosahedral heteroborane model systems $X_2B_{11}H_{13}$ (X = C, Si, Ge, Sn) and $Y_2B_{11}H_{11}$ (Y = P, As, Sb, Bi)

Twenty-eight unique isomers of 13-vertex diheteroboranes are possible. Along with this, eight different heteroatoms are being considered. Therefore the requirement for a systematic approach to this investigation arises. From the $[B_{13}H_{13}]^{2-}$ optimised geometry, simply replacing appropriate {BH} fragments with heteroatom fragments may work in some cases, for example with the smaller heteroatoms. However in cases where the heteroatom being included is larger than the boron vertex being replaced, the nuclear-nuclear repulsion caused by having short contacts around the heteroatoms will cause the cage to expand in the first instance. This expansion may possibly drive an isomerisation of the cage away from the target isomer, leading to loss of the stability datum for that isomer, *i.e.* a local minimum would be missed.

To avoid this, a system of constraints was constructed whereby atoms may move away from (or towards) the centre of the cage while all angles remain fixed. This was achieved through internal coordinates, using three 'dummy' atoms X^1, X^2 and X^3 (see Figure 5.6, below) where only the V–X^1 distances (where V is a cage vertex) were allowed to vary. The same constraints were applied to substituent hydrogen atoms, where the initial guess H-X distances were taken from optimised $[B_{13}H_{13}]^{2-}$.

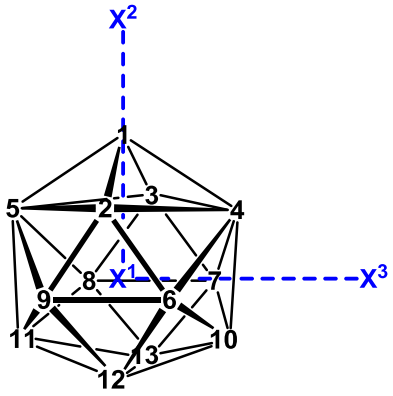

Figure 5.6 – Dummy atom system used for constrained 13-vertex heteroborane optimisations. Distances V–X^1 vary, angles V-X^1-X^2 are fixed and dihedral angles V-X^1-X^2-X^3 fixed (V = cage vertex).

Appropriate boron vertices were replaced with heteroatoms to give each isomer. Conducting optimisations produced under these constraints then produced a set of geometries, which were the best possible guess geometries for unconstrained calculations.

The unconstrained optimisations were carried out and any isomerisations tracked. If isomerisation occurred, this was likely to be due to the isomer being unstable, rather than its loss being a function of the geometry of the model. Analytical frequency calculations were carried out on all optimised geometries and those characterised as minima represent the full list of 'stable' isomers. Relative energies of the stable group 14 $X_2B_{11}H_{13}$ and group 15 $Y_2B_{11}H_{11}$ diheteroborane isomers are plotted below in Figures 5.7 and 5.8 respectively.

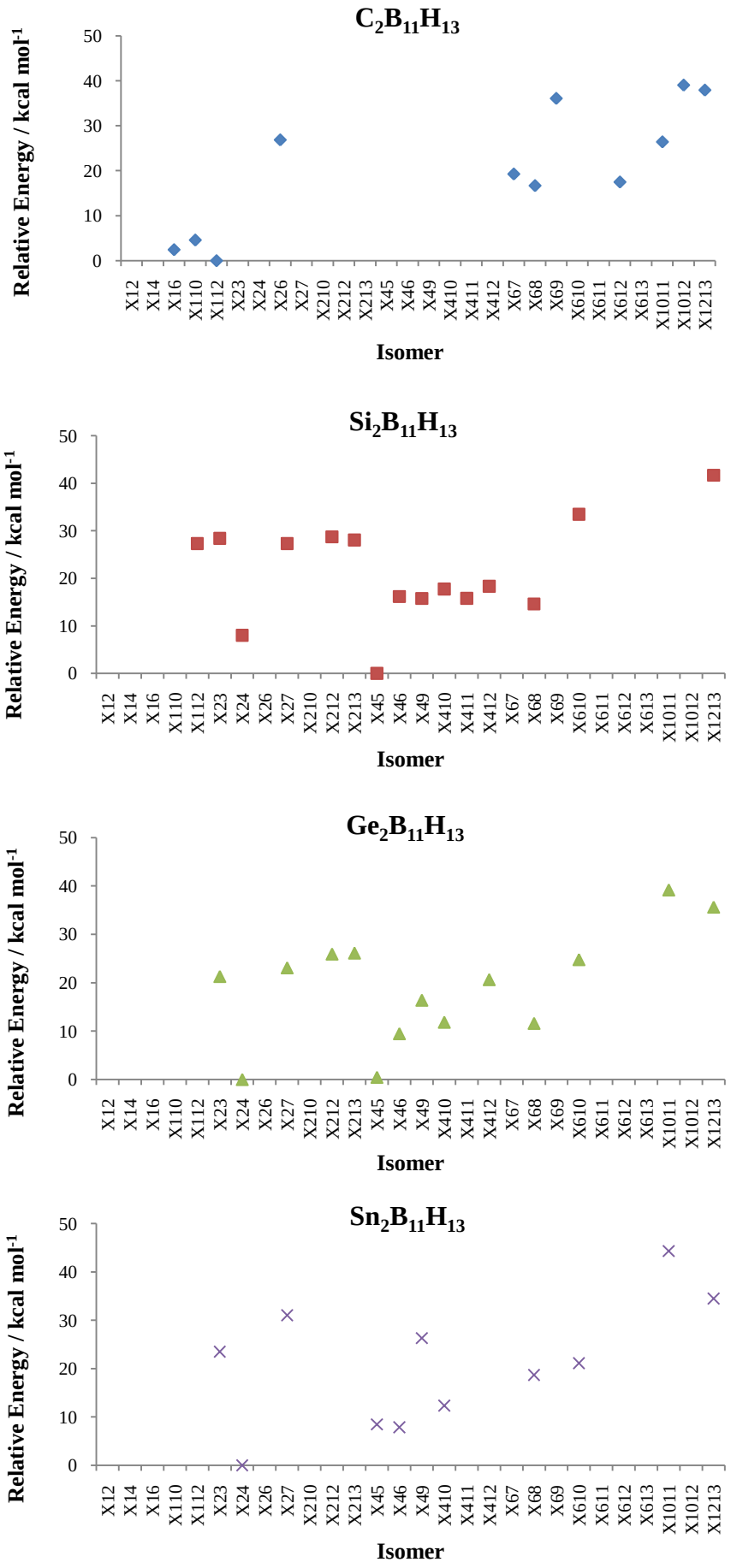

Figure 5.7 – Plots of relative energies of 13-vertex group 14 diheteroborane isomers, $X_2B_{11}H_{13}$.

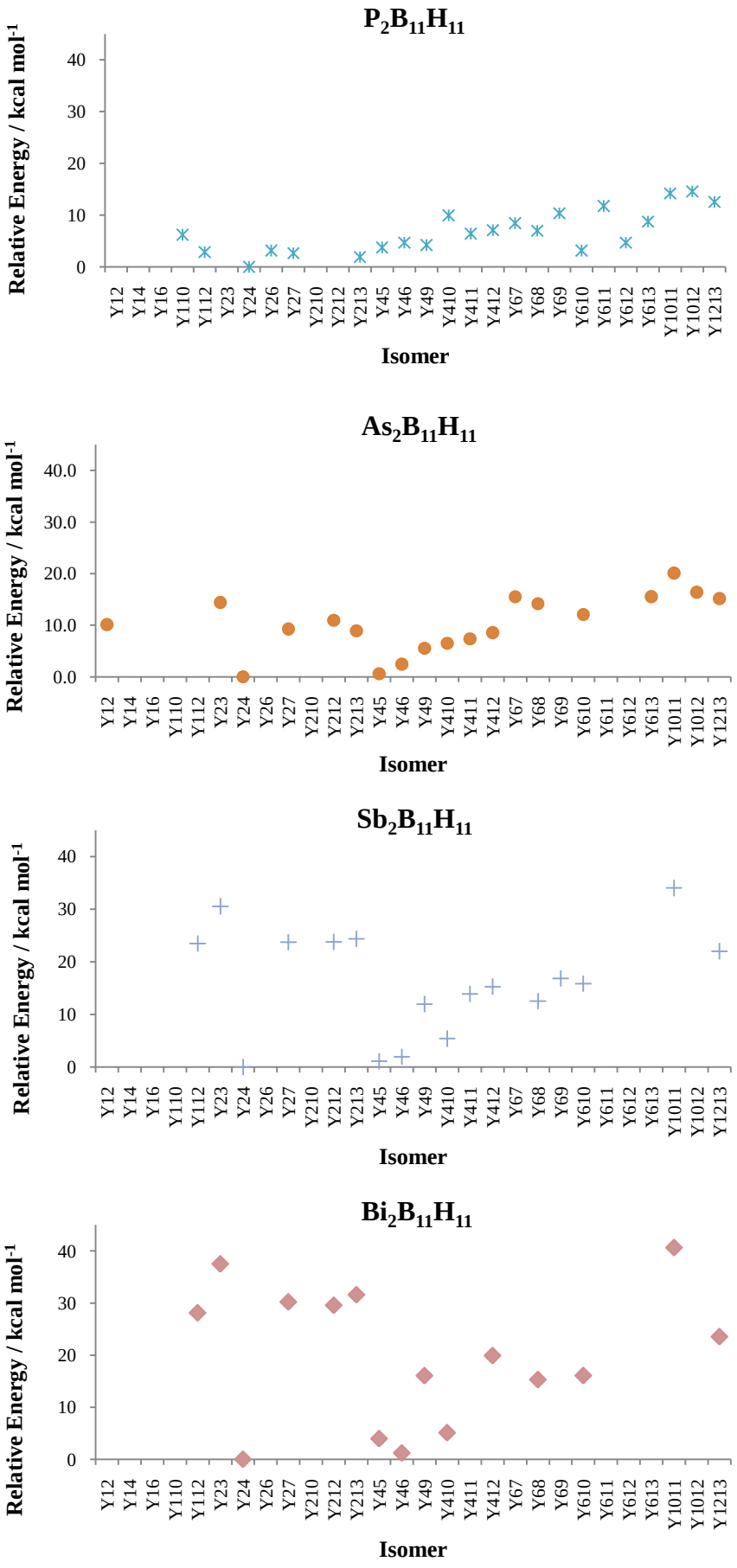

Figure 5.8 – Plots of relative energies of 13-vertex group 15 diheteroborane isomers, $Y_2B_{11}H_{11}$.

The number of stable isomers found changes considerably with the heteroatom used and is summarised in Table 5.1, below. Carbon and tin give the fewest stable isomers, emphasising their incompatibility with boron, which appears to be mostly size-based; carbon through its smaller atomic radius and tin through its larger atomic radius compared with boron. Electronegativity is also evident, where Sn gives less isomers than Sb and Bi, which are larger, but closer to B in electronegativity. Phosphorus is shown to be the most compatible with boron, as 20 stable isomers were computed, reinforced by the smallest energy range of all of the plots in Figures 5.7 and 5.8. In general, by this measure of the number of stable isomers, the group 15 heteroboranes appear to be more stable than those of group 14.

Table 5.1 – Numbers of stable docosahedral or henicosahedral geometries found in $X_2B_{11}H_{13}$ and $Y_2B_{11}H_{11}$.

X	No. 13-vertex Minima	Y	No. 13-vertex Minima
C	11	**P**	20
Si	13	**As**	19
Ge	13	**Sb**	16
Sn	11	**Bi**	14

5.4.1. 13-vertex carboranes $C_2B_{11}H_{13}$

Figure 5.10 gives the geometries of the 11 stable 13-vertex carboranes found. Four isomers with C in the 4-connected vertex 1 were found; 1,2-, 1,6-, 1,10- and 1,12-*closo*-$C_2B_{11}H_{13}$ where 1,2-*closo*-$C_2B_{11}H_{13}$ is computed as having a henicosahedral geometry with equivalent carbon vertices, while the remaining isomers were docosahedral (see Figure 5.9, below). In the remaining seven isomers, both carbon vertices are 5-connected.

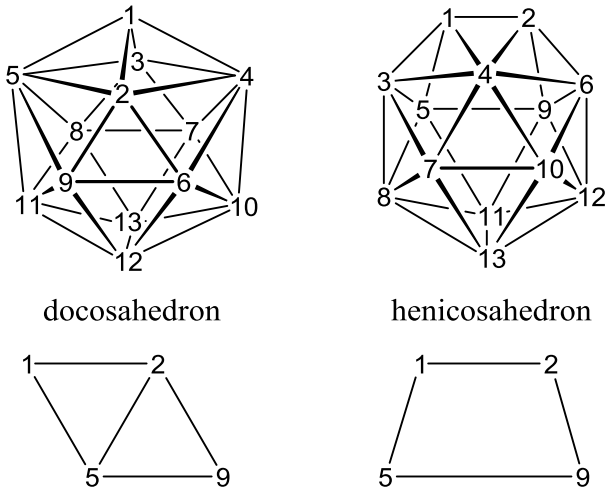

Figure 5.9 – Docosahedral and henicosahedral geometries, related by the 2–5 connection.

The thermodynamic order of the 1,X-isomers was 1,2- < 1,10- < 1,6- < 1,12-*closo*-$C_2B_{11}H_{13}$ with energies of 17.5, 4.6, 2.5 and 0.0 kcal mol^{-1} respectively.

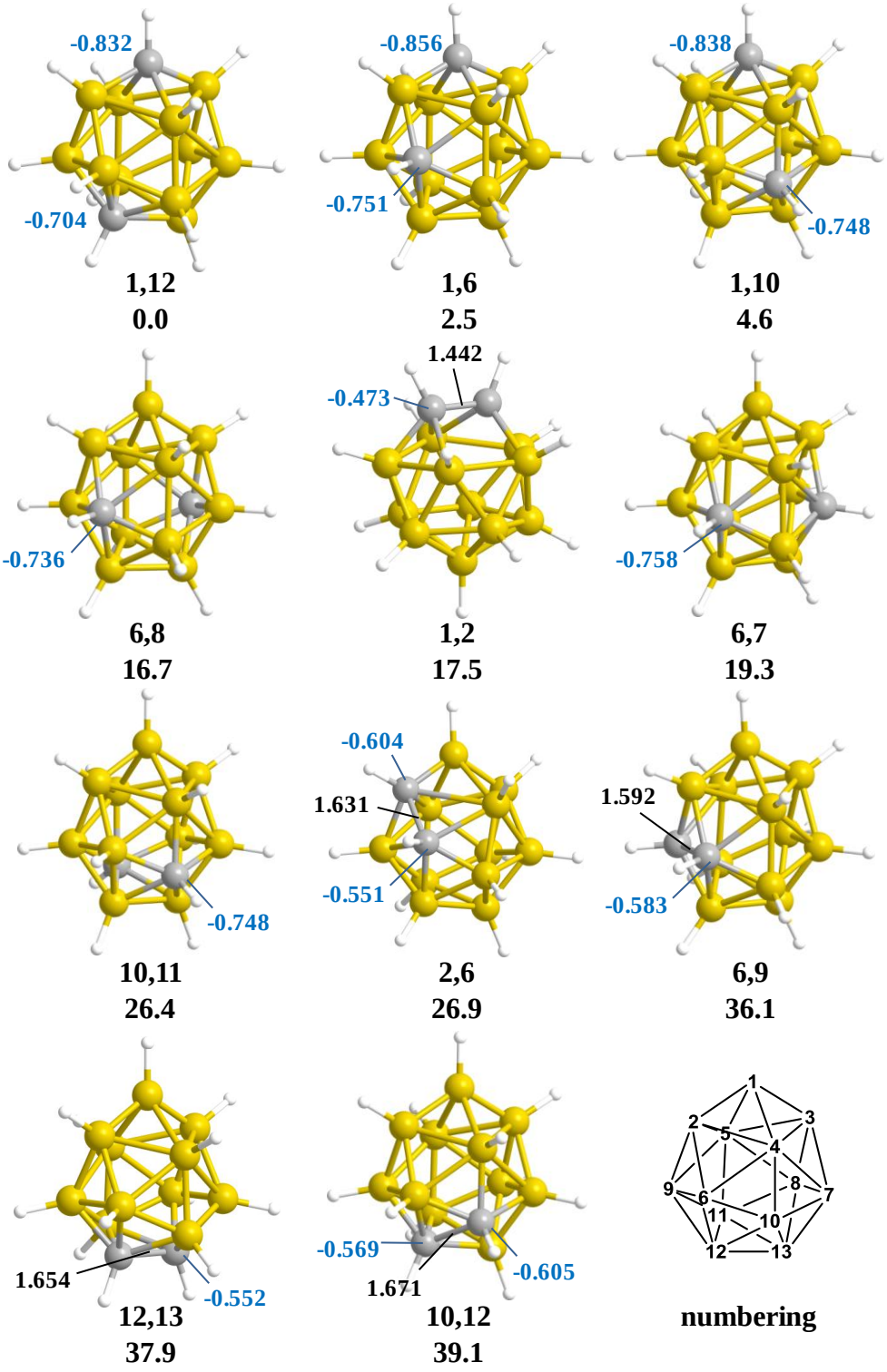

Figure 5.10 – Geometries of stable *closo*-$C_2B_{11}H_{13}$ isomers, showing carbon positions, relative energies in kcal mol^{-1}, C–C connection lengths (in black) and natural charges on C (blue).

The remaining isomers have higher energies, which can be related to the fact that both of the carbon vertices are 5-connected. The trend within these isomers is 6,8- < 6,7- < 10,11- < 2,6- < 6,9- < 12,13- < 10,12-*closo*-$C_2B_{11}H_{13}$, where the four least stable exhibit

a direct C–C connection, showing this is again a destabilising property related to a Coulombic interaction. The C–C distances were computed to be 1.631, 1.592, 1.654 and 1.671 Å for 2,6-, 6,9-, 12,13- and 10,12-*closo*-$C_2B_{11}H_{13}$ respectively, thus there is not a strong correlation between the stability of a particular isomer and the C–C bond length. No stable isomers were computed with carbon-based vertices occupying 6-connected sites. Therefore the factors contributing to these energies are the number of connections, where the isomers are stabilised with $\{CH\}^+$ 4- > 5- > 6-connected, and the relative positions of carbon vertices, where isomers with distant carbon atoms are stabilised. The henicosahedral 1,2-*closo*-$C_2B_{11}H_{13}$ isomer is discussed later.

To investigate the isomer energies further, natural charges were computed. The carbon atoms carry negative charges (shown in blue in Figure 5.10) and those on boron centres (not shown) are less negative or slightly positive. The magnitude of the negative charge on carbon atoms was assessed with respect to the relative stability of each isomer. In general, more negative charges coincide with a lower connectivity, linking the vertex with electronegativity. The charge on carbon is most negative where it occupies vertex 1, where the average charge, $\langle q(C1) \rangle = -0.842$. Where C occupies a 5-connected site and is not directly connected to another carbon atom, the charge is less negative; $\langle q(C_{5c}) \rangle = -0.743$. Where there is a direct connection between carbons in 5-connected sites, in 2,6-, 6,9-, 12,13- and 10,12-*closo*-$C_2B_{11}H_{13}$, the negative average charge on carbon is again lowered, to $\langle q(C_{5c}–C_{5c}) \rangle = -0.575$.

It is therefore clear that a carborane is most stable where its carbons carry the largest possible negative charge and that this is dictated by the vertices the carbon atoms adopt. This is coupled with the proximity of the two carbon vertices (which is most apparent where there is a direct C–C connection). The order of stability of 6,X-*closo*-$C_2B_{11}H_{13}$ isomers (which cover all of these structural features) is 1,6- > 6,8- > 6,7- > 2,6- > 6,9-*closo*-$C_2B_{11}H_{13}$. As shown in Table 5.2, this order can be rationalised by the connectivities and proximities of the carbon-based vertices and when these features are equivalent, in 2,6- and 6-9-*closo*-$C_2B_{11}H_{13}$, their relative energies are explained by the charge carried by C.

Table 5.2 – Relative energies and structural differences in 6,X-*closo*-$C_2B_{11}H_{13}$ isomers (X = 1, 8, 7, 2, 9).

X	Relative Energy / kcal mol^{-1}	Connectivity of X	Structural notes	q(C6)	q(CX)
1	2.5	4	*meta*, inequivalent	-0.751	-0.856
8	16.7	5	distant, equivalent	-0.736	-0.736
7	19.3	5	*meta*, equivalent	-0.758	-0.758
2	26.9	5	connected, inequivalent	-0.551	-0.604
9	36.1	5	connected, equivalent	-0.583	-0.583

As stated before, the 1,2-*closo*-$C_2B_{11}H_{13}$ is henicosahedral and therefore both carbon vertices are effectively 4-connected. However, the charge carried by each carbon atom is -0.473, which is the smallest negative charge seen. It also exhibits a very short C–C connection of 1.442 Å. It may be that in this case, the carbon-based unit is essentially exopolyhedral, with a localised C–C interaction.

5.4.2. Other group 14 13-vertex diheteroboranes $X_2B_{11}H_{13}$ (X = Si, Ge, Sn)

The monoheteroborane study showed that the remaining group 14 elements, Si, Ge and Sn, share a common trend in site preference, favouring more connections. Selected geometries (displaying the range in computed energies and structural types found) from the stable isomers of sila-, germa- and stannaboranes are given in Figures 5.11, 5.12 and 5.13 respectively. The changes in destabilising factors (the number of connections to the heteroatoms and the proximity of the heteroatoms) will be compared for X = Si, Ge and Sn and contrasted with those observed in the carboranes.

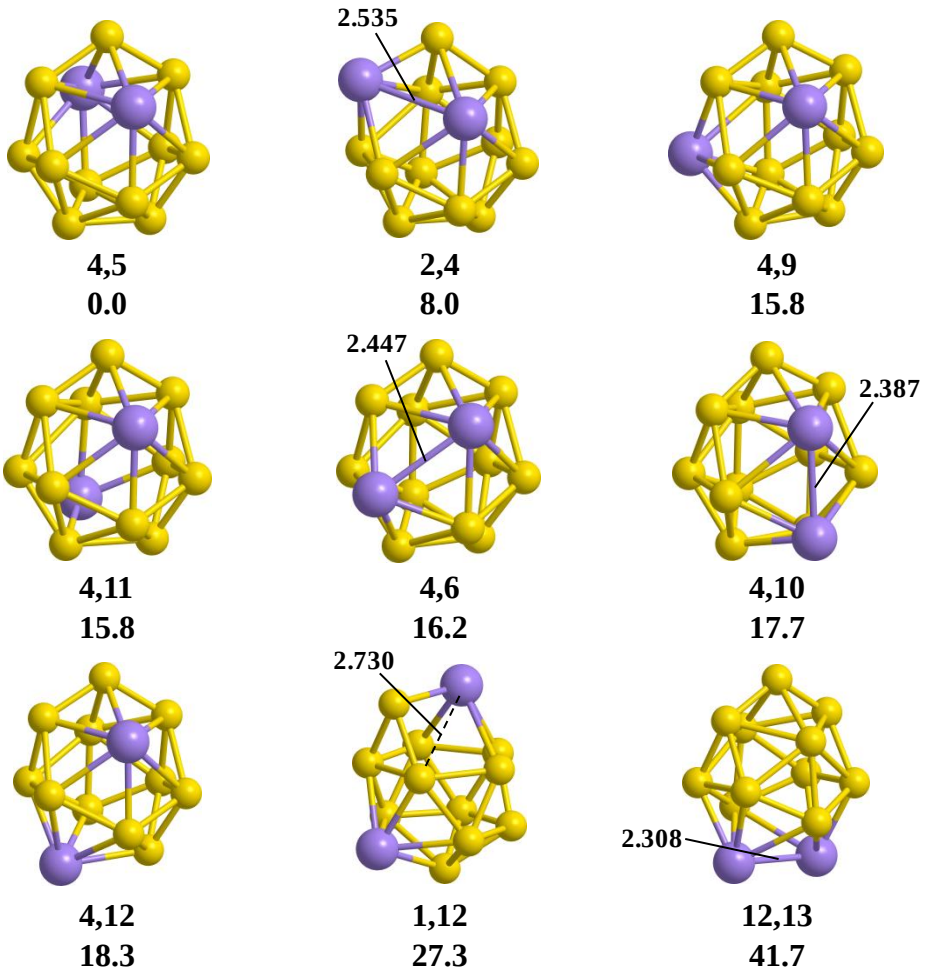

Figure 5.11 – Geometries of selected 13-vertex silaboranes, showing relative energies in kcal mol^{-1} and bond distances in Ångstroms where applicable. Hydrogens omitted for clarity.

For X = Si, the global minimum, 4,5-*closo*-$Si_2B_{11}H_{13}$ where both heteroatoms are 6-connected, displays a preference for high-connected Si vertices in silaboranes, as seen in the 13-vertex monoheteroboranes. Moreover, only one, highly distorted isomer (1,12-*closo*-$Si_2B_{11}H_{13}$) was found with Si in vertex 1. Isomers with adjacent silicon atoms are evenly distributed across the computed energy range, suggesting there is no preference in terms of the proximity of Si-based vertices. This is consistent with the relative energies in the 12-vertex silaboranes which all fall within 1 kcal mol^{-1} and the similar electronegativities of boron and silicon. The relative stability of a silaborane appears, therefore, to be dictated simply by the number of connections of each $\{SiH\}^+$ vertex.

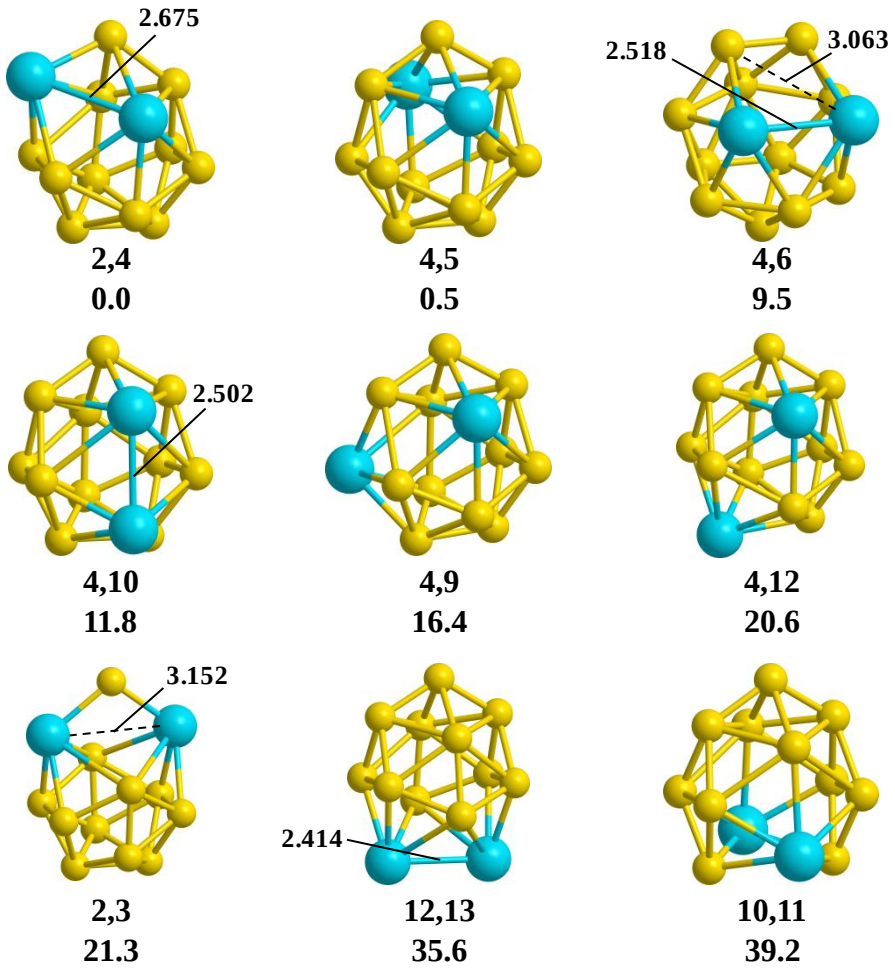

Figure 5.12 – Geometries of selected 13-vertex germaboranes, showing relative energies in kcal mol^{-1} and bond distances in Ångstroms where applicable. Hydrogens omitted for clarity.

The germaboranes demonstrate the same preference as the silaboranes for higher-connected heteroatoms, as predicted from the monoheteroborane anion study. Moreover, a preference for adjacent heteroatoms is now seen and isomers with Ge–Ge connections are relatively stabilised in comparison to their silaborane analogues. For example, 2,4-*closo*-$Ge_2B_{11}H_{13}$ is the global minimum, suggesting the effect of directly connected heteroatoms has become stabilising in the germaboranes and indeed it appears to be as stabilising as having both Ge atoms in 6-connected sites as in the 4,5-*closo*-$Ge_2B_{11}H_{13}$ isomer, which is found at 0.5 kcal mol^{-1}. This observation is, again, consistent with the 12-vertex diheteroboranes, where *ortho*-germaborane was found to be the global minimum. In general, the trend in germaborane stabilities, with respect to structural features is $\{GeH\}^+$ 6-connected with Ge–Ge connections > both 6-connected > mixed 5- and 6-connected > both 5-connected, where the final category leads to highly distorted geometries, such as that seen in 2,3-*closo*-$Ge_2B_{11}H_{13}$.

The third most stable 13-vertex germaborane isomer was found to be the henicosahedral 4,6-*closo*-$Ge_2B_{11}H_{13}$ at ΔE = 9.5 kcal mol^{-1}. Here, however, the germanium vertices occupy different positions than the carbon atoms in the henicosahedral carborane, 1,2-*closo*-$C_2B_{11}H_{13}$.

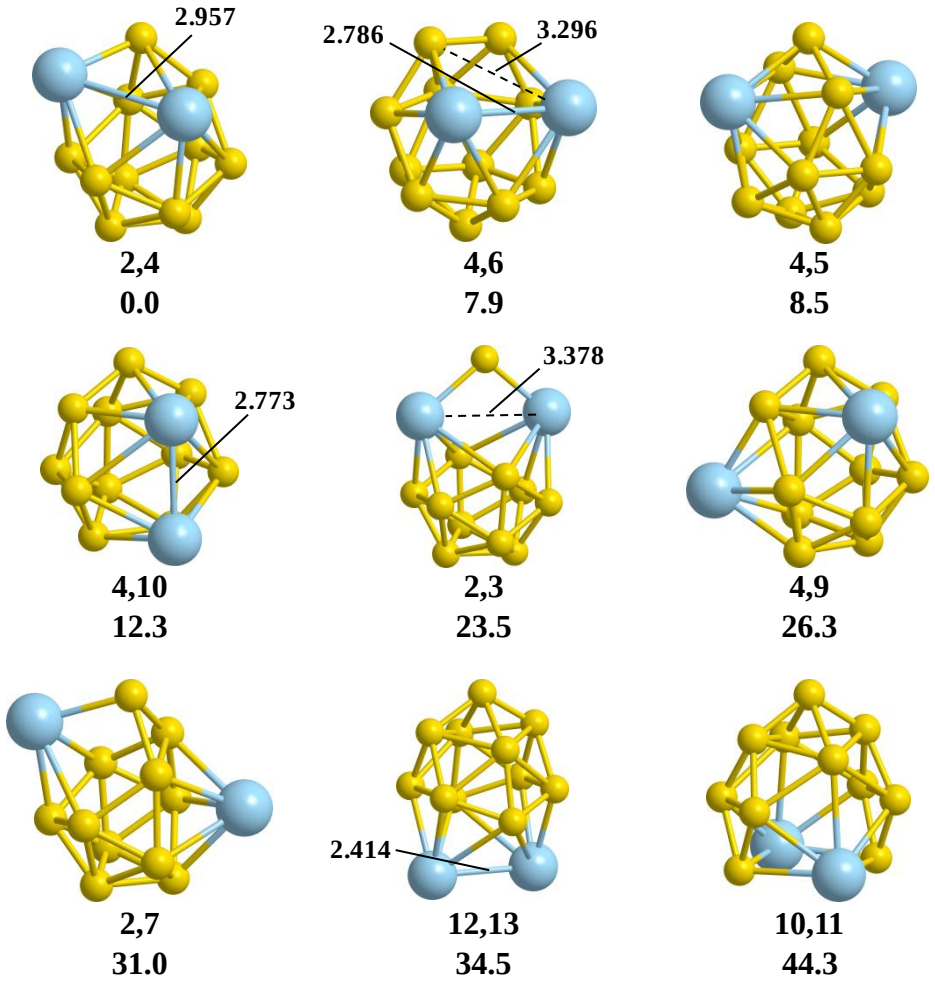

Figure 5.13 – Geometries of selected 13-vertex stannaboranes, showing relative energies in kcal mol^{-1} and Sn–Sn bond distances in Ångstroms where applicable. Hydrogens omitted for clarity.

In the supraicosahedral stannaboranes, the trends seen in the sila- and germaboranes are further reinforced. Sn–Sn connections are prevalent in the low energy geometries, while low-connected Sn centres are in the higher energy stable and unstable geometries. The 2,4- and 4,6-*closo*-$Sn_2B_{11}H_{13}$ isomers were found to be the first and second most stable isomers for X = Sn at 0.0 and 7.9 kcal mol^{-1} respectively. This indicates that the stabilising effect of having a direct Sn–Sn connection now overrules the stabilisation of having both Sn centres in 6-connected sites, as 4,5-*closo*-$Sn_2B_{11}H_{13}$, the third most stable isomer, is found at 8.5 kcal mol^{-1}. However the above, coupled with the highly distorted geometries seen, is indicative of a poor match between tin and boron and can be attributed to the difference in atomic radii. The 2,3-*closo*-$Sn_2B_{11}H_{13}$ isomer, while

high in energy, is the most stable of those with both tin-based vertices in 5-connected sites. This may suggest its highly distorted geometry, exhibiting a bridging boron centre (B1), allows a weak metal-metal bond with a Sn···Sn distance of 3.378 Å.

5.4.3. The "unstable" 6,8-*closo*-$X_2B_{11}H_{13}$ isomer (X = Si, Ge, Sn)

The case of 6,8-*closo*-$X_2B_{11}H_{13}$ was interesting. Where X = C, the expected docosahedral geometry was found, however where X = Si, Ge and Sn, the initial target isomer was lost and the geometry optimisation revealed a new 13-vertex structure (see Figure 5.14, below).

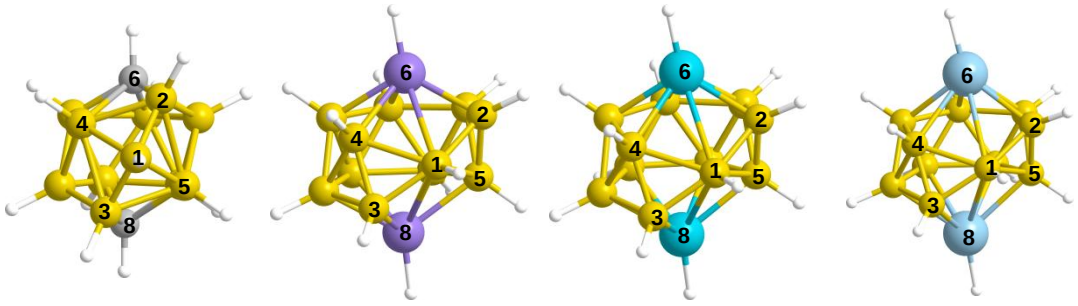

6,8-*closo*-$C_2B_{11}H_{13}$ 16.7 **6,8-*closo*-$Si_2B_{11}H_{13}$ 14.6** **6,8-*closo*-$Ge_2B_{11}H_{13}$ 11.6** **6,8-*closo*-$Sn_2B_{11}H_{13}$ 22.4**

Figure 5.14 – 6,8-*closo*-$X_2B_{11}H_{13}$ (X = C, Si, Ge, Sn), showing relative energies with respect the global minimum for each heteroatom.

In this geometry, the cage has isomerised to allow both X atoms adopt 6-, rather than 5-connected sites at opposite ends of the molecule and cause B1 atom to adopt a 6-connected site bridging the two heteroatoms. In addition, B2 and B3 become 4-connected. This geometry can be related to the docosahedron by rotation of the B2-B1-B3 fragment as labelled in Figure 5.14, together with D-S-D isomerisations in the 1-4-6-2 and 1-3-8-5 diamonds (see Figure 5.15, below).

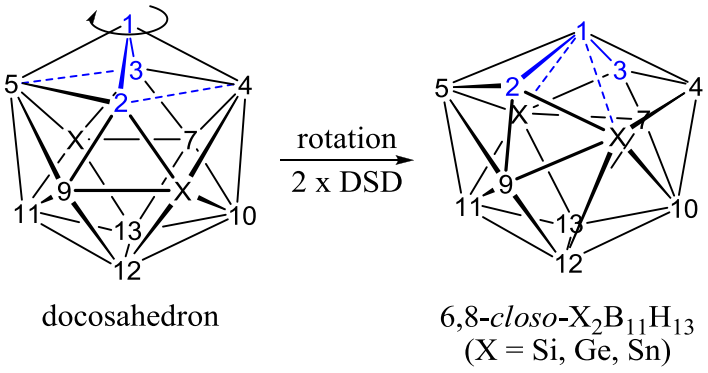

Figure 5.15 – Proposed isomerisation from a docosahedral geometry to the optimised structure of the 6,8-*closo*-$X_2B_{11}H_{13}$ isomer (X = Si, Ge, Sn).

A compound exhibiting this geometry has not been reported in the literature, but given there are two 4-connected and three 6-connected sites, it may be realised experimentally through production of a $M_3C_2B_8$ species. Such a species would exhibit two stabilised 4-connected carbon centres and two stabilised metal centres (where metal fragments are known to preferentially adopt 6-connected sites).

5.4.4. Group 15 13-vertex diheteroboranes $Y_2B_{11}H_{11}$ (Y = P, As, Sb, Bi)

Selected geometries (displaying the range of computed energies and structural types seen) from the stable isomers of phospha-, arsena-, stiba- and bismaboranes are given in Figures 5.16, 5.17, 5.18 and 5.19 respectively.

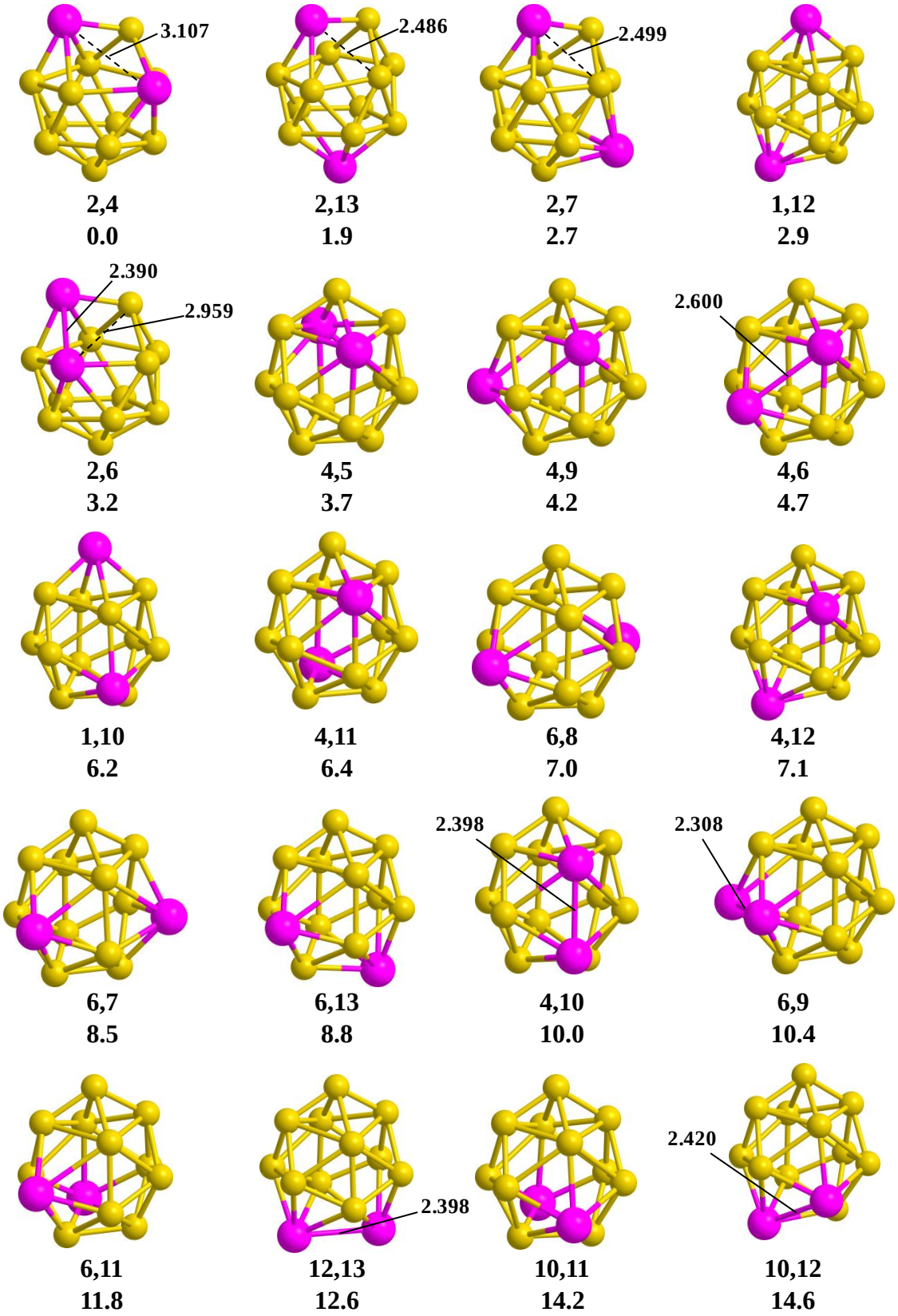

Figure 5.16 – Geometries of stable 13-vertex phosphaboranes, showing relative energies in kcal mol^{-1}, P–P bond distances and shortest diagonal (of 1-2-5-9 face) in henicosahedral geometries in Ångstroms where applicable. B–H hydrogen atoms omitted for clarity.

The 13-vertex phosphaboranes were found to exhibit the largest number of stable isomers, which can be attributed to phosphorus being most 'boron like' in terms of the

combination of electronegativity and atomic radius. As a result, the isomers with direct P–P connections are evenly distributed across the energy range. However, the above geometries reveal the effect of the larger atomic radius of the phosphorus atoms, as structures with phosphorus in a 6-connected site are slightly favoured. Additionally, an increased proportion of henicosahedral geometries is seen, highlighted in Figure 5.16 by lengthened P2···B4 connections. 2,4-*closo*-$P_2B_{11}H_{11}$, found to be the global minimum, has adjacent phosphorus atoms diagonally opposite each other on the four-membered face, although at a distance of 3.107 Å which does not suggest a significant P–P interaction. 2,13- and 2,7-*closo*-$P_2B_{11}H_{11}$ have shorter P2–B4 diagonals (2.486 and 2.499 Å respectively). 2,6-*closo*-$P_2B_{11}H_{11}$, which differs from 2,4-*closo*-$P_2B_{11}H_{11}$ by having a P–P connection (at 2.390 Å), was found at 3.2 kcal mol^{-1}. However, this small energy difference reinforces the observation that there is not a significant destabilisation with respect to the proximity of the heteroatoms. At higher energies, there is a prevalence of isomers with one or both phosphorus atoms in vertices 6 to 13 which exhibit less distortion of the docosahedral geometries. Perhaps this also relates to the sizes of the atoms, since higher relative energies are found where the strain caused by inclusion of a large P vertex cannot be relieved by distortion of the cage. The key observation in the phosphaboranes is the small energy range and large number of stable isomers essentially suggesting a lack of structural preference and therefore a good match between phosphorus and boron.

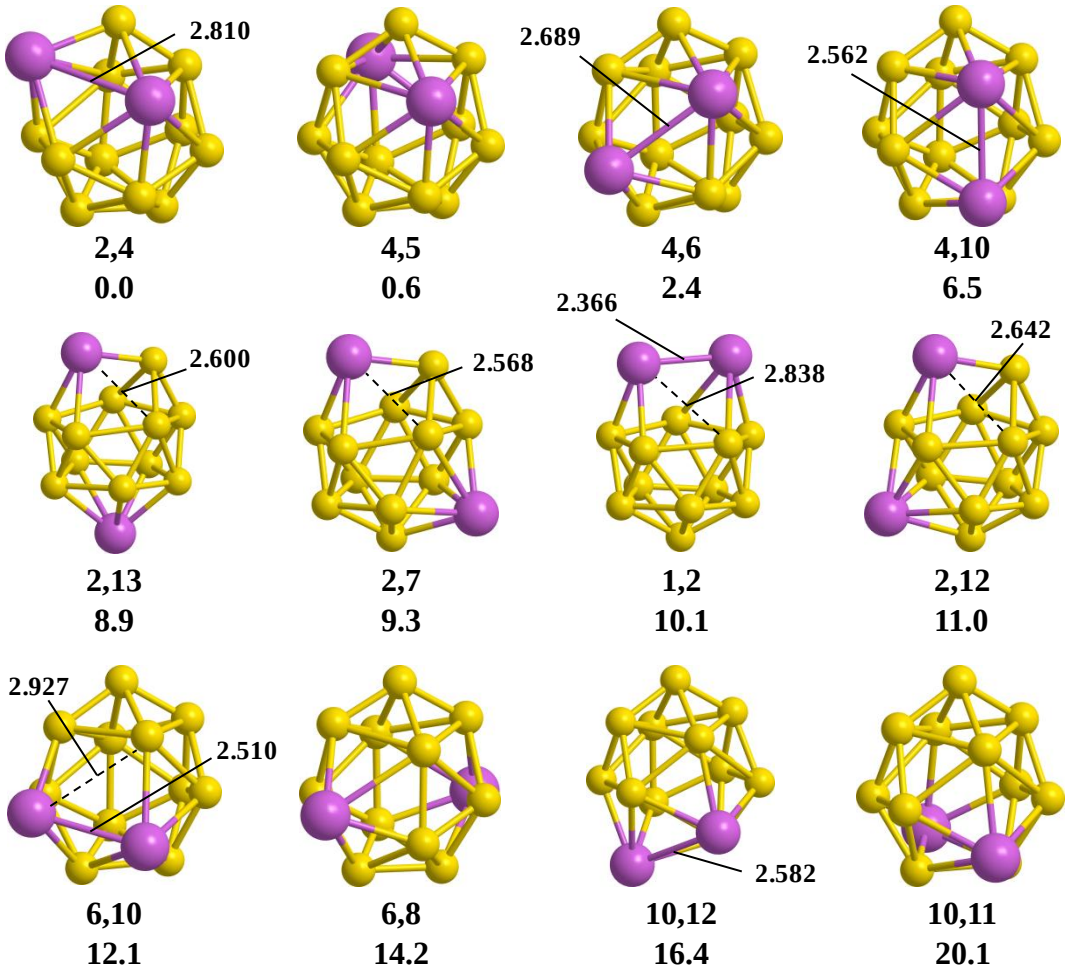

Figure 5.17 – Geometries of selected stable 13-vertex arsenaboranes, showing relative energies in kcal mol^{-1}, As–As bond distances and shortest diagonal (of the 1-2-5-9 face) in henicosahedral geometries in Ångstroms where applicable. B–H hydrogen atoms omitted for clarity.

The arsenaboranes produce only one less stable isomer than the phosphaboranes, despite having double the mismatch in atomic radius (B = 85 pm *cf.* P = 100 pm and As = 115pm). In changing from phosphorus to arsenic, the global minimum has not changed, however as we move down group 15, structural preferences begin to arise as isomers with 6-connected As vertices are stabilised. The distorted geometries of 1,2- and 6,10-*closo*-$As_2B_{11}H_{11}$ reinforce this observation as the cage distortion appears to allow for a shorter As–As interaction and less As–B bonding. 6,10-*closo*-$As_2B_{11}H_{11}$ exhibits a 4-membered As6-B2-B4-As10 face and, by comparison with other isomers in Figure 5.17 with either an As6 or As10 vertex, the distortion giving a 4-membered face is a lengthened As6···B4 distance of 2.927 Å by movement of the B4 vertex.

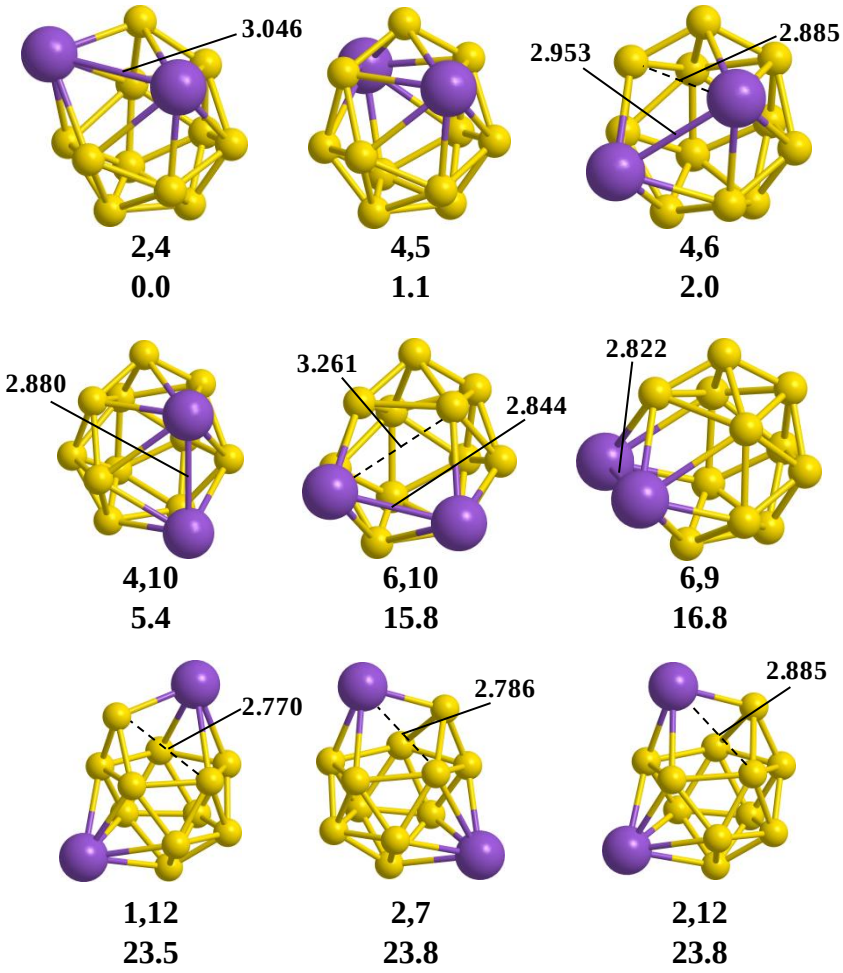

Figure 5.18 – Geometries of selected stable 13-vertex stibaboranes, showing relative energies in kcal mol^{-1}, Sb–Sb bond distances and shortest diagonal (of the 1-2-5-9 face) in henicosahedral geometries in Ångstroms where applicable. B–H hydrogen atoms omitted for clarity.

The 13-vertex stibaboranes show, again, an increase in relative stability of geometries exhibiting 6-connected heteroatoms as well as those with direct Sb–Sb connections. The 2,4-*closo*-$Sb_2B_{11}H_{11}$ isomer is the most stable, where the long Sb–Sb interaction of 3.046 Å (*cf.* an atomic radius of 145 pm) is shorter than the P···P distance in the 2,4-*closo*-$P_2B_{11}H_{11}$ henicosahedron, despite the increased atomic radius. If this is considered to be a bonding interaction, the geometry is therefore docosahedral. The next five most stable isomers shown, 4,5-, 4,6-, 4,10-, 6,10- and 6,9-*closo*-$Sb_2B_{11}H_{11}$ (E = 1.1, 2.0, 5.4, 15.8 and 16.8 kcal mol^{-1} respectively) demonstrate the relative strengths of the stabilisations seen by having a 6-connected Sb vertex and a direct Sb–Sb connection. 4,5-*closo*-$Sb_2B_{11}H_{11}$ exhibits two 6-connected Sb vertices and no Sb–Sb connection, relative to which the 4,6-*closo*-$Sb_2B_{11}H_{11}$ isomer is destabilised in that one Sb atom has become 5-connected, but stabilised by a Sb–Sb connection. The 4,10-*closo*-$Sb_2B_{11}H_{11}$ isomer retains one 6-connected Sb centre, but the other, Sb10, is in a vertex where, as seen in the 13-vertex phosphaboranes, a stabilisation *via* distortion of

the cage is not possible. There is a sharp rise in relative energy to the 6,10- and 6,9-*closo*-$Sb_2B_{11}H_{11}$ isomers, associated with both antimony atoms being 5-connected. They exhibit relatively similar Sb–Sb distances of 2.844 and 2.822 Å respectively, and so their energy difference of 1 kcal mol^{-1} may be related to there being a stabilising distortion in 6,10-*closo*-$Sb_2B_{11}H_{11}$; the B4···Sb6 connection is lengthened to 3.261 Å, whereas there is relatively little distortion in the 6,9-*closo*-$Sb_2B_{11}H_{11}$ isomer.

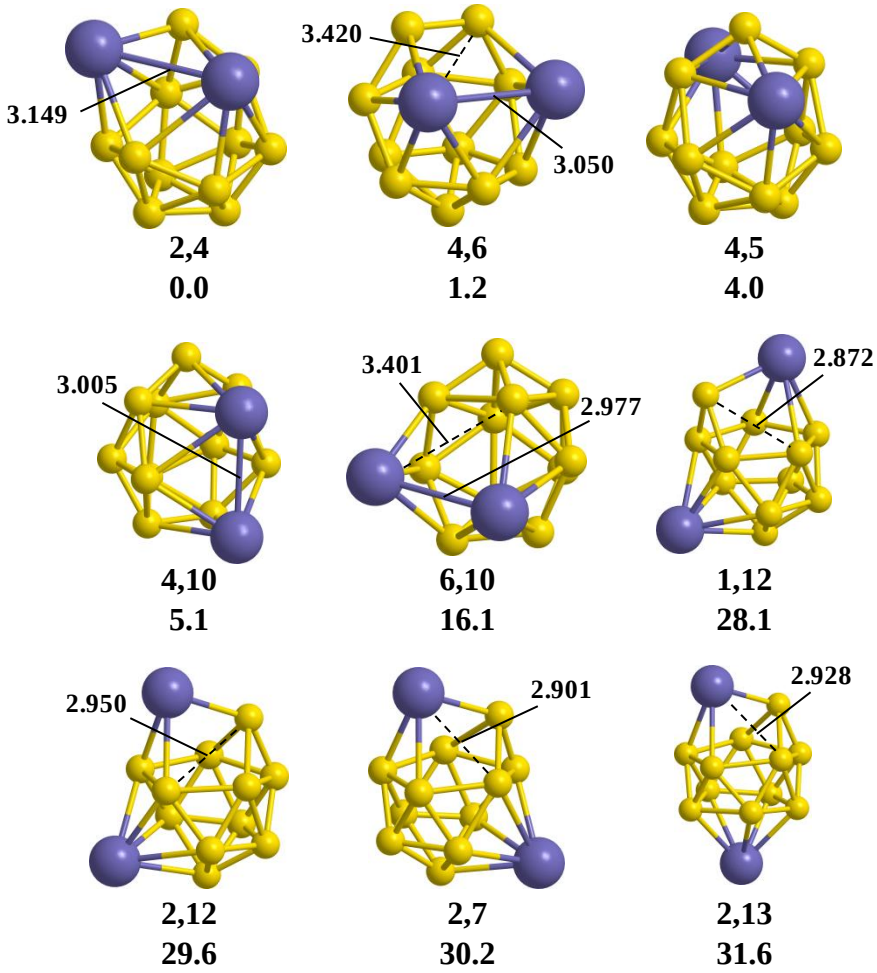

Figure 5.19 – Geometries of selected stable 13-vertex bismaboranes, showing relative energies in kcal mol^{-1}, Bi–Bi bond distances and shortest diagonal (of the 1-2-5-9 face) in henicosahedral geometries in Ångstroms where applicable. B–H hydrogen atoms omitted for clarity.

The final element investigated as a heteroatom in $Y_2B_{11}H_{11}$ was bismuth. Fourteen isomers were found to be stable, which is the lowest number for the group 15 elements, in agreement with the large difference in atomic radii between boron and bismuth.

The trends in 13-vertex bismaborane isomers largely continue those of the earlier group 15 elements. Cages with 6-connected Bi vertices are favoured, as are cages with direct Bi–Bi connections, where now the latter appears to be the stronger effect as the 4,5-*closo*-$Bi_2B_{11}H_{11}$ isomer is only the third most stable. This emphasises the emergence of

metal–metal bonding as we go down the Periodic Table, as seen in the group 14 heteroboranes.

The global minima for all 13-vertex isomers, $Y_2B_{11}H_{11}$ (Y = P, As, Sb, Bi), were found to be represented by the 2,4-*closo*-$Y_2B_{11}H_{11}$ isomer, however, these fall into two different structural types (see Table 5.3, below). For Y = P, the geometry is best described as henicosahedral, since the phosphorus vertices are deemed unconnected. In contrast, for Y = As, Sb and Bi, the heteroatoms are thought to be connected and therefore the geometries are considered to be docosahedral.

Table 5.3 – Structural type of the 2,4-*closo*-$Y_2B_{11}H_{11}$ isomers (Y = P, As, Sb, Bi)

Y	Y···Y Distance / Å	Structural type
P	3.107	Henicosahedral
As	2.810	Docosahedral
Sb	3.046	Docosahedral
Bi	3.149	Docosahedral

5.5. 12-vertex *nido* phosphaboranes, [*nido*-$P_2B_{10}H_{10}$]$^{2-}$

The parallel experimental part of this work aims to reduce and capitate with {BPh}$^{+}$ 1,2-*closo*-$P_2B_{10}H_{10}$ (*ortho*-phosphaborane) to produce the first supraicosahedral phosphaborane.[15] The following section describes computational work carried out to predict which 13-vertex isomer (or isomers) would be most likely to form. In order to make this prediction, the 12-vertex *nido* isomers must be computed (as seen in Chapters 1 and 2 for carboranes), since the *nido* intermediate greatly influences the nature of the capitated species. Calculations focussed on the reduction and isomerisation of *ortho*-phosphaborane.

The 12-vertex *nido* fragment is a fragment of the docosahedron with the 6-connected vertex 4 removed. The resulting geometry has C_s symmetry and has eight unique vertices (see insert in Figure 5.20 for numbering). Substituting a heteroatom into each of these unique vertices gives geometries of either C_s (vertices 1, 2, 7 and 10) or C_1 symmetry (vertices 3, 4, 8 and 9). The symmetry is further reduced on insertion of the second heteroatom, resulting in diheteroborane *nido* fragments corresponding to 38 unique isomers.

The internal coordinates used for the 13-vertex diheteroboranes were adapted by removal of vertex 4 to give a *nido* topology. Constrained optimisations were conducted and subsequently re-optimised after removal of the constraints, producing the following stable minima of [*nido*-$P_2B_{10}H_{10}$]$^{2-}$.

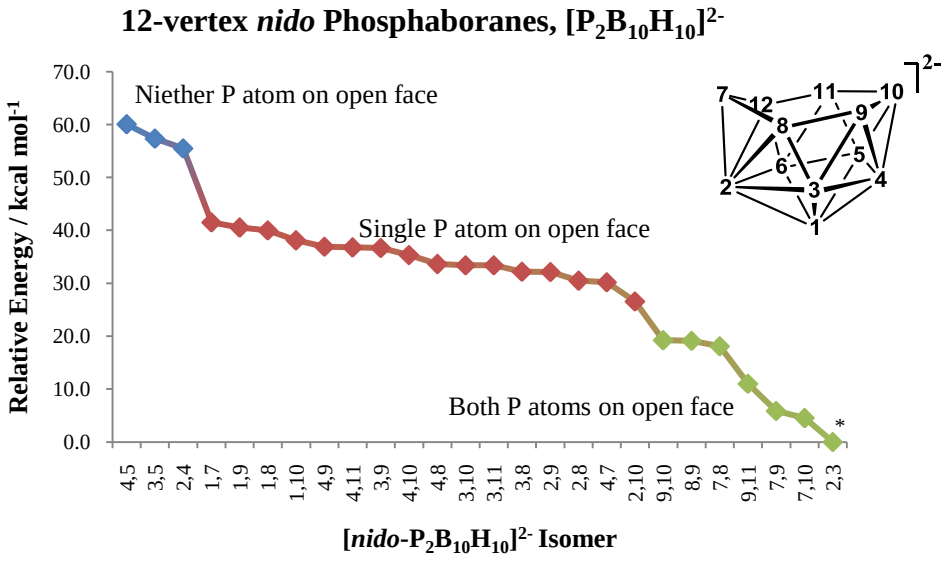

Figure 5.20 – Graph of stable [*nido*-$P_2B_{10}H_{10}$]$^{2-}$ isomers in order of increasing stability.

Figure 5.20 shows that isomers of [*nido*-$P_2B_{10}H_{10}]^{2-}$ with both phosphorus atoms on the open face (in vertices 7-12) are lowest in energy and those with both phosphorus atoms away from the face (in vertices 1-6) are highest in energy. Isomers with just one on the open face are intermediate in energy (selected geometries given in Figure 5.21, below). This is consistent with the trend seen in [*nido*-$C_2B_{10}H_{12}]^{2-}$ isomers found in Chapter 2. Indeed this preference for heteroatoms on the open face was found to be a driving force in the isomerisation of *nido* carboranes.

The lowest energy isomer found, [2,3-*nido*-$P_2B_{10}H_{10}]^{2-}$, is a special case as it does not exhibit the expected geometry and will be discussed in detail later.

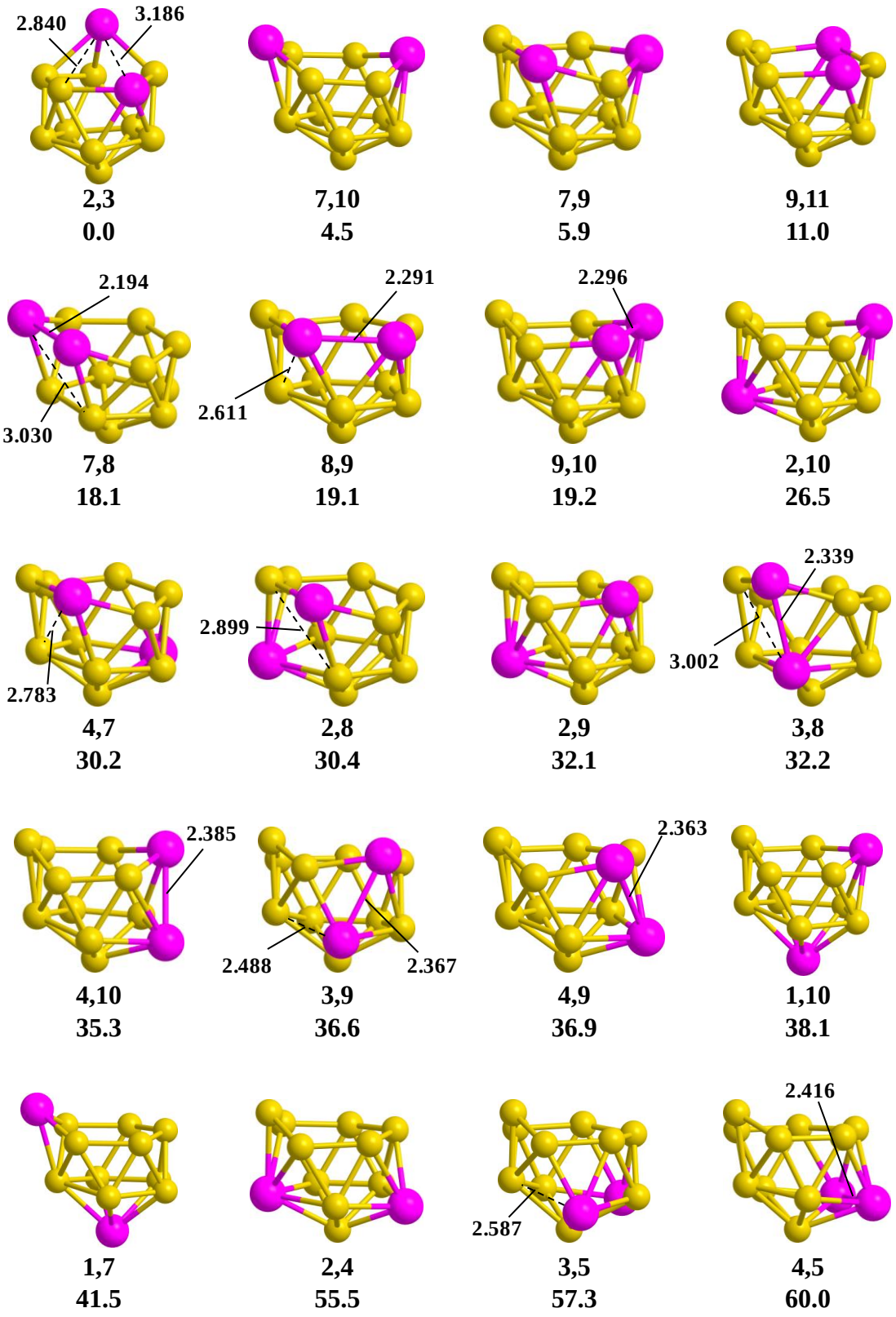

Figure 5.21 – Geometries of selected stable 12-vertex *nido*-phosphaboranes dianions, showing relative energies in kcal mol^{-1}, P–P bond distances and lengthened connections in Ångstroms where applicable. B–H hydrogen atoms omitted for clarity.

From the above geometries, two further trends are also seen; structures with low-connected P vertices (P7) are stabilised and those with direct P–P connections are

destabilised. This is an unexpected observation since the relative stabilities of 13-vertex *closo*-phosphaboranes reveal preference for high-connected sites and little dependence on the P···P proximity and now, as *nido* dianionic species, the phosphaboranes exhibit the same trends seen in the carboranes. This may be associated with the increased charge of the system, which favours isomers which are better set up to remove electron density from the cage. Isomers with lower-connected phosphorus vertices would allow stabilisation of the cage by increased localisation of the phosphorus lone pairs. This hypothesis is supported by experimental work[15] which suggests *nido* phosphaboranes are better Lewis bases than *closo* phosphaboranes. In addition, parallel experimental and computational work (Chapter 3, Section 3.2.1) to stabilise *nido* carboranes suggest this can be done with electron withdrawing C-substituents.

The most stable isomer, [2,3-*nido*-$P_2B_{10}H_{10}]^{2-}$, is unusual in that it does not exhibit typical *nido* fragment topology. It is therefore not numbered following the conventional system, but since it was found through isomerisation of the [2,3-*nido*-$P_2B_{10}H_{10}]^{2-}$ constrained geometry it retains this numbering. The geometry does not exhibit a 6-membered open face, and is in fact a nido fragment of a 1,6-*closo*-$P_2B_{11}H_{11}$ henicosahedron (the enantiomer of the global minimum, 2,4-*closo*-$P_2B_{11}H_{11}$, see Section 5.3.5) where a 4-connected vertex 2 has been removed giving a 5 atom open face (see Figure 5.22, below).

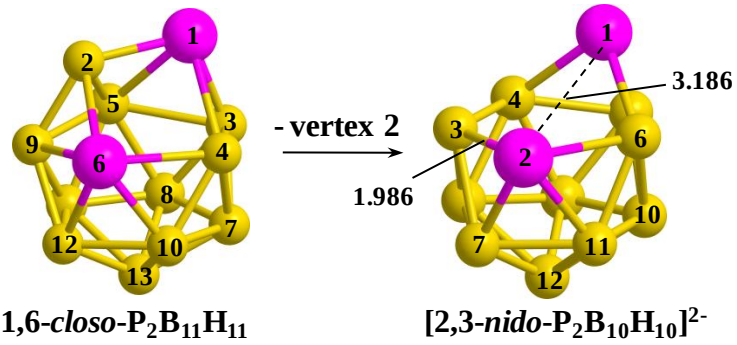

Figure 5.22 – The topology of [2,3-*nido*-$P_2B_{10}H_{10}]^{2-}$, arising from the loss of B2 from 1,6-*closo*-$P_2B_{11}H_{11}$. B–H hydrogen atoms omitted for clarity.

The above goes against the convention set out in the Wade-Williams-Rudolph structural matrix[16] as the lowest-connected rather than the highest-connected boron is removed from the 13-vertex geometry to give the 12-vertex *nido* species.

5.6. Computed reduction and isomerisation of 1,2-*closo*-$P_2B_{10}H_{10}$

The computational reduction of *ortho*-phosphaborane was done in two steps. First the doublet monoanion was optimised, using unrestricted DFT, following addition of $1e^-$ to *ortho*-phosphaborane. The resulting geometry showed an increased P–P distance from 2.358 Å in the neutral species to 2.823 Å in [*ortho*-phosphaborane]$^-$ (see Figure 5.23, below).

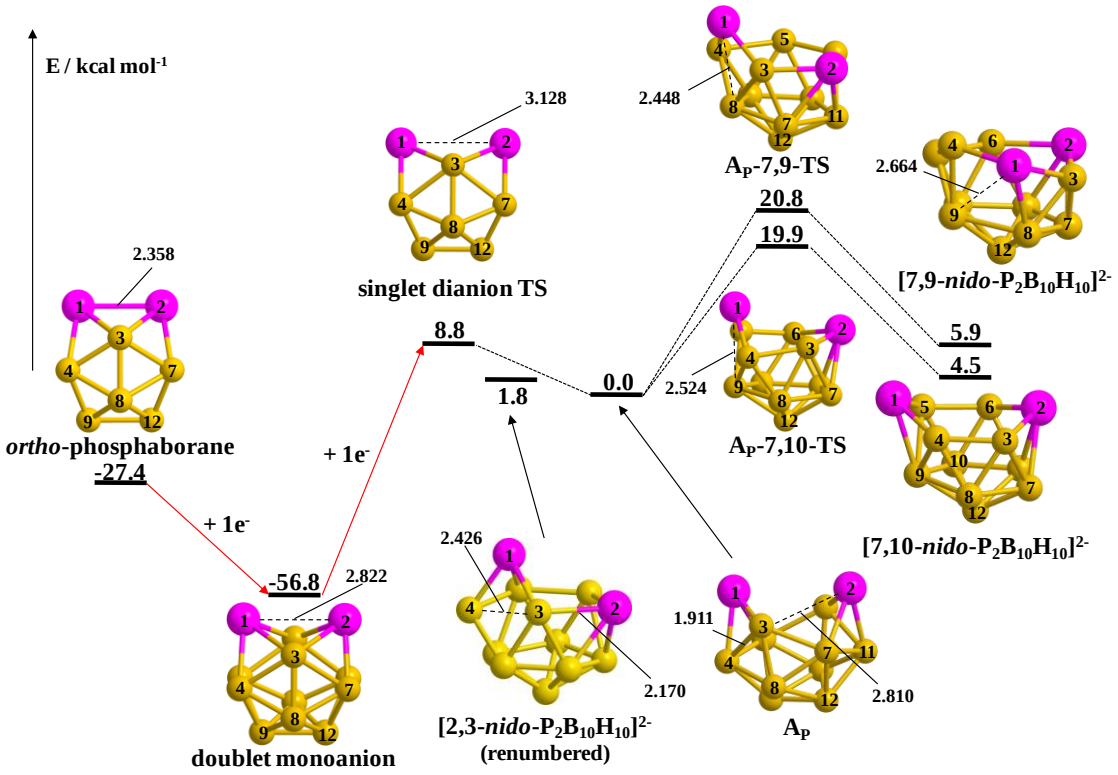

Figure 5.23 – Computational 2e reduction of *ortho*-phosphaborane. Energies in kcal mol^{-1}.

The optimised geometry of the singlet dianion shows a further increase P–P distance to 3.128 Å while C_{2v} symmetry is maintained, similar to the reduction of diphenyl-*ortho*-carborane. Frequency calculations on the C_{2v} $[P_2B_{10}H_{10}]^{2-}$ dianion showed, however, this geometry was a transition state, where the negative eigenvalue corresponds to a twisting of the structure about its rotational symmetry axis. IRC calculations confirmed this to be a symmetrical transition state relating two enantiomeric C_2 symmetric minima, **A_P**, which is closely related to [2,3-*nido*-$P_2B_{10}H_{10}]^{2-}$ by lengthening of the P2–B3 distance from 2.170 to 2.810 Å and shortening of the B3···B4 distance from 2.426 to 1.911 Å in **A_P** ($\Delta E = 1.8$ kcal mol^{-1}).

This leads to the conclusion that the [*nido*-$P_2B_{10}H_{10}]^{2-}$ isomer formed kinetically by reduction, **A_P**, is in fact the thermodynamically most stable isomer. Isomerisations to the second and third most stable isomers, [7,10-*nido*-$P_2B_{10}H_{10}]^{2-}$ and [7,9-*nido*-

$P_2B_{10}H_{10}]^{2-}$, are then considered as these exhibit a 6-membered open face and are therefore thought to promote capitation (in parallel to the reduced diphenyl-*ortho*-carborane species investigated in Chapter 3).

5.7. Proposed capitation of A_P

Three closely related pathways to capitated species may be envisaged. Two alternative D-S-D processes, **A** or **B** would give [7,9-*nido*-$P_2B_{10}H_{10}]^{2-}$ or [7,10-*nido*-$P_2B_{10}H_{10}]^{2-}$ respectively. Capitation of the 6-membered face may then take place. These isomerisations $\mathbf{A_P}$ to 7,9- and [7,10-*nido*-$P_2B_{10}H_{10}]^{2-}$ were characterised with $\Delta E^{\ddagger}$ = 20.8 and 19.9 kcal mol^{-1} respectively (see Figure 5.23, above). The third alternative (**C**) would be where isomerisation to [2,3-*nido*-$P_2B_{10}H_{10}]^{2-}$ takes place with ΔE = +1.8 kcal mol^{-1} (no transition state was characterised in this case). The 5-membered face, rather than a 6-membered face, is then capitated. Which of these three proposed processes, if any, is the true mechanism could be determined by crystallographic characterisation of the capitated species, if this does prove experimentally possible.

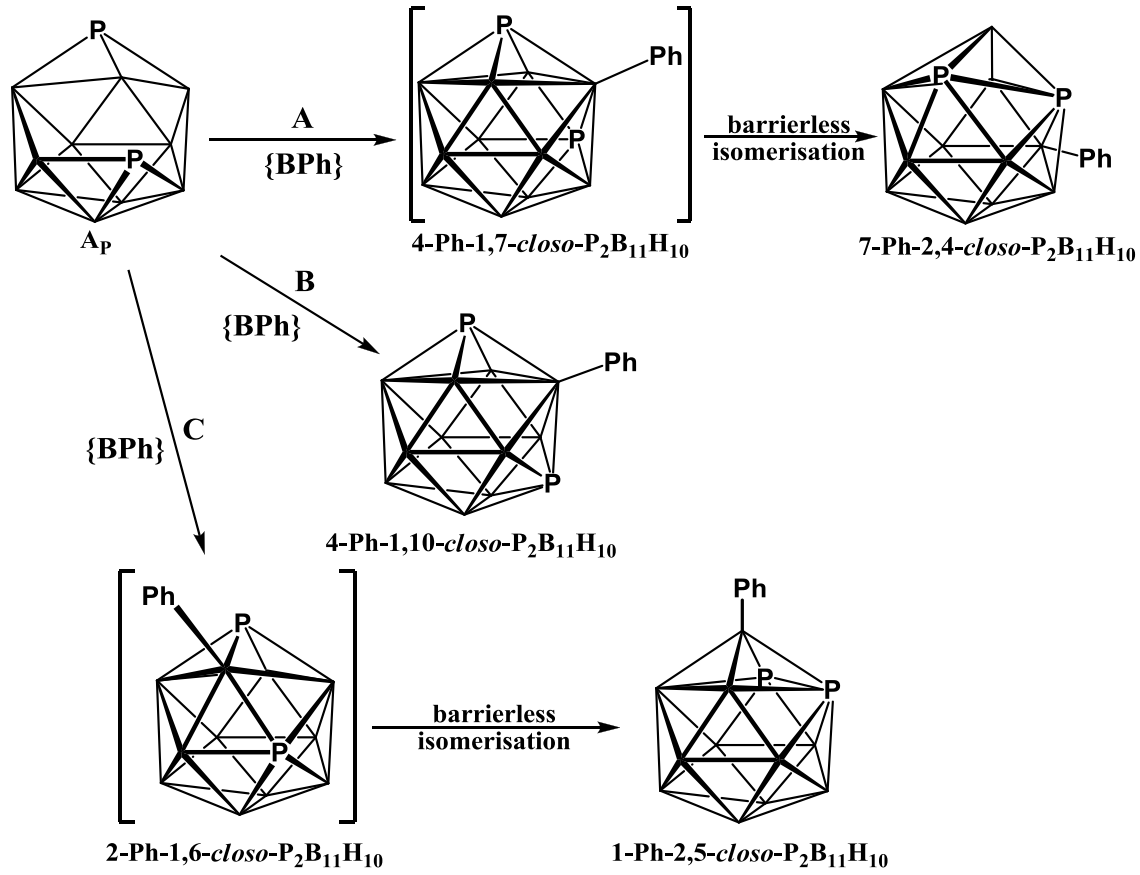

Figure 5.24 – Possible capitation processes of reduced *ortho*-phosphaborane. A – isomerisation to [7,9-$P_2B_{10}H_{10}]^{2-}$, followed by capitation and isomerisation to 7-Ph-2,4-$P_2B_{11}H_{10}$; B – Isomerisation to [7,10-$P_2B_{10}H_{10}]^{2-}$ and capitation to give 4-Ph-1,10-$P_2B_{11}H_{10}$; C – isomerisation to [2,3-*nido*-$P_2B_{10}H_{10}]^{2-}$, followed by capitation and isomerisation to give 1-Ph-2,5-$P_2B_{11}H_{10}$.

Processes A, B and C, shown in Figure 5.24, show capitation of [7,9-*nido*-$P_2B_{10}H_{10}]^{2-}$ with {BPh} to give 4-Ph-1,7(1,6)-*closo*-$P_2B_{11}H_{10}$, capitation of [7,10-*nido*-$P_2B_{10}H_{10}]^{2-}$ would give 4-Ph-1,10-*closo*-$P_2B_{11}H_{10}$ and direct capitation of [2,3-*nido*-$P_2B_{10}H_{10}]^{2-}$ would give 1-Ph-2,5-*closo*-$P_2B_{11}H_{10}$.

5.8. Conclusions and future work

A significant insight was gained in the trends of main group heteroborane stabilities in both 12- and 13-vertex cases. Differences in electronegativity and atomic radii between the heteroatom and boron were shown to contribute to these trends.

Predictions as to the potential isomeric product of reduction and capitation of *ortho*-phosphaborane with {BPh} were made and await experimental results to measure their significance.

5.9. References

1. a) D. M. Schubert, W. S. Rees, C. B. Knobler and M. F. Hawthorne, *Organometallics*, 1990, **9**, 2938-2944; b) H. S. Wong and W. N. Lipscomb, *Inorg. Chem.*, 1975, **14**, 1350-1357; c) L. I. Zakharkin, G. G. Zhigareva, K. A. Lysenko, M. Y. Antipin and P. V. Petrovskii, *Russ. J. Gen. Chem.*, 2001, **71**, 196-200; d) D. Joosten, I. Weissinger, M. Kirchmann, C. Maichle-Mössmer, F. M. Schappacher, R. Pöttgen and L. Wesemann, *Organometallics*, 2007, **26**, 5696-5701.
2. J. L. Little, M. A. Whitesell, R. W. Chapman, J. G. Kester, J. C. Huffman and L. J. Todd, *Inorg. Chem.*, 1993, **32**, 3369-3372.
3. R. W. Chapman, J. G. Kester, K. Folting, W. E. Streib and L. J. Todd, *Inorg. Chem.*, 1992, **31**, 979-983.
4. D. Seyferth, K. D. Buchner, W. S. Rees, L. Wesemann, W. M. Davis, S. S. Bukalov, L. A. Leites, H. Bock and B. Solouki, *J. Am. Chem. Soc.*, 1993, **115**, 3586-3594.
5. C. Nickl, D. Joosten, K. Eichele, C. Maichle-Mössmer, K. Törnroos and L. Wesemann, *Angew. Chem. Int. Ed.*, 2009, **48**, 7920-7923.
6. W. Keller, G. Sawitzki and W. Haubold, *Inorg. Chem.*, 2000, **39**, 1282-1287.
7. J. L. Little, S. S. Pao and K. K. Sugathan, *Inorg. Chem.*, 1974, **13**, 1752-1756.
8. J. L. Little, *Inorg. Chem.*, 1979, **18**, 1598-1600.
9. F. A. Kiani and M. Hofmann, *Dalton Trans.*, 2006, 686-692.
10. a) F. A. Kiani and M. Hofmann, *Inorg. Chem.*, 2005, **44**, 3746-3754; b) F. A. Kiani and M. Hofmann, *Inorg. Chem.*, 2004, **43**, 8561-8571; c) F. A. Kiani and M. Hofmann, *J. Mol. Model.*, 2006, **12**, 597-609.
11. M. Hofmann, M. A. Fox, R. Greatrex, P. v. R. Schleyer and R. E. Williams, *Inorg. Chem.*, 2001, **40**, 1790-1801.
12. F. A. Kiani and M. Hofmann, *Eur. J. Inorg. Chem.*, 2005, **2005**, 2545-2553.
13. A. L. Allred, *J. Inorg. Nucl. Chem.*, 1961, **17**, 215-221.
14. J. C. Slater, *J. Chem. Phys.*, 1964, **39**, 3199-3204.
15. R. McLellan and A. J. Welch, *unpublished results*.
16. R. E. Williams, *Inorg. Chem.*, 1971, **10**, 210-214.

Chapter 6 – Computational Chemistry of Bis(carboranes)

6.1. Introduction

The present study is concerned with the potential of bis(carboranes) in polyhedral expansion chemistry; the aim of experimental workers was to synthesise the first examples of bis(carboranes) and bis(metallacarboranes) with greater than 12 vertices per cage and the aim of computational work was rationalise experimental results.

Bis(carboranes) are a family of carborane compounds consisting of two carborane cages joined by a single C–C, B–B or C–B bond. These include 1,1′-bis(*ortho*-carborane),[1, 2] 1,1′-bis(*meta*-carborane)[2] and 1,1′-bis(*para*-carborane).[3, 4] Syntheses were originally carried out by Hawthorne, through reaction of diacetylene with two equivalents of decaborane, resulting in C–C connected 1,1′-bis(*ortho*-carborane).[1] Zakharkin later produced the 1,1′-bis(*para*-carborane) analogue, adopting $CuCl_2$ mediated coupling of monolithiated *para*-carboranes.[3] This method was further developed by Hawthorne and seen to also produce 1,1′-bis(*ortho*-carborane) and 1,1′-bis(*meta*-carborane), though with side products of oligomers and C–B-connected species. The contemporary method uses Ullmann-type chemistry,[5] adopting CuCl, and typically gives a 50% improvement in yields of 1,1′-bis(*ortho*-carborane).[6]

Previous work on the applications of bis(carboranes) saw their use as bidentate ligands in transition metal chemistry, for example, in the synthesis of $[M\{1,1'\text{-bis}(ortho\text{-carborane})\}_2]^{2-}$ (M = Co, Ni, Cu).[7] More applicable to this work are studies by Getman, Knobler and Hawthorne in which the reduction chemistry of 1,1′-bis(*ortho*-carborane) was reported,[8, 9] which will be discussed in the following section.

Calculations on bis(carboranes) were performed using methods previously described in this thesis, *via* the Gaussian 03 program; the BP86 functional was used along with 6-31G** basis sets for C, B and H and the SDD pseudo-potential and associated basis sets for Ru.

6.2. Reduction of bis(carboranes)

6.2.1. Computational 4e reduction of 1,1′-bis(*ortho*-carborane)

Details of the computational 4e reduction of 1,1′-bis(*ortho*-carborane) are given in Figure 6.1, below.

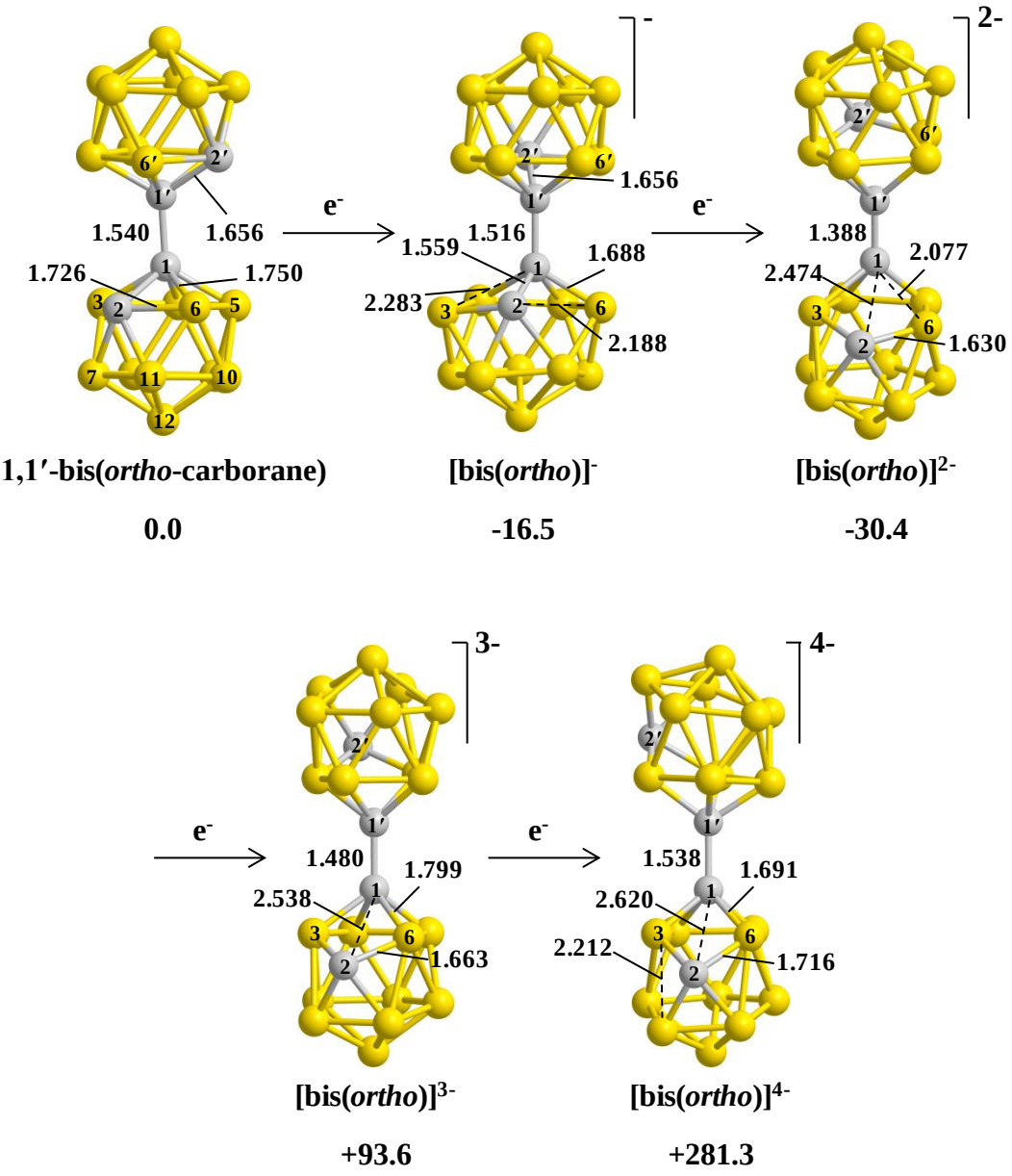

Figure 6.1 – Computational reduction of 1,1′-bis(*ortho*-carborane) to its tetraanion, with selected distances in Ångstroms and energies in kcal mol^{-1}. Hydrogen atoms omitted for clarity.

Addition of 1e to 1,1′-bis(*ortho*-carborane) results in formation of **[bis(*ortho*)]$^{-}$**, which exhibits a distortion of one *ortho*-carborane cage and a relative stabilisation (E = -16.5 kcal mol^{-1}). The lower cage (as shown in Figure 6.1, above) exhibits two 4-membered faces after 1e reduction, and the C1–C2 connection is shortened from 1.656 Å to 1.559 Å. The C1–C1′ distance has also become shorter, suggesting an increased bond order

between the cages. The upper cage shows no distortion, where the C1′–C2′ distance remains at 1.656 Å. Indeed, the geometry of the lower cage closely resembles that of singly reduced *ortho*-carborane, which exhibits two equivalent 4-membered faces and a C1–C2 distance of 1.559 Å (see Figure 6.2, below). This suggests the cages are reduced independently at this stage. Adding a second electron produces a further stabilisation in energy, to -30.4 kcal mol^{-1}, as well as a further distortion of the lower cage, which is now mirrored in the upper cage. The equivalent cages, **[bis(*ortho*)]$^{2-}$**, each exhibit a 5-membered face with long C1–C2 and C1–B6 connections of 2.474 Å and 2.077 Å respectively. This distortion is therefore now more closely related to that seen in reduced diphenyl-*ortho*-carborane, where the C1–C2 connection is lengthened to 2.388 Å (see Figure 6.2, below). A short C1–C1′ connection of 1.388 Å is seen in **[bis(*ortho*)]$^{2-}$**, suggesting increased multiple bond character. These features suggest communication between the cages, in strong agreement with experimental results, which will be discussed in Section 6.4.[9]

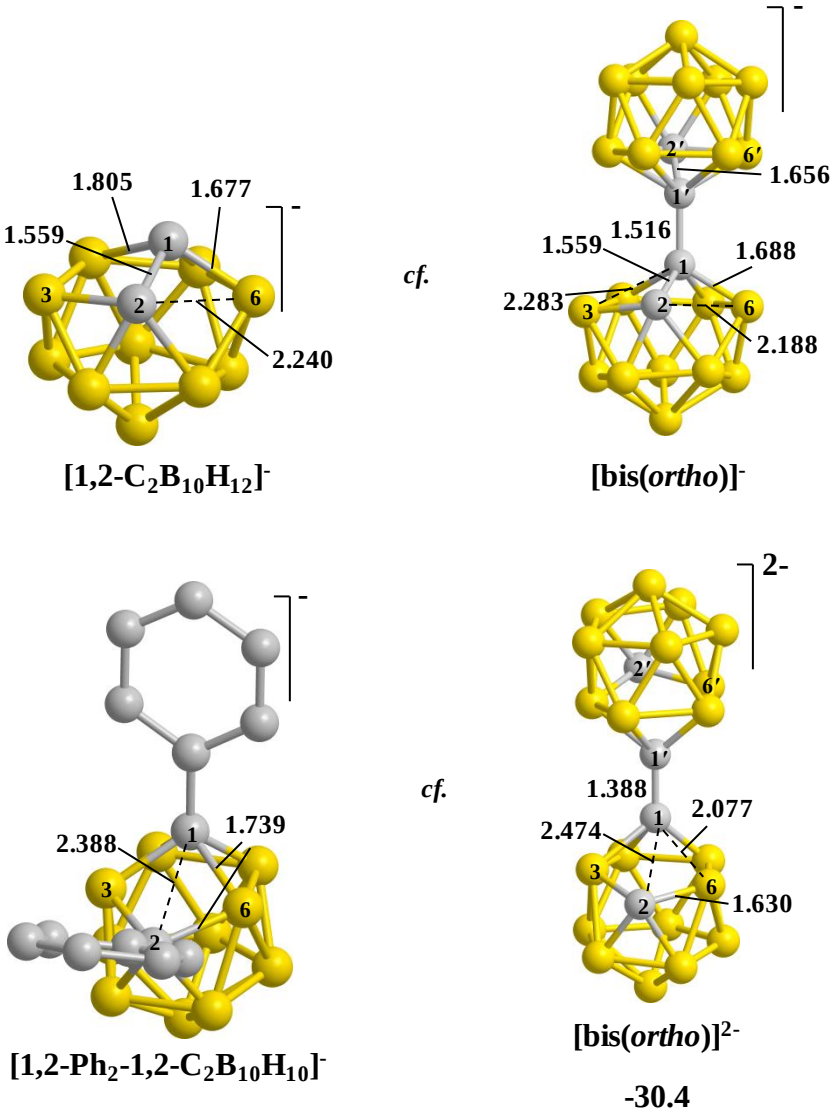

Figure 6.2 – Computed monoanions of *ortho*-carborane and diphenyl-*ortho*-carborane for comparison with the monoanion and dianion of 1,1′-bis(*ortho*-carborane) respectively, with selected distances given in Ångstroms. Hydrogen atoms omitted for clarity.

The addition of a third electron, to give **[bis(*ortho*)]$^{3-}$**, sees further lengthening of the C1–C2 connections from 2.474 Å to 2.538 Å but shortening of the C1–B6 connections from 2.077 Å to 1.799 Å. The C1–C1′ connection is now lengthened to 1.480 Å, where previously reduction had shortened the bond. This reduction also produces a large increase in energy to +93.6 kcal mol^{-1}. The final electron addition produces a 'bis(basket)' tetraanion, **[bis(*ortho*)]$^{4-}$**. The geometry exhibits two 4-membered faces per cage; C1-B6-C2-B3 and C2-B7-B8-B3. The C1–C1′ distance is further lengthened to 1.538 Å, close to that of the neutral geometry, 1.540 Å. The increased multiple bond character of the intermediate anions has therefore become reversed. This may suggest that the first two electrons added occupy an orbital with a C1–C1′ bonding component, whereas the next two electrons occupy the corresponding antibonding orbital. The

relative energy of **[bis(*ortho*)]$^{4-}$** reveals a destabilisation with addition of the fourth electron, at E = +281.3 kcal mol^{-1}. The energetic trend with reduction of 1,1′-bis(*ortho*-carborane) is that, with respect to the neutral species, the dianion is stabilised, at -30.4 kcal mol^{-1}, and the tetraanion is destabilised, at +281.3 kcal mol^{-1}. Similarly, in the reduction of diphenyl-*ortho*-carborane, with respect to the neutral species, the mono- and dianions are found at -38.0 and +2.5 kcal mol^{-1} respectively. This is therefore in agreement with the structural effects of reduction and is likely related to similar π-bonding between the cage carbon atoms and their substituent.

The first intermediate of 4e reduction, **[bis(*ortho*)]$^{4-}$**, is 17.6 kcal mol^{-1} above *rac*-[7,7′-bis(7,9-*nido*-$C_2B_{10}H_{11}$)]$^{4-}$, which was the global minimum implied experimentally by metallation (as a mixture of *racemic* and *meso* diastereoisomers, discussed in Section 6.2.2).[10] The isomerisation of **[bis(*ortho*)]$^{4-}$** to **[7,7′-bis(7,9-*nido*-$C_2B_{10}H_{11}$)]$^{4-}$** was found to be closely related to that in reduced diphenyl-*ortho*-carborane, from **A_{Ph}** to [7,9-*nido*-$C_2B_{10}H_{12}$]$^{2-}$, seen in Chapter 3.

6.2.2. Computational 4e reduction of 1,1′-bis(*meta*-carborane)

The reduction of 1,1′-bis(*meta*-carborane) was found to be directly analogous to that of *meta*-carborane, which gave [7,9-*nido*-$C_2B_{10}H_{12}$]$^{2-}$. Here each pair of electrons added gives a {7,9-*nido*-$C_2B_{10}H_{11}$} fragment in one cage while the other is a spectator (see Figure 6.3, below).

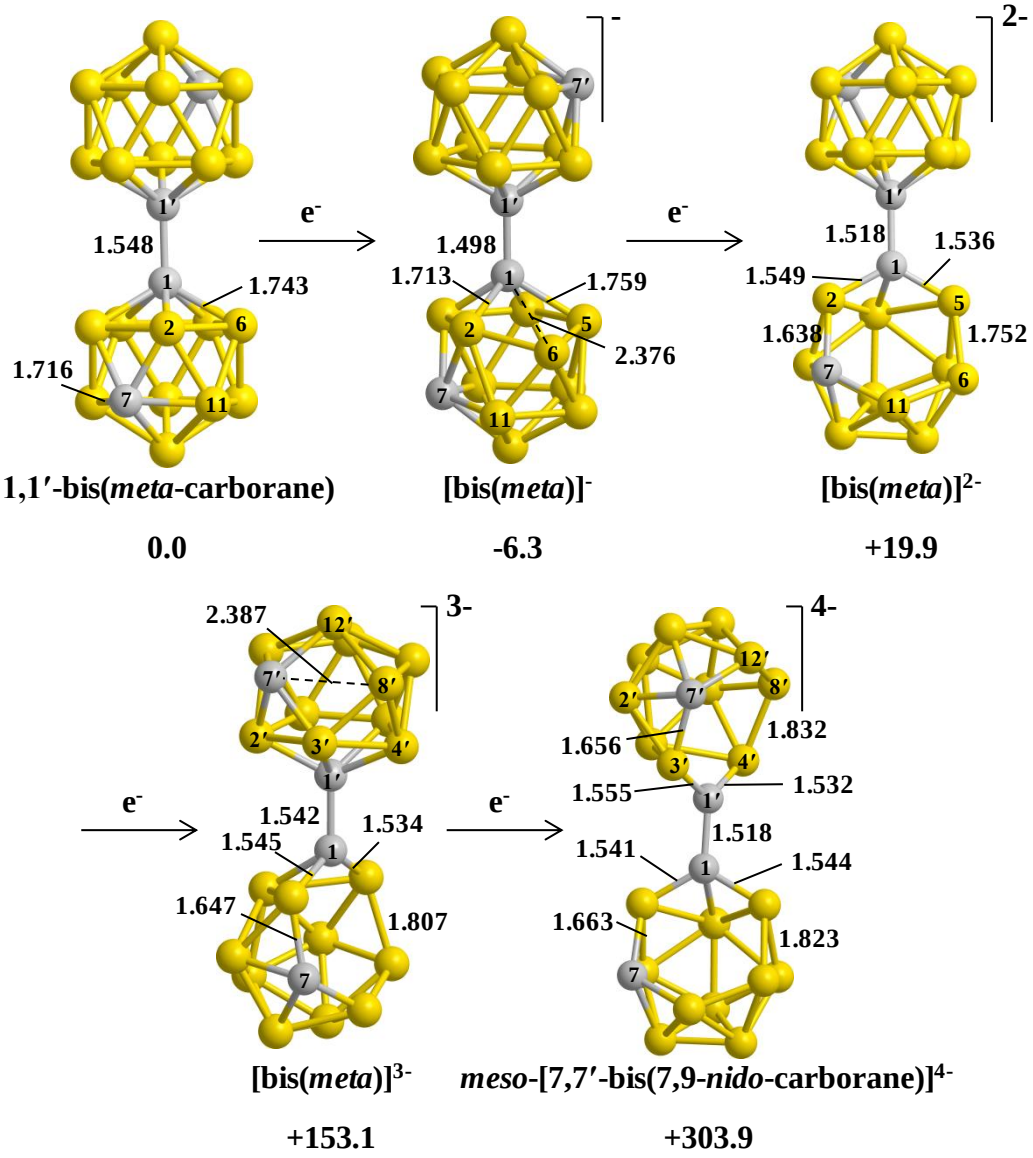

Figure 6.3 – Computational reduction of 1,1′-bis(*meta*-carborane) to its tetraanion, with selected distances in Ångstroms and energies in kcal mol^{-1}. Hydrogen atoms omitted for clarity.

The two cages of 1,1′-bis(*meta*-carborane) are seen to open to give *meso*-[7,7′-bis(7,9-*nido*-$C_2B_{10}H_{11}$)]$^{4-}$ directly in two 2e stages, however each stages exhibits a different (but related) mechanism.

The first 1e reduction produces a lengthening of the C1–B6 connection of the lower cage from 1.743 Å to 2.376 Å in **[bis(*meta*)]$^{-}$**, while there is no distortion in the upper cage. The second electron addition directly produces a {7,9-*nido*-$C_2B_{10}H_{11}$}$^{2-}$ fragment in the lower cage in **[bis(*meta*)]$^{2-}$**. Addition of a third electron, to give **[bis(*meta*)]$^{3-}$**, now causes distortion in the upper cage, with little further distortion of the lower *nido* fragment. The C7′–B8′ connection in **[bis(*meta*)]$^{3-}$** is lengthened to 2.387 Å from 1.709 Å in **[bis(*meta*)]$^{2-}$**, therefore differing from the monoanion in the connection lengthened (C7′–B8′ rather than C1–B6), but consistent with it in that the distortion is linked to a

carbon vertex. At this stage of the reduction, the way in which the cage opens determines which diastereoisomer of **[7,7′-bis(7,9-*nido*-$C_2B_{10}H_{11}$)]$^{4-}$** is formed. From these calculations, the *meso* form is found on the addition of the forth electron. However, the *rac* form (in which both cages are equivalent by C_2 symmetry) is just 0.2 kcal mol^{-1} less stable and the barrier to its formation may also be comparable.

The C1–C1′ bond length is not related to the negative charge in the reduction of 1,1′-bis(*meta*-carborane). The largest change is seen in the formation of the monoanion, where it is shortened from 1.548 Å to 1.498 Å. This contrasts with features exhibited by 1,1′-bis(*ortho*-carborane) and, along with the observation that the cages reduce separately, suggests that there is little electronic communication between the cages of 1,1′-bis(*meta*-carborane). The energy changes with reduction are generally destabilising, where in contrast to **[bis(*ortho*)]$^{2-}$**, the dianion is less stable than the neutral species, at +19.9 kcal mol^{-1}. This appears, however, to be a reflection on the relative stability of 1,1′-bis(*meta*-carborane), which is 29.7 kcal mol^{-1} more than 1,1′-bis(*ortho*-carborane).

6.2.3. Computational 4e reduction of 1,1′-bis(*para*-carborane)

The computational 4e reduction of 1,1′-bis(*para*-carborane) is given in Figure 6.4, below.

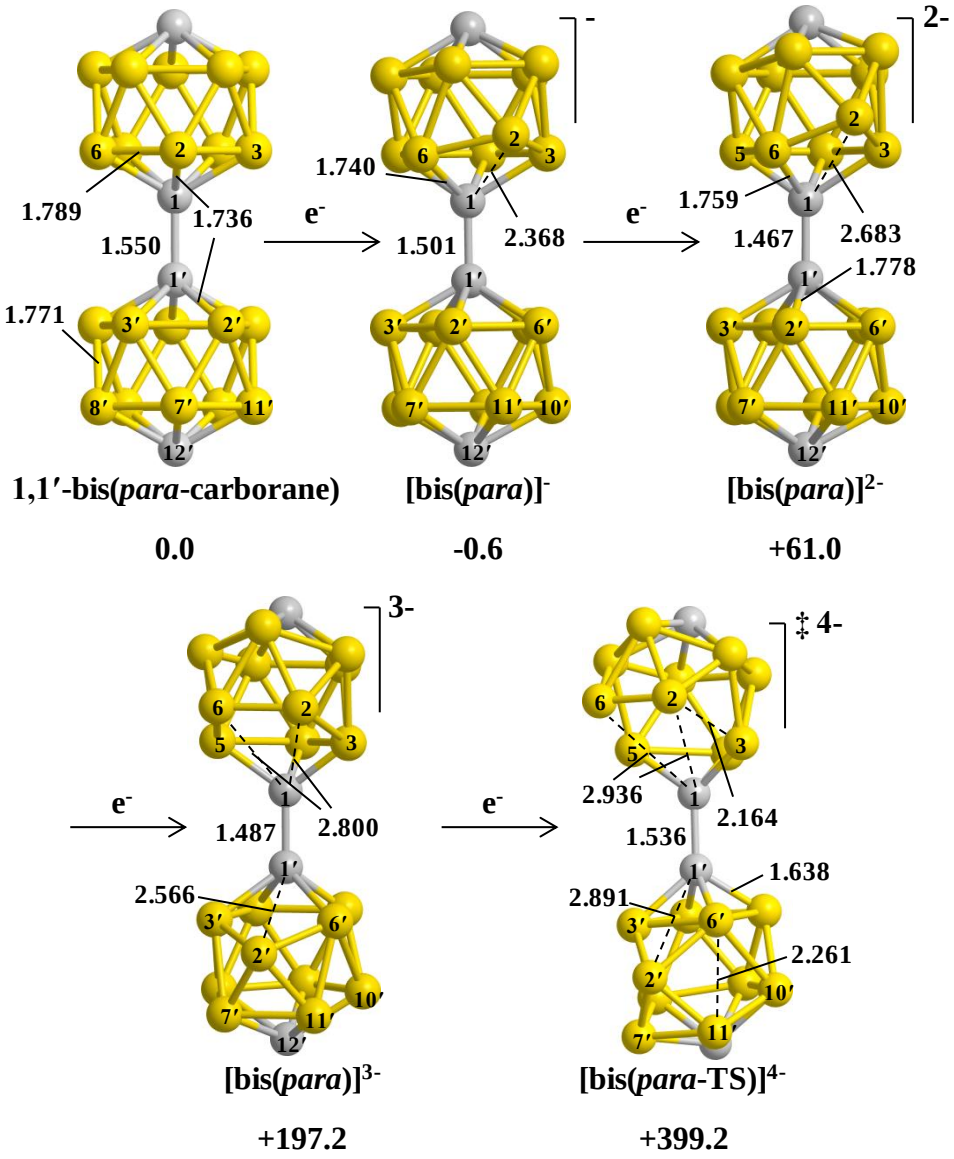

Figure 6.4 – Computational reduction of 1,1′-bis(*para*-carborane) to its tetraanion. Selected distances are given in Ångstroms and energies in kcal mol^{-1}. Hydrogen atoms are omitted for clarity.

The first 1e reduction of 1,1′-bis(*para*-carborane), giving **[bis(*para*)]$^{-}$**, causes a lengthening of the C1–B2 connection in the upper cage (as shown) from 1.736 Å to 2.368 Å and the C1–C1′ bond is shortened from 1.550 to 1.501 Å, while there is only a nominal change in the relative energy. In **[bis(*para*)]$^{2-}$**, the C1–B2 connection is lengthened further to 2.683 Å as the C1–C1′ bond is shortened to 1.467 Å. The third electron addition causes distortions of both cages in **[bis(*para*)]$^{3-}$**. In the upper cage, the C1–B2 connection is further lengthened to 2.800 Å and the C1–B6 connection also lengthens from 1.759 Å in **[bis(*para*)]$^{2-}$** to become equivalent to C1–B2 in **[bis(*para*)]$^{3-}$**. In the lower cage, the C1′–B2′ connection is lengthened from 1.778 Å, in the dianion, to 2.566 Å. The C1–C1′ bond is now lengthened to 1.487 Å.

In **[bis(*para*)]$^{4-}$**, the C1–C1′ distance is increased to 1.536 Å, the C1–B2 and C1–B6 connections are increased to 2.936 Å and the C1′–B2′ distance is increased to 2.891 Å. The B2–B3 and B5–B6 connections in the upper cage are now also significantly lengthened from 1.789 in the neutral geometry to 2.164 Å and the B6′–B11′ and B3′–B7′ connections are lengthened from 1.771 Å in the neutral geometry to 2.261 Å in the tetraanion. The tetraanion, **[bis(*para*-TS)]$^{4-}$**, was computed as a transition state, hence its isomerisation was characterised (see Figure 6.5, below).

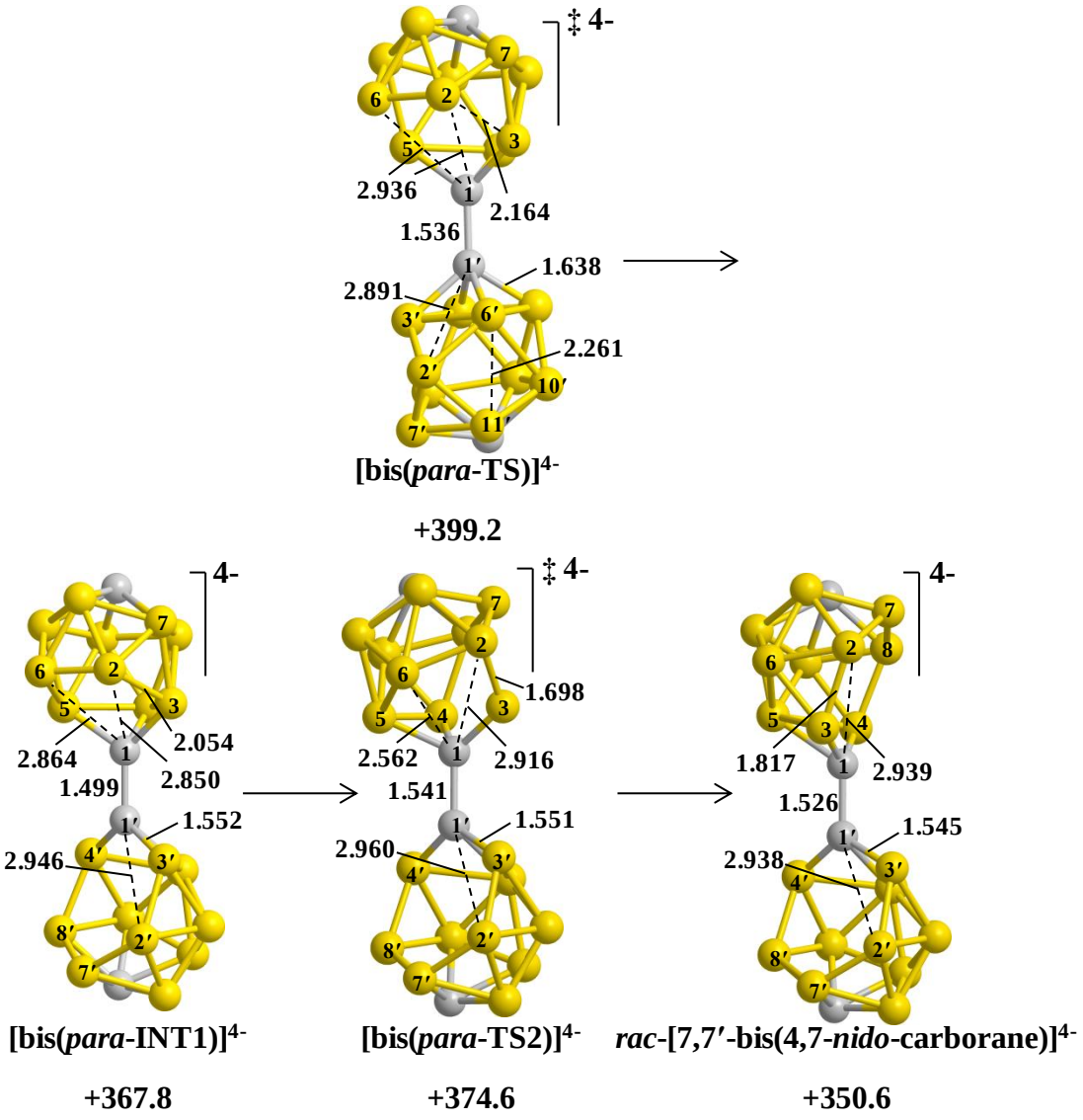

Figure 6.5 – Initial isomerisation of [bis(*para*-TS)]$^{4-}$ to a bis(*nido*) geometry. Selected distances are given in Ångstroms and energies in kcal mol^{-1}. Hydrogen atoms are omitted for clarity.

Subjecting **[bis(*para*-TS)]$^{4-}$** to IRC calculations saw rearrangement of the lower cage to a {4,7-*nido*-$C_2B_{10}H_{11}$} fragment in **[bis(*para*-INT1)]$^{4-}$**. A scan lengthening the C1–B2 connection of the upper cage (in order to break the local C_s symmetry) then led to **[bis(*para*-TS2)]$^{4-}$** and subsequently to *rac*-[7,7′-bis(4,7-*nido*-carborane)]$^{4-}$, 51.0 kcal

mol^{-1} above *rac*-[7,7′-bis(7,9-*nido*-carborane)]$^{4-}$. As seen in the reduction of 1,1′-bis(*meta*-carborane), the way in which the symmetry is broken determines which diastereoisomer is formed. In this case, however, the symmetry was broken manually, rather than by the addition of an electron, suggesting either diastereoisomer would be formed through the same energy barrier.

The reduction of 1,1′-bis(*para*-carborane) is therefore analogous to the 2e reduction of *para*-carborane, in that the kinetic product of reduction is a high energy species, [4,7-*nido*-$C_2B_{10}H_{12}$]$^{2-}$ (see Chapter 2, Section 2.2). It is therefore reasonable to speculate that multiple products may be seen in polyhedral expansion experiments carried out on this compound, as with its single cage analogue where five isomers of $L_nMC_2B_{10}H_{12}$ are found on capitation of reduced *para*-carborane with $\{ML_n\}^{2+}$ and that each of these would be formed as a mixture of *racemic* and *meso* diasteroisomers.

It is interesting to note that the doubly reduced bis(carboranes) are relatively stable in comparison with the carborane dianions, in terms of the relative energy change computed on the addition of 2e. For example, **[bis(*ortho*)]$^{2-}$** was found at -30.4 kcal mol^{-1} with respect to 1,1′-bis(*ortho*-carborane), whereas the 2e reduction of *ortho*-carborane coincided with an energy change of +57.3 kcal mol^{-1} (see Chapter 2, Section 2.2.9) and the 2e reduction of diphenyl-*ortho*-carborane resulted in an energy change of +1.5 kcal mol^{-1} (see Chapter 3, Section 3.2.1). This may have implications in experimental work as it could possibly allow the selective polyhedral expansion of a single cage within a bis(carborane).

6.2.4. Comparison of the LUMOs of bis(carborane) and [bis(carborane)]$^{2-}$ species

An interesting issue in the 4e reductions of bis(carboranes) is the apparent communication between the cages during reduction, especially in the case of 1,1′-bis(*ortho*-carborane). To investigate this, the LUMOs of the neutral and dianionic bis(carborane) species were computed (see Figure 6.6, below).

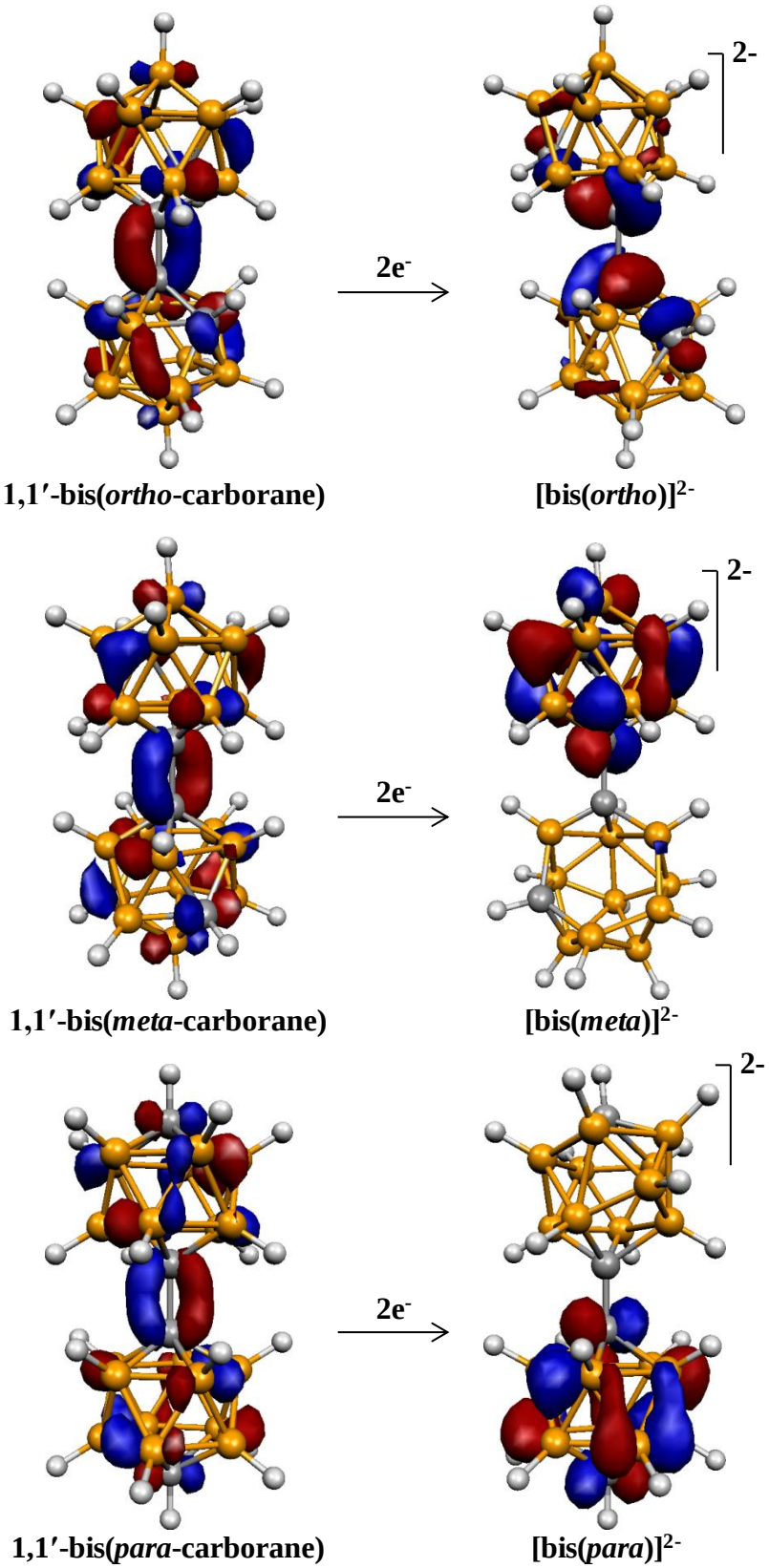

Figure 6.6 – LUMOs of 1,1′-bis(*ortho*-carborane), 1,1′-bis(*meta*-carborane) and 1,1′-bis(*para*-carborane) and their corresponding dianions.

The most significant observation is that the LUMOs of the neutral bis(carboranes) exhibit C1–C1′ π-bonding character for all three isomers. This is consistent with this bond being shortened upon addition of the first electron. From the dianionic species,

the distortion with reduction can also be rationalised through the LUMO. In **[bis(*ortho*)]$^{2-}$** the LUMO exhibits antibonding character across the C1–C1′ bond, consistent with the large increase in the bond length, from 1.388 to 1.480 Å upon further reduction. There is therefore a clear communication between the cages in 1,1′-bis(*ortho*-carborane) and its reduced forms. **[bis(*meta*)]$^{2-}$** and **[bis(*para*)]$^{2-}$** exhibit LUMOs based solely on the undistorted cage, and are therefore non-bonding between the cages, consistent with these species exhibiting a small change in their C1–C1′ bond length with reduction, increasing by only 0.024 and 0.020 Å respectively. Communication between cages is therefore more limited in these species.

6.3. Computational 4e oxidation of [7,7′-bis(7,9-*nido*-$C_2B_{10}H_{12}$)]$^{4-}$

In the study of carborane REDOX chemistry, described in Chapter 2, the oxidation of [7,9-*nido*-$C_2B_{10}H_{12}$]$^{2-}$ was considered as the oxidation of reduced intermediates is a common cause of failure to afford products in polyhedral expansion experiments. It is also well known that there is a REDOX relationship between *ortho*-carborane, *meta*-carborane and [7,9-*nido*-$C_2B_{10}H_{12}$]$^{2-}$ (see Figure 6.7, below).[11]

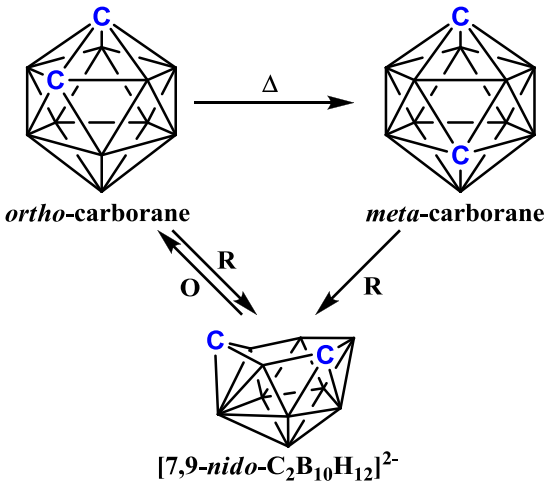

Figure 6.7 – Thermal and REDOX processes relating *ortho*-carborane, *meta*-carborane and [7,9-*nido*-$C_2B_{10}H_{12}$]$^{2-}$.

We were, therefore, in a position to determine, computationally, whether the same relationship exists for the bis(carborane) analogues. Figure 6.8, shows the computational 4e oxidation of [7,7′-bis(7,9-*nido*-$C_2B_{10}H_{12}$)]$^{4-}$.

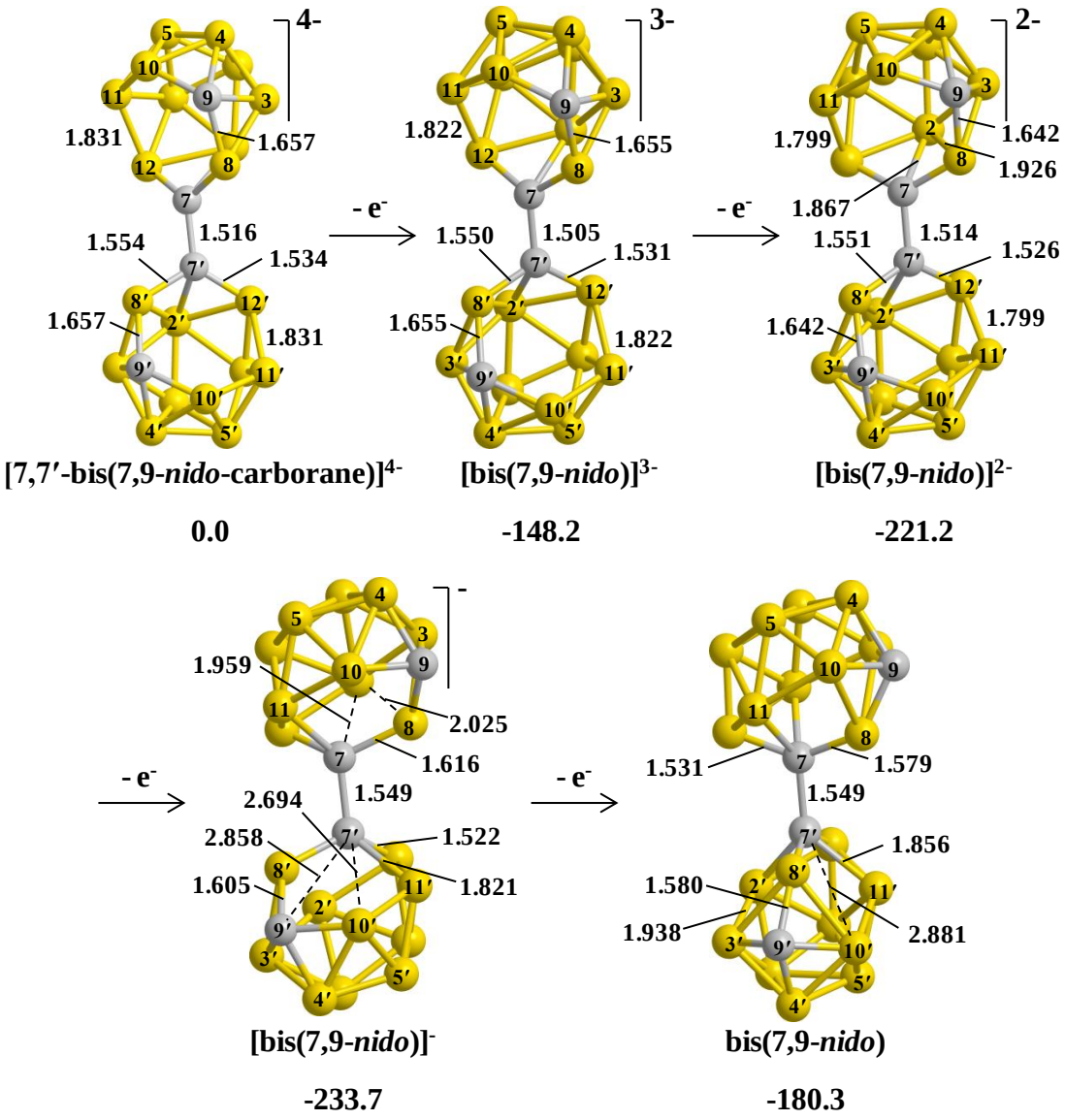

Figure 6.8 – Computational oxidation of 7,7′-bis(7,9-*nido*-carborane). Selected distances are given in Ångstroms and energies in kcal mol^{-1}. Hydrogen atoms omitted for clarity.

Removal of the first two electrons from **[7,7′-bis(7,9-*nido*-$C_2B_{10}H_{12}$)]$^{4-}$** to give the dianion, **[bis(7,9-*nido*)]$^{2-}$**, causes very little distortion of the cages. C_2 symmetry is retained, suggesting communication between the cages, since electron density is necessarily removed from both cages equally. On the third oxidation, to the monoanion, significant distortion is seen. The C7 and B8 vertices move into the 6-membered open face of the cages (which remain equivalent by C_2 symmetry) by elongation of the C7–B2 and B8–B2 connections from 1.867 to 1.959 Å and from 1.926 to 2.025 Å (shown in the upper cages in Figure 6.8). This produces two inequivalent 5-membered faces in each cage. Oxidation to the neutral species produces a bis(basket) geometry, where each cage fragment is C_s (the whole molecule retaining C_2 symmetry) and directly equivalent to the first intermediate of the 2e oxidation of [7,9-*nido*-

$C_2B_{10}H_{12}]^{2-}$, **7,9-ox-INT1** (see Figure 6.9 and Chapter 2, Section 2.2.11). The distances shown are, in general, longer in **7,9-ox-INT1** than in **bis(7,9-*nido*)**, which may perhaps be attributed to the communication between the bis(carborane) cages allowing a slightly more open structure.

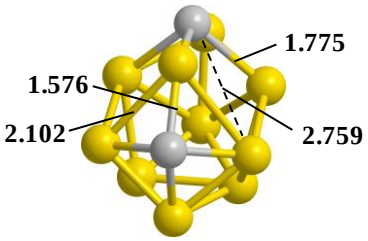

7,9-ox-INT1

Figure 6.9 – The product of 2e oxidation of [7,9-*nido*-$C_2B_{10}H_{12}]^{2-}$ for comparison with bis(7,9-*nido*). Hydrogen atoms omitted for clarity.

The changes in relative energy with oxidation of [7,7′-bis(7,9-*nido*-$C_2B_{10}H_{12}$)]$^{4-}$ complement those seen in the bis(carborane) reductions. Here there is a large stabilisation going from the tetraanion to the dianion, followed by a relatively small destabilisation going from the dianion to the neutral species.

6.4. Comparison of computational bis(carborane) results with experimental structures

Experimental geometries have been resolved crystallographically for **1,1′-bis(*ortho*-carborane)**,[6] **[bis(*ortho*)]$^{2-}$**[9] and the doubly protonated tetraanion, **[1,1′-(H)$_2$-1,1′-bis(*ortho*-carborane)]$^{2-}$**.[8] A comparison of the experimentally derived structures and computed geometries is given in Figure 6.10, below.

In general the computed geometries reproduce the experimentally derived structures well. The structures of the protonated species, **[bis(*ortho*)(H)$_2$]$^{2-}$** and **BPh-H$^+$** (discussed in Chapter 3) reveals a further link between these species. The same topology being found in the protonated *nido* structures suggests a common global minimum, in agreement with their computational reductions.

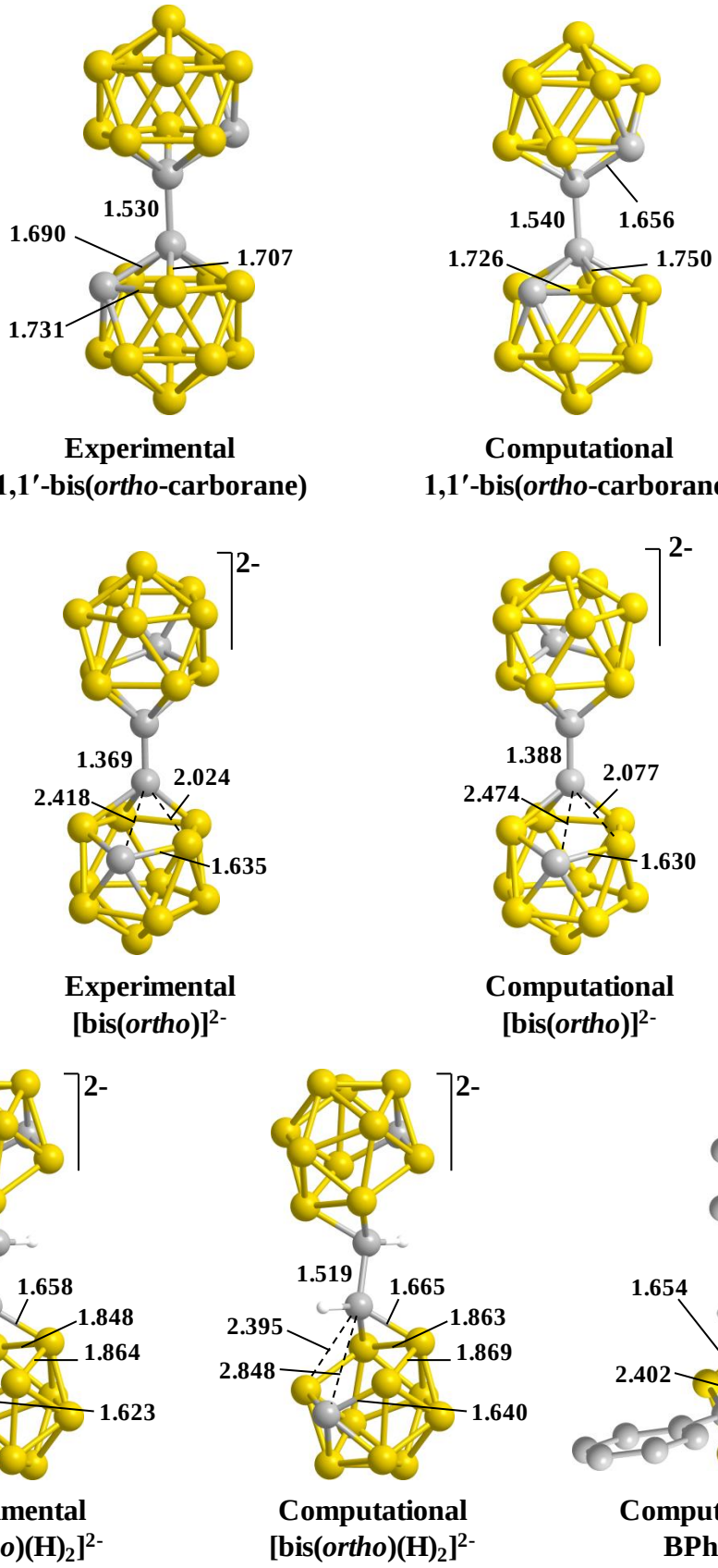

Figure 6.10 – Comparison between computational and experimental structures of 1,1′-bis(*ortho*-carborane), its dianion and its doubly protonated tetraanion [bis(*ortho*)$(H)_2]^{2-}$ and the singly protonated dianion of diphenyl-*ortho*-carborane, BPh-H^+. Distances are given in Ångstroms. Cage hydrogen atoms omitted for clarity.

6.5. Polyhedral expansion of 1,1′-bis(*ortho*-carborane)

The experimental workers involved in this study found unexpected, novel chemistry when attempting polyhedral expansion of 1,1′-bis(*ortho*-carborane) to produce a supraicosahedral ruthenacarborane. It was discovered that reaction of exhaustively reduced 1,1′-bis(*ortho*-carborane) with two equivalents of the $\{Ru(p\text{-cymene})\}^{2+}$ fragment at room temperature produced 1-(1′,2′-*closo*-$C_2B_{10}H_{11}$)-4-{($C_{10}H_{14}$)Ru(*p*-cymene)}-4,1,6-*closo*-$RuC_2B_{10}H_{11}$ (**1**), the structure of which was determined crystallographically and is shown in Figure 6.11, below.[12]

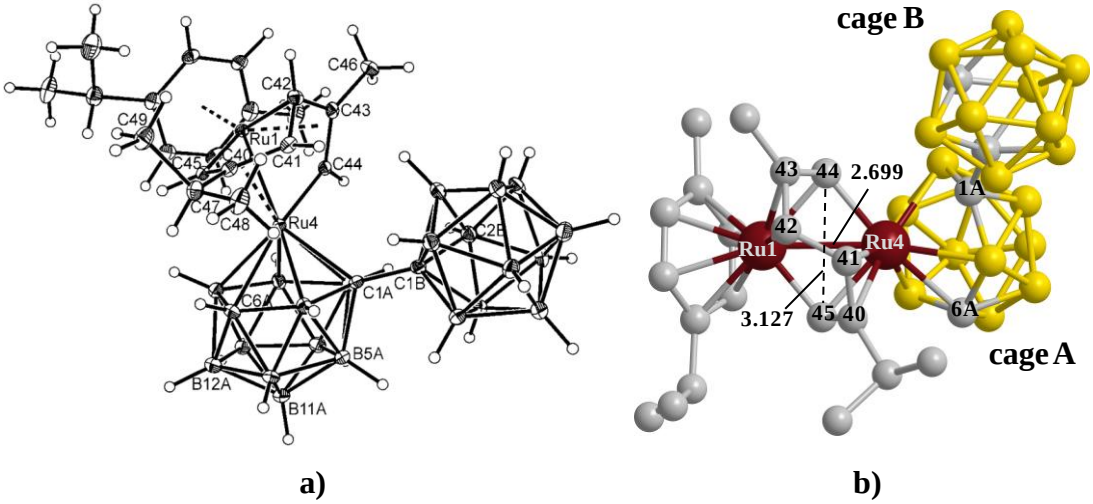

Figure 6.11 – a) View of 1 with thermal ellipsoids drawn at 50% probability and b) alternative 3D view of 1 highlighting the transition metal core (hydrogen atoms omitted for clarity).

1 exhibits a 12-vertex carborane cage (cage B), a 13-vertex ruthenacarborane cage (cage A), a second $\{Ru(p\text{-cymene})\}^{2+}$ fragment and a central $\{C_{10}H_{14}\}^{2-}$ fragment bound to both Ru1 and Ru4 (*cis* to the carbon vertices of cage A). This has resulted from cleavage of a C–C bond in one *p*-cymene unit. **1** is an example of a fly-over complex,[13] which is a bimetallic system containing a $\{\mu\text{-}\sigma,\eta^3\text{:}\eta^3,\sigma\text{-}C_6\}^{2-}$ fly-over bridging ligand (highlighted in Figure 6.11 b, above) and therefore reductive cleavage of the arene has occurred. The C44–C45 bond has been cleaved to give σ-bonds from C44 to Ru4 and from C45 to Ru1 of 2.042 and 2.061 Å respectively, where are complemented by allylic η^3 binding of C44-C43-C42 to Ru1 and of C41-C40-C45 to Ru4. A Ru1–Ru4 distance of 2.699 Å is consistent with a bonding interaction, which is formulated as a dative Ru1→Ru4 bond. In this formulation, Ru1 has 18 electrons including the d^8 metal centre, 6e from *p*-cymene and 4e from the bridging ligand and Ru4 has 16 electrons, where cage A and the bridging ligand are both 4e donors. A dative bond therefore satisfies the 18 electron rule in both metal centres.

The cleavage of aromatic C–C bonds is notoriously difficult. Existing chemistry for achieving this includes gas phase processes conducted at high temperatures,[14] biochemical processes,[15] and oxidative[16] or reductive[17] cleavage reactions, the last two of which require significant modification of the aromatic precursors. Furthermore, this study represents the first formation of a fly-over bridge complex from an arene, where they have previously been formed through the condensation of substituted alkynes, and as such proposed as intermediates in the cyclotrimerisation of alkynes to arenes. It is also unusual in that fly-over bridge complexes normally exhibit the largest bridge carbon substituents on the terminal carbon atoms. The above result was therefore rather unexpected and so the mechanism of formation of **1** was sought, through computational techniques.

6.5.1. Mechanism of formation of 1

The formation of **1** is described below, where Figure 6.12 shows formation of the precursor to C–C cleavage.

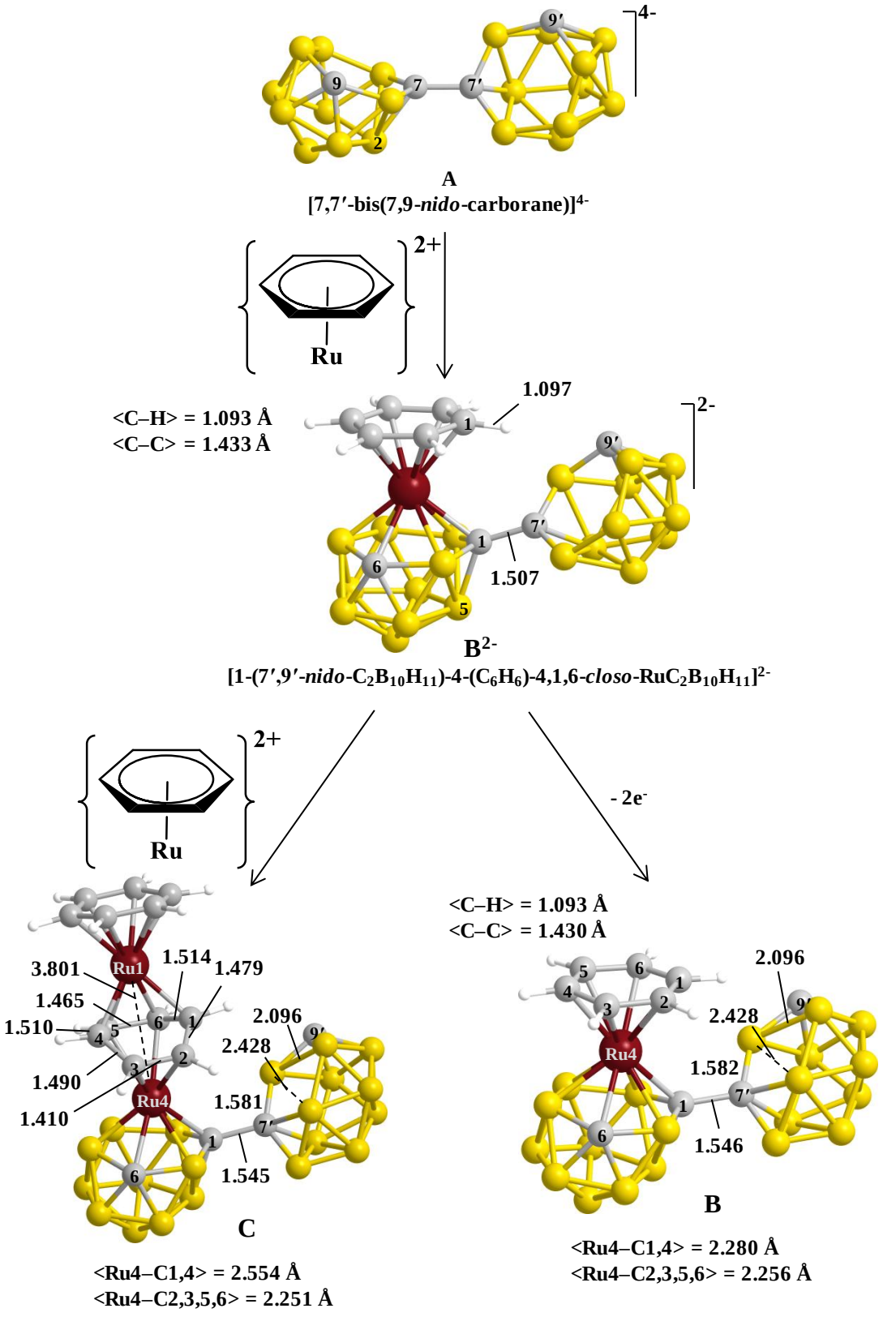

Figure 6.12 – Construction of the model reactant, C *via* [7,7′-bis(7,9-*nido*-carborane)]$^{4-}$ (A) and singly metallated B^{2-}. B is provided for comparison of the carborane cage with the in C.

In order to find the mechanism of C–C bond cleavage to form **1**, the model reactant was first constructed by combining [7,7′-bis(7,9-*nido*-carborane)]$^{4-}$ (**A**) and two {Ru(benzene)}$^{2+}$ fragments. **A** was modelled as the reactant as this was suggested by

experiment, where the structure of **1** implies **A** as the reduced species. **1** does not distinguish between diastereoisomers of **A** however, for simplicity, only the *rac* form is considered here. {Ru(*p*-cymene)}$^{2+}$ was replaced with {Ru(benzene)}$^{2+}$ for computational expediency. The model reactant was constructed in a stepwise fashion in order to understand why only one of the carborane cages is expanded. On adding the first ruthenium fragment and optimising, the dianionic species, [1-(7′,9′-*nido*-$C_2B_{10}H_{11}$)-4-(C_6H_6)-4,1,6-*closo*-$RuC_2B_{10}H_{11}$]$^{2-}$ (**B**$^{2-}$) was formed. **B**$^{2-}$ exhibits a 13-vertex metallacarborane cage and a 12-vertex *nido* carborane cage. There is evidence in **B**$^{2-}$ for an interaction between the carborane cage and the benzene ligand in an elongation of the benzene C1–H bond to 1.097 Å, which is lengthened with respect to the other benzene C–H bonds, possibly arising from donation from the *nido* carborane into the σ(C1–H)* antibonding orbital.

The addition of a second {Ru(*p*-cymene)}$^{2+}$ fragment to the model, followed by optimisation, directly gave **C**. The newly added ruthenium fragment is coordinated by the existing benzene ligand, forming a triple-decker compound. The alternative coordinating site, the pendant {*nido*-$C_2B_{10}H_{11}$}$^{2-}$ fragment, is blocked by the bulky 13-vertex ruthenacarborane and so the doubly expanded 1,1′-bis(4-(benzene)-4,1,6-*closo*-$RuC_2B_{10}H_{11}$) could not be optimised. Addition of the second {Ru(benzene)}$^{2+}$ fragment would therefore initially result in a zwitterionic system, where Ru1 is dicationic and the 12-vertex pendant carborane is dianionic. However, **C** exhibits two distinguishing geometrical features that contradict this. Firstly, the geometry exhibited by the pendant 12-vertex carborane cage, cage B, is topologically identical to that computed in the oxidations of [7,9-*nido*-$C_2B_{10}H_{12}$]$^{2-}$ and of **A**. Secondly, the central benzene ring of the triple-decker fragment is distorted.

The apparent oxidation of cage B was assessed by conducting a computational 2e oxidation of **B**$^{2-}$, giving **B**. The same distortion of the carborane cage is seen, verifying that 2e have been removed from the pendant carborane cage. Also apparent is the shortening of the benzene C1–H bond, which is directed towards cage B, from 1.097 Å in **B**$^{2-}$ to 1.093 Å in **B**, which is consistent with a loss of electron donation into the σ(C1–H)* orbital.

Distortion of the central benzene ring was assessed through the C–C bond lengths in the C_6 unit (see Figure 6.13, below). This is η^4-bound to Ru1 through C4-C5-C6-C1 and η^2:η^2-bound to Ru4 through the C5–C6 and C2–C3 bonds. The ring exhibits two shorter C–C bonds and four longer C–C bonds. The C5–C6 bond is longer than C2–C3

at 1.465 and 1.410 Å respectively, which is consistent with C5–C6 being coordinated to both ruthenium atoms. The C1–C2, C3–C4, C4–C5 and C6–C1 bonds are longer than C5–C6 and C2–C3. Of the former four, the C1–C2 and C3–C4 bonds are the shorter, consistent with neither being coordinated to a metal centre.

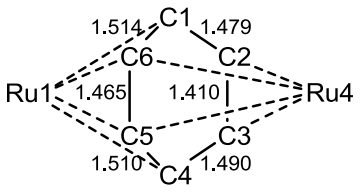

Figure 6.13 – C–C bond lengths (Å) of the central C_6 ring in C.

To assess whether the benzene ring was reduced coincidentally with the pendant carborane oxidation, the LUMOs of benzene were computed. The first and second LUMOs of benzene are a degenerate pair of e_{1g} symmetry, shown in Figure 6.14, below, labelled **a** and **b** to aid discussion. Due to the C_1 symmetry of **C**, however, these orbitals would lose their degeneracy. If the benzene ring is considered to be reduced, the above bond groupings would be consistent with occupation of **a**. It is therefore thought that 2 electrons have been transferred from cage B to the LUMO of the central benzene ring.

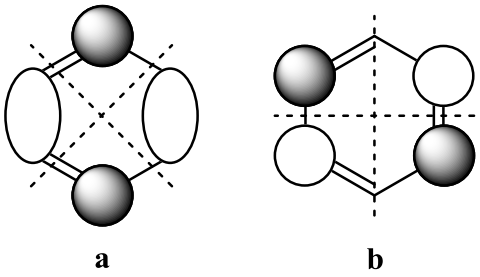

Figure 6.14 – Degenerate (e_{1g}) LUMOs of benzene.

The driving force behind this process is thought to be the association of opposing charges, whereby the dicationic Ru1 centre is distant from the dianionic cage B prior to electron transfer. The internal REDOX process therefore results in a large electrostatic stabilisation.

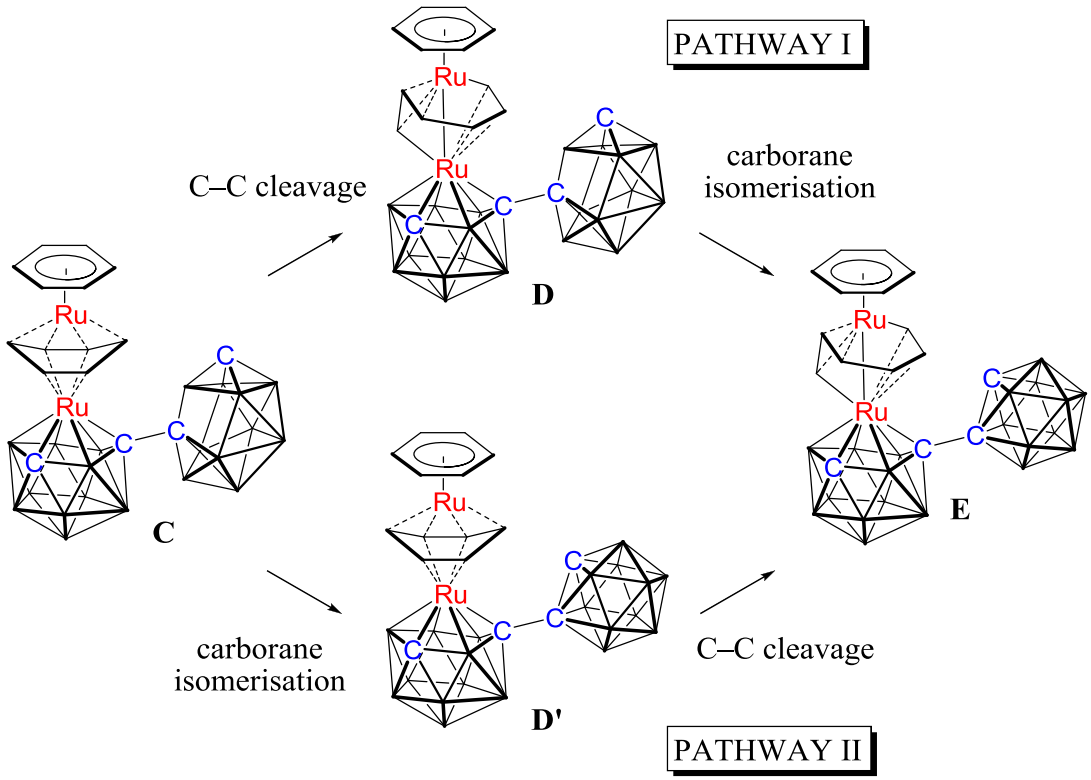

Figure 6.15 – Pathways for formation of E from C, where the two steps of the process can come in either order.

The reaction mechanism from **C** to **E** (the computational model of **1**) requires two main processes to occur; the C–C bond cleavage of the reduced benzene and the isomerisation of the basket 12-vertex carborane, cage B, to *ortho*-carborane. The latter is known from previous work to be a single step process (see Chapter 2, Section 2.5.1).[18] Figure 6.15, above shows two alternative pathways which differ in the order of these key steps. Four of the C–C bonds are elongated in **C**, however, only the longest, C6–C1, is considered as its cleavage would lead to the experimental product, where the resulting bridging ligand is *cis* with respect to the carbon vertices of cage A. The pathways characterised are described in Figure 6.16, below.

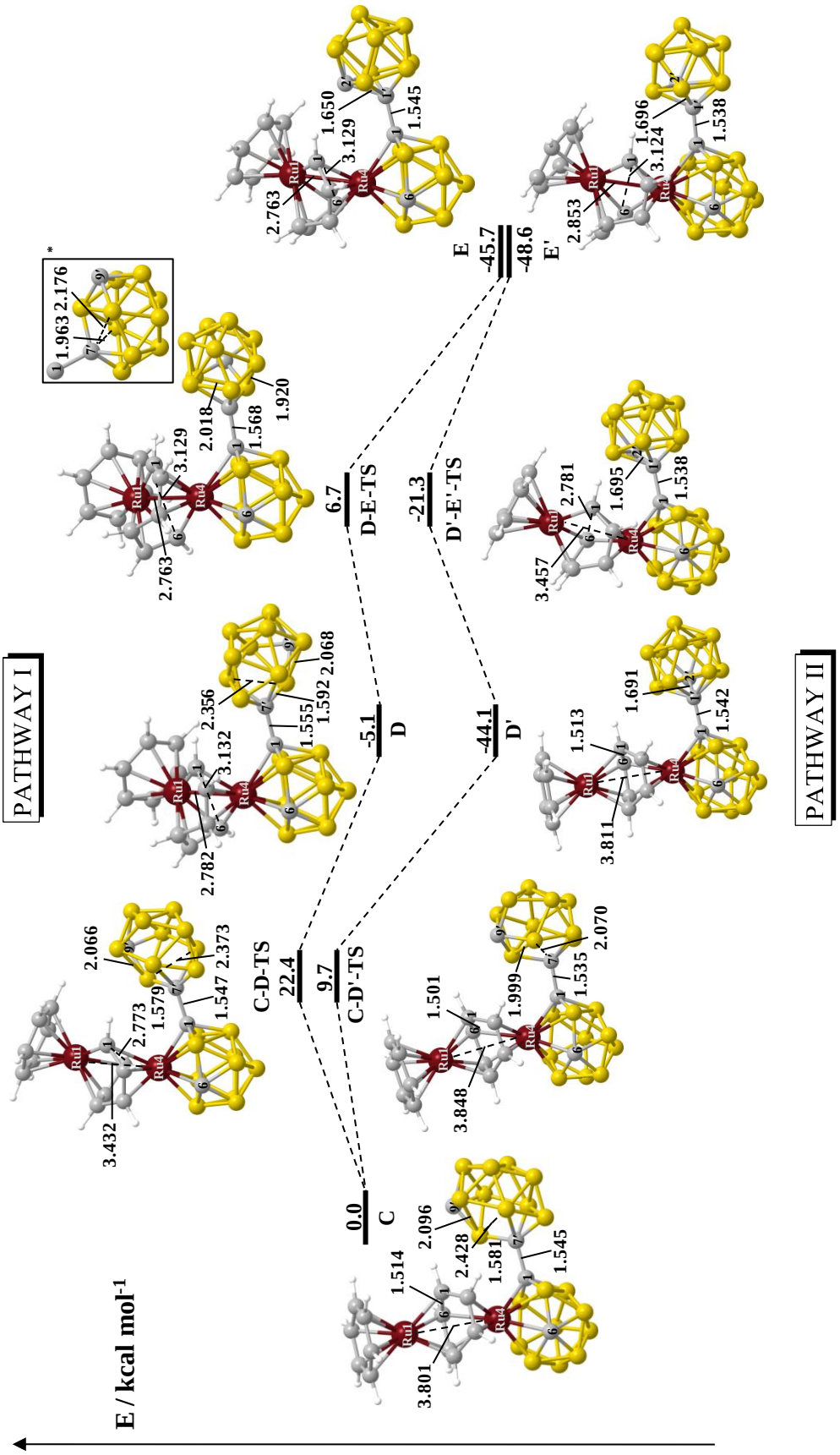

Figure 6.16 – Computed pathways to E, with geometries given for pathway I. Cage hydrogen atoms omitted for clarity. *Highlighted geometry of cage B in D-E-TS.

To locate the C–C cleavage step in pathway I, the C1–C6 distance in **C** was increased. **C-D-TS** was found at +22.4 kcal mol^{-1}, where the C1–C6 distance had lengthened from 1.514 to 2.773 Å. **C-D-TS** exhibits a shortened Ru1···Ru4 distance of 3.432 Å. Characterisation of this transition state gave **D** at -5.1 kcal mol^{-1}, in which the C1···C6 bond is fully broken (3.132 Å) and the Ru1–Ru4 bond is fully formed (2.782 Å). Therefore, **D** exhibits the key features of the final fly-over complex. Cage B, has rotated during this process, seemingly due to steric interactions with the intact benzene ligand. The transition state for closing of the pendant carborane, **D-E-TS**, was located at +6.7 kcal mol^{-1}, where the distortion of the cage is directly analogous to that seen previously, in the mono(carborane) analogue. The final minimum, **E**, was then found through IRC calculations. **E** is a conformational isomer of the experimental product, **1**, where the bridging ligand is inverted.

In pathway II, the steps are reversed. In the first step, cage B is closed in the same way as before, through **C-D′-TS** at 9.7 kcal mol^{-1} to give **D′** at -44.1 kcal mol^{-1}. **D′** is similar to **C** around the central reduced benzene ring and so the transition state for formation of the fly-over complex can be found in the same way, through increasing the C1–C6 distance. The transition state, **D′-E′-TS**, at -21.3 kcal mol^{-1} exhibits a reduced Ru1···Ru4 distance, from 3.811 Å in **D′** to 3.457 Å in **D′-E′-TS** and the C1–C6 bond is lengthened from 1.513 Å to 2.718 Å. Characterisation of **D′-E′-TS** gives **E′**.

Pathway II was found to be comparable with pathway I, where the barriers to C–C cleavage were computed at $\Delta E^{\ddagger}$ = +22.4 and +22.8 kcal mol^{-1} in pathways I and II respectively and the barrier to carborane isomerisations were computed at $\Delta E^{\ddagger}$ = +9.7 and +11.8 kcal mol^{-1} respectively. The final products, **E** and **E'**, differ by rotation of cage B. This is a reflection on the order of the two steps: where the carborane isomerisation is the first step, its rotation is not triggered by the formation of the fly-over bridging ligand.

The experimental Ru1–Ru4 connection is least well reproduced in the computed models of **1**, where the Ru1–Ru4 distance is 2.763 Å and 2.853 Å in **E** and **E'** respectively and 2.699 Å in **1**. However, the large difference in the two computed Ru1–Ru4 bond lengths may suggest this distance is relatively flexible.

6.6. Suggestions for new bis(carborane) experiments

It was concluded from the above that attempts to doubly metallate reduced bis(carborane) were being prevented by the first metal fragment blocking the addition of the second. A fragment containing two potential capitating centres was therefore considered computationally. One possibility was a functionalised arene, bound η^6 to Ru, which would metallate one *nido* fragment of the reduced bis(carborane), with an arene substituent which would itself be capable of capitating the other *nido* fragment. The compound identified was dichloro(phenyl)borane ($PhBCl_2$), shown in Figure 6.17, which could replace the *p*-cymene ligand in $[Ru(p\text{-cymene})Cl_2]_2$ to give $[Ru(PhBCl_2)Cl_2]_2$, potentially a source of both $\{Ru(arene)\}^{2+}$ and $\{B(R)\}^{2+}$ fragments. The effect of the inter-cage distance was also considered through a bis(carborane) analogue with a methylene spacer between the carborane cages (currently being investigated experimentally[19]) which could potentially be doubly metallated.

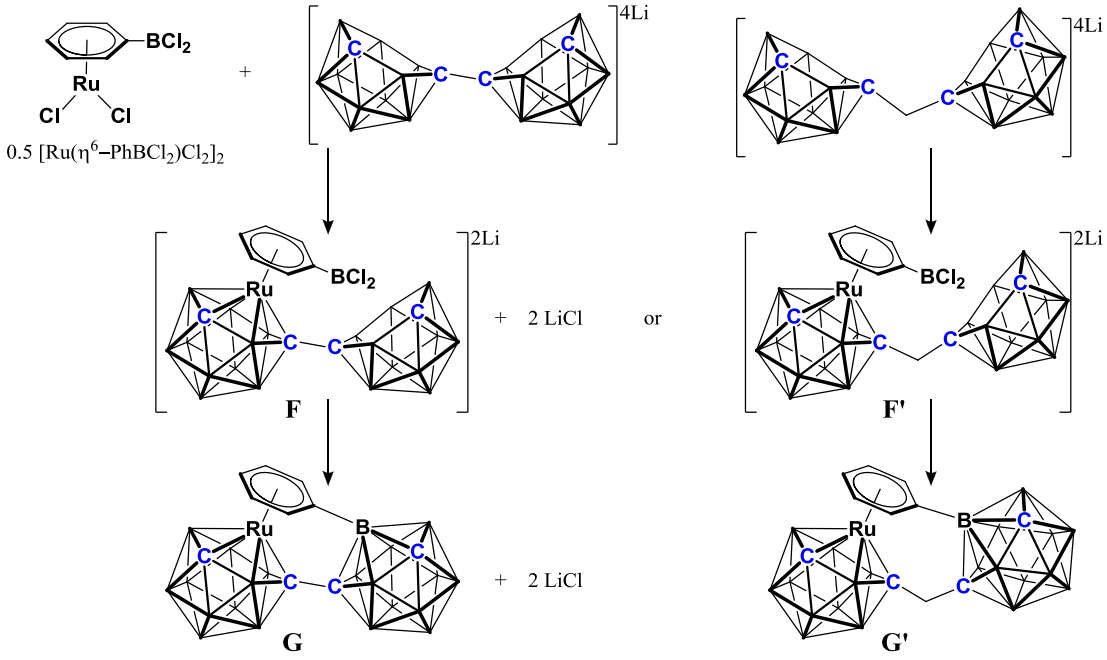

Figure 6.17 – Proposed double capitation of bis(carborane) tetraanions by $[Ru(PhBCl_2)Cl_2]_2$.

The structures of dianionic species, **F** and **F'**, and neutral species, **G** and **G'**, were computed. This allowed the energy change, ΔE, for each reaction (**a** and **b**, in Figure 6.18, below) to be assessed.

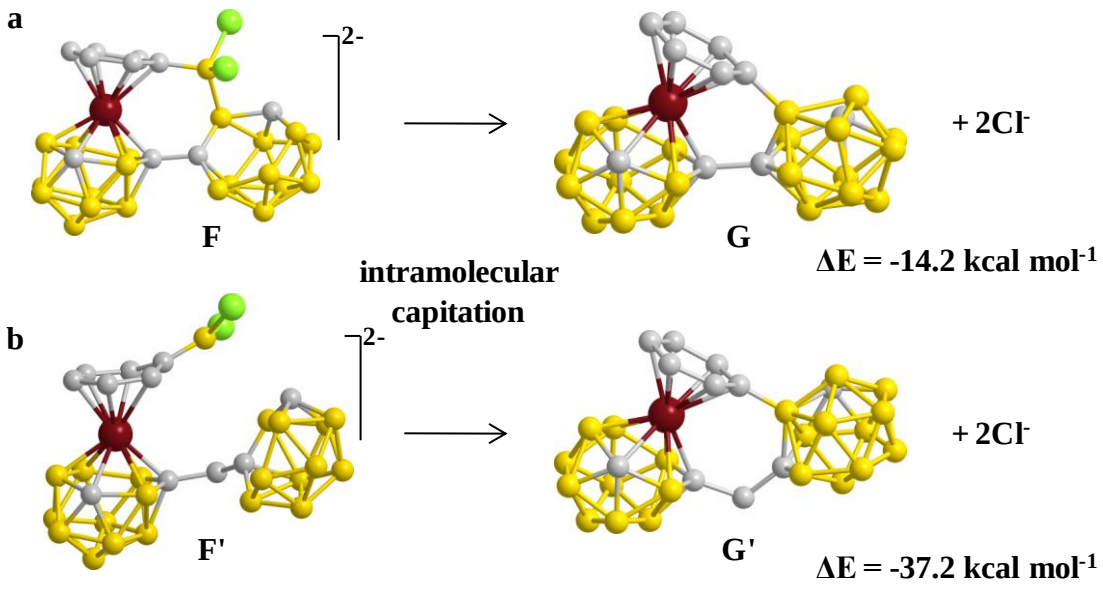

Figure 6.18 – Second steps of proposed double capitation of reduced bis(carborane) fragments. Hydrogen atoms omitted for clarity.

The above processes, proposed as intramolecular capitation, produce metallacarborane-carborane species. Though the computed ΔE of these reactions are not wholly reliable, they do provide some qualitative information. For instance, **G'** was found to be more stable than **G**, owing to its less strained 6-membered metallacyclic unit and docosahedral carborane cage (where that of **G** is computed with a 4-membered B2-C6-B10-B4 face).

Discussions with experimental co-workers suggest the above chemistry may be viable, but as a two step process, whereby a $Ru(COD)Cl_2$ could be used to give initial metallation before displacement of the labile COD ligand with dichloro(phenyl)borane, which would then lead to the second capitation.

6.7. Conclusions

The REDOX chemistry of bis(carborane) species was investigated computationally. In general, distortions in the carborane cages were found to be closely related to analogous mono(carborane) compounds investigated in Chapters 2. A notable exception was the reduction of 1,1′-bis(*ortho*-carborane), which exhibited cage distortions analogous with *ortho*-carborane on addition of a single electron but displayed more similarities with diphenyl-*ortho*-carborane thereafter. 1,1′-bis(*ortho*-carborane) also exhibits strong communication between the cages, attributed to a C–C π-bonding interaction, computed as being present in both the neutral and the dianionic minima.

The formation of a fly-over bridge complex from arene-containing precursors was found by experimental co-workers, revealing aromatic C–C bond cleavage by a metallacarborane. Calculations revealed a 2 electron reductive cleavage process where an internal electron transfer was driven by the spatial association of opposing charges, resulting in a reduced arene containing triple-decker intermediate, **C**. A thermal process giving C–C bond cleavage was located, with a barrier of +22.4 kcal mol^{-1}.

Finally, a process was computed, where a $\{Ru(\eta^6\text{-PhB})\}^{4+}$ fragment was proposed to overcome the steric barrier toward double capitation of a reduced bis(carboranes) with separate dicationic metal fragments.

6.8. References

1. a) J. A. Dupont and M. F. Hawthorne, *J. Am. Chem. Soc.*, 1964, **86**, 1643-1643; b) T. E. Paxson, K. P. Callahan and M. F. Hawthorne, *Inorg. Chem.*, 1973, **12**, 708-709.
2. X. Yang, W. Jiang, C. B. Knobler, M. D. Mortimer and M. F. Hawthorne, *Inorg. Chim. Acta*, 1995, **240**, 371-378.
3. L. I. Zakharkin and A. I. Kovredov, *Izv. Akad. Nauk SSSR, Ser. Khim.*, 1973, 1428.
4. X. Yang, W. Jiang, C. B. Knobler and M. F. Hawthorne, *J. Am. Chem. Soc.*, 1992, **114**, 9719-9721.
5. P. E. Fanta, *Chem. Rev.*, 1964, **64**, 613-632.
6. S. Ren and Z. Xie, *Organometallics*, 2008, **27**, 5167-5168.
7. D. E. Harwell, J. McMillan, C. B. Knobler and M. F. Hawthorne, *Inorg. Chem.*, 1997, **36**, 5951-5955.
8. T. D. Getman, C. B. Knobler and M. F. Hawthorne, *Inorg. Chem.*, 1992, **31**, 101-105.
9. T. D. Getman, C. B. Knobler and M. F. Hawthorne, *J. Am. Chem. Soc.*, 1990, **112**, 4593-4594.
10. D. Ellis, G. M. Rosair and A. J. Welch, *Chem. Commun.*, 2010, **46**, 7394-7396.
11. a) G. B. Dunks, R. J. Wiersema and M. F. Hawthorne, *J. Am. Chem. Soc.*, 1973, **95**, 3174-3179; b) L. I. Zakharkin and V. N. Kalinin, *Dokl. Akad. Nauk SSSR*, 1966, **169**, 590.
12. D. Ellis, D. McKay, S. A. Macgregor, G. M. Rosair and A. J. Welch, *Angew. Chem. Int. Ed.*, 2010, **49**, 4943-4945.
13. a) R. J. Baxter, G. R. Knox, J. H. Moir, P. L. Pauson and M. D. Spicer, *Organometallics*, 1998, **18**, 206-214; b) L. Brammer, M. Green, A. G. Orpen, K. E. Paddick and D. R. Saunders, *J. Chem. Soc., Dalton Trans.*, 1986, 657-667.
14. R. M. Pope, S. L. VanOrden, B. T. Cooper and S. W. Buckner, *Organometallics*, 1992, **11**, 2001-2003.
15. T. D. H. Bugg and C. J. Winfield, *Nat. Prod. Rep.*, 1998, **15**, 513-530.
16. Y. Yoshida, K. Mohri, K. Isobe, T. Itoh and K. Yamamoto, *J. Org. Chem.*, 2009, **74**, 6010-6015.
17. C. Krempner, H. Reinke and R. Wustrack, *Inorg. Chem. Commun.*, 2007, **10**, 239-242.

18. B. W. Hutton, F. MacIntosh, D. Ellis, F. Herisse, S. A. Macgregor, D. McKay, V. Petrie-Armstrong, G. M. Rosair, D. S. Perekalin, H. Tricas and A. J. Welch, *Chem. Commun.*, 2008, 5345-5347.
19. D. Ellis and A. J. Welch, *Unpublished Results*.

Chapter 7 – Theoretical Background

7.1. Introduction

This chapter will provide a brief description of the theoretical basis of the work described in this thesis. Key concepts and approximations are introduced, leading to Hartree-Fock (HF) theory, before introducing density functional theory (DFT) and its applications to chemical systems.

7.2. The Schrödinger equation

The time-independent, non-relativistic Schrödinger equation[1] (Equation 7.1) is the fundamental equation of quantum mechanics.

$$\hat{H}\Psi = E\Psi \qquad (Eq.7.1)$$

Here, $\hat{H}$ is the Hamiltonian operator which acts on the wavefunction, Ψ, of the system to return the energy of the system, *E*. This therefore represents an eigenvalue equation, where *E* is the eigenvalue and Ψ is the eigenfunction.

$$\hat{H} = -\frac{1}{2}\sum_{i=1}^{N}\nabla_i^2 - \frac{1}{2}\sum_{A=1}^{M}\frac{1}{M_A}\nabla_A^2 - \sum_{i=1}^{N}\sum_{A=1}^{M}\frac{Z_A}{r_{iA}} + \sum_{i=1}^{N}\sum_{j>i}^{N}\frac{1}{r_{ij}} + \sum_{A=1}^{M}\sum_{B>A}^{M}\frac{Z_A Z_B}{R_{AB}} \qquad (Eq.7.2)$$

The Hamiltonian operator, defined in Equation 7.2, above, consists of five terms: the kinetic energy of *N* electrons, the kinetic energy of *M* nuclei, the potential energy due to electrons-nucleus interactions, the potential energy between the electrons and the potential energy between the nuclei.

In the solution to the Schrödinger equation lies all of the information required to describe a chemical system, however, its solution cannot be found exactly. Indeed, in 1929, Dirac remarked on this subject,[2] *"The fundamental laws necessary for the mathematical treatment of a large part of physics and the whole of chemistry are thus completely known, and the difficulty lies only in the fact that application of these laws leads to equations that are too complex to be solved."*

Methodologies developed to describe chemical systems, including HF and DFT, are therefore designed to evaluate the Schrödinger equation through a series of approximations which are described below.

The first such simplification of the Schrödinger equation is the Born-Oppenheimer (BO) approximation. This takes advantage of the large discrepancy in masses between nuclei

and electrons, because of which the lighter electrons move far faster than the more massive nuclei. If we therefore consider the nuclei fixed and the electrons moving within this field, *i.e.* regarding their motions as decoupled, Equation 7.2 may be reduced to the electronic Hamiltonian, below.

$$\hat{H} = -\frac{1}{2}\sum_{i=1}^{N} \nabla_i^2 - \sum_{i=1}^{N}\sum_{A=1}^{M} \frac{Z_A}{r_{iA}} + \sum_{i=1}^{N}\sum_{j>i}^{N} \frac{1}{r_{ij}} \equiv \hat{T} + \hat{V}_{Ne} + \hat{V}_{ee} \qquad (Eq.\,7.3)$$

where the kinetic energy of the nuclei has been set to zero and the nuclear-nuclear repulsion is simply a constant, which may be added to the electronic energy provided by this Hamiltonian to give the total energy of the system. The remaining terms represent the kinetic energy of the electrons, the potential energy due to electron-nucleus interactions and the potential energy between the electrons.

The magnitude of the error caused by the BO approximation is at its largest in small systems. In the dihydrogen molecule this represents one 10 thousandth of the total energy. This, however, exceeds the accuracy of current methods for solving the electronic part of the Schrödinger equation and so this approximation is minor in comparison with other errors.[3]

The wavefunction, Ψ, is dependent on the 3*N* spatial and *N* spin coordinates of the particles described. In an electronic wavefunction, spatial and spin coordinates of electrons 1, 2, ... *N* are represented by elements $\vec{x}_1, \vec{x}_2, \ldots \vec{x}_N$. The square of the wavefunction then gives the probability of finding electrons 1, 2, ... *N* in volume elements $d\vec{x}_1, d\vec{x}_2, \ldots d\vec{x}_N$, *i.e.*

$$|\Psi(\vec{x}_1, \vec{x}_2, \ldots \vec{x}_N)|^2 d\vec{x}_1, d\vec{x}_2, \ldots d\vec{x}_N \qquad (Eq.\,7.4)$$

We are then faced with a series of constraints that Ψ must obey; the indistinguishability of electrons, the Pauli Exclusion Principle and the normalisation of the wavefunction (which aids its computation). With the physical interpretation of Ψ given in Equation 7.4, having indistinguishable electrons means the square of the wavefunction is unchanged by the interchange of any two electrons:

$$|\Psi(\vec{x}_1, \vec{x}_2, \ldots \vec{x}_i, \vec{x}_j, \ldots \vec{x}_N)|^2 = |\Psi(\vec{x}_1, \vec{x}_2, \ldots \vec{x}_j, \vec{x}_i, \ldots \vec{x}_N)|^2 \qquad (Eq.\,7.5)$$

Electrons are fermions and have spin = ½. Such particles have an antisymmetric wavefunction, therefore the interchange of electrons must result in a change in sign of

the wavefunction (Equation 7.6, below). This gives rise to the (required) property of antisymmetry and a generalisation of the Pauli exclusion principle.

$$\Psi(\vec{x}_1, \vec{x}_2, \dots \vec{x}_i, \vec{x}_j, \dots \vec{x}_N) = -\Psi(\vec{x}_1, \vec{x}_2, \dots \vec{x}_j, \vec{x}_i, \dots \vec{x}_N) \qquad (Eq.\,7.6)$$

The final requirement is that the wavefunction is normalised. This simply means the probability of finding *N* electrons in all space must be exactly 1. Algebraically, this takes the following form.

$$\int \dots \int |\Psi(\vec{x}_1, \vec{x}_2, \dots \vec{x}_N)|^2 d\vec{x}_1, d\vec{x}_2, \dots d\vec{x}_N = 1 \qquad (Eq.\,7.7)$$

7.3. The variational principle

While the exact solution to the Schrödinger equation is not known beyond hydrogenic systems, it does exhibit a property which renders the extrapolation of the exact solution possible. This is that it adheres to the variational principle, which states that the ground state wavefunction of a system, Ψ_0, by definition must provide the lowest possible energy, E_0, for a given Hamiltonian.

If a 'guess' wavefunction, Ψ_{trial}, is acted upon by the Hamiltonian operator, $\widehat{H}$, it will provide the expectation value of the associated observable (the energy) thus

$$\langle \widehat{H} \rangle = \int \dots \int \Psi^*_{trial} \widehat{H} \ \Psi_{trial} d\vec{x}_1, d\vec{x}_2, \dots d\vec{x}_N \equiv \langle \Psi^*_{trial} | \widehat{H} | \Psi_{trial} \rangle \qquad (Eq.\,7.8)$$

where $\langle \widehat{H} \rangle$ is the expectation value of $\widehat{H}$, Ψ^*_{trial} represents the complex conjugate of Ψ_{trial} and the "bracket notation" used in Equation 7.8 is shorthand for the integral over *N* volume elements. Through the variational principle, this leads to the expression below (Equation 7.9).

$$\langle \Psi^*_{trial} | \widehat{H} | \Psi_{trial} \rangle = E_{trial} \geq E_0 = \langle \Psi^*_0 | \widehat{H} | \Psi_0 \rangle \qquad (Eq.\,7.9)$$

This prescribes that the aim of a quantum chemical method is to generate a wavefunction for a given system, and evaluate the electronic energy through operation of its Hamiltonian. The best wavefunction is that providing the smallest energy. The energy is delivered by operation of some potential, *v*, on the wavefunction. However the potential itself is dependent on the wavefunction. This therefore represents a self-consistent field (SCF) problem, whereby Ψ is generated by *v*, but also generates *v*. As a result, quantum chemical methods may also be described as SCF methods.

7.4. The Slater determinant

Since there are an infinite number of possible wavefunctions for a given system, the likelihood of finding Ψ_0, where the energy of the trial wavefunction is uniquely equal to the ground state energy, is small. A manageable subset is therefore required which gives a satisfactory approximation to the true wavefunction and is physically robust. This can be achieved by approximating the many (*N*) electron wavefunction, $\Psi(\vec{x}_1, \vec{x}_2, \ldots \vec{x}_i, \vec{x}_j, \ldots \vec{x}_N)$, to a product, of *N* one electron wavefunctions, $\chi_i(\vec{x}_i)$, also known as 'spin orbitals' as

$$\chi_i(\vec{x}_i) = \phi(\vec{r})\sigma(s), \qquad \sigma(s) = \alpha, \beta \qquad (Eq.7.10)$$

where ϕ is the position and σ is the spin of the electron.

A direct product would not satisfy the physical requirements of an electronic wavefunction; as Equation 7.11 shows, each wavefunction is directly associated to a particular electron, meaning electrons are not indistinguishable. Moreover, the Hartree product wavefunction, Ξ, is not antisymmetric to interchange of electrons, *i.e.* it does not fulfil the requirement of Equation 7.6.

$$\Xi = \chi_1(\vec{x}_1)\chi_2(\vec{x}_2) \ldots \chi_N(\vec{x}_N) \qquad (Eq.7.11)$$

An antisymmetric product is therefore required and this, as suggested by Fock, is provided by the Slater determinant, Φ_{SD}:

$$\Psi_0 \approx \Phi_{\mathrm{SD}} = \frac{1}{\sqrt{N!}} \begin{vmatrix} \chi_1(\vec{x}_1) & \chi_2(\vec{x}_1) & \cdots & \chi_N(\vec{x}_1) \\ \chi_1(\vec{x}_2) & \chi_2(\vec{x}_2) & \cdots & \chi_N(\vec{x}_2) \\ \vdots & \vdots & \ddots & \vdots \\ \chi_1(\vec{x}_N) & \chi_2(\vec{x}_N) & \cdots & \chi_N(\vec{x}_N) \end{vmatrix} \qquad (Eq.7.12)$$

where $\frac{1}{\sqrt{N!}}$ ensures the wavefunction is normalised. The determinant includes every electron in every wavefunction, therefore satisfying indistinguishability. Furthermore, two fundamental properties of a determinant are that swapping two rows (equivalent to interchange of two electrons) changes the sign of the determinant and having two equal columns the same gives $\Phi_{\mathrm{SD}} = 0$, which satisfies Pauli's exclusion principle.

The use of a Slater determinant is therefore a convenient and efficient approximation to the true wavefunction. It does however, only allow for a single electronic configuration, which is particularly inaccurate for systems with low-lying excited states that can interact with the ground state wavefunction. $\Psi_0 \approx \Phi_{\mathrm{SD}}$ may therefore be considered a

large approximation. Methods such as full configuration interaction (CI), and approaches that approximate it, such as Complete Active Space Self Consistent Field (CASSCF), circumvent this by representing the wavefunction as a product of multiple determinants. These methods entail high computational expense, however, and so only so-called "single reference" methods will be considered here.

7.5. The Hartree-Fock approximation

The first method to be considered is the Hartree-Fock (HF) method, which adopts a single Slater determinant and the HF Hamiltonian (described in this section) to approximate the Schrödinger equation through the first application of the SCF methodology to a quantum chemical problem:

$$\widehat{H}_{HF}\Phi_{\mathrm{SD}} = E_{HF}\Phi_{\mathrm{SD}} \qquad (Eq.7.13)$$

The HF method uses the variational principle to minimise E_{HF} (the expectation value of $\widehat{H}_{HF}$ acting upon the Slater determinant) self-consistently, by improving the spin orbitals, $\chi_i(\vec{x}_i)$ which make up Φ_{SD}:

$$E_{HF} = \langle\Phi_{\mathrm{SD}}|\widehat{H}_{HF}|\Phi_{\mathrm{SD}}\rangle = \sum_{i}^{N}\left(|i|\hat{h}|i|\right) + \frac{1}{2}\sum_{i}^{N}\sum_{j}^{N}[(ii|jj) - (ij|ji)] \quad (Eq.7.14)$$

This expression, however, is problematic in that the second term requires the solution to a two electron operator and does lend itself to computational treatment.

Roothaan and Hall[4] independently showed that the Hartree-Fock equations could then be converted into a series of equations for the coefficients of linear combinations of atomic orbitals (LCAO). This is arranged in the form of a matrix equation which is more easily solved computationally:

$$Fc = Sc\varepsilon \qquad (Eq.7.15)$$

where F is an $N \times N$ matrix, where each element is a form of Equation 7.16,below (N = number of basis functions), S is an $N \times N$ matrix of overlap integrals, c is an $N \times N$ matrix of unknown coefficients and ε is a diagonal matrix of orbital energies.

$$\hat{\mathrm{f}}_{\mathrm{i}}\chi_{\mathrm{i}} = \varepsilon_{\mathrm{i}}\chi_{\mathrm{i}} \qquad (Eq.7.16)$$

such that

$$E_{HF} = \langle \Phi_{\mathrm{SD}} | \hat{H}_{HF} | \Phi_{\mathrm{SD}} \rangle = \sum_{i=1}^{N} \hat{\mathrm{f}}_{\mathrm{i}} \chi_{\mathrm{i}} = \sum_{i=1}^{N} \varepsilon_{\mathrm{i}} \chi_{\mathrm{i}} \qquad (Eq. 7.17)$$

where $\hat{\mathrm{f}}_i$ is the Fock operator and ε_i is the orbital energy.

In essence, the Slater determinant is an eigenfunction of the Hamiltonian operator defined in turn as a sum of Fock operators. This has the effect of allowing the solution to the eigenfunction problem to consist of one electron problems, shown in Equation 7.18.

$$\hat{\mathrm{f}}_i = -\frac{1}{2}\nabla_i^2 - \sum_{A}^{M} \frac{Z_A}{r_{iA}} + \hat{V}_{HF}(i) \equiv \hat{T} + \hat{V}_{Ne} + \hat{V}_{HF} \qquad (Eq. 7.18)$$

where $\hat{V}_{HF}$ is the Hartree-Fock potential, which, to satisfy Equation 7.3, describes the potential between electrons. In Hartree Fock theory, this term is taken as a potential that considers the average repulsive interaction of *N*-1 electrons felt by the i^{th} electron and consists of two terms: $\hat{J}$, the Coulomb operator and $\hat{K}$, the exchange operator.

$$\hat{V}_{HF}(\vec{x}_1) = \sum_{j}^{N} \left(\hat{J}_j(\vec{x}_1) - \hat{K}_j(\vec{x}_1) \right) \qquad (Eq. 7.19)$$

The Coulomb operator, which is likened to repulsion of like charges in classical mechanics, is given by

$$\hat{J}_j(\vec{x}_1) = \int |\chi_j(\vec{x}_2)|^2 \frac{1}{r_{12}} d\vec{x}_2 \qquad (Eq. 7.20)$$

It was shown before that the square of a wavefunction integrated over a given volume is equal to the probability of finding an electron in that volume. The expression given in Equation 7.20, above is therefore the potential exerted by the average charge distribution of an electron in spin orbital χ_j upon an electron at position $\vec{x}_1$, weighted by the probability of finding electron 2 in spin orbital χ_j.

The exchange operator has a stabilising effect, however, it is often described as having "no physical interpretation". Its definition, when operating on a spin orbital, is given in Equation 7.21, below.

$$\hat{K}_j(\vec{x}_1)\chi_i(\vec{x}_1) = \int \chi_j^*(\vec{x}_2) \frac{1}{r_{12}} \chi_i(\vec{x}_2) d\vec{x}_2 \, \chi_j(\vec{x}_1) \qquad (Eq. 7.21)$$

This describes the potential associated with exchanging the electrons between two spin orbitals and is a consequence of antisymmetry. As it is integrated over spin coordinates and is dependent on orthonormal spin orbitals, opposing spins would give zero contributions. Exchange is therefore a property of parallel spins only.

The final property of the HF method is that the phenomenon of 'self-interaction' is overcome. Self-interaction is introduced by the Coulomb operator (Equation 7.20) as the case of $i = j$ is allowed. This has the unphysical effect of producing a non-zero Coulomb operator, $\hat{J}_j(\vec{x}_1)$, where an electron is interacting with itself. As a result, even hydrogenic exhibit electron-electron repulsion. In the HF method this is fully accounted for, however, through the exchange operator:

$$\hat{K}_j(i) = \hat{J}_j(i) \; for \; i = j \qquad (Eq. 7.22)$$

This ensures that the potential (Equation 7.19) goes to zero for this case. However, self-interaction will arise as a problem in DFT (Section 7.10).

7.6. Electron correlation

A major contribution to electron correlation is due to the difference between the average and instantaneous electron-electron interactions, known as dynamic correlation, and is represented as

$$\hat{V}_{ee} = \sum_{i=1}^{N} \sum_{j>i}^{N} \frac{1}{r_{ij}} \qquad (Eq. 7.23)$$

The effective potential used in HF, $\hat{V}_{HF}(\vec{x}_1)$, made up of Coulomb and exchange operators, is a single-electron operator, and crucially, the term in Equation 7.23, above is taken into account only in an average way. The electron correlation energy is therefore often defined as

$$E_{HF}^{C} = E_0 - E_{HF} \qquad (Eq. 7.24)$$

E_{HF}^{C} is absent from the HF approximation and so it is the error between the HF energy and the true ground state energy. From the variational principle, it is known that the correlation energy is stabilising, which reflects the idea that like charges repel one another. Without electron correlation, electrons can be considered to be, on average, closer together, as their motions are not linked, leading to an increased electron-electron repulsion energy.

The terms making up *E*, including electron kinetic energy, electron-nuclear attraction, Coulomb repulsion and exchange, described by Hartree-Fock, plus electron correlation can be summarised as[5]

$$E = E_T + E_V + E_J + E_X + E_C \qquad (Eq.7.25)$$

where the first three terms contribute most to *E*; for example in Ne, *E* = -129.4 a.u. and E_T, E_V, E_J, E_X and E_C contribute by +129, -312, +66, -12 and -0.4 a.u. respectively. So-called 'post Hartree-Fock' or wavefunction methods, which use HF as a starting point, aim to systematically improve the HF approximation by describing the electron correlation term, E_C. However, such methods become increasingly computationally expensive, scaling formally as N^4 in HF up to N^7 in more modern methods (where *N* is the number of basis functions). DFT methods, discussed below, use an alternative approach of improving the external potential, in order to account for the effect of electron correlation, through electron density, while remaining computationally inexpensive, formally scaling as N^3 in its simplest form. As will be discussed, however, it is difficult to systematically improve their treatment of exchange and correlation. In general in DFT implementations, expressions for electron-nuclear and Coulomb potential energies are common, whereas the exchange and correlation expressions (referred to as exchange correlation functionals, $V_{XC}[\rho]$) are the focus of development.

7.7. Electron density

The electron density is an experimentally observable property of chemical systems (used, for example, in X-Ray crystallography) and is defined in quantum mechanics as the probability of finding an electron in a particular point in space. This concept has been shown previously, in Equation 7.4, which can now be modified to give:

$$\rho(\vec{r}_1) = N \int \dots \int |\Psi(\vec{x}_1, \vec{x}_2, \dots \vec{x}_N)|^2 d\vec{s}_1, d\vec{x}_2, \dots d\vec{x}_N \qquad (Eq.7.26)$$

where $\rho(\vec{r}_1)$ is the electron density. As this functional is dependent only on the position of the electron, the total electron density of the chemical system can therefore be described by just 3 variables. The fact that the electron density is independent of the remaining variables describing the wavefunction (the spin of electron 1 and the spatial and spin coordinates of all other electrons) means, however, that the above expression is not unique.

7.8. The Hohenberg-Kohn theorems

Modern DFT sees its foundation in two theorems published in 1964 by Hohenberg and Kohn (HK).[6] The first theorem consists of a proof by *reductio ad absurdum* that the ground state electron density uniquely determines the Hamiltonian operator. The second proved that their approach was viable, through application of the variational principle to the electron density.

This work led to the Nobel Prize in Chemistry for Walter Kohn in 1998, which he shared with John Pople, whose work on basis sets will be discussed later.

7.8.1. The first Hohenberg-Kohn theorem – proof of DFT

The proof proceeds by first assuming two different external potentials, $\hat{V}_{ext} \neq \hat{V}'_{ext}$, corresponding to different (non-degenerate) ground state wavefunctions, $\Psi_0 \neq \Psi'_0$, and therefore differing ground state energies, $E_0 \neq E'_0$, while producing the same electron density, $\rho(\vec{r}_1)$, which is allowed by Equation 7.26. This leads to Equation 7.27.

$$\hat{H} = \hat{T} + \hat{V}_{ext} + \hat{V}_{ee} \neq \hat{H}' = \hat{T} + \hat{V}'_{ext} + \hat{V}_{ee} \qquad (Eq.\,7.27)$$

It follows then, by the variational principle, that if the primed wavefunction, Ψ'_0, is used with the unprimed Hamiltonian operator, $\hat{H}$, to resolve its expectation value, this would be greater than the unprimed ground state energy, E_0, *i.e.*

$$E_0 < \langle \Psi'_0 | \hat{H} | \Psi'_0 \rangle = E'_0 + \langle \Psi'_0 | \hat{H} - \hat{H}' | \Psi'_0 \rangle \qquad (Eq.\,7.28)$$

Equation 7.27 allows the expansion of the final term to give:

$$E_0 < E'_0 + \langle \Psi'_0 | \hat{T} + \hat{V}_{ext} + \hat{V}_{ee} - \hat{T} - \hat{V}'_{ext} - \hat{V}_{ee} | \Psi'_0 \rangle \qquad (Eq.\,7.29)$$

$$E_0 < E'_0 + \langle \Psi'_0 | \hat{V}_{ext} - \hat{V}'_{ext} | \Psi'_0 \rangle \qquad (Eq.\,7.30)$$

Repeating the above derivation with the complementary primed and unprimed expressions gives:

$$E'_0 < E_0 - \langle \Psi_0 | \hat{V}_{ext} - \hat{V}'_{ext} | \Psi_0 \rangle \qquad (Eq.\,7.31)$$

The combination of Equations 7.30 and 7.31 is then the ‘absurd’ statement that

$$E_0 + E'_0 < E'_0 + E_0 \qquad (Eq.\,7.32)$$

concluding, therefore, that there exists only one (unique) potential that will generate the true ground state electron density, ρ_0. Hence the ground state electron density, ρ_0, reflects a unique external potential, $\hat{V}_{ext}$, and leads to the true ground state energy. Thus, the ground state energy is generated from the ground state electron density and its components are functionals of ρ_0:

$$E_0[\rho_0] = T[\rho_0] + E_{ee}[\rho_0] + E_{Ne}[\rho_0] \qquad (Eq. 7.33)$$

The final term in Equation 7.33 can be said to be system dependent as it involves the nuclei as well as the electron density, whereas $T[\rho_0]$ and $E_{ee}[\rho_0]$ are dependent on the electron density only. These terms, including the kinetic energy, the classical Coulomb repulsion, the self-interaction correction, the exchange energy and electron correlation, may therefore be grouped into a single functional, $F_{HK}[\rho]$, the Hohenberg-Kohn functional. This functional would then provide, from the electron density, all of the information needed to describe a chemical system. Unfortunately the form of the functional is unknown, thus its definition is the holy grail of density functional theory.

7.8.2. The second Hohenberg-Kohn theorem – the variational principle

The second theorem given by Hohenberg and Kohn (in the same publication) addresses the issue that since the ground state electron density is required for the above proof, it is necessary to be certain the electron density used is indeed that of the ground state.

The density functional, $F_{HK}[\rho]$, delivers the ground state energy of a system when given the ground state density, ρ_0. Therefore, where a trial electron density is used, ρ_{trial}, an associated trial Hamiltonian, $\hat{H}_{trial}[\rho]$, is produced, giving a trial wavefunction, $\Psi_{trial}[\rho]$. If it is then assumed the true Hamiltonian, $\hat{H}$, is known, Equation 7.9 can be applied as:

$$\langle \Psi_{trial}[\rho] | \hat{H} | \Psi_{trial}[\rho] \rangle = E_{trial}[\rho] \geq E_0 = \langle \Psi_0 | \hat{H} | \Psi_0 \rangle \qquad (Eq. 7.34)$$

This proves the density functional can be used to find the energy of a system and that energy can be solved self-consistently. As this energy is variational, minimisation of the energy, by adjustment of the electron density, will lead to the ground state energy, where $\rho_{trial} \equiv \rho_0$ (within a given external potential).

7.9. The Kohn-Sham approach

In 1965, Kohn and Sham (KS) made developments towards the application of DFT to chemical systems,[7] by suggesting an approximation of the universal functional, $F_{HK}[\rho_0]$. The most pressing task, at the time of writing, was to find an expression for the kinetic energy of electrons as it contributes the largest amount to the total energy of the unknown quantities of E_T, E_X and E_C. Conveniently, an expression existed for the kinetic energy operator in Hartree-Fock theory, which could be adopted through the introduction of orbital:

$$\hat{T}_{HF} = -\frac{1}{2}\sum_{i}^{N}\langle\chi_i|\nabla^2|\chi_i\rangle \qquad (Eq.7.35)$$

where χ_i represent spin orbitals. In KS, this has the effect of creating a system of N non-interacting (as if neutral) fermions, each occupying a spin orbital. These are then placed in a Slater determinant, which approximates the wavefunction of the system, but crucially exactly represent the true wavefunction of the system of non-interacting fermions.

Kohn and Sham saw this could be exploited in DFT, where an equivalent non-interacting system could be set up and used with an effective potential, $V_S(\vec{r})$:

$$\hat{H}_S = -\frac{1}{2}\sum_{i}^{N}\nabla_i^2 + \sum_{i}^{N}V_S(\vec{r}_i) \qquad (Eq.7.36)$$

A Slater determinant, Θ_S, is then set up with spin orbitals, $\varphi_i(\vec{x}_i)$, known as Kohn-Sham orbitals:

$$\Theta_S = \frac{1}{\sqrt{N!}}\begin{vmatrix} \varphi_1(\vec{x}_1) & \varphi_2(\vec{x}_1) & \dots & \varphi_N(\vec{x}_1) \\ \varphi_1(\vec{x}_2) & \varphi_2(\vec{x}_2) & \dots & \varphi_N(\vec{x}_2) \\ \vdots & \vdots & \ddots & \vdots \\ \varphi_1(\vec{x}_N) & \varphi_2(\vec{x}_N) & \dots & \varphi_N(\vec{x}_N) \end{vmatrix} \qquad (Eq.7.37)$$

essentially equivalent to Equation 7.12. It follows then that equivalent expressions to Equation 7.16 and 7.18 can also now be adopted:

$$\hat{f}^{KS}\varphi_i = \varepsilon_i\varphi_i \qquad (Eq.7.38)$$

$$\hat{f}^{KS} = -\frac{1}{2}\nabla^2 + V_S(\vec{r}) \qquad (Eq.7.39)$$

This system, while artificial, allows for the kinetic energy of non-interacting particles to be accounted for exactly. The remaining kinetic energy and the connection of this artificial system to the true chemical system being examined is then determined by the effective potential, $V_S(\vec{r})$. This requires that the total electron density of the non-interacting system, as given by the sum of the squares of the Kohn-Sham orbitals, should be equal to the ground state electron density of the true system, *i.e.*

$$\rho_S(\vec{r}) = \sum_i^N \sum_s |\varphi_i(\vec{r}, s)|^2 = \rho_0(\vec{r}) \qquad (Eq. 7.40)$$

A large part of the true kinetic energy, *T*, is therefore found exactly by this method as:

$$T_S = -\frac{1}{2}\sum_i^N \langle \varphi_i | \nabla^2 | \varphi_i \rangle ; \;\; T_S \leq T \qquad (Eq. 7.41)$$

The density functional, $F_{HK}[\rho]$, can then be modified to:

$$F[\rho(\vec{r})] = T_S[\rho(\vec{r})] + J[\rho(\vec{r})] + E_{XC}[\rho(\vec{r})] \qquad (Eq. 7.42)$$

where $E_{XC}[\rho(\vec{r})]$ is the exchange correlation energy:

$$E_{XC}[\rho(\vec{r})] \equiv (T[\rho] - T_S[\rho]) + (E_{ee}[\rho] - J[\rho]) = T_C[\rho] + E_{ncl}[\rho] \quad (Eq. 7.43)$$

where $T_C[\rho]$ is the kinetic energy arising from electron correlation and $E_{ncl}[\rho]$ is the energy of the combined non-classical terms of the self-interaction correction, the exchange energy and the correlation potential energy.

7.10. Exchange-correlation functional approaches

As remarked by Walter Kohn in his 1998 address to the Nobel Foundation,[8] "So far DFT has been presented as a formal *mathematical framework* for viewing electronic structure from the perspective of the electron density... to make concrete use of it we require effective approximations for $F_{HK}[\rho]$ in the HK formulation, and for $E_{XC}[\rho(\vec{r})]$ in the KS formulation." This section will introduce methods used to provide expressions for $V_{XC}[\rho(\vec{r})]$.

7.10.1. The local density approximation

The local density approximation (LDA) and related local spin-density approximation (LSDA) are the starting points for most exchange-correlation functionals. LDA is based

on the hypothetical uniform electron gas (UEG) model. This neutral system is defined as electrons moving within a field of positive charges (to render the system neutral) such that the number of electrons, *N*, and the volume of the system, *V*, tend to infinity while their ratio (the electron density) remains constant.

$$N \to \infty, V \to \infty, \frac{N}{V} = \rho \qquad (Eq. 7.44)$$

While this model is not a realistic approximation of a chemical system, it has the advantage of having a near exact form of $E_{XC}[\rho(\vec{r})]$. This is defined as

$$E_{XC}^{LDA}[\rho(\vec{r})] = \int \rho(\vec{r}) \varepsilon_{XC}\big(\rho(\vec{r})\big)\, d\vec{r} \qquad (Eq. 7.45)$$

where $\varepsilon_{XC}\big(\rho(\vec{r})\big)$ is the single electron exchange-correlation energy of a UEG with density $\rho(\vec{r})$. This can be further decomposed to separate the exchange and correlation parts:

$$\varepsilon_{XC}\big(\rho(\vec{r})\big) = \varepsilon_X\big(\rho(\vec{r})\big) + \varepsilon_C\big(\rho(\vec{r})\big) \qquad (Eq. 7.46)$$

The exchange part of this is known, and given by

$$\varepsilon_X = -\frac{3}{4}\sqrt[3]{\frac{3\rho(\vec{r})}{\pi}} \qquad (Eq. 7.47)$$

while the correlation part is not known, but has been accurately determined numerically.[9]

In order to discern information from real chemical systems, an interface must be found between the electron density of the real system and the UEG (illustrated by the scheme in Figure 7.1). This requires the chemical system to be divided into an array of finite volumes (normally referred to as the 'integration grid'); each volume is then assigned a single electron exchange correlation energy, $\varepsilon_{XC}\big(\rho(\vec{r})\big)$ from a UEG constructed from the electron density of that volume. The total exchange correlation energy, $E_{XC}^{LDA}[\rho(\vec{r})]$, calculated through Equation 7.45. The coarseness of the integration grid is therefore an important consideration in DFT calculations as a finer grid would give a better approximation.

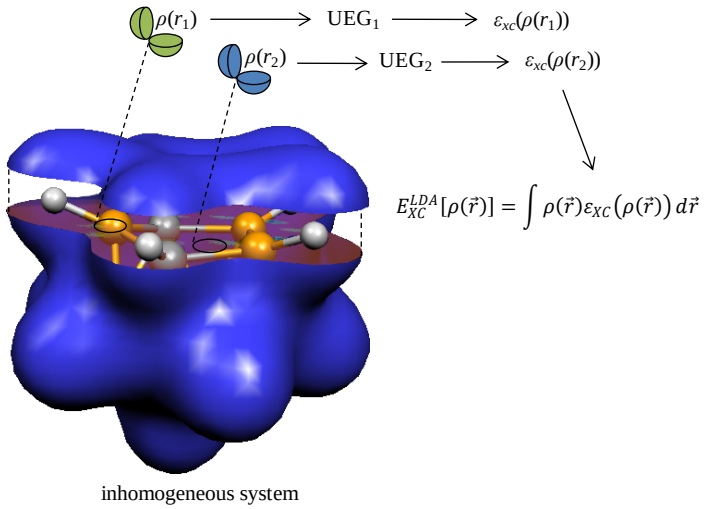

Figure 7.1 – Schematic for the conversion of electron densities into exchange correlation energies under the LDA method.

7.10.2. The generalised gradient approximation

For chemical problems, the LDA and LSD methods were found to exhibit large errors with respect to experiment, most notably the 'overbinding' problem, which results in, for example, overestimated atomisation energies. The next step to improving the LDA functional was to include the reduced gradient of the density, supplementing $\rho(\vec{r})$ with $\nabla\rho(\vec{r})$, giving

$$E_{XC}^{GGA}[\rho_\alpha, \rho_\beta] = \int f(\rho_\alpha, \rho_\beta, \nabla\rho_\alpha, \nabla\rho_\beta)\, d\vec{r} \qquad (Eq.\,7.48)$$

which can be further divided into exchange and correlation functional components:

$$E_{XC}^{GGA} = E_X^{GGA} + E_C^{GGA} \qquad (Eq.\,7.49)$$

As described in Section 7.5, HF allows *J* and *K* to cancel in hydrogenic systems, here exchange and correlation functionals are separated to aid development, however, this may lead to self-interaction.

The exchange functional can be expressed as

$$E_X^{GGA} = E_X^{LDA} - \sum_\sigma \int F(s_\sigma)\rho_\sigma^{4/3}\, d\vec{r} \qquad (Eq.\,7.50)$$

where s_σ is the dimensionless reduced gradient of the density for spin σ:

$$s_\sigma(\vec{r}) = \frac{|\nabla\rho_\sigma(\vec{r})|}{\rho_\sigma^{4/3}(\vec{r})} \qquad (Eq.\,7.51)$$

The first such functional was published by Becke in 1988[10] (abbreviated to B):

$$F^B = \frac{\beta s_\sigma^2}{1 + 6\beta s_\sigma \sinh^{-1} s_\sigma} \qquad (Eq. 7.52)$$

where an empirical parameter, β = 0.0042, is introduced as the least-squares fit to exact exchange energies of nobel gases He to Rn. Functionals based on the reduced gradient are described as *pure* GGA functionals.

Many correlation functionals are available, including Perdew's 1986 functional[11] (P86), the 1991 functional of Perdew and Wang[12] (PW91) and the 1988 Lee, Yang and Parr[13] functional (LYP). The latter is unusual in that it is not based on the uniform electron gas model, rather on the computed correlation energy of the helium atom. It therefore contains a single parameter.

The combination of exchange and correlation functionals (where any two may be combined) is usually described by their respective acronyms. For example, BP86 is the combination of Becke's exchange functional and Perdew's correlation functional, likewise BLYP uses Lee, Yang and Parr's correlation functional. Since their implementation, these two functional combinations have been the most popular of this type.

7.10.3. Hybrid functionals

Hybrid functionals were proposed to take advantage of the Hartree-Fock exchange term, which is exact, and apply this to Kohn-Sham orbitals, then add a pure DFT correlation energy to give E_{XC}. Simply:

$$E_{XC} = E_X^{exact} + E_C^{KS} \qquad (Eq. 7.53)$$

However, this produced greater errors with respect to experiment than GGA functionals in which both E_X and E_C are approximated. This can be attributed to the combination of a delocalised exchange component and a localised correlation component, preventing rigorous cancellation and again emphasising that separation of the exchange and correlation terms is convenient, however it is not know whether this is a valid approach.

In 1993, Becke introduced the B3PW91 hybrid functional.[14] It used HF exchange with DFT-based exchange and correlation functionals, to varying extents, given below.

$$E_{XC}^{B3} = E_{XC}^{LSD} + a(E_X^{exact} - E_X^{LSD}) + b\Delta E_X^B + c\Delta E_C^{PW91} \qquad (Eq. 7.54)$$

where *a*, *b* and *c* are semiempirical parameters determining the amount of correction for exact exchange ($\Delta E_X^{exact} = E_X^{exact} - E_X^{LSD}$), GGA-derived exchange ($\Delta E_X^B = E_X^B - E_X^{LSD}$) and correlation energy ($\Delta E_C^{PW91} = E_C^{PW91} - E_C^{LSD}$) corrections respectively. Fitting to experimental data for atomisation energies, ionisation potentials, proton affinities, and total atomic energies (of first and second row systems) led to values of *a* = 0.20, *b* = 0.72 and *c* = 0.81.

The most popular hybrid functional, and indeed the most popular DFT method used today is B3LYP. This uses the above B3 method with the LYP correlation functional rather than PW91:

$$E_{XC}^{B3LYP} = E_{XC}^{LSD} + a\Delta E_X^{exact} + b\Delta E_X^B + c\Delta E_C^{LYP} \qquad (Eq. 7.55)$$

where the same values of *a*, *b*, *c* were adopted.[15]

7.10.4. *meta*-GGA functionals

Another approach to improve the GGA functionals is through the *meta*-GGA functionals. These are a family of functionals which include the next higher order derivative of the kinetic energy density, the Laplacian, in analogy to use of the second derivative in a Taylor expansion. For example, the TPSS exchange correlation functional, developed by Tao, Perdew, Staroverov and Scuseria.[16] This is generalised as

$$E_{XC}^{mGGA}[\rho_\alpha, \rho_\beta] = \int f(\rho_\alpha, \rho_\beta, \nabla\rho_\alpha, \nabla\rho_\beta, \tau_\alpha, \tau_\beta)\, d\vec{r} \qquad (Eq. 7.56)$$

where τ_α is the Laplacian of the electron density for electrons of spin α.

7.10.5. Dispersion-corrected functionals

One of the current challenges in density functional theory is to account for weak non-covalent interactions or dispersion forces. Functionals designed to address this issue include Grimme's DFT-D functionals[17] and Truhlar's M06 suite of functionals.[18] These adopt two different methods; the former uses a semiempirical dispersion correction, which can be added to existing exchange correlation functionals, while the latter consists of four functionals (M06, M06-L, M06-2X and M06-HF) parameterised to account for dispersion.

DFT-D functionals compute energies as

$$E_{DFT-D} = E_{KS-DFT} + E_{disp} \qquad (Eq. 7.57)$$

where E_{KS-DFT} is the total energy given by the chosen density functional and E_{disp} is an empirical dispersion correction, related to the Leonard-Jones potential, and given by

$$E_{disp} = -s_6 \sum_{i=1}^{N_{at}-1} \sum_{j=i+1}^{N_{at}} \frac{C_6^{ij}}{R_{ij}^6} f_{dmp}(R_{ij}) \qquad (Eq. 7.58)$$

Here, s_6 is a scaling factor dependent on the density functional, N_{at} is the number of atoms, C_6^{ij} is the dispersion coefficient for atom pair *ij*, R_{ij} is the interatomic distance and f_{dmp} is a damping function adopted to avoid singularities at $R_{ij} \to 0$. Dispersion coefficients are derived from PBE0 (a so-called parameter free hybrid DFT functional) calculations of ionisation potentials and static dipole polarisabilities.

The M06 family of functionals are all *meta*-GGA-based, but have varying extents of exact exchange (those with exact exchange may therefore be considered hybrid-*meta*-GGA functionals). M06 itself has 27%, M06-2X has double that of M06, at 54%, M06-L has 0% and M06-HF has 100% exact exchange. Each have been developed and parameterised with specific aims in mind, for instance M06-L, which is purely a *meta*-GGA functional, is suggested by the authors for application to transition metal systems, where generally GGA and *meta*-GGA functionals are found to perform better than hybrid functionals. While the M06 functionals perform well, the extent of parameterisation is relatively large, where the M06 and M06-HF functionals employ 36 and 33 parameters respectively.

7.11. Basis sets

Thus far, the dependence of HF and DFT methods upon orbitals has been discussed, however the mathematic form of these orbitals has not. This is provided by basis sets, $\{\eta_\mu\}$, consisting of basis functions, which model orbitals, χ_i. Wavefunction methods are explicitly reliant on the size of the basis set, since $\Psi \approx \Phi_{SD} = \frac{1}{\sqrt{N!}} det\,\{\chi_1(\vec{x}_1)\chi_2(\vec{x}_2) \ldots \chi_N(\vec{x}_N)\}$. The accuracy of wavefunction calculations is therefore maximised as $\{\eta_\mu\} \to \infty$. DFT implementations are, however, less reliant on basis sets size as they are used only to construct the density:

$$\rho(\vec{r}) = \sum_i^N |\varphi_i(\vec{r})|^2 \qquad (Eq. 7.59)$$

The basis functions that most basis sets consist of generally fall into two main groups: Slater-type orbitals (STO) and Gaussian-type orbitals (GTO). Slater-type orbitals are given by

$$\eta^{STO} = Nr^{n-1}e^{-\zeta r}Y_{lm}(\Theta, \phi) \qquad (Eq. 7.60)$$

where N is a normalisation factor, such that $\langle \eta_\mu | \eta_\mu \rangle = 1$, n, l and m are quantum numbers, ζ determines the spatial extent of the orbital and Y is a function describing the angular shape of the orbital. Slater-type orbitals, at first glance, appear to be the ideal choice of basis functions, as they are asymptotically equivalent to atomic orbitals, mimicking exact eigenfunctions of the H atom (and other hydrogenic systems). However, the integrals of Slater-type orbitals, required in calculations of, for example, Coulombic terms, have no analytical form and must be solved numerically. Most quantum chemical software packages therefore adopt GTOs (a notable exception being the ADF code, discussed in the next section), which are expressed as

$$\eta^{GTO} = Nx^l y^m z^n e^{-\alpha r^2} \qquad (Eq. 7.61)$$

where L = $l + m + n$ defines the orbital type (s, p, d, etc.) and the exponent, α determines its size (small α corresponding to a diffuse orbital). The prevalence of GTOs in implementations of wavefunction and density functional codes is due to computational convenience, as the two electron integrals involving GTOs have analytical solutions. The shapes of GTOs do not represent atomic orbitals well, however, as the slope goes to zero as $r \to 0$ (rather than the desired cusp) and as $r \to \infty$ the decay of the GTO is too rapid. This can be overcome, however, by using a linear combination of GTOs to form contracted Gaussian functions (CGF). In this way, a number of primitive Gaussian functions (normally 3-6) can be used to represent a single basis function, where

$$\eta_\tau^{CGF} = \sum_a^A d_{a\tau}\eta_a^{GTO} \qquad (Eq. 7.62)$$

The coefficient, $d_{a\tau}$, provides the ability to give the CGF a shape mimicking that of a single STO, and the contraction overall reduces the number of functions being computed, as the GTOs are fixed following contraction. Typically, however, 3 times more GTOs than STOs are required to describe a chemical system to similar accuracy.

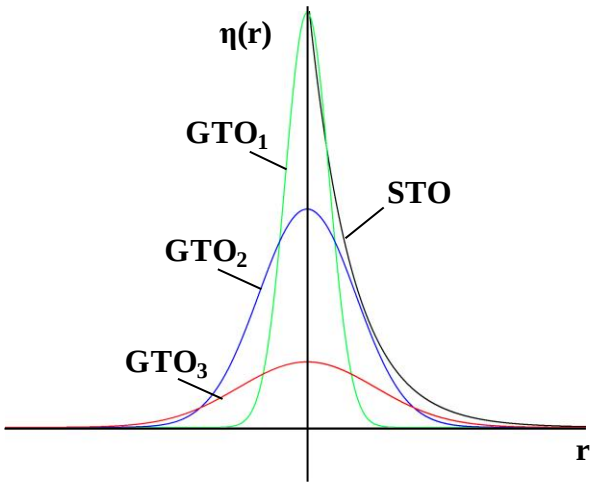

Figure 7.2 – Schematic of STO (black) compared with GTOs (green, blue and red) vs r.

The simplest basis sets, known as minimal basis sets, consist of one function (or one contracted function) per atomic orbital. For example, the STO-3G basis sets use three Gaussian-type orbitals contracted to one CGF to represent an atomic orbital. As an example, use of this basis set in representing methane would be 5 basis functions for carbon (one for each of the 1s, 2s and 2p orbitals) contracted from 15 primitives, and one basis function for each hydrogen atom. The result of using these basis sets is a relatively inflexible set of orbitals and a correspondingly high energy; a larger basis set will always deliver a lower energy, as dictated by the variational principal.

The size of the basis sets are increased by increasing the number of functions used to represent each orbital (typically in the valence shell). The first of these are the "double-zeta", where two functions are used to represent each valence orbital, the term zeta referring to, for historical reasons, the exponent of the STO, despite the use of GTOs. This provides increased flexibility as each CGF can be adjusted independently. Examples of these include the 3-21G and 6-31G basis sets developed by Pople and co-workers.[19] In the former, three primitive GTOs are contracted to a single CGF to represent the core orbitals, whereas in the valence, two CGFs are used, contracted from two and one GTOs respectively. Within the double-zeta framework, the accuracy of the basis sets can be further improved through the addition of polarisation functions[20] and diffuse functions. The former is done by including a function of higher angular momentum in the valence shell (*e.g.* p-orbitals in hydrogen and d-orbitals in carbon), which better allows for orbital overlap. The inclusion of diffuse functions is achieved by the addition of orbitals with small exponents, extending the length of the orbital "tail".

The basis sets adopted throughout most of this thesis are the 6-31G** basis sets, which use 6 GTOs, contracted to a single CGF to represent the core orbitals and two GTOs contracted from three and one primitive GTOs to represent the valence orbitals. The valence is further augmented with polarisation functions.

When computing systems with post 3rd Row elements, especially transition metal systems, where a large number of electrons occupy the core shells, functions known as pseudopotentials may be adopted. These adopt relativistic effective core potentials (RECP) to represent the core electron shells, rather than modelling the core electrons explicitly and use associated basis sets to model the valence. This decreases the calculation cost. Additionally relativistic effects, are modelled by pseudopotentials, but are not by Pople-type basis sets. The pseudopotential adopted in this work is the Stuttgart-Dresden (SDD) pseudopotential.[21]

7.12. Gaussian and Amsterdam Density Functional (ADF) codes

Two quantum chemical software packages, Gaussian03[22] and ADF2009,[23] were used in the work described in this thesis. Gaussian is the most widely-used software used by computational chemists today and includes implementations of wavefunction and DFT methodologies. The Amsterdam Density Functional (ADF) code is less used, however provides some advantages as described in Chapter 4, when the interactions between chemical fragments are to be analysed. ADF a is purely DFT-based software. Perhaps the largest difference between Gaussian and ADF is in the basis sets used. In Gaussian, Gaussian-type orbital basis sets are used, whereas in ADF, Slater-type orbitals are favoured. Additionally, in ADF relativistic effects are accounted for explicitly, rather than implicitly through pseudopotentials.

7.13. Benchmarking of DFT methods with carborane systems

DFT functionals were benchmarked for geometries of *ortho*-, *meta*- and *para*-carborane and [7,9-*nido*-$C_2B_{10}H_{12}]^{2-}$ and [7,10-*nido*-$C_2B_{10}H_{12}]^{2-}$ which represent the most stable minima of neutral and dianionic carboranes (see Chapter 2). First, BP86 energies were computed (using Gaussian03) using double-zeta polarised (6-31G**), triple-zeta polarised (6-311G**) and diffuse triple-zeta polarised (6-311++G**) basis sets. Single point energies at the 6-31G** geometries, as well as energies of fully optimised geometries at each level were computed. The results of this are summarised in Table 7.1, below.

Table 7.1 - Optimised and single point energies of selected carboranes using BP86 with double-zeta, triple-zeta and diffuse triple-zeta basis sets. Energies in kcal mol^{-1} relative to *ortho*-carborane.

	E_{OPT}	E_{SP}	E_{SP}	E_{OPT}	E_{OPT}
Basis Set	6-31G**	6-311G**//6-31G**	6-311++G**//6-31G**	6-311G**	6-311++G**
ortho	0.0	0.0	0.0	0.0	0.0
meta	-15.4	-15.3	-15.3	-15.2	-15.2
para	-18.1	-18.0	-18.0	-18.0	-18.0
[7,9-*nido*]$^{2-}$	38.4	23.5	21.8	23.5	21.7
[7,10-*nido*]$^{2-}$	39.8	24.8	23.1	24.8	23.1

In the neutral carborane species there was very little relative energy difference made on increasing basis set size (from 6-31G** to 6-311G**) nor is there a difference made in using a more diffuse basis set (6-311++G**). Additionally, across all five species, there is no significant change in relative energy achieved over single point by optimising with larger basis sets. The only change was in the energies of the *nido* dianions with respect to the neutral geometries, where the effect of moving from a double-zeta to a triple-zeta basis set was large (*ca*. 15 kcal mol^{-1} in both cases) and the effect of moving to a diffuse basis set was evident, but almost a factor of ten smaller (*ca*. 1.7 kcal mol^{-1}). Importantly, the energies between the two dianions were, however, unchanged.

Table 7.2 - Optimised and single point energies of selected carborane species using a range of pure GGA and hybrid functionals with diffuse triple-zeta basis set, 6-311++G.**

SP Energy / kcal mol^{-1}	BP86	BLYP	OLYP	BPW91	B3LYP	O3LYP	B3PW91
ortho	0.0	0.0	0.0	0.0	0.0	0.0	0.0
meta	-15.3	-15.7	-15.1	-15.3	-16.3	-15.6	-16.0
para	-18.0	-18.4	-17.7	-18.0	-19.1	-18.2	-18.7
[7,9-*nido*]$^{2-}$	21.8	24.3	40.7	29.1	23.7	38.5	31.2
[7,10-*nido*]$^{2-}$	23.1	25.8	42.1	30.4	25.7	40.1	33.0
OPT Energy / kcal mol^{-1}	BP86	BLYP	OLYP	BPW91	B3LYP	O3LYP	B3PW91
ortho	0.0	0.0	0.0	0.0	0.0	0.0	0.0
meta	-15.2	-15.5	-14.9	-15.2	-16.2	-15.4	-15.8
para	-18.0	-18.4	-17.7	-18.0	-19.1	-18.2	-18.6
[7,9-*nido*]$^{2-}$	21.7	24.2	40.7	29.1	23.6	38.5	31.2
[7,10-*nido*]$^{2-}$	23.1	25.8	42.1	30.4	25.7	40.2	33.0

The above data (Table 7.2) summarises the effect of changing DFT functional on single point and optimised energies of neutral and dianionic carborane species. However, no significant differences are seen in the relative energies, except in the difference in energy between dianionic and neutral species. Energy differences for the neutral, *closo*, species ranged between -17.7 to -19.1 kcal mol^{-1}, and between 1.3 and 2.1 kcal mol^{-1} in the dianionic *nido* fragments, **[7,9-*nido*]$^{2-}$** and **[7,10-*nido*]$^{2-}$**. Therefore, no preference in

functional was found for assessing energy differences between geometries of the same charge (the predominant type of comparison made in this work), since ΔΔE (the change in relative energies between functionals) was relatively small.

Relative energies between species of different charges are made occasionally in this thesis, and is the key comparison made in Chapter 3, which considers the oxidation of **[7,9-*nido*]**$^{2-}$ to ***ortho*** through an neutral intermediate geometry. Care was therefore taken to use a reference system in that case and to link the work closely with experiment.

7.14. References

1. E. Schrödinger, *Phys. Rev.*, 1926, **28**, 1049-1070.
2. P. A. M. Dirac, *Proc. R. Soc. Lond. A*, 1929, **123**, 714-733.
3. F. Jensen, *Introduction to Computational Chemistry*, John Wiley & Sons Ltd., Chichester, UK, 1999.
4. a) C. C. J. Roothaan, *Rev. Mod. Phys.*, 1951, **23**, 69-89; b) G. G. Hall, *Proc. R. Soc. Lond. A*, 1951, **205**, 541-552.
5. P. M. W. Gill, *in Encyclopedia of Computational Chemistry, pp. 678-689*, John Wiley and Sons, Chichester, UK, 1998.
6. P. Hohenberg and W. Kohn, *Phys. Rev.*, 1964, **136**, B864-B871.
7. W. Kohn and L. J. Sham, *Phys. Rev.*, 1965, **140**, A1133-A1138.
8. W. Kohn, *Rev. Mod. Phys.*, 1999, **71**, 1253-1266.
9. D. M. Ceperley and B. J. Alder, *Phys. Rev. Lett.*, 1980, **45**, 566-569.
10. A. D. Becke, *Phys. Rev. A*, 1988, **38**, 3098-3100.
11. J. P. Perdew, *Phys. Rev. B*, 1986, **33**, 8822-8824.
12. J. P. Perdew and Y. Wang, *Phys. Rev. B*, 1992, **45**, 13244-13249.
13. C. Lee, W. Yang and R. G. Parr, *Phys. Rev. B*, 1988, **37**, 785-789.
14. A. D. Becke, *J. Chem. Phys.*, 1993, **98**, 5648-5652.
15. P. J. Stephens, F. J. Devlin, C. F. Chabalowski and M. J. Frisch, *J. Phys. Chem.*, 1994, **98**, 11623-11627.
16. a) J. Tao, J. P. Perdew, V. N. Staroverov and G. E. Scuseria, *Phys. Rev. Lett.*, 2003, **91**, 146401-146404; b) J. P. Perdew, J. Tao, V. N. Staroverov and G. E. Scuseria, *J. Chem. Phys.*, 2004, **120**, 6898-6911.
17. a) S. Grimme, *J. Comp. Chem.*, 2004, **25**, 1463-1473; b) S. Grimme, *J. Comp. Chem.*, 2006, **27**, 1787-1799; c) J. Antony and S. Grimme, *Phys. Chem. Chem. Phys.*, 2006, **8**, 5287-5293.
18. Y. Zhao and D. Truhlar, *Theor. Chem. Acc.*, 2008, **120**, 215-241.
19. W. J. Hehre, R. Ditchfield and J. A. Pople, *J. Chem. Phys.*, 1972, **56**, 2257-2261.
20. P. C. Hariharan and J. A. Pople, *Theor. Chim. Acta*, 1973, **28**, 213-222.
21. a) A. Bergner, M. Dolg, W. Kuechle, H. Stoll and H. Preuss, *Mol. Phys.*, 1993, **80**, 1431-1441; b) M. Kaupp, P. v. R. Schleyer, H. Stoll and H. Preuss, *J. Chem. Phys.*, 1991, **94**, 1360-1366; c) M. Dolg, H. Stoll, H. Preuss and R. M. Pitzer, *J. Phys. Chem.*, 1993, **97**, 5852-5859.
22. M. J. Frisch, G. W. Trucks, H. B. Schlegel, G. E. Scuseria, M. A. Robb, J. R. Cheeseman, J. A. Montgomery, Jr., T. Vreven, K. N. Kudin, J. C. Burant, J. M.

Millam, S. S. Iyengar, J. Tomasi, V. Barone, B. Mennucci, M. Cossi, G. Scalmani, N. Rega, G. A. Petersson, H. Nakatsuji, M. Hada, M. Ehara, K. Toyota, R. Fukuda, J. Hasegawa, M. Ishida, T. Nakajima, Y. Honda, O. Kitao, H. Nakai, M. Klene, X. Li, J. E. Knox, H. P. Hratchian, J. B. Cross, V. Bakken, C. Adamo, J. Jaramillo, R. Gomperts, R. E. Stratmann, O. Yazyev, A. J. Austin, R. Cammi, C. Pomelli, J. W. Ochterski, P. Y. Ayala, K. Morokuma, G. A. Voth, P. Salvador, J. J. Dannenberg, V. G. Zakrzewski, S. Dapprich, A. D. Daniels, M. C. Strain, O. Farkas, D. K. Malick, A. D. Rabuck, K. Raghavachari, J. B. Foresman, J. V. Ortiz, Q. Cui, A. G. Baboul, S. Clifford, J. Cioslowski, B. B. Stefanov, G. Liu, A. Liashenko, P. Piskorz, I. Komaromi, R. L. Martin, D. J. Fox, T. Keith, M. A. Al-Laham, C. Y. Peng, A. Nanayakkara, M. Challacombe, P. M. W. Gill, B. Johnson, W. Chen, M. W. Wong, C. Gonzalez and J. A. Pople, *Gaussian 03*, *Revision D.01*, Gaussian, Inc., Wallingford CT, 2004.

23. E. J. Baerends, J. Autschbach, D. Bashford, A. Bérces, F. M. Bickelhaupt, C. Bo, P. M. Boerrigter, L. Cavallo, D. P. Chong, L. Deng, R. M. Dickson, D. E. Ellis, M. van Faassen, L. Fan, T. H. Fischer, C. F. Guerra., A. Ghysels, A. Giammona, S. J. A. van Gisbergen, A. W. Götz, J. A. Groeneveld, O. V. Gritsenko, M. Grüning, F. E. Harris, P. van den Hoek, C. R. Jacob, H. Jacobsen, L. Jensen, G. van Kessel, F. Kootstra, M. V. Krykunov, E. van Lenthe, D. A. McCormack, A. Michalak, M. Mitoraj, J. Neugebauer, V. P. Nicu, L. Noodleman, V. P. Osinga, S. Patchkovskii, P. H. T. Philipsen, D. Post, C. C. Pye, W. Ravenek, J. I. Rodríguez, P. Ros, P. R. T. Schipper, G. Schreckenbach, M. Seth, J. G. Snijders, M. Solà, M. Swart, D. Swerhone, G. te Velde, P. Vernooijs, L. Versluis, L. Visscher, O. Visser, F. Wang, T. A. Wesolowski, E. M. van Wezenbeek, G. Wiesenekker, S. K. Wolff, T. K. Woo, A. L. Yakovlev and T. Ziegler, *ADF2009.01*, SCM, Theoretical Chemistry, Vrije Universiteit, Amsterdam, The Netherlands, 2009.

Unprecedented steric deformation of *ortho*-carborane†

Brian W. Hutton, Fraser MacIntosh, David Ellis, Fabien Herisse, Stuart A. Macgregor,* David McKay, Victoria Petrie-Armstrong, Georgina M. Rosair, Dmitry S. Perekalin, Hugo Tricas and Alan J. Welch*

Received (in Cambridge, UK) 25th June 2008, Accepted 15th August 2008
First published as an Advance Article on the web 19th September 2008
DOI: 10.1039/b810702e

The reduction and subsequent oxidation of *meta*-carboranes containing bulky groups attached to the cage C atoms affords sterically-crowded *ortho*-carboranes with unprecedentedly long C–C connectivities.

Although it has been appreciated for more than 45 years that *ortho*-carborane, 1,2-*closo*-$C_2B_{10}H_{12}$, has a distorted icosahedral geometry,[1] its accurate structure has been determined only relatively recently. In 1996 Davidson, Wade *et al.*[2] used the acidic nature of the carborane CH units to form a supramolecular dimer with hexamethylphosphoramide, locking the CH units in C–H···O hydrogen bonds and so overcoming the disorder that had frustrated previous attempts to obtain an accurate structure crystallographically; the two independent C–C distances measured at 150 K were 1.629(6) and 1.630(6) Å. Later, Rankin and co-workers[3] redetermined the gas phase structure of *ortho*-carborane by electron diffraction, improving on the accuracy of previous determinations[4] and affording C1–C2 1.624(8) Å, in excellent agreement with the results of a parallel computational study, 1.621 Å.

The C–C distance in *ortho*-carborane can be lengthened to *ca.* 1.8 Å by attaching bulky substituents to the cage C atoms,[5] or to nearly 1.9 Å by incorporating the cage C atoms in suitable exopolyhedral cycles.[6] Alternatively, the C–C distance can be extended *electronically* by π-donor substituents at one cage C atom to distances >2 Å,[7] but such species can be argued to have formal skeletal electron counts in excess of the $(2n + 2)$ (n = no. of vertices) normally associated with *closo* species[8] and so bear closer comparison with $(2n + 3)$ carborane radical anions[9] or $(2n + 4)$ *nido* dianions.[8] The electronic causes for long C–C distances in neutral and anionic *ortho*-carboranes as a function of various substituents have been explored computationally.[10] Herein we report unprecedented lengthening of the C1–C2 connectivity of *ortho*-carborane, to 2.15 Å, and related deformation of the carborane icosahedron by intramolecular steric crowding alone.

When *ortho*-carborane is doubly deprotonated and allowed to react with two equivalents of the substituted fulvene **1** (**a**, R = Me) the known,[11] singly-substituted, product 1-$CMe_2(C_5H_5)$-1,2-*closo*-$C_2B_{10}H_{11}$ is afforded on aqueous work-up, implying that the $CMe_2(C_5H_5)$ substituent is already too bulky to 1,2-disubstitute by this approach. However, double deprotonation of *meta*-carborane, 1,7-*closo*-$C_2B_{10}H_{12}$ (**I**), followed by treatment with two equivalents of **1** readily yields the disubstituted species 1,7-$\{CR_2(C_5H_5)\}_2$-1,7-*closo*-$C_2B_{10}H_{10}$ (**2a**, R = Me; **2b**, R_2 = Pm) (Pm = pentamethylene) on work-up (Scheme 1).‡ In **2** there are two isomeric forms of the cyclopentadienyl ring, with the CH_2 function α or β; by ^{1}H NMR spectroscopy the ratio α : β is 1 : 2 for **2a** and 2 : 9 for **2b**. Compounds **2** are converted to the corresponding bis-ferrocenyl species 1,7-$(CR_2Fc)_2$-1,7-*closo*-$C_2B_{10}H_{10}$ **3a** and **3b** {Fc = (η-C_5H_4)Fe(η-C_5H_5)} by standard means.

It is well established that 2e reduction of *meta*-carborane followed by reoxidation affords *ortho*-carborane.[12] Similarly, reduction (Na, THF) then reoxidation of compounds **3** produces the crowded substituted *ortho*-carboranes **4a** and **4b**. By this (indirect) method may be prepared *ortho*-carborane derivatives with substantially sterically demanding groups attached to the two cage carbon atoms that are not possible starting from *ortho*-carborane directly.

Crystallographic study§ of **4a** and **4b** reveals the extent of the steric crowding within. Molecules of **4a** have effective C_2 symmetry about an axis from the mid-point of C1–C2 to the mid-point of B9–B12, with the Me groups of the CMe_2Fc substituents interdigitated about this axis and the Fc units oriented away from both the C1/C2 region and the BH cage vertices. The C1–C2 distance is 1.9378(16) Å. In **4b** (Fig. 1) the CPmFc substituent on C2 has an orientation that corresponds to the CMe_2Fc substituent in **4a**, but the other CPmFc substituent (on C1) has rotated so that its Pm group is side-on to the Pm group on C21 not face-on (which presumably would be untenable). Nevertheless, the C1–C2 distance in **4b** is 2.156(4) Å, easily the longest such distance experimentally recorded for a true $(2n + 2)$ *ortho*-carborane derivative. Further evidence for the severe intramolecular crowding in **4b** is the presence of two H···H distances of 2 Å (H12B···H26B 1.995 Å, H12B···H22A 1.997 Å) and distortion of the Fc group on C211 as a result of the forced orientation of the adjacent Pm group; the C211–C215 ring is tilted at C211 (the C21–C211 bond meets the plane at 11.38°) and the two Cp rings on Fe2 subtend a dihedral angle of 11.65°.

As the cage carbon atoms C1 and C2 are progressively forced apart by steric crowding, the boron atoms to which they are both connected, B3 and B6, are pulled together, the B3···B6 separation reducing from 2.886 Å (average) in *ortho*-carborane,[2] to 2.756 Å in **4a** to 2.663 Å in **4b**. Concomitantly, a smaller,

Department of Chemistry, School of Engineering & Physical Sciences, Heriot–Watt University, Edinburgh, UK EH14 4AS.
E-mail: a.j.welch@hw.ac.uk, s.a.macgregor@hw.ac.uk;
Fax: +44 131 451 3180/+ 44 131 451 3180;
Tel: +44 131 451 3217/+44 131 451 8031

† Electronic supplementary information (ESI) available: Experimental procedures; views of all structures; computational details. CCDC 688279–688284. For ESI and crystallographic data in CIF or other electronic format see DOI: 10.1039/b810702e

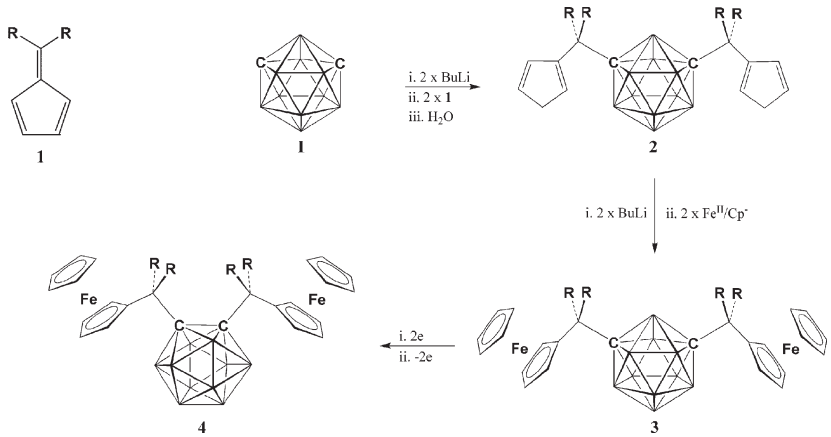

Scheme 1 Synthesis of compounds **2–4** (**a**, R = Me; **b**, R_2 = Pm). For **2** the β,β isomer of the C_5 ring is arbitrarily shown.

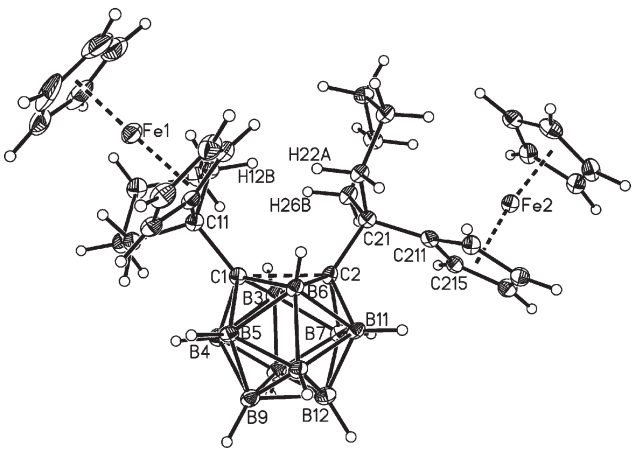

Fig. 1 Perspective view of compound **4b** (50% probability ellipsoids); C1–C2 2.156(4) Å.

second-order, effect is a lengthening of the B3–B8 and B6–B10 connectivities, from (averages¶) 1.766(8) Å in *ortho*-carborane,[2] to 1.794(3) Å in **4a** to 1.818(7) Å in **4b**, to become the longest B–B distances in the last.

Why do the *meta*-carborane derivatives **3** convert to the crowded *ortho*-carborane derivatives **4** on reduction and reoxidation? Why do they not simply reclose on oxidation to the less crowded (and thermodynamically preferred) original *meta*-carborane species? In Fig. 2 are presented the results of a DFT study‖ on the reoxidation of [7,9-*nido*-$C_2B_{10}H_{12}]^{2-}$, the product of 2e reduction of *ortho*- (and *meta*-) carborane. Two-electron oxidation of [7,9-*nido*-$C_2B_{10}H_{12}]^{2-}$ affords a basket-shaped intermediate 4.8 kcal mol^{-1} above the dianion. This intermediate (**INT**) isomerises to *ortho*-carborane *via* a transition state (**TS1**) with an activation energy of +9.2 kcal mol^{-1}, or, alternatively, isomerises to *meta*-carborane *via* an alternative transition state (**TS2**) with an activation energy of +16.7 kcal mol^{-1}. Clearly, therefore, oxidation of [7,9-*nido*-$C_2B_{10}H_{12}]^{2-}$ will preferentially afford *ortho*-carborane over *meta*-carborane. **INT** and **TS2** have been previously characterised by Brown and McKee[13] (*o-m*-INT and *o-m*-TS2, respectively, in ref. 13) in their computational study of the isomerisation of *ortho*- to *meta*-carborane by a non-TFR (TFR = triangular face rotation) pathway, but **TS1** has not previously been reported. It is significant that **TS1** in this

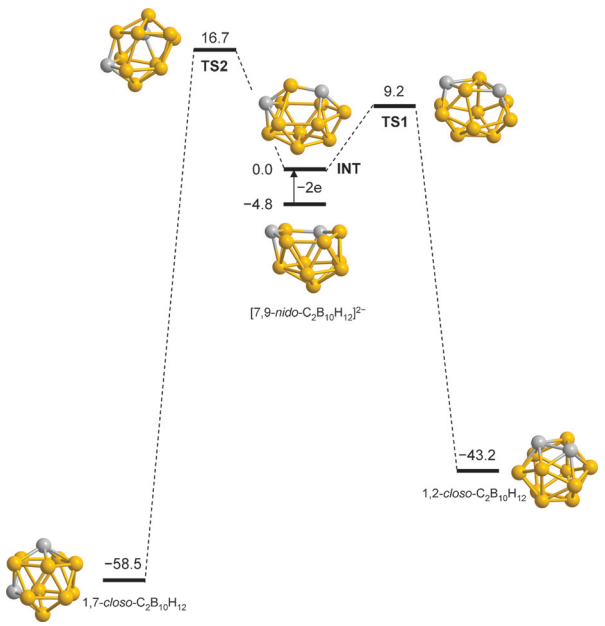

Fig. 2 Computational study of the 2e oxidation of [7,9-*nido*-$C_2B_{10}H_{12}]^2$. All energies in kcal mol^{-1}.

study is considerably more stable than *o-m*-TS1 in McKee's study, and thus that the profile from *ortho*- to *meta*-carborane in Fig. 2, with an overall activation energy of 59.9 kcal mol^{-1}, is computed to be more favourable than McKee's non-TFR pathway and comparable with his TFR route.

The deformation of the C1C2B3B6 diamond of *ortho*-carborane in the sterically crowded compounds **4** is reminiscent of that of the C1C2M3B6 unit in semi-pseudo-*closo*[14] and pseudo-*closo*[15] metallacarboranes which we and others first studied a decade or more ago, but this is the first time such a deformation has been described in carboranes. In pseudo-*closo* metallacarboranes there is a pronounced shift to high frequency of $\langle\delta(^{11}B)\rangle$, the weighted average ^{11}B chemical shift, compared to analogous undistorted species. A similar phenomenon is observed here. $\langle\delta(^{11}B)\rangle$ barely changes on metallation from **2a** to **3a** and **2b** to **3b**, lying between −11 and −12 ppm in all cases. However, as *meta* **3a** converts to *ortho* **4a** $\langle\delta(^{11}B)\rangle$ moves 4.3 ppm to high

frequency, and as *meta* **3b** converts to the even more distorted *ortho* **4b** the average shift is even greater, 6.5 ppm.

In conclusion, by utilising the fact that *meta*-carboranes can be converted to *ortho*-carboranes by successive reduction and reoxidation, we have prepared unprecedented, sterically-crowded, (2*n* + 2) skeletal electron *ortho*-carborane derivatives which relieve that crowding by severe structural deformation. We have previously proposed (derivatised) sterically crowded metallacarboranes as potential vehicles by which to study the mechanism(s) of isomerisation of carboranes experimentally, a possibility which relies on the ability of the crowded species to isomerise at relatively low temperatures. However, results so far[16] indicate only limited agreement between theoretical predictions (on carboranes) and experimental results (on metallacarboranes), possibly linked to the greater electronic complexity of metallacarboranes. It may be that our ability now to prepare severely crowded carboranes could revive interest in this area. In this context it is informative to note that *ortho*-carborane **4b** converts to *meta*-carborane **3b** in refluxing toluene.[17]

We thank the EPSRC for support.

Notes and references

‡ *Selected NMR spectroscopic data* ($CDCl_3$, 298 K): for **2a**: ^{1}H: Major (β) isomer; δ 6.42 (m, 1H, CH), 6.30 (m, 1H, CH), 6.23 (m, 1H, CH), 2.87 (m, 2H, CH_2), 1.31* (s, 6H, CH_3). Minor (α) isomer; δ 6.62, 1H, CH), 6.37 (m, 1H, CH), 6.05 (m, 1H, CH), 2.93 (m, 2H, CH_2), 1.31* (s, 6H, CH_3). Relative integrals given are internal and the ratio of α : β is 1 : 2. * = coincident resonance. $^{11}B\{^1H\}$: δ −6.4 (2B), −12.0 (6B), −14.2 (2B), $\langle\delta(^{11}B)\rangle$ −11.34.

For **2b**: ^{1}H: Major (β) isomer; δ 6.38 (m, 2H, CH), 6.03 (m, 1H, CH), 2.98 (br m, 2H, CH_2 [C_5H_5]), 2.08 (br d, 2H, CH_2 [Pm]), 1.45 (br m, 8H, CH_2 [Pm]). Minor (α) isomer; δ 6.47 (m, 1H, CH), 6.32 (m, 1H, CH), 6.18 (m, 1H, CH), 2.83 (br m, 2H, CH_2 [C_5H_5]), 1.90 (br d, 2H, CH_2 [Pm]), 1.03 (br m, 8H, CH_2 [Pm]). Relative integrals given are internal and the ratio of α : β is 2 : 9. $^{11}B\{^1H\}$: δ −6.6 (2B), −12.3 (6B), −14.7 (2B), $\langle\delta(^{11}B)\rangle$ −11.65.

For **3a**: ^{1}H: δ 4.15 (m, 4H, C_5H_4), 4.10 (s, 10H, Cp), 4.01 (m, 4H, C_5H_4), 1.38 (s, 12H, CH_3). $^{11}B\{^1H\}$: δ −6.7 (2B), −12.2 (6B), −14.1 (2B), $\langle\delta(^{11}B)\rangle$ −11.50.

For **3b**: ^{1}H: δ 4.15 (m, 4H, C_5H_4), 4.07 (s, 10H, Cp), 3.98 (m, 4H, C_5H_4), 2.17 (m, 4H, CH_2), 1.90 (m, 8H, CH_2), 1.59 (m, 6H, CH_2), 1.37 (m, 2H, CH_2). $^{11}B\{^1H\}$: δ −5.9 (2B), −12.4 (8B), $\langle\delta(^{11}B)\rangle$ −11.12.

For **4a**: ^{1}H: δ 4.24 (m, 4H, C_5H_4), 4.15 (m, 4H, C_5H_4), 4.12 (s, 10H, Cp), 1.87 (s, 12H, CH_3). $^{11}B\{^1H\}$: δ −2.6 (2B), −6.6 (4B), −7.9 (2B), −12.6 (2B), $\langle\delta(^{11}B)\rangle$ −7.25.

For **4b**: ^{1}H: δ 4.23 (m, 4H, C_5H_4), 4.19 (m, 4H, C_5H_4), 4.11 (s, 10H, Cp), 2.63 (m, 4H, CH_2), 2.33 (m, 4H, CH_2), 2.24 (m, 4H, CH_2), 1.73 (m, 6H, CH_2), 1.52 (m, 2H, CH_2). $^{11}B\{^1H\}$: δ −0.7 (4B), −3.7 (4B), −14.2 (2B), $\langle\delta(^{11}B)\rangle$ −4.61.

§ *Crystal data*: for **2a** (mixture of α,α; β,β and α,β isomers): $C_{18}H_{32}B_{10}$, M = 356.54, monoclinic, $P2$, a = 14.804(3), b = 10.428(3), c = 27.942(6) Å, β = 100.501(15)°, V = 4241.3(17) Å^3, Z = 8, D_c = 1.117 Mg m^{-3}, μ = 0.055 mm^{-1}, $F(000)$ = 1520. θ_{max} = 24.69°. 7586/59 225 independent reflections (R_{int} = 0.1145), R_1 = 0.0621, wR_2 = 0.1403, S = 1.016 for data with $I > 2\sigma(I)$.

For **2b**: $C_{24}H_{40}B_{10}$ (β,β isomer), M = 436.66, monoclinic, Cc, a = 21.315(4), b = 8.1515(16), c = 15.649(3) Å, β = 112.03(3)°, V = 2520.6(9) Å^3, Z = 4, D_c = 1.151 Mg m^{-3}, μ = 0.058 mm^{-1}, $F(000)$ = 936, θ_{max} = 26.12°. 2424/13998 reflections (R_{int} = 0.0399), R_1 = 0.0582, wR_2 = 0.1515, S = 1.152, $I > 2\sigma(I)$.

For **3a**: $C_{28}H_{40}B_{10}Fe_2$, M = 596.40, triclinic, $P-1$, a = 10.187(2), b = 12.513(3), c = 13.387(2) Å, α = 96.618(8), β = 112.070(7), γ = 112.308(8)°, V = 1395.2(5) Å^3, Z = 2, D_c = 1.420 Mg m^{-3}, μ = 1.060 mm^{-1}, $F(000)$ = 620, θ_{max} = 28.03°. 6521/25611 reflections (R_{int} = 0.0533), R_1 = 0.0411, wR_2 = 0.0893, S = 1.018, $I > 2\sigma(I)$.

For **3b**: $C_{34}H_{48}B_{10}Fe_2$, M = 676.52, triclinic, $P-1$, a = 9.808(8), b = 12.947(10), c = 14.060(11) Å, α = 73.99(2), β = 78.525(15), γ = 70.027(18)°, V = 1601(2) Å^3, Z = 2, D_c = 1.403 Mg m^{-3}, μ = 0.933 mm^{-1}, $F(000)$ = 708, θ_{max} = 28.11°. 7594/11459 reflections (R_{int} = 0.0356), R_1 = 0.0471, wR_2 = 0.0984, S = 1.008, $I > 2\sigma(I)$.

For **4a**: $C_{28}H_{40}B_{10}Fe_2$, M = 596.40, monoclinic, $P2_1/n$, a = 8.7366(14), b = 16.920(3), c = 19.641(3) Å, β = 100.783(7)°, V = 2852.1(8) Å^3, Z = 4, D_c = 1.389 Mg m^{-3}, μ = 1.037 mm^{-1}, $F(000)$ = 1240, θ_{max} = 32.63°. 9673/71 682 reflections (R_{int} = 0.0462), R_1 = 0.0323, wR_2 = 0.0760, S = 1.034, $I > 2\sigma(I)$.

For **4b**: $C_{34}H_{48}B_{10}Fe_2$, M = 676.52, monoclinic, $P2_1/n$, a = 15.1029(17), b = 15.4587(19), c = 15.6930(18) Å, β = 118.556(6)°, V = 3218.2(7) Å^3, Z = 4, D_c = 1.396 Mg m^{-3}, μ = 0.928 mm^{-1}, $F(000)$ = 1416, θ_{max} = 25.14°. 5648/47 044 reflections (R_{int} = 0.0885), R_1 = 0.0492, wR_2 = 0.1275, S = 1.053, $I > 2\sigma(I)$.

¶ E.s.d.'s of the mean of N independent observations given by the expression $\sigma^2 = (\sigma_1^2 + \sigma_2^2)$ if N = 2, or $\sigma^2 = \{\sum_{i=1}^{i=N}(\chi^i - \bar{\chi})^2\}/(N-1)$ where χ^i is the ith and $\bar{\chi}$ the mean value if $N > 2$.

‖ Calculations run with Gaussian 03 with the BP86 functional and 6-31G** basis sets. See ESI† for full details.†

1 T. L. Heying, J. W. Ager, Jr, S. L. Clark, D. J. Mangold, H. L. Goldstein, M. Hillman, R. J. Polak and J. W. Szymanski, *Inorg. Chem.*, 1963, **2**, 1089.

2 M. G. Davidson, T. G. Hibbert, J. A. K. Howard, A. Mackinnon and K. Wade, *Chem. Commun.*, 1996, 2285.

3 A. R. Turner, H. E. Robertson, K. B. Borisenko, D. W. H. Rankin and M. A. Fox, *Dalton Trans.*, 2005, 1310.

4 R. K. Bohn and M. D. Bohn, *Inorg. Chem.*, 1971, **10**, 350, and references therein.

5 *E.g.* Y.-J. Lee, S.-J. Kim, C.-H. Kang, J. Ko, S. O. Kang and P. J. Carroll, *Organometallics*, 1998, **17**, 1109.

6 (*a*) *E.g.* F. Teixidor, C. Viñas, J. Rius, C. Miravitlles and J. Casabó, *Inorg. Chem.*, 1990, **29**, 149; (*b*) D.-H. Kim, J. Ko, K. Park, S. Cho and S. O. Kang, *Organometallics*, 1999, **18**, 2738.

7 (*a*) D. A. Brown, W. Clegg, H. M. Colquhoun, J. A. Daniels, I. R. Stephenson and K. Wade, *J. Chem. Soc., Chem. Commun.*, 1987, 889; (*b*) T. D. Getman, C. B. Knobler and M. F. Hawthorne, *Inorg. Chem.*, 1992, **31**, 101; (*c*) K. Chui, H.-W. Li and Z. Xie, *Organometallics*, 2000, **19**, 5447; (*d*) L. A. Boyd, W. Clegg, R. C. B. Copley, M. G. Davidson, M. A. Fox, T. G. Hibbert, J. A. K. Howard, A. Mackinnon, R. J. Peace and K. Wade, *Dalton Trans.*, 2004, 2786.

8 K. Wade, *J. Chem. Soc. D*, 1971, 792.

9 M. A. Fox, C. Nervi, A. Crivello and P. J. Low, *Chem. Commun.*, 2007, 2372.

10 J. M. Oliva, N. L. Allan, P. v. R. Schleyer, C. Viñas and F. Teixidor, *J. Am. Chem. Soc.*, 2005, **127**, 13538.

11 E. Hong, Y. Kim and Y. Do, *Organometallics*, 1998, **17**, 2933.

12 (*a*) G. B. Dunks, R. J. Wiersema and M. F. Hawthorne, *J. Am. Chem. Soc.*, 1973, **95**, 3174; (*b*) L. I. Zakharkin, V. N. Kalinin and L. S. Podvisotskaya, *Bull. Acad. Sci. USSR, Div. Chem. Sci.*, 1966, 1444.

13 C. A. Brown and M. L. McKee, *J. Mol. Model.*, 2006, **12**, 653.

14 (*a*) *E.g.* Rh. Ll. Thomas and A. J. Welch, *J. Chem. Soc., Dalton Trans.*, 1997, 631; (*b*) F. Teixidor, C. Viñas, M. A. Flores, G. M. Rosair, A. J. Welch and A. S. Weller, *Inorg. Chem.*, 1998, **37**, 5394.

15 (*a*) *E.g.* Z. G. Lewis and A. J. Welch, *J. Organomet. Chem.*, 1992, **430**, C45; (*b*) P. T. Brain, M. Bühl, J. Cowie, Z. G. Lewis and A. J. Welch, *J. Chem. Soc., Dalton Trans.*, 1996, 231; (*c*) A. J. Welch and A. S. Weller, *Inorg. Chem.*, 1996, **35**, 4548; (*d*) A. J. Welch, Steric Effects in Metallacarboranes, , in *Metal Clusters in Chemistry*, ed. P. Braunstein, L. A. Oro and P. R. Raithby, Wiley-VCH, Weinheim Germany, 1999, p. 26; (*e*) F. Teixidor, M. A. Flores, C. Viñas, R. Sillanpää and R. Kivekäs, *J. Am. Chem. Soc.*, 2000, **122**, 1963; (*f*) A. V. Safronov, F. M. Dolgushin, P. V. Petrovskii and I. T. Chizhevsky, *Organometallics*, 2005, **24**, 2964; (*g*) L. S. Alekseev, F. M. Dolgushin, A. A. Korlyukov, I. A. Godovikov, E. V. Vorontsov and I. T. Chizhevsky, *Organometallics*, 2007, **26**, 3868.

16 (*a*) *E.g.* S. Robertson, D. Ellis, G. M. Rosair and A. J. Welch, *Appl. Organomet. Chem.*, 2003, **17**, 518; (*b*) S. Robertson, D. Ellis, G. M. Rosair and A. J. Welch, *J. Organomet. Chem.*, 2003, **680**, 286; (*c*) S. Robertson, R. M. Garrioch, D. Ellis, T. D. McGrath, B. E. Hodson, G. M. Rosair and A. J. Welch, *Inorg. Chim. Acta*, 2005, **358**, 1485.

17 B. W. Hutton and A. J. Welch, unpublished results.

Adducts of the supraicosahedral stannacarborane 1,6-Me_2-4,1,6-*closo*-$SnC_2B_{10}H_{10}$; synthetic, structural and computational studies†

Peter D. Abram, David McKay, David Ellis, Stuart A. Macgregor,* Georgina M. Rosair, Rodrigo Sancho and Alan J. Welch*

Received 1st December 2008, Accepted 13th January 2009
First published as an Advance Article on the web 18th February 2009
DOI: 10.1039/b821417d

The 13-vertex stannacarborane 1,6-Me_2-4,1,6-*closo*-$SnC_2B_{10}H_{10}$ reacts with the Lewis bases 2,2′-bipyridine, 1,10-phenanthroline, 4,4′-dimethybipyridine and 4,4′-diphenylbipyridine, in toluene, to precipitate bright-yellow adducts 1,6-Me_2-4-(L_2)-4,1,6-*closo*-$SnC_2B_{10}H_{10}$ (**1–4**, respectively) in good yield. Compounds **1–3** have been characterised by NMR spectroscopy and single-crystal X-ray diffraction. Compound **4** is somewhat less stable in solution but has also been studied crystallographically. Adduct formation retains the docosahedral structure of 1,6-Me_2-4,1,6-*closo*-$SnC_2B_{10}H_{10}$ but is accompanied by polyhedral distortion arising from significant increases in Sn-C and Sn-B2 distances. This distortion is described in terms of either a *slipping* or *hinging* of the {SnL_2} fragment. In the molecular structures of **1–4** it is evident that the Sn lone pair of electrons is stereochemically active since the L_2 ligand is clearly inclined with respect to the polyhedron. Both the inclination and orientation of L_2 are rationalised by the results of DFT calculations on 4,1,6-*closo*-$SnC_2B_{10}H_{12}$. Calculations on models of the adducts **1**, **3** and **4** reproduce the structural distortion that accompanies adduct formation, but appear to underestimate somewhat the strength of Sn-L_2 bonding.

Introduction

The icosahedral stannacarboranes 1,2-R_2-3,1,2-*closo*-$SnC_2B_9H_9$ (R = H[1] or Me[2]) and their pentagonal bipyramidal analogue 2,3-($SiMe_3$)$_2$-1,2,3-*closo*-$SnC_2B_4H_4$[3] have long been recognised as interesting molecules in that, despite the presence of a lone pair of electrons on the Sn atom, they function as Lewis acids, giving rise to adducts with classic Lewis bases *eg.* pyridine or 2,2′-bipyridine (bipy). Moreover, although the position and orientation of the ligating atoms in these adducts implies that the Sn lone pair is fully *stereochemically active* it appears to be *chemically inert* since these stannacarboranes show no Lewis base properties towards classic acceptors like BH_3.

Interest in icosahedral stannacarboranes has recently been enhanced by work on the related stannaborate [*closo*-$SnB_{11}H_{11}]^{2-}$,[4] shown by Wesemann and co-workers to be an excellent Lewis base to a wide variety of transition-metal fragments,[5] and the intermediate monocarbon species [1,2-*closo*-$SnCB_{10}H_{11}]^-$,[6] which appears to have both σ-donor and π-acceptor properties. Very recently the systematic changes in the donor/acceptor properties of the series [*closo*-$SnB_{11}H_{11}]^{2-}$ [1,2-*closo*-$SnCB_{10}H_{11}]^-$ and 3,1,2-*closo*-$SnC_2B_9H_{11}$ have been investigated by Fox, Marder and Wesemann using DFT calculations.[7]

A few years ago we reported the synthesis and characterisation of 4,1,6-*closo*-$SnC_2B_{10}H_{12}$ and 1,6-Me_2-4,1,6-*closo*-$SnC_2B_{10}H_{10}$, the first supraicosahedral p-block metallacarboranes.[8] We were interested to discover if the Lewis acid behaviour of the smaller stannacarboranes extended also to these 13-vertex systems, and here describe the synthesis and structures of the adducts 1,6-Me_2-4-(L_2)-4,1,6-*closo*-$SnC_2B_{10}H_{10}$ for L_2 = bipy, 1,10-phenanthroline (*o*-phen), 4,4′-dimethyl-2,2′-bipyridine (Me_2bipy) and 4,4′-diphenyl-2,2′-bipyridine (Ph_2bipy). We also report DFT calculations on 4,1,6-*closo*-$SnC_2B_{10}H_{12}$ and its adducts which successfully reproduce the distortions in these species and rationalise both the orientation and the inclination of the chelating ligand in these adducts, complementing the computational study of Fox *et al.*[7]

Results and discussion

Synthesis and spectroscopy

The 13-vertex stannacarborane 1,6-Me_2-4,1,6-*closo*-$SnC_2B_{10}H_{10}$ (**I**, see line diagram for numbering) readily reacts with bipy, *o*-phen, Me_2bipy and Ph_2bipy, in toluene, to precipitate the bright-yellow adducts 1,6-Me_2-4-(bipy)-4,1,6-*closo*-$SnC_2B_{10}H_{10}$ (**1**), 1,6-Me_2-4-(*o*-phen)-4,1,6-*closo*-$SnC_2B_{10}H_{10}$ (**2**), 1,6-Me_2-4-(Me_2bipy)-4,1,6-*closo*-$SnC_2B_{10}H_{10}$ (**3**) and 1,6-Me_2-4-(Ph_2bipy)-4,1,6-*closo*-$SnC_2B_{10}H_{10}$ (**4**) in good yield (57–80%).

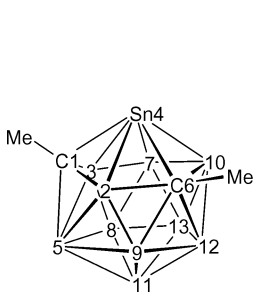

I

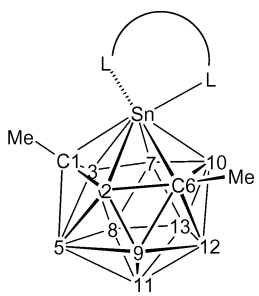

1 - 4

Department of Chemistry, School of Engineering & Physical Sciences, Heriot-Watt University, Edinburgh, UK EH14 4AS. E-mail: a.j.welch@hw.ac.uk, s.a.macgregor@hw.ac.uk; Fax: +44 (0)131 451 3180; Tel: +44 (0)131 451 3217; Tel: +44 (0)131 451 8031

† CCDC reference numbers 697455–697458. For crystallographic data in CIF or other electronic format see DOI: 10.1039/b821417d

Compounds **1–3** are analytically pure by C, H and N microanalysis without the need for chromatography, and appear to be stable for reasonable periods as solids in air and as tetrahydrofuran (THF) or CH_2Cl_2 solutions. They have been characterised by IR spectroscopy, ^{1}H and ^{11}B NMR spectroscopies, mass spectrometry and single-crystal X-ray diffraction studies. Compound **4** is less stable, and reliable microanalysis could not be obtained. Equally, NMR spectra of solutions of **4** always contained evidence of significant decomposition. Nevertheless, the structural identity of **4** was unequivocally established by a crystallographic study.

The IR spectra of **1–4** as CH_2Cl_2 solutions all show ν_{max} 2520–2530 cm^{-1} (B–H). Mass spectra of **1–3** do not yield the molecular ion but simply show envelopes centred on 291 and 171 corresponding to M-L_2 and M-{SnL_2}, respectively, as well as a peak for the appropriate chelating ligand (*i.e.* M-{$SnMe_2C_2B_{10}H_{10}$}).

Only the *o*-phen ligand is conformationally predisposed to chelation and consequently all the ^{1}H NMR resonances of **2** in the aromatic region of the spectrum are simply shifted to low frequency by *ca.* 0.3 ppm relative to those of the free ligand. Both the (room temperature) ^{1}H and ^{11}B NMR spectra of **1–3** in CD_2Cl_2 show evidence for an intramolecular fluctional process, given the asymmetric structures revealed by crystallographic study (*vide supra*). Thus the ^{11}B{^{1}H} spectra have a 2:1:3:1:3 pattern of resonances (high frequency to low frequency) between δ +8 and –9 (all resonances becoming doublets on retention of proton coupling, $^1J_{BH}$ 117–156 Hz), whilst in the ^{1}H spectrum is only a single resonance assigned to the cage-bound CH_3 groups (δ 2.5–3.0) in addition to unique resonances for only half the L_2 ligand (for L_2 = Me_2bipy we did not distinguish which CH_3 resonance was due to the bipy ligand and which to the cage). Thus we assume that, in solution at room temperature, **1–3** are C_s-symmetric on the NMR timescale, *via* the same double diamond-square-diamond process we have previously described for **I**.[8] This would afford an idealised 2:2:2:1:1:1:1 pattern in the ^{11}B spectra, from which the observed pattern is easily obtained by two 2 + 1 co-incidences.

Molecular structures

The structures of the adducts **1–4** have all been established by single-crystal diffraction studies. Similar perspective views of the four molecules are presented in Fig. 1–4, respectively, and Table 1 lists selected molecular parameters (first entries, normal type).

In all cases the basic docosahedral structure of the cage of **I** has been retained on coordination of the L_2 ligand, but with some distortion. Notably, addition of the bipy, *o*-phen, Me_2bipy and Ph_2bipy ligands results in increased (with one apparent exception, Sn4-B7 in **3**) Sn-cage atom distances, most dramatically Sn4-C1 (2.41 to 2.69–2.75 Å), Sn4-B2 (2.64 to 3.00–3.06 Å) and Sn4-C6 (2.67 to 3.02–3.17 Å). Increases in Sn4-B10 and Sn4-B3 are smaller (*ca.* 0.15 Å) and Sn4-B7 remains essentially unchanged. For these reasons, the Sn4-C1,B2,C6 connectivities in Fig. 1–4 are shown as dashed lines only.

Distortions of icosahedral and pentagonal bipyramidal stannacarborane polyhedra on the addition of Lewis bases to the Sn atom have been noted previously. Thus, on moving from 2,3-$(SiMe_3)_2$-1,2,3-*closo*-$SnC_2B_4H_4$ to 1,1-bipy-2,3-$(SiMe_3)_2$-1,2,3-*closo*-$SnC_2B_4H_4$ the Sn-C distances increase from *ca.* 2.50 Å to >2.70 Å.[3b,c] Equally, although the icosahedral species 1,2-Me_2-3,1,2-*closo*-$SnC_2B_9H_9$ has also not been crystallographically characterised, its structure has recently been computed in C_s symmetry resulting in Sn-C *ca.* 2.55 Å,[7] considerably shorter than the measured Sn-C distances, 2.86 and 2.88 Å, in 1,2-Me_2-3-bipy-3,1,2-*closo*-$SnC_2B_9H_9$.[2] These structural changes have previously

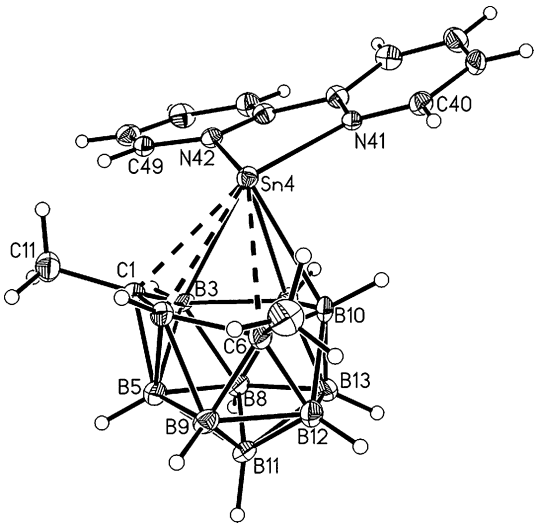

Fig. 1 Perspective view of compound **1**. Thermal ellipsoids are drawn at 50% probability level, except for H atoms.

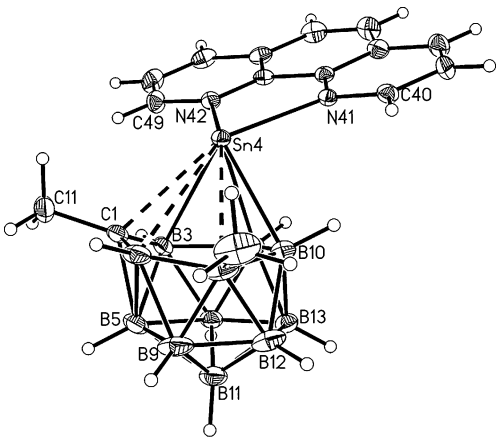

Fig. 2 Perspective view of compound **2**. Thermal ellipsoids as for Fig. 1.

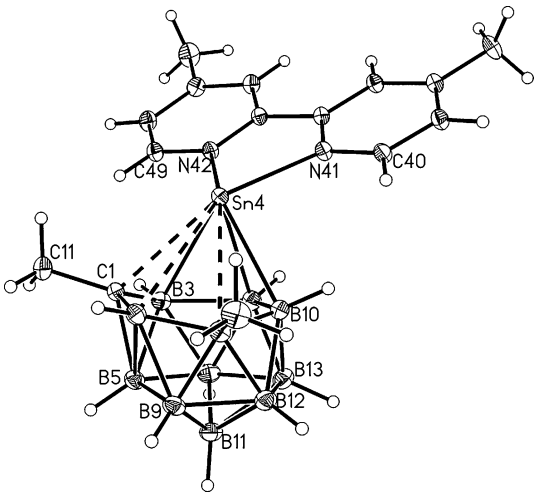

Fig. 3 Perspective view of compound **3**. Thermal ellipsoids as for Fig. 1.

Table 1 Normal type—selected molecular parameters (Å, °) in **I** and compounds **1–4** by crystallographic analysis. Italics—selected molecular parameters (Å, °) in the related model compound **A–D** by DFT calculation

	I/A	1/B	2	3/C	4/D
Sn4-C1	2.411(3) *2.416*	2.717(3) *2.582*	2.725(3)	2.7502(14) *2.594*	2.692(7) *2.595*
Sn4-B2	2.639(4) *2.652*	3.033(4) *2.923*	3.027(3)	3.0642(17) *2.937*	3.008(8) *2.937*
Sn4-C6	2.672(4) *2.700*	3.173(4) *2.992*	3.064(3)	3.1182(15) *3.005*	3.025(7) *3.005*
Sn4-B10	2.425(4) *2.433*	2.620(4) *2.541*	2.547(3)	2.5561(17) *2.548*	2.530(9) *2.547*
Sn4-B7	2.453(4) *2.471*	2.471(4) *2.468*	2.463(3)	2.4135(17) *2.471*	2.473(11) *2.469*
Sn4-B3	2.592(4) *2.634*	2.717(4) *2.689*	2.750(3)	2.7215(17) *2.695*	2.7552(7) *2.694*
Sn4-N41		2.389(3) *2.638*	2.425(2)	2.3854(12) *2.619*	2.374(6) *2.618*
Sn4-N42		2.384(3) *2.593*	2.397(2)	2.3611(13) *2.573*	2.347(7) *2.570*
Δ	0.274 *0.287*	0.651 *0.517*	0.582	0.665 *0.525*	0.549 *0.525*
Δ_Δ		0.377 *0.230*	0.308	0.391 *0.238*	0.275 *0.238*
z	3.407 *3.419*	3.689 *3.596*	3.665	3.656 *3.606*	3.650 *3.605*
θ		21.2 *27.2*	20.6	26.4 *26.6*	19.0 *26.8*

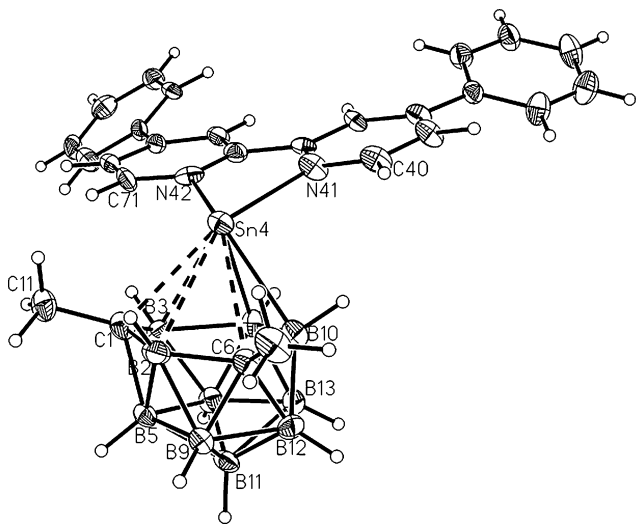

Fig. 4 Perspective view of compound **4**. Thermal ellipsoids as for Fig. 1.

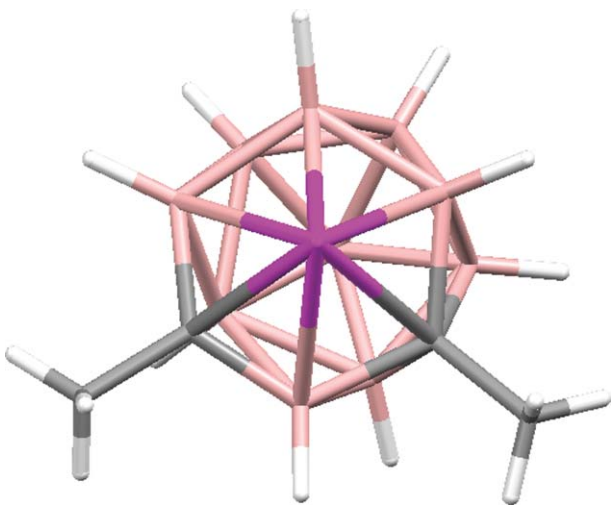

Fig. 5 View of **I** perpendicular to the best plane through atoms B5, B9, B12, B13 and B8.

been described in terms of a *slip distortion*. Slip distortions, in which there is a pronounced lateral movement of the metal atom across the carborane ligand face, in a direction away from the cage carbon atoms, have been studied theoretically for the $L_2SnC_2B_4$ system[9] but are perhaps best known in icosahedral metallacarboranes of the type $L_2PtC_2B_9$.[10]

In such icosahedral metallacarboranes, of either the 3,1,2-MC_2B_9, 2,1,7-MC_2B_9 or 2,1-MCB_{10} isomeric type, it is usual to quantify the slip distortion, Δ, with respect to the centroid of the lower pentagon of $5 \times$ B atoms.[10] For the docosahedral compound **I** and adducts **1–4** the appropriate analogous reference plane is B5B9B12B13B8. As is evident from Table 1, the Sn atom in **I** is already displaced from a position above the centroid of this B_5 pentagon, having $\Delta = 0.27$ Å, but on formation of the adducts **1–4** this slipping parameter increases to between 0.55 and 0.67 Å. The increase in slip with respect to that in **I** is defined as Δ_Δ. The greatest slip is in the Me_2bipy compound **3** and the smallest is in the Ph_2bipy derivative **4**, *i.e.* the stronger the Lewis base the weaker the Sn–cage interactions (note, however, that the Sn-N distances do not easily fit with this simple description). Fig. 5 and Fig. 6 are projections onto the best (least-squares) plane through the lower pentagon of **I** and **1** (similar views for **2–4** are essentially equivalent to that for **1**) and clearly show that the direction of increased slippage is towards a position above B7, fully consistent with the substantial increases noted in Sn4-C1, Sn4-B2 and Sn4-C6 distances. However, since there is also a (smaller) increase in the Sn4-B10 and Sn4-B3 connectivities on adduct formation, and Sn4-B7 is effectively unchanged, an alternative description of the structural change accompanying L_2 addition to **I** would be a *hinge distortion* (pivoting about an axis parallel to B3-B10 and passing through B7) rather than a slip distortion. With increased hinging the Sn atom is located further above the reference B_5 plane. We define z as the perpendicular displacement of Sn above the least-squares plane through atoms B5B9B12B13B8 and note that z increases from 3.40 Å in **I** to 3.65–3.69 Å in **1–4**.

The bipy ligand in **1** is significantly twisted about its central C–C bond (dihedral angle between NC_5 planes 15.2°) whereas much less twist is evident in the Me_2bipy ligand in **3** and the Ph_2bipy ligand in **4** (dihedral angles 0.3 and 4.5°, respectively). The *o*-phen ligand in **2**, of course, is required to have co-planar NC_5 rings. In **2**, **3** and **4** we note significantly different Sn-N distances, always shorter to N42, whereas the Sn-N distances in **1** are effectively identical. That Sn-N42 is shorter than Sn-N41 may be rationalised by fact that N42 is almost exactly *trans* to C6 whilst N41 is *trans* to the C1-B2 edge and the relative *trans* influences of B and C atoms in carborane ligands (caused by the localisation of the frontier orbitals of *nido* carboranes

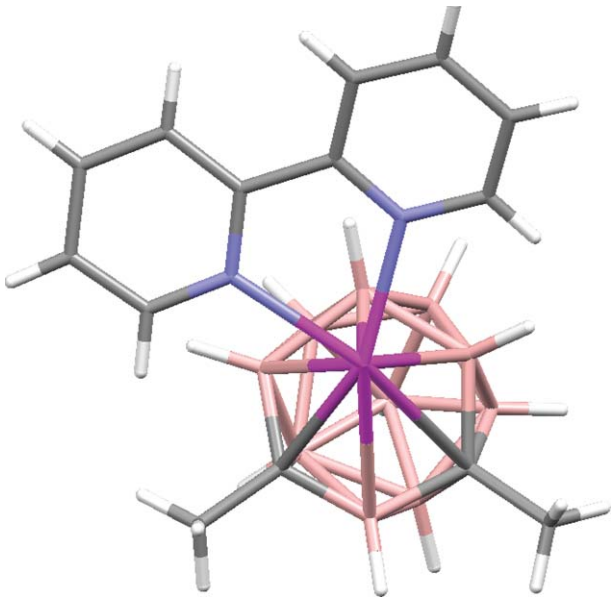

Fig. 6 View of **1** perpendicular to the best plane through atoms B5, B9, B12, B13 and B8.

away from the C atoms in the open face).[10b] Although initially established for icosahedral metallacarboranes the same arguments can clearly be extended to supraicosahedral species, as already noted for other 4,1,6-MC_2B_{10} compounds 4-dppe-4,1,6-*closo*-$NiC_2B_{10}H_{10}$ [dppe = 1,2-bis(diphenylphosphino)ethane],[11] [4-(η-cod)-4,1,6-*closo*-$RhC_2B_{10}H_{10}]^-$ (cod = 1,5-cyclooctadiene)[12] and 4,4-$(PMe_2Ph)_2$-4,1,6-*closo*-$PtC_2B_{10}H_{10}$,[13] as well as for compounds **2–4** herein. We assume that the identical Sn-N distances in **1** are related to the twist of the bipy ligand.

In compounds **1–4** the L_2 ligands are clearly inclined with respect to the carborane cage. We quantify this inclination by θ, the dihedral angle between the least-squares planes through B5B9B12B13B8 and Sn4N41CCN42. Values of θ are given in Table 1. As is evident from these, and clearly visible from comparison of Fig. 1–4, θ is greatest for **3**, least for **4** and intermediate for **1** and **2**. There therefore appears to be a direct correlation between Δ and θ.

Computational studies

In an attempt to reproduce and understand some of the structural features of compounds **1–4** we have performed DFT calculations on 4,1,6-*closo*-$SnC_2B_{10}H_{12}$ (**A**, a model for **I**), its bipy adduct **B** (a model for **1**), its Me_2bipy adduct **C** (a model for **3**) and its Ph_2bipy adduct **D** (a model for **4**).

The frontier molecular orbitals of **A** are shown in Fig. 7. Orbital energies of the HOMO and LUMO (–6.72 and –3.25 eV, respectively) are consistent with those previously calculated.[7] Because model compound **A** lacks symmetry there are significant contributions from several atoms to all the frontier orbitals, but nevertheless it is evident that the HOMO is essentially a Sn lone pair outward pointing over B2. The LUMO, LUMO + 1 and LUMO + 2 also have major contributions from the Sn atom, and one can rationalise the orientation of L_2 ligands in compound **1–4** most easily from the form and direction of LUMO and LUMO + 2.

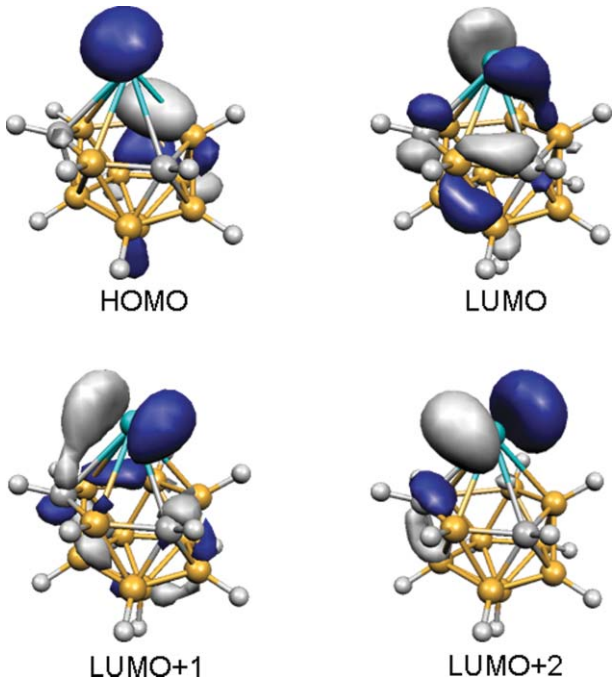

Fig. 7 The frontier molecular orbitals of **A**, 4,1,6-*closo*-$SnC_2B_{10}H_{12}$, by DFT calculation.

The Sn lone pair in **A** is retained as the HOMO of **B**, as is clearly shown in Fig. 8. In Fig. 9 is presented a view of the optimised structure of **B** projected onto the B5B9B12B13B8 reference plane, and comparison of this with Fig. 6, the equivalent view of **1**, confirms that the calculations faithfully reproduce the overall structure and conformation. Similar views of **C** and D show essentially equivalent structural features.

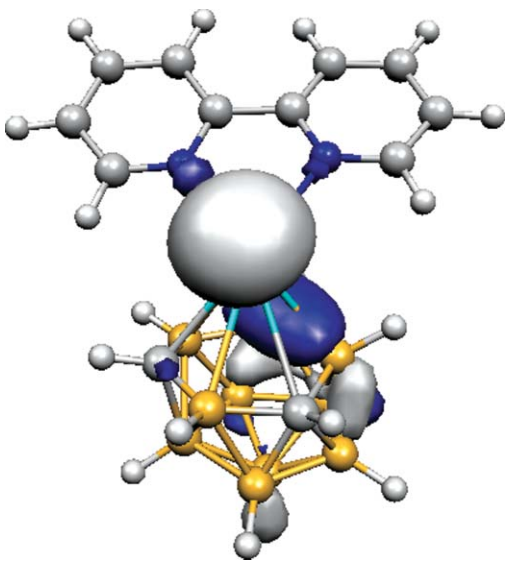

Fig. 8 The HOMO of **B**, 4-(bipy)-4,1,6-*closo*-$SnC_2B_{10}H_{12}$, by DFT calculation.

Molecular parameters arising from the computational studies are given in Table 1 (second entries, italicised type) alongside the appropriate experimental values. For **I** (experimental) *vs* **A** (computational) there is excellent agreement in terms of Sn-cage

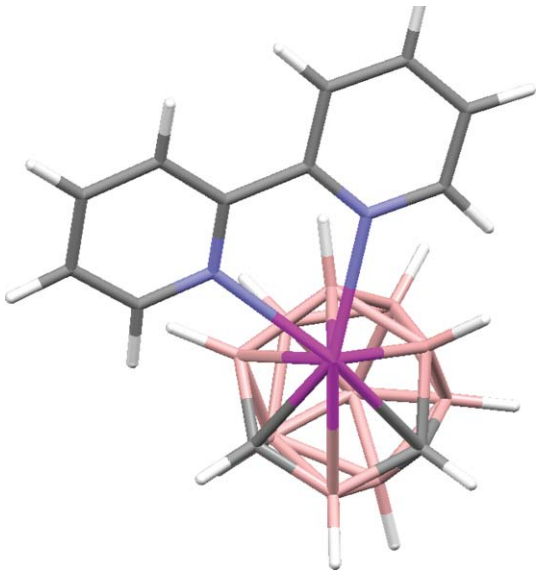

Fig. 9 View of **B** perpendicular to the best plane through atoms B5, B9, B12, B13 and B8. Compare with Fig. 6.

distances and the related parameters Δ and z. Note also that the computed Sn-cage distances here correspond very well with those of Fox *et al.*[7] For the computational adducts **B**, **C** and **D** (models for the real adducts **1**, **3** and **4**, respectively) there appears to be a systematic underestimation of the strength of the Sn-L_2 bonding; Sn-N distances are 0.2–0.25 Å too long (although the relative shortness of Sn-N42 over Sn-N41 is correctly reproduced) whilst, to compensate, Sn-cage distances are generally too short (minor exceptions being Sn-B7 in **C** and Sn-B10 in **D**). The underestimation of the Sn-L_2 bonding is further reflected in smaller Δ (and, hence, Δ_4) and z values for the model adducts relative to their respective real molecules. Computation also reveals no perceptible difference between Me_2bipy model **C** and the Ph_2bipy model **D** (corresponding molecular parameters within 0.003 Å or 0.02°), but, given that the calculations appear to poorly model the Sn-L_2 bonding, it is not surprising that subtle variations in the nature of the bipy ligand are not reproduced.

To assess the origin of these geometric deviations in the Sn-L_2 adducts, further calculations were performed on **B**, **C** and **D** where the effects of both the functional (B3LYP, TPSS), the basis set (triple-ζ or additional diffuse functions) and the methodology (MP2/6-31G**) employed were tested. In no case was a significant change in geometry computed. Instead the longer computed Sn-L_2 distances appear to reflect the relatively soft potential associated with the Sn-N bonds. Reoptimising **B** with the Sn-N distances fixed at the values determined experimentally in **2** gave a structure only 2.8 kcal mol^{-1} higher in energy than fully optimised **B**. Thus the geometries of these Sn-L_2 adducts may be sensitive to subtle environmental effects and the difficulty in reproducing the Sn-N bonds may arise by comparing a gas-phase optimised structure with experimental data derived from the solid state.

Conclusions

These studies have shown that the supraicosahedral stannacarborane 1,6-Me_2-4,1,6-*closo*-$SnC_2B_{10}H_{10}$ functions as a Lewis acid towards bipy, *o*-phen and substituted bipy in a manner similar to related icosahedral and sub-icosahedral species. In all cases adduct formation results in significantly increased *slipping* or *hinging* of the Sn atom, resulting from dramatic increases in Sn-C and Sn-B2 distances, and there appears to be a correlation between the Lewis base strength of the ligand and the extent of the molecular distortion. DFT calculations on model compounds successfully reproduce the general structural features of these adducts.

Experimental

Synthesis

Experiments were performed under dry, oxygen-free N_2, using standard Schlenk techniques with some subsequent manipulations in the open laboratory. All solvents were freshly distilled from the appropriate drying agents under nitrogen immediately before use [CH_2Cl_2 and CH_3CN; CaH_2: THF, diethylether, toluene and light petroleum (bp 40–60 and 60–80 °C); sodium wire] or were stored over 4 Å molecular sieves and were degassed (3 × freeze–pump–thaw cycles) before use. IR spectra were recorded from CH_2Cl_2 solutions, using a Perkin-Elmer Spectrum RX FT spectrophotometer. NMR spectra at 400.1 MHz (^{1}H) or 128.4 MHz (^{11}B) were recorded on a Bruker DPX-400 spectrometer at ambient temperature from CD_2Cl_2 solutions. EI mass spectrometry was carried out using a Kratos Concept mass spectrometer. Elemental analyses were determined by the departmental service. 1,6-Me_2-4,1,6-*closo*-$SnC_2B_{10}H_{10}$ was synthesised according to ref. 8. All other reagents and solvents were supplied commercially.

1,6-Me_2-4-(bipy)-4,1,6-*closo*-$SnC_2B_{10}H_{10}$ (1). A solution of 1,6-Me_2-4,1,6-*closo*-$SnC_2B_{10}H_{10}$ (72 mg, 0.25 mmol) in dry, degassed, toluene (10 mL) was added to a dry, degassed, toluene solution (10 mL) of 2,2′-bipyridine (47 mg, 0.30 mmol). The resulting yellow suspension was stirred for 24 h. The toluene was removed using a gas-tight syringe, leaving a yellow solid. This solid was washed with petroleum ether (2 × 10 mL) and any remaining solvent was removed *in vacuo* to afford the product as a yellow solid (86 mg, 77%). $C_{14}H_{24}B_{10}N_2Sn$ requires C 37.61, H 5.41, N 6.26. Found C 37.19, H 5.37, N 6.24%. IR, ν_{max} 2524 cm^{-1} (B–H). $^{11}B\{^1H\}$ NMR, δ 6.89 (2B), 4.50 (1B), –0.74 (3B), –4.33 (1B), –8.35 (3B). ^{1}H NMR, δ 8.95 (d, 2H, bipy), 8.30 (d, 2H, bipy), 8.20 (d of d, 2H, bipy), 7.70 (d of d, 2H, bipy), 2.50 (s, 6H, CH_3). MS, *m*/*z* 291 (M – bipy), 171 (M – Sn{bipy}), 154 (M – $SnMe_2C_2B_{10}H_{10}$). X-Ray diffraction quality crystals were grown by diffusion of 40–60 petroleum ether and a THF solution of **1** at 5 °C.

1,6-Me_2-4-(*o*-phen)-4,1,6-*closo*-$SnC_2B_{10}H_{10}$ (2). In an analogous manner a dry, degassed, toluene solution (10 mL) of 1,10-phenanthroline (54 mg, 0.30 mmol) was treated with a solution of 1,6-Me_2-4,1,6-*closo*-$SnC_2B_{10}H_{10}$ (80 mg, 0.27 mmol) in dry, degassed, toluene (10 mL). The yield of **2** was 94 mg (74%). $C_{16}H_{24}B_{10}N_2Sn$ requires C 40.79, H 5.13, N 5.95. Found C 40.04, H 5.32, N 5.70%. IR, ν_{max} 2528 cm^{-1} (B–H). $^{11}B\{^1H\}$ NMR, δ 7.25 (2B), 4.57 (1B), –0.80 (3B), –4.57 (1B), –8.38 (3B). ^{1}H NMR, δ 9.30 (d, 2H, phen), 8.65 (d, 2H, phen), 8.10 (s, 2H, phen), 8.00 (d of d, 2H, phen), 2.55 (s, 6H, CH_3). MS, *m*/*z* 291 (M – phen), 171 (M – Sn{phen}), 179 (M – $SnMe_2C_2B_{10}H_{10}$). Crystals suitable for X-ray diffraction grown by slow diffusion of 40–60 petroleum ether and a THF solution of **2** at 5 °C.

Table 2 Crystallographic data for compounds **1–4**

	1	**2**	**3**	**4**
Formula	$C_{14}H_{24}B_{10}N_2Sn$	$C_{16}H_{24}B_{10}N_2Sn{\cdot}C_4H_8O$	$C_{16}H_{28}B_{10}N_2Sn{\cdot}CD_2Cl_2$	$C_{26}H_{32}B_{10}N_2Sn{\cdot}CD_2Cl_2$
M	447.14	543.27	562.13	686.26
Crystal system	Monoclinic	Monoclinic	Monoclinic	Orthorhombic
Space group	$P2_1/n$	$P2_1/c$	$P2_1/c$	$Pna2_1$
a/Å	7.9073(8)	7.7876(14)	10.7196(7)	11.4342(11)
b/Å	16.9367(14)	19.350(3)	16.3778(11)	16.0203(16)
c/Å	14.7949(13)	16.543(2)	15.0928(10)	17.1455(18)
β/°	95.924(4)	94.301(7)	106.260(3)	
U/Å^3	1970.8(3)	2485.9(7)	2543.8(3)	3140.7(5)
Z	4	4	4	4
F(000)/e	888	1096	1120	1376
D_{calc}/Mg m^{-3}	1.507	1.452	1.468	1.451
μ(Mo Kα)/mm^{-1}	1.297	1.046	1.224	1.007
θ_{max}/°	26.30	30.62	37.85	27.63
Data measured	96417	67045	95280	96034
Unique data, n	5927	7628	13000	12491
R_{int}	0.0494	0.0525	0.0467	0.0703
R, wR_2 (obs. data)	0.0405, 0.0847	0.0345, 0.0801	0.0329, 0.1137	0.0695, 0.1588
S	0.940	1.081	0.959	1.026
Abs. str. parameter, x				0.12(3)
Variables, p	278	385	333	398
E_{max}, E_{min}/e Å^{-3}	0.680, –1.175	1.038, –1.114	3.141, –3.045	1.739, –1.667

1,6-Me$_2$-4-(Me$_2$bipy)-4,1,6-*closo*-SnC$_2$B$_{10}$H$_{10}$ (3). Likewise, a solution of 1,6-Me$_2$-4,1,6-*closo*-SnC$_2$B$_{10}$H$_{10}$ (40 mg, 0.137 mmol) in dry, degassed, toluene (10 mL) was stirred with a dry, degassed, toluene solution (10 mL) of 4,4′-dimethyl-2,2′-bipyridine (25 mg, 0.14 mmol) to afford 53 mg (80%) of **3**. $C_{16}H_{28}B_{10}N_2Sn$ requires C 40.44, H 5.94, N 5.89. Found C 40.52, H 6.06, N 5.85%. IR, ν_{max} 2523 cm^{-1} (B–H). $^{11}B\{^1H\}$ NMR, δ 6.91 (2B), 4.20 (1B), –1.07 (3B), –4.54 (1B), –8.64 (3B). ^1H NMR, δ 8.75 (d, 2H, Me$_2$bipy), 8.08 (s, 2H, Me$_2$bipy), 7.48 (d, 2H, Me$_2$bipy), 2.59 (s, 6H, CH_3), 2.49 (s, 6H, CH_3). MS, m/z 291 (M – Me$_2$bipy), 182 (M-SnMe$_2$C$_2$B$_{10}$H$_{10}$). Crystals by slow evaporation of a CD_2Cl_2 solution of **3** at room temperature.

1,6-Me$_2$-4-(Ph$_2$bipy)-4,1,6-*closo*-SnC$_2$B$_{10}$H$_{10}$ (4). Similarly, a solution of 1,6-Me$_2$-4,1,6-*closo*-SnC$_2$B$_{10}$H$_{10}$ (30 mg, 0.10 mmol) in dry, degassed, toluene (10 mL) was allowed to react with a dry, degassed, toluene solution (10 mL) of 4,4′-diphenyl-2,2′-bipyridine (32 mg, 0.10 mmol), yielding 33 mg (57%) of **4**. Microanalytical data unavailable. IR, ν_{max} 2530 cm^{-1} (B–H). The product was crystallised by slow evaporation of a CD_2Cl_2 solution of **4** at room temperature.

Crystallography†

Intensity data were collected from single crystals on a Bruker X8 APEX2 diffractometer, with crystals mounted in inert oil on a cryoloop and cooled to 100 K by an Oxford Cryosystems Cryostream. Crystals of compounds **2** and **3** were single, but those of **1** and **4** were twinned. For these, indexing with CELL_NOW[14] revealed that **1** was a three-component non-merohedral twin and that **4** was a two-component non-merohedral twin. Empirical absorption corrections were made using the program TWINABS[15] (**1** and **4**, R_{int} values quoted from merging with TWINABS) and SADABS[16] (**2** and **3**). The structures were solved by direct methods and refined by full-matrix least-squares using the SHELXTL program suite.[17] All non-hydrogen atoms were refined with anisotropic displacement parameters. In **2** there is one molecule of THF of solvation, while in **3** and **4** is one molecule of CD_2Cl_2 of solvation. In the case of **1** cage H atoms were restrained to B–H 1.10(2) Å. For **4**, the cage H atom on B5 was restrained to B–H 1.10(2) Å and the H atoms on B2, B3, B7, B8, B10 and B11 were constrained to ideal positions with B–H 1.10 Å. In all cases, H atoms on methyl groups and ligands were constrained to ideal positions with C–H 0.98 Å and C–H 0.95 Å respectively. All H atom thermal parameters were set to 1.2 × U_{eq} of the attached B or C atom. Table 2 contains further experimental details.

Calculations

All geometries were optimised without constraints using Gaussian 03, Revision C.02[18] employing the BP86 functional.[19] 6-31G** basis sets were used for B, C, N and H atoms[20] whilst for Sn the Stuttgart relativistic ECP[21] and the associated SDD basis set were employed with additional d-polarization functions.[22] Local minima were confirmed as such through analytical frequency calculations. Geometry measurements were made using Mercury[23] and orbital representations generated *via* Molekel.[24] Test calculations employing the B3LYP[25] and TPSS[26] functionals as well as the MP2 methodology were performed. In addition, basis set effects were monitored by recomputing the BP86 results with 6-311G** and 6-31++G** basis sets on B, C, N and H atoms.

Acknowledgements

We thank the EPSRC (PDA supported by DTA studentship; DE and DMcK funded by project EP/E02971X/1) and Prof. T. B. Marder (University of Durham) for a preprint of ref. 7. RS was the recipient of a Socrates scholarship from the Universidad de Zaragoza, Spain.

Notes and references

1 R. W. Rudolph, R. L. Voorhees and R. E. Cochoy, *J. Am. Chem. Soc.*, 1970, **92**, 3351.

2 P. Jutzi, P. Galow, S. Abu-Orabi, A. M. Arif, A. H. Cowley and N. C. Norman, *Organometallics*, 1987, **6**, 1024.
3 (*a*) N. S. Hosmane, N. N. Sirmokadam and R. H. Herber, *Organometallics*, 1984, **3**, 1665; (*b*) N. S. Hosmane, P. de Meester, N. N. Maldar, S. B. Potts, S. S. C. Chu and R. H. Herber, *Organometallics*, 1986, **5**, 772; (*c*) N. S. Hosmane, R. D. Barreto, M. A. Tolle, J. J. Alexander, W. Quintana, U. Siriwardane, S. G. Shore and R. E. Williams, *Inorg. Chem.*, 1990, **29**, 2698.
4 R. W. Chapman, J. G. Kester, K. Folting, W. E. Streib and L. J. Todd, *Inorg. Chem.*, 1992, **31**, 979.
5 T. Gädt and L. Wesemann, *Organometallics*, 2007, **26**, 2474 and references therein.
6 D. Joosten, I. Weissinger, M. Kirchmann, C. Maichle-Mössmer, F. M. Schappacher, R. Pöttgen and L. Wesemann, *Organometallics*, 2007, **26**, 5696.
7 M. A. Fox, T. B. Marder and L. Wesemann, *Canad. J. Chem.*, 2009, **87**, 63.
8 N. M. M. Wilson, D. Ellis, A. S. F. Boyd, B. T. Giles, S. A. Macgregor, G. M. Rosair and A. J. Welch, *Chem. Commun.*, 2002, 464.
9 J. A. Maguire, G. P. Ford and N. S. Hosmane, *Inorg. Chem.*, 1988, **27**, 3354.
10 (*a*) D. M. P. Mingos, M. I. Forsyth and A. J. Welch, *J. Chem. Soc., Chem. Commun.*, 1977, 605; (*b*) D. M. P. Mingos, M. I. Forsyth and A. J. Welch, *J. Chem. Soc., Dalton Trans.*, 1978, 1363.
11 M. A. Laguna, D. Ellis, G. M. Rosair and A. J. Welch, *Inorg. Chim. Acta*, 2003, **347**, 161.
12 B. E. Hodson, T. D. McGrath and F. G. A. Stone, *Organometallics*, 2005, **24**, 1638.
13 K. J. Dalby, D. Ellis, S. Erhardt, R. D. McIntosh, S. A. Macgregor, K. Rae, G. M. Rosair, V. Settels, A. J. Welch, B. E. Hodson, T. D. McGrath and F. G. A. Stone, *J. Am. Chem. Soc.*, 2007, **129**, 3302.
14 *CELL_NOW*, G. M. Sheldrick, University of Göttingen, Germany, 2005.
15 *TWINABS*, G. M. Sheldrick, University of Göttingen, Germany, 2007.
16 *SADABS*, V2.05; G. M. Sheldrick, University of Göttingen, Germany, 2005.
17 *SHELXTL*, V6.10; Bruker-AXS, Madison, WI, USA, 2000.
18 M. J. Frisch, G. W. Trucks, H. B. Schlegel, G. E. Scuseria, M. A. Robb, J. R. Cheeseman, J. A. Montgomery, Jr., T. Vreven, K. N. Kudin, J. C. Burant, J. M. Millam, S. S. Iyengar, J. Tomasi, V. Barone, B. Mennucci, M. Cossi, G. Scalmani, N. Rega, G. A. Petersson, H. Nakatsuji, M. Hada, M. Ehara, K. Toyota, R. Fukuda, J. Hasegawa, M. Ishida, T. Nakajima, Y. Honda, O. Kitao, H. Nakai, M. Klene, X. Li, J. E. Knox, H. P. Hratchian, J. B. Cross, V. Bakken, C. Adamo, J. Jaramillo, R. Gomperts, R. E. Stratmann, O. Yazyev, A. J. Austin, R. Cammi, C. Pomelli, J. Ochterski, P. Y. Ayala, K. Morokuma, G. A. Voth, P. Salvador, J. J. Dannenberg, V. G. Zakrzewski, S. Dapprich, A. D. Daniels, M. C. Strain, O. Farkas, D. K. Malick, A. D. Rabuck, K. Raghavachari, J. B. Foresman, J. V. Ortiz, Q. Cui, A. G. Baboul, S. Clifford, J. Cioslowski, B. B. Stefanov, G. Liu, A. Liashenko, P. Piskorz, I. Komaromi, R. L. Martin, D. J. Fox, T. Keith, M. A. Al-Laham, C. Y. Peng, A. Nanayakkara, M. Challacombe, P. M. W. Gill, B. G. Johnson, W. Chen, M. W. Wong, C. Gonzalez and J. A. Pople, *GAUSSIAN 03 (Revision C.02)*, Gaussian, Inc., Wallingford, CT, 2004.
19 (*a*) H. L. Schmider and A. D. Becke, *J. Chem. Phys.*, 1998, **108**, 9624; (*b*) J. P. Perdew, *Phys. Rev. B*, 1986, **33**, 8822.
20 (*a*) W. J. Hehre, R. Ditchfield and J. A. Pople, *J. Chem. Phys.*, 1972, **56**, 2257; (*b*) P. C. Hariharan and J. A. Pople, *Theor. Chim. Acta*, 1973, **28**, 213.
21 (*a*) A. Bergner, M. Dolg, H. Kuechle, H. Stoll and H. Preuss, *Mol. Phys.*, 1993, **80**, 1431; (*b*) M. Kaupp, P. v. R. Schleyer, H. Stoll and H. Preuss, *J. Chem. Phys.*, 1991, **94**, 1360; (*c*) M. Dolg, H. Stoll, H. Preuss and R. M. Pitzer, *J. Phys. Chem.*, 1993, **97**, 5852.
22 A. Höllworth, M. Böhme, S. Dapprich, A. W. Ehlers, A. Gobbi, V. Jonas, K. F. Köhler, R. Syegmann, A. Veldkamp and G. Frenking, *Chem. Phys. Lett.*, 1993, **208**, 237.
23 *Mercury*, version 1.4.2, Cambridge Crystallographic Data Center, Cambridge, UK, 2006.
24 P. Flükiger, H. P. Lüthi, S. Portmann and J. Webe, *Molekel*, version 4.0, Swiss National Supercomputing Centre CSCS, Manno, Switzerland, 2000.
25 A. D. Becke, *J. Chem. Phys.*, 1993, **98**, 5648.
26 J. M. Tao, J. P. Perdew, V. N. Staroverov and G. E. Scuseria, *Phys. Rev. Lett.*, 2003, **91**, 146401.

Synthetic, structural and computational studies on adducts of the 4,1,2-SnC_2B_{10} supraicosahedral stannacarborane†

Peter D. Abram, David McKay, David Ellis, Stuart A. Macgregor,* Georgina M. Rosair and Alan J. Welch*

Received 29th October 2009, Accepted 2nd December 2009
First published as an Advance Article on the web 27th January 2010
DOI: 10.1039/b922644c

The stannacarborane 1,2-μ-$(CH_2)_3$-4,1,2-*closo*-$SnC_2B_{10}H_{10}$ (**1**) and its adducts with 2,2′-bipyridine (bipy), 1,10-phenanthroline (*o*-phen) and 4,4′-diphenyl-2,2′-bipyridine (Ph_2bipy), 1,2-μ-$(CH_2)_3$-4-(bipy)-4,1,2-*closo*-$SnC_2B_{10}H_{10}$ (**2**), 1,2-μ-$(CH_2)_3$-4-(*o*-phen)-4,1,2-*closo*-$SnC_2B_{10}H_{10}$ (**3**) and 1,2-μ-$(CH_2)_3$-4-(Ph_2bipy)-4,1,2-*closo*-$SnC_2B_{10}H_{10}$ (**4**), respectively, together with the analogous compound 1,2-μ-{$C_6H_4(CH_2)_2$}-4-(bipy)-4,1,2-*closo*-$SnC_2B_{10}H_{10}$ (**5**) have been prepared and characterised. In solution at ambient temperature, compounds **1–5** all display NMR spectra which are interpreted in terms of (time-averaged) C_s molecular symmetry, but whilst (effectively) C_s symmetry is retained in the structures of **2–5** in the crystal (*i.e.* henicosahedral cage structures are observed), **1** has a (C_1-symmetric) docosahedral structure. A method for quantifying the "percentage docosahedral character" of 13-vertex 1,2-C_2 heteroboranes is described, based on the angles around the C1C2B9B5 quadrilateral. The structures of "carbons adjacent" **1–5** all reveal less slipping of the Sn atom (or {SnL_2} fragment) across the C_2B_4 carborane face than has previously been observed in analogous "carbons apart" 4,1,6-*closo*-SnC_2B_{10} species, a surprising result in the context of previous studies of slipping in icosahedral platinacarboranes. A computational study of "carbons adjacent" and "carbons apart" icosahedral and supraicosahedral platinacarboranes has revealed that the origin of this observation is steric control of the slipping distortion in both "carbons apart" species and in the "carbons adjacent" 13-vertex species, with orbital interactions proving dominant only in the case of the "carbons adjacent" icosahedral compound.

Introduction

In 2002 we reported the first supraicosahedral p-block metallacarboranes 4,1,6-*closo*-$SnC_2B_{10}H_{12}$ and 1,6-Me_2-4,1,6-*closo*-$SnC_2B_{10}H_{10}$, arising from reduction of 1,2-*closo*-$C_2B_{10}H_{12}$ or its C,C′-dimethyl analogue, followed by treatment with $SnCl_2$.[1] Very recently we described a number of adducts of the dimethyl species with chelating Lewis bases L_2.[2] The structures of these adducts, studied both crystallographically and computationally, confirmed that the supraicosahedral stannacarboranes resemble their icosahedral[3] and sub-icosahedral[4] analogues in their Lewis acid behaviour, giving rise to adducts in which (i) there is an enhanced slip of the Sn atom relative to the uncomplexed precursor and (ii) the stereochemical influence of the Sn lone pair of electrons is clearly evident.

The slip of metal atoms across a carborane ligand face was thoroughly studied with respect to icosahedral {L_2M}C_2B_9 species more than 30 years ago (M = Pt or Pd, L = typically phosphine).[5] A key finding of this work was that the slip distortion, Δ, was greater in 3,1,2-MC_2B_9 species (cage C atoms adjacent)[5] than in 2,1,7-MC_2B_9 species (cage C atoms separated),[6] a result that was rationalised by the results of molecular orbital (MO) calculations at the extended Hückel level.

In 4,1,6-MC_2B_{10} supraicosahedral compounds the cage C atoms are separated by a single B atom, as they are in 2,1,7-MC_2B_9 icosahedral species. A known 13-vertex C-adjacent isomer is 4,1,2-MC_2B_{10}, but to prepare this it is usually necessary to first tether the cage C atoms of 1,2-*closo*-C_2B_{10} icosahedra with a short exopolyhedral tether, to prevent their separation in the initial reduction step, the same strategy used to prepare the first supraicosahedral carborane.[7] Following our report of 4,1,6-SnC_2B_{10} species, Xie prepared such a 4,1,2-SnC_2B_{10} compound and determined the structures of its adducts with MeCN, THF and dme (dme = dimethoxyethane).[8]

In view of the superficial similarity in the relationship between 4,1,6-SnC_2B_{10} and 4,1,2-SnC_2B_{10} and that between 2,1,7-MC_2B_9 and 3,1,2-MC_2B_9, we wondered if adducts of 4,1,2-SnC_2B_{10} compounds would also show increased slip distortions relative to their 4,1,6-SnC_2B_{10} cousins. Hence we report here the results of synthetic and structural studies on a number of adducts of 4,1,2-SnC_2B_{10} stannacarboranes using exclusively bidentate L_2 bases similar to those we used in our earlier work. Surprisingly, the 4,1,2-SnC_2B_{10} species are *less* slipped than their 4,1,6-SnC_2B_{10} analogues. We trace the origin of this unexpected result by computational studies of model compounds.

Department of Chemistry, School of Engineering & Physical Sciences, Heriot-Watt University, Edinburgh, UK EH14 4AS. E-mail: a.j.welch@hw.ac.uk, s.a.macgregor@hw.ac.uk; Fax: +44 (0)131 451 3180; Tel: +44 (0)131 451 3217 +44 (0)131 451 8031

† Electronic supplementary information (ESI) available: Computational models and additional plots referred to in the text. CCDC reference numbers 751644–751648 (compounds **1–5** respectively). For ESI and crystallographic data in CIF or other electronic format see DOI: 10.1039/b922644c

Results and discussion

Synthesis and spectroscopy

Reduction of 1,2-μ-$(CH_2)_3$-1,2-*closo*-$C_2B_{10}H_{10}$ by sodium in THF in the presence of naphthalene, followed by treatment with $SnCl_2$, affords a modest yield of the pale yellow stannacarborane 1,2-μ-$(CH_2)_3$-4,1,2-*closo*-$SnC_2B_{10}H_{10}$ (**1**) after work-up. Compound **1** was initially characterised by mass spectrometry and NMR spectroscopy. The highest mass signal in the mass spectrum appears as a characteristic heteroborane envelope from 298 to 308 with the most intense peak at m/z 302. In the ^{1}H NMR spectrum are multiplets of equal intensity between δ 3.20 and 1.90 due to the tether protons, whilst the $^{11}B\{^1H\}$ spectrum consists of five signals between δ +8.0 and –0.5, of relative ratio 2 : 4 : 1 : 1 : 2 from high frequency to low frequency, all of which become doublets on retention of proton coupling. The molecular structure of **1**, subsequently determined crystallographically (*vide infra*), is that of an asymmetric docosahedral cage, and the presence of a mirror plane implied by the $^{11}B\{^1H\}$ spectrum is readily rationalised by a diamond-trapezium-diamond fluctional process in solution, similar to that proposed for the transition-metal metallacarboranes 1,2-μ-$(CH_2)_3$-4,4-$(PMe_2Ph)_2$-4,1,2-*closo*-$PtC_2B_{10}H_{10}$ and 1,2-μ-$(CH_2)_3$-4-dppe-4,1,2-*closo*-$NiC_2B_{10}H_{10}$ (dppe = $Ph_2PCH_2CH_2PPh_2$),[9] which is rapid on the NMR timescale.

Room temperature reaction of a toluene solution of **1** and toluene solutions of 2,2′-bipyridine (bipy), 1,10-phenanthroline (*o*-phen) and 4,4′-diphenyl-2,2′-bipyridine (Ph_2bipy) result in immediate precipitation of the yellow adducts 1,2-μ-$(CH_2)_3$-4-(bipy)-4,1,2-*closo*-$SnC_2B_{10}H_{10}$ (**2**), 1,2-μ-$(CH_2)_3$-4-(*o*-phen)-4,1,2-*closo*-$SnC_2B_{10}H_{10}$ (**3**) and 1,2-μ-$(CH_2)_3$-4-(Ph_2bipy)-4,1,2-*closo*-$SnC_2B_{10}H_{10}$ (**4**), respectively, in good yields. The ^{1}H NMR spectra of **2–4** all show, in addition to resonances due to the bipy, *o*-phen or Ph_2bipy ligands, four multiplets in the ratio 2 : 2 : 1 : 1 at δ 3.15–2.95, 2.85–2.65, 2.05–1.90 and 1.80–1.65, respectively, assigned to the protons of the $(CH_2)_3$ tether. Peaks in the $^{11}B\{^1H\}$ NMR spectra of **2–4** are shifted to low frequency compared to those in **1**, appearing as a 3 : 2 : 2 : 2 : 1 pattern for **2** and **3** and a 3 : 2 : 4 : 1 for **4**, between δ +4.0 and –11.0. The ^{1}H and ^{11}B spectra imply (at least time-averaged) C_s molecular symmetry in solution (assuming, in the latter, that the integral-3 resonances are 2+1 co-incidences and the integral-4 resonance is a 2+2 co-incidence). As will be discussed subsequently, the structures of **2–4** in the solid state are effectively henicosahedral (Fig. 1, right) and C_s-symmetric for a 4,1,2-SnC_2B_{10} heteroatom pattern.

To provide a link between these adducts of the $(CH_2)_3$-tethered stannacarborane **1** and the MeCN, THF and dme adducts of 1,2-μ-{$C_6H_4(CH_2)_2$}-4,1,2-*closo*-$SnC_2B_{10}H_{10}$ previously reported by Xie,[8] we have further treated a toluene solution of 1,2-μ-{$C_6H_4(CH_2)_2$}-4,1,2-*closo*-$SnC_2B_{10}H_{10}$ with bipy to afford the bright yellow bipyridyl adduct 1,2-μ-{$C_6H_4(CH_2)_2$}-4-(bipy)-4,1,2-*closo*-$SnC_2B_{10}H_{10}$ (**5**). In compound **5** the ^{1}H NMR spectrum is unremarkable, with appropriate resonances in terms of multiplicity, integral and chemical shift, for the protons of the bipy ligand and α,α-*o*-xylylene tether. Peaks in the $^{11}B\{^1H\}$ NMR spectrum are considerably broader than those of **2–4**, but nevertheless a clear 2 : 2 : 2 : 1 : 1 : 2 pattern, from δ +7.5 to –10.5, is evident. Again, the NMR spectra of **5** imply a C_s-symmetric molecule, at least in solution at room temperature.

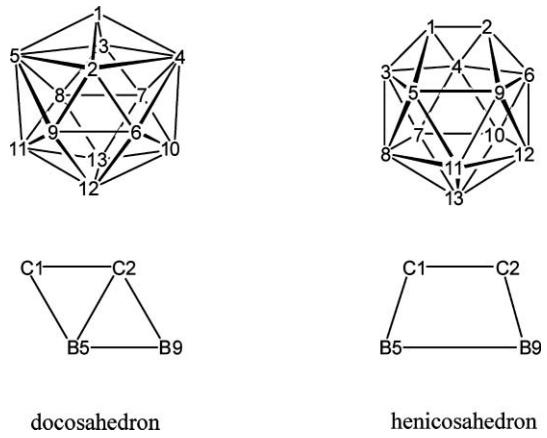

Fig. 1 The docosahedron (left) and henicosahedron (right) and numbering schemes.

Molecular structures

The molecular structures of compounds **1–5** have all been determined by single-crystal diffraction studies.

We have previously shown[9] that 4,1,2-MC_2B_{10} compounds can exist in the solid-state with either docosahedral or henicosahedral structures, the topological difference between which is the formal absence of a C2–B5 connectivity in the latter. Thus, in the docosahedron the C1C2B9B5 unit is a diamond, with a measureable difference in C1–C2–B9 and C2–C1–B5 angles and a measureable difference in C2–B9–B5 and B9–B5–C1 angles, whereas in the henicosahedron the C1C2B9B5 unit is trapezoidal and the C1–C2–B9 and C2–C1–B5 angles are equal, as are the C2–B9–B5 and B9–B5–C1 angles (Fig. 1). For the series of metallacarboranes 1,2-μ-$(CH_2)_3$-4-L-4,1,2-*closo*-$MC_2B_{10}H_{10}$ we found a continuum of structure type from henicosahedral (ML = CoCp, Ru{*p*-cym} {*p*-cym = $C_6H_4Me^iPr$-1,4}), through intermediate (ML = Pt{PMe_2Ph}$_2$) to essentially docosahedral (ML = Ni{dppe}, although both the platinum and nickel species were clearly fluctional in solution *via* a henicosahedral intermediate as noted above.

In the present study it is immediately apparent that the cage of the ligand-free stannacarborane **1** (Fig. 2) appears to be best described as docosahedral, whilst those of the adducts **2–5** (Fig. 3–6) are best described as henicosahedral. To place these and other 1,2-C_2 carboranes and heterocarboranes quantitatively on the continuum of structure type from docosahedral to henicosahedral we define the angle ϕ as the average of the differences between angles C1–C2–B9 and C2–C1–B5 and angles C2–B9–B5 and B9–B5–C1, *i.e.*

$$\phi = (|\text{C1–C2–B9} - \text{C2–C1–B5}| + |\text{C2–B9–B5} - \text{B9–B5–C1}|)/2$$

For a C_s-symmetric henicosahedron ϕ = 0, and ϕ increases as the C2–B5 distance shortens and the structure becomes docosahedral. Table 1 lists ϕ values for all structurally characterised 13-vertex 1,2-C_2 carboranes and heterocarboranes of which we are aware. The "most docosahedral" species, 1,2-μ-$(CH_2)_3$-4-dppe-4,1,2-*closo*-$NiC_2B_{10}H_{10}$, has ϕ = 41.55°. We now define x,

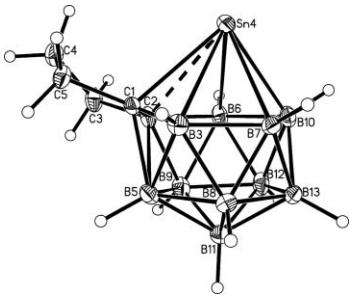

Fig. 2 Perspective view of compound **1**. Thermal ellipsoids are drawn at the 50% probability level except for H atoms.

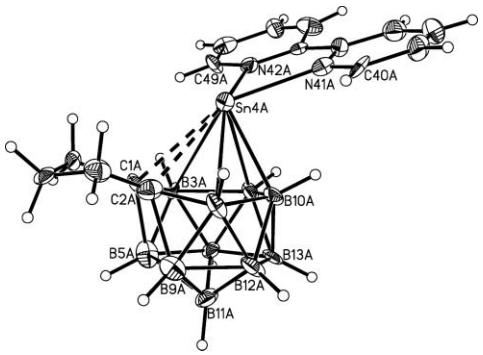

Fig. 3 Perspective view of compound **2** (molecule α). Thermal ellipsoids are drawn at the 40% probability level except for H atoms.

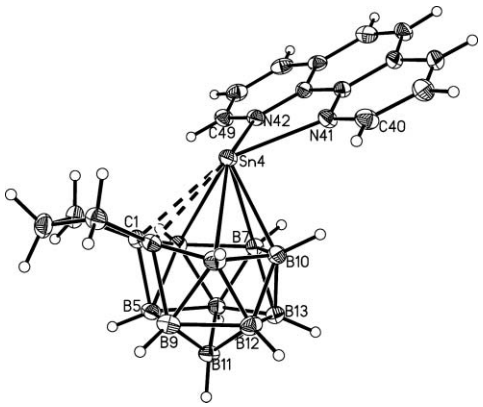

Fig. 4 Perspective view of compound **3**. Thermal ellipsoids as for Fig. 2.

the "percentage docosahedral character", as $x = (\phi/41.55) \times 100\%$.‡ For a perfect henicosahedron $x = 0\%$ and for the docosahedral nickelacarborane $x = 100\%$. By this approach the percentage docosahedral character of all 13-vertex 1,2-C_2 carboranes and heterocarboranes can be assessed on a common scale. The 1,2-C_2B_{11} carboranes are all essentially henicosahedral. The 4,1,2-MC_2B_{10} metallacarboranes appear to be predominantly henicosahedral,§ but are somewhat more spread, displaying henicosahedral, docosahedral and effectively intermediate, *e.g.* 1,2-μ-$(CH_2)_3$-4,4-$(PMe_2Ph)_2$-4,1,2-*closo*-$PtC_2B_{10}H_{10}$ (**III**), structures.

‡ Since our docosahedral model compound is chosen arbitrarily it may be that future species will be "more docosahedral" and have x values >100%.

§ However this has not always been recognised, *e.g.* in ref. 8 the line diagrams of the adducts are drawn as docosahedral whilst the crystallographically-determined structures are clearly henicosahedral.

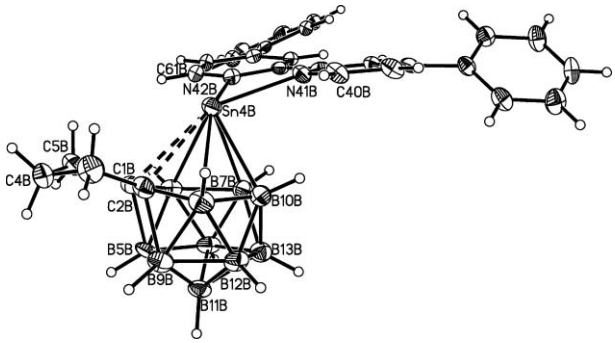

Fig. 5 Perspective view of compound **4** (molecule β). Thermal ellipsoids as for Fig. 2.

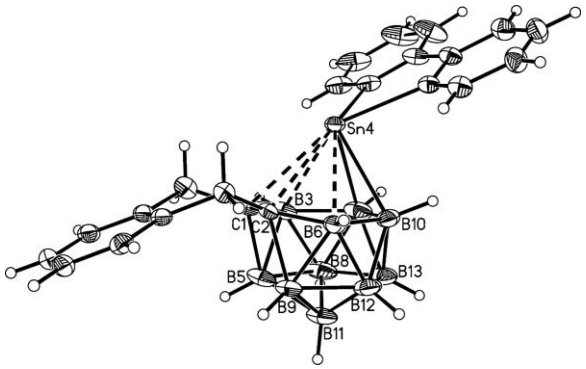

Fig. 6 Perspective view of compound **5**. Thermal ellipsoids as for Fig. 2.

The ligand-free stannacarborane **1** has $x = 80.3\%$ and is confirmed as essentially docosahedral, whilst the adducts **2–5**, with x between 0.0 and 21.6, are essentially henicosahedral.

This report constitutes the first time a ligand-free 4,1,2-SnC_2B_{10} species has been structurally characterised. Table 2 hosts selected molecular parameters for compounds **1–5** studied, where Δ is the slip distortion of the Sn atom measured relative to the centroid of the B5B9B12B13B8 least-squares plane, Δ_Δ is the additional slip accompanying adduct formation, z is the perpendicular distance of the Sn atom from that least-squares plane and θ is the inclination of the L_2 ligand, the dihedral angle between B5B9B12B13B8 and Sn4N41CCN42 planes. In **1** the Sn-cage atom distances vary somewhat from the corresponding distances in 1,6-Me_2-4,1,6-*closo*-SnC_2B_{10},[1] connectivities to vertex atoms 1, 2, 3 and 7 being longer (by 0.04–0.13 Å) whilst those to 6 and 10 are shorter (by 0.09 and 0.05 Å respectively). Moreover, there is greater internal variation in these distances, 0.35 Å in **1** compared to 0.26 Å in the 4,1,6-SnC_2B_{10} species, in spite of which the Sn atom in **1** is less slipped (Δ = 0.14 Å) than that in the 4,1,6-isomer (Δ = 0.27 Å).[2] As noted in the introduction, in studies of isomeric icosahedral platinacarboranes in which the two cage C atoms were both adjacent[5] and non-adjacent,[6] it was found that the greater slip distortion occurred in the former case. Thus the measurement of a smaller slip in **1** (C atoms adjacent) compared to that in 1,6-Me_2-4,1,6-*closo*-SnC_2B_{10} (C atoms non-adjacent) is significant. We return to this point later.

The molecular structures of the bipy, *o*-phen and Ph_2bipy adducts of **1**, compounds **2–4**, respectively, are shown in Fig. 3–5 (compounds **2** and **4** crystallise with two independent molecules in the asymmetric fraction of the unit cell; only molecule A is

Table 1 Structural analysis of the cages of 13-vertex 1,2-C_2 heteroboranes[a]

Compound	Type	CCDC refcode	Reference	ϕ/°	x
I	4,1,2-CoC_2B_{10}	GAQHIQ	9	0.20	0.5
II	4,1,2-RuC_2B_{10}	GAQHOW	9	0.33	0.8
III	4,1,2-PtC_2B_{10}	GAQHUC	9	28.44	68.4
IV	4,1,2-NiC_2B_{10}	GAQJAK	9	41.55	100
V	4,1,2-CoC_2B_{10}	BOKZAC	10	32.53, 41.32[b]	78.3, 99.4
VI	4,1,2-SnC_2B_{10}	GUZSOJ	8	0.93	2.2
VII	4,1,2-SnC_2B_{10}	GUZSUP	8	4.23	10.2
VIII	4,1,2-SnC_2B_{10}	GUZTAW	8	4.98	12.0
IX	4,1,2-CoC_2B_{10}	POYHEQ	11	6.17	14.8
X	4,1,2-NaC_2B_{10}	BIYVOU	12	3.32	8.0
XI	4,1,2-ZrC_2B_{10}	IYUVED	13	9.41	22.6
XII	4,1,2-ZrC_2B_{10}	IYUVIH	13	0.66	1.6
XIII	1,2-C_2B_{11}	TUSGAP	7	11.61	27.9
XIV	1,2-C_2B_{11}	JEWZER	14	0.00[c]	0
XV	1,2-C_2B_{11}	JEWZAN	14	6.70	16.1
XVI	1,2-C_2B_{11}	NEGSUO	15[d]	2.99, 6.09[e]	7.2, 14.7
1	4,1,2-SnC_2B_{10}		this work	33.37	80.3
2	4,1,2-SnC_2B_{10}		this work	7.46, 0.97[e]	18.0, 0.02
3	4,1,2-SnC_2B_{10}		this work	4.68	11.3
4	4,1,2-SnC_2B_{10}		this work	6.76, 8.98[c]	16.3, 21.6
5	4,1,2-SnC_2B_{10}		this work	5.80	14.0

I, 1,2-μ-$(CH_2)_3$-4-Cp-4,1,2-*closo*-$CoC_2B_{10}H_{10}$; **II**, 1,2-μ-$(CH_2)_3$-4-(*p*-cym)-4,1,2-*closo*-$RuC_2B_{10}H_{10}$; **III**, 1,2-μ-$(CH_2)_3$-4-$(PMe_2Ph)_2$-4,1,2-*closo*-$PtC_2B_{10}H_{10}$; **IV**, 1,2-μ-$(CH_2)_3$-4-dppe-4,1,2-*closo*-$NiC_2B_{10}H_{10}$; **V**, 1-Me-4-(PEt_3)-4,6/7-μ-{$Co(PEt_3)_2$-μ-$(H)_2$}-4,1,2-*closo*-$CoC_2B_{10}H_{10}$; **VI**, 1,2-μ-{$C_6H_4(CH_2)_2$}-4-MeCN-4,1,2-*closo*-$SnC_2B_{10}H_{10}$; **VII**, 1,2-μ-{$C_6H_4(CH_2)_2$}-4-thf-4,1,2-*closo*-$SnC_2B_{10}H_{10}$; **VIII**, 1,2-μ-{$C_6H_4(CH_2)_2$}-4-dme-4,1,2-*closo*-$SnC_2B_{10}H_{10}$; **IX**, 1-CN-4-Cp-4,1,2-*closo*-$CoC_2B_{10}H_{11}$; **X**, [[1,2-μ-{$C_6H_4(CH_2)_2$}-4-thf-4,1,2-*closo*-$NaC_2B_{10}H_{10}$.$Na(thf)_2$]$_2$]$_n$; **XI**, [4,4′-$(Cl)_2$-4,4′-Zr-(1,2-μ-{$C_6H_4(CH_2)_2$}-1,2-*closo*-$C_2B_{10}H_{10})_2$]$^{2-}$ (monoclinic); **XII**, [4,4′-$(Cl)_2$-4,4′-Zr-(1,2-μ-{$C_6H_4(CH_2)_2$}-1,2-*closo*-$C_2B_{10}H_{10})_2$]$^{2-}$ (triclinic); **XIII**, 1,2-μ-{$C_6H_4(CH_2)_2$}-3-Ph-1,2-*closo*-$C_2B_{11}H_{10}$; **XIV**, 1,2-Me_2-1,2-*closo*-$C_2B_{11}H_{11}$; **XV**, 1,2-μ-{$Me_2Si(CH_2)_2$}-1,2-*closo*-$C_2B_{11}H_{11}$; **XVI**, 1,2-μ-{$C_6H_4(CH_2)_2$}-1,2-*closo*-$C_2B_{11}H_{11}$.[a] ConQuest (version 1.11) search of the Cambridge Structural Database (September 2009 update) at the Daresbury Laboratory. [b] C2 disordered over vertices 2 and 3. [c] Crystallographically-imposed C_s symmetry. [d] This paper reports four further, similar, species, two of which have multiple crystallographically-independent molecules, but all are essentially docosahedral, with C1–B9 and C2–B5 distances ranging from 2.139(3) to 2.629(3) Å. [e] Two crystallographically-independent molecules.

Table 2 Selected molecular parameters (Å, °) in experimental compounds **1–5** and model compounds **A** and **B**[a]

	1	**A**	**2α**	**2β**	**B**	**3**	**4α**	**4β**	**5**
Sn4–C1	2.545(2)	*2.549*	2.813(17)	2.879(18)	*2.832*	2.803(2)	2.821(4)	2.782(4)	2.849(4)
Sn4–C2	2.727(3)	*2.762*	2.92(2)	2.824(17)	*2.787*	2.820(2)	2.797(4)	2.864(5)	2.852(4)
Sn4–B6	2.582(3)	*2.560*	2.95(2)	2.82(2)	*2.742*	2.899(3)	2.732(5)	2.988(6)	2.872(4)
Sn4–B10	2.375(3)	*2.365*	2.50(2)	2.43(2)	*2.458*	2.521(2)	2.469(5)	2.604(6)	2.550(5)
Sn4–B7	2.492(3)	*2.514*	2.46(2)	2.47(2)	*2.535*	2.448(2)	2.585(5)	2.441(5)	2.485(5)
Sn4–B3	2.692(3)	*2.675*	2.786(19)	2.897(19)	*2.903*	2.755(2)	2.949(5)	2.671(5)	2.775(5)
C1–C2	1.445(3)	*1.463*	1.40(3)	1.44(3)	*1.437*	1.433(3)	1.431(6)	1.420(6)	1.430(5)
C2–B5[b]	2.056(4)	*1.954*	2.33(3)	2.45(3)	*2.434*	2.410(3)	2.359(7)	2.378(7)	2.399(6)
Sn4–N41			2.419(16)	2.399(15)	*2.623*	2.4481(17)	2.433(4)	2.462(4)	2.382(3)
Sn4–N42			2.396(15)	2.396(14)	*2.608*	2.4460(18)	2.419(4)	2.415(4)	2.418(3)
Δ[c]	0.144	*0.117*	0.392	0.410	*0.330*	0.341	0.331	0.400	0.320
Δ_Δ[d]			0.248	0.266	*0.212*	0.197	0.187	0.256	0.176
z[e]	3.455	*3.432*	3.644	3.644	*3.612*	3.631	3.648	3.635	3.661
θ[f]			24.26	25.68	*31.23*	30.16	27.13	16.04	29.51
ϕ[g]	33.37	*28.8*	7.46	0.97	*3.3*	4.68	8.98	6.76	5.80
x[h]	80.3	*69.2*	18.0	0.02	*7.8*	11.3	21.6	16.3	14.0

[a] **A** is the optimised model of compound **1** and **B** the optimised model of compound **2**. In both model compounds the exopolyhedral –$(CH_2)_3$– tethers were replaced by two H substituents. Optimisation was performed using Gaussian 03. Optimised parameters shown italicised for emphasis. [b] For the henicosahedral species **2–5** the smaller of the C2–B5 and C1–B9 distances is quoted, since these molecules could be numbered in one of two enantiomorphic ways. [c] Δ is the slipping parameter of the Sn4 atom, defined as its displacement, parallel to the best (least-squares) plane through B5B9B12B13B8, from the point directly above the centroid of that plane. [d] Δ_Δ is the increase in slipping for compounds **2–5** relative to **1**. [e] z is the perpendicular displacement of the Sn4 atom from the B5B9B12B13B8 plane. [f] θ is the inclination of the bipyridyl ligand, the dihedral angle between Sn4N41CCN42 and B5B9B12B13B8 planes. [g] ϕ is defined in the text as $(|C1–C2–B9 – C2–C1–B5| + |C2–B9–B5 – B9–B5–C1|)/2$. [h] x is the "percentage docosahedral character", defined as $(\phi/41.55) \times 100\%$.

shown in Fig. 3 and only **B** is shown in Fig. 5). Structurally, adduct formation is accompanied by (i) a change in cage structure from essentially docosahedral (x = 80.3% in **1**) to essentially henicosahedral (x = 0–21.6% in **2–4**), (ii) increased slipping of the Sn atom, from Δ = 0.14 Å to Δ = 0.33–0.41 Å and (iii) a slight reduction (*ca.* 0.01–0.04 Å) in the length of the C1–C2 connectivity. The slipping is predominantly away from cage C atoms, as evidenced by significantly increased Sn–C1/C2 and Sn–B3/B6 distances (averages¶ of 2.64 Å in **1** to 2.81–2.86 Å in **2–4** for Sn–C1/C2, and 2.64 Å in **1** to 2.83–2.86 Å in **2–4** for Sn–B3/B6) although the fact that Sn–B7/B10 also increases (average 2.43 Å in **1** to 2.47–2.52 Å in **2–4**) means that the overall structural change is more complicated and, indeed, we note that the Sn atom in **2–4** is displaced further from the B_5 reference plane (3.63–3.65 Å) than it is in **1** (3.45 Å). A similar phenomenon accompanied adduct formation of 1,6-Me_2-4,1,6-*closo*-SnC_2B_{10}.[2] The increase in slipping that accompanies adduct formation, Δ_Δ, is 0.19–0.27 Å in **2–4**, less than in the isomeric 4,1,6-SnC_2B_{10} species (0.28–0.39 Å).[2] Since they both start from a smaller base and change by less, overall, therefore, the slipping parameters in the carbons adjacent compounds **2–4**, 0.33–0.41 Å, are *ca.* 0.2–0.25 Å smaller than in the 4,1,6 species. The origins of this unexpected result are discussed subsequently. The slight shortening of C1–C2 as a consequence of increasing slip is reminiscent of the situation in slipped icosahedral 3,1,2-MC_2B_9 species in which case the origin has been traced to reduced depopulation of a carborane ligand orbital which is C/C bonding in nature.

The bipy, *o*-phen and Ph_2bipy ligands in **2–4** are oriented such that their N atoms are opposite the cage C atoms. This reflects the greater *trans* influence of the facial boron atoms, B3, B7, B10 and B6, over the (facial) carbon atoms, C1 and C2. Thus Sn–C bonding is somewhat weaker than Sn–B bonding (further evidence for this is the direction of slip of the Sn atom) and, to compensate, the bipy, *o*-phen and Ph_2bipy ligands position themselves *trans* to cage C with the Sn lone pair of electrons *trans* to B. In the related 4,1,6-SnC_2B_{10} adducts a broadly similar orientation of the exopolyhedral ligands was observed, with one N atom *trans* to the degree-5 C atom C6 and the other *trans* to the connectivity between the degree-4 C atom C1 and the degree-5 B atom B2.[2] In bipyridyl adducts of 4,1,10-SnC_2B_{10} the exopolyhedral ligand lies *trans* to the degree-5 C atom C10, whilst in 4,1,12-SnC_2B_{10} it lies *trans* to the degree-4 C atom C1,[16] these results affording the ranking of *trans* influence as $B_{degree\text{-}5} > C_{degree\text{-}4} > C_{degree\text{-}5}$. The origin of the general result that the carbon atoms in heterocarboranes have a relatively weak *trans* influence lies in the fact that the frontier molecular orbitals of carborane ligands are predominantly localised on the facial boron atoms.[5]

The stereochemical influence of the Sn lone pair of electrons is reflected not only in the orientation of the bipy, *o*-phen and Ph_2bipy ligands in **2–4** but also in their inclination, at an angle θ of *ca.* 30° to the B5B9B12B13B8 reference plane. A slight difference in inclination angle (θ = 16°) exists for **4**B although we note that in **4** there is clear evidence of intermolecular π–π interactions in the crystal. Sn–N distances in **2–4** are 2.42–2.46 Å, somewhat longer than those (2.35–2.43 Å) in the related 4,1,6-SnC_2B_{10} adducts,[2] which may be related to the smaller slipping distortions in the present compounds.

We determined the structure of **5** (Fig. 6) for comparison with that of **2**, to see if the two different tethers, μ-$(CH_2)_3$- and μ-{$C_6H_4(CH_2)_2$}-, had any effect on structure. Although the comparison is somewhat compromised by the relatively poor precision of the structural determination of **2** (a consequence of poor crystal size and quality) it is evident from the data in Table 2 that any differences are minor. One interesting feature of the structure of **5** is that the C_6 ring of the tether and the Sn4N41CCN42 sequence are nearly co-planar (dihedral angle 8.14°). In the crystal both the α,α-*o*-xylylene tether and the bipy ligand are involved in quasi-graphitic interactions with equivalent units across inversion centres.

The overall similarity between the molecular structures of **2** and **5** provides a link between the structures of our supraicosahedral 4,1,2-SnC_2B_{10} adducts and those of Xie, who used the μ-{$C_6H_4(CH_2)_2$}-tethered carborane and MeCN, THF and dme as external ligands (compounds **VI**, **VII** and **VIII**, respectively, of Table 1). Even though he used a mixture of mono- and bidentate Lewis bases in his study Xie concluded *"a stronger base leads to an increased slip distortion of the tin from the centre of the C_2B_4 bonding face"*.[8] However, Xie based this conclusion on measured Sn–cage atom distances, and did not actually calculate the slip distortions. In view of our interest in this general family of compounds we have calculated Δ for Xie's compounds (0.205, 0.253 and 0.223 Å, respectively, measuring slip with respect to the lower B_5 pentagon, or 0.320, 0.377 and 0.365 Å, respectively, measuring slip with respect to the centroid of the upper C_2B_4 ring) and find no such correlation.

Computational studies

A significant conclusion from the structural studies above is that the slipping distortion in the "carbons adjacent" 4,1,2-SnC_2B_{10} stannacarborane **1** is less than in its "carbons apart" 4,1,6- analogue 1,6-Me_2-4,1,6-*closo*-$SnC_2B_{10}H_{10}$,[1] and that this difference is maintained in the adducts of **1** reported here compared to adducts of 1,6-Me_2-4,1,6-*closo*-$SnC_2B_{10}H_{10}$.[2] This is in contrast to established work on the slipping distortions in icosahedral platina- or palladacarboranes[5,6] where the reverse is true. To check whether this difference is due to the change from icosahedral to supraicosahedral or from group 10 element to Sn, we have calculated Δ for the supraicosahedral platinacarboranes 1,2-μ-$(CH_2)_3$-4,4-$(PMe_2Ph)_2$-4,1,2-*closo*-$PtC_2B_{10}H_{10}$[9] and 4,4-$(PMe_2Ph)_2$-4,1,6-*closo*-$PtC_2B_{10}H_{12}$.[17] These are 0.08 and 0.52 Å, respectively, clearly revealing a fundamental difference between icosahedral and supraicosahedral metallacarboranes in terms of the magnitude of metal slipping as a function of C atom position.

To probe the origins of this difference, we have extended our previous density functional theory (DFT) calculations[18] on 13-vertex stannacarboranes[2] to include the "carbons-adjacent" species **1** and **2** reported here. In addition, we have revisited the structural trends in icosahedral and supraicosahedral platinacarboranes noted above.[5,17] Calculations on **1** and **2** employed the model systems **A** and **B** respectively, where the exopolyhedral–$(CH_2)_3$– tethers were replaced by two H substituents. Table 2 shows that key computed and derived distances in **A** and **B** compare well with those determined experimentally for **1** and **2** although, as noted

¶ Since compounds **2–4** are essentially henicosahedral with local mirror symmetry passing through the cage it is necessary to average Sn–C1 and Sn–C2, Sn–B3 and Sn–B6, and Sn–B7 and Sn–B10.

in our previous studies,[2] there is a tendency to overestimate the Sn–cage interactions in the bipy adduct **B**.

In order to assess the factors controlling the degree of slipping in 12- and 13-vertex metallacarboranes we turned to the family of platinacarboranes, specifically icosahedral 3,3-$(PEt_3)_2$-3,1,2-*closo*-$PtC_2B_9H_{11}$ (**XVII**)[5] and 1,7-Me_2-2,2-$(PMe_2Ph)_2$-2,1,7-*closo*-$PtC_2B_9H_9$ (**XVIII**)[6] and supraicosahedral 1,2-μ-$(CH_2)_3$-4,4-$(PMe_2Ph)_2$-4,1,2-*closo*-$PtC_2B_{10}H_{10}$ (**III**)[9] and 4,4-$(PMe_2Ph)_2$-4,1,6-*closo*-$PtC_2B_{10}H_{12}$ (**XIX**).[17] Focussing on these platinum systems has the benefit of benchmarking the approach adopted here against earlier studies of slipping in the icosahedral species.[5] In the calculations, species **XVII**, **XVIII**, **III** and **XIX** were represented by simplified models **C**, **D**, **E** and **F** respectively, in which all phosphine ligands were replaced by PH_3 and all exopolyhedral C-substituents were replaced by H (see Fig. 7 for line diagrams of all the model compounds **A–F**). As found previously[17] the calculations reproduce the experimental structures well, both in terms of the orientations of the $\{Pt(PH_3)_2\}$ fragments relative to the open face of the carborane cage and the slipping parameters (see Table 3 for the latter; full computed geometries are supplied in the ESI†).

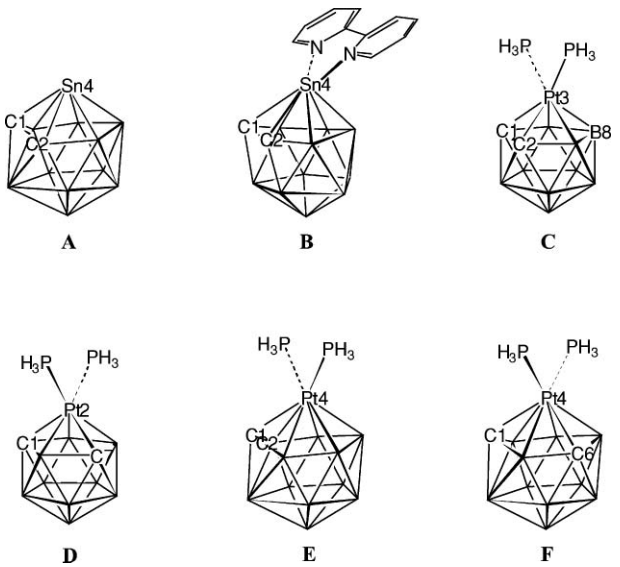

Fig. 7 Line diagrams and numbering of computational models **A–F**.

The origins of the slipping distortions in **C–F** were investigated by considering the interaction of the $\{Pt(PH_3)_2\}^{2+}$ fragment with the appropriate *nido*-$\{C_2B_n\}^{2-}$ cage ($n = 9$, 10). In the analysis we have made use of the energy decomposition scheme available within the Amsterdam Density Functional (ADF) code.[19] In this approach the interaction between two fragments can be broken up into "steric" and "orbital interaction" energy terms. The steric interaction is overall destabilising and is composed of the electrostatic interaction derived from the different charge distributions associated with each fragment, as well as a Pauli repulsion term due to interaction of occupied orbitals in each fragment. The orbital interaction arises from the overlap of occupied orbitals on one fragment with unoccupied orbitals of the other and is therefore stabilising. Where appropriate, this term can be further factored into contributions arising within different orbital symmetries. Symmetry therefore greatly facilitates

Table 3 Comparison of experimentally- (X-ray diffraction) and computationally- (DFT) determined connectivities and slip distances (Å) and conformations (χ, °) in platinacarboranes

(i) 12-vertex compounds

	XVII[5]	**C**[a]		**XVIII**[6]	**D**[a]
CCDC	EPTBOR10		CCDC	CMPBPT10	
Pt3–C1	2.530(7)	2.794	Pt2–C1[c]	2.442(7)	2.465
Pt3–C2	2.613(7)	[b]	Pt2–C7	2.452(8)	[b]
Pt3–B4	2.283(8)	2.240	Pt2–B6	2.261(8)	2.283
Pt3–B7	2.277(8)	[b]	Pt2–B11	2.255(9)	[b]
Pt3–B8	2.264(8)	2.212	Pt2–B3	2.270(9)	2.253
Pt3–P1	2.2759(18)	2.379	Pt2–P1[d]	2.303(2)	2.381
Pt3–P2	2.2843(18)	[b]	Pt2–P2	2.249(2)	2.342
Δ	0.411	0.699	Δ	0.141	0.081
χ^e	75.9	90	χ^e	10.1	0

(ii) 13-vertex compounds

	III[9]	**E**[f]		**XIX**[17]	**F**[f]
CCDC	GAQHUC		CCDC	HEYZOB	
Pt4–C1	2.381(8)	2.396	Pt2–C1	2.1652(12)	2.153
Pt4–C2	2.626(8)	2.855	Pt2–B2	2.4438(15)	2.439
Pt4–B3	2.322(8)	2.299	Pt2–B3	2.3961(14)	2.442
Pt4–B6	2.301(7)	2.292	Pt2–C6	2.8131(13)	2.894
Pt4–B7	2.305(7)	2.279	Pt2–B7	2.2631(14)	2.230
Pt4–B10	2.265(7)	2.236	Pt4–B10	2.3692(14)	2.412
Pt4–P1[g]	2.3046(18)	2.383	Pt2–P1[h]	2.2710(3)	2.346
Pt4–P2	2.3001(17)	2.398	Pt2–P2	2.3129(4)	2.420
Δ	0.080	0.195	Δ	0.518	0.583
χ^i	61.1	68.2	χ^i	148.7	141.3

[a] Structure optimised in C_s symmetry. [b] Equivalent to previous distance by symmetry. [c] Molecule renumbered relative to that in reference 6. [d] P1 lies over B3. [e] Conformation defined as dihedral angle between PtP_2 and PtB_3 planes, where the three B atoms in the latter are those that lie in the cage mirror plane. [f] Structure optimised in C_1 symmetry. [g] P1 lies over B6. [h] P1 lies over B7–B10. [i] Conformation defined as dihedral angle between PtP_2 and C1B10B11 planes, where $0 < \chi < 90$ represents, in projection, one phosphine ligand lying in the B3 quadrant and $90 < \chi < 180$ represents one phosphine ligand lying in the B7 quadrant.

the analysis and so for this reason the geometries of **C** and **D** (and **E**, see below) were recomputed in C_s symmetry with the ADF code. Importantly, this did not significantly affect the extent of slipping compared to the data in Table 3 where no symmetry constraint was applied.

In the following we will consider how the steric and orbital interaction energy terms vary as the $\{Pt(PH_3)_2\}^{2+}$ fragment is moved across the open face of the $\{C_2B_n\}^{2-}$ fragment. The approach adopted is shown in Fig. 8 for the "carbons adjacent" icosahedral model **C**. Initially, the Pt atom of the $\{Pt(PH_3)_2\}^{2+}$ fragment is placed directly above the centroid of the lower $\{B_5\}$ belt ($\Delta = 0$) and then displaced, either toward ($-\Delta$) or away

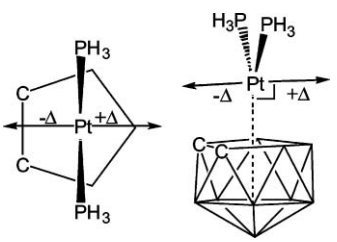

Fig. 8 Definition of slipping in the model compound **C**.

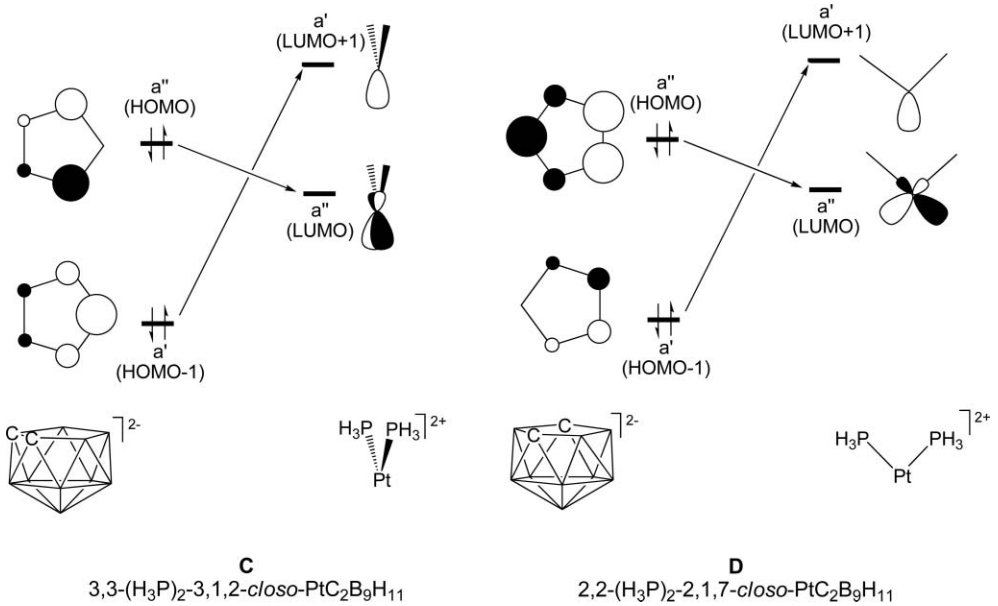

C
3,3-$(H_3P)_2$-3,1,2-*closo*-$PtC_2B_9H_{11}$

D
2,2-$(H_3P)_2$-2,1,7-*closo*-$PtC_2B_9H_{11}$

Fig. 9 Frontier orbital interactions in **C** and **D**.

(+Δ) from the carbon atoms, along the vector perpendicular to this Pt-centroid axis which passes through the position of the metal atom in the $\{Pt(PH_3)_2\}^{2+}$ fragment in the fully-optimised geometry. In all cases except **F** (see below) this analysis could be performed such that C_s symmetry was maintained throughout. At each point thus generated the steric and orbital interaction terms were calculated without any relaxation of either the $\{Pt(PH_3)_2\}^{2+}$ or $\{C_2B_n\}^{2-}$ fragments. Although this approach will tend therefore to exaggerate the various contributions to the interaction energy, the trends within these terms should be secure.

Previously, the orientation and slipping of the $\{Pt(PR_3)_2\}^{2+}$ fragment in **XVII/C** have been rationalised in terms of preferential frontier molecular orbital interactions (see Fig. 9‖). Thus strong overlap of the $\{Pt(PR_3)_2\}^{2+}$ a″ LUMO with the HOMO of the $C_2B_9H_{11}^{2-}$ cage dictates a perpendicular orientation of the $\{Pt(PR_3)_2\}^{2+}$ moiety with respect to the mirror plane of the cage. Positive slipping towards a position above B8 arises *via* maximising bonding overlap between the $\{Pt(PR_3)_2\}^{2+}$ LUMO+1 and the a′ HOMO−1 of the $\{C_2B_9H_{11}\}^{2-}$ fragment which is strongly localised on the B atoms of the open face (especially B8). For the carbons apart isomer, **XVIII/D**, the a″ HOMO–LUMO interaction again controls $\{Pt(PH_3)_2\}^{2+}$ fragment orientation which in this case lies in the cage mirror plane. The a′ HOMO-1 of the $\{C_2B_9H_{11}\}^{2-}$ fragment now displays little localisation and this, coupled to the relatively even distribution of the $\{C_2B_9H_{11}\}^{2-}$ HOMO means that only a minor slipping is seen.

The results of the energy decomposition analyses for these 12-vertex systems are shown in Fig. 10, with **C** on the left hand side and **D** on the right. For **C** the total interaction energy shown in plot (a) finds a minimum value at Δ ≈ +0.7 Å and appears to be a compromise between the orbital interaction term [plot (b), in purple] which is most stabilising at Δ *ca.* +1.0 Å and steric interactions [plot (b), in green] which minimise at Δ *ca.* +0.2 Å. Plot (c) shows that the stabilising a″ orbital interaction (in blue) is the more significant orbital interaction, it being more stabilising at higher Δ; the a′ interaction (in red) does, however, also contribute to the positive slip. Thus, although the a″ orbital interaction is the most important single contribution to the positive slipping (as revealed by the earlier EHMO analysis[5]) the present approach highlights the role played by other factors, especially the steric interaction, in controlling the detailed extent of slipping.

For model species **D** the total energy is dominated by the steric interaction term with the relevant two plots being nearly superimposable. In contrast, the orbital interaction is only weakly dependent on Δ and this arises from counteracting trends in the a′ and a″ contributions. This weak dependence of the orbital interaction on Δ is again consistent with the EHMO study.[5] What emerges in the present study is the far greater importance of the steric interaction term in determining the extent of slipping in the "carbons apart" 12-vertex system, a feature that will also be prominent in rationalising the structures of the 13-vertex systems.

Results of the energy decomposition analysis for the 13-vertex model systems **E** and **F** are shown in Fig. 11 and some further comment is required on the models used in these cases. Both **E** and **F** exhibit C_1 structures in their fully optimised forms. For **E**, in order to facilitate the analysis, a henicosahedral C_s structure was adopted which corresponds to a transition state that interconverts two equivalent docosahedral minima. This C_s structure is only 7.3 kcal mol^{-1} above the C_1 minimum and allows C_s symmetry to be maintained upon displacement of $\{Pt(PH_3)_2\}^{2+}$ to ±Δ. Test calculations on the C_1 form indicate that the outcomes of the analysis are not significantly affected by this simplification (see ESI†). For **F** no convenient close-lying C_s structure exists and so the analysis was performed on the fully optimised C_1 form.

As shown in Fig. 11, for **E** (left hand side) the destabilising steric interaction is minimised around Δ = 0.0 while the orbital interaction terms are actually least stabilising at that point. Displacement in either direction therefore enhances the overall orbital

‖ The fragmentation of **C** employed here, into doubly charged $\{C_2B_9H_{11}\}^{2-}$ and $\{Pt(PH_3)_2\}^{2+}$ fragments, differs from that used previously,[5] where neutral $\{C_2B_9H_{11}\}$ and $\{Pt(PH_3)_2\}$ fragments were used.

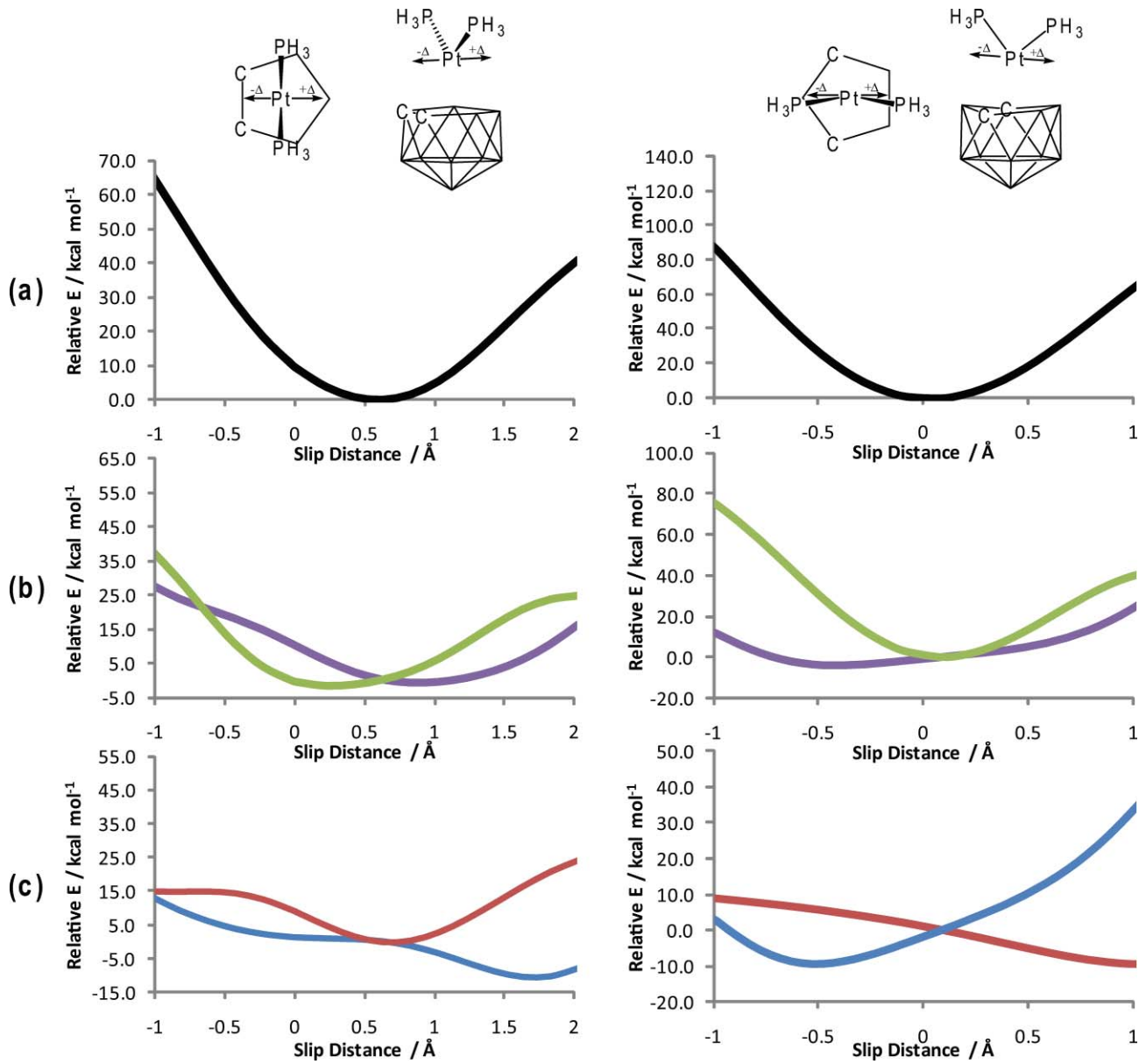

Fig. 10 Energy decomposition analyses for **C** (left) and **D** (right). Plots are (a) total interaction energy, (b) steric (green) and orbital (purple) interaction energy terms and (c) a′ (red) and a″ (blue) orbital interaction terms *vs.* Δ.

interaction, however, this does not outweigh the destabilisation arising from the steric interaction. The net result is that only a small negative slipping occurs. Orbital interactions are therefore less important in determining Δ in this case and for this reason the contributions from a′ and a″ symmetry are relegated to the ESI.† For **F** the somewhat larger positive slipping is again seen to result primarily from the steric interaction term that minimises around Δ *ca.* +0.5 Å. This is only slightly perturbed by the orbital interaction term, resulting in an overall slip of Δ *ca.* +0.6 Å.

Conclusions

The ligand-free 4,1,2-SnC_2B_{10} compound **1** and its bipy, *o*-phen and Ph_2bipy adducts **2–4** have been prepared and fully characterised, together with the bipy adduct **5** of the known species 1,2-μ-{$C_6H_4(CH_2)_2$}-4,1,2-*closo*-$SnC_2B_{10}H_{10}$. In the solid state compound **1** has a docosahedral structure, whilst **2–5** are essentially henicosahedral. A method of quantifying the "percentage docosahedral character" of a *closo*-13-vertex cluster is described. The "carbons adjacent" compounds **1–5** are all significantly less slipped than analogous "carbons apart" 4,1,6-SnC_2B_{10} species, an apparently surprising result in the context of earlier work on "carbons adjacent" and "carbons apart" icosahedral platinacarboranes. However, a computational study of "carbons adjacent" and "carbons apart" 12- and 13-vertex platinacarboranes reveals that only in one case, that of the "carbons adjacent" 12-vertex metallacarborane, is the degree of slipping determined by orbital effects. For all the other systems studied (12-vertex "carbons apart" and both "carbons apart" and "carbons adjacent" 13-vertex species) orbital effects are less

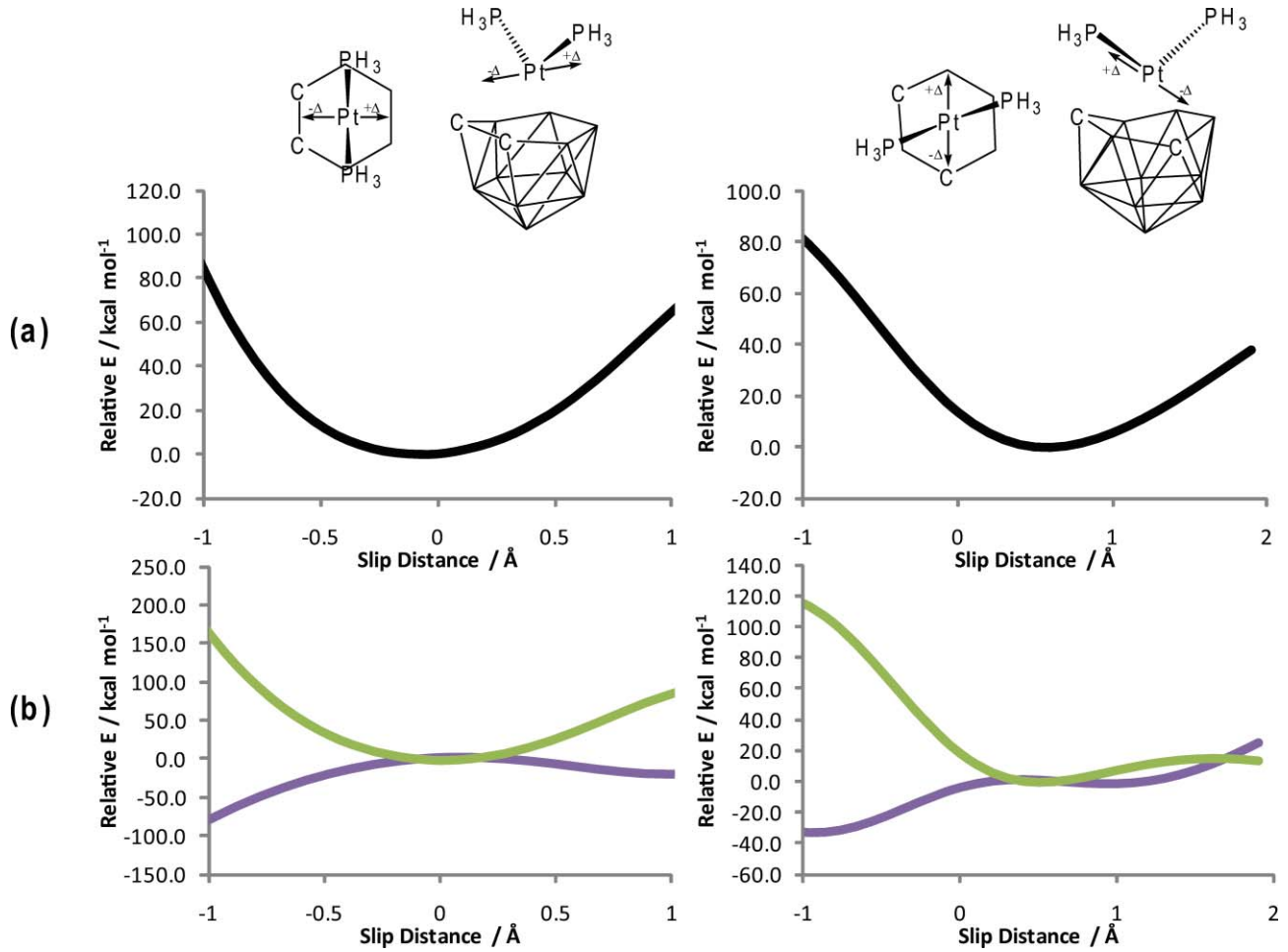

Fig. 11 Energy decomposition analyses for **E** (left) and **F** (right). Plots are (a) total interaction energy, (b) steric (green) and orbital (purple) interaction energy terms *vs.* Δ.

significant and the degree of slipping reflects the dominant role played by steric interactions.

Experimental

Synthesis

Experiments were performed under dry, oxygen-free N_2, using standard Schlenk techniques, although subsequent manipulations were sometimes performed in the open laboratory. All solvents were freshly distilled from the appropriate drying agents under nitrogen immediately before use [CH_2Cl_2; CaH_2: THF, toluene and 40–60 petroleum ether; sodium wire] or were stored over 4 Å molecular sieves and were degassed (3 × freeze–pump–thaw cycles) before use. IR spectra were recorded from CH_2Cl_2 solutions on a Perkin-Elmer Spectrum RX FT spectrophotometer. NMR spectra at 400.1 MHz (^{1}H) or 128.4 MHz (^{11}B) were recorded on a Bruker DPX-400 spectrometer from CD_2Cl_2 solutions at room temperature. EI mass spectrometry was carried out using a Kratos Concept mass spectrometer. Elemental analyses were determined by the departmental service (compound **1** only; for **2–5** only sufficient material was obtained for NMR and crystallographic studies). 1,2-μ-$(CH_2)_3$-1,2-*closo*-$C_2B_{10}H_{10}$[20] and 1,2-μ-{$C_6H_4(CH_2)_2$}-4,1,2-*closo*-$SnC_2B_{10}H_{10}$[8] were prepared by literature methods or slight variations thereof. All other reagents and solvents were supplied commercially.

1,2-μ-$(CH_2)_3$-4,1,2-*closo*-$SnC_2B_{10}H_{10}$ (1). A solution of 1,2-μ-$(CH_2)_3$-1,2-*closo*-$C_2B_{10}H_{10}$ (150 mg, 0.81 mmol) in dry, degassed, THF (20 mL) was stirred with sodium pieces (130 mg, 5.7 mmol) and naphthalene (*ca.* 10 mg) at room temperature for 48 h. The resulting dark-green solution was transferred *via* cannula to a dry, degassed, frozen (–196 °C) solution of $SnCl_2$ (153 mg, 0.81 mmol) in THF (10 mL), and the reagents then allowed to warm to 0 °C with stirring. The crude, dark brown reaction mixture was evaporated to dryness and then suspended in CH_2Cl_2 (40 mL). The mixture was filtered and all volatiles were removed *in vacuo*, yielding a white solid (60 mg, 25%). $C_5H_{16}B_{10}Sn$ requires C 19.8, H 5.82. Found C 19.9, H 5.44%. IR, ν_{max} 2547 cm^{-1} (B–H). ^{11}B{^{1}H} NMR, δ 7.73 (2B), 6.45 (4B), 4.12 (1B), 1.06 (1B), –0.27 (2B). ^{1}H NMR, δ 3.20–3.10 (m, 2H, $(CH_2)_3$), 2.85-2.75 (m, 2H, $(CH_2)_3$), 2.05–1.90 (m, 2H, $(CH_2)_3$). MS: *m*/*z* 302 (M^+), 119 ($M-C_5H_{16}B_{10}$). Recrystallisation by diffusion of a CH_2Cl_2 solution and 40–60 petroleum ether at –30 °C afforded pale-yellow diffraction-quality block crystals of **1**.

1,2-μ-$(CH_2)_3$-4-(bipy)-4,1,2-*closo*-$SnC_2B_{10}H_{10}$ (2). A solution of **1** (10 mg, 0.03 mmol) in dry, degassed toluene (5 mL) was added

to a dry, degassed toluene solution (3 mL) of 2,2′-bipyridine (6 mg, 0.04 mmol), and the resulting yellow suspension stirred for 24 h. On settling, the toluene was removed using a gas-tight syringe, leaving a yellow solid which was washed with petroleum ether (2 × 10 mL) and dried *in vacuo* to afford **2** as a yellow solid (10 mg, 73%). IR, ν_{max} 2518 cm^{-1} (B–H). ^{11}B{^{1}H} NMR, δ 3.55 (3B), 2.30 (2B), –4.05 (2B), –5.16 (2B), –10.78 (1B). ^{1}H NMR, δ 8.99 (d, 2H, bipy), 8.22 (d, 2H, bipy), 8.13 (d of d, 2H, bipy), 7.69 (d of d, 2H, bipy), 3.05–2.95 (m, 2H, $(CH_2)_3$), 2.77–2.68 (m, 2H, $(CH_2)_3$), 1.99–1.90 (m, 1H, $(CH_2)_3$), 1.78–1.66 (m, 1H, $(CH_2)_3$). Small crystals were grown by vapour diffusion of 40–60 petroleum ether and a CH_2Cl_2 solution of **2** at 5 °C.

1,2-μ-$(CH_2)_3$-4-(*o*-phen)-4,1,2-*closo*-$SnC_2B_{10}H_{10}$ (3). Likewise, a solution of **1** (30 mg, 0.10 mmol) in dry, degassed toluene (10 mL) was stirred with a dry, degassed toluene solution (10 mL) of 1,10-phenanthroline (20 mg, 0.11 mmol) to afford 31 mg (64%) of **3**. IR, ν_{max} 2540 cm^{-1} (B–H). ^{11}B{^{1}H} NMR, δ 3.73 (3B), 2.36 (2B), –4.25 (2B), –5.07 (2B), –10.69 (1B). ^{1}H NMR, δ 9.34 (d, 2H, phen), 8.59 (d, 2H, phen), 8.05 (s, 2H, phen), 8.00 (d of d, 2H, phen), 3.15–3.05 (m, 2H, $(CH_2)_3$), 2.82–2.72 (m, 2H, $(CH_2)_3$), 2.05–1.95 (m, 1H, $(CH_2)_3$), 1.80–1.70 (m, 1H, $(CH_2)_3$). Crystals by solvent diffusion of 40–60 petroleum ether and a CH_2Cl_2 solution of **3** at 5 °C.

1,2-μ-$(CH_2)_3$-4-(Ph_2bipy)-4,1,2-*closo*-$SnC_2B_{10}H_{10}$ (4). In the same way, a solution of **1** (10 mg, 0.03 mmol) in dry, degassed toluene (10 mL) was allowed to react with a dry, degassed toluene solution (10 mL) of 4,4′-diphenyl-2,2′-bipyridine (12 mg, 0.04 mmol), yielding 15 mg (82%) of **4**. IR, ν_{max} 2522 cm^{-1} (B–H). ^{11}B{^{1}H} NMR, δ 3.70 (3B), 2.41 (2B), –4.13 (4B), –10.79 (1B). ^{1}H NMR, δ 9.03 (d, 2H, Ph_2bipy), 8.45 (2, 2H, Ph_2bipy), 7.91 (d, 2H, Ph_2bipy), 7.82–7.73 (m, 4H, Ph_2bipy), 7.64–7.55 (m, 6H, Ph_2bipy), 3.05–2.99 (m, 2H, $(CH_2)_3$), 2.80–2.70 (m, 2H, $(CH_2)_3$), 2.01–1.920 (m, 1H, $(CH_2)_3$), 1.78–1.69 (m, 1H, $(CH_2)_3$). The product was crystallised by solvent diffusion of 40–60 petroleum ether and a CH_2Cl_2 solution of **4** at 5 °C.

1,2-μ-{$C_6H_4(CH_2)_2$}-4-(bipy)-4,1,2-*closo*-$SnC_2B_{10}H_{10}$ (5). A solution of 1,2-μ-{$C_6H_4(CH_2)_2$}-4,1,2-*closo*-$SnC_2B_{10}H_{10}$ (70 mg, 0.192 mmol) in dry, degassed toluene (10 mL) was added to a dry, degassed toluene solution (10 mL) of 2,2′-bipyridine (90 mg, 0.575 mmol), and the resulting yellow suspension stirred for 24 h. After settling, the toluene was removed using a gas-tight syringe, leaving a yellow solid, subsequently washed with petroleum ether (2 × 10 mL) and dried *in vacuo* to afford **5** as a yellow solid (61 mg, 61%). IR, CH_2Cl_2, ν_{max} 2521 cm^{-1} (B–H). ^{11}B{^{1}H} NMR, δ 7.19 (br, 2B), 4,16 (br, 2B), 2.92 (br, 2B), –3.65 (br, 1B), –5.62 (br, 1B), –10.48 (br, 2B). ^{1}H NMR, δ 8.87 (d, 2H, bipy), 8.24 (d, 2H, bipy), 8.04 (d of d, 2H, bipy), 7.60 (d of d, 2H, bipy), 7.27–7.10 (m, 4H, $C_6H_4(CH_2)_2$), 3.98 (d, 2H, $C_6H_4(CH_2)_2$), 3.82 (d, 2H, $C_6H_4(CH_2)_2$). Diffraction-quality crystals were grown by slow evaporation of a CH_2Cl_2 solution of **5** at room temperature.

Crystallography

Intensity data from **1** and **3–5** were collected from single crystals on a Bruker X8 APEX2 diffractometer using Mo-Kα X-radiation, with crystals mounted in inert oil on a cryoloop and cooled to 100 K by an Oxford Cryosystems Cryostream. Data from compound **2**, which affords only very small crystals were collected by the EPSRC National Crystallographic Service at Southampton using a Bruker-Nonius APEX II diffractometer equipped with a Bruker-Nonius FR591 rotating anode and confocal mirror monochromator with Mo-Kα X-radiation at 120 K. The structures were solved by direct methods and refined by full-matrix least-squares. All non-H atoms were refined with anisotropic displacement parameters, although it was necessary to restrain the anisotropy, in **2**, of four B atoms and four C atoms (two methylene, one solvent and one bipy) and, in **4**, of three B atoms, one cage C and one bipy C atom, using the ISOR command.[21] In compound **2** there is $\frac{1}{4}$ molecule of CH_2Cl_2 per molecule of stannacarborane, and in **5** the solvent was modelled as $\frac{1}{3}$ molecule of hexane per molecule of stannacarborane. The crystal of **1** was treated as a two-component twin, indexed using CELL_NOW,[22]

Table 4 Crystallographic data for compounds **1–5**

	1	**2**	**3**	**4**	**5**
Formula	$C_5H_{16}B_{10}Sn$	$C_{15}H_{24}B_{10}N_2Sn\cdot\frac{1}{4}\,CH_2Cl_2$	$C_{17}H_{24}B_{10}N_2Sn$	$C_{27}H_{32}B_{10}N_2Sn$	$C_{20}H_{26}B_{10}N_2Sn\cdot\frac{1}{3}C_6H_{14}$
M	302.97	480.38	483.17	611.34	549.94
Crystal system	Monoclinic	Monoclinic	Monoclinic	Monoclinic	Monoclinic
Space group	$P2_1/c$	$P2_1/c$	$P2_1/n$	$P2_1/c$	$P2_1/n$
a/Å	11.520(3)	10.1522(8)	8.2556(14)	7.58370(10)	11.8737(7)
b/Å	7.4934(17)	18.4533(17)	23.479(4)	37.9500(8)	14.0561(8)
c/Å	14.040(3)	22.9010(19)	10.8500(15)	19.5831(4)	15.2938
β (°)	92.078(10)	93.834(5)	98.566(9)	96.6860(10)	109.310(3)
U/Å^3	1211.2(5)	4280.7(6)	2079.6(6)	5597.71(18)	2408.9(2)
Z	4	8	4	8	4
F(000)/e	584	1908	960	2464	1107
D_c/Mg m^{-3}	1.661	1.491	1.543	1.451	1.516
μ(Mo-Kα)/mm^{-1}	2.062	1.261	1.236	0.935	1.077
θ_{max} (°)	27.53	27.59	34.33	23.61	28.62
Data measured	31929	26476	67393	77776	54270
Unique data, n	3577	9313	8582	8186	6141
R_{int}	0.0643	0.1057	0.1006	0.0712	0.0690
R, wR_2 (obs. data)	0.0251, 0.0792	0.1885, 0.3476	0.0392, 0.0788	0.0376, 0.0695	0.0396, 0.0889
S	1.150	2.375	0.967	1.076	0.932
Variables	164	533	301	721	346
E_{max}, E_{min}/e Å^{-3}	0.733, –0.637	1.931, –1.824	1.307, –1.411	0.986, –0.771	1.175, –1.100

scaled and absorption corrected using TWINABS[23] and refined using HKLF5 which includes both components. Data from **2** were also treated as a two-component twin but refined using the twin law –1 0 0 0 –1.0 0 1.65 0 1 and HKLF4 data. This proved to be the best model and data set for these crystals arising from many attempts including the use of synchrotron data. Data from **3–5** was corrected for absorption using SADABS.[24] For **3**, **5** and some H atoms in **1**, cage-bound H atoms were located in difference Fourier maps and freely refined. Cage H atoms of **4** and the remaining cage H atoms in **1** were constrained to B–H 1.10 Å. In all cases, H atom thermal parameters were set to $1.2 \times U_{eq}$ of the attached B or C atom. Table 4 contains further experimental details.

Calculations

All geometries were optimised without constraints using Gaussian 03, Revision C.02[18] employing the BP86 functional.[25] 6-31G** basis sets were used for B, C, H and N atoms[26] whilst for P, Pt and Sn the Stuttgart relativistic ECP[27] was employed with additional d-polarization functions for P and Sn. Local minima were confirmed as such through analytical frequency calculations. Energy decomposition analyses were performed with ADF2009.01,[19] applying symmetry constraints, if appropriate, as described in the text. The BP86 function was employed and ZORA/TZ2P basis sets were used for all atoms. Geometry measurements were made using Mercury.[28]

Acknowledgements

We thank the EPSRC for funding (PDA supported by DTA studentship; DE and DMcK supported by project EP/E02971X/1) and the EPSRC National Crystallographic Service at the University of Southampton for data from compound **2**.

Notes and References

1 N. M. M. Wilson, D. Ellis, A. S. F. Boyd, B. T. Giles, S. A. Macgregor, G. M. Rosair and A. J. Welch, *Chem. Commun.*, 2002, 464.
2 P. D. Abram, D. McKay, D. Ellis, S. A. Macgregor, G. M. Rosair, R. Sancho and A. J. Welch, *Dalton Trans.*, 2009, 2345.
3 (*a*) R. W. Rudolph, R. L. Voorhees and R. E. Cochoy, *J. Am. Chem. Soc.*, 1970, **92**, 3351; (*b*) P. Jutzi, P. Galow, S. Abu-Orabi, A. M. Arif, A. H. Cowley and N. C. Norman, *Organometallics*, 1987, **6**, 1024.
4 (*a*) N. S. Hosmane, N. N. Sirmokadam and R. H. Herber, *Organometallics*, 1984, **3**, 1665; (*b*) N. S. Hosmane, P. de Meester, N. N. Maldar, S. B. Potts, S. S. C. Chu and R. H. Herber, *Organometallics*, 1986, **5**, 772.
5 D. M. P. Mingos, M. I. Forsyth and A. J. Welch, *J. Chem. Soc., Dalton Trans.*, 1978, 1363.
6 A. J. Welch, *J. Chem. Soc., Dalton Trans.*, 1975, 1473.
7 A. Burke, D. Ellis, B. T. Giles, B. E. Hodson, S. A. Macgregor, G. M. Rosair and A. J. Welch, *Angew. Chem., Int. Ed.*, 2003, **42**, 225.
8 K.-H. Wong, H.-S. Chan and Z. Xie, *Organometallics*, 2003, **22**, 1775.
9 R. McIntosh, D. Ellis, J. Gil-Lostes, K. J. Dalby, G. M. Rosair and A. J. Welch, *Dalton Trans.*, 2005, 1842.
10 G. K. Barker, M. P. Garcia, M. Green, F. G. A. Stone and A. J. Welch, *J. Chem. Soc., Chem. Commun.*, 1983, 137.
11 K. J. Donaghy, P. J. Carroll and L. G. Sneddon, *J. Organomet. Chem.*, 1998, **550**, 77.
12 G. Zi, H.-W. Li and Z. Xie, *Organometallics*, 2001, **20**, 3836.
13 W.-C. Kwong, H.-S. Chan, Y. Tang and Z. Xie, *Organometallics*, 2004, **23**, 3098.
14 J. Zhang, L. Deng, H.-S. Chan and Z. Xie, *J. Am. Chem. Soc.*, 2007, **129**, 18.
15 L. Deng, H.-S. Chan and Z. Xie, *J. Am. Chem. Soc.*, 2006, **128**, 5219.
16 P. D. Abram, D. Ellis, G. M. Rosair and A. J. Welch, *Chem. Commun.*, 2009, 5403.
17 K. J. Dalby, D. Ellis, S. Erhardt, R. D. McIntosh, S. A. Macgregor, K. Rae, G. M. Rosair, V. Settles, A. J. Welch, B. E. Hodson, T. D. McGrath and F. G. A. Stone, *J. Am. Chem. Soc.*, 2007, **129**, 3302.
18 *Gaussian 03, Revision C.02*, M. J. Frisch, G. W. Trucks, H. B. Schlegel, G. E. Scuseria, M. A. Robb, J. R. Cheeseman, J. A. Montgomery Jr., T. Vreven, K. N. Kudin, J. C. Burant, J. M. Millam, S. S. Iyengar, J. Tomasi, V. Barone, B. Mennucci, M. Cossi, G. Scalmani, N. Rega, G. A. Petersson, H. Nakatsuji, M. Hada, M. Ehara, K. Toyota, R. Fukuda, J. Hasegawa, M. Ishida, T. Nakajima, Y. Honda, O. Kitao, H. Nakai, M. Klene, X. Li, J. E. Knox, H. P. Hratchian, J. B. Cross, V. Bakken, C. Adamo, J. Jaramillo, R. Gomperts, R. E. Stratmann, O. Yazyev, A. J. Austin, R. Cammi, C. Pomelli, J. W. Ochterski, P. Y. Ayala, K. Morokuma, G. A. Voth, P. Salvador, J. J. Dannenberg, V. G. Zakrzewski, S. Dapprich, A. D. Daniels, M. C. Strain, O. Farkas, D. K. Malick, A. D. Rabuck, K. Raghavachari, J. B. Foresman, J. V. Ortiz, Q. Cui, A. G. Baboul, S. Clifford, J. Cioslowski, B. B. Stefanov, G. Liu, A. Liashenko, P. Piskorz, I. Komaromi, R. L. Martin, D. J. Fox, T. Keith, M. A. Al-Laham, C. Y. Peng, A. Nanayakkara, M. Challacombe, P. M. W. Gill, B. Johnson, W. Chen, M. W. Wong, C. Gonzalez and J. A. Pople, Gaussian Inc., Wallingford, CT, USA, 2004.
19 *ADF2009.01*, E. J. Baerends, J. Autschbach, D. Bashford, A. Bérces, F. M. Bickelhaupt, C. Bo, P. M. Boerrigter, L. Cavallo, D. P. Chong, L. Deng, R. M. Dickson, D. E. Ellis, M. van Faassen, L. Fan, T. H. Fischer, C. F. Guerra, A. Ghysels, A. Giammona, S. J. A. van Gisbergen, A. W. Götz, J. A. Groeneveld, O. V. Gritsenko, M. Grüning, F. E. Harris, P. van den Hoek, C. R. Jacob, H. Jacobsen, L. Jensen, G. van Kessel, F. Kootstra, M. V. Krykunov, E. van Lenthe, D. A. McCormack, A. Michalak, M. Mitoraj, J. Neugebauer, V. P. Nicu, L. Noodleman, V. P. Osinga, S. Patchkovskii, P. H. T. Philipsen, D. Post, C. C. Pye, W. Ravenek, J. I. Rodríguez, P. Ros, P. R. T. Schipper, G. Schreckenbach, M. Seth, J. G. Snijders, M. Solà, M. Swart, D. Swerhone, G. te Velde, P. Vernooijs, L. Versluis, L. Visscher, O. Visser, F. Wang, T. A. Wesolowski, E. M. van Wezenbeek, G. Wiesenekker, S. K. Wolff, T. K. Woo, A. L. Yakovlev and T. Ziegler, SCM, Theoretical Chemistry, Vrije Universiteit, Amsterdam, The Netherlands, 2009, http://www.scm.com.
20 T. E. Paxson, M. K. Kaloustian, G. M. Tom, R. J. Wiersema and M. F. Hawthorne, *J. Am. Chem. Soc.*, 1972, **94**, 4882.
21 *CELL_NOW*, G. M. Sheldrick, University of Göttingen, Germany, 2005.
22 *TWINABS*, G. M. Sheldrick, University of Göttingen, Germany, 2007.
23 *SADABS, V2.05*, G. M. Sheldrick, University of Göttingen, Germany, 2005.
24 *SHELXTL, V6.10*, Bruker-AXS, Madison, WI, USA, 2000.
25 (*a*) H. L. Schmider and A. D. Becke, *J. Chem. Phys.*, 1998, **108**, 9624; (*b*) J. P. Perdew, *Phys. Rev. B: Condens. Matter*, 1986, **33**, 8822.
26 (*a*) W. J. Hehre, R. Ditchfield and J. A. Pople, *J. Chem. Phys.*, 1972, **56**, 2257; (*b*) P. Hariharan and J. A. Pople, *Theor. Chim. Acta*, 1973, **28**, 213.
27 (*a*) A. Bergner, M. Dolg, H. Kuechle, H. Stoll and H. Preuss, *Mol. Phys.*, 1993, **80**, 1431; (*b*) M. Kaupp, P. v. R. Schleyer, H. Stoll and H. Preuss, *J. Chem. Phys.*, 1991, **94**, 1360; (*c*) M. Dolg, H. Stoll, H. Preuss and R. M. Pitzer, *J. Phys. Chem.*, 1993, **97**, 5852.
28 *Mercury, version 1.4.2*, Cambridge Crystallographic Data Center, Cambridge, UK, 2006.

Supraicosahedral indenyl cobaltacarboranes†‡

Greig Scott,[a] Amelia McAnaw,[a] David McKay,[a] Alan S. F. Boyd,[a] David Ellis,[a] Georgina M. Rosair,[a] Stuart A. Macgregor,*[a] Alan J. Welch,*[a] Franco Laschi,[b] Fulvio Rossi[b] and Piero Zanello*[b]

Received 15th February 2010, Accepted 9th April 2010
First published as an Advance Article on the web 4th May 2010
DOI: 10.1039/c003067h

13-vertex indenyl cobaltacarboranes with 4,1,6-, 4,1,10- and 4,1,2-CoC_2B_{10} architectures have been synthesised by reduction of the corresponding *closo* carborane and metallation with an {(η-C_9H_7)Co} fragment. Variants of the 4,1,6-isomer were prepared with no, one and two methyl groups on cage C atoms, whilst 4,1,2-species were obtained both with two methyl groups and a trimethylene tether on the cage C atoms. Thermolysis of the 4,1,6-isomers yielded the corresponding 4,1,8-isomers, which in turn were converted to 4,1,12-isomers by thermolysis at higher temperatures. Alternatively relatively mild heating of the 4,1,10-isomer led to the 4,1,12-isomer directly. Products were characterised by mass spectrometry, ^{1}H and ^{11}B NMR spectroscopies and, in most cases, elemental analysis, and nine compounds were studied crystallographically. The 4,1,6-, 4,1,8-, 4,1,10- and 4,1,12- species have docosahedral cages whilst the 4,1,2-species are henicosahedral. In the structural studies attention focused on the orientation of the indenyl ligand with respect to the carborane ligand since this affords experimental information on the metal-cage bonding through the *structural indenyl effect*. There is a general tendency for the indenyl ligand to adopt orientations in which the ring junction C atoms lie *trans* to cage B atoms. In cases where the orientation is not compromised by the presence of a non-H substituent on the face of the carborane there is generally good agreement between the experimental orientation and that computed by DFT calculations for the related naphthalene ferracarboranes (η-$C_{10}H_8$)$FeC_2B_{10}H_{12}$. The presence of C-methyl substituents in the indenyl cobaltacarboranes tends to override this preference except in the case of 1,6-Me_2-4-(η-C_9H_7)-4,1,6-*closo*-$CoC_2B_{10}H_{10}$ where the indenyl ligand instead is forced to incline away from the cage methyl groups. In DCM solution the 4,1,6-, 4,1,8-, 4,1,10- and 4,1,12- isomers of (η-C_9H_7)$CoC_2B_{10}H_{12}$ exhibit two, stepwise, 1-electron reductions assigned to Co(III)/Co(II)/Co(I) couples at less negative potentials than those of the corresponding Cp compounds. Moreover these reductions are easier for those isomers (4,1,6- and 4,1,10-) in which there are two cage C atoms in the carborane face to which the metal atom is bound. By spectroelectrochemical and EPR measurements it is concluded that the reductions of these indenyl cobaltacarboranes are largely metal-based.

Introduction

There is considerable current interest in supraicosahedral heteroboranes.[1] The synthesis and development of the chemistry of boron-based polyhedral compounds with more than 12 vertices in the cluster is both academically challenging and of potential importance, as such compounds could prove to be of value in a range of applications from weakly co-ordinating anions in homogeneous catalysis[2] to new and effective agents for the delivery of high concentration of boron to tumour sites in Boron-Neutron Capture Therapy.[3]

In theoretical studies of supraicosahedral heteroboranes $[B_nH_n]^{2-}$, Lipscomb[4] and later Schleyer[5] have shown that the preferred structures of 13-, 14- and 15-vertex clusters involve degree-6 vertices, *i.e.* vertices with six cage connectivities. The preferred 13-vertex cluster is the docosahedron (Fig. 1, left) which features two degree-6 vertices (vertices 4 and 5) and is the structure found for very many 13-vertex heteroboranes, including the first such species to be prepared, 4-(η-C_5H_5)-4,1,6-*closo*-$CoC_2B_{10}H_{12}$.[1a,1b,6] An interesting variant on the docosahedron is the henicosahedron (Fig. 1, right), topologically related to the former by the formal breaking of the 2–5 connectivity. The henicosahedron retains only one degree-6 vertex (vertex 4) and is frequently observed in species in which there are two cage carbon atoms held adjacent by an exopolyhedral tether, including the first 13-vertex carborane.[1c]

[a]*Department of Chemistry, Heriot-Watt University, Edinburgh, UK EH14 4AS. E-mail: a.j.welch@hw.ac.uk, s.a.macgregor@hw.ac.uk; Fax: +44 (0)131 451 3180; Tel: +44 (0)131 451 3217, +44 (0)131 451 8031*
[b]*Dipartimento di Chimica dell'Università di Siena, Via De Gasperi 2, 53100, Siena, Italy. E-mail: Zanello@unisi.it; Fax: +39 (0)577 234254; Tel: +39 (0)577 234262*

† Dedicated to Professor David Rankin on the occasion of his retirement and in recognition of his outstanding achievements in structural chemistry.

‡ Electronic supplementary information (ESI) available: Electronic supplementary information (ESI) available: Tables S1–S6; computational models. Table S7; spectroelectrochemical data for compounds **1**, **3**, **8** and **9** and their 1-electron reduced anions. Figs. S1–S6; perspective views of single molecules of compounds **4**, **7–10** and **12**. Fig. S7; cyclic voltammogram of 1,2-*closo*-$C_2B_{10}H_{12}$. Fig. S8; second derivative X-band EPR spectrum of [**1**]$^-$. CCDC reference numbers 766296–766300, 766301–766304. For ESI and crystallographic data in CIF or other electronic format see DOI: 10.1039/c003067h

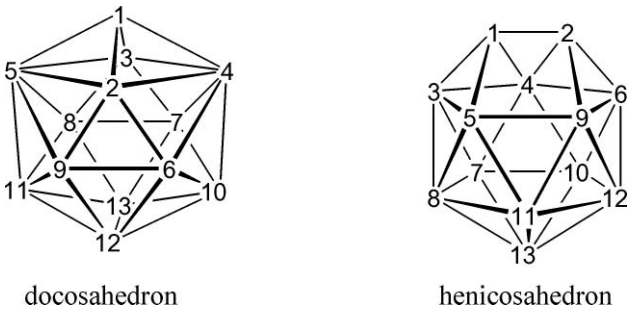

Fig. 1 The docosahedron (left) and henicosahedron (right) and numbering schemes.

It is clear that fragments with relatively diffuse frontier orbitals (*e.g.* transition-metal fragments) are better able to stabilise degree-6 polyhedral sites than those with more contracted orbitals (*e.g.* {BH} and especially {CH} fragments)[7] and it is therefore not surprising that the vast majority of supraicosahedral heteroboranes known are metal-containing species. Equally, the archetypal synthetic route to supraicosahedral heteroboranes is reduction followed by capitation (addition of a new vertex),[1a,1b] and the need for the precursor to be reducible has meant that the vast majority of supraicosahedral heteroboranes are metallacarboranes, with the overall synthetic process to 13-vertex species being reduction of an icosahedral carborane followed by metallation.

A ubiquitous metal fragment used in this chemistry is {CpCo} (Cp = η-C_5H_5). Early studies using this fragment described the initial 13-vertex metallacarborane 4,1,6-CoC_2B_{10} from reduction/metallation of 1,2-C_2B_{10} or 1,7-C_2B_{10} and from it, by progressive thermolysis, two further isomers, 4,1,8-CoC_2B_{10} and 4,1,12-CoC_2B_{10}.[1a,1b] The 4,1,6-isomer was crystallographically characterised shortly after its synthesis,[6] but the first crystallographic confirmation of 4,1,8- and 4,1,12-isomers (as Cp* analogues, Cp* = η-C_5Me_5) followed some 30 years later.[8] The isomerisation sequence 4,1,6-MC_2B_{10} → 4,1,8-MC_2B_{10} → 4,1,12-MC_2B_{10} parallels the well-known thermal isomerisation of carboranes[9] in that the C atoms are progressively separated. However, yields of (particularly) 4,1,12-isomers by thermolysis starting from 4,1,6-isomers are sometimes relatively low, and for some metal fragments, *e.g.* {(arene)Ru}, very high temperatures are required.[10] A few years ago we described, from reduction/metallation of 1,12-C_2B_{10}, a new isomer, 4,1,10-MC_2B_{10}, which can be used as a more convenient precursor to 4,1,12- species.[11] One example of a further isomer, 4,1,11-MC_2B_{10}, has been afforded in trace amounts by reduction and metallation ({arene)Ru}) of 1,12-Ph_2-1,12-*closo*-$C_2B_{10}H_{10}$.[12] All the 13-vertex metallacarboranes noted above are docosahedral in structure. Finally, 4,1,2-MC_2B_{10} species, which may have either docosahedral or henicosahedral structures, are formed by reduction and metallation of tethered 1,2-C_2B_{10} carboranes.[13]

Examples of all the above isomers of 13-vertex MC_2B_{10} metallacarboranes (except the 4,1,11- isomer) are known with the {CpCo} metal fragment.[1a,1b,8,11,13] In this paper we report the synthesis, characterisation and structural study of 4,1,6-, 4,1,8-, 4,1,10, 4,1,12- and 4,1,2-CoC_2B_{10} species featuring {(indenyl)Co} fragments. In η-indenyl compounds the ring junction carbon atoms are relatively weakly bound to the metal atom since their p_π atomic orbitals are part of both the η-bonded C_5 ring and the free C_6 ring. This gives rise not only to a *kinetic indenyl effect* (in which indenyl compounds undergo ligand substitution reactions much more rapidly than analogous Cp compounds)[14] but also to a *structural indenyl effect* if the co-ligands on the metal have differing *trans* influences. We have previously shown that this is manifested in icosahedral indenyl metallacarboranes as a distinct orientational preference for the indenyl ligand.[15] In the present paper we make use of this phenomenon to probe, both experimentally and computationally, the relative *trans* influences of cage C and B atoms in supraicosahedra where the cage atoms directly bound to metal are cluster vertices of differing degrees.

Finally we report electrochemical, spectroelectrochemical and EPR studies of selected supraicosahedral indenyl cobaltacarboranes and their Cp analogues, to better understand the electronic structures of these species and probe their capacity for further expansion *via* reduction/capitation reactions.

Results and discussion

Synthesis and spectroscopy

The supraicosahedral indenyl cobaltacarborane species 4-(η-C_9H_7)-4,1,6-*closo*-$CoC_2B_{10}H_{12}$ (**1**), 1,6-Me_2-4-(η-C_9H_7)-4,1,6-*closo*-$CoC_2B_{10}H_{10}$ (**2**), 1(or 6)-Me-4-(η-C_9H_7)-4,1,6-*closo*-$CoC_2B_{10}H_{11}$ (**5**), 4-(η-C_9H_7)-4,1,10-*closo*-$CoC_2B_{10}H_{12}$ (**8**) and 1,2-μ-$(CH_2)_3$-4-(η-C_9H_7)-4,1,2-*closo*-$CoC_2B_{10}H_{10}$ (**11**) were prepared as brown or orange solids in moderate yields by Na or Li reduction of the corresponding carborane (**1**, 1,2-*closo*-$C_2B_{10}H_{12}$; **2**, 1,2-Me_2-1,2-*closo*-$C_2B_{10}H_{10}$; **5**, 1-Me-1,2-*closo*-$C_2B_{10}H_{11}$; **8**, 1,12-*closo*-$C_2B_{10}H_{12}$; **11**, 1,2-μ-$(CH_2)_3$-1,2-*closo*-$C_2B_{10}H_{10}$) and treatment of the *nido* dianion thus formed with Li[C_9H_7] and $CoCl_2$, followed by air-oxidation. For **1**, **2**, **5** and **11** the initial reduction proceeds in THF, but for **8** it is necessary to use liquid NH_3. These syntheses thus parallel those of the corresponding supraicosahedral cyclopentadienyl cobaltacarboranes.[1a,1b,11,13] Compounds **1**, **2** and **5** have docosahedral 4,1,6-CoC_2B_{10} architectures in the solid state (*vide infra* for structures of **1** and **2**) but are fluctional in solution *via* a double diamond-square-diamond process first suggested by Hawthorne[1b] and later confirmed by us computationally (for the related 4-arene-4,1,6-RuC_2B_{10} system).[16] For **1** and **2** this fluctional process affords time-averaged C_s molecular symmetry (including rendering cage carbon atoms 1 and 6 equivalent), clearly evident in the $^{11}B\{^1H\}$ and ^1H NMR spectra. However, compound **5** is asymmetrically C_{cage}-substituted, so never attains C_s symmetry in spite of any fluctionality (which therefore cannot be confirmed, but, given the fluctionality of both **1** and **2**, such fluctionality of **5** is highly likely) and presents nine resonances in the $^{11}B\{^1H\}$ spectrum (one integral-2 co-incidence). Consequently, in the absence of a crystallographic study we do not know whether in the solid state compound **5** is methyl-substituted at C1 or C6, but since **5** was expressly made only as a precursor of the target compound **7** we have not addressed this point further.

Compound **8** has a docosahedral 4,1,10-CoC_2B_{10} architecture (*vide infra*) and thus a cage which has C_s symmetry. The NMR spectra of **8** confirm overall molecular C_s symmetry, meaning that the indenyl ligand must be undergoing rotation (or at least substantial libration) about the Co···cage axis in solution at room temperature. Such a process is fully expected. ^{11}B and ^1H ($C_{cage}H$)

chemical shifts in **8** are in excellent agreement with those in the analogous Cp compound.[11]

The tethered compound **11** has a henicosahedral 4,1,2-CoC_2B_{10} cage structure, similar to that of its Cp analogue,[13] which, together with indenyl rotation or libration, affords the molecule the C_s symmetry which is evident in solution. Compound **12**, 1,2-Me_2-4-(η-C_9H_7)-4,1,2-*closo*-$CoC_2B_{10}H_{10}$, is also a 4,1,2-CoC_2B_{10} species with a similar henicosahedral structure, but it is untethered. This compound is prepared, albeit in relatively poor yield, by reduction and metallation of the silyl-tethered carborane 1,2-μ-($CH_2SiMe_2CH_2$)-1,2-*closo*-$C_2B_{10}H_{10}$. It has previously been shown that this carborane can be reduced and boronated to afford a tethered 13-vertex carborane which readily loses its tether on chromatography on silica.[17] The synthesis of **12** following chromatographic work-up clearly parallels this process, but nevertheless constitutes, as far as we are aware, the first preparation of an untethered 4,1,2-MC_2B_{10} species. Spectroscopically compound **12** strongly resembles the tethered compound **11**, with a 2 : 2 : 1 : 1 : 2 : 2 pattern in the $^{11}B\{^1H\}$ spectrum from δ *ca.* +17 to *ca.* −10.

The remaining cobaltacarboranes, 4-(η-C_9H_7)-4,1,8-*closo*-$CoC_2B_{10}H_{12}$ (**3**), 1,8-Me_2-4-(η-C_9H_7)-4,1,8-*closo*-$CoC_2B_{10}H_{10}$ (**4**), 1-Me-4-(η-C_9H_7)-4,1,8-*closo*-$CoC_2B_{10}H_{11}$ (**6**), 8-Me-4-(η-C_9H_7)-4,1,8-*closo*-$CoC_2B_{10}H_{11}$ (**7**), 4-(η-C_9H_7)-4,1,12-*closo*-$CoC_2B_{10}H_{12}$ (**9**) and 1,12-Me_2-4-(η-C_9H_7)-4,1,12-*closo*-$CoC_2B_{10}H_{10}$ (**10**), were all prepared by thermal isomerisations. Heating **1** to reflux in THF affords a good yield of the 4,1,8-CoC_2B_{10} isomer **3**, whilst similar thermolysis of **2** produces the disubstituted analogue **4** also in high yield. Compounds **3** and **4** are immediately identified as 4,1,8-CoC_2B_{10} species by the occurrence of a relatively high frequency resonance in their ^{11}B NMR spectra, δ *ca.* +21 - +23, such high frequency signals having previously been reported for 4-(η-C_5H_5)-4,1,8-*closo*-$CoC_2B_{10}H_{12}$ and 4-(η-C_5Me_5)-4,1,8-*closo*-$CoC_2B_{10}H_{12}$.[1b,8] That **3** and **4** are asymmetric is confirmed by the observation of two close, but clearly distinguished, integral-1 multiplets at δ *ca.* 5.8 (**3**) and 5.6 (**4**) in the ^1H NMR spectra assigned to protons H41 and H43 of the indenyl ligand. The H42 protons, which appear as an apparent triplet, resonate at somewhat lower frequency. The ^1H spectra of the asymmetric compounds, **5**–**7**, **9** and **10** have similar features.

THF reflux of the monosubstituted 4,1,6-CoC_2B_{10} species **5** affords, as anticipated, a mixture of orange **6** and **7** as major products (combined yield 61%). These compounds could not readily be separated chromatographically, but fortunately the desired isomer **7** preferentially crystallised as a pure species, allowing its complete characterisation. This then allowed spectroscopic characterisation of **6** by subtraction of the resonances due to **7** from NMR spectra of the mixture. Also formed in the thermolysis of **5**, in a combined yield of 21%, was a brown band which clearly was not a single compound from its ^{11}B and ^1H NMR spectra and which we tentatively assume to be a mixture of 1-Me-4-(η-C_9H_7)-4,1,12-*closo*-$CoC_2B_{10}H_{11}$ and 12-Me-4-(η-C_9H_7)-4,1,12-*closo*-$CoC_2B_{10}H_{11}$.

Heating compound **4** to reflux in toluene (or, alternatively, simply heating **2** to reflux in toluene) affords the disubstituted 4,1,12-CoC_2B_{10} isomer **10** in good yield. Once again the identity of **10** was readily suggested from its ^{11}B NMR spectrum, since the highest frequency ^{11}B resonance of 4,1,12-MC_2B_{10} species (δ *ca.* +10 in **10**) is measurably lower than that of analogous 4,1,6- and 4,1,8- compounds.[1b,8] We have previously shown[11] that a better route to 4,1,12-MC_2B_{10} species is the mild thermolysis of 4,1,10-MC_2B_{10} isomers, and, indeed, compound **8** effectively converts quantitatively to **9** under only THF reflux. Like **10**, compound **9** has the highest frequency resonance in its ^{11}B spectrum at relatively high field (δ *ca.* +9).

Molecular structures

General comments. The crystallographically-determined structures of the docosahedral cobaltacarboranes **1**, **2**, **4**, **7**, **8**, **9** and **10** are shown in perspective in Fig. 2–3 and Figs. S1–S5 (see Supplementary Material‡), respectively, together with the atomic numbering schemes. In all cases one cage C atom, C1, occupies the unique degree-4 polyhedral vertex whilst Co4 and B5 are both in degree-6 sites. All other vertices are degree-5. In **1** and **2** the second cage C atom is at position 6, in **4** and **7** at position 8, in **8** position 10 and in **9** and **10** position 12. Key structural parameters are collated in Table 1 and full lists of interatomic distances and angles have been deposited as Supplementary Material.‡

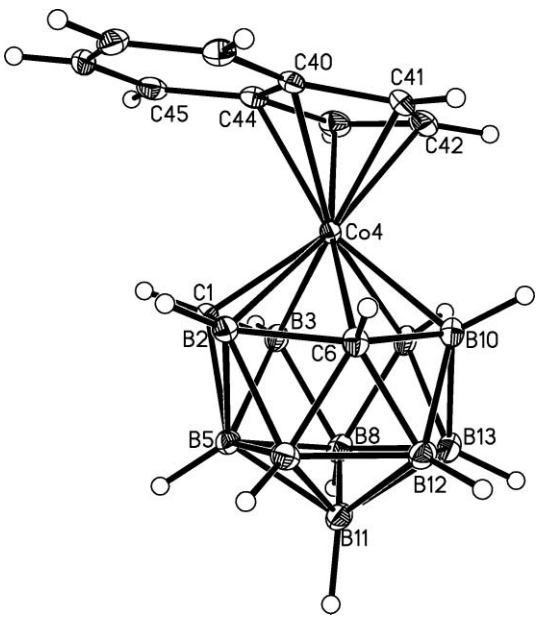

Fig. 2 Perspective view of compound **1**. Displacement ellipsoids drawn at the 50% probability level except for H atoms.

Molecular parameters within the cages of the 4,1,6-CoC_2B_{10} species **1** and **2** are in good agreement with those in the related species 4-(η-C_5H_5)-4,1,6-*closo*-$CoC_2B_{10}H_{12}$[6] and 4-(η-C_5Me_5)-4,1,6-*closo*-$CoC_2B_{10}H_{12}$.[8] Equally, the cages of the 4,1,8-CoC_2B_{10} compounds **4** (both crystallographically-independent molecules **A** and **B**) and **7**, the 4,1,10-CoC_2B_{10} species **8**, and the 4,1,12-CoC_2B_{10} isomers **9** and **10** stand comparison with those reported for Cp or Cp* analogues (Cp* = C_5Me_5).[8,11] However, the only 4,1,8- and 4,1,12-cobaltacarboranes previously to have been studied crystallographically (Cp* species) were partially disordered,[8] and the Cp analogues are very seriously disordered,[8] so the structures of **4**, **7** and **10** (**9** is partially disordered itself) represent the most accurate determinations to date of this family of compounds. All the docosahedral structures reported herein

Table 1 Selected molecular dimensions (Å, °) in compounds **1**, **2**, **4**, **7**, **8**, **9** and **10**

	1	2	4A	4B	7	8	9	10
Co4–C1	2.0175(15)	2.0458(10)	2.049(2)	2.041(2)	2.0169(19)	2.0392(18)	2.090(10)	2.0500(19)
Co4–B2	2.1828(17)	2.1886(12)	2.192(3)	2.216(3)	2.201(2)	2.217(2)	2.179(7)	2.202(2)
Co4–X6[a]	2.1734(15)	2.2290(11)	2.167(3)	2.175(3)	2.183(2)	2.163(2)	2.119(5)	2.132(2)
Co4–Y10	2.1249(17)	2.1064(12)	2.156(3)	2.140(3)	2.135(2)	2.1023(17)	2.119(5)[b]	2.128(2)
Co4–B7	2.1795(17)	2.1528(12)	2.133(3)	2.132(3)	2.152(2)	2.142(2)	2.179(7)[c]	2.189(2)
Co4–B3	2.2365(18)	2.2438(12)	2.193(3)	2.183(3)	2.195(2)	2.201(2)	2.178(11)	2.196(2)
Co4–C40	2.1642(15)	2.1777(10)	2.137(2)	2.143(2)	2.1394(19)	2.1328(17)	2.141(4)	2.1385(19)
Co4–C41	2.0527(16)	2.0418(10)	2.038(2)	2.033(2)	2.0396(19)	2.0470(18)	2.048(5)	2.058(2)
Co4–C42	2.0228(16)	2.0234(10)	2.052(2)	2.057(2)	2.027(2)	2.0555(18)	2.028(7)	2.043(2)
Co4–C43	2.0342(15)	2.0452(11)	2.070(2)	2.081(2)	2.062(2)	2.0642(18)	2.048(5)[d]	2.051(2)
Co4–C44	2.1469(14)	2.2046(11)	2.146(2)	2.157(2)	2.142(2)	2.1596(17)	2.141(4)[e]	2.1392(19)
C40–C41	1.440(2)	1.4320(15)	1.441(3)	1.445(3)	1.436(3)	1.446(3)	1.440(6)	1.434(3)
C41–C42	1.422(2)	1.4226(15)	1.413(4)	1.403(4)	1.427(3)	1.425(3)	1.409(7)	1.417(3)
C42–C43	1.426(2)	1.4205(16)	1.417(3)	1.411(4)	1.414(3)	1.417(3)	1.409(7)[f]	1.418(3)
C43–C44	1.445(2)	1.4450(15)	1.429(3)	1.435(3)	1.436(3)	1.446(3)	1.440(6)[g]	1.439(3)
C44–C40	1.438(2)	1.4342(15)	1.436(3)	1.432(3)	1.437(3)	1.436(2)	1.452(9)	1.441(3)
τ[h]	36.1	36.2	–113.3	112.4	–41.5	95.0	–39.3	123.2
χ[i]	8.6	15.1	4.6	8.4	7.1	4.5	8.3	3.8

[a] For **1** and **2** X = C, Y = B; for **4**, **7**, **9** and **10** X = Y = B; for **8** X = B, Y = C. [b] Co4–B10 = Co4–B6 by symmetry. [c] Co4–B7 = Co4–B2 by symmetry. [d] Co4–C43 = Co4–C41 by symmetry. [e] Co4–C44 = Co4–C40 by symmetry. [f] C42–C43 = C41–C42 by symmetry. [g] C43–C44 = C40–C41 by symmetry. [h] τ is the torsion angle A–B–Co4–C1 where A is the midpoint of C40–C44 and B is the centroid of the C_5 ring. [i] χ is the dihedral angle between C_5 and B5B9B12B13B8 least-squares planes.

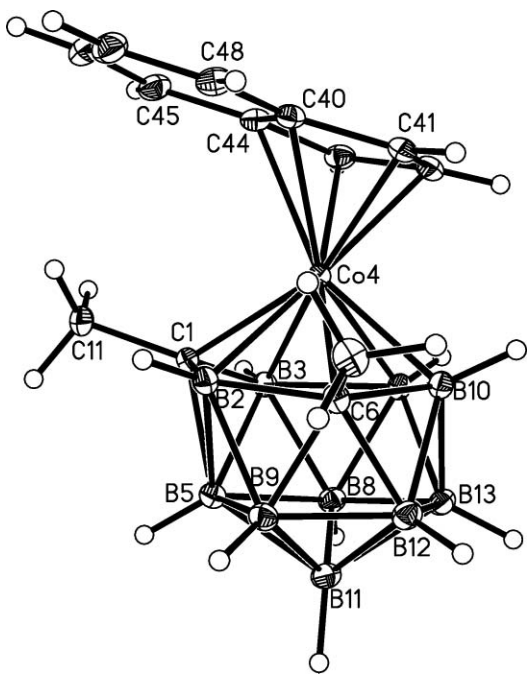

Fig. 3 Perspective view of compound **2**. Displacement ellipsoids as for **1**.

have characteristically long connectivities to the degree-6 B atom B5, with B2–B5 and B6–B5 both *ca*. 2 Å.[18]

Compounds **11** and **12** have henicosahedral cages, as has been previously established for the Cp analogue of **11**.[13] See Fig. 4 and S6,‡ respectively, for perspective views of **11** and **12**, and Table 2 for key molecular dimensions. The henicosahedron is characterised by a trapezoidal C1C2B9B5 face and thus the cage has effective C_s symmetry about the plane through Co4, B11 and B13. Sometimes 13-vertex metallacarboranes have cages which lie between purely docosahedral and purely henicosahedral, and we have recently described a convenient method of quantifying the position of

Table 2 Selected molecular dimensions (Å, °) in compounds **11** and **12**

	11	12
Co4–C1	2.090(2)	2.0762(19)
Co4–C2	2.044(2)	2.0686(19)
Co4–B6	2.233(2)	2.191(2)
Co4–B10	2.173(2)	2.183(2)
Co4–B7	2.156(2)	2.183(2)
Co4–B3	2.178(2)	2.172(2)
Co4–C40	2.134(2)	2.1508(19)
Co4–C41	2.038(2)	2.034(2)
Co4–C42	2.052(2)	2.0377(19)
Co4–C43	2.0882(19)	2.0861(19)
Co4–C44	2.168(2)	2.1887(18)
C40–C41	1.439(3)	1.440(3)
C41–C42	1.426(3)	1.425(3)
C42–C43	1.416(3)	1.417(3)
C43–C44	1.437(3)	1.434(3)
C44–C40	1.439(3)	1.445(3)
τ_2[a]	–79.7	–84.8
χ[b]	11.6	11.2
ϕ[c]	10.0	1.9
x[d]	24.1	4.5

[a] τ_2 is the torsion angle A–B–Co4–D where A is the midpoint of C40–C44, B is the centroid of the C_5 ring, and D is the midpoint of C1–C2. [b] χ is the dihedral angle between C_5 and B5B9B12B13B8 least-squares planes. [c] ϕ is $(|C1–C2–B9 – C2–C1–B5| + |C2–B9–B5 – B9–B5–C1|)/2$. See ref. 19. [d] x is the "percentage docosahedral character", defined as $(\phi/41.44)\times100\%$. See ref. 19.

a particular cage on this continuum.[19] To do this we calculate the angle ϕ from the interior angles of the C1C2B9B5 quadrilateral and define x, the "percentage docosahedral character", as $(\phi/41.44)\times100\%$. For **11** and **12** x is 24.1% and 4.5%, respectively; both are clearly henicosahedral, but **12** the more so.

In all the structures determined the Co–C distances to the ring junction carbon atoms (C40 and C44) are typically 0.1–0.15 Å longer than those to the other η-bound indenyl carbon atoms (C41, C42 and C43), confirming that the ring junction C atoms

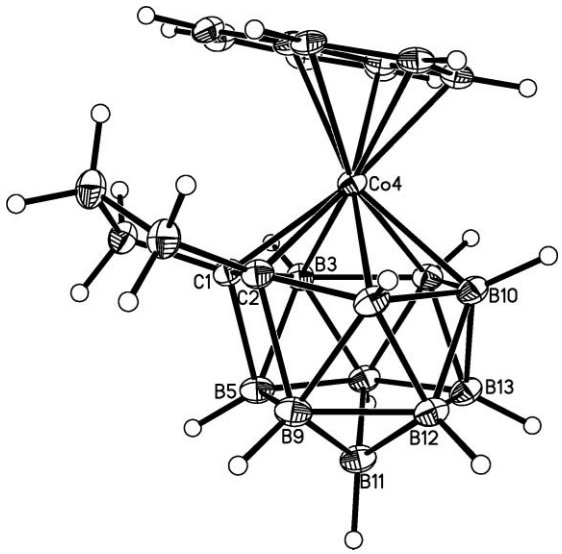

Fig. 4 Perspective view of compound **11**. Displacement ellipsoids as for **1**.

are more weakly bound to the metal atom. Thus we can anticipate orientational preferences for the indenyl ligand which reflect the relative *trans* influences of the cage atoms through a structural indenyl effect.

Indenyl orientations. We have prepared and structurally studied these indenyl cobaltacarboranes to probe the Co-cage bonding *via* the indenyl orientations. As noted in the introduction, the ring junction carbon atoms C40 and C44 have a weaker *trans* influence than C41, C42 and C43 and therefore tend to align themselves *trans* to the cage atoms with the strongest *trans* influence. In the icosahedral model indenyl cobaltacarborane 3-(η-C_9H_7)-3,1,2-*closo*-$CoC_2B_9H_{11}$ this leads to a cisoid arrangement of ring junction and carborane C atoms,[15] *i.e.* the ring junction atoms lie *trans* to a facial B–B connectivity (presumably a *cis* arrangement, which would require eclipsed 5-membered rings, is disfavoured on steric grounds). This indenyl orientation can be therefore taken to infer that in an icosahedral metallacarborane the facial B atoms have a greater *trans* influence than the facial C atoms, and the origin of this has been traced to the fact that the frontier molecular orbitals of the [7,8-*nido*-$C_2B_9H_{11}]^{2-}$ ligand are predominantly localised on the boron atoms of the open face, not the carbon atoms.[20] Thus, having established that indenyl orientation can give information on the differing *trans* influences of facial atoms in the unprejudiced case where all polyhedral vertices are of degree-5, we plan to use the indenyl orientations in the present compounds to probe the relative *trans* influences of facial atoms in supraicosahedral metallacarboranes, whose different isomeric forms have both degree-5 and degree-4 facial C atoms and several different types of facial B atoms. For 3-(η-C_9H_7)-3,1,2-*closo*-$CoC_2B_9H_{11}$ we complemented the structural study with a computational analysis at the EHMO level.[15] In the present study we have supplemented the structural work with the results of DFT calculations on various isomers of the related naphthalene ferracarboranes (η-$C_{10}H_8$)$FeC_2B_{10}H_{12}$ (Tables S1–S5 in Supplementary Material summarise minimum energy structures for each isomer). We chose to use the {($C_{10}H_8$)Fe} fragment as opposed to {(C_9H_7)Co} to avoid any complications that might arise from having parallel 5- and 6-membered rings which must sometimes be staggered and sometimes eclipsed.[21]

A few previous studies have already furnished some information on *trans* influences in supraicosahedra. For 4,1,6-MC_2B_{10} compounds the differing Ni–P distances in 4-(dppe)-4,1,6-*closo*-$NiC_2B_{10}H_{12}$,[18] differing Pt–P distances in 4,4-($Me_2PhP)_2$-4,1,6-*closo*-$PtC_2B_{10}H_{12}$,[22] orientation of the {$Mo(C_3H_5)(CO)_2$} fragment in [4-(η-C_3H_5)-4,4-$(CO)_2$-4,1,6-*closo*-$MoC_2B_{10}H_{12}]^-$[18] and orientation of the bipy ligand in a number of 1,6-Me_2-4-(bipy)-4,1,6-*closo*-$SnC_2B_{10}H_{10}$ species[23] have all been interpreted in terms of relatively weak *trans* influences of the facial C atoms. This theme continues in the 4,1,2- species 1,2-μ-(tether)-4-(bipy)-4,1,2-*closo*-$SnC_2B_{10}H_{10}$.[19] In the 4,1,10 compound 1,10-Me_2-4-(bipy)-4,1,10-*closo*-$SnC_2B_{10}H_{10}$ we are able to conclude, from the inclination of the bipy ligand, that the degree-4 C atom has a stronger *trans* influence than the degree-5 C atom, and on isomerising this species to its 4,1,12- analogue, that the single C atom remaining in the carborane ligand face has a weaker *trans* influence than all the B atoms.[24] Whilst these studies have provided some useful results the present one is the most comprehensive in that the orientation of a single exopolyhedral ligand is used for an extensive range of supraicosahedral isomers. Moreover, in bipy stannacarboranes the bipy (and related) ligands point towards where the metal-cage bonding is weakest, whereas in indenyl metallacarboranes the indenyl ligand junction atoms point towards where the metal-cage bonding is strongest, so these two types of system provide complementary information.

To define the indenyl orientation in the docosahedral species **1**, **2**, **4**, **7**, **8**, **9** and **10** we use τ, the torsion angle A–B–Co4–C1 where A is the midpoint of C40–C44 and B is the centroid of the C_5 ring, with τ defined as *ca.* +60° if A lies above B2 and *ca.* –60° if A lies above B3. Fig. 5 shows a common view of the metal-bonded carborane faces of these compounds and the varying indenyl orientations displayed.

For **1** we find that τ is 36.1°, with C40/C44 lying *trans* to the B7–B10 connectivity. In the 4,1,6-MC_2B_{10} isomer there are three facial boron atoms in a sequence, B3, B7 and B10, with the fourth, B2, sandwiched between the two carbon atoms. We could reasonably assume that the combined *trans* influence of three adjacent B atoms would outweigh that of a single one and, indeed, as we have already shown, the orientation of bipy and related ligands in 4,1,6-stannacarboranes shows that the weakest *trans* influence lies in the C1B2C6 region.[23] Hence in **1** we would expect C40/C44 to orient *trans* to a B–B connectivity but could not easily have assumed whether that would be B3–B7 or B7–B10.

To help illuminate this problem we have turned to computational chemistry and have used DFT calculations to explore the potential energy profile for rotation of the naphthalene ligand about the metal-cage axis in the related compound 4-(η-$C_{10}H_8$)-4,1,6-*closo*-$FeC_2B_{10}H_{12}$. Fig. 6(a) shows the profile obtained. The minimum energy found for rotation of the naphthalene ligand is at τ = *ca.* 50° which agrees moderately well with the observed orientation of the indenyl ligand in **1** (τ = 36.1°). For reasons explained above we are modelling an η^5-C_9H_7 ligand with an η^6-$C_{10}H_8$ one (together with an associated change in the metal). Everything else being equal, an η^6 ligand over a 6-membered carborane face is naturally going to show local minima at τ = *ca.* 0, 60, 120, 180, 240 and 300° as these correspond to staggered orientations, and it is for this reason that the computed minimum for the

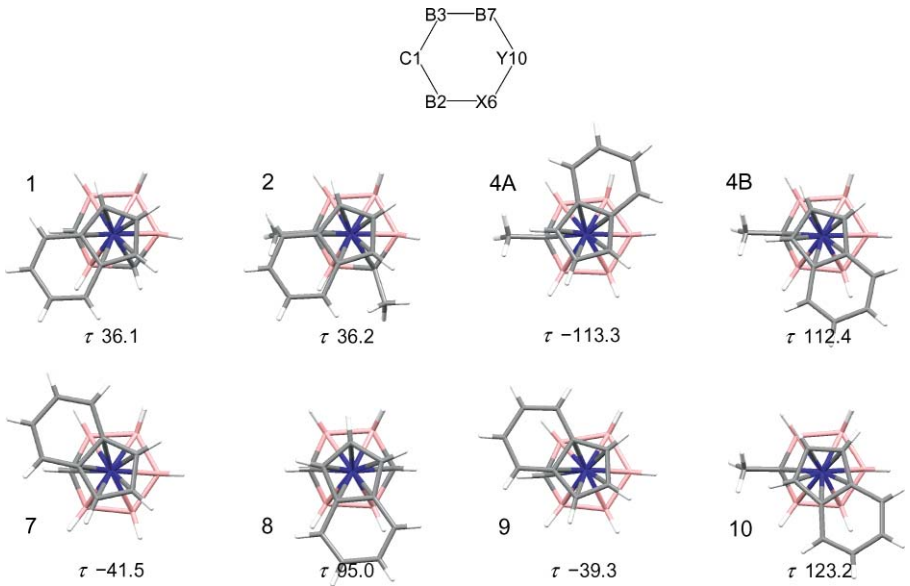

Fig. 5 The indenyl orientation in compounds **1**, **2**, **4**, **7**, **8**, **9** and **10** viewed perpendicular to the C_5 indenyl ring and projected onto a common view of the C1B2 × 6Y10B7B3 carborane ligand face (for **1** and **2** X = C, Y = B; for **4**, **7**, **9** and **10** X = Y = B; for **8** X = B, Y = C).

4,1,6- naphthalene ferracarborane is somewhat greater τ than that observed experimentally for the indenyl cobaltacarborane. The barrier to rotation of the naphthalene ligand in the computational model is calculated to be *ca.* 4.7 kcal mol^{-1} with the least stable conformation residing at $\tau = 285°$ (−75°). In the dimethyl analogue **2** effectively the same orientation is observed experimentally (τ = 36.2°) in spite of such an orientation generating steric crowding between the methyl substituents on C1 and C6 and the 6-membered ring of the indenyl ligand. The consequence of this crowding is that the indenyl ligand in **2** is significantly more inclined with respect to the carborane than it is in **1**, clearly evident in comparison of Fig. 2 and Fig. 3, and quantified by χ, the dihedral angle between C40C41C42C43C44 and B5B9B12B13B8 least-squares planes. For **1** χ is only 8.6° whilst for **2** it has increased to 15.1°. To completely avoid methyl/indenyl crowding in **2** would require an orientation defined by $\tau = -120°$ (A above B7) but this would clearly be electronically unfavourable.

Our preferred 4,1,8- indenyl cobaltacarborane for structural study would have been the parent, non-substituted, compound **3**, but unfortunately this could not be persuaded to crystallise. The dimethyl analogue **4** did crystallise, however. Nevertheless, seeking a derivative of **3** that did not have a substituent on the upper carborane ligand face (which might compromise the orientational preference of the indenyl ligand) we targeted the 8-Me species **7**. This required the initial synthesis of the mono-substituted 4,1,6-isomer **5** which, although likely to be fluctional in solution at room temperature,[1b,16] could be either 1-Me or 6-Me in the solid state. Thermolysis of **5** afforded a 1 : 2 mixture of 1-Me and 8-Me substituted 4,1,8- isomers **6** and **7**, respectively, from which the required species **7** preferentially crystallised. Thus we have structurally characterised two 4,1,8- indenyl cobaltacarboranes, **4** and **7**, and since in **4** there are two crystallographically-independent molecules **A** and **B** we have access to three molecular structures.

The measured τ values for the three structures are very different, −113.3° for **4A**, 112.4° for **4B** and −41.5° for **7**. Consideration of the calculated profile for naphthalene rotation in 4-(η-$C_{10}H_8$)-4,1,8-*closo*-$FeC_2B_{10}H_{12}$, shown in Fig. 6(b), would imply that a τ value close to +45° (C40/C44 *trans* to the B7–B10 connectivity) might have been anticipated. The measured τ value for **7**, with C40/C44 *trans* to B6–B10, corresponds to the "second-best" predicted orientation ($\tau = 310°$, *i.e.* −50°) although the difference between these two orientations is only *ca.* 0.8 kcal mol^{-1}, well within the normal range of simple crystal packing forces. In **4A** the indenyl ligand is rotated away from its position in **7** by 72° (one ratchet of the pentagon) presumably to relieve Me/indenyl crowding, whilst in **4B** the twist is 72° away from the idealised orientation for (presumably) the same reason. Note that, unlike the situation for **2**, a simple rotation of the indenyl ligand by this amount to relieve crowding affords a perfectly feasible alternative orientation in which C40/C44 are still *trans* to B atoms which bind strongly to the metal atom. Indeed, the observed orientations in **4A** and **4B** correspond to clear local minima in the computed profile for (η-$C_{10}H_8$)-4,1,8-*closo*-$FeC_2B_{10}H_{12}$. In **2** the avoidance of Me/indenyl crowding by rotation would place C40/C44 *trans* to the highly unfavourable C1B2C6 sequence so the indenyl ligand inclines instead.

In **8** τ is 95.0°, *i.e.* the ring junction atoms of the indenyl ligand lie approximately *trans* to B3 and B7 (clearly an equivalent orientation would be τ = −95°, with C40/C44 *trans* to B2 and B6). We conclude from this orientation that in the 4,1,10-CoC_2B_{10} isomer the boron atoms in the carborane ligand face have a greater *trans* influence than either the degree-4 or degree-5 carbon atoms. Fig. 6(c), which summarises the computational study of naphthalene rotation in the corresponding naphthalene ferracarborane, is less helpful in this case than for the 4,1,6- and 4,1,8- isomers, being both relatively shallow (<2 kcal mol^{-1}) and dominated simply by minima at staggered and maxima at eclipsed conformations of the naphthalene and carborane 6-atom faces.

Compounds **9** and **10** have 4,1,12-CoC_2B_{10} architectures. The profile for naphthalene rotation in the related species 4-(η-$C_{10}H_8$)-4,1,12-*closo*-$FeC_2B_{10}H_{12}$ is shown in Fig. 6(d). The

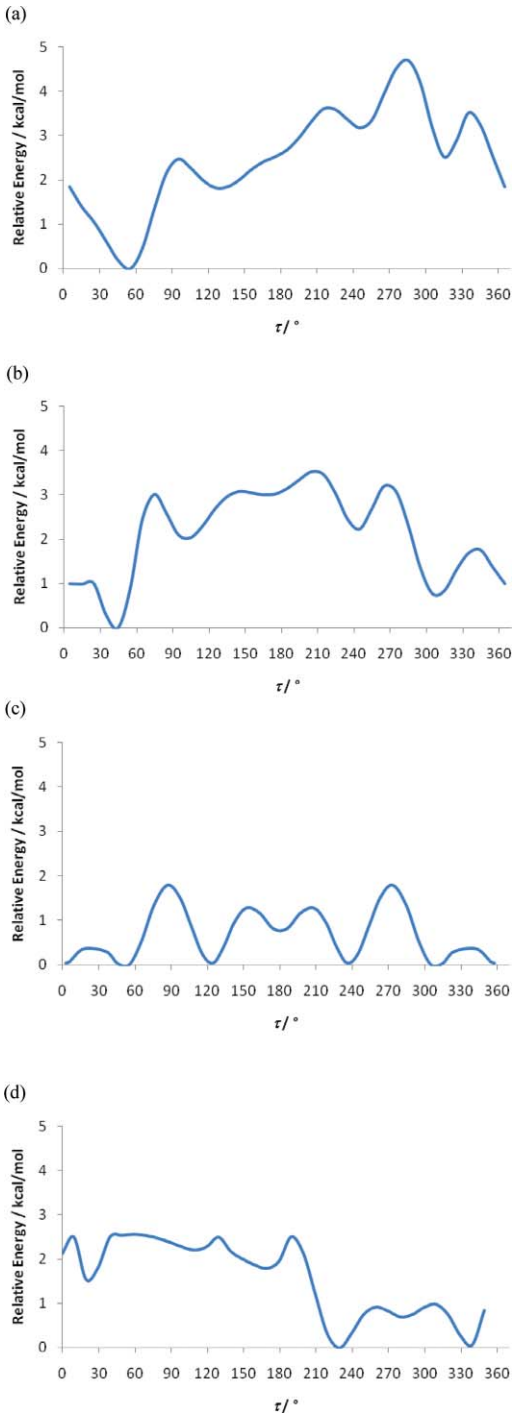

Fig. 6 Relative energy (kcal mol^{-1}) *versus* τ (°) for naphthalene rotation in the model compounds (a) 4-(η-$C_{10}H_8$)-4,1,6-*closo*-$FeC_2B_{10}H_{12}$, (b) 4-(η-$C_{10}H_8$)-4,1,8-*closo*-$FeC_2B_{10}H_{12}$, (c) 4-(η-$C_{10}H_8$)-4,1,10-*closo*-$FeC_2B_{10}H_{12}$ and (d) 4-(η-$C_{10}H_8$)-4,1,12-*closo*-$FeC_2B_{10}H_{12}$.

orientation of the indenyl ligand in the non-methylated **9** (τ = –39.3°, with C40/C44 *trans* to B6–B10) is moderately close to one of two nearly-equienergetic minima calculated for the naphthalene ferracarborane at τ = –21°. In **10** the presence of the methyl substituent on C1 clearly compromises the indenyl orientation since the measured value of τ, 123.2°, corresponds to a relatively unstable region of the naphthalene ferracarborane plot.

The orientations of the indenyl ligand relative to the carborane in the henicosahedral 4,1,2-CoC_2B_{10} species **11** and **12** are very similar and are summarised in Fig. 7. Since there are now two degree-4 carbon atoms in the cage we describe the orientation subtly differently, with τ_2 defined as the torsion angle A–B–Co4–D where A is the midpoint of C40–C44, B is the centroid of the C_5 ring, and D is the midpoint of C1–C2. We would predict from first principles that for the related henicosahedral naphthalene ferracarborane 4-(η-$C_{10}H_8$)-4,1,2-*closo*-$FeC_2B_{10}H_{12}$, in the absence of significant steric effects, the strongest M–B bonding would be to B7 and B10, corresponding to a τ_2 value of 0° (in 4,1,2- indenyl stannacarboranes it is clear that the weakest metal–cage bonding is to C1 and C2),[19] and this is supported by the profile shown in Fig. 7 in which the most stable conformation is computed for $\tau_2 = 0°$. The observed conformations, with $\tau_2 = ca.$ –80°, presumably result from crowding between the indenyl ligands and C_{cage} substituents but these nevertheless correspond to a (relatively deep) local minimum in the plot for the naphthalene ferracarborane. Note that these conformations still have the 6-membered ring of the indenyl ligand adjacent to the substituent on C1, and, although this results in more crowding than in **4** and **10**, they are presumably acceptable since they allow C40/C44 to lie *trans* to B atoms; indenyl rotation away from the C_{cage} substituents to the extent observed in **4** and **10** would have the junction atoms *trans* to cage C, a situation confirmed as unfavourable in the plot in Fig. 7. It is assumed to

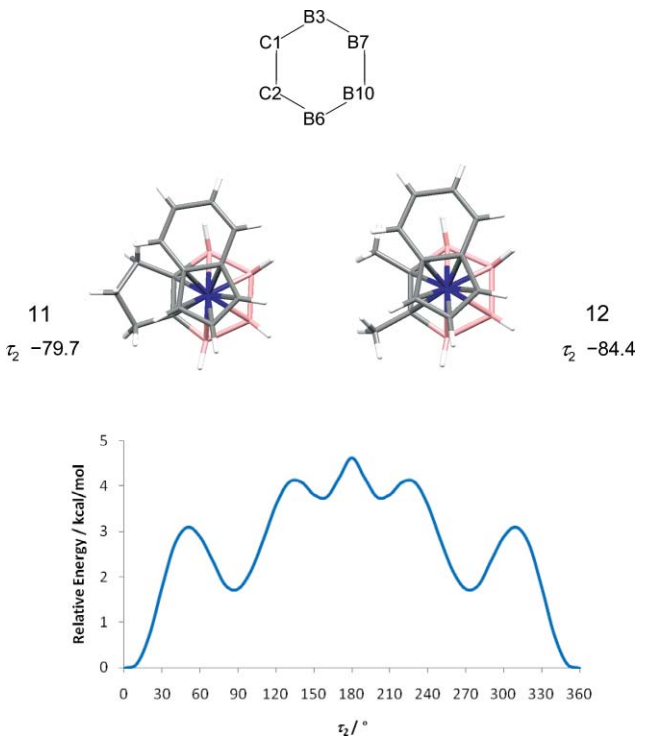

Fig. 7 (Upper) The indenyl orientation in compounds **11** and **12** viewed perpendicular to the C_5 indenyl ring and projected onto a common view of the C1C2B6B10B7B3 carborane ligand face. (Lower) Relative energy (kcal mol^{-1}) *versus* τ_2 (°) for naphthalene rotation in the model compound 4-(η-$C_{10}H_8$)-4,1,2-*closo*-$FeC_2B_{10}H_{12}$.

Table 3 Formal electrode potentials (V, *vs.* SCE), peak-to-peak separation (mV), and peak-current ratio for the reduction processes exhibited by compounds **1**, **3**, **8** and **9** and related species

Complex	$E^{\circ\prime}$ (1st reduction)	ΔE_p[a]	i_{pa}/i_{pc}[a]	$E^{\circ\prime}$ (2nd reduction)	ΔE_p[a]	i_{pa}/i_{pc}[a]	Solvent
4-Cp-4,1,8-*closo*-$CoC_2B_{10}H_{12}$ (**3Cp**)	–0.98	59	1.0	–1.95	67	0.5	THF
	–1.13	59	1.0	–1.95[b]	88	[c]	CH_2Cl_2
4-Cp-4,1,12-*closo*-$CoC_2B_{10}H_{12}$ (**9Cp**)	–0.98	59	1.0	–1.99[b]	91	0.3	THF
	–1.12	87	1.0	–1.96	96	0.4	CH_2Cl_2
$[CpCo(\eta\text{-}C_6H_6)]^{2+}$[d]	+0.39	65[a]	1.0	–0.56	65[a]	0.9	PC[e]
4-(η-C_9H_7)-4,1,6—*closo*-$CoC_2B_{10}H_{12}$ (**1**)	–0.41	69	1.0	–1.78[f,a]	—	—	THF
	–0.56	79	1.0	–1.80[g,a]	—	—	CH_2Cl_2
4-(η-C_9H_7)-4,1,8-*closo*-$CoC_2B_{10}H_{12}$ (**3**)	–0.69	59	1.0	–1.82[f,a]	—	—	THF
4-(η-C_9H_7)-4,1,10-*closo*-$CoC_2B_{10}H_{12}$ (**8**)	–0.39	61	1.0	–1.82[f,a]	—	—	THF
	–0.54	58	1.0	–1.81	92	0.7[a]	CH_2Cl_2
4-(η-C_9H_7)-4,1,12-*closo*-$CoC_2B_{10}H_{12}$ (**9**)	–0.69	62	1.0	–1.81[f,a]	—		THF
	–0.85	80	1.0	–2.01	171[h]	0.3[h]	CH_2Cl_2
3-Cp-3,1,2-*closo*-$CoC_2B_9H_{11}$[i]	–1.18	—	—	–2.23			THF
3-(η-C_9H_7)-3,1,2-*closo*-$CoC_2B_9H_{11}$[j]	–0.85	—	—	–1.87	—	—	CH_2Cl_2

[a] Measured at 0.1 V s^{-1}. [b] Coupled to slow chemical complications. [c] Difficult to evaluate because close to the solvent discharge. [d] See ref. 27. [e] PC = propylene carbonate. [f] Peak potential value for processes coupled to fast chemical complications (see text). [g] From Osteryang Square Wave Voltammetry. [h] Measured at 2.0 Vs^{-1} [i] See ref. 25 and 26. [j] See ref. 15 and 26.

be for this reason that χ values measured for **11** and **12**, *ca.* 11°, are greater than for all the docosahedral species except **2**.

Electrochemistry, spectroelectrochemistry and EPR spectroscopy

To investigate the electrochemical response of supraicosahedral indenyl cobaltacarboranes we have studied the 4,1,6-, 4,1,8-, 4,1,10- and 4,1,12- isomers **1**, **3**, **8** and **9**, respectively, together with, for comparative purposes, the (already known)[1a,1b] Cp analogues of **3** and **9**, **3Cp** and **9Cp** respectively. Table 3 summarises the electrochemical results. Fig. 8 compares the cyclic voltammetric behaviour of 4-Cp-4,1,8-*closo*-$CoC_2B_{10}H_{12}$ (**3Cp**) with that of **3**, and substantially reflects the redox activity of the two series of 13-vertex derivatives in THF solution.

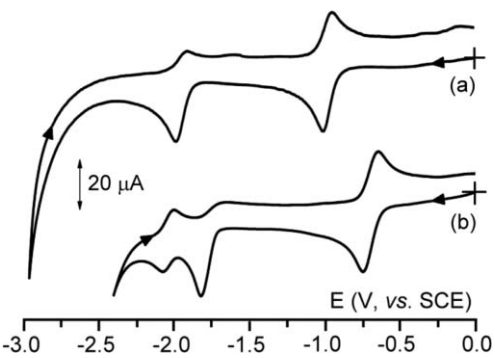

Fig. 8 Cyclic voltammetric responses recorded at a gold electrode in THF solution of (a) **3Cp** (1.2×10^{-3} mol dm^{-3}) and (b) compound **3** (1.1×10^{-3} mol dm^{-3}). $[NBu_4][PF_6]$ (0.2 mol dm^{-3}) supporting electrolyte. Scan rate 0.1 V s^{-1}. $T = 293$ K.

The cyclopentadienyl complex **3Cp** undergoes two consecutive reduction processes, which, in agreement with the behaviour of the related species 3-Cp-3,1,2-*closo*-$CoC_2B_9H_{11}$[25,26] and $[CpCo(\eta\text{-}C_6H_6)]^{2+}$[27] are conceivably assigned to the stepwise one-electron sequence Co(III)/Co(II)/Co(I).

Controlled potential coulometry of **3Cp** corresponding to the first cathodic process ($E_w = -1.2$ V) consumes one-electron *per* molecule. In spite of the apparent stability of the electrogenerated Co(II) monoanion [4-Cp-4,1,8-*closo*-$CoC_2B_{10}H_{12}]^-$ on the short time scale of cyclic voltammetry (the peak-current ratio i_{pa}/i_{pc} remains equal to 1 in the scan rate range 0.02 V s^{-1} to 2.00 V s^{-1}), cyclic voltammetric tests on the solution resulting from exhaustive reduction showed that about 60% of the original complex decomposed. No significant improvement in the stability of the Co(II) monoanion has been achieved at $T = 275$ K (at lower temperatures the solubility of the complexes tends markedly to decrease). To the best of our knowledge no experimental data exist on the long term stability of the related Co(II) monoanion [3-Cp-3,1,2-*closo*-$CoC_2B_9H_{11}]^-$ (equally, no structural data for this monoanion exists in the Cambridge Crystallographic Database).[28] The second reduction of **3Cp** is clearly coupled to chemical complications even in the short time scales of cyclic voltammetry,[29] as the pertinent current ratio is notably less than 1 (see Table 3).

In the case of the indenyl 4,1,8- species **3**, exhaustive one-electron reduction ($E_w = -1.0$ V) of the original burnt orange solution generates the corresponding, quite stable, carmine red monoanion [4-(η-C_9H_7)-4,1,8-*closo*-$CoC_2B_{10}H_{12}]^-$ ([**3**]$^-$). In turn, as is illustrated in Fig. 8, the second reduction is accompanied by the rapid generation of a new, presently unidentified, species which displays a reversible reduction (at $E^{\circ\prime} = -2.05$ V).

As expected, corresponding reduction potentials for indenyl cobaltacarboranes are less negative than those of analogous Cp species since the indenyl ligand is a poorer electron donor and thus the reduction processes are easier. This phenomenon clearly has the same origin as both the kinetic and structural indenyl effects and has previously been noted in comparative electrochemical studies of analogous icosahedral indenyl and Cp cobaltacarboranes.[15,25]

An interesting feature of the electrochemical studies is that corresponding reductions are easier for the 4,1,6- and 4,1,10-indenyl cobaltacarboranes **1** and **8**, in which the metal-bonded face is C_2B_4, than for the 4,1,8- and 4,1,12- isomers **3** and **9**, where the metal-bonded face is CB_5. This observation supports and extends preliminary first reduction potentials previously reported for the Cp analogues of **1**, **3** and **9**,[1b] and is fully consistent with recent electrochemical results on various isomers of $CpFeC_3B_8H_{11}$.[30] The origin of this effect appears to be the higher electronegativity of the

carbon atoms with respect to the boron atoms. In this connection, the very easy one-electron reduction of $[CpCo(\eta\text{-}C_6H_6)]^{2+}$[27] further supports such a conclusion.

Table 3 also reveals clear evidence of differences as a function of the solvent. In fact, in CH_2Cl_2 solution, not only is the Co(III)/Co(II) reduction generally shifted towards negative potential values by about 0.15 V with respect to THF, but also the rate of the chemical complication following the Co(II)/Co(I) step decreases in CH_2Cl_2 solution. In particular, as illustrated in Fig. 9 which shows the cyclic voltammetry of compound **8** in CH_2Cl_2, the chemical complication is too slow to give rise to the spurious product arising from the second reduction recorded in THF solution (see, for example, Fig. 8b).

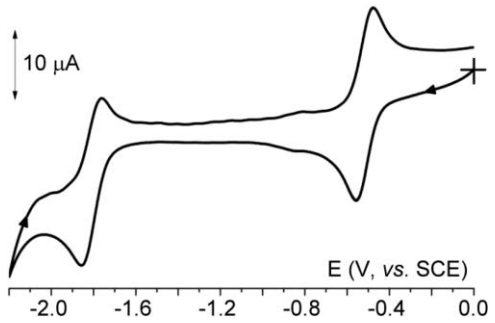

Fig. 9 Cyclic voltammetric response recorded at a gold electrode in CH_2Cl_2 solution of compound **8** (1.0×10^{-3} mol dm^{-3}). $[NBu_4][PF_6]$ (0.2 mol dm^{-3}) supporting electrolyte. Scan rate 0.1 V s^{-1}. $T = 293$ K.

Finally, in order to have a more complete electrochemical picture of the complexes under examination, we have looked at the redox activity of the family of isomeric $C_2B_{10}H_{12}$ carboranes. In agreement with previous investigations,[31] 1,2-*closo*-$C_2B_{10}H_{12}$ affords a detectable reduction within the cathodic window of THF (up to −3.2 V, *vs*. SCE). As illustrated in Fig. S7 (see Supplementary Material), it undergoes an irreversible reduction at $E_p = -2.66$ V, which, by comparison with the one-electron oxidation of ferrocene, fully supports the chemical evidence of a two-electron process. In contrast, no reduction process is detected for the 1,7- and 1,12- isomers, suggesting that their cathodic reduction is masked by the solvent discharge.

In view of the stability of the Co(II) monoanions of the indenyl derivatives, we have followed the Co(III)/Co(II) process in THF solution by UV-vis spectroelectrochemistry as well as by EPR spectroscopy. As a representative example, Fig. 10 shows the spectral trends recorded upon one-electron reduction of compound **1** in THF solution (in macroelectrolysis, the original burnt orange solution turns orange). The slight decrease and shift of the main band at 323 nm, which can be assigned to MLCT or LMCT charge transfer, is accompanied by the corresponding increase of a band at 383 nm coupled to a broad band at about 474 nm, which are reminiscent of *d*-*d* transitions in Co(II) sandwich complexes.[32] The appearance of the isosbestic point at 368 nm attests to the chemical reversibility of the redox change **1**/[**1**]$^-$. Similar spectroelectrochemical behaviour has been observed for the Co(III)/Co(II) reduction of all the indenyl compounds and pertinent data are compiled in Table S7 (see Supplementary Material).

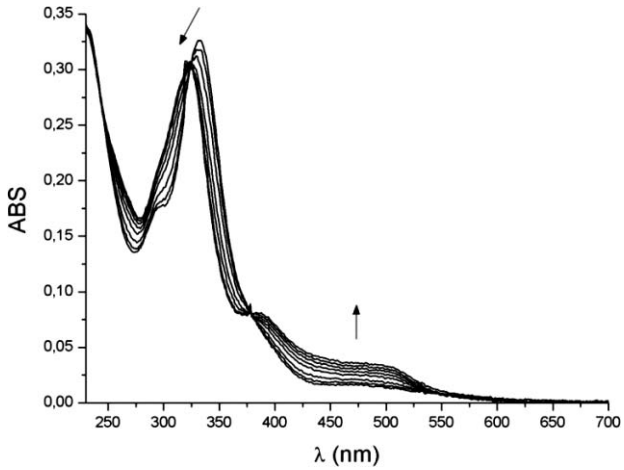

Fig. 10 Spectroelectrochemical profiles recorded in a OTTLE cell upon progressive one-electron reduction of compound **1** in THF solution. Scan rate: 250 μV s^{-1}. Supporting electrolyte: $[TBA][PF_6]$ (0.2 mol dm^{-3}).

In order to lend further support to the Co-centred nature of the neutral/monoanion passage in the present complexes, we carried out EPR spectroscopic measurements on the electrogenerated monoanions. As a representative example, Fig. 11 shows the liquid nitrogen X-band EPR spectrum (first derivative mode) of [4-(η-C_9H_7)-Co-4,1,6-*closo*-$C_2B_{10}H_{12}$]$^-$ ([**1**]$^-$) recorded in THF solution. Analysis of the spectrum can be suitably accounted for by a $S = \frac{1}{2}$ Hamiltonian assuming the anisotropic Zeeman and metal hyperfine interactions as fundamental paramagnetic terms.[33] The g_i values of the broad anisotropic signal differ from the value of $g_{free\text{-}electron} = 2.0023$, as expected in the presence of an important Co(II) spin–orbit coupling constant contribution to the experimental lineshape (^{59}Co: $I = {}^7/_2$, natural abundance = 100%; Co(II) $3d^7$ low-spin, $\lambda_{Co} < 0$).[32] The best fit of the experimental lineshape has been computer simulated assuming an anisotropic

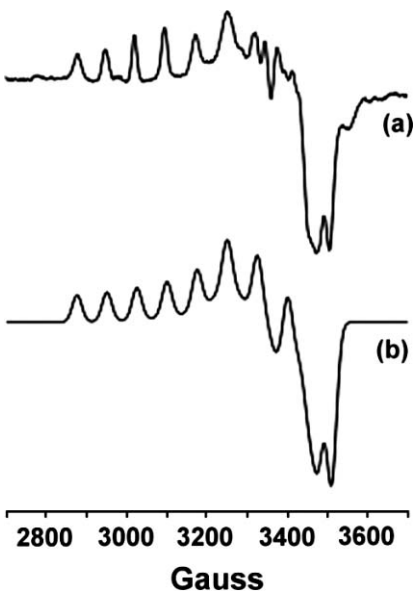

Fig. 11 X-band EPR spectrum of [4-(η-C_9H_7)-4,1,6-*closo*-$CoC_2B_{10}H_{12}$]$^-$ ([**1**]$^-$). Experimental (a) and simulated (b) spectrum. THF solution. $T =$ 105 K. $\nu = 9.467$ GHz.

lineshape with three different g_i values in a partially resolved rhombic spectrum.[34]

Unfortunately, in the high field region the g_m (medium field) and g_h (high field) absorptions are largely overlapping thus affording a broad and poorly resolved spectral pattern with reduced resolution of the hyperfine (hpf) from $+^7/_2$ to $-^7/_2$ Co(II) m_I multiplets.[32] Such behaviour is somewhat reminiscent of the EPR features of related cyclopentadienyl(arene)cobalt(II) complexes.[27]

The multiple derivative approach (first and second derivative modes) allows a better determination of the paramagnetic features of the monoanion:

$$g_l = 2.155(8),\ g_m = 2.023(8),\ g_h = 1.974(8)$$

$$a_l = 75(5)\ \text{G},\ a_m = 25(5)\ \text{G},\ a_h = 20(5)\ \text{G}$$

$$\Delta H_l = 12(4),\ \Delta H_m = 22(4),\ \Delta H_h = 13(4)$$

The second derivative spectrum (see Fig. S8 in the Supplementary Material‡) shows that the number of hpf splittings is lower than the expected eight, likely due to the cited linewidth effects in the high field region. As a consequence, ΔH_m and ΔH_h mask the underlying hpf signals: $\Delta H_{m,l} \geq a(\text{Co})_{m,l}$. Accordingly, no EPR evidence for superhyperfine (shpf) coupling with the other magnetically active nuclei (^{1}H, $I = \frac{1}{2}$, natural abundance = 99.98%; ^{10}B, $I = 3$, natural abundance = 19.6%; ^{11}B, $I = {}^3/_2$, natural abundance = 80.4%) has been detected. Pertinent paramagnetic parameters are collected in Table 4, together with those of the other indenyl cobaltacarborane monoanions examined, [**8**]$^-$ and [**9**]$^-$.

The EPR features show that the 3*d* Co AOs play a fundamental role in the SOMO of the Co(II) species, while minor contributions arise from the orbitals of other atoms. In other words only a minor part of the unpaired spin density is delocalised on the indenyl moiety and carborane cage. This conclusion is fully supported by the results of DFT calculations and, as a typical example, Fig. 12 shows the LUMO of 4-(η-C_9H_7)-4,1,6-*closo*-$CoC_2B_{10}H_{12}$ when τ = –42.3° (Table S6, Supplementary Material‡). For this compound in this orientation the LUMO composition is 41.4% Co atom, 33.6% indenyl ligand and 25.0% carborane cage.

The μ_{eff} values calculated from the $< g >$ values are close to the theoretical value obtained with the spin-only approximation (1.73) and in good agreement with the value of cobaltocene (1.76 μB).[35] Raising the temperature, the glassy paramagnetic signal rapidly decays and at the glassy-fluid transition the frozen solution becomes EPR-silent. Such a temperature-dependent paramagnetic behaviour is not unusual in the presence of active electron spin relaxation processes able to induce noticeable line broadening of the experimental linewidths. Actually, the EPR relaxation rates are dramatically increased by the effective fastening of the thermally induced intramolecular dynamics under fast motion conditions.[33,36]

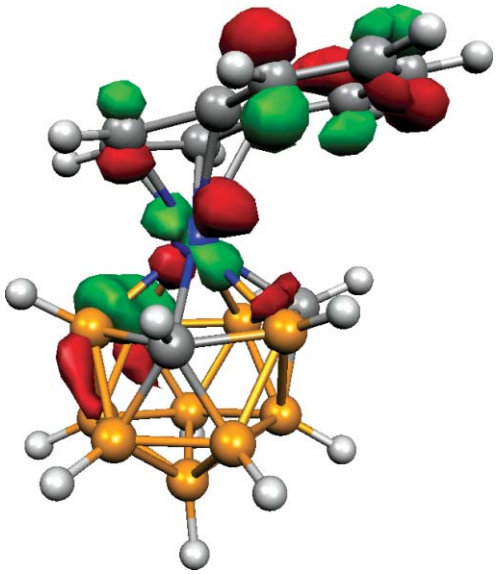

Fig. 12 The LUMO of 4-(η-C_9H_7)-4,1,6-*closo*-$CoC_2B_{10}H_{12}$ when τ = –42.3°, by DFT calculation.

In summary, and as anticipated, the observed paramagnetic features of the three anionic Co(II) complexes adequately support the conclusion that the reduction processes for 13-vertex cobaltacarboranes are centred on the metal atom. Moreover, as demonstrated by the electrochemical results, reductions of the neutral species are easier if there are two cage C atoms in the carborane ligand face to which the metal is bound, *i.e.* the 4,1,6- and 4,1,10-isomers. However, the available experimental evidence is that of all the known isomers of MC_2B_{10} only the 4,1,8- and 4,1,12-species can be expanded to 14-vertex bimetallacarboranes by the sequential process of 2-electron reduction and metallation.[37,38] This process is illustrated in Fig. 13 and shows that the initial *closo* metallacarborane cage must be transformed as a consequence of reduction into a *nido* cage. This must mean that, in spite of the facts that (i) the reduction of 13-vertex metallacarboranes is initially

Table 4 X-Band EPR Parameters of the 1-electron reduced anions of **1**, **8** and **9** in THF glassy solutions. T = 105 K. $< g > = (g_l + g_m + g_h)/3$ (l, low-field; m, medium-field; h, high-field); $< a > = (a_l + a_m + a_h)/3$; $<\Delta H > = (\Delta H_l + \Delta H_m + \Delta H_h)/3$; a_i in Gauss

Reduced species	g	$< g >$	a	$< a >$	μ_{eff}
[4-(η-C_9H_7)-4,1,6-*closo*-$CoC_2B_{10}H_{12}$]$^-$ ([**1**]$^-$)	$g_l = 2.155(8)$ $g_m = 2.023(8)$ $g_h = 1.974(8)$	2.051(8)	$a_l = 75(5)$ $a_m = 25(5)$ $a_h = 20(5)$	40(5)	1.77
[4-(η-C_9H_7)-4,1,10-*closo*-$CoC_2B_{10}H_{12}$]$^-$ ([**8**]$^-$)[a]	$g_l = 2.125(8)$ $g_m = 1.978(8)$ $g_h = 1.978(8)$	2.027(8)	$a_l = 74(6)$ $a_m = 34(6)$ $a_h = 34(6)$	47(6)	1.75
[4-(η-C_9H_7)-4,1,12-*closo*-$CoC_2B_{10}H_{12}$]$^-$ ([**9**]$^-$)[a]	$g_l = 2.185(8)$ $g_m = 2.088(8)$ $g_h = 1.987(8)$	2.087(8)	$a_l = 73(6)$ $a_m = 119(6)$ $a_h = 66(6)$	86(6)	1.81

[a] Experimental parameters.

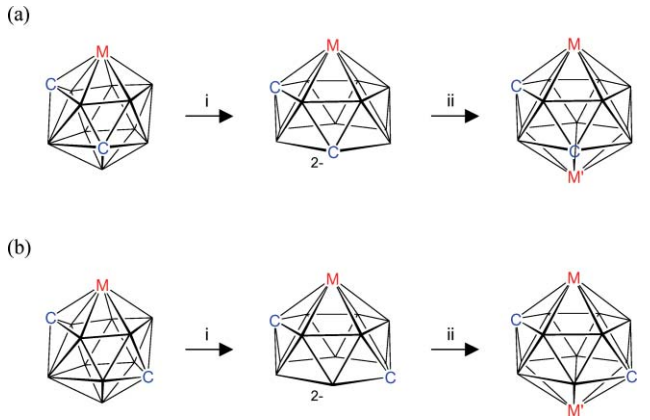

Fig. 13 Reduction and metallation of (a) 4,1,8-MC_2B_{10} 13-vertex metallacarboranes to afford 1,14,2,9-$MM'C_2B_{10}$ 14-vertex bimetallacarboranes and (b) 4,1,12-MC_2B_{10} 13-vertex metallacarboranes to afford 1,14,2,10-$MM'C_2B_{10}$ 14-vertex bimetallacarboranes. i = reduction. ii = metallation. See ref. 37 and 38.

metal-centred and (ii) the 4,1,6- and 4,1,10- isomers are the easiest to reduce, only for the 4,1,8- and 4,1,12- isomers can there be an accessible pathway to a stable *nido* dianion. The structures of the 14-vertex bimetallacarboranes (bicapped square antiprisms) have metal atoms in the degree-6 capping vertices and one cage C atom in each of the hexagonal belts. Having a cage C atom in the open face of the *nido* dianion will stabilise that ion since facial atoms are only of degree-4. Presumably for the 4,1,6- and 4,1,10-MC_2B_{10} isomers (where both cage C atoms are connected to M) the barrier to isomerisation of the reduced form in which a cage C atom moves to the open face is insurmountable.

Conclusions

In 13-vertex indenyl cobaltacarboranes the orientation of the indenyl ligand with respect to the metallacarborane cage can provide unique experimental information on the relative *trans* influences of the B and C atoms in the carborane ligand face to which the metal is bound. In cases where there are no substituents (other than H atoms) on these facial atoms there is generally good agreement between the indenyl orientations found by crystallographic study and those predicted by DFT calculations on models of the analogous naphthalene ferracarborane. However, the presence of even a single methyl group as substituent at a cage C atom can change the electronically-preferred orientation through methyl/indenyl steric interaction. Indenyl cobaltacarboranes are easier to reduce that analogous cyclopentadienyl compounds, and, of the various 13-vertex isomers, the 4,1,6- and 4,1,10- species are the easiest to reduce in a process that is shown to be cobalt-centred.

Experimental

Synthesis

Experiments were performed under dry, oxygen-free N_2, using standard Schlenk techniques, although subsequent manipulations were sometimes performed in the open laboratory. All solvents were freshly distilled from the appropriate drying agents under nitrogen immediately before use (CH_2Cl_2; CaH_2: THF, toluene and 40–60 petroleum ether; sodium wire) or were stored over 4 Å molecular sieves and were degassed (3 × freeze-pump-thaw cycles) before use. Preparative TLC employed 20 × 20 cm Kieselgel F_{254} glass plates. NMR spectra at 400.1 MHz (^{1}H) or 128.4 MHz (^{11}B) were recorded on a Bruker DPX-400 spectrometer from $CDCl_3$ solutions (unless otherwise stated) at room temperature. Electron impact mass spectrometry (EIMS) was carried out using a Kratos Concept mass spectrometer. Elemental analyses were determined by the departmental service (HWU). The carboranes 1,2-*closo*-$C_2B_{10}H_{12}$ and 1,12-*closo*-$C_2B_{10}H_{12}$ were purchased from Katchem (Czech Republic) and used as supplied, whilst 1-Me-1,2-*closo*-$C_2B_{10}H_{11}$,[39] 1,2-μ-$(CH_2)_3$-1,2-*closo*-$C_2B_{10}H_{10}$[40] and 1,2-μ-$(CH_2SiMe_2CH_2)$-1,2-*closo*-$C_2B_{10}H_{10}$[41] were prepared by literature methods or slight variations thereof. 1,2-Me_2-1,2-*closo*-$C_2B_{10}H_{10}$ was prepared by treatment of Li_2[1,2-*closo*-$C_2B_{10}H_{10}$] with MeI in Et_2O.[42] All other reagents and solvents were supplied commercially.

4-(η-C_9H_7)-4,1,6-*closo*-$CoC_2B_{10}H_{12}$ (1). 1,2-*closo*-$C_2B_{10}H_{12}$ (0.700 g, 4.85 mmol) was dissolved in degassed THF (30 mL). Na metal (0.34 g, 14.79 mmol) was added and the solution stirred overnight. In a separate Schlenk tube a solution of Li[C_9H_7] was prepared by adding indene (1.69 mL, 14.55 mmol) and *n*-BuLi (6.40 mL, 16.00 mmol) to degassed THF (10 mL) in an ice bath, stirring the solution at room temperature for 1 h, then at reflux for 15 min, giving a dark red solution. Excess Na was removed from the reduced carborane solution which was then added to the Li[C_9H_7] solution. The resulting red solution was cooled in an ice bath, and $CoCl_2$ (2.330 g, 17.95 mmol) was added, affording a brown solution which was stirred at room temperature overnight then aerially oxidised (0.5 h). The solution was filtered through a short silica column eluting with DCM to afford a brown solution, removal of solvent from which yielded a brown solid. This was further purified by column chromatography (1 : 4 DCM:40-60 petroleum ether), followed by preparative TLC on silica (3 : 2 DCM:40-60 petroleum ether, R_f 0.62) yielding, as major product, 4-(η-C_9H_7)-4,1,6-*closo*-$CoC_2B_{10}H_{12}$ (**1**) as a brown solid on removal of solvent (0.730 g, 47.3%). $C_{11}H_{19}B_{10}Co$ requires C 41.5, H 6.02. Found for **1**: C 41.6, H 6.18%. ^{11}B{^{1}H} NMR: δ 14.54 (1B), 1.95 (2B), –0.52 (1B), –3.80 (3B), –11.90 (2B), –16.89 (1B). ^{1}H NMR: δ 7.70 (m, 2H, C_6H_4), 7.60 (m, 2H, C_6H_4), 5.90 (d, 2H, C_5H_3), 5.60 (t, 1H, C_5H_3), 3.70 (br s, 2H, $C_{cage}H$). EIMS: envelope centred on *m*/*z* 317 (M^+). Crystals grown by solvent diffusion of diethyl ether into a THF solution of **1** at –30 °C.

1,6-Me_2-4-(η-C_9H_7)-4,1,6-*closo*-$CoC_2B_{10}H_{10}$ (2). Similarly 1,6-Me_2-4-(η-C_9H_7)-4,1,6-*closo*-$CoC_2B_{10}H_{10}$ (**2**) was the major band afforded (R_f 0.62 eluting with 3 : 2 DCM:40–60 petroleum ether) as a brown solid (0.340 g, 33.8%) from 1,2-Me_2-1,2-*closo*-$C_2B_{10}H_{10}$ (0.500 g, 2.90 mmol), Na metal (0.24 g, 10.4 mmol), freshly prepared Li[C_9H_7] (8.70 mmol) and $CoCl_2$ (1.393 g, 10.73 mmol). $C_{13}H_{23}B_{10}Co$ requires C 45.1, H 6.69. Found for **2**: C 44.9, H 6.77%. ^{11}B{^{1}H} NMR: δ 15.08 (1B), 4.87 (2B), 0.33 (1B), –0.47 (1B), –4.79 (2B), –7.28 (2B), –12.05 (1B). ^{1}H NMR, δ 7.80 (m, 2H, C_6H_4), 7.60 (m, 2H, C_6H_4), 5.80 (d, 2H, C_5H_3), 5.75 (t, 1H, C_5H_3), 2.15 (s, 6H, CH_3). EIMS: envelope centred on *m*/*z* 346 (M^+). Crystals grown by solvent diffusion of 40–60-petroleum ether into a CH_2Cl_2 solution of **2** at –30 °C.

4-(η-C_9H_7)-4,1,8-*closo*-$CoC_2B_{10}H_{12}$ (3). Compound **1** (0.208 g, 0.65 mmol) was stirred at reflux overnight in THF (25 mL). Removal of solvent from the resulting brown solution yielded a bronze solid. Preparative TLC on silica (3 : 2 DCM:40–60 petroleum ether) separated 4-(η-C_9H_7)-4,1,8-*closo*-$CoC_2B_{10}H_{12}$ (**3**) as a bronze product at R_f 0.77 (0.153 g, 73.6%) from minor amounts of the corresponding 4,1,12- isomer (R_f 0.84) and unchanged 4,1,6- isomer (R_f 0.60). $^{11}B\{^1H\}$ NMR: δ 22.61 (1B), 9.32 (1B), 7.43 (1B), 6.34 (1B), –0.92 (1B), –5.80 (1B), –7.23 (1B), –8.69 (1B), –9.72 (1B), –12.52 (1B). ^1H NMR: δ 7.60 (m, 2H, C_6H_4), 7.50 (m, 2H, C_6H_4), 5.86 (m, 1H, C_5H_3), 5.80 (m, 1H, C_5H_3), 5.10 (app. t, 1H, C_5H_3), 3.75 (br s, 1H, $C_{cage}H$), 2.50 (br s, 1H, $C_{cage}H$). EIMS: envelope centred on m/z 317 (M^+).

1,8-Me_2-4-(η-C_9H_7)-4,1,8-*closo*-$CoC_2B_{10}H_{10}$ (4). Similarly, compound **2** (0.200 g, 0.58 mmol) was heated to reflux in THF (25 mL) to afford, following TLC on silica (3 : 2 DCM:40–60 petroleum ether, R_f 0.75), 1,8-Me_2-4-(η-C_9H_7)-4,1,8-*closo*-$CoC_2B_{10}H_{10}$ (**4**) as an orange solid (0.133 g, 66.5%) together with a smaller amount (57 mg, 28.5%) of the corresponding 4,1,12-isomer. $C_{13}H_{23}B_{10}Co$ requires C 45.1, H 6.69. Found for **4**: C 44.9, H 6.71%. $^{11}B\{^1H\}$ NMR: δ 21.23 (1B), 13.23 (1B), 10.79 (1B), 5.22 (1B), 3.34 (1B), –2.11 (1B), –2.57 (1B), –2.97 (1B), –5.67 (1B), –13.19 (1B). ^1H NMR: δ 7.60 (m, 2H, C_6H_4), 7.50 (m, 2H, C_6H_4), 5.65 (m, 1H, C_5H_3), 5.60 (m, 1H, C_5H_3), 5.25 (app. t, 1H, C_5H_3), 2.60 (s, 3H, CH_3), 1.75 (s, 3H, CH_3). EIMS: envelope centred on m/z 346 (M^+). Crystals grown by solvent diffusion of 40–60 petroleum ether into a CH_2Cl_2 solution of **4** at –30 °C.

1(or 6)-Me-4-(η-C_9H_7)-4,1,6-*closo*-$CoC_2B_{10}H_{11}$ (5). Following the procedure outlined above for compound **1**, 1-Me-1,2-*closo*-$C_2B_{10}H_{11}$ (0.245 g, 1.55 mmol) was reduced with Na (0.089 g, 3.90 mmol) and then treated with freshly prepared Li[C_9H_7] (4.65 mmol) and $CoCl_2$ (0.745 g, 5.74 mmol) to afford dark brown 1(or 6)-Me-4-(η-C_9H_7)-4,1,6-*closo*-$CoC_2B_{10}H_{11}$ (**5**) after aerial oxidation and work-up involving column chromatography on silica (1 : 4 DCM:40–60 petroleum ether). Yield 0.208 g, 40.4%. $C_{12}H_{21}B_{10}Co$ requires C 43.4, H 6.37. Found for **5**: C 43.3, H 6.52%. $^{11}B\{^1H\}$ NMR: δ 14.32 (1B), 8.20 (1B), –0.10 (1B), –2.38 (2B), –3.43 (1B), –4.59 (1B), –7.59 (1B), –10.21 (1B), –16.46 (1B). ^1H NMR: δ 7.86 (m, 1H, C_6H_4), 7.66 (m, 2H, C_6H_4), 7.33 (m, 1H, C_6H_4), 6.12 (m, 1H, C_5H_3), 5.73 (m, 1H, C_5H_3), 5.61 (app. t, 1H, C_5H_3), 2.62 (s, 3H, CH_3), 2.48 (br s, 1H, $C_{cage}H$). EIMS: envelope centred on m/z 332 (M^+).

1-Me-4-(η-C_9H_7)-4,1,8-*closo*-$CoC_2B_{10}H_{11}$ (6) and 8-Me-4-(η-C_9H_7)-4,1,8-*closo*-$CoC_2B_{10}H_{11}$ (7). Compound **5** (0.100 g, 0.30 mmol) was heated to reflux in THF (25 mL) to afford, following TLC on silica (3 : 2 DCM:40–60 petroleum ether), progressively a brown band (R_f 0.87) tentatively identified by ^{11}B and ^1H NMR spectroscopies as a mixture of 1-Me-4-(η-C_9H_7)-4,1,12-*closo*-$CoC_2B_{10}H_{11}$ and 12-Me-4-(η-C_9H_7)-4,1,12-*closo*-$CoC_2B_{10}H_{11}$ (combined yield 0.021 g, 21%), an orange band (R_f 0.80, 0.067 g, 67%) and finally a second brown band (R_f 0.64, compound **5** by NMR spectroscopy, 0.005 g, 5%). The orange band gave a clean EI mass spectrum with an envelope centred on m/z 332 (M^+), but in NMR spectra appeared to be a mixture of two isomers, in approximately a 2 : 1 ratio. The major component was preferentially crystallised by solvent diffusion of 40–60 petroleum ether into a CH_2Cl_2 solution at –30 °C. Major isomer, 8-Me-4-(η-C_9H_7)-4,1,8-*closo*-$CoC_2B_{10}H_{11}$ (**7**): $^{11}B\{^1H\}$ NMR: δ 20.44 (1B), 11.66 (1B), 8.71 (1B), 4.62 (1B), 2.09 (1B), –2.74 (1B), –3.52 (1B), –7.07 (2B), –12.63 (1B). ^1H NMR: δ 7.53 (m, 4H, C_6H_4), 5.83 (m, 1H, C_5H_3), 5.79 (m, 1H, C_5H_3), 5.04 (app. t, 1H, C_5H_3), 3.75 (br s, 1H, $C_{cage}H$), 1.75 (s, 3H, CH_3), from spectra of redissolved crystals. Minor isomer, 1-Me-4-(η-C_9H_7)-4,1,8-*closo*-$CoC_2B_{10}H_{11}$ (**6**): $^{11}B\{^1H\}$ NMR: δ 23.16 (1B), 11.23 (1B), 8.88 (1B), 6.77 (1B), 0.26 (1B), –5.20 (1B), –6.26 (2B), –7.30 (1B), –13.22 (1B). ^1H NMR: δ 7.53 (m, 4H, C_6H_4), 5.67 (m, 1H, C_5H_3), 5.62 (m, 1H, C_5H_3), 5.27 (app. t, 1H, C_5H_3), 2.42 (br s, 1H, $C_{cage}H$), 1.53 (s, 3H, CH_3), from difference spectroscopy.

4-(η-C_9H_7)-4,1,10-*closo*-$CoC_2B_{10}H_{12}$ (8). Ammonia (30 mL) was condensed onto 1,12-*closo*-$C_2B_{10}H_{12}$ (1.000 g, 6.94 mmol) at –78 °C. Na metal (1.116 g, 48.70 mmol) was added and the resulting dark blue solution left stirring at –78 °C for 3 h. After warming to room temperature and evaporation of ammonia the resulting Na_2[7,10-*nido*-$C_2B_{10}H_{12}$] was dissolved in degassed THF (40 mL) giving a purple solution. This was then added to a freshly prepared Li[C_9H_7] solution (20.82 mmol). Following a further addition of $CoCl_2$ (3.330 g, 25.68 mmol) and stirring at room temperature overnight, aerial oxidation (0.5 h) afforded the final product. Purification as for compound **1** concluding with preparative TLC on silica (3 : 2 DCM:40–60 petroleum ether, R_f 0.60) yielded brown 4-(η-C_9H_7)-4,1,10-*closo*-$CoC_2B_{10}H_{12}$ (**8**) (1.050 g, 47.5%) as the major product. A small amount of the corresponding 4,1,12- isomer was also visible (R_f 0.80, see next). $C_{11}H_{19}B_{10}Co$ requires C 41.5, H 6.02. Found for **8**: C 41.6, H 6.14%. $^{11}B\{^1H\}$ NMR, CD_2Cl_2: δ 4.92 (2B), 3.86 (2B), –7.26 (1B), –9.79 (3B), –12.77 (2B). ^1H NMR, CD_2Cl_2: δ 7.70 (m, 2H, C_6H_4), 7.55 (m, 2H, C_6H_4), 5.80 (d, 2H, C_5H_3), 5.65 (t, 1H, C_5H_3), 5.05 (br s, 1H, $C_{cage}H$), 1.90 (br s, 1H, $C_{cage}H$). EIMS: envelope centred on m/z 317 (M^+). Crystals grown by solvent diffusion of 40–60 petroleum ether into a CH_2Cl_2 solution of **8** at –30 °C.

4-(η-C_9H_7)-4,1,12-*closo*-$CoC_2B_{10}H_{12}$ (9). Compound **8** (0.850 g, 2.67 mmol) was stirred at reflux overnight in THF (25 mL). The resulting brown solution was cooled to room temperature, and solvent removed leaving a brown solid. Preparative TLC on silica (3 : 2 DCM:40–60 petroleum ether) yielded 4-(η-C_9H_7)-4,1,12-*closo*-$CoC_2B_{10}H_{12}$ (**9**) as a brown band at R_f 0.80 (0.775 g, 91.2%). $C_{11}H_{19}B_{10}Co$ requires C 41.5, H 6.02. Found for **9**: C 41.4, H 6.02%. $^{11}B\{^1H\}$ NMR: δ 8.78 (1B), 6.67 (1B), 3.99 (1B), 3.15 (1B), –2.78 (1B), –10.02 (2B), –14.32 (1B), –15.85 (1B), –17.32 (1B). ^1H NMR: δ 7.55 (m, 2H, C_6H_4), 7.45 (m, 2H, C_6H_4), 5.86 (m, 1H, C_5H_3), 5.76 (m, 1H, C_5H_3), 5.15 (app. t, 1H, C_5H_3), 3.70 (br s, 1H, $C_{cage}H$), 3.15 (br s, 1H, $C_{cage}H$). EIMS: envelope centred on m/z 317 (M^+). Crystals grown by solvent diffusion of 40–60 petroleum ether into a CH_2Cl_2 solution of **9** at –30 °C.

1,12-Me_2-4-(η-C_9H_7)-4,1,12-*closo*-$CoC_2B_{10}H_{10}$ (10). Compound **4** (0.075 g, 0.22 mmol) was stirred at reflux overnight in toluene (25 mL). Preparative TLC on silica (1 : 1 DCM:40–60 petroleum ether) yielded 1,12-Me_2-4-(η-C_9H_7)-4,1,12-*closo*-$CoC_2B_{10}H_{10}$ (**10**) as a dark brown band at R_f 0.86 (0.056 g, 74.7%) (also recovered from the TLC plates was unchanged compound **4**, 0.013 g, 17.3%). $C_{13}H_{23}B_{10}Co$ requires C 45.1, H 6.69. Found for **10**: C 44.9, H 6.76%. $^{11}B\{^1H\}$ NMR: δ 10.18 (1B), 8.97 (1B), 8.21 (1B), 4.23 (1B), 1.86 (1B), –5.19 (1B), –5.75 (1B), –8.02 (1B),

–14.36 (2B). ^{1}H NMR: δ 7.55 (m, 4H, C_6H_4), 5.64 (m, 1H, C_5H_3), 5.55 (m, 1H, C_5H_3), 5.31 (app. t, 1H, C_5H_3), 2.38 (s, 3H, CH_3), 1.72 (s, 3H, CH_3). EIMS: envelope centred on m/z 346 (M^+). Crystals grown by solvent diffusion of 40–60 petroleum ether into a CH_2Cl_2 solution of **10** at –30 °C.

1,2-μ-$(CH_2)_3$-4-(η-C_9H_7)-4,1,2-*closo*-$CoC_2B_{10}H_{10}$ (11). Following the procedure similar to that detailed for compound **1**, the brown product 1,2-μ-$(CH_2)_3$-4-(η-C_9H_7)-4,1,2-*closo*-$CoC_2B_{10}H_{10}$ (**11**) was prepared (R_f 0.59 eluting with 3 : 2 DCM:40–60 petroleum ether) as a brown solid (0.150 g, 23.4%) from 1,2-μ-$(CH_2)_3$-1,2-*closo*-$C_2B_{10}H_{10}$ (0.330 g, 1.79 mmol), Li metal (0.124 g, 17.90 mmol), freshly prepared Li[C_9H_7] (5.37 mmol) and $CoCl_2$ (0.860 g, 6.62 mmol) in THF (25 mL). $C_{14}H_{23}B_{10}Co$ requires C 46.9, H 6.47. Found for **11**: C 46.7, H 6.52%. ^{11}B{^{1}H} NMR: δ 16.24 (2B), 7.64 (2B), 5.54 (1B), 2.25 (1B), –4.67 (2B), –10.45 (2B). ^{1}H NMR, δ 7.66 (m, 2H, C_6H_4), 7.47 (m, 2H, C_6H_4), 5.92 (d, 2H, C_5H_3), 5.26 (t, 1H, C_5H_3), 2.69 (m, 2H, CH_2), 2.47 (m, 2H, CH_2), 2.08 (m, 1H, CH_2), 1.96 (m, 1H, CH_2). EIMS: envelope centred on m/z 357 (M^+). Crystals grown by vapour diffusion of 40–60 petroleum ether into a THF solution of **11** at room temperature.

1,2-$(CH_3)_2$-4-(η-C_9H_7)-4,1,2-*closo*-$CoC_2B_{10}H_{10}$ (12). 1,2-μ-$(CH_2SiMe_2CH_2)$-1,2-*closo*-$C_2B_{10}H_{10}$ (0.250 g, 1.09 mmol) was treated with Li metal (0.075 g, 10.90 mmol) in THF (25 mL) for 24 h. To the resulting yellow solution, cooled to 0 °C, was added freshly prepared Li[C_9H_7] (3.27 mmol) and $CoCl_2$ (0.523 g, 4.03 mmol). Following overnight stirring the mixture was aerially oxidised (0.5 h) and filtered through a short silica column. TLC, eluting with 3 : 2 DCM:40–60 petroleum ether, yielded progressively orange compound **4** (0.007 g, 1.9%), brown compound **2** (0.020 g, 9.5%), and finally brown 1,2-$(CH_3)_2$-4-(η-C_9H_7)-4,1,2-*closo*-$CoC_2B_{10}H_{10}$ (**12**) (R_f 0.48, 0.020 g, 5.0%). $C_{13}H_{23}B_{10}Co$ requires C 45.1, H 6.69. Found for **12**: C 45.2, H 6.81%. ^{11}B{^{1}H} NMR: δ 17.02 (2B), 11.93 (2B), 4.58 (1B), 2.28 (1B), –6.72 (2B), –9.41 (2B). ^{1}H NMR, δ 7.67 (m, 2H, C_6H_4), 7.48 (m, 2H, C_6H_4), 5.97 (d, 2H, C_5H_3), 5.37 (t, 1H, C_5H_3), 1.95 (s, 6H, CH_3). EIMS: envelope centred on m/z 345 (M^+). Crystals grown by solvent diffusion of 40–60 petroleum ether into a THF solution of **12** at –30 °C.

Crystallography

Intensity data were collected from single crystals on a Bruker X8 APEX2 diffractometer using Mo-Kα X-radiation, with crystals mounted in inert oil on a cryoloop and cooled to 100 K by an Oxford Cryosystems Cryostream. The structures were solved by direct methods and refined by full-matrix least-squares.[43] In compound **8** there is a molecule of CH_2Cl_2 per molecule of cobaltacarborane, and in **11** a molecule of THF per molecule of cobaltacarborane. The structure of **9** is partially disordered across a crystallographic mirror plane and stable refinement required the application of restraints [B2–B3, 1.9(2) Å; C1–B2, 1.53(2) Å; C1–B3A, 1.53(2) Å]. For compounds **1**, **2**, **4**, **7**, **8** and **10** and for H5 of **12**, cage-bound H atoms were located in difference Fourier maps and freely refined. Cage H atoms of **11** and all other cage H atoms (except H5) of **12** were set in idealised positions (B–H 1.12 Å), whilst for **9** B–H and C_{cage}–H distances were restrained to 1.10(2) Å. Non-cage H atoms were set in idealised positions in all compounds (CH_2, C–H 0.99 Å; CH_3, C–H 0.98 Å; CH [5-membered ring], C–H 1.0 Å; CH [6-membered ring], C–H 0.95 Å). In all cases, H atom thermal parameters were set to 1.2×U_{eq} of the attached B or C atom. Table 5 contains further experimental details.

Table 5 Crystallographic data

	1	**2**	**4**	**7**	**8**	**9**	**10**	**11**	**12**
Formula	$C_{11}H_{19}B_{10}Co$	$C_{13}H_{23}B_{10}Co$	$C_{13}H_{23}B_{10}Co$	$C_{12}H_{21}B_{10}Co$	$C_{11}H_{19}B_{10}Co\cdot CH_2Cl_2$	$C_{11}H_{19}B_{10}Co$	$C_{13}H_{23}B_{10}Co$	$C_{14}H_{23}B_{10}Co\cdot C_4H_8O$	$C_{13}H_{23}B_{10}Co$
M	318.29	346.34	346.34	332.32	403.22	318.29	346.34	430.46	346.34
Crystal system	Triclinic	Triclinic	Monoclinic	Triclinic	Monoclinic	Orthorhombic	Monoclinic	Monoclinic	Orthorhombic
Space group	*P*bar*1*	*P*bar*1*	*C*2/*c*	P*bar*1	$P2_1/n$	*Pnma*	$P2_1/c$	$P2_1/n$	*Pbca*
a/Å	7.1142(5)	8.0489(6)	56.627(8)	7.2421(3)	11.4396(5)	17.3193(17)	10.1626(10)	8.7797(12)	13.4744(11)
b/Å	9.1272(6)	9.0351(8)	8.8716(10)	9.1848(4)	8.7217(3)	11.7891(11)	10.2041(9)	23.658(3)	14.6459(13)
c/Å	11.9007(7)	11.9980(9)	13.7968(19)	12.8122(6)	19.2249(9)	7.2997(7)	16.7251(11)	10.2905(14)	17.2983(15)
α (°)	75.946(3)	98.473(3)		101.925(2)					
β (°)	88.019(3)	96.184(3)	100.226(4)	99.156(3)	107.299(2)		102.048(4)	104.090(7)	
γ (°)	78.059(3)	101.756(4)		102.443(2)					
U/Å^3	733.29(8)	836.31(12)	6821.0(15)	795.54(6)	1831.36(13)	1490.4(2)	1696.2(3)	2073.1(5)	3413.7(5)
Z	2	2	16	2	4	4	4	4	8
F(000)/e	324	356	2848	340	816	648	712	896	1424
D_c/Mg m^{-3}	1.442	1.375	1.349	1.387	1.462	1.418	1.356	1.379	1.348
μ(Mo-Kα)/mm^{-1}	1.149	1.014	0.995	1.063	1.219	1.131	1.000	0.836	0.994
θ_{max} (°)	30.98	32.45	26.50	29.25	28.50	28.36	30.67	26.40	27.49
Data measured	15837	22402	55490	15146	46198	31925	44880	41272	57987
Unique data, n	4413	5401	6994	4002	4640	1945	5232	4229	3913
R_{int}	0.0322	0.0297	0.0744	0.0340	0.0476	0.0471	0.0572	0.0637	0.0795
R, wR_2 (obs. data)	0.0314, 0.0952	0.0257, 0.0663	0.0358, 0.0830	0.0361, 0.0819	0.0349, 0.0731	0.0710, 0.1645	0.0408, 0.1022	0.0345, 0.0739	0.0320, 0.0713
S	1.025	1.041	0.971	1.070	1.131	1.367	1.080	1.041	1.055
Variables	235	252	517	227	262	137	222	271	227
E_{max}, E_{min}/e Å^{-3}	0.505, –0.508	0.507, –0.295	0.362, –0.373	0.383, –0.449	0.406, –0.345	1.229, –2.541	0.688, –0.439	0.331, –0.382	0.369, –0.339

Electrochemistry, spectroelectrochemistry and EPR

Materials and apparatus for electrochemistry, spectroelectrochemistry and EPR spectroscopy have been described elsewhere.[44] Potential values are referred to the Saturated Calomel Electrode (SCE). Under the present experimental conditions, the one-electron oxidation of ferrocene occurs at $E^{\circ\prime} = +0.39$ V in CH_2Cl_2 solution and at $E^{\circ\prime} = +0.53$ V in THF solution.

Calculations

All geometries were optimised without constraints using Gaussian 03, Revision D.01[45] employing the BP86 functional.[46] 6-31G** basis sets were used for B, C and H atoms[47] whilst for Fe and Co the Stuttgart relativistic ECP[48] and the associated basis sets were employed. Local minima were confirmed as such through analytical frequency calculations. Geometry measurements were made using Mercury[49] and orbital representations generated *via* Molekel.[50]

Acknowledgements

AJW and SAM thank the EPSRC (GS supported by DTA studentship; DE and DMcK supported by project EP/E02971X/1) and the Carnegie Trust (AMcA) for funding. PZ and FL gratefully acknowledge the financial support of the University of Siena (PAR servizi).

References

1 *e.g.* (*a*) G. B. Dunks, M. M. McKown and M. F. Hawthorne, *J. Am. Chem. Soc.*, 1971, **93**, 2541; (*b*) D. F. Dustin, G. B. Dunks and M. F. Hawthorne, *J. Am. Chem. Soc.*, 1973, **95**, 1109; (*c*) A. Burke, D. Ellis, B. T. Giles, B. E. Hodson, S. A. Macgregor, G. M. Rosair and A. J. Welch, *Angew. Chem., Int. Ed.*, 2003, **42**, 225; (*d*) L. Deng and Z. Xie, *Coord. Chem. Rev.*, 2007, **251**, 2452.
2 *e.g.* C. A. Reed, *Acc. Chem. Res.*, 1998, **31**, 133, and references therein.
3 *e.g.* R. F. Barth, J. A. Coderre, M. G. H. Vicente and T. E. Blue, *Clin. Cancer Res.*, 2005, **11**, 3987, and references therein.
4 L. D. Brown and W. N. Lipscomb, *Inorg. Chem.*, 1977, **16**, 2989.
5 P.v.R. Schleyer, K. Najafian and A. M. Mebel, *Inorg. Chem.*, 1998, **37**, 6765.
6 M. R. Churchill and B. G. DeBoer, *J. Chem. Soc., Chem. Commun.*, 1972, 1326.
7 (*a*) E. D. Jemmis, *J. Am. Chem. Soc.*, 1982, **104**, 7017; (*b*) R. B. King, *Inorg. Chem.*, 2001, **40**, 6369; (*c*) R. B. King, *J. Organomet. Chem.*, 2007, **692**, 1773.
8 A. Burke, R. McIntosh, D. Ellis, G. M. Rosair and A. J. Welch, *Collect. Czech. Chem. Commun.*, 2002, **67**, 991.
9 D. Grafstein and J. Dvorak, *Inorg. Chem.*, 1963, **2**, 1128.
10 S. Zlatogorsky, D. Ellis, G. M. Rosair and A. J. Welch, *Chem. Commun.*, 2007, 2178.
11 D. Ellis, M. E. Lopez, R. McIntosh, G. M. Rosair, A. J. Welch and R. Quenardelle, *Chem. Commun.*, 2005, 1348.
12 S. Zlatogorsky, M. J. Edie, D. Ellis, S. Erhardt, M. E. Lopez, S. A. Macgregor, G. M. Rosair and A. J. Welch, *Angew. Chem., Int. Ed.*, 2007, **46**, 6706.
13 R. McIntosh, D. Ellis, J. Gil-Lostes, K. J. Dalby, G. M. Rosair and A. J. Welch, *Dalton Trans.*, 2005, 1842.
14 (*a*) A. J. Hart-Davis and R. J. Mawby, *J. Chem. Soc. A*, 1969, 2403; (*b*) F. Basolo, *Coord. Chem. Rev.*, 1982, **43**, 7; (*c*) M. J. Calhorda, *Chem.–Eur. J.*, 2002, **8**, 868.
15 D. E. Smith and A. J. Welch, *Organometallics*, 1986, **5**, 760.
16 A. Burke, D. Ellis, D. Ferrer, D. L. Ormsby, G. M. Rosair and A. J. Welch, *Dalton Trans.*, 2005, 1716.
17 J. Zhang, L. Deng, H. -S. Chan and Z. Xie, *J. Am. Chem. Soc.*, 2007, **129**, 18.
18 M. A. Laguna, D. Ellis, G. M. Rosair and A. J. Welch, *Inorg. Chim. Acta*, 2003, **347**, 161.
19 P. D. Abram, D. McKay, D. Ellis, S. A. Macgregor, G. M. Rosair and A. J. Welch, *Dalton Trans.*, 2010, **39**, 2412.
20 D. M. P. Mingos, M. I. Forsyth and A. J. Welch, *J. Chem. Soc., Dalton Trans.*, 1978, 1363.
21 The synthesis and characterisation of naphthalene ferra- and ruthenacarboranes is currently underway; G. Scott, D. Ellis, G. M. Rosair and A. J. Welch, to be published.
22 K. J. Dalby, D. Ellis, S. Erhardt, R. D. McIntosh, S. A. Macgregor, K. Rae, G. M. Rosair, V. Settles, A. J. Welch, B. E. Hodson, T. D. McGrath and F. G. A. Stone, *J. Am. Chem. Soc.*, 2007, **129**, 3302.
23 P. D. Abram, D. McKay, D. Ellis, S. A. Macgregor, G. M. Rosair, R. Sancho and A. J. Welch, *Dalton Trans.*, 2009, 2345.
24 P. D. Abram, D. Ellis, G. M. Rosair and A. J. Welch, *Chem. Commun.*, 2009, 5403.
25 W. E. Geiger Jr., W. L. Bowden and N. El Murr, *Inorg. Chem.*, 1979, **18**, 2358.
26 M. Corsini, F. Fabrizi de Biani and P. Zanello, *Coord. Chem. Rev.*, 2006, **250**, 1351, and references therein.
27 U. Koelle, B. Fuss, M. V. Rajasehharan, B. L. Ramakrishna, J. H. Ammeter and M. C. Bohm, *J. Am. Chem. Soc.*, 1984, **106**, 4152.
28 F. H. Allen, *Acta Crystallogr., Sect. B: Struct. Sci.*, 2002, **58**, 380.
29 P. Zanello, *Inorganic Electrochemistry: Theory, Practice and Application*, RSC, Oxford, UK, 2003.
30 R. H. Herber, A. R. Kudinov, P. Zanello, I. Nowik, D. S. Perekalin, V. I. Meshcheryakov, K. A. Lyssenko, M. Corsini and S. Fedi, *Eur. J. Inorg. Chem.*, 2006, 1786.
31 (*a*) M. V. Yarosh, T. V. Baranova, V. L. Shirokii, A. A. Érdman and N. A. Maier, *Russ. J. Electrochem.*, 1993, **29**, 1125; (*b*) M. V. Yarosh, T. V. Baranova, V. L. Shirokii, A. A. Érdman and N. A. Maier, *Russ. J. Electrochem.*, 1994, **30**, 366.
32 V. I. Meshcheryakov, P. S. Kitaev, K. A. Lyssenko, Z. S. Starikowa, P. V. Petrovskii, Z. Janoušek, M. Corsini, F. Laschi, P. Zanello and A. R. Kudinov, *J. Organomet. Chem.*, 2005, **690**, 4745.
33 (*a*) F. E. Mabbs and D. Collins, *Electron Paramagnetic Resonance of d Transition Metal Compounds*, Elsevier, New York, USA, 1992; (*b*) R. S. Drago, *Physical Methods for Chemists*, Saunders College Publishing, New York, USA, 1992.
34 M. Romanelli, *Sim. Program GPN1Cu23*, Department of Chemistry, University of Florence, Italy, 1995.
35 M. F. Rettig and R. S. Drago, *J. Am. Chem. Soc.*, 1969, **91**, 1361.
36 J. Ammeter, N. Oswald and R. Bucher, *Helv. Chim. Acta*, 1975, **58**, 671.
37 W. J. Evans and M. F. Hawthorne, *J. Chem. Soc., Chem. Commun.*, 1974, 38.
38 D. Ellis, M. E. Lopez, R. McIntosh, G. M. Rosair and A. J. Welch, *Chem. Commun.*, 2005, 1917. We believe that it will also be possible to expand 4,1,11-MC_2B_{10} species to 14-vertex derivatives, but as yet insufficient amounts of this isomer are available. See ref. 12.
39 T. L. Heying, J. W. Ager Jr., S. L. Clark, D. J. Mangold, H. L. Goldstein, M. Hillman, R. J. Polak and J. W. Szymanski, *Inorg. Chem.*, 1963, **2**, 1089.
40 T. E. Paxon, M. K. Kaloustian, G. M. Tom, R. J. Wiersema and M. F. Hawthorne, *J. Am. Chem. Soc.*, 1972, **94**, 4882.
41 T. L. Heying, J. W. Ager Jr., S. L. Clark, R. P. Alexander, S. Papetti, J. A. Reid and S. I. Trotz, *Inorg. Chem.*, 1963, **2**, 1097.
42 S. Zlatogorsky, D. Ellis and A. J. Welch, unpublished results. This represents an improvement on the original synthesis; H. D. Smith, T. A. Knowles and H. Schroeder, *Inorg. Chem.*, 1965, **4**, 107.
43 *SHELXTL, V6.10*, Bruker-AXS, Madison, WI, USA, 2000.
44 F. Fabrizi de Biani, A. Ienco, F. Laschi, P. Leoni, F. Marchetti, L. Marchetti, C. Mealli and P. Zanello, *J. Am. Chem. Soc.*, 2005, **127**, 3076.
45 M. J. Frisch, G. W. Trucks, H. B. Schlegel, G. E. Scuseria, M. A. Robb, J. R. Cheeseman, J. A. Montgomery Jr., T. Vreven, K. N. Kudin, J. C. Burant, J. M. Millam, S. S. Iyengar, J. Tomasi, V. Barone, B. Mennucci, M. Cossi, G. Scalmani, N. Rega, G. A. Petersson, H. Nakatsuji, M. Hada, M. Ehara, K. Toyota, R. Fukuda, J. Hasegawa, M. Ishida, T. Nakajima, Y. Honda, O. Kitao, H. Nakai, M. Klene, X. Li, J. E. Knox, H. P. Hratchian, J. B. Cross, V. Bakken, C. Adamo, J. Jaramillo,

R. Gomperts, R. E. Stratmann, O. Yazyev, A. J. Austin, R. Cammi, C. Pomelli, J. W. Ochterski, P. Y. Ayala, K. Morokuma, G. A. Voth, P. Salvador, J. J. Dannenberg, V. G. Zakrzewski, S. Dapprich, A. D. Daniels, M. C. Strain, O. Farkas, D. K. Malick, A. D. Rabuck, K. Raghavachari, J. B. Foresman, J. V. Ortiz, Q. Cui, A. G. Baboul, S. Clifford, J. Cioslowski, B. B. Stefanov, G. Liu, A. Liashenko, P. Piskorz, I. Komaromi, R. L. Martin, D. J. Fox, T. Keith, M. A. Al-Laham, C. Y. Peng, A. Nanayakkara, M. Challacombe, P. M. W. Gill, B. Johnson, W. Chen, M. W. Wong, C. Gonzalez and J. A. Pople, *Gaussian 03*, Gaussian, Inc., Wallingford CT, USA, 2004.

46 (*a*) H. L. Schmider and A. D. Becke, *J. Chem. Phys.*, 1998, **108**, 9624; (*b*) J. P. Perdew, *Phys. Rev. B: Condens. Matter*, 1986, **33**, 8822.

47 (*a*) W. J. Hehre, R. Ditchfield and J. A. Pople, *J. Chem. Phys.*, 1972, **56**, 2257; (*b*) P. C. Hariharan and J. A. Pople, *Theor. Chim. Acta*, 1973, **28**, 213.

48 (*a*) A. Bergner, M. Dolg, W. Kuechle, H. Stoll and H. Preuss, *Mol. Phys.*, 1993, **80**, 1431; (*b*) M. Kaupp, P.v.R. Schleyer, H. Stoll and H. Preuss, *J. Chem. Phys.*, 1991, **94**, 1360; (*c*) M. Dolg, H. Stoll, H. Preuss and R. M. Pitzer, *J. Phys. Chem.*, 1993, **97**, 5852.

49 C. F. Macrae, I. J. Bruno, J. A. Chisholm, P. R. Edgington, P. McCabe, E. Pidcock, L. Rodriguez-Monge, R. Taylor, J. van de Streek and P. A. Wood, *J. Appl. Crystallogr.*, 2008, **41**, 466.

50 P. Flükiger, H. L. Lüthi, S. Portmann, J. Weber, *MOLEKEL 4.3*, Swiss Center for Scientific Computing, Manno, Switzerland, 2002.

Metallacarboranes

DOI: 10.1002/anie.201001555

Room-Temperature C–C Bond Cleavage of an Arene by a Metallacarborane**

David Ellis, David McKay, Stuart A. Macgregor, Georgina M. Rosair, and Alan J. Welch**

The activation and cleavage of C–C bonds by transition-metal species is an area of intense current interest,[1] and, although they are still relatively rare, a number of systems that afford the breaking of C–C single bonds are known.[2–4] In contrast, the cleavage of aromatic C–C bonds is considered to be extraordinarily difficult. Six-carbon aromatic rings can be cleaved in the gas phase at high temperatures,[5] whereas under less extreme conditions such rings are cleaved by enzymes, an important part of the global carbon cycle.[6] However, there are very few reports of low-temperature cleavage reactions of aromatic rings in nonbiological systems. Of the examples that are known, (biomimetic) oxidative cleavage is the more common process but is generally regarded as difficult to control,[7] whereas reductive cleavage is much more rare.[8] However, both oxidative and reductive cleavage reactions typically involve significant initial chemical modification of the aromatic ring. Sattler and Parkin recently described the cleavage of a C–C bond in an aromatic heterocycle (a quinoxaline) at 90 °C.[9] We report herein the unprecedented cleavage of an aromatic C–C bond in a simple arene at room temperature by a metallacarborane without other chemical modification to the arene.

Treatment of 1,1′-bis(*o*-carborane),[10–11] 1-(1′,2′-*closo*-$C_2B_{10}H_{11}$)-2-*closo*-$C_2B_{10}H_{11}$ (Figure 1), with an excess of Li in THF in the presence of naphthalene and subsequent reaction with $[\{Ru(p\text{-cymene})Cl_2\}_2]$ (*p*-cymene = 1-*i*Pr,4-MeC_6H_4), affords the dark red metallacarborane 1-(1′,2′-*closo*-$C_2B_{10}H_{11}$)-4-{$C_{10}H_{14}$Ru(*p*-cymene)}-4,1,6-*closo*-$RuC_2B_{10}H_{11}$ as the only isolable product (in ca. 20% yield) after workup (involves TLC methods). The product was characterized by mass spectroscopy, ^{1}H and ^{11}B{^{1}H} NMR spectroscopy, and ultimately by single-crystal X-ray diffraction.[12]

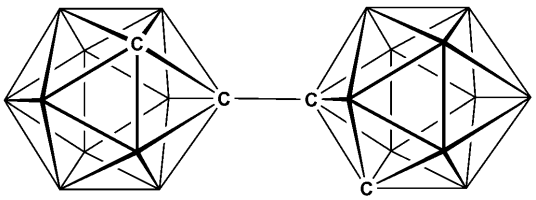

Figure 1. 1,1′-bis(*o*-carborane).

In the ^{1}H spectrum there are, in addition to broad $C_{cage}H$ resonances at approximately $\delta = 4.7$ and 2.2 ppm, the normal resonances assigned to the $CH_3C_6H_4CHMe_2$ protons of a η^6-*p*-cymene ligand in an asymmetric complex (four dd between $\delta = 6.5$ and 5.5 ppm with ^3J and ^4J couplings of ca. 6 Hz and 1.5 Hz, respectively). However, the signals normally assigned to the $CH_3C_6H_4CHMe_2$, $CH_3C_6H_4CHMe_2$, and $CH_3C_6H_4CHMe_2$ protons all appear doubled. In addition there are two high-frequency doublet resonances ($\delta = 9.6$, 9.4 ppm) and two additional resonances ($\delta = 4.5$, 4.1 ppm) which appear as apparent triplets. Collectively these data suggest that there are two different $C_{10}H_{14}$ units in the product; one is a regular η^6-*p*-cymene ligand but the other appears to have been subjected to a major structural change. The ^{11}B{^{1}H} spectrum is relatively uninformative with nine resonances between $\delta = 6$ and -25 ppm, including a multiple signal at $\delta = -10.6$ ppm that accounts for ten boron atoms. The mass spectrum confirms the molecular formula as $C_{25}H_{50}B_{20}Ru_2$ (envelope centered on *m*/*z* 757) which implies bis(carborane) plus two $\{RuC_{10}H_{14}\}$ units, but, as is evident from the NMR spectra, the molecule is asymmetric and one of the *p*-cymene ligands has been substantially altered. A crystallographic study resulted in the molecular structure shown in Figure 2. Figure 3 shows an alternative view of the central part of the molecule.

The molecule consists of a 13-vertex docosahedral ruthenacarborane (cage A) with a 4,1,6-RuC_2B_{10} architecture, the

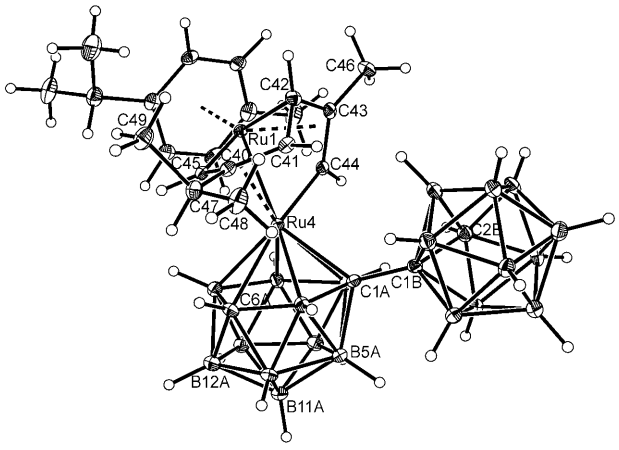

Figure 2. Perspective view of 1-(1′,2′-*closo*-$C_2B_{10}H_{11}$)-4-{$C_{10}H_{14}$Ru(*p*-cymene)}-4,1,6-*closo*-$RuC_2B_{10}H_{11}$. Thermal ellipsoids drawn at 50% probability.

[*] Dr. D. Ellis, D. McKay, Prof. S. A. Macgregor, Dr. G. M. Rosair, Prof. A. J. Welch
Department of Chemistry, Heriot-Watt University
Edinburgh EH14 4AS (UK)
Fax: (+44) 131-451-3217
E-mail: s.a.macgregor@hw.ac.uk
a.j.welch@hw.ac.uk

[**] We thank the EPSRC for support (project EP/E02971X/1).
Supporting information for this article is available on the WWW under http://dx.doi.org/10.1002/anie.201001555.

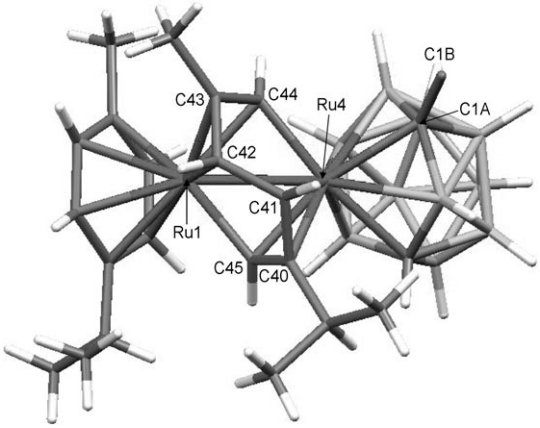

Figure 3. Alternative view of part of 1-(1′,2′-*closo*-$C_2B_{10}H_{11}$)-4-{$C_{10}H_{14}$Ru-(*p*-cymene)}-4,1,6-*closo*-$RuC_2B_{10}H_{11}$).

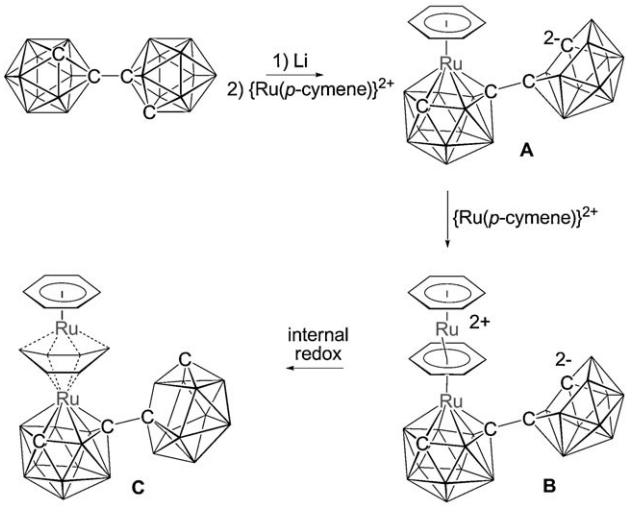

Figure 4. Proposed mechanism for the formation of intermediate **C** (the alkyl groups of the *p*-cumene ligand were disregarded in the calculation).

normal isomer obtained upon reduction and metallation of *o*-carborane.[13] Carborane cage B has not been expanded and remains a 1,2-C_2B_{10} icosahedron, connected to cage A at vertex C1A. A second Ru atom, Ru1, is bonded to Ru4 [Ru-Ru = 2.6984(4) Å] and to Ru1 is bound a conventional η^6-*p*-cymene ligand. Ru4 and Ru1 are additionally linked by (what was) the second *p*-cymene ligand, which has undergone cleavage of the C44–C45 bond. The C41-C40-C45 unit is η^3 bonded to Ru4 and the C42-C43-C44 unit is η^3 bonded to Ru1, complemented by σ bonds between C42 and Ru1 and between C44 and Ru4.

Therefore, the molecule is an example of a "fly-over bridge" compound,[14] in which the *p*-cymene ligand C40–C46 has been converted into a $[\mu\text{-}\sigma,\eta^3\text{:}\eta^3,\sigma\text{-}C_6]^{2-}$ ligand by reductive cleavage of the C44–C45 bond. Fly-over bridge compounds are well-established in organometallic chemistry, but all previously reported examples have been the result of condensation of three alkyne molecules onto a dimetal center. Upon heating, or treatment with Br_2[15] or trimethylamine-*N*-oxide,[16] fly-over bridge compounds can afford arenes by oxidative ring closure, lending support to the view that fly-over compounds represent intermediates in the metal-promoted cyclotrimerization of alkynes into arenes, at least by one possible pathway. However, as far as we are aware, the present species represents the first example of a fly-over bridge compound formed in the reverse direction, that is, from an arene.

The mechanism by which this compound is formed is clearly of great interest and we have investigated this using density functional theory (DFT) calculations (with the *p*-cymene ligand replaced by benzene for computational expedience).[17] The components of the molecule can be assembled as depicted in Figure 4. Initial four-electron reduction of 1,1′-bis(*o*-carborane)[18] gives a bis(nido) species, one face of which is capped by a $\{Ru(C_6H_6)\}^{2+}$ fragment to give intermediate **A**. The second $\{Ru(C_6H_6)\}^{2+}$ unit is then added, resulting in the formally zwitterionic triple-decker intermediate **B**. Calculations on plausible model structures of **B**, however, led instead to an alternative form, **C**. The geometry of **C** suggests that an internal redox process had occurred, whereby two electrons have been transferred from the pendant nido cage in **B** into the central C_6H_6 ligand. Evidence for this transfer is 1) the geometry of the pendant cage B exhibits a basket-shaped structure, which is the initial (kinetic) consequence of two-electron oxidation of a *nido*-C_2B_{10} cage,[19] and 2) the boat-like structure of the sandwiched $\{C_6H_6\}$ moiety, consistent with its reduction and the disruption of its aromaticity (Figure 5).

The central $\{C_6H_6\}$ moiety in **C** interacts with both Ru centers, although in different ways (see Figure 5 for a view of the DFT optimized structure of **C** and Figure 6 which shows the central $\{RuC_6H_6Ru\}$ core). With Ru1 an η^4-binding mode is computed involving the C41-C40-C45-C44 unit, whereas with Ru4 an $\eta^2\text{:}\eta^2$ interaction is seen with the C42–C43 and C40–C45 bonds. As a result most of the ring C–C bonds lengthen substantially and lie in the range 1.47–1.52 Å (only C42–C43 is relatively unaffected at 1.41 Å). Elongation of C44–C45 then allowed the location of a C–C bond-cleavage transition state, TS(**C**–**D**) ($E = +21.3$ kcal mol^{-1}), in which lengthening of the C44–C45 distance to 2.77 Å is accompanied by rotation about the C41–C42 bond [the C40-C41-C42-C43 torsion is 46.6° in **C**; compared to 89.8° in TS(**C**–**D**)]. Characterization of this transition state led to intermediate **D** ($E = -4.0$ kcal mol^{-1}) in which both the $\{\mu\text{-}\sigma,\eta^3\text{:}\eta^3,\sigma\text{-}C_6\}$ binding mode and a Ru–Ru bond (Ru1-Ru4 = 2.76 Å) have been established. Electron counting suggests the Ru–Ru interaction is best formulated as a dative bond in which Ru1 donates two electrons to Ru4.

The second step in the formation of the product involves isomerization of the C_2B_{10} group of cage B from a basket to an icosahedral geometry. This isomerization occurs in an analogous fashion to that described previously[19] via TS(**D**–**E**) with a barrier of only 10.7 kcal mol^{-1}. During this process the $\{RuC_6H_6Ru\}$ core is largely a spectator and the only significant change is a slight lengthening of the Ru1–Ru4 distance to 2.85 Å. TS(**D**–**E**) leads to the very stable product species **E** ($E = -42.0$ kcal mol^{-1}). **E** is a simple isomer of the crystallographically determined structure in which the fly-

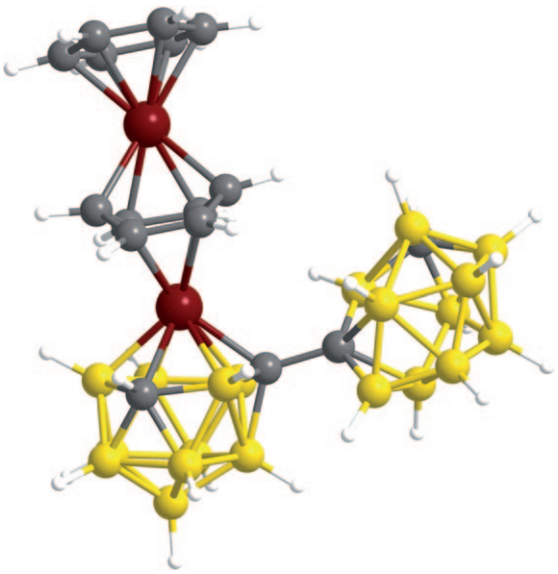

Figure 5. Computed structure of intermediate **C**. C gray, B yellow, Ru red, H white.

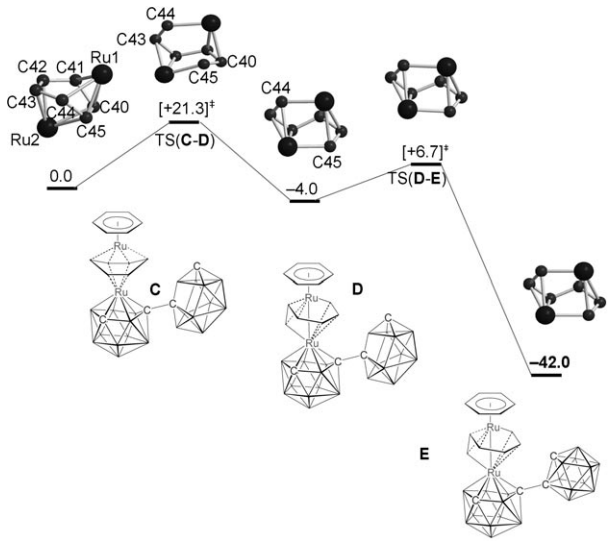

Figure 6. Computed reaction profile (kcal mol^{-1}) for C–C bond cleavage in intermediate **C** to form a fly-over bridge compound. Geometry changes within the central {RuC_6H_6Ru} core are shown at the top of the figure.

over bridging ligand adopts an alternative conformation (the computed energy of the actual structure is −56.1 kcal mol^{-1}), but nevertheless this computational study identifies the key features of the probable mechanism of cleavage of the C44–C45 bond and reveals that the energy barriers for this mechanism are modest.

In conclusion, we have discovered a unique system in which an aromatic C–C bond in a simple arene is reductively cleaved at room temperature with no other chemical modification, and we have used DFT calculations to elucidate an accessible reaction pathway by which this could occur. Central to the cleavage is an internal redox step in which the pendant reduced carborane is oxidized and transfers two electrons to the central arene of a triple decker intermediate. We are currently exploring the scope and implications of this reaction.

Received: March 15, 2010
Published online: June 10, 2010

Keywords: boron · metallaboranes · redox chemistry · ruthenium · X-ray diffraction

[1] C.-H Jun, *Chem. Soc. Rev.* **2004**, *33*, 610–618.
[2] B. Rybtchinski, D. Milstein, *Angew. Chem.* **1999**, *111*, 918–932; *Angew. Chem. Int. Ed.* **1999**, *38*, 870–883.
[3] M. Albrecht, G. van Koten, *Angew. Chem.* **2001**, *113*, 3866–3898; *Angew. Chem. Int. Ed.* **2001**, *40*, 3750–3781.
[4] M. E. van der Boom, D. Milstein, *Chem. Rev.* **2003**, *103*, 1759–1792.
[5] eg. R. M. Pope, S. L. VanOrden, B. T. Cooper, S. W. Buckner, *Organometallics* **1992**, *11*, 2001–2003.
[6] eg. T. D. H. Bugg, C. J Winfield, *Nat. Prod. Rep.* **1998**, *15*, 513–530.
[7] eg. Y. Yoshida, K. Mohri, K. Isobe, T. Itoh, K. Yamamoto, *J. Org. Chem.* **2009**, *74*, 6010–6015.
[8] eg. C. Krempner, H. Reinke, R. Wustrack, *Inorg. Chem. Commun.* **2007**, *10*, 239–242.
[9] A. Sattler, G. Parkin, *Nature* **2010**, *463*, 523–526.
[10] J. A. Dupont, M. F. Hawthorne, *J. Am. Chem. Soc.* **1964**, *86*, 1643.
[11] S. Ren, Z. Xie, *Organometallics* **2008**, *27*, 5167–5168.
[12] Crystallography: a crystal was mounted in inert oil on a glass fiber and cooled to 100(2) K on a Bruker X8 APEX2 diffractometer equipped with $Mo_{K\alpha}$ *X*-radiation. Intensity data were corrected for absorption semi-empirically and structures solved by direct and difference-Fourier methods. Cage C atoms C6A and C2B were unambiguously identified on the basis of refined (as B) U_{eq} values and interatomic distances. Refinement[20] was by full-matrix least-squares analysis on F^2. Crystal data for **1**: $C_{24}H_{50}B_{20}Ru_2{\cdot}2\,CH_2Cl_2$, $M = 926.83$, orthorhombic, $P2_12_12_1$, $a = 9.9886(10)$, $b = 19.6115(19)$, $c = 21.631(2)$ Å, $V = 4237.3(7)$ Å^3, $Z = 4$, $\rho_{cald} = 1.453$ Mg m^{-3}, $\mu = 0.987$ mm^{-1}, $F(000) = 1864$. 12759 out of 90211 independent reflections collected to $\theta_{max} = 30.60°$ ($R_{int} = 0.0574$), $R_1 = 0.0308$, $wR_2 = 0.0631$ for data with $I > 2\sigma(I)$, $S = 1.119$, Flack parameter 0.00(13), largest peak 0.62 and deepest hole −0.77 e Å^{-3}. CCDC 769687 (**1**) contains the supplementary crystallographic data for this paper. These data can be obtained free of charge from The Cambridge Crystallographic Data Centre via www.ccdc.cam.ac.uk/data_request/cif.
[13] M. R. Churchill, B. G. DeBoer, *J. Chem. Soc. Chem. Commun.* **1972**, 1326–1327.
[14] O. S. Mills, G. Robinson, *Proc. Chem. Soc.* **1964**, 187.
[15] U Krüerke, W. Hübel, *Chem. Ber.* **1961**, *94*, 2829–2856.
[16] R. J. Baxter, G. R. Knox, J. H. Moir, P. L. Pauson, M. D. Spicer, *Organometallics* **1999**, *18* 206–214.
[17] Calculations were run with Gaussian 03 and employed the BP86 functional and 6-31G** basis sets for B, C, and H and the Stuttgart-Dresden pseudopotentials and associated basis set for Ru. See the Supporting Information for details.
[18] T. D. Getman, C. B. Knobler, M. F. Hawthorne, *Inorg. Chem.* **1992**, *31*, 101–105.
[19] B. W. Hutton, F. MacIntosh, D. Ellis, F. Herisse, S. A. Macgregor, D. McKay, V. Petrie-Armstrong, G. M. Rosair, D. S. Perekalin, H. Tricas, A. J. Welch, *Chem. Commun.* **2008**, 5345–5347.
[20] G. M. Sheldrick, SHELXTL version 6.10, Bruker AXS Inc., Madison, Wisconsin, **2000**.

